OXFORD SERIES ON NEUTRON SCATTERING IN CONDENSED MATTER • 15

Applications of Neutron Powder Diffraction

ERICH H. KISI AND
CHRISTOPHER J. HOWARD

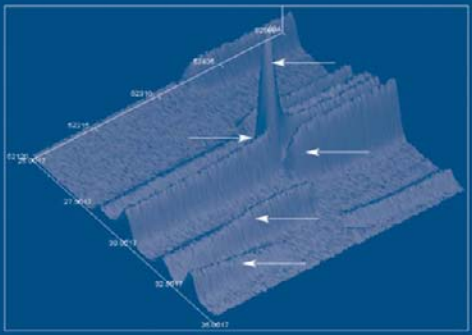

OXFORD SCIENCE PUBLICATIONS

APPLICATIONS OF NEUTRON POWDER DIFFRACTION

OXFORD SERIES ON NEUTRON SCATTERING IN CONDENSED MATTER

1. W.G. Williams: *Polarized neutrons*
2. E. Balcar and S.W. Lovesey: *Theory of magnetic neutron and photon scattering*
3. V.F. Sears: *Neutron optics*
4. M.F. Collins: *Magnetic critical scattering*
5. V.K. Ignatovich: *The physics of ultracold neutrons*
6. Yu. A. Alexandrov: *Fundamental properties of the neutron*
7. P.A. Egelstaff: *An introduction to the liquid state*
8. J.S. Higgins and H.C. Benoît: *Polymers and neutron scattering*
9. H. Glyde: *Excitations in liquid and solid helium*
10. V. Balucani and M. Zoppi: *Dynamics of the liquid state*
11. T.J. Hicks: *Magnetism in disorder*
12. H. Rauch and S. Werner: *Neutron interferometry*
13. R. Hempelmann: *Quasielastic neutron scattering and solid state diffusion*
14. D.A. Kean and V.M. Nield: *Diffuse neutron scattering from crystalline materials*
15. E.H. Kisi and C.J. Howard: *Applications of neutron powder diffraction*

APPLICATIONS OF NEUTRON POWDER DIFFRACTION

Erich H. Kisi
School of Engineering, The University of Newcastle, Australia

Christopher J. Howard
School of Engineering, The University of Newcastle, Australia

OXFORD
UNIVERSITY PRESS

OXFORD
UNIVERSITY PRESS
Great Clarendon Street, Oxford OX2 6DP

Oxford University Press is a department of the University of Oxford.
It furthers the University's objective of excellence in research, scholarship,
and education by publishing worldwide in

Oxford New York

Auckland Cape Town Dar es Salaam Hong Kong Karachi
Kuala Lumpur Madrid Melbourne Mexico City Nairobi
New Delhi Shanghai Taipei Toronto

With offices in

Argentina Austria Brazil Chile Czech Republic France Greece
Guatemala Hungary Italy Japan Poland Portugal Singapore
South Korea Switzerland Thailand Turkey Ukraine Vietnam

Oxford is a registered trade mark of Oxford University Press
in the UK and in certain other countries

Published in the United States
by Oxford University Press Inc., New York

© Oxford University Press 2008

The moral rights of the authors have been asserted
Database right Oxford University Press (maker)

First Published 2008

All rights reserved. No part of this publication may be reproduced,
stored in a retrieval system, or transmitted, in any form or by any means,
without the prior permission in writing of Oxford University Press,
or as expressly permitted by law, or under terms agreed with the appropriate
reprographics rights organization. Enquiries concerning reproduction
outside the scope of the above should be sent to the Rights Department,
Oxford University Press, at the address above

You must not circulate this book in any other binding or cover
and you must impose the same condition on any acquirer

British Library Cataloguing in Publication Data
Data available

Library of Congress Cataloging in Publication Data
Data available

Typeset by Newgen Imaging Systems (P) Ltd., Chennai, India
Printed in Great Britain
on acid-free paper by
Biddles Ltd., www.biddles.co.uk

ISBN 978–0–19–851594–4

1 3 5 7 9 10 8 6 4 2

Contents

Preface **ix**

Acknowledgements **xi**

Image Acknowledgements **xii**

Glossary of symbols **xiii**

1 Introduction to neutron powder diffraction **1**
1.1 What is neutron powder diffraction? 1
1.2 The role of neutron powder diffraction 2
1.3 Milestones in the development of neutron powder diffraction 3

2 Theory – the bare essentials **18**
2.1 Neutrons for diffraction 18
2.2 Samples for diffraction – the structure of condensed matter 20
2.3 Neutron scattering by the sample 39
2.4 The powder diffraction pattern 49

3 Basic instrumentation and experimental techniques **65**
3.1 Where to find neutron powder diffraction facilities 65
3.2 Constant wavelength neutron diffractometers 70
3.3 TOF neutron diffractometers 77
3.4 Comparison of CW and TOF diffractometers 80
3.5 Experiment design 80
3.6 Sample preparation 100

4 Elements of data analysis **106**
4.1 Preliminaries 106
4.2 Visual inspection 109
4.3 Phase identification 113
4.4 Unit cell parameters 118

4.5 Peak shapes and widths 124
4.6 Whole pattern fitting 131

5 Crystal structures 134
5.1 Neutron powder diffraction and crystal structures 134
5.2 More crystallography – description of crystal structures 135
5.3 Reflection conditions and space group determination 146
5.4 Solving structures 150
5.5 Structure refinement – the Rietveld method 155
5.6 Le Bail extraction 177
5.7 Practical considerations in structure refinement 178
5.8 Structure solution and refinement – examples 182

6 *Ab initio* structure solution 192
6.1 Introduction 192
6.2 Unit cell determination (powder pattern indexing) 193
6.3 Intensity extraction 205
6.4 Structure solution 212
6.5 Advanced refinement techniques 232
6.6 Looking ahead 249

7 Magnetic structures 251
7.1 Introduction 251
7.2 Crystallography and symmetry of magnetic structures 252
7.3 Magnetic scattering and diffraction 260
7.4 Solving magnetic structures 267
7.5 Recent examples 273

8 Quantitative phase analysis 284
8.1 Introduction 284
8.2 Theory 285
8.3 Individual peak methods 287
8.4 Whole pattern analysis 292
8.5 Evaluation of the techniques 293
8.6 Practical examples 294

9 Microstructural data from powder patterns 308
9.1 Introduction 308
9.2 Particle size 309
9.3 Microstrains 330
9.4 Combined size and strain broadening 340

9.5 Chemical and physical gradients 346
9.6 Line defects – dislocation broadening 358
9.7 Plane defects and stacking disorder 368
9.8 Texture 374

10 Diffuse scattering – thermal, short-range order, gaseous, liquid, and amorphous scattering 381
10.1 Introduction 381
10.2 Thermal diffuse scattering 382
10.3 Short-range order scattering 385
10.4 Scattering from gases, liquids, and amorphous solids 395

11 Stress and elastic constants 403
11.1 Stresses, strains, and elastic constants in nature and industry 403
11.2 Influence of elastic strains on the powder diffraction pattern 414
11.3 Neutron diffraction residual stress analysis 420
11.4 Determination of single crystal elastic constants from polycrystalline samples 438

12 New directions 443
12.1 Introduction 443
12.2 Neutron sources 443
12.3 Components 444
12.4 Diffractometers 446
12.5 Data analysis 449
12.6 New problems for study by neutron powder diffraction 453
12.7 Closing remarks 458

Appendix 1 459

Appendix 2 462

References 463

Index 481

This page intentionally left blank

Preface

Neutron powder diffraction patterns were recorded in 1945 at the Graphite Reactor, Oak Ridge, so it can be quite reasonably claimed that neutron powder diffraction is the longest established use of thermal neutrons in studies of condensed matter. Over the ensuing period, there has been continual development of instrumentation and methods for data analysis leading to an ever expanding range of applications. Nowadays, at major neutron sources, neutron powder diffraction is challenged only by small angle neutron scattering as regards the number of scientists who make use of it and its breadth of application. Its popularity may in part be due to a degree of familiarity because of similarities with the ubiquitous X-ray powder diffraction method, and in part that the relatively fast throughput on modern diffractometers means a large number of experiments can be accommodated. The real value of the technique, however, derives from its capacity to yield valuable information on the systems under study that is not readily accessible by other means. The technique is used extensively in physics, chemistry, crystallography, mineralogy, materials science, and engineering where good use is made of its complementarity with X-ray and electron diffraction.

Despite the long history, and perhaps because of the availability of texts on X-ray powder diffraction, there is as yet no single volume covering the theory, practicalities, and applications of neutron powder diffraction. This book is intended to fill this gap. Herein we have tried to synthesize the necessary material from many fields into a monograph that will support research utilizing neutron powder diffraction. As for all books that utilize crystallographic techniques, this book draws heavily on the foundations laid down in the X-ray diffraction literature as well as early works on neutron diffraction in general (e.g. Bacon 1975). However, we have attempted to make the coverage much broader to encapsulate the many areas in which neutron powder diffraction is being used. It therefore contains a synthesis of established techniques illustrated by example and some original work on the relation between displacement parameters and occupancies, on the use of group theoretical software in the solution of magnetic structures, on anisotropic particle size broadening, and on the analysis of peak shapes from samples containing gradients. We have also attempted to make the book relatively stand alone. It was our wish that a working knowledge of the field could be obtained from the book without extensive forays into the literature. As such, we begin with a very basic introduction to neutron diffraction by way of a summary of the basic strengths of the method and a discourse on its development over the last six decades (Chapter 1). This is followed by a brief outline of the types of structure to be encountered in a powder diffraction experiment, their description, and the theory underlying the

powder diffraction pattern (Chapter 2). Thereafter, the basic experimental methods (Chapter 3) and preliminary data analysis (Chapter 4) are treated. There follow chapters concerned with the various applications of neutron powder diffraction beginning with a bracket of chapters concerning structure analysis and solution. In Chapter 5, we explore crystallographic fundamentals and their application to crystal structure analysis. Chapter 6 expands into the realm of *ab initio* crystal structure solution and Chapter 7 deals with the investigation and solution of magnetic structures – a strength of neutron diffraction from its earliest beginnings due to the strong interaction between the atomic moments and the magnetic moment of the neutron. The following chapters stray outside the standard crystallographic mould beginning with Chapter 8 concerning the use of neutron powder diffraction for quantitative phase analysis – an area where it holds particular advantages over competing techniques due to an absence of microabsorption. Microstructural analysis is not a traditional strength of neutron diffraction due to historically low resolution; however, the rapid expansion in the availability of high-resolution diffractometers makes good estimates of microstructural parameters such as crystallite size, strain distribution, or even dislocation and stacking fault densities readily accessible (Chapter 9). In Chapter 10, we have explored the various kinds of diffuse scattering both from the perspective of obtaining better models for the background of powder patterns and with a view to investigating more poorly crystalline materials or materials containing poorly crystallized portions. From here we explore the reciprocal realms of residual stress analysis and elastic constant determination in Chapter 11. Here once again, neutron diffraction has particular advantages, this time due to the large penetration depth of neutrons in most practical materials. In the final chapter (Chapter 12), we have chosen to highlight advances that are more recent or which we feel have great potential to deliver a deeper understanding of the condensed states of matter.

The broad topic coverage and the depth to which we have covered the topics makes the book suitable for a broad audience. Even those hardy professionals who run neutron powder diffractometers at major neutron sources may find new insights inside. However, the major audience is that much larger number of scientists from varied fields who use or will want to use neutron powder diffraction in the course of their work. The book is primarily aimed at graduate students, postdoctoral staff, and senior researchers in science and engineering with an interest in the technique. With proper instruction, Chapters 1–5 and 8 and selected parts of Chapters 6, 7, 9, and 11 should be accessible to senior undergraduates. As with all books, the choice of subject matter and its treatment is somewhat idiosyncratic. Where possible, we have illustrated each topic or subtopic with examples. Usually, we have been able to bring our own experience to bear in the preparation and discussion of the examples (Chapters 2–6, 8, 9, 11, and 12). In others, we have had to rely to a greater extent on literature sources (Chapters 7 and 10) but hope we have done so adequately. We hope that the book serves as a useful adjunct to the library of anyone interested in the structure of condensed matter.

Acknowledgements

We are indebted to many people who have contributed to the existence of this book. We are thankful to Kevin Knight of the ISIS facility for sowing the seeds of the project, Prof. Steven Lovesey the series editor for accepting our proposal, and the commissioning editors at Oxford University Press for their continuing encouragement and assistance. Assistance with typing of the manuscript by Carol Watkins, Amanda Turner, and Katrina Gordon is gratefully acknowledged. Many thanks also to David Carr of ANSTO for his careful scrutiny of Chapter 11 and to friends and colleagues for their many words of encouragement over the years. A special thank you to Jennifer Forrester and Heather Goodshaw for their generous efforts in proof reading and correction in the closing stages of the writing. Naturally, the final and greatest thanks are to our long-suffering families, Katrina, Patrick, and Marnie K. and Sue, Andrew, and Alexandra H. to whom we owe our sanity.

Erich Kisi and Chris Howard,
Newcastle, December 2007.

Image Acknowledgements

The authors wish to thank the many publishers and individuals who granted permission to reproduce figures from cited sources. These include the American Physical Society (Fig. 1.2-1.9 and Fig. 7.10), Blackwell Publishing (Fig. 5.14, 5.15, 8.2, 8.7, 8.9, 11.5, 11.6 and 12.3), Cambridge University Press (Fig. 9.23), Prof. B.T.M. (Terry) Willis (Fig. 10.1), Dover Publications (Fig. 6.4, 9.18, 9.19, 9.32, 9.33, 10.4), Elsevier (Fig. 2.12, 7.11, 7.13, 7.14, 7.16-7.21, 8.10, 9.36 and 10.2), Institute of Materials Engineering Australia (Fig. 6.8), Institute of Physics London (Fig. 4.2, 4.3, 5.13, 9.5, 9.26), International Centre for Diffraction Data (Fig. 4.6), the International Union for Crystallography (Fig. 4.12, 5.12, 6.9, 9.29- 9.31, 9.40, 11.13, 12.1), John Wiley (Fig. 2.11a), Oxford University Press (Fig. 2.13, 2.15-2.17, 7.3-7.6, 7.8 and 11.1), Plenum Press (Fig. 7.1, 7.2), Royal Australian Chemical Institute (Fig. 8.3), Taylor and Francis (Fig. 11.11, 11.14 and 11.16), the American Chemical Society (Fig. 12.2), the Royal Society (Fig. 9.34 and 9.35) and Trans Tech Publications (Fig. 9.8 and 9.16). Figures 9.27 and 9.28 are from *VAN VLACK, L.H., ELEM MAT SCIENCE, 4th, © 1980*, reproduced by permission of Pearson Education, Inc, Upper Saddle River, New Jersey. Figures 2.24, 2.25, 11.4, 11.7 and 11.10 are from *CULLITY, B.D. ELEMENTS OF X-RAY DIFFRACTION, 2nd, © 1978*, reproduced by permission of Pearson Education, Inc, Upper Saddle River, New Jersey.

Glossary of symbols

$\hat{}$ over vector	denotes unit vector
A	attenuation factor
$\boldsymbol{a}^*, \boldsymbol{b}^*, \boldsymbol{c}^*$	reciprocal lattice translation vectors
$a^*, b^*, c^*, \alpha^*, \beta^*, \gamma^*$	parameters of reciprocal lattice cell
$\boldsymbol{a}, \boldsymbol{b}, \boldsymbol{c}$	lattice translation vectors
A, B, C, D, E, F	the constants in $1/d^2 = h^2A + k^2B + l^2C + klD + hlE + hkF$
$a, b, c, \alpha, \beta, \gamma$	lattice parameters
b	neutron nuclear scattering length; Burger's vector (Chapter 9)
$\bar{b}, b_{\text{coh}}$	mean scattering length, coherent scattering length
$B_{\text{iso}} = 8\pi^2 U_{\text{iso}}$	'B-factor'
C	number of constraints
c	speed of light
$d^* = 1/d$	interplanar spacing in reciprocal space
d_{hkl}	interplanar spacing, (hkl) planes
d^0_{hkl}	stress free spacing, (hkl) planes
D	mean crystallite diameter
D_0, D_1, D_{hkl}	direction-dependent crystallite diameters
$d\sigma/d\Omega$	differential scattering cross section
e	charge on the electron
E	neutron energy; activation energy; elastic modulus
f	magnetic form factor; X-ray form factor
$f(x), g(x), h(x) = f(x)*g(x)$	sample profile, instrument profile, observed profile
$F(\xi), G(\xi), H(\xi)$	Fourier transforms of $f(x), g(x), h(x)$
$F_{hkl}, F(hkl), F(\boldsymbol{h})$	structure factor for hkl diffraction peak
g	Landé splitting factor
$g(r)$	pair correlation function, radial distribution function
$g(r)_{A-B}$	partial pair-distribution functions
$G(\boldsymbol{r}, t)$	time-dependent correlation function

$G(t - t_k)$	normalized profile function (TOF)
$G(x)$	Gaussian profile function
$G(2\theta - 2\theta_k)$	normalized profile function (CW)
$GoF = R_{wp}/R_{\mathrm{exp}}$	Goodness of fit
H	full width at half maximum (FWHM)
h	Planck's constant; height of detector aperture
H_G, H_L, H_I	FWHM: Gaussian, Lorentzian, or instrument contributions
hkl	reflection indices
(hkl), $\{hkl\}$	a lattice plane, symmetry equivalent planes
$[HKL]$	a prominent vector of the reciprocal lattice
$\boldsymbol{H}_{hkl} = h\mathbf{a}^* + k\mathbf{b}^* + l\mathbf{c}^*$	reciprocal lattice vector normal to (hkl) planes
$I(SRO)$	short-range order scattering
I_1	intensity of first-order TDS
I_{hkl}, I_k	integrated intensity of hkl peak (kth peak)
I_k('obs')	Estimate of integrated intensity of the kth reflection derived from the y_{ik}('obs')
J	Multiplicity
$j(Q)$	short-range order scattering (normalized)
K	Scherrer constant
$\boldsymbol{k}$	wavevector; wavevector of scattered neutrons
$\boldsymbol{k}_0$	wavevector of incident neutrons
K_0, K_1	constants in a generalized Scherrer equation
k_B	Boltzmann's constant
L	Lorentz factor; length of neutron flight path (TOF)
$L(x)$	Lorentzian profile function
M	$B(\sin\theta/\lambda)^2$
m	neutron mass; mass of vibrating atom (Chapter 6)
M_{20}	figure of merit, based on first 20 observed peaks
m_e	mass of electron
M_p	mass of one formula unit, phase p
m_p	mass of phase p
n	n-fold rotation axes; number of atoms per unit cell; number of detectors in detector bank
N	number of observations; number of counts
N_{c}	number of cells per unit volume
$p = (e^2\gamma/2m_ec^2)gJf$	magnetic scattering length
P	number of parameters
$\boldsymbol{P}$	polarization vector (neutron); transformation matrix (Chapter 5)
$P(UVW)$	Patterson function, three-dimensional case

P_{hkl}	preferred orientation correction factor, at *hkl* reflection
$P_{HKL}(\phi)$	density of [*HKL*] poles at angle ϕ from a symmetry axis
$pV(x)$	pseudo-Voigt profile function
$\boldsymbol{q}$	magnetic interaction vector; location relative to a reciprocal lattice point (Chapters 9 and 10)
$Q = 4\pi \sin\theta/\lambda$	
$\boldsymbol{Q} = \boldsymbol{P}^{-1}$	inverse transformation matrix
r	distance of detector from sample
$\boldsymbol{r}, \boldsymbol{R}$	position vectors
R, R_{DS}	parameters in March function
r, θ, ϕ	spherical polar coordinates
$r_{\mathrm{AA}}, r_{\mathrm{BB}}$	interatomic distances for pairs of atoms
R_{exp}	expected profile *R*-factor
$R_G = \langle r^2 \rangle^{1/2}$	radius of gyration
r_i	distance of shell *i* from an atom at the origin
r_{mn}	distance between pair of atoms, m, n
$\boldsymbol{r}_n$	position vector, *n*th atom
R_p, R_{wp}, R_B	profile *R*-factor, weighted profile *R*-factor, Bragg *R*-factor
r_α, r_β	fractions of α, β sites occupied by *A*, *B* atoms, respectively
S	scale factor (Chapters 5 and 8); long-range order parameter (Chapters 2 and 10)
$\overline{S}$	sum of squared differences
$S(Q)$	'structure factor' for liquids
S, L, J	atomic spin, orbital, and total angular momentum quantum numbers
S_{A-B}	partial structure factors
S_p	scale factor for phase *p*
T	absolute temperature; overall temperature (displacement) factor
t_i	location of the *i*th step (TOF)
$T_j\ (\boldsymbol{\kappa})$	temperature factor, applying to scattering from *j*th atom
t_k	true position of *k*th peak (TOF)
$\boldsymbol{u}$	displacement from ideal atomic position (due e.g. to thermal vibration)
$\langle u^2 \rangle$	average mean square displacement
U, V, W	peak width parameters (CW)
$[uvw]$, $\langle uvw \rangle$	direction, symmetry equivalent directions

U_{eq}	equivalent isotropic displacement parameter (physical units)
U^{ij}	anisotropic displacement parameters (physical units)
U_{iso}	isotropic displacement parameter
V	sample volume
v	speed of neutron
$V(x)$	Voigt function
V_{c}	unit cell volume
V_p	unit cell volume, phase p
v_{s}	sound velocity
w_i	statistical weight at ith step
w_p	weight fraction of phase p
x	a variable, e.g. $x = 2\theta - 2\theta_k$ or $x = t - t_k$
x, y, z	Cartesian coordinates; atomic coordinates (fractional)
x_0, x_1	fractions of host and substituting elements
x_A, x_B	fractions of A, B atoms in binary system
$Y(2\theta)$	calculated diffraction profile
y_i	intensity (count) at ith step
y_{ib}	background contribution at ith step
y_{ic}, y_i(calc)	calculated count at ith step
y_{ik}('obs')	Estimate following Rietveld refinement of contribution of kth reflection to y_i(obs)
y_{obs}, y_i(obs)	observed count at ith step
y_α, y_β	fractions of α, β sites in binary system
Z_p	number of formula units per unit cell, phase p
α	angle between $\boldsymbol{\kappa}$ and $\boldsymbol{\mu}$ (Chapters 2 and 7); angle [hkl] makes with [HKL] (Chapters 5 and 11)
α, β	time constants describing rise and fall of neutron pulse
$\alpha_0, \alpha_1, \beta_0, \beta_1$	parameters determining above time constants
α_i	Cowley short-range order parameters
$\boldsymbol{\beta} = (\beta^{ij})$	anisotropic displacement parameters (dimensionless)
$\beta, \beta_G, \beta_I, \beta_S$	integral breadths
γ	neutron magnetic moment
$\varepsilon, \varepsilon_{hkl}$	strain, strain along [hkl]
η	Lorentzian fraction in pseudo-Voigt peak
θ	half the scattering angle
θ_{c}	critical angle for total external reflection
θ_{D}	Debye temperature

θ_k	Bragg angle, kth peak
$2\theta_i$	location of the ith step
$2\theta_k$	true position of kth peak (CW)
$\boldsymbol{\kappa} = \boldsymbol{k} - \boldsymbol{k}_0$	scattering vector
λ	neutron wavelength
μ	linear attenuation coefficient
$\boldsymbol{\mu}$	magnetic moment (atom)
μ/ρ	mass absorption coefficient
μ_B	Bohr magneton
μ_i, μ_{ai}, μ_{si}	linear attenuation coefficients for specific element i
μ_n	neutron magnetic moment
ν	Poisson's ratio
ρ	theoretical density
$\rho(r)$	density function
$\rho(x, y, z)$	scattering density
ρ'	actual density
$\rho'(x, y)$	projected scattering density
ρ_a	average density
$\rho_{A-B}(r)$	conditional probabilities
ρ_d	dislocation density
$\rho_j(\boldsymbol{u})$	scattering density (at jth atom)
σ	stress (Chapter 11); standard deviation; scattering cross section; peak width parameter (TOF)
σ^2	variance
σ_a	absorption cross section
$\sigma_{\text{coh}} = 4\pi b^2$	coherent scattering cross section
σ_{incoh}	incoherent scattering cross section
σ_{total}	total scattering cross section
Φ_0	incident neutron flux
χ^2	measure of goodness of fit
ψ	wave function
ω	vibrational frequency

This page intentionally left blank

1

Introduction to neutron powder diffraction

1.1 WHAT IS NEUTRON POWDER DIFFRACTION?

Neutrons are among the fundamental building blocks of atomic nuclei and are released by a variety of nuclear processes. They are produced in abundance by the fission of uranium in nuclear reactors. Alternatively, they may be produced by nuclear reactions such as the bombardment of beryllium by α-particles ($^{9}_{4}\mathrm{Be} + {}^{4}_{2}\mathrm{He} \rightarrow {}^{12}_{6}\mathrm{C} + {}^{1}_{0}\mathrm{n}$) or by spallation due to collisions of high-energy particles such as protons with a heavy metal target. The wave-particle duality in quantum mechanics means that neutrons have wave-like properties, including the ability to be diffracted by suitably spaced objects.

Of particular interest in condensed matter research are neutrons with wavelengths comparable to the radii of atoms ($\sim 1-2 \times 10^{-10}$ m). These so-called thermal neutrons are strongly diffracted by the ordered arrangements of atoms in crystals, in an analogous way to the well-known phenomenon of X-ray diffraction. Like its X-ray counterpart, neutron diffraction provides a wealth of information on the structure of the diffracting sample.

Powder diffraction is concerned with samples that are polycrystalline[1] or composed of many different crystals. As the name suggests they may be in the form of a powder but, especially in the materials sciences, are also commonly polycrystalline solids. There may be a number of phases present in different proportions, each with its own structure and microstructure. Each phase in the sample produces a characteristic diffraction pattern that can be used to study crystal structures, atomic substitutions, phase transformations, and chemical reactions. The relative intensities of the diffraction patterns, from individual crystalline phases in a multiphase sample, can be used to conduct quantitative phase analysis and shifts in the positions of diffraction peaks can be used to study strains due to either residual or externally applied stresses. Finally, subtle features of the diffraction pattern such as the shape and width of the diffraction peaks can, in favourable circumstances, provide microstructural detail such as particle size and shape, strain distributions, dislocation densities, and stacking fault or twinning models.

The fundamental scattering processes underpinning neutron diffraction are different from those in X-ray diffraction and so whilst the two techniques are in many

[1] Some non-crystalline matter may also be present (Chapter 10).

ways analogous, neutron and X-ray diffraction patterns obtained from a given sample differ substantially. In many ways, these differences serve to make the two techniques complementary; however, neutron powder diffraction has many advantages and can provide many types of information not readily obtained in other ways. The role of neutron powder diffraction in modern research is discussed briefly in §1.2. In §1.3, milestones in the development of neutron powder diffraction are used to introduce concepts and research areas that are expanded more fully in the succeeding chapters.

1.2 THE ROLE OF NEUTRON POWDER DIFFRACTION

Neutron powder diffraction is complementary to many other materials characterization techniques such as X-ray diffraction and electron microscopy. Because of this and the large capital costs associated with intense neutron sources, neutron diffraction is rarely the first technique used to study a particular material. More commonly, a range of samples have already been studied using other techniques and neutron diffraction is used in a highly specialized way to provide critical information or facilitate a critical *in situ* experiment. The complementarity between neutron diffraction and, for example, X-ray and electron diffraction arises primarily because the scattering process is quite different. The details of how and why they differ is a matter for Chapter 2. Here it is sufficient to list the differences as being:

(i) Nuclear scattering – scattering length not atomic number dependent.
  (a) Light element visibility is good.
  (b) Adjacent elements in the periodic table are often readily distinguished.
(ii) Nuclear scattering – isotopes have different scattering lengths.
  (a) Contrast matching in random structures.
  (b) Can detect different isotopic behaviour (e.g. hydrogen and deuterium).
(iii) Scattering is weak and absorption is usually low – high penetration depth.
  (a) Big samples are easily studied.
  (b) Complex sample environments are readily used.
  (c) Depth profiling in large samples is relatively easy.
  (d) Count rates and practical resolution limit are generally lower than for synchrotron X-ray sources.
(iv) Nuclear scattering – no form factor.
  (a) Good for studying phenomena requiring data over a large range of interplanar spacings (Q range), for example, isotropic, anisotropic, or even anharmonic displacement parameters.
(v) Magnetic scattering – magnetic structures.

All these differences apply to single crystal *and* powder diffraction. Why then the focus on powder diffraction? There is little doubt that single crystal techniques are superior for *ab initio* structure solution. However, a large majority of the materials of interest in physics, materials science, and many in solid state chemistry are not readily available in single crystal form. Many functional materials are intrinsically highly twinned (e.g. ferroelectrics) or deliberately multi-phase

(e.g. engineering alloys such as steels, partially stabilized zirconia ceramics, and composite materials). Such microstructurally complex materials often have properties quite different from those of the individual components and hence they form a system which should be studied as a whole. Herein lies the role of neutron powder diffraction. It is a technique that benefits from all of the advantages listed earlier, but can be used to study a wide range of real materials. Possibly of even greater importance, these materials can easily be studied in a wide variety of sample environments that simulate real service or synthesis conditions. The value of such *in situ* experiments cannot be overstated. They reveal, in a single measurement sequence, the phase evolution and kinetics against a variety of physical parameters such as temperature, pressure, electric field, magnetic field, and so on. Transient phases are readily studied as are a variety of microstructural parameters.

In addition to being complementary to X-ray diffraction, neutron powder diffraction is also often used in conjunction with other neutron scattering techniques. These include single crystal neutron diffraction in crystal structure and magnetic structure studies; small angle neutron scattering in microstructural studies; diffuse scattering in crystallization studies; and inelastic neutron scattering in the study of phase transformations and critical phenomena.

The unusual characteristics of neutron powder diffraction highlighted here have been used to good advantage in a very wide range of applications that will be explored in detail in the chapters that follow. In §1.3, we have prepared a summary of the development of neutron powder diffraction which we feel will be valuable for the researcher entering the field for the first time or even for old hands wishing to reappraise the development of the field.

1.3 MILESTONES IN THE DEVELOPMENT OF NEUTRON POWDER DIFFRACTION

Significant milestones in the development of neutron powder diffraction are shown on the timeline in Fig. 1.1. Instrumental developments are shown on the left of the timeline and scientific milestones on the right. The diffraction of neutrons was first demonstrated in 1936, by Mitchell and Powers and independently by von Halban and Preiswerk (1936), just 4 years after Chadwick's suggestion of the 'possible existence of a neutron'. This was time enough for it to be recognized (1) that a neutron would have wave characteristics, with wavelength given by the de Broglie relation:

$$\lambda = h/mv \tag{1.1}$$

where m and v are mass and speed of neutron, and h is the Planck's constant; (2) that neutrons from a radium/beryllium source could be slowed by collisions in a paraffin moderator to speeds giving wavelengths comparable with interatomic spacings in solids; and (3) that in consequence these 'thermal' neutrons could be diffracted by the regularly spaced atoms in crystalline solids. The diffraction of X-rays from crystalline solids was already well established. A schematic of the Mitchell and

1932
Discovery of the neutron (Chadwick)

1936
First diffraction of neutrons (Mitchell & Powers, von Halban & Preiswerk)
On the magnetic scattering of neutrons (Bloch)

1939
First BF_3 neutron detector (Korff & Danforth)

1939
Full theory of the magnetic scattering of neutrons (Halpern & Johnson)

1940
Measurement of neutron magnetic moment (Alvarez & Bloch)

1943
Graphite reactor goes critical at Oak Ridge

1946
Oak Ridge neutron powder diffractometer

1946–48
First diffraction patterns (Wollan & Shull)
Simple structures, NaCl, NaH, NaD
Some neutron scattering lengths determined
Isotopic substitution

1949
MnO shown to be antiferromagnetic (Shull & Smart)
Atomic ordering in FeCo alloy (Shull & Siegel)

1951
Polarised neutron beams (Shull)
Expanded table of neutron scattering lengths (Shull & Wollan)

1951–55
Hydrogen containing structures, e.g. ammonium halides (Goldschmidt & Hurst, Levy & Peterson), uranium deuteride UD_3
Cation distribution in spinels, e.g. $MgAl_2O_4$ (Bacon)
Magnetic structures – antiferromagnets, e.g. MnF_2 (Erickson); ferrimagnets, e.g. magnetite Fe_3O_4: ferromagnets, e.g. Fe, Co, Ni, Ni_3Fe
Magnetism in perovskites, $La_{1-x}Ca_xMnO_3$ (Wollan & Koehler)

1952
First use of ^{3}He filled proportional counter (Batchelor)

1956
DIDO reactor goes critical, Harwell (several reactors built to this design)

1956–67
Structure of $PbTiO_3$ (Shirane, Pepinsky & Frazer)
Atomic ordering in alloys – Ni_3Mn
Ferroelastic switching in $Cu_{0.15}Mn_{0.85}$
Magnetic structures – antiferromagnetic, spiral structure in Au_2Mn, "umbrella" arrangement of spins in antiferromagnetic CrSe, antiferromagnetic structures of haematite Fe_2O_3 and ilmenite $FeTiO_3$, rare earth iron perovskites, e.g. $ErFeO_3$
Atomic and magnetic ordering in Mn alloys, including Heusler alloys

1958
Optical analysis of neutron powder diffractometer (Caglioti, Paoletti & Ricci)

1962
Development of high pressure ^{3}He detector (Mills, Caldwell & Morgan)

1965
High Flux Beam Reactor (HFBR) at Brookhaven

1967
Rietveld method for structural refinement from powder data (Rietveld, 1967, 1969)

1968–69

Fig. 1.1 (Continues)

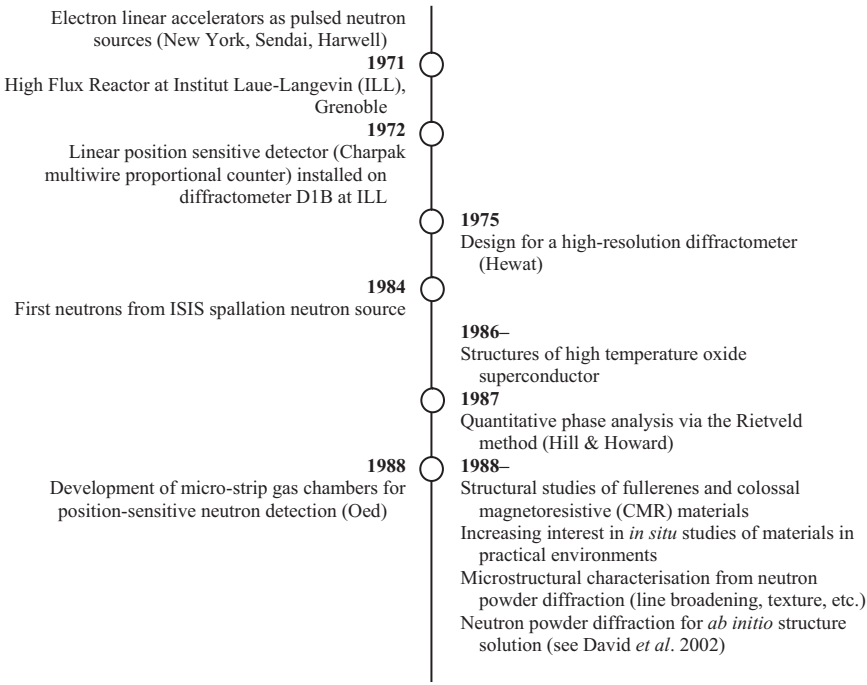

Fig. 1.1 Some key events in the development of neutron powder diffraction.

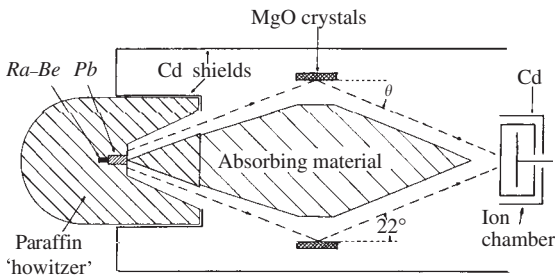

Fig. 1.2 Schematic diagram of the apparatus used to demonstrate the (wave-like) diffraction of neutrons (Mitchell and Powers 1936).

Powers experiment is reproduced in Fig. 1.2. Neutrons from the Ra/Be source, with an estimated wavelength of 1.6 Å after moderation, were directed towards the (100) face of an MgO single crystal, interplanar spacing $d = 4.2$ Å, at angle 22° for which the Bragg condition:

$$\lambda = 2d \sin\theta \tag{1.2}$$

would be satisfied. The number of neutrons reaching the detector was greatly enhanced when the Bragg condition was satisfied, as compared with when the crystal was rotated so it was not.

The prospect that a neutron might carry a magnetic moment also attracted interest around the same time. In a short insightful paper appearing in the same year, Bloch (1936) considered the consequences of a magnetic neutron, and outlined many of the applications of the magnetic scattering of neutrons pursued to the present day. A demonstration that the neutron carried a magnetic moment, based on the scattering from magnetized iron, was published in the following year. The next few years saw an impressive development of the theory of the magnetic scattering of neutrons, and the magnetic moment of the neutron was measured to good precision in 1940 (Alvarez and Bloch 1940).

The early demonstrations of neutron single crystal diffraction would have been of little practical value; the theory of magnetic scattering would have fallen into disuse; and the diffraction of neutrons from polycrystalline materials never observed were it not for the development of much more intense neutron sources. The first suitably intense neutron sources were nuclear reactors. Reactors utilize a self-sustaining chain reaction in which thermal neutrons cause the fission of ^{235}U nuclei accompanied by the release of several high-energy (MeV) neutrons and considerable energy. The neutrons are slowed to thermal energies by collisions in a moderator, and these thermal neutrons cause further fission. A self-sustaining chain reaction was first demonstrated in Chicago in December 1942. Driven by the weapons programme, and unfettered by regulatory requirements, the first full-scale nuclear reactor, the 'Clinton Pile', was commissioned at Oak Ridge in November 1943. Another reactor CP-3 commenced operation at Argonne (near Chicago) in 1944. The Clinton Pile operated at a power level of about 3.5 MW, and produced a thermal neutron flux density of about 10^{12} neutrons cm^{-2}s^{-1}. In 1966 the Clinton Pile was designated a 'historic landmark' (http://www.ornl.gov/graphite/graphite.html), and opened to the public.

The main wartime application of these reactors was the production of man-made elements and isotopes, including plutonium. Another application was in obtaining neutron scattering cross sections by measuring the transmission of nearly mono-energetic beams of neutrons. These beams were produced by diffraction from crystals. The wavelength (energy) is selected by varying the d-spacing and the angle of incidence θ (eqn (1.2)). After World War II, scientists were soon pursuing their scientific interests, so that by the early months of 1946 (according to Shull 1995), the first neutron powder diffraction patterns, from polycrystalline NaCl and from light and heavy water, had been recorded. Wollan and Shull (1948) published a selection of these early patterns, along with a schematic of the instrument used (reproduced in Fig. 1.3).

This early schematic provided a simple template of how neutron powder diffraction patterns could be recorded: a mono-energetic beam of neutrons produced from a single crystal of NaCl (the monochromating crystal) was directed onto the sample. The neutron detector was rotated around the sample so as to count scattered

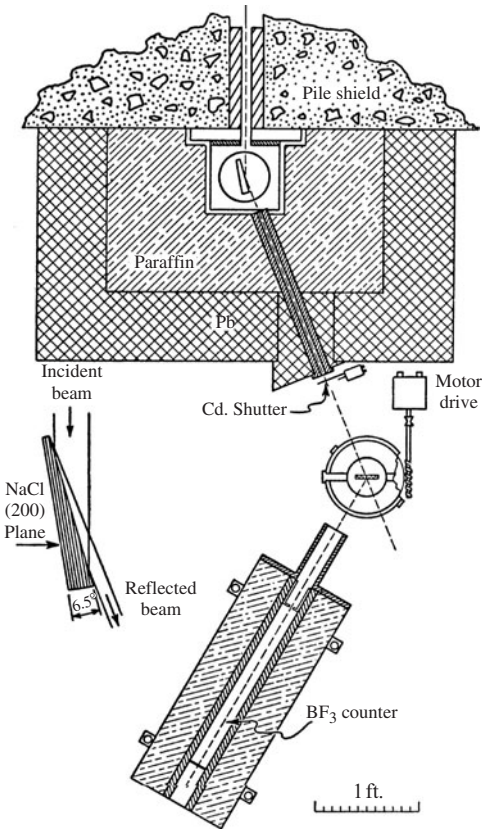

Fig. 1.3 The first neutron powder diffractometer used at the Oak Ridge National Laboratory in the 1940s (reproduced from Wollan and Shull 1948).

neutrons as a function of angle. In the 'transmission geometry' shown, the sample is positioned so that the sample normally bisects the angle between the incident and scattered neutron beam. A point to be noticed in the photograph (Fig. 1.4) is that the weight of the counter shielding, intended to keep stray neutrons out, is so great that cables are required for support. An early pattern, recorded from powdered diamond, is reproduced in Fig. 1.5.

An urgent task was to quantify the interaction of neutrons with various isotopes or elements. From the strength of this interaction and the pertinent atomic positions, diffracted intensities can be calculated. Neutrons interact with atoms via *either* the interaction of the neutron with the nucleus or the interaction of the magnetic moment of the neutron with magnetic moments on the atoms themselves. We focus for the moment on the nuclear scattering. Because the nucleus is so much smaller than the neutron wavelength, this nuclear scattering is as from a point and accordingly is isotropic. In most circumstances, the strength of this scattering can

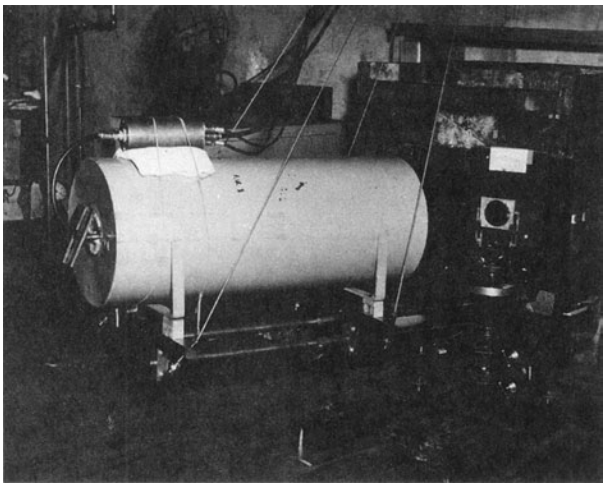

Fig. 1.4 Photograph of the earliest neutron powder diffractometer at Oak Ridge (reproduced from Shull 1995).

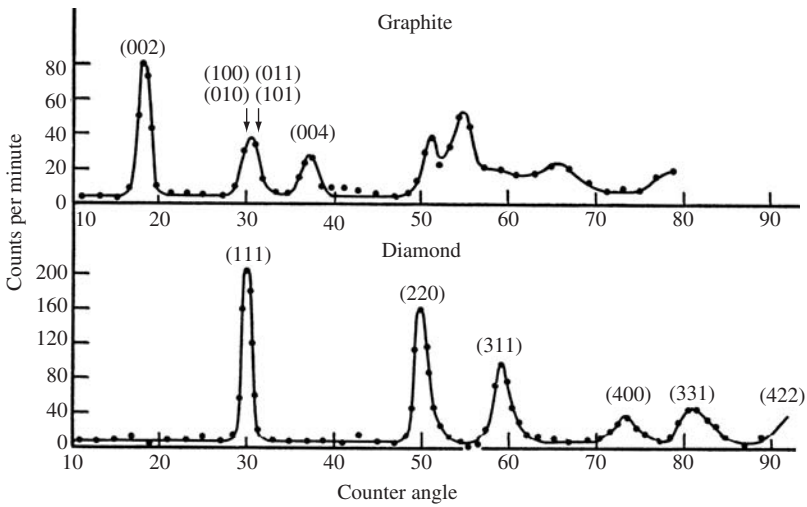

Fig. 1.5 Neutron powder diffraction patterns recorded from powdered graphite and diamond (reproduced from Wollan and Shull 1948).

be summarized in a single number, the coherent scattering amplitude or scattering length, b, though the scattering length does depend on the particular isotope involved[2] (see §2.3). Nuclear scattering lengths cannot be calculated theoretically,

[2] In the case of nuclei with non-zero spin, the scattering length also depends on whether the neutron spin is parallel or antiparallel to the nuclear spin.

so the task was to measure them. Elements comprising single isotopes with zero nuclear spin provided the starting point for this work, since for such elements the scattering is entirely coherent and the scattering cross-section is:

$$\sigma_{\text{total}} = \sigma_{\text{coh}} = 4\pi b^2 \tag{1.3}$$

So from relatively simple transmission measurements, scattering lengths can be derived. In the earliest studies (Wollan and Shull 1948), the absolute value of the scattering length for carbon obtained from powdered diamond (almost pure ^{12}C) was used as a reference. Some scattering lengths (e.g. for Al) were determined by comparing intensities in the diffraction patterns from these elements with those in the diffraction pattern from powdered diamond. Other scattering lengths were obtained by intensity measurements in diffraction patterns from simple compounds; from such measurements both scattering lengths and relative phases (e.g. negative scattering lengths for Li, Mn, and ^{1}H) were extracted. Results were cross-checked by reference to other zero-spin isotopically pure materials. By 1951, neutron diffraction patterns had been recorded from over 100 elements or compounds; scattering length data (amplitude and sign) had been tabulated for nearly 60 elements or separated nuclides (Shull and Wollan 1951); and the foundations for neutron powder diffraction were firmly established.

A number of interesting and significant problems were addressed in this early period. The most obvious applications involved favourable neutron scattering lengths, which were exploited to study systems not amenable to study by X-rays. The crystal structure of sodium hydride, NaH, was the first application of this kind (Shull *et al.* 1948). It was confirmed that, as suspected, NaH adopts the rock salt (NaCl) structure. At the same time scattering lengths and scattering cross sections for Na and H were determined. The rock salt structure is such that the intensities for the 111 and 200 reflections are proportional to $(b_{\text{Na}} - b_{\text{H/D}})^2$ and $(b_{\text{Na}} + b_{\text{H/D}})^2$, respectively[3] – the 111 reflection is thus weaker than the 200 reflection if the scattering lengths have the same signs and *vice versa* (Fig. 1.6). The conclusions are that b_{Na} and b_{D} have the same sign, taken to be positive, whereas b_{H} is negative.

The crystal structure of ammonium chloride, ND_4Cl, was another early application of this kind (Goldschmidt and Hurst 1951; Levy and Peterson 1952). Since hydrogen atoms are difficult to locate using X-rays (the X-ray scattering by its single electron being small), the solution of crystal structures of hydrogen-containing materials has represented an important application of neutron powder diffraction from the earliest history to the present day.

Neutron diffraction offers potential advantages not only when X-ray scattering is weak (the case just discussed) but also in distinguishing elements with very similar X-ray form factors. The elements Fe and Co with 26 and 27 electrons, respectively, are examples. The alloy FeCo is cubic, but depending on its preparation the elements may be randomly distributed (disordered) or regularly arranged

[3] This approximation ignores differences between the atoms in respect of their thermal vibrations.

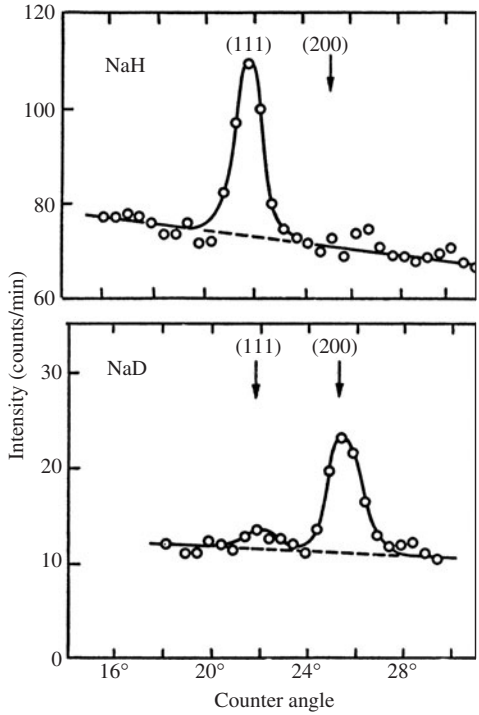

Fig. 1.6 Diffraction pattern from NaH illustrating the effect of opposite sign scattering lengths for Na and H (reproduced from Shull 1995).

such that each atom is surrounded by atoms of the other kind (ordered). The random and ordered arrangements could not be distinguished using X-ray diffraction, but were readily distinguished by Shull and Siegel (1949) from neutron diffraction. In fact this potential of neutrons for study of ordered and disordered alloys had been realized much earlier, in that Nix *et al.* (1940) attempted a neutron study of the FeNi system in the days before reactors, using a Ra/Be source.

The magnetic scattering of neutrons, mentioned earlier, led to other very important applications. The interaction is between the magnetic moment of the neutron and the atomic magnetic moments due to unpaired electrons. Since these are spread over dimensions comparable with the neutron wavelengths, an angle-dependent magnetic form factor results. The magnetic form factor can be calculated from theoretical electron densities, or determined experimentally. The magnetic interaction depends on the form factor, the *directions* of the neutron magnetic moment, the atomic magnetic moment, and the neutron trajectory.[4]

[4] This geometrical factor is important but not especially simple – it depends on a vector triple product – full details are presented in Chapters 2 and 8.

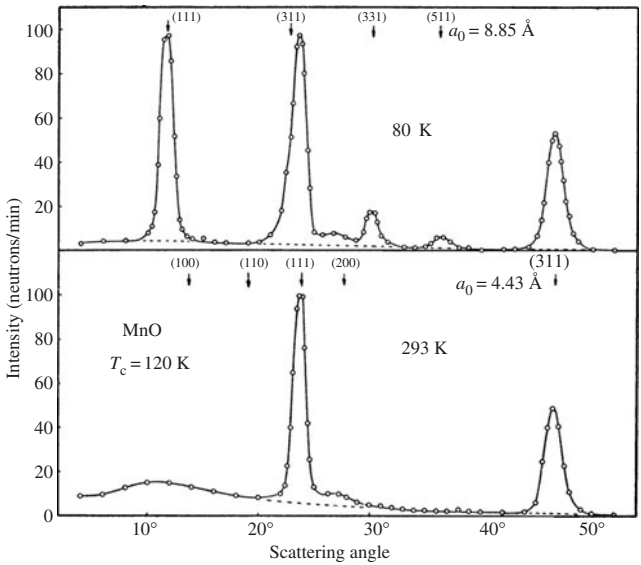

Fig. 1.7 Neutron powder diffraction patterns from MnO recorded above (293 K) and below (80 K) the Curie temperature (reproduced from Shull *et al.* 1951a).

The first and perhaps still most significant application of neutron powder diffraction to the magnetic interaction was the detection of antiferromagnetism and the elucidation of the magnetic structure of MnO (Shull and Smart 1949; Shull *et al.* 1951a). The Mn^{2+} ion has five unpaired electrons in $3d$ orbitals (spin $S = 5/2$) and a correspondingly large magnetic moment ($5\mu_B$). At room temperature, the atomic moments in paramagnetic MnO are randomly oriented and the magnetic scattering contributes only very broad features to the neutron diffraction pattern. The magnetic susceptibility and specific heat of MnO show anomalies in the vicinity of 120 K, yet no macroscopic magnetization develops, and X-rays had revealed no change in crystal structure (from the rock salt structure) at this temperature. The 120 K transition was thought to be the onset of an antiferromagnetic ordered arrangement of atomic moments, with as many moments aligned in one direction as in the opposite one. Such an arrangement leads to repeat distances in the magnetic structure larger than in the crystal structure, and thence to additional peaks in the neutron diffraction pattern. Neutron diffraction patterns recorded from MnO in its paramagnetic phase, at 293 K, and in its antiferromagnetic phase, at 80 K, are compared in Fig. 1.7. The additional peaks, corresponding to the larger repeat distances in the magnetic structure, and confirming the antiferromagnetic ordering, are seen to be strong.

The magnetic structure suggested by Shull *et al.* (1951a) is shown schematically in Fig. 1.8. A high-resolution low-temperature X-ray study revealed a very slight

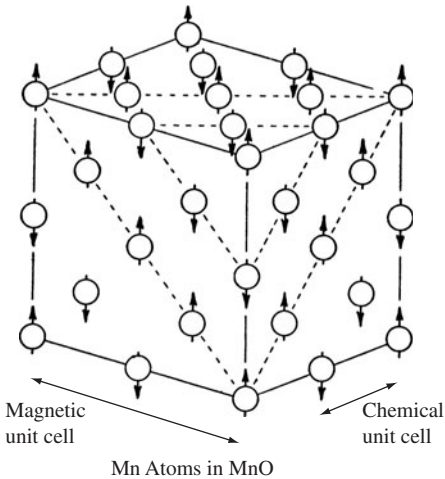

Fig. 1.8 Magnetic structure for MnO proposed by Shull, Strauser, and Wollan (reproduced from Shull *et al.* 1951a).

distortion from cubic symmetry in consequence of the magnetic ordering. Shull *et al.* (1951a) completed the first experimental determination of the magnetic form factor for the Mn^{2+} ion as part of the same study.

Though the important features of the Shull *et al.* structure are correct, a subsequent neutron study at sufficient resolution to reveal the rhombohedral distortion (Roth 1958) also revealed that the magnetic moments are aligned not along the cube edges (as indicated in Fig. 1.8) but in directions normal to the body diagonal. The magnetic structure of the tetragonal fluoride MnF_2, in its low-temperature antiferromagnetic phase, was another study in early times (Erickson 1953). In this case the conclusion that atomic moments are aligned parallel and antiparallel to the fourfold axis stands unchallenged to the present day.

Neutron powder diffraction was also used to determine magnetic structures involving ferromagnetic and ferrimagnetic ordering (Shull *et al.* 1951b). Ferromagnetic ordering (atomic magnetic moments in parallel alignment) in elements such as Fe and Co does not result in increased repeat distances, so the magnetic diffraction coincides with the nuclear diffraction peaks. The two can be distinguished, however, since magnetic scattering shows strong angular dependence whereas nuclear scattering is isotropic. More interesting perhaps was the application to the atomically ordered ferromagnetic alloy Ni_3Fe (Shull and Wilkinson 1955) – the magnetic contribution to the additional 'superlattice' peaks depends on $(\mu_{Ni} - \mu_{Fe})^2$, and from this quantity together with the mean atomic moment per atom $\left|\frac{3}{4}\mu_{Ni} + \frac{1}{4}\mu_{Fe}\right|$ determined from saturation magnetization, the two separate atomic moments were derived. Ferrimagnetic ordering (atomic magnetic moments aligned, some in one direction and some in the opposite direction, but resulting

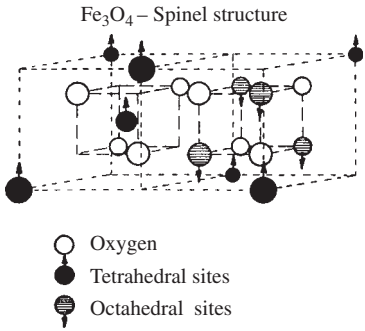

Fig. 1.9 Magnetic structure of Fe_3O_4 as determined by Shull *et al.* (1951b).

in net magnetization) does not necessarily lead to any additional reflections. The elucidation of the details of the ferrimagnetic ordering in α-Fe_2O_3 (haematite) and Fe_3O_4 (magnetite, see Fig. 1.9) was an impressive achievement of the early research.

Work on the atomic and magnetic arrangements in various ferrites, $MgFe_2O_4$, $ZnFe_2O_4$, and $NiFe_2O_4$ (Corliss *et al.* 1953; Hastings and Corliss 1953), was similarly impressive. In ferromagnetically or ferrimagnetically ordered materials, there is the possibility of aligning the atomic magnetic moments by applying a strong magnetic field. This leads in turn to the possibility of manipulating the geometrical factor (previously mentioned) so as to remove the magnetic contribution to the scattering from some or all of the magnetic species in the sample – a valuable aid in the solution of magnetic structures.

The neutron powder diffraction study of the magnetic properties of the perovskite-type compounds $La_{1-x}Ca_xMnO_3$ carried out by Wollan and Koehler (1955) at Oak Ridge represented something of a *tour de force*. The main mechanism for charge compensation in this system is the change from Mn^{3+} to Mn^{4+} as Ca^{2+} is substituted for La^{3+}. The study involved switching off the magnetic contributions from ferromagnetic ordering by applying a strong magnetic field (as indicated just earlier), while the antiferromagnetic contributions were switched off simply by raising the temperature. The study revealed a veritable zoo of low-temperature ferro- and antiferromagnetically ordered structures, and also provided some evidence, on the basis of their different magnetic contributions, of an ordered arrangement ('charge ordering') of the Mn^{3+} and Mn^{4+} ions. This work is still attracting interest (Millis 1998) because systems such as this based on $LaMnO_3$ exhibit the giant magneto-resistive effect, and 'charge ordering' has become a field of study in its own right.

The majority of early studies used the Oak Ridge neutron powder diffractometer (Wollan and Shull 1948), or instrumentation at the graphite reactors at Brookhaven (BGRR) or Harwell. Before long, more research reactors were built providing higher fluxes of thermal neutrons, so neutron diffraction became rather

more widely available. The multi-purpose Harwell DIDO reactor, commissioned in 1956, and at 26 MW power producing a thermal neutron flux density of about 2×10^{14} neutrons $cm^{-2}\,s^{-1}$, was an important new facility for neutron diffraction, and the prototype for a class of multi-purpose medium flux reactors at which significant programmes in neutron diffraction were established. The High Flux Beam Reactor (HFBR) commissioned at the Brookhaven Laboratory (USA) in 1965, providing a thermal neutron flux of 5×10^{14} neutrons $cm^{-2}\,s^{-1}$, was the first reactor built expressly for carrying out research using neutron beams. However, because of the increasing use of single crystal diffraction in crystallographic studies, along with a shift in emphasis to areas such as inelastic scattering, for a time neutron powder diffraction and its applications languished.

The renaissance of neutron powder diffraction can be traced to the development of computer power to support computer-based techniques for data analysis, most notably the Rietveld method (Rietveld 1967, 1969). Here the intensities of the diffraction peaks are calculated for a model crystal (and magnetic) structure; next these peaks are located at angles determined by neutron wavelength and lattice parameters; and finally the intensities distributed according to assumptions about widths and shapes of diffraction peaks and how these vary across the pattern. Parameters describing crystal structure, peak widths and shapes, background, and an overall scale are varied so as to obtain the best fit between the calculated pattern and that observed. The method was demonstrated by refinements of structures of tungsten trioxide (Rietveld 1967), and a selection of metal uranates (Loopstra and Rietveld 1969; Rietveld 1969). The method did not have immediate impact, but within a few years, it had been used successfully at Harwell by Hewat to study structural phase transitions in ferroelectrics (Hewat 1973), by Taylor and coworkers at Lucas Heights on uranium halides (Taylor *et al.* 1973; Taylor and Wilson 1974, 1975), and by Cheetham, Von Dreele, and others at Oxford in neutron studies of complex oxides (Von Dreele and Cheetham 1974; Anderson *et al.* 1975). A review published just 10 years after Rietveld's first paper listed some 170 structures that had been refined from neutron powder diffraction data by the Rietveld method (Cheetham and Taylor 1977). The focus in the early work was on crystal structure refinement (Chapter 5), that is, on extracting just those parameters that describe the crystal structure. It has been recognized subsequently that other parameters such as peak width, peak shape, scale factors, and peak positions also carry useful information (see Chapters 8, 9, and 11).

A second reactor intended for neutron beam research, the High Flux Reactor (HFR) at the Institut Laue-Langevin (ILL), Grenoble, was being constructed at about the same time as the potential of the Rietveld method was being recognized. The HFR at the ILL, operating at 58 MW power, produces a thermal neutron flux density of about 1.5×10^{15} neutrons $cm^{-2}\,s^{-1}$, and is still today the pre-eminent reactor-based centre for neutron beam research. These two developments, that is, the development of the Rietveld method and the construction of a new high-flux neutron source, were combined in the proposal by Hewat (1975) for a new generation high-resolution neutron powder diffractometer. The development of

the Rietveld method (and subsequently other computer-based methods for data analysis) made it possible to analyse patterns containing many overlapping peaks. The method would work better and allow larger structures to be solved using powder methods with patterns of higher resolution. Accordingly, Hewat (1975) designed a 'conventional' high-resolution powder diffractometer for installation at the HFR that would give resolution at the limits indicated by crystallite size broadening together with reasonable intensities. The high resolution would be achieved by using a high angle of incidence onto the monochromator crystal, θ_M, together with tight collimation of the primary and final diffracted beams. Intensity would be recovered from careful matching of the various horizontal divergences involved, by relaxing counter apertures to accept a considerable degree of vertical divergence, and by simultaneously recording data in a number (32 proposed) of detectors. Hewat claimed that the design should permit the refinement (by the Rietveld method) of nuclear and magnetic structures having unit cells of up to 3500 $Å^3$ volume. Hewat did not immediately secure a position for his diffractometer at the HFR reactor face, but instead constructed a diffractometer, D1A, with a bank of 11 detectors on a guide tube at the ILL (Hewat and Bailey 1976). Though the specifications of this diffractometer were less ambitious, its influence has been great; this because of the science it has supported (e.g. crystal structure of the 90 K superconductor, $YBa_2Cu_3O_7$, Capponi *et al.* 1987), as well as its role in encouraging the development of high-resolution neutron powder diffractometers elsewhere (e.g. on the HIFAR reactor at Lucas Heights – Howard *et al.* 1983). The high-resolution diffractometer, D2B, installed at the reactor face about 10 years later, and carrying 64 detectors, can be considered as the eventual implementation of the original Hewat design (Hewat 1986). Subsequent upgrades have included replacing individual detectors with 128 vertical position sensitive detectors to form the Super-D2B (see Chapter 12).

It was around the same time as the introduction of the Rietveld method that accelerator-based production of neutrons by spallation gained some acceptance (e.g. LINAC at Harwell – Moore and Kasper 1968; Windsor and Sinclair 1982). These developments culminated in a new kind of neutron source – the pulsed spallation neutron source pioneered by the KENS source in Tsukuba Japan (1980) followed closely by IPNS at Argonne, USA (1981) and ISIS at Didcot, UK (1984). In these sources, a proton beam is accelerated to high energy (typically 800 MeV) in a proton synchrotron and made incident on to a heavy metal target. Neutrons are spalled from the nuclei of the target. The protons are grouped in tightly bunched pulses which repeat at short time intervals (typically 50 Hz). Neutrons so generated are partially moderated before travelling down flight tubes to various diffractometers. Pulsed spallation sources usually use neutrons with a wide range of wavelengths (energies) directly and rely on the different velocities of the different wavelengths to conduct time-of-flight (TOF) analysis (Chapter 3). This development has been advantageous in a number of ways. First, since the resolution of a TOF instrument depends largely on the total length of the instrument, to access higher resolution *cet. par.* merely requires building a larger diffractometer whereas

for constant wavelength instruments, resolution is acquired by *reducing* the size of collimating apertures with associated difficulty and loss of intensity. Second, the TOF technique allows fixed geometry which is advantageous in the installation of a very large detector coverage and also in the use of ancillary equipment (no moving parts). This development process has culminated in the instrument HRPD at ISIS, currently the world's highest resolution neutron powder diffractometer.

A somewhat later though parallel development process has occurred for high-intensity neutron diffractometers capable of recording patterns very rapidly so that parametric studies of phase transitions and other transient phenomena can be conducted. This process began with the introduction of multi-wire position sensitive detectors (e.g. the 400 element detector on D1B at ILL, *c.* 1978) and has progressed to the TOF instrument GEM at ISIS with four steradians solid angle of detector coverage which can record several diffraction patterns per minute. The ultimate in rapid neutron powder diffraction was enabled by the invention of the microstrip detector (Oed 1988) and its implementation on the diffractometer D20 at ILL (Convert *et al.* 1997). This instrument (and its more recent Australian counterpart WOMBAT) can record patterns in a few hundred milliseconds in continuous mode or $<30\,\mu s$ in stroboscopic mode (Chapter 12).

In a major adjunct to the Rietveld refinement method, Hill and Howard (1987) devised a method for using the Rietveld refinement scale factors derived from multi-phase diffraction patterns to extract accurate, usually standardless, quantitative phase analyses from neutron powder diffraction data. This method, development in parallel for X-rays, (Bish and Howard 1988) has been widely adopted in the X-ray diffraction community and, despite several advantages over X-rays, only selectively adopted in the neutron diffraction community, primarily for analysing the results of time-resolved or *in situ* studies (Chapter 8).

Armed with the benefits of software, source, and instrumentation developments, there have been many examples of high impact studies using neutron powder diffraction. One of the most widely known applications is in solving the crystal structures of high-temperature oxide superconductors. The first successful determination of the crystal structure of the 90 K superconductor, $YBa_2Cu_3O_7$, stands as the most celebrated recent application of neutron powder diffraction. This application provides another illustration of the value of neutron diffraction in locating oxygen atoms in the presence of heavier elements. The discovery of superconductivity in $(La,Ba)_2CuO_4$, followed quickly by the discovery of the 90 K superconductor $YBa_2Cu_3O_7$, led to unprecedented interest in superconductivity, and intensely competitive efforts, largely with X-ray diffraction, to establish the crystal structure of the latter compound. The race to determine the structure was won by scientists using neutron powder diffraction because the relative neutron scattering length of oxygen is comparable to the scattering length of the metal ions. Since it was later discovered that the key to the superconductivity lies in the detailed electronic transitions within the partially occupied planes of oxygen ions, the detailed crystal structure was seminal. The publications arising from this work (Capponi *et al.* 1987; Jorgenson *et al.* 1987) are among the most highly

cited of any relying on neutron powder diffraction. Other high-profile applications have included work on the crystal structures of fullerenes (David *et al.* 1991, 1992) and in the study of colossal magnetoresistance or CMR materials (Mitchell *et al.* 1996).

The availability of higher resolution diffractometers has meant that the powder diffraction techniques developed for the study of microstructures using X-rays have been able to be adapted to neutron diffraction (Chapter 9). They have similarly enabled forays into the world of the *ab initio* solution of large crystal structures (Chapters 6 and 12). Similarly, the availability of very high-intensity powder diffractometers has encouraged a far greater number of *in situ* studies of materials in realistic simulated service environments or during actual synthesis.

In closing, we acknowledge that this overview has emphasized a relatively few large neutron sources and, for reasons of brevity, has overlooked many significant contributions made to neutron powder diffraction around the world at the smaller neutron sources.

2

Theory – the bare essentials

2.1 NEUTRONS FOR DIFFRACTION

In Chapter 1, it was noted that neutrons can exhibit wave-like properties, which can be used to advantage in the study of condensed matter. The properties of the neutron are summarized in Fig. 2.1.

It is apparent that key properties such as wavelength are dependent on the speed of the neutron and hence its energy. The relationship between the neutron velocity and wavelength is governed by the de Broglie equation:

$$\lambda = h/mv \tag{2.1}$$

where h is Planck's constant. Taking the conventional units (λ in Å and v in km s^{-1}) eqn (2.1) can be simplified to $\lambda = 3.956/v$. Neutron sources (discussed in more detail in Chapter 3) produce neutrons with a relatively wide spectrum of energies. For example, a typical reactor source produces a flux of neutrons with a Maxwellian distribution:

$$\phi(\lambda) \propto \frac{1}{\lambda^5}\exp\left(\frac{-h^2}{2mk_{\mathrm{B}}T\lambda^2}\right) \tag{2.2}$$

where $\phi(\lambda)$ is the neutron flux (neutrons per second) through a unit area with wavelengths in the range $\lambda-(\lambda+d\lambda)$; m is the neutron mass; k_{B} is Boltzman's constant; and T is the absolute temperature of the moderator with which the neutrons have come into thermal equilibrium by repeated inelastic collisions. It is apparent from eqn (2.2) that the wavelength distribution can be substantially modified by the use of a moderator at a different temperature. The core of a reactor source usually produces 'thermal' neutrons, that is, those moderated at the temperature of the reactor core moderator, $T \sim 300$ K. The influence of changing moderator temperature is shown in Fig. 2.2 for three commonly used configurations; a hot source at 2000 K, a thermal source at 330 K, and a cold source at 20 K. The peak of the Maxwellian (in Å) occurs at:

$$\lambda = \frac{h}{\sqrt{5mk_{\mathrm{B}}T}} \tag{2.3}$$

giving 0.446, 1.15, and 4.46 Å for the curves shown in Fig. 2.2. Neutrons for diffraction need to be optimized against several criteria. The interplanar spacings in most materials of interest are in the range 0.5–5 Å and so wavelengths in this

Properties of the neutron

Mass (m)	1.68×10^{-27} kg
Charge	0
Spin	1/2
Magnetic moment (μ_n)	−1.913 nuclear magneton
Wavelength (λ)	h/mv
Wavevector ($\boldsymbol{k}$)	magnitude $2\pi/\lambda$
Momentum ($\boldsymbol{p}$)	$\hbar\boldsymbol{k}$
Energy (E)	$1/2\ mv^2 = \dfrac{h^2}{2m\lambda^2}$

Fig. 2.1 Properties of the neutron.

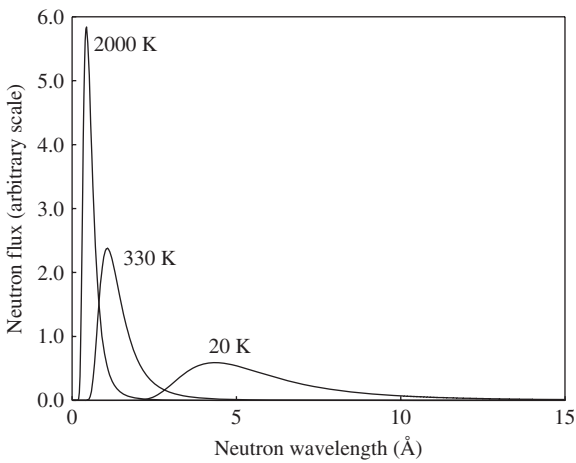

Fig. 2.2 The Maxwellian distribution of neutron wavelengths produced within moderators at different temperatures.

range are the most beneficial for keeping the diffraction pattern within certain physical constraints (e.g. Bragg cut-off – §3.2.1). The energy of such neutrons is in the range 327–3.27 meV, the same order as thermal and magnetic excitations in crystals. This does not greatly influence powder diffraction patterns *per se*, but does influence the magnitude of the thermal and/or magnetic diffuse scattering which must be taken into account in some kinds of very precise work.

Consistent with their electrical neutrality, the absorption cross section of thermal neutrons is low for most elements but this is dependent on the neutron velocity, being proportional to $1/v$. Exceptions with much higher absorption include the commonly used shielding materials B, Gd (as Gd_2O_3), and Cd. A more complete discussion of neutron absorption cross sections can be found in §2.3.3 and Squires (1978).

As will be established in §2.4, the intensity of the scattered neutrons is proportional to wavelength cubed (λ^3). An additional factor proportional to λ arises due to the efficiency of neutron detectors. All of these diverse effects must be considered in detail when planning a neutron diffraction experiment. The selection of wavelength to optimize the information content of the resulting powder patterns is dealt with in §3.5. In general, the wavelengths used are in the range 0.7–2.5 Å.

A particular characteristic of neutrons that distinguishes them from other radiations used for diffraction experiments (X-rays and electrons) is that they possess a substantial magnetic moment (Fig. 2.1).[5] This magnetic moment can interact in various ways with the sample; see for example Marshall and Lovesey (1971), Squires (1978), and Hicks (1995). Of particular interest here is elastic scattering from magnetic spin or orbital moments in magnetic atoms giving rise to strong diffraction effects in the presence of magnetic order. This allows a detailed study to be made of the magnetic structures of materials and forms the subject of Chapter 7.

A consequence of magnetic scattering is that a beam of neutrons formed by diffraction from a magnetized crystal monochromator will be polarized with respect to the neutron spins and magnetic moment. The diffraction of polarized neutrons from materials and the polarization analysis of the diffracted beams is a powerful tool in the study of magnetic structure.

2.2 SAMPLES FOR DIFFRACTION – THE STRUCTURE OF CONDENSED MATTER

Having reviewed the properties of the neutron beam, it is now necessary to briefly review the spectrum of physical states that diffraction samples may take, how to describe them, and how they inter-relate. Materials studied by powder diffraction are the different forms of condensed matter. The forms of condensed matter differ mainly in the degree to which their constituent atoms or molecules are ordered or disordered.

The structure of a condensed matter sample and its degree of order may be conveniently considered in terms of the correlation of the characteristics of a given atom (i.e. its position, type, magnetic moment, etc.) with the characteristics of the other atoms in the sample. It is the nature and strength of these correlations that defines both the category of condensed matter into which a particular sample falls *and* the kinds of neutron diffraction effects that can be observed from it. We can imagine an overarching mathematical expression or *correlation function* that contains *all* of this information for *all* of the types of atoms in the system. The complete correlation function must include information concerning the atom

[5] X-rays are also capable of magnetic scattering giving rise to scattered intensities usually of order 10^{-4}–10^{-5} of the non-magnetic scattering. At synchrotron sources, anomalous scattering techniques have recently been developed to enhance the magnetic scattering signal (see, e.g. Stirling and Cooper 1999), however neutrons are still used for the study of most magnetic systems.

species, its position, magnetic moment, and kinetic behaviour. The number of degrees of freedom associated with each atom is very great and a single correlation function to describe the entire system is not practical. However, much can be learned by considering only one kind of correlation (e.g. positional) and developing a partial correlation function. One widely used correlation function $G(\boldsymbol{r}, t)$ describes the number density of the atoms in a system, as a function of time t and position $\boldsymbol{r}$ with respect to a fixed atom at the origin (Marshall and Lovesey 1971). Time is included in the correlation function for completeness, although the time structure of correlation functions is studied by inelastic neutron scattering rather than diffraction. In fact, correlation functions are not often used in powder diffraction except in cases where a sample may contain highly disordered regions as is discussed in Chapter 10. As an example, in a perfect crystalline sample, once the crystal structure is known, the state of any atom in the crystal and its relationship to any other may be readily determined (see §2.2.1). In that case, $G(r)$ is merely a set of delta functions, each positioned at the radius of successive shells of atoms. Real crystals do of course have imperfections or defects that reduce the perfection of the correlation and lead to interesting diffraction effects. Ranked in order of increasing perfection, we may distinguish liquids, glasses, liquid crystals, disordered crystals, and notionally perfect crystals. This spectrum is illustrated in Fig. 2.3. These degrees of order are dealt with in the succeeding sections with the major emphasis on crystalline materials that form the majority of powder diffraction samples.

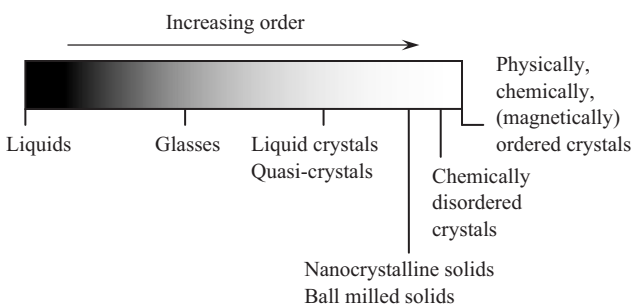

Fig. 2.3 A schematic illustration of the spectrum of ordered states in condensed matter.

2.2.1 The perfect crystalline state (three-dimensional long-range positional and chemical order)

A vast majority of the materials studied by powder diffraction are composed from crystals with a relatively high degree of perfection, that is, in the right hand 2% of Fig. 2.3. The atoms (ions, molecules) in a perfect crystal are arranged in a three-dimensional periodic array. This three-dimensional periodicity is responsible

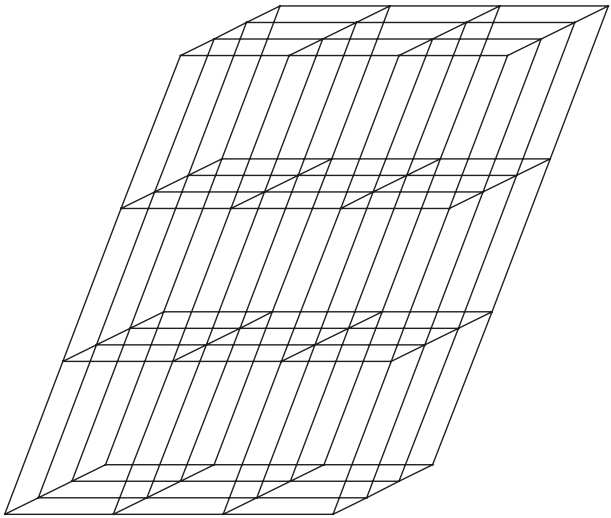

Fig. 2.4 A general three-dimensional space lattice.

for many of the interesting properties of crystalline solids; so that texts on the solid state almost always begin with a discussion of crystal structures (see, e.g. Kittel 1976). In such a perfect crystal, if it were of infinite extent, the structure would be the same when viewed from any origin chosen within the bounds of the crystal. In other words, the position and identity of each atom is known from a relatively small sample. Over the past 90 years, crystallographers have devised powerful methods for describing crystal structures in the most efficient way.

We begin with the periodicity of the structure. This periodicity may be conveniently represented by a three-dimensional space lattice as illustrated in Fig. 2.4. The infinite lattice is generated by endless repetition of three lattice translation vectors, $\boldsymbol{a}$, $\boldsymbol{b}$, and $\boldsymbol{c}$ along x, y, and z axes, respectively. This means that for any atom at coordinates $(x_1\boldsymbol{a}, y_1\boldsymbol{b}, z_1\boldsymbol{c})$, there is an identical atom at $((x_1 + p)\boldsymbol{a}, (y_1 + q)\boldsymbol{b}, (z_1 + r)\boldsymbol{c})$ where p, q, and r are any integers. The axes are chosen to meet several criteria to be discussed in later chapters, including minimizing the enclosed volume and reflecting the symmetry of the atom arrangement being described. There is no requirement for the axes chosen to be Cartesian and in practice, Cartesian axes are the exception rather than the rule. Although in their vector form, the lattice translation vectors $\boldsymbol{a}$, $\boldsymbol{b}$, and $\boldsymbol{c}$ give a complete description of the crystal lattice and the parallelepiped bounded by them known as the *unit cell*, the unit cell is more commonly described in terms of the edge lengths, a, b, and c and inter-axial angles, α, β, and γ. These six quantities are known as the lattice parameters.

Table 2.1 Lattice parameters of the seven crystal systems.

System	Lattice parameter conditions
Triclinic	$a \neq b \neq c,\ \alpha \neq \beta \neq \gamma \neq 90°$
Monoclinic	$a \neq b \neq c,\ \alpha = \beta = 90°, \gamma \neq 90°$
Orthorhombic	$a \neq b \neq c,\ \alpha = \beta = \gamma = 90°$
Trigonal	$a = b = c,\ \alpha = \beta = \gamma \neq 90°$
Hexagonal	$a = b \neq c,\ \alpha = \beta = 90°, \gamma = 120°$
Tetragonal	$a = b \neq c,\ \alpha = \beta = \gamma = 90°$
Cubic	$a = b = c,\ \alpha = \beta = \gamma = 90°$

In the most general case, the lattice is triclinic and $a \neq b \neq c$ and $\alpha \neq \beta \neq \gamma$. Other lattices, now possessing higher symmetry, can be constructed with some of the lattice parameters equal. For example, the orthorhombic lattice has $a \neq b \neq c$ and $\alpha = \beta = \gamma = 90°$. In all, seven distinct crystal systems result from the different combinations. The conditions on the lattice parameters of the seven systems are given in Table 2.1.

The lattice and unit cell are constructed to take advantage of the periodicity of the crystal and produce an efficient description of the crystal. If this were the only purpose, then we would always choose a unit cell of minimum volume – a so-called primitive unit cell. In fact, there are always alternative unit cells that may be chosen to describe the same crystal structure. In some cases, the underlying symmetry of the lattice is different from the symmetry of the primitive unit cell. In that case, a larger unit cell is chosen. Cells chosen in this way are centred cells, that is, they contain sub-translations that introduce extra symmetry. For example, the cubic close-packed structure, commonly adopted by many metallic elements, has face-centred cubic symmetry. The face-centred cell is generated by the face-centring translations [1/2, 1/2, 0], [1/2, 0, 1/2], and [0, 1/2, 1/2]. The primitive unit cell is actually rhombohedral with $a = b = c = a_{\text{cubic}}/\sqrt{2}$ and $\alpha = 60°$ with a single basis atom located at the origin. Cells may be constructed that are body-centred, one-face centred, or all-face centred. Combining all of the centrings with the seven crystal systems, we have 14 crystal lattices, known as the Bravais Lattices. The Bravais lattices are illustrated in Fig. 2.5.

We have proceeded thus far without paying any attention to the contents of the unit cells, apart from recognizing that they are all identical in a perfect crystal. Once we have determined the contents of the unit cell, that is, the position and identity of all the atoms therein, and the lattice translations (or lattice parameters), the structure is uniquely described. Mathematically, we may refer to the unit cell contents as a basis and the position of atom n in the unit cell is given by

$$\boldsymbol{r}_n = x_n\mathbf{a} + y_n\boldsymbol{b} + z_n\boldsymbol{c} \tag{2.4}$$

where x_n, y_n, and z_n are the fractional coordinates of the nth atom with respect to the unit cell origin. Taking x, y, and z in the range 0–1 ensures that all of the

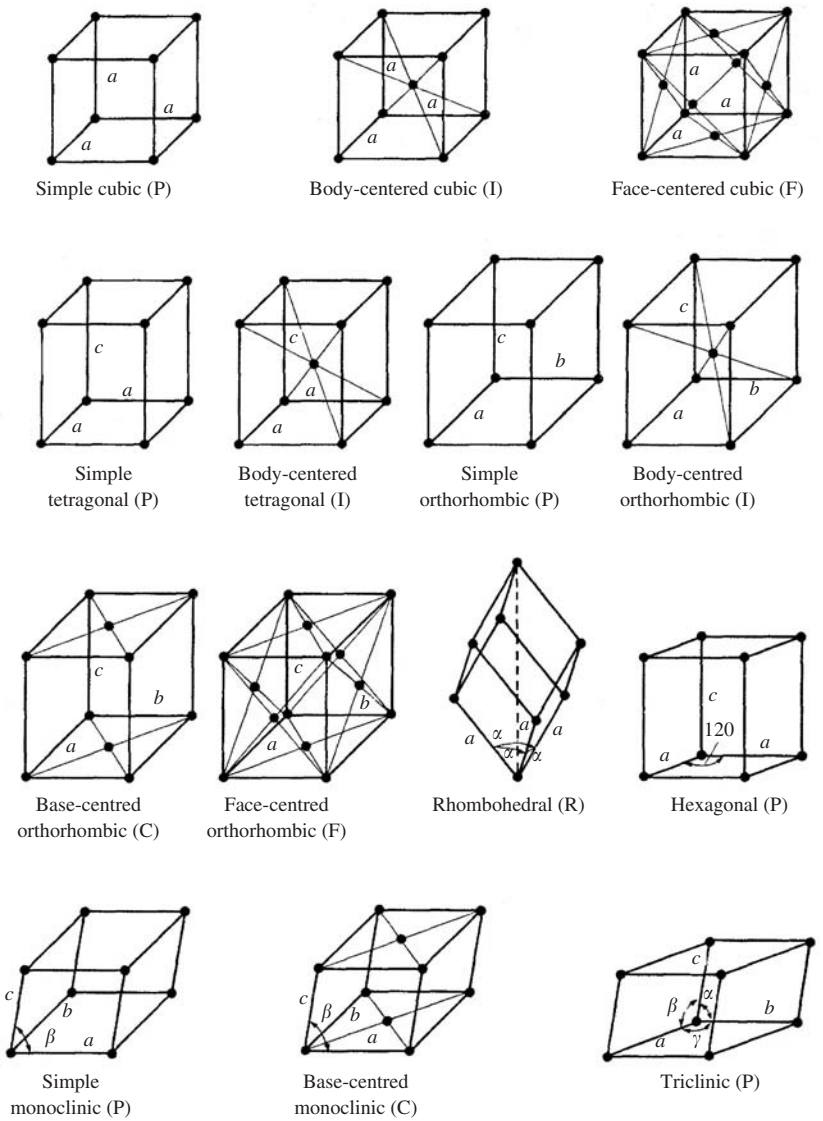

Fig. 2.5 The 14 Bravais lattices.

atoms lie within the unit cell. Examples of simple crystal structures, their unit cells, and bases are shown in Fig. 2.6. The influence of symmetry of the basis set and centring translations on the description of crystal structures is explored in more detail in §5.2.

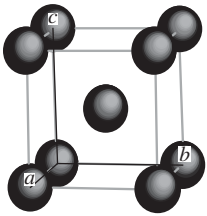

(a)
Material: Fe
Structure: Body-centred cubic
a: 2.866 Å
Basis: Fe (0, 0, 0)
Atoms:
Fe (0, 0, 0), (½, ½, ½)

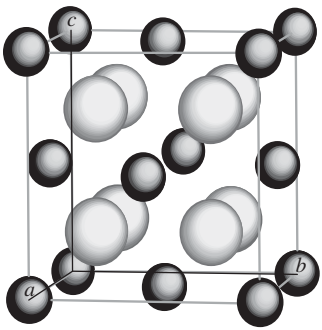

(b)
Material: ZrO_2
Structure: Cubic fluorite
a: 5.110 Å
Basis: Zr (0, 0, 0)
O (¼, ¼, ¼)
Atoms:
Zr (0, 0, 0), (½, ½, 0), (½, 0, ½), (0, ½, ½)
O (¼, ¼, ¼), (¼, ¾, ¼), (¾, ¼, ¼), (¾, ¾, ¼)
(¼, ¼, ¾), (¼, ¾, ¾), (¾, ¼, ¾), (¾, ¾, ¾)

Fig. 2.6 Two simple crystal structures: (a) body-centred cubic iron and (b) the fluorite structure of cubic zirconia.

In describing crystal structures and phase transitions, and particularly in interpreting diffraction patterns, it is important to have a shorthand method of representing directions and planes in crystal structures. Consider first a vector from the origin of the unit cell to the point ($x_i = u$, $y_i = v$, $g_i = w$) in Fig. 2.6 where x_i, y_i, and z_i are defined in eqn (2.4). The corresponding direction is referred to by the indices [*uvw*].[6] By convention, *u*, *v*, and *w* are multiplied or divided by a common scaling integer to make them adopt minimum integer values. For example, [0.25 0.5 0.75] becomes [1 2 3] and [0.33 1 2] becomes [1 3 6]. Any vector parallel to [*uvw*] also has indices [*uvw*], since the lattice is infinite and we may take the origin at any point in it. Hence the line joining (u_1, v_1, w_1) to (u_2, v_2, w_2) has indices $n[u_2 - u_1\ v_2 - v_1\ w_2 - w_1]$ where *n* is the scaling integer. [*uvw*] may be normalized into a unit vector by dividing by its length (e.g. $(u^2 + v^2 + w^2)^{1/2}$ in orthogonal unit cells). For example, the cube diagonal of a cubic lattice has the indices [1 1 1] and the corresponding unit vector is $1/\sqrt{3}$ [1 1 1] (or $[1/\sqrt{3}\ 1/\sqrt{3}\ 1/\sqrt{3}]$). The components of this unit vector are the direction cosines, more commonly referred to as l_1, l_2, and l_3. They are extremely valuable in the tensor transformations required for manipulating

[6] Negative indices are indicated by a bar over the number concerned, for example [−2 1 0] becomes [$\bar{2}$10]).

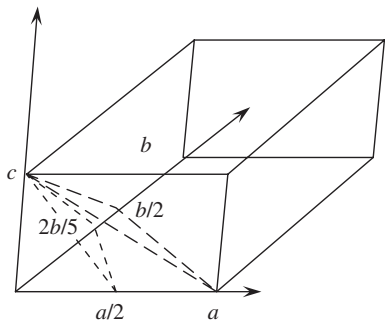

Fig. 2.7 The derivation of Miller indices for planes from axial intercepts. Miller indices for the two planes shown are (121), (452).

the many anisotropic properties of crystals such as elasticity (Chapter 11), piezoelectric moduli, and optical properties. Taking the negative of all indices merely reverses the direction of the vector, for example $[uvw]$ and $[\bar{u}\bar{v}\bar{w}]$ are oppositely directed but otherwise identical. In any Bravais lattice, some directions are equivalent. For example, in a cubic lattice [1 0 1], [1 1 0], [0 1 1], $[01\bar{1}]$, $[10\bar{1}]$, and $[1\bar{1}0]$ are equivalent. In a tetragonal lattice, [1 0 1] and [0 1 1] are equivalent but [1 1 0] is not. Symmetry equivalent directions can be grouped and considered together in most situations and this grouping is indicated by angular brackets ⟨ ⟩. For example, in the cubic example earlier, ⟨1 1 0⟩ represents [1 1 0], [1 0 1], [0 1 1], $[1\bar{1}0]$, $[10\bar{1}]$, $[01\bar{1}]$, and their negatives. In the tetragonal example, ⟨1 1 0⟩ represents only [1 1 0], $[1\bar{1}0]$, and their negatives. The others are represented by ⟨1 0 1⟩ (or ⟨0 1 1⟩).

A related system is used for the description of lattice planes. Any plane in the lattice not passing through the origin will intercept a unit cell at discrete points or fractional intercepts along the three unit cell edges as shown in Fig. 2.7. These intercepts may be used to uniquely describe the plane except when the plane lies parallel to one or more unit cell edges. To avoid problems posed by fractional intercepts at infinite distance, the plane is described by its Miller indices (hkl), the *inverse* of the fractional intercepts. Some examples of the derivation of Miller indices from plane intercepts are shown in Fig. 2.7. Greater detail may be found in books on elementary crystallography and diffraction such as Azároff (1968), Buerger (1980), Cullity (1978), Hammond (1990), and Tilley (2006). Each plane described by the Miller indices (hkl) is actually a member of an infinite set of parallel, equally spaced planes. This is illustrated in Fig. 2.8 for some simple examples. The symbol (hkl) may be taken to mean one individual plane or the whole set.[7] Unlike crystal direction indices, where the scaling integer is used to reduce u, v, and w to minimum integer values, Miller indices are used unscaled.

[7] Again negative indices are indicated with a bar, for example $(-1\ 1\ 3)$ becomes $(\bar{1}\ 1\ 3)$.

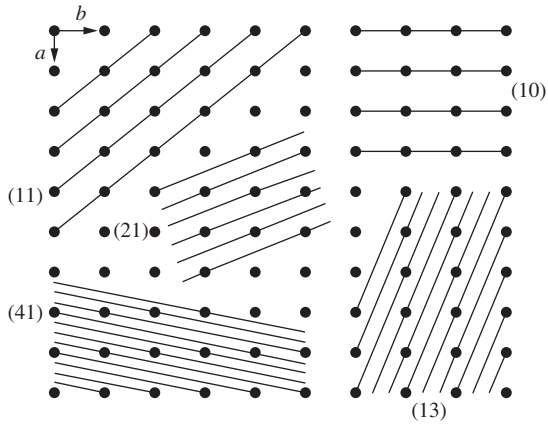

Fig. 2.8 Two-dimensional illustration of groups of planes (lines) with the same Miller indices.

This is because different sets of planes may be parallel (e.g. (1 1 0), (2 2 0), (3 3 0), etc.), but the Miller indices also define the relative spacing between the planes. That is, the spacing of (*nh nk nl*) is $1/n$ times the spacing of (*hkl*). We will later call this the *d-spacing* of (*hkl*) and define a reciprocal lattice made from points separated by d along directions defined by the plane normals. As with lattice directions, some planes with different Miller indices are actually identical under the symmetry operations of the lattice. This is indicated by grouping in parentheses { }. For example, $(1\,1\,1)$, $(\bar{1}\,1\,1)$, $(1\,\bar{1}\,1)$, $(1\,1\,\bar{1})$ in a cubic crystal are all equivalent and may be represented as $\{1\,1\,1\}$.

Hexagonal crystal structures are described on a unit cell with $a = b \neq c$ and $\alpha = \beta = 90°$, $\gamma = 120°$. The hexagonal symmetry (i.e. sixfold rotation about the c-axis) introduces an element of arbitrariness into the selection of axes. This means that the Miller indices of some planes that are equivalent, for example, $(1\,0\,0)$, $(1\,\bar{1}\,0)$ do not appear similar. To remedy this, the four Miller–Bravais indices (*hkil*) are used. Formally, i is the intercept along an axis that makes an angle 90° to c and 120° to both a and b. The fourth index i is not independent of h and k. They must conform to the relationship:

$$h + k = -i \tag{2.5}$$

When Miller–Bravais indices are used, our example earlier becomes $(1\,0\,\bar{1}\,0)$ and $(1\,\bar{1}\,0\,0)$ and the relationship is clear. More details of Miller–Bravais indices and their use may be found in crystallographic texts such as Azároff (1968) or Hammond (1990). Some authors also use the fourth index for directions in hexagonal crystals, however this is not necessary.

2.2.2 Departures from perfection (restricting the three-dimensional long-range order)

In the previous section, convenient representations for perfect crystals of infinite extent were discussed. Everyday experience tells us that crystals are not infinite in extent and the average purity of even laboratory compounds (98%–99.9%, say) indicates a chemical imperfection every 50–1000 atoms or so. These and other departures from our perfect crystal condition lead to a degree of uncertainty in the position and identity (atomic magnetic moment, etc.) of each atom; and in many cases to recognizable diffraction effects. These in turn may be used to study the underlying departures from perfection.

The most easily understood departure from perfection is the finite size of the crystal. As the name suggests, neutron powder diffraction is conducted on powdered or other polycrystalline samples consisting of rather small crystallites. A typical unit cell for an inorganic solid has dimensions in the range 2.5–25 Å. We see then that the extent of the crystals in a typical crystallite of 2–20 μm (20,000–200,000 Å) diameter does not seriously detract from our infinite crystal approximation; that is, the crystallites are 10^3–10^5 unit cells in diameter. When crystals smaller than 0.5 μm are present in the sample, the departure from an infinite crystal begins to become significant and leads to appreciable broadening of the diffraction peaks as discussed in §4.5 and §9.2.

The next effect that we will discuss is the displacement of atoms from their ideal or mean positions. Thermal vibration is the most common cause of atom displacements in materials. This persists even at temperatures close to absolute zero, where the zero point motion is still readily detected by careful diffraction experiments. At room temperature, the root mean square thermal vibrations in an inorganic solid are typically of order 0.1 Å. This causes an uncertainty in our knowledge of the phase difference between neutrons scattered from atoms within the lattice planes. Figure 2.9 shows a simple illustration of the effect where atoms displaced from the diffracting 'plane' no longer scatter in-phase as will be discussed in §2.4.2 and §5.5.2.

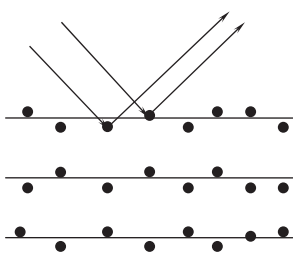

Fig. 2.9 Illustration of how the thermal vibration of atoms introduces a path length and phase difference between neutrons scattered by atoms which would have scattered in-phase in a perfect static structure.

In some fields, the preparation of relatively pure compounds is considered straightforward (chemistry) whilst in others the presence of elements in solid solution is either unavoidable (geology/mineralogy) or desirable to modify properties (materials science/physics). The presence of dissolved (or solute) atoms, either accidental (impurities) or deliberate (alloys or dopants), disrupts the crystalline perfection in two ways; the chemical disorder and positional disorder introduced by solute atoms. Dissolved atoms may be present substitutionally, that is replacing host atoms within the crystal structure or interstitially, occupying the spaces between the solvent atoms. Both kinds of solute perturb the local interatomic distances. This may be thought of as an atomic size effect (Warren 1969, 1990). Perturbations in the first shell of atomic positions around a solute atom are usually in the range 0 to ~0.2 Å and the perturbation or interatomic strain decays with the inverse square of the distance from the solute atom. A level of uncertainty in the atomic positions is introduced. This uncertainty or distribution in atomic positions has a very similar effect on the diffraction pattern to thermal vibration of the atoms. Since the diffracting sample constitutes an ergodic system we cannot, from a single diffraction pattern, distinguish between time-averaged thermal vibrations and distance-averaged 'static' displacements due to solute atoms and defects. The use of diffraction patterns collected over a substantial temperature range and a suitable model for the thermal properties of the solid can in some instances be used to isolate static displacement effects (Kisi 1988; Cheary 1991; Argyriou 1994; Ma and Kisi 1998). These techniques are discussed further in §6.5.3. The second effect of solute atoms is in lowering the degree of chemical order by introducing a level of uncertainty as to the type of atom that will be found occupying a particular crystallographic site in a particular unit cell. In a random solid solution, we describe this kind of structure by composing an 'average' unit cell and recognizing that the sites are fractionally occupied by two or more atom types. A simple example is shown in Fig. 2.10.

As the amount of solute increases, both the positional disorder and chemical disorder provide an impetus for structural change. In favourable circumstances close to integer atomic ratios (e.g. Fe_3Al), many such solid solutions become fully ordered into new crystal structures. The peaks in the correlation function sharpen up and the uncertainty in the chemical occupancy is removed. The changes are

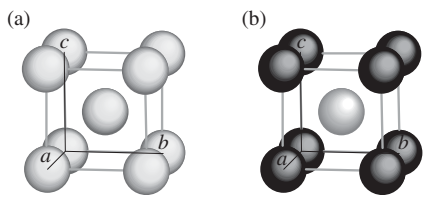

Fig. 2.10 The two β-brass (CuZn) structures; (a) with Cu and Zn disordered over both the origin and unit cell body centre position (bcc) and (b) with Cu and Zn fully ordered.

illustrated in Fig. 2.10(b). The new crystal structure has a new diffraction pattern related to, though easily distinguished from that due to the parent phase. Structural changes such as these are termed order–disorder transitions and have been widely studied. At intermediate compositions or at high temperatures, there may be some degree of ordering on a local scale but not extending throughout the crystal. This kind of behaviour for a binary system composed from two atom types A and B occupying sites α and β, respectively, in the stoichiometric ordered structure, is usually described by a long-range order parameter S (Warren 1969, 1990) to be discussed in §10.3.4 given by:

$$S = \frac{(r_\alpha - x_A)}{y_\beta} = \frac{(r_\beta - x_B)}{y_\alpha} \tag{2.6}$$

in which x_A represents the atom fraction of A, x_B the atom fraction of B, r_α the fraction of α-sites (correctly) occupied by an A atom, r_β the fraction of correctly occupied B atom sites, y_α is the overall fraction of α-sites, and y_β the fraction of β-sites.

In the absence of long- or short-range order, solute atoms influence the *intensities* of the diffraction peaks which can in turn be used as a powerful means of measuring the solute content on the various crystallographic sites (see Chapter 5). Short-range order has its greatest influence on the diffraction pattern in the diffuse (or background) scattering as discussed in Chapter 10. Long-range order leads to new structures or superlattices that are easily recognized by the appearance of new diffraction peaks in the pattern.

A related, though distinct type of departure from crystalline perfection is the departure from Dalton's law of definite proportions, that is, non-stoichiometry. Some compounds can exist over a range of chemical compositions. TiC_x is a classic example where $0.6 < x < 1$ (Storms 1967). The structure accommodates these departures from stoichiometry by forming either vacancies of one species (C in this example) or interstitial atoms of the other species (Ti here). Changes of this kind have quite different effects on the diffraction pattern and diffraction-based techniques are the only ones capable of uniquely determining the true structure.

Special cases of non-stoichiometry may be induced by alloying when, for example, an ionic material is doped with cations or anions of different valence to the host. In order to maintain charge balance, anion vacancies, anion interstitials, cation vacancies, or cation interstitials may form depending on the relative valence of solute and solvent ions and their relative size. A classic example is in zirconia ceramics doped with trivalent or divalent cations, for example, using Y_2O_3 or MgO. These materials form very mobile anion vacancies that facilitate ionic conduction and the materials are used as solid electrolytes in fuel cells and as high-temperature resistive heating elements (Green *et al.* 1989). More rarely, non-stoichiometry is observed in intermetallic compounds such as γ-brasses due to Fermi-surface–Brillouin zone interactions (Jones 1960; Kisi and Browne 1991).

Departures from perfection of a purely physical nature can occur by a number of mechanisms illustrated in Fig. 2.11. Very often when examining diffraction

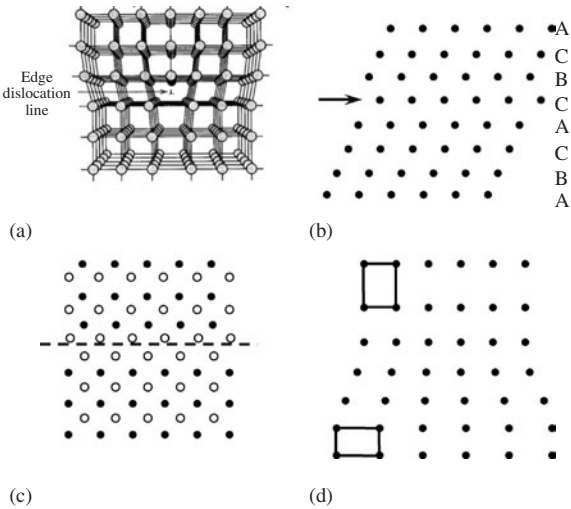

Fig. 2.11 Various crystal imperfections or defects that can influence the neutron diffraction pattern. Shown are (a) an edge dislocation (adapted from Callister 2003), (b) a stacking fault (arrowed) in a two-dimensional stacking sequence, (c) an anti-phase domain boundary, and (d) a 90° domain wall in a ferroic crystal. The atom displacements or strains are greatly exaggerated in (a) and (d).

patterns recorded from affected samples, these mechanisms are all grouped as 'strains'. Apart from the strains in solid polycrystalline samples described later, pure strains are very rare in powder diffraction samples. In a vast majority of cases, the observed diffraction effects are really a result of crystal imperfections or physical defects, although these may lead to genuine lattice strains. Point defects such as vacancies and interstitials in numbers great enough to cause a diffraction signature can only arise from the chemical mechanisms already described. Line defects or *dislocations* cause highly oriented strain fields that are compressive above the dislocation core and tensile below for edge dislocations; or pure shear strains for screw dislocations (see, e.g. Weertman and Weertman 1964; Ashby and Jones 2005). The strains cause a local distribution of interatomic spacings that may extend 100 Å or more from the dislocation core as shown schematically in Fig. 2.11(a). Therefore, a high dislocation density leads to very profound diffraction effects, as we will discuss in §9.6. This effect is more commonly seen in metallic materials where dislocations are generated in large numbers by processes such as plastic deformation or the absorption of hydrogen to form metal hydrides. In some circumstances, errors occur in the sequence of atomic planes within a structure to generate planar defects as illustrated in Fig. 2.11(b). Such *stacking faults* interrupt the crystal periodicity in one dimension but leave it intact in the other two. In extreme cases, the stacking in one direction can become completely random, although it is more common that stacking faults form at random with

some average probability. When the faulting probability is high (i.e. the stacking fault energy is low), the crystal may lower its energy by ordering the stacking faults at regular intervals to form a new crystal structure much as the random solute atoms of a solid solution discussed earlier may order into new structures. Materials that exhibit series of structures through modified stacking sequences in one dimension are said to exhibit *polytypism*. SiC is among the most prolific generators of polytypic structures; over 70 are known with sequences from 2 to 36 layers thick (Trigunayat 1991). Other kinds of planar defects include anti-phase domains and twins. Both represent ways in which crystals sometimes partition into small perfect regions bounded by very narrow boundaries where the perfect crystalline state is disturbed. Anti-phase domains are regions within an ordered solid solution or intermetallic compound where the ordering pattern is reversed compared with adjacent domains as shown in Fig. 2.11(c). Twins are likewise regions of relatively perfect crystal that are related to each other by a small shear displacement. Anti-phase domain wall boundaries and twin boundaries have quite a different (local) structure to the rest of the crystal and as such can give diffraction effects if present at a sufficient density. A further kind of domain occurs in ferroelastic, ferroelectric, and ferromagnetic crystals. These crystals have a spontaneous strain, spontaneous electric polarization, or spontaneous magnetization, respectively. Crystals of these ferroic materials are most often subdivided into small domains within which the elastic, electric, or magnetic polarization opposes those of other domains such that overall the crystal has no net polarization. The domain walls have a finite extent and if the polarization has a large crystal *distortion* (e.g. to tetragonal or rhombohedral symmetry) associated with it, then relatively large strains will accumulate in the domain walls as illustrated in Fig. 2.11(d). Domain walls can make a significant contribution to the diffraction patterns of ferroic crystals – a relatively recent field of study that is considered in §9.5.

All of the departures from perfection above can be present in single crystal and polycrystalline samples alike. The remaining effects in the section are all peculiar to polycrystalline samples. The finite size of real crystals has been alluded to earlier. A special case arises in nanocrystalline materials ($d \sim$ 1–20 nm diameter) where atoms at the surface of crystals can, in extreme cases, outnumber those in the bulk. These materials are of interest because they represent one of many intermediate states between crystalline solids and the amorphous (or glassy) solids discussed in §2.2.4.

Solid polycrystalline samples, such as a majority of engineering materials, rocks, and mineralogical specimens, can differ from powdered materials in a number of interesting ways. First, the materials have usually been formed at elevated temperature and cooled to room temperature before study. Due to a combination of constraint from surrounding crystals, thermal expansion anisotropy and elastic anisotropy, quite large residual strains and strain distributions can accumulate. The situation is worst in materials that cannot easily plastically deform such as rocks and ceramics, and rather less common in metallic materials. These residual strains are undesirable in a majority of cases, as they lead to residual stresses that

add to externally applied stresses causing premature failure. The second imperfection sometimes found in solid polycrystals but rarely seen in single crystals is compositional inhomogeneity. This most commonly occurs in materials processing when there is one or more volatile species present during high-temperature sample preparation. A gradation in chemical composition naturally is accompanied by a gradation of all the crystal structure parameters and therefore leads to very strong diffraction effects.

The final departure from perfection that is most commonly seen in polycrystalline samples is the simultaneous presence of two or more phases. This is a very commonplace occurrence in geological specimens, rocks, and ores being very commonly composed of large collections of minerals. Similarly, modern engineering materials usually contain more than one phase at some time during their synthesis, fabrication, and very often in the final product. In many instances the multi-phase nature of engineering materials is deliberate to modify the properties. Prominent examples include precipitation hardening by distribution of ultra-fine second phase particles created by a heat treatment sequence. Each phase in a multi-phase material contributes its own diffraction pattern to the overall experimentally determined pattern. This is the basis of the most widespread use of X-ray powder diffraction, that is, for phase identification in unknown samples. In this regard, with suitable computational techniques, the analysis of X-ray and neutron powder diffraction patterns may be taken much further to provide quantitative phase analysis (QPA), a subject discussed at length in Chapter 8. Neutron powder diffraction has advantages in this area because of greater penetration depth to give a statistically meaningful sample size and (usually) minimal micro-absorption. Diffraction-based techniques are among only a few that can provide a quantitative phase analysis. To do so under ambient conditions is very useful, but of even greater importance is the ability with neutron powder diffraction to study *in situ*, the evolving mixture of phases as a function of temperature, time, pressure, electric field, magnetic field, pH, or other environmental or process variables. Naturally, many (or in rare cases all) of the previous defects or departures from the infinite perfect crystal model can occur within individual phases in a multi-phase mixture. Disentangling the individual contributions to a complex powder diffraction pattern is one of the supreme challenges of the field and also most rewarding in the richness of the information that it can provide. The tools to do so are introduced in §2.3 and §2.4, expanded in Chapter 4 and applied to real materials and problems in the succeeding chapters. First, however, we pause to examine several of the less well-ordered states of condensed matter in progressively greater departures from three-dimensional crystalline perfection.

2.2.3 Lower and higher dimensional forms of order – the loss of lattice periodicity

This section encompasses several very different types of order that have in common the fact that the translational periodicity of the lattice is broken in one, two, or three

dimensions, for some or all of the basis atoms whilst preserving a high degree of symmetry.

The first example in this section is that of incommensurate superlattices. Early in §2.2.2, we discussed how a superlattice may form in a solid solution by ordering of formerly random solute atoms to well-defined crystallographic sites. In that discussion, a tacit assumption was made that the new unit cell volume would be an integer multiple of the disordered cell volume. In a small fraction of cases this is not true and the superlattice is said to be incommensurate (or out of step) with the base structure. The shorthand description of the structure through an exactly specified unit cell is inadequate. The approach that is usually taken is to describe the position of the incommensurate atom(s) as a set of fractional coordinates (x, y, z) plus a vector describing the perturbation from the commensurate position $(\delta_x, \delta_y, \delta_z)$. The perturbation may have one, two, or three non-zero elements leading to one-, two-, or three-dimensional incommensurate structures. In a later section (§2.2.6), we discuss the special case of magnetic structures which may be incommensurate with the underlying crystal structure.

The second type of material with reduced long-range order is the liquid crystals. These are really a special case of electric field-induced alignment of polar molecules. In the unexcited state they have a liquid-like structure (see §2.2.5); however, in an applied field they can adopt one-, two-, or three-dimensional order. Unlike the incommensurate structures above where the lattice periodicity is intact for most of the basis atoms, in a lower dimensional (one or two) liquid crystal the liquid-like state persists in the other dimensions.

A further degeneration of the lattice periodicity is possible in the quasi-crystals such as $AlMn_6$. Quasi-crystals have highly ordered arrangements of atoms which show very strong rotational symmetry (see Chapter 5). In particular, they exhibit rotational symmetries (e.g. fivefold) that, when combined with lattice translations, cannot completely tile a two- or three-dimensional space without leaving gaps. Hence quasi-crystals have no lattice periodicity whatever and yet they can in some cases grow to relatively large dimensions (e.g. 1–2 mm in diameter) and give a strong diffraction pattern. Most studies have been conducted using powder diffraction and neutron diffraction has made quite a contribution. Having no lattice, it is impossible to establish a three-dimensional unit cell. Mathematical means for describing quasi-crystals that involve examining three-dimensional slices through a six-dimensional space have been developed; however, they are beyond the scope of this volume. The reader is referred to Kramer (1987) and Senechal (1995) for further information. It is worth noting that similar analysis methods may be applied to incommensurate superlattices involving six-, five-, or four-dimensional spaces for structures that are incommensurate in three, two, or one dimension(s), respectively.

2.2.4 Glasses (solids with no long-range order)

Glasses are non-crystalline solids. Many of the gross physical properties exhibited by glasses are similar to those exhibited by crystalline solids. They are mechanically stiff and able to sustain shear forces (unlike liquids). Metallic glasses are electrically and thermally conducting and may be ferromagnetic. Ionic glasses such as silica behave very similarly to their crystalline counterparts. Yet the detailed properties of glasses are often interestingly different from crystalline solids. The structure of a glass is difficult to explain and indeed it was many years after the advent of the science of diffraction-based crystallography in 1912 that an understanding of the structure of glasses was generated for example by the work of Warren (1933, 1934) and others. The picture that emerged was one of randomized atom position combined with interatomic distances that are nonetheless, on average, within 5%–10% or so of their crystalline equivalents. No unit cell can be constructed since each part of the material is different, and yet diffraction effects can be observed. It is here that the pair correlation function introduced in §2.2 comes into its own. Consider first a mono-atomic glass such as amorphous C. The pair correlation function has strong peaks around 1.52, 2.88 Å, and so on as shown in Fig. 2.12(a); however, these peaks are very broad in comparison to those for crystals, reflecting the high degree of disorder in the structure. Nonetheless, the material shown achieves the remarkable coordination number of 3.9 (number of nearest neighbours – from the area of the first peak) which closely approaches the value of 4 for crystalline diamond (Robertson 2002).

In polyatomic glasses (e.g. SiO_2) the situation is more complex as shown in Fig. 2.12(b). A pair-correlation function can be constructed for each chemical pair (Si–Si, Si–O, O–O). By using this kind of analysis, it is possible to show that glassy SiO_2 is composed of SiO_4 tetrahedra, just as are the crystalline forms (quartz, crystobalite, tridymite, etc.). These tetrahedra are highly ordered and contain strong covalent bonds. The difference between the glass and the crystalline form is that in the former, a great variety of rotations of tetrahedra is allowed about the shared O atoms at the tetrahedral vertices. Glasses are interesting in their own right (e.g. SiO_2 has almost zero thermal expansion; metallic glasses can have interesting magnetic properties), but are also interesting as pre-cursors to new crystalline states that may be difficult or impossible to attain directly from the liquid. This is an emerging field, particularly when many new amorphous or partially amorphous states can be readily achieved by high-energy mechanical milling (mechanical alloying). It leads to the analytically difficult situation of diffraction patterns containing contributions from both crystalline and amorphous phases (see Chapter 10).

2.2.5 Liquids (rapid atomic or molecular motion)

Structurally, at an instant in time, simple liquids are not too dissimilar from glasses. However, they have the additional feature that the constituent atoms or molecules

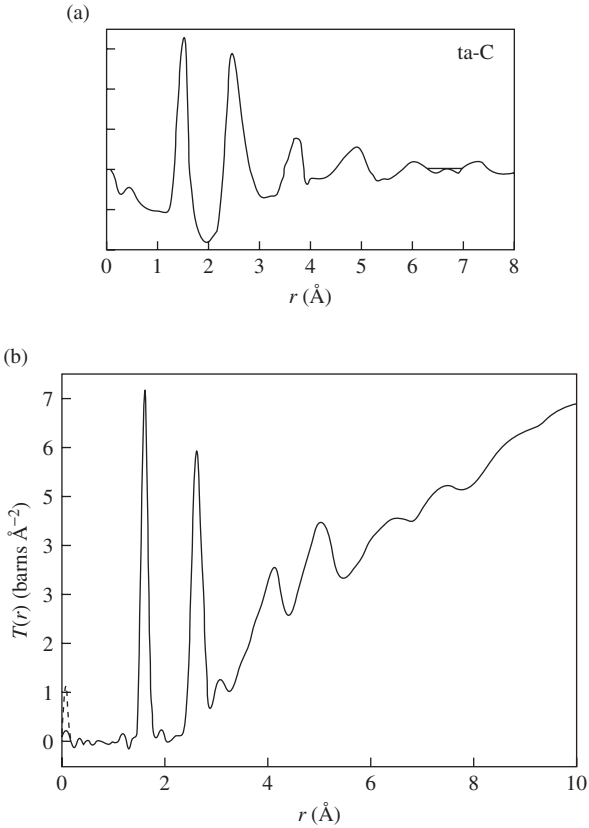

Fig. 2.12 Radial distribution functions derived from neutron scattering studies of (a) amorphous carbon (Robertson 2002) and (b) amorphous SiO_2 (Grimley *et al.* 1990).

are in rapid motion. Nonetheless some interatomic distances are more favoured than others, leading to diffraction effects. The diffraction pattern of a liquid is similar to that of the amorphous or glassy phase of the same material except that the features are broader, reflecting a less well-defined correlation function. There is some distinction between simple or monoatomic liquids, where the higher order scattering is rapidly damped, and molecular liquids, where quite strong diffraction can occur. Liquids are seldom deliberately present in powder diffraction sample. Exceptions include the *in situ* study of precipitation and solidification phenomena, and the *in situ* study of electrolytic processes.

2.2.6 Magnetic order

In addition to the atomic positions and chemical identity of the atoms in condensed matter, there are a number of other attributes that may form ordered structures.

The major one of interest to neutron scattering is the magnetic moment possessed by some atoms. Just as the atoms interact by physical and chemical means to form highly ordered crystal structures, so too can the magnetic moments interact to form magnetic structures, albeit through more subtle mechanisms. The kinds of magnetic order that are possible parallel the kinds of structural order already discussed; however, additional complexity is possible because (i) the magnetic moment is a vector and (ii) the magnetic structure is superimposed on the crystal structure. The description given here is of necessity very brief and does not do justice to this complex and fascinating field. More detailed accounts may be found in books on magnetism such as Crangle (1977) and on magnetic neutron diffraction such as Izyumov and Ozerov (1970). Least ordered is the paramagnetic state[8] where, in the absence of an externally applied magnetic field, the magnetic moments are uncorrelated and rapidly fluctuating. This is the magnetic equivalent of the liquid state and little can be learned from a simple powder diffraction pattern. At the other end of the spectrum of order is the ferromagnetic state in which, even in the absence of an external magnetic field, the magnetic moments are fully aligned over volumes of crystal many unit cells in size. The magnetic unit cell for a ferromagnetic structure is identical to the underlying structural unit cell[9] as illustrated in Fig. 2.13(a). The magnetic diffraction peaks therefore occur at the same Bragg angles as the crystal structure peaks and add extra intensity to them as discussed in Chapter 7. Ferromagnetic materials have a large spontaneous magnetization even in the absence of an externally applied field and are the basis for many technical magnet applications. In more complex materials, more than one kind of magnetic atom can be present. If in such materials all of the magnetic moments are spontaneously parallel, the material is again a ferromagnet; if they are antiparallel, the material is termed a ferrimagnet. A third simple arrangement occurs when the antiparallel arrangement is present in a material containing only one magnetic atom. This latter type, called antiferromagnets, has no net magnetization at zero applied field (Fig. 2.13(b)). In antiferromagnetic and some ferrimagnetic materials, the magnetic unit cells are multiples of the underlying primitive crystal unit cell meaning that additional (purely magnetic) neutron diffraction peaks will be present in the diffraction pattern (§7.2).

Still more complex structures arise because the magnetic moments of the atoms are not constrained to parallel a crystal direction (e.g. [1 0 0], [1 1 0], etc.). Hence the moments can vary in a helical fashion around a vector (helimagnets). In the simplest cases, this vector is a simple lattice translation vector [1 0 0], [0 1 0], or [0 0 1]. More complex structures where the magnetic structure is incommensurate with the crystal structure are possible (Fig. 2.13(c)). This can arise because (i) the period of rotation of the moment about a low-index lattice vector is incommensurate with the underlying structure or (ii) the vector about which the moment rotates has one or more irrational indices. Other structures in which the moments undergo

[8] The diamagnetic state is not considered here.
[9] Sometimes referred to as the chemical unit cell.

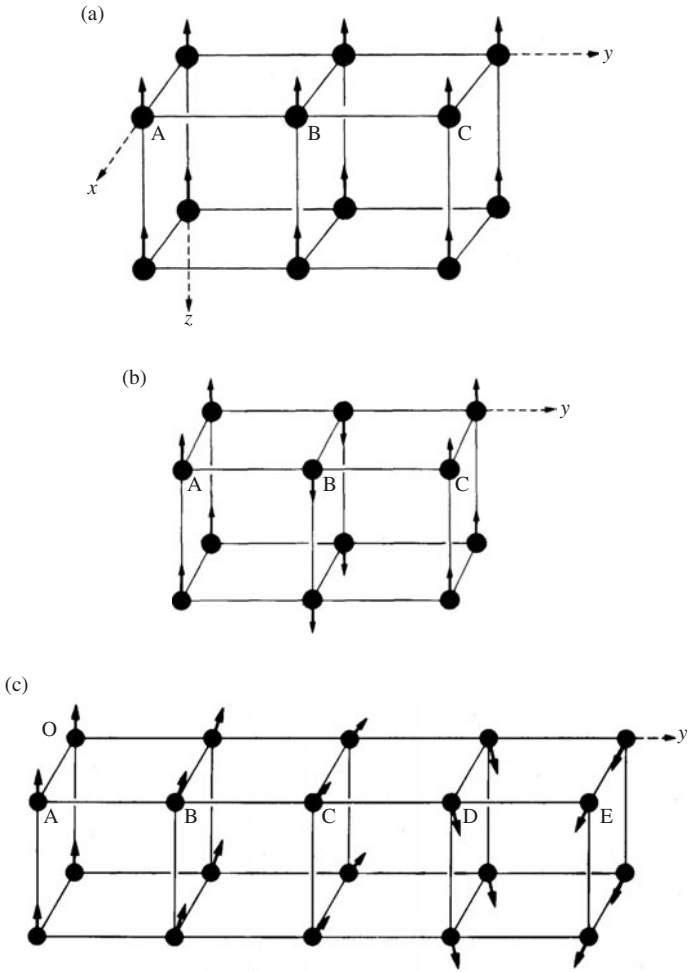

Fig. 2.13 Some examples of magnetic structures; (a) ferromagnetic, (b) antiferromagnetic, and (c) helical or spiral structures (Bacon 1975).

a conical modulation, a sinusoidal modulation, or a square-wave modulation have been described and an introduction may be found in books such as Bacon (1975) and Izyumov and Ozerov (1970).

Lying between the multitude of ordered magnetic states described earlier and the disordered or paramagnetic state are the spin glasses. Spin glasses occur in solid solution phases in some alloy systems and as the name suggests, are the magnetic analogue to the true glasses (§2.2.4). Spin glasses are fully ordered with respect to atomic position (i.e. they are crystalline); however, the occupation of the atomic positions by different elements is random (i.e. they are chemically disordered).

Many magnetic materials undergo magnetic phase transitions in response to changes in temperature, pressure, composition, or magnetic field. Neutron powder diffraction is an essential tool in understanding such transitions and in mapping out magnetic phase diagrams.

2.3 NEUTRON SCATTERING BY THE SAMPLE

In §1.2, a number of features of neutron diffraction that enable it to make a valuable contribution to condensed matter research were outlined. The fundamental process underpinning neutron diffraction is the interaction of the neutron with individual atoms in the sample; a process that differs substantially from the more common X-ray scattering. The theory of thermal neutron scattering is the subject of several excellent texts (see, e.g. Marshall and Lovesey 1971; Squires 1978; Balcar and Lovesey 1989). We present here only those results that are essential to the successful conduct and interpretation of neutron powder diffraction experiments. Interested readers are referred to these more comprehensive accounts for greater detail.

2.3.1 Nuclear scattering by individual atoms

Whereas X-rays are scattered from the electron distribution, neutrons are scattered primarily by atomic nuclei. In the special case of magnetic materials, neutrons are also scattered by the interaction of the neutron magnetic moment with the magnetic moment(s) of the atoms – a property of the electron distribution.[10] The size of the scattering object (i.e. the electron distribution) in both X-ray and magnetic neutron scattering is comparable in size to the wavelength of the X-rays or neutrons. This leads to interference effects between the incident wave and the scattered wave for all but the directly transmitted wave and is responsible for the familiar X-ray form factor (e.g. Klug and Alexander 1974; Cullity 1978). The nuclear scattering of neutrons, on the other hand, is isotropic except for very minor contributions from Foldy scattering and Schwinger scattering (e.g. Bacon 1975).

The scattering geometry is illustrated in Fig. 2.14. An incident neutron of wavevector $\boldsymbol{k}$ is scattered by the sample (target), and the scattered wave is sampled by a neutron detector at a position defined by the polar angles θ, ϕ and subtending a solid angle $d\Omega = \sin\theta\, d\theta\, d\phi$.

For an incident neutron flux of N (neutrons per second per unit area), the scattered neutron flux measured by the detector will be

$$N\left(\frac{d\sigma}{d\Omega}\right) d\Omega \tag{2.7}$$

[10] Electrons with unpaired spins in particular.

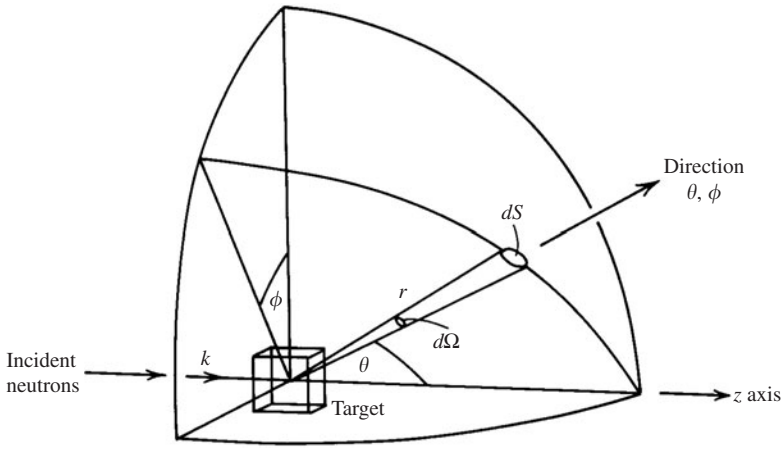

Fig. 2.14 Geometry of a neutron scattering experiment (Marshall and Lovesey 1971; Squires 1978).

which defines the differential scattering cross section $d\sigma/d\Omega$. We have assumed at this stage that the scattering nucleus is rigidly fixed in place and that no transfer of energy takes place between the nucleus and the neutron, that is, the scattering is completely elastic. If the incident neutrons are described by a plane wave $\psi = \mathrm{e}^{ikz}$, the scattered wave may be represented by the spherical wave $\psi = -(b/r)\mathrm{e}^{ikr}$. Here $k = 2\pi/\lambda$ is the wave number, and r is the distance from the scattering nucleus to the detector. The constant b is a very important quantity in neutron diffraction and is known as the *scattering length*. It has the dimensions of length and is the neutron equivalent of the X-ray scattering factor or form factor (f). The scattering cross section can be obtained by integrating eqn (2.7) or by noting the definition:

$$\begin{aligned}\sigma &= \text{flux of scattered neutrons/incident flux}\\ &= 4\pi r^2 v \frac{\left|(-b/r)\ \mathrm{e}^{ikr}\right|^2}{v\left|\mathrm{e}^{ikz}\right|^2}\\ &= 4\pi b^2 \qquad (2.8)\end{aligned}$$

for neutron velocity v. The scattering length b is a complex quantity with the imaginary part being responsible for neutron absorption. Fortunately, most elements and isotopes have relatively small absorption and b can be regarded as a real constant. Exceptions include the well-known neutron-shielding materials Cd, Gd, and B. In problems related to the calculation of diffracted intensities, it is possible to treat the real and imaginary portions separately as the scattering cross section (σ_s) and the absorption cross section (σ_a).

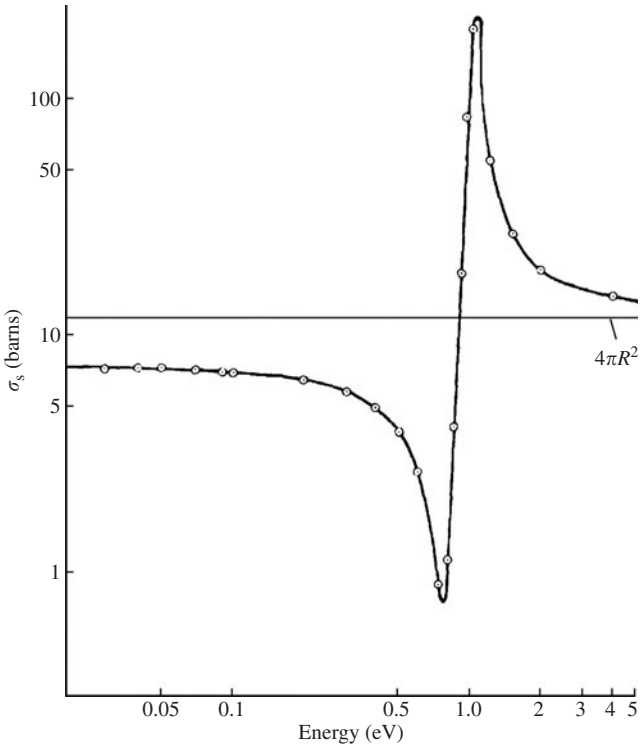

Fig. 2.15 Dependence of the neutron scattering length b on the neutron wavelength at energies affected by a nuclear resonance (Bacon 1975).

The energy (or wavelength) dependence of the nuclear neutron scattering cross section has the general form of Fig. 2.15. There is a substantial range of energies over which the scattering cross section is relatively constant as well as large variations in cross section close to the energy of a nuclear resonance. The curve is not unlike the energy dependence of X-ray scattering close to an absorption edge. At energies below the resonance, b and σ_s are displaced negatively by an amount that depends on the detailed nuclear structure. In some cases b is negative indicating a phase shift on scattering that differs by 180° from nuclei with positive b.[11] At energies above the resonance, the cross section is asymptotic to the surface area of the nucleus $4\pi R^2$. This latter quantity is the expected value of σ_s for collisions of rigid spheres (potential scattering) and if this were the only kind of scattering for all elements, would lead to a systematic increase in σ_s with increasing atomic number. However, because of the influence of nuclear resonances above (or less

[11] The sign of b is somewhat arbitrary. It is chosen as positive for a 180° phase shift on scattering – a situation valid for most nuclei.

commonly below or within) the thermal energy range ~0.01–0.08 eV (1–2.9 Å), this is not observed. A second consequence of resonance scattering is that different isotopes of the same element have different nuclear energy levels and hence different values of σ_s and b. The scattering length that is observed for the natural isotopic mixture (or any other) is the weighted average of b for the collection of isotopes present.

To illustrate these points, we will shortly discuss examples of scattering lengths for various elements and isotopes; however, it is first necessary to consider what proportion of the scattering cross section σ_s is available to take part in interference effects such as diffraction.

2.3.2 Scattering by assemblies of atoms – coherent and incoherent scattering

In any assembly of atoms, there will inevitably be variations in the scattering potential about some mean value. These may arise due to human intervention (alloying or doping), occur by accident (impurity atoms), or be an inevitable attribute of the system (isotopic mixture and distribution of nuclear spins). Analysis of the scattering from a system containing a random distribution of scattering nuclei (Squires 1978) leads to the following expression for the differential scattering cross section:

$$\frac{d\sigma}{d\Omega} = |\bar{b}|^2 \left| \sum_n \exp(i\boldsymbol{\kappa} \cdot \boldsymbol{r}_n) \right|^2 + N\overline{\left|b - \bar{b}\right|^2} \tag{2.9}$$

where $\bar{b}$ is the mean scattering length for all atoms in the system, $\boldsymbol{\kappa}$ is the scattering vector (difference in wavevector of scattered and incident neutrons §2.4.1), $\boldsymbol{r}_n$ is the position vector of the nth atom in the system, and N is the number of atoms in the system. Making the substitutions:

$$\left(\frac{d\sigma}{d\Omega}\right)_{\text{coherent}} = \left|\bar{b}\right|^2 |\Sigma_n \exp(i\boldsymbol{\kappa} \cdot \boldsymbol{r}_n)|^2$$

$$\left(\frac{d\sigma}{d\Omega}\right)_{\text{incoherent}} = N\overline{\left|b - \bar{b}\right|^2} \tag{2.10}$$

we obtain

$$\left(\frac{d\sigma}{d\Omega}\right) = \left(\frac{d\sigma}{d\Omega}\right)_{\text{coherent}} + \left(\frac{d\sigma}{d\Omega}\right)_{\text{incoherent}} \tag{2.11}$$

It is clear from eqns (2.10) and (2.11) that interference effects can only arise from the coherent scattering and is proportional to the mean scattering squared $|\bar{b}|^2$. Deviations from the mean scattering lead only to incoherent scattering that is proportional to the variance of the distribution $\overline{|b - \bar{b}|^2}$. This result was introduced in terms of any deviation from the mean scattering; however, this is strictly true only if there is no correlation between the scattering length and position within

the scattering sample. This distinction has lead historically to a divergence of nomenclature. The term incoherent scattering is reserved for sources of scattering potential variation that were inviolate and considered a natural part of the system in the early days of neutron scattering research, that is, spin incoherence and isotope incoherence.[12] Other sources of scattering potential variation such as alloying can, for the same system, be made to vary from truly random (i.e. incoherent) to fully ordered by simple heat treatment procedures. In these cases, scattering due to deviation from the mean is termed diffuse scattering (see Chapter 10).

2.3.3 Coherent scattering lengths and absorption cross sections

Many of the applications of neutron powder diffraction rely on the different systematics of the scattering length (compared with X-rays) and the low absorption of most elements for thermal neutrons. It is therefore appropriate to reflect on the numerical values taken by the coherent scattering length b_{coh} (hereafter b) and the total scattering cross section σ_{s} for some prominent examples. Table 2.2 summarizes the coherent scattering length and absorption cross section for a number of elements and isotopes. A complete listing is given in Koester *et al.* (1991). Alongside the scattering lengths in Table 2.2, X-ray form factors in electron units at $\sin\theta/\lambda = 0.3$ are given for comparison.

Variation of b between isotopes of the same element is demonstrated using Cu, at the top of the table, as an example. The scattering lengths of ^{63}Cu and ^{65}Cu differ by 40%. These are then weighted by the natural abundance of the isotopes giving the mean value 7.718 fm. The ability to distinguish between adjacent elements in the periodic table is illustrated by comparing Cu with Zn. As a rough rule of thumb, the ability to distinguish different elements (isotopes, ions, etc.) is proportional to the square of the ratio of their scattering lengths. With thermal neutrons, the scattering length of Cu is 36% greater than the scattering length of Zn whereas with X-rays, the difference is only 4%. Therefore, in structures containing both Cu and Zn, these elements are far more readily distinguished using neutrons. Modern X-ray diffraction methods can in some instances resolve differences as small as this; however in ionically bonded crystals, where the oxidation state of each element may not be known, the uniqueness of the solution cannot be guaranteed. Using Cu and Zn, for example, Cu^{1+} and Zn^{2+} have essentially identical X-ray scattering characteristics – especially as far as powder diffraction is concerned. At the other end of the scale is the ability with neutrons to locate low atomic number elements in the presence of heavy elements. From Table 2.2 we can see that Pb and O have comparable neutron scattering lengths whereas with X-rays the scattering from oxygen is some 215 times weaker than that from lead (*cet. par.*). Even more extreme is the comparison with hydrogen, an element that is extremely difficult

[12] In more recent times it has become possible to alter the isotopic mixture which substantially alters the isotope incoherence and the use of polarised neutrons strongly affects the spin incoherence. The terminology has remained.

Table 2.2 Coherent scattering lengths and absorption cross sections for selected isotopes from Koester *et al.* (1991).

Element	Isotope	b_{coh} (fm)	$\sigma_{s(tot)}$ (10^{-24} cm^2)	σ_a (10^{-24} cm^2)	f	Isotopic abundance (%)
Cu		7.718(4)	8.03(3)	3.78(2)	19.9	
	63	6.43(2)				69.17
	65	10.61(2)				30.83
Zn		5.680(5)	4.131(10)	1.10(2)	20.8	
Pb		9.405(3)	11.118(7)	0.171(2)	60.9	
O		5.803(4)	4.232(6)	0.00019(2)	4.09	
C		6.6460(12)	5.551(3)	0.00350(7)	2.50	
	12	6.6511(16)				98.90
	13	6.19(9)				1.10
Zr		7.16(3)	6.46(14)	0.185(3)	27.0	
Ti		−3.438(2)	4.35(3)	6.09(13)	13.2	
	46	4.93(6)				8.2
	47	3.63(12)				7.4
	48	−6.08(2)				73.8
	49	1.04(5)				5.4
	50	6.18(8)				5.2
H		−3.739(1)	82.02(6)	0.3326(7)	0.25	
	1	−3.741(1)				99.985
	2	6.671(4)				0.015
	3	4.792(27)				–
B		5.30(4)−2.13(3)i	5.24(11)	767(8)	1.99	
	10	−0.1(3)−1.006(3)i	3.1(4)	3835(9)		20.0
	11	6.65(4)	5.77(10)	0.0055(33)		80.0
Gd		6.5(5)	180(2)	49700(125)	45.9	
	155	6.0(1)−17.0i	66(6)	61100(400)		14.8
	157	−11.4(2)−71.9(2)i	1044(8)	259000(700)		15.7
V		−0.0443(14)	0.510(6)	0.508(4)	14.0	

Where not stated, the values are for the natural isotopic mix.

to locate with X-rays. In the field of metal hydrides, neutron powder diffraction has been the principal structural analysis tool for more than five decades. The negative scattering length of hydrogen provides extra contrast, however the large incoherent scattering cross section $\left(\sigma_s \approx 80 \times 10^{-24}\,\text{cm}^2\right)$ makes the use of H experimentally difficult. Incoherent scattering removes neutrons from the incident beam – acting in an analogous way to absorption. Unlike absorbed neutrons though, the incoherently scattered neutrons find their way into the background of the diffraction pattern. In a powder diffraction experiment, the entire sample scatters into the background whereas only those crystallites oriented to satisfy Bragg's law scatter coherently into the diffracted peaks (see §2.4). Taken together

these effects lead to very poor diffraction patterns. One remedy is to use the heavier isotope deuterium (^{2}H or sometimes D) which has greatly reduced incoherent scattering.

The existence of two hydrogen isotopes with scattering lengths of opposite sign has been used to advantage in some small angle neutron scattering (SANS) studies of solutions and suspensions by 'contrast matching'. By mixing heavy and light water in the correct proportions, an average scattering length of zero can be obtained. Particles or molecules within the solution are then the only scattering objects contributing to the SANS pattern.

A solid-state analogue has been known for some time in the form of 'null-matrix' alloys. The first and most widely exploited example was an alloy of titanium and zirconium (Sidhu *et al.* 1956). Ti and Zr adopt the same room temperature crystal structure (hexagonal close-packed) and they form a random solid solution.[13] From the values of b in Table 2.2, it can be seen that an alloy of 32.44 at% Zr and 67.56 at% Ti will have an average scattering length of zero. Aside from their novelty value, these alloys have found application in the construction of ancillary equipment for neutron diffraction including sample holders and high-pressure cells. A form of contrast matching is occasionally used in the solution of the crystal structures of solids. A good example is the use by Thompson *et al.* (1987b) of isotopically enriched Ni to prepare $LaNi_5D_6$ such that the majority of the coherent scattering was from the D. This enabled previously unknown deuterium ordering to be discovered and characterized.

Finally, from Table 2.2 it can be seen that, in general, the absorption cross section is quite small, often smaller than the scattering cross section. Two counter examples are shown, B and Gd. One isotope of boron, ^{10}B, has a resonance at thermal neutron energies. This leads to a complex scattering length and strong absorption. Even though the natural isotopic abundance of ^{10}B is only 20%, natural boron nonetheless has a high-absorption cross section and is used as a neutron-shielding material in various forms. The last example given is gadolinium which has two strongly resonant isotopes and extreme absorption. The absorption is so effective that even a thin layer (Gd paint) provides sufficient absorption for many applications. It is used in the preparation of Soller collimators and other precise instrumentation.

2.3.4 Magnetic scattering

Our treatment so far has dealt only with nuclear scattering. As mentioned at the beginning of §2.3.1, the magnetic moment of the neutron also allows it to interact with the orbital and spin magnetic moments of atoms in a solid. Although only a small fraction of the periodic table elements carry such magnetic moments,

[13] Some short-range ordering occurs in some circumstances depending on the thermal history of the alloy.

the vector nature of these magnetic moments ensures a vast array of possible magnetic structures (§2.2.6) and causes the magnetic scattering to be a vector process rendering a simple scalar scattering length (e.g. b_{coh}) insufficient.

The magnetic scattering from a single atom (or ion) is due to unpaired electron spins. Since the scattering object, the electron distribution, is comparable in size to the wavelength of thermal neutrons, interference effects occur leading to a magnetic form factor. Figure 2.16 illustrates this for the Mn^{2+} ion. The X-ray scattering form factor is shown for comparison and it can be seen that the magnetic form factor falls more rapidly because only outer electrons are involved in magnetic scattering. This has implications for the design of magnetic neutron diffraction experiments that are discussed in Chapter 7.

The geometry of magnetic neutron scattering is shown in Fig. 2.17. Unit vectors, $\hat{\boldsymbol{\kappa}}$, $\hat{\boldsymbol{\mu}}$, and $\hat{\boldsymbol{P}}$ define the scattering vector, magnetic moment of the atom, and polarization vector, respectively. It is useful to define a magnetic interaction vector $\boldsymbol{q}$ as:

$$\boldsymbol{q} = \hat{\boldsymbol{\kappa}} \times \left(\hat{\boldsymbol{\mu}} \times \hat{\boldsymbol{\kappa}}\right) = \hat{\boldsymbol{\mu}} - \left(\hat{\boldsymbol{\kappa}} \cdot \hat{\boldsymbol{\mu}}\right)\hat{\boldsymbol{\kappa}} \quad \text{with } |q| = \sin\alpha \tag{2.12}$$

where α is the angle between $\hat{\boldsymbol{\kappa}}$ and $\hat{\boldsymbol{\mu}}$. We may then write the differential magnetic neutron scattering cross section per atom for an ordered magnetic structure:

$$\left(\frac{d\sigma}{d\Omega}\right)_{\text{mag}} = q^2 S^2 \left(\frac{e^2\gamma}{m_e c^2}\right)^2 f^2 \tag{2.13}$$

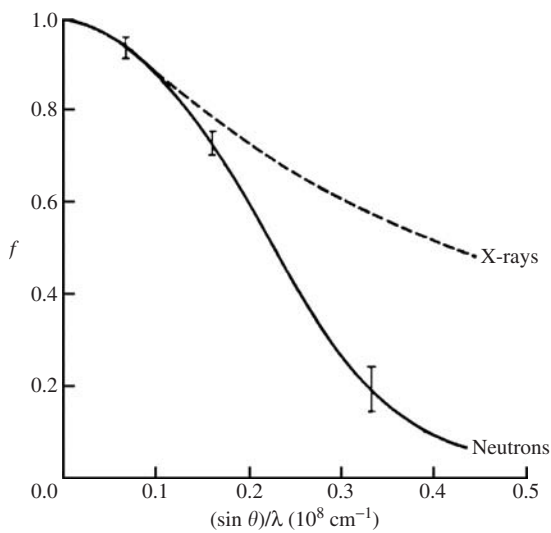

Fig. 2.16 The magnetic form factor for Mn^{2+} compared with the (normalized) X-ray form factor (Bacon 1975).

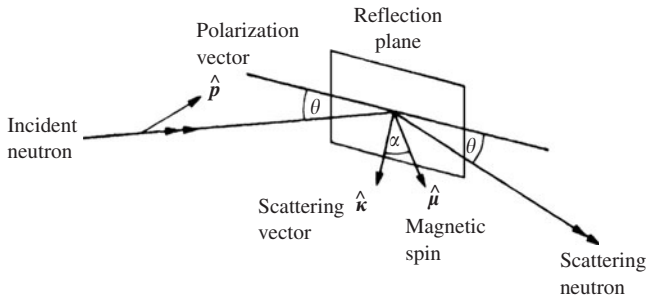

Fig. 2.17 The geometry of magnetic scattering (adapted from Bacon 1975).

in the special case where spin moments only are to be considered. Here S is the spin quantum number of the atom involved, e is the charge on the electron, m_e its mass, c the speed of light, γ is the magnetic moment of the neutron (1.913 nuclear magnetons), and f is the magnetic form factor. It is important to note that, through the quantum number S, the scattering cross section depends on the valence state of the atom or ion (e.g. Fe^{2+} and Fe^{3+} have S equal to 2 and 5/2, respectively, as well as different form factors). In cases where orbital moments also contribute, $2S$ is replaced by gJ where g is the Landé splitting factor:

$$g = 1 + \frac{J(J+1) + S(S+1) - L(L+1)}{2J(J+1)} \tag{2.14}$$

For a system containing many atoms, the degree of correlation between the magnetic moments of the atoms is critical. As discussed in §2.2.6, this may vary from zero (paramagnetic) to close to unity (e.g. ferromagnet far below the Curie temperature). For a completely disordered or paramagnetic system, the average of q over all orientations is $\pi/4$ and the scattering is incoherent, that is, it gives rise to no interference or diffraction effects. It does however contribute to the background of the powder pattern. This contribution is not isotropic like the nuclear incoherent scattering discussed in §2.3.2 because of the form factor f. In fact, this was one of the most successful early methods for measuring magnetic form factors.

When the atomic magnetic moments are highly correlated as in the ordered magnetic structures, the magnetic scattering is coherent and gives rise to strong diffraction effects.[14] This is the primary type of magnetic scattering of interest in this volume. Just as in the discussion of coherent nuclear scattering, it was convenient to define a coherent scattering length b_{coh}, we define the magnetic

[14] At intermediate levels of correlation, the treatment is complex and forms the subject of a separate volume in this series (Hicks 1995).

scattering length:

$$p = \left(\frac{e^2\gamma}{2m_e c^2}\right) gJf \tag{2.15}$$

An important consideration is how the magnetic scattering interacts with the nuclear scattering. The vector nature of magnetic scattering means that the magnetic scattering is highly dependent on the polarization of the incident neutron beam. The total cross section may be considered as containing five terms:

$$\sigma_{\text{tot}} = \sigma_{\text{coh}} + \sigma_{\text{incoh}} + \sigma_{\text{NM}} + \sigma_{\text{M}} + \sigma_{\text{pol}} \tag{2.16}$$

where σ_{coh} and σ_{incoh} are the coherent and incoherent nuclear scattering cross sections previously defined, σ_{NM} is the nuclear–magnetic interference term, σ_{M} is the magnetic scattering cross section (eqn (2.13)), and σ_{pol} is the polarization-dependent term. Ignoring incoherent scattering and considering only simple magnetic structures with co-linear moments, the differential cross section becomes:

$$\frac{d\sigma}{d\Omega} = b^2 + 2bp\hat{\boldsymbol{P}} \cdot \boldsymbol{q} + p^2 q^2 \tag{2.17}$$

where $\hat{\boldsymbol{P}}$ is a unit vector defining the polarization direction of the incident neutron beam. Note that in this very simple structure, the pure polarization terms (σ_{pol}) are zero and we are left with the nuclear, magnetic, and nuclear–magnetic interaction terms only. If the incident neutron beam is unpolarized, the interaction term averages to zero (i.e. $\hat{\boldsymbol{P}}$ can take all possible orientations) leaving:

$$\frac{d\sigma}{d\Omega} = b^2 + p^2 q^2 \tag{2.18}$$

Examples of how these effects are manifest in neutron powder diffraction patterns are given in Chapter 7.

2.3.5 Inelastic scattering

We have proceeded thus far on the assumption that all of the interactions between incident neutrons and atoms are elastic.[15] In reality this is not the case, and inelastic collisions are quite common. During the inelastic collision of a neutron and an atom, the neutron energy (and hence wavelength) is altered. The energy exchange is with some dynamic process in the sample – either quantized lattice vibrations (phonons) or quantized spin fluctuations (magnons). Inelastic scattering is not generally of primary interest in powder diffraction experiments. It does however give rise to two important effects that need to be taken into account in very careful work.

[15] Tantamount to assuming infinite mass for the scattering atom.

First, the scattering cross section varies depending on the degree to which the atom is bound. The relationship is

$$\sigma_{\text{free}} = \left(\frac{A}{A+1}\right)^2 \sigma_{\text{bound}} \tag{2.19}$$

where A is the atomic mass. This is most apparent in hydrogen where the bound cross section is four times the free cross section. In general, we use σ_{bound} when studying condensed states of matter and in any case the difference rapidly falls to zero as the atomic mass increases. In some dilute hydride systems, some account for this effect may be required.

Second, inelastically scattered neutrons do not take part in the strong diffraction effects that are of primary concern in powder diffraction patterns. However, they are not isotropically distributed. Although the inelastic interaction is with a highly correlated dynamic process in the sample, it is common for the scattering to peak under the elastic diffraction peaks. Examples include thermal diffuse scattering (§10.2) and quasi-elastic scattering (e.g. see Marshall and Lovesey 1971). In principle, it is possible to remove the inelastically scattered neutrons with the aid of an analyser crystal between the sample and the detector. The crystal is set to diffract only elastically scattered neutrons into the detector. This method is seldom used in neutron powder diffraction as it seriously lowers the intensity of the recorded diffraction pattern and limits the kinds of detector configurations that may be employed.

2.4 THE POWDER DIFFRACTION PATTERN

To this point, we have described the characteristics of the neutrons used for diffraction (§2.1), the kinds of short- and long-range physical and chemical order that can be found in condensed matter (§2.2) and focussed on the scattering of thermal neutrons from individual atoms in the scattering system (§2.3). It is now possible to examine how all three of these combine to give a neutron powder diffraction pattern. It has already been apparent in §2.3.2 that the coherent scattering from the system involves the phase relationships between scattering from the different atoms in the system. This phase term lends to strong interference effects particularly in systems such as crystalline solids, with strong correlations between atom positions. Hence we begin our discussion with diffraction from a perfect crystalline solid.

2.4.1 The directions of diffracted beams from a perfect crystal

Consider a two-dimensional lattice with a unit scattering body placed rigidly at each lattice point.[16] The phase difference between two lattice points can be visualized

[16] Later we will replace these with atoms – the result is substantially the same.

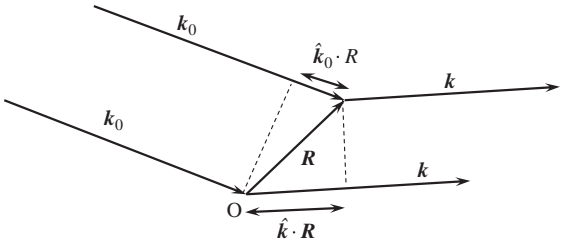

Fig. 2.18 Scattering from two lattice points located at O and O + $\boldsymbol{R}$ of an incident wave of wavevector $\boldsymbol{k}_0$ into a scattered wave of wavevector $\boldsymbol{k}$. The unit vectors $\hat{\boldsymbol{k}}_0$ and $\hat{\boldsymbol{k}}$, given by $\frac{\lambda}{2x}\boldsymbol{k_0}$ and $\frac{\lambda}{2\pi}\boldsymbol{k}$ define the path difference, $\hat{\boldsymbol{k}} \cdot \boldsymbol{R} - \hat{\boldsymbol{k}}_0 \cdot \mathbf{R} = \frac{\lambda}{2\pi}(\boldsymbol{k} - \boldsymbol{k_0}) \cdot \mathbf{R}$, between waves scattered at O and at O + $\boldsymbol{R}$.

with the aid of Fig. 2.18. In the figure, incident neutrons with wavevector $\boldsymbol{k}_0$ are scattered at the origin and a lattice point defined by the vector $\boldsymbol{R}$ in a direction defined by the wavevector $\boldsymbol{k}$ into a distant detector. The wavevectors are defined as vectors in the propagation direction of length $2\pi/\lambda$. The path difference is then $\frac{\lambda}{2\pi}(\boldsymbol{k} - \boldsymbol{k}_0) \cdot \boldsymbol{R}$ and the phase difference $(\boldsymbol{k} - \boldsymbol{k}_0) \cdot \boldsymbol{R}$ where $(\boldsymbol{k} - \boldsymbol{k}_0)$ is known as the scattering vector and is given the symbol $\boldsymbol{\kappa}$. The contribution of the lattice point at $\boldsymbol{R}$ to the scattered neutron wave will therefore involve the phase term, $\exp(i\boldsymbol{\kappa} \cdot \boldsymbol{R})$. Using the earlier definition of the wavevectors, the magnitude of the scattering vector can be easily shown to be

$$\kappa = \frac{4\pi \sin\theta}{\lambda} \tag{2.20}$$

Recalling that a crystal lattice may be considered as being composed of many sets of parallel planes, we next consider diffraction from a single plane of lattice points. If the origin is chosen to be within the same plane, there are only two conditions giving constructive interference (i.e. a phase shift of zero). These are (i) $\boldsymbol{k}$ parallel to $\boldsymbol{k}_0$, that is, in the direction of the transmitted beam or (ii) scattering vector $\boldsymbol{\kappa}$ perpendicular to the lattice plane so that all $\boldsymbol{\kappa} \cdot \boldsymbol{R} = 0$. In the second case, the diffracted beam makes the same angle θ with the diffracting plane as the incident beam does. This symmetrical geometry has led to the diffracted beams being commonly referred to as 'reflections'.

As we know from §2.2.1, a perfect crystal lattice is not planar or two-dimensional but rather three-dimensional. We can however consider it to be constructed from many planes of atoms stacked together. We have already considered how planes in a crystal can be described by the three Miller indices (*hk1*). Recalling that the Miller indices (*hkl*) actually describe not one but the entire stack of identical planes, we can analyse the phase shift for neutrons scattered from successive planes with the aid of Fig. 2.19. In the figure we can see that the path difference for neutrons reflected by successive planes is $2d_{hkl} \sin\theta$, where d_{hkl} is the distance between

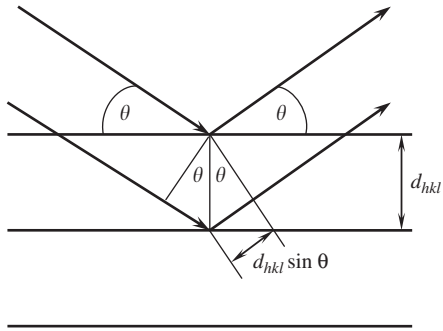

Fig. 2.19 Schematic illustration of how the path length difference between successive planes in a crystal is given by $2d_{hkl}\sin\theta$ leading to the familiar form of Bragg's law.

successive planes in the stack. The interplanar spacing is a very important concept in powder diffraction and we will return to it soon.

When the path length difference is an integral number of wavelengths, $n\lambda$, then constructive interference will occur between beams diffracted from all planes in the stack[17] leading to the well-known form of Bragg's law:

$$n\lambda = 2d_{hkl}\sin\theta \tag{2.21}$$

It is apparent that two experimental arrangements may be used to record a powder diffraction pattern from many types of crystal planes simultaneously. In the first, a single fixed wavelength is used and detectors are either scanned or positioned in a continuous arc over a wide range of θ (commonly 0°–80° θ or 0°–160° 2θ). In the second, the detector(s) are at a fixed diffraction angle θ_D and neutrons of many wavelengths are used to record the pattern. This method requires a precise method of determining the wavelength of the neutrons entering the detector(s) – a requirement easily met by pulsing or chopping the incident neutron beam and using the neutron time of flight (TOF) to determine the velocity and hence the wavelength from eqn (2.2). These two alternative arrangements will be referred to throughout the book as 'constant wavelength (CW)' and 'time-of-flight (TOF)' experiments, respectively.

Returning to our consideration of diffraction, we can simplify the task of representing a three-dimensional crystal composed from many types of infinite stacks of planes by using the reciprocal lattice concept. We present here only the essential elements and refer the interested reader to standard works on crystallography and solid-state physics (Kittel 1976; Cullity 1978; Hammond 1990).

[17] We are considering only kinematic diffraction here where each plane is assumed to be irradiated by an incident beam unmodified by its passage through the preceding planes, that is, no extinction effects are considered.

For every 'real' crystal lattice with translation vectors $\boldsymbol{a}$, $\boldsymbol{b}$, and $\boldsymbol{c}$, a *reciprocal lattice* may be defined with translation vectors given by

$$\boldsymbol{a}^* = s\left(\frac{\boldsymbol{b}\times\boldsymbol{c}}{\boldsymbol{a}\cdot(\boldsymbol{b}\times\boldsymbol{c})}\right)$$
$$\boldsymbol{b}^* = s\left(\frac{\boldsymbol{c}\times\boldsymbol{a}}{\boldsymbol{a}\cdot(\boldsymbol{b}\times\boldsymbol{c})}\right)$$
$$\boldsymbol{c}^* = s\left(\frac{\boldsymbol{a}\times\boldsymbol{b}}{\boldsymbol{a}\cdot(\boldsymbol{b}\times\boldsymbol{c})}\right) \tag{2.22}$$

where s is an arbitrary scaling constant and the quantity $\boldsymbol{a}\cdot(\boldsymbol{b}\times\boldsymbol{c})$ in the denominator represents the unit cell volume (V_c). This definition implies $\boldsymbol{a}^*\cdot\boldsymbol{a} = s$, $\boldsymbol{a}^*\cdot\boldsymbol{b} = 0$, and so on. Note that the wave vectors $\boldsymbol{k}$, $\boldsymbol{k}_0$, and the scattering vector $\boldsymbol{\kappa}$ are in reality vectors in reciprocal space (consider their units $(\text{Å})^{-1}$). It is a fundamental property of the reciprocal lattice that each infinite stack of planes (hkl) in the crystal is represented by a single point. Such a point in reciprocal space is often considered to lie at the end of a reciprocal space vector defined by

$$\boldsymbol{H}_{hkl} = h\boldsymbol{a}^* + k\boldsymbol{b}^* + l\boldsymbol{c}^* \tag{2.23}$$

where h, k, and l are integers.

$\boldsymbol{H}_{hkl}$ is always perpendicular to the real space plane (hkl) and has a length given by s/d_{hkl}, that is, proportional to the reciprocal of the interplanar spacing. The astute reader will have noted that the real and reciprocal spaces are analogous to the time and frequency domains in signal processing and will not be surprised when we later discover that it is convenient to move between the two spaces using Fourier transforms. The significance of the reciprocal lattice in understanding diffraction is firstly apparent by re-writing Bragg's law as $4\pi\sin\theta/\lambda = 2\pi/d_{hkl}$ or taking note of eqn (2.20), we can write[18]

$$|\boldsymbol{\kappa}| = 2\pi\,|\boldsymbol{H}_{hkl}| \tag{2.24}$$

Since both the scattering vector (see Fig. 2.19) and reciprocal lattice vector $\boldsymbol{H}_{hkl}$ are perpendicular to the diffracting planes (hkl), it is not difficult to extend the equality that represents diffraction in reciprocal space to

$$\frac{\boldsymbol{\kappa}}{2\pi} = \boldsymbol{H}_{hkl} \quad\text{or}\quad \frac{(\boldsymbol{k}-\boldsymbol{k_0})}{2\pi} = \left(h\boldsymbol{a}^* + k\boldsymbol{b}^* + l\boldsymbol{c}^*\right) \tag{2.25}$$

That is, diffraction can only occur if the scattering vector divided by 2π, ends on a reciprocal lattice point. A convenient graphical representation for fixed wavelength experiments is the Ewald construction where a sphere of radius $1/\lambda$ is superimposed on to the reciprocal lattice of the crystal. A two-dimensional representation is shown in Fig. 2.20. The incident wave vector $\boldsymbol{k_0}$ has only one direction but because

[18] Here we adopt the crystallographic convention by taking $s = 1$. In some physics texts, the value $s = 2\pi$ is used.

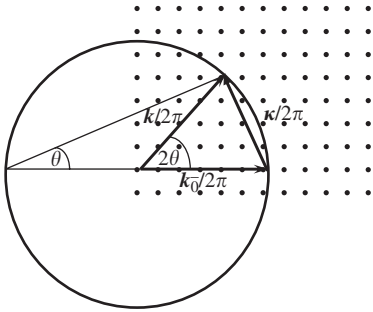

Fig. 2.20 Ewald construction in reciprocal space. Shown is a two-dimensional section through the sphere of reflection of radius $1/\lambda$. Incident and scattered wavevectors $\boldsymbol{k_0}/2\pi$ and $\boldsymbol{k}/2\pi$ and the scattering vector $\boldsymbol{\kappa}/2\pi$ are shown in bold. The diffraction condition is exactly satisfied when $\boldsymbol{\kappa}/2\pi$ ends on a reciprocal lattice point.

the scattered wave can in principle take any direction, it is represented by the sphere of reflection (a circle in Fig. 2.20). The condition in eqn (22) is met whenever the sphere intersects a reciprocal lattice point. For a given incident wave vector $\boldsymbol{k}_0$, the number of diffracted beams is determined by the number of reciprocal lattice points on the sphere of reflection which in most crystal orientations will be zero. In some orientations, one and occasionally more than one diffracted beam will be excited.

To visualize diffraction from an ideal polycrystalline sample in which uniformly sized, strain and defect-free crystallites are randomly oriented is our next goal. Here we require a figure such as Fig. 2.21.

The effect of a statistically large number of crystallites perfectly randomly oriented is to take an ensemble of superimposed reciprocal lattices in every possible orientation. This means that for a given value of d_{hkl} the single reflection produced in Fig. 2.20 is replaced by a continuum of diffracted beams all making the Bragg angle 2θ with the transmitted beam. These beams form a cone centred on the incident beam direction. Since a crystal has many (hkl) planes with a variety of d-spacings (d_{hkl}), a constant wavelength powder diffraction pattern consists of sets of concentric cones known as Debye–Scherrer cones, which intercept a detector arc, usually placed in a horizontal plane.[19] The situation is illustrated in Fig. 2.22. The resulting diffraction pattern, plotted as neutron counts per angular interval (I) versus the diffraction angle 2θ, is also shown in Fig. 2.22. It is clear from this treatment that all planes with the same d_{hkl} will be superimposed in the powder pattern.

The Ewald sphere construction for TOF experiments is more complex. First, because a wide band of wavelengths is used, there is no longer a single Ewald

[19] This differs from X-ray powder diffractometers which are usually mounted so that the detector sweeps out a vertical arc.

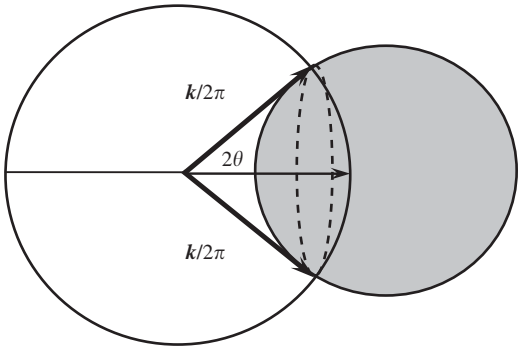

Fig. 2.21 Ewald construction for powder diffraction. The random orientation of crystallites in the sample cause the reciprocal lattice points to be replaced by concentric spheres of which only one is shown. The intersection of this sphere with the sphere of reflection leads to a cone of diffraction indicated by the dashed line.

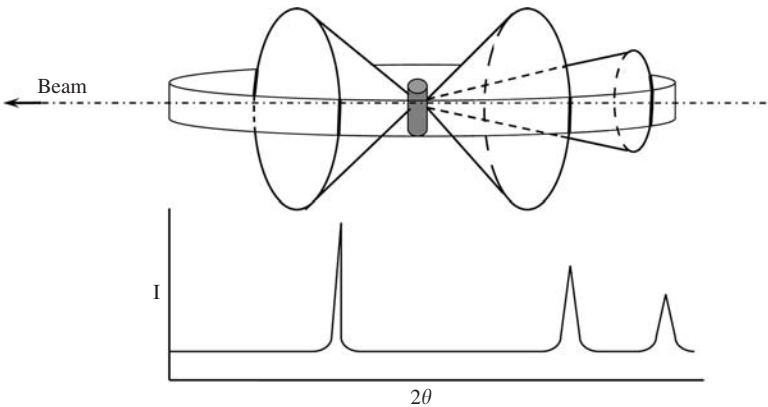

Fig. 2.22 Interception of Debye–Scherrer cones of diffracted neutrons by a horizontal detector bank or position sensitive detector in the standard CW diffractometer arrangement, and the resulting diffraction pattern.

sphere but rather a continuum of spheres ranging from the innermost of radius $1/\lambda_{max}$ to the outermost at a radius $1/\lambda_{min}$. Second, the diffraction angle is usually fixed in TOF experiments. Therefore the directions of $\boldsymbol{k}_0$ and $\boldsymbol{k}$ are constant. In general, even for a single crystal, this continuum of Ewald spheres will intersect many reciprocal lattice points and hence excite many diffracted beams. All of these lie on a conic surface similar to the Debye–Scherrer cone. Randomization of the reciprocal lattice orientation to simulate a random polycrystal merely has the effect

of smoothing out the cone to make it continuous, like a genuine Debye–Scherrer cone.

The final stage in understanding the directions in which diffracted beams will be produced is to examine the connection between the crystal structure (described in §2.2.1) and the interplanar spacing d_{hkl}. Because the interplanar spacings will be uniquely determined by the unit cell geometry (i.e. the crystal class – cubic, tetragonal, etc.) and the cell dimensions, the direction of diffracted beams is determined purely by the shape and size of the unit cell. As a simple example, for a cubic structure, we have

$$\frac{1}{d^2} = \frac{h^2 + k^2 + l^2}{a^2} \tag{2.26}$$

similarly, for a tetragonal crystal structure,

$$\frac{1}{d^2} = \frac{h^2 + k^2}{a^2} + \frac{l^2}{c^2} \tag{2.27}$$

Appropriate equations for the other crystal classes are given in Appendix 1 along with relationships for the unit cell volume and interplanar angles. Substituting eqn (2.27) into Bragg's law gives

$$\sin^2\theta = \left[\frac{h^2 + k^2}{a^2} + \frac{l^2}{c^2}\right]\frac{\lambda^2}{4} \tag{2.28}$$

For known unit cell dimensions, this can be used to calculate the Bragg angle in a constant wavelength experiment or the neutron wavelength in a TOF experiment. Alternatively, measured Bragg angles or wavelengths can be used to determine unknown lattice parameters using the methods discussed in §4.4.

Although precisely measured directions of diffracted beams can tell us very accurately what the unit cell parameters of the structure are, they tell us nothing about the contents of the unit cell – for that we must determine and understand the intensities of the diffracted beams.

2.4.2 Adding the basis – the intensity of diffracted beams from an ideal polycrystalline sample

In our discussion of diffraction from a perfect crystal, we have treated the crystal as though it were composed of perfect planes of uniform scattering density. This is far from true. First, the scattering density is concentrated within atoms (or nuclei for nuclear neutron diffraction) that may have different scattering lengths (b) and second, for any but the simplest structures, there are relatively few flat planes of atoms. Fortunately neither of these invalidates eqn (2.25) governing the conditions under which diffracted beams are allowed to form. Equation (2.25) may be re-interpreted as stating that any 'objects' whose separation parallel to the scattering vector is d_{hkl} will scatter in-phase. These same objects (atoms say) will

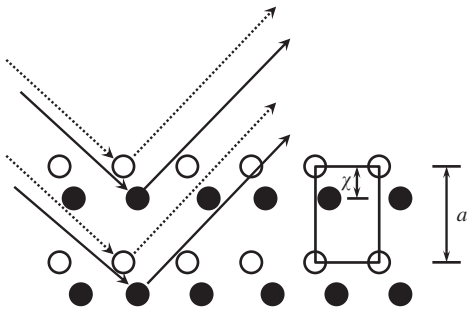

Fig. 2.23 Diffraction from a simple two-dimensional structure with a basis comprising two atoms; one shown as a filled circle and the other as an open circle. The unit cell is shown outlined as are the unit cell parameter a and the coordinate χ of the dark atom parallel to the scattering vector (perpendicular to the diffracting planes).

form scattered waves that are partly or wholly out of phase with other atoms not so spaced. Hence the phase of the total scattered wave will be altered. The situation is illustrated in Fig. 2.23 for a simple two-dimensional example.

At the Bragg angle for diffraction from the planes of atoms shown, the phase difference between the pairs of light atoms is 2π ($\equiv$ zero). The phase difference between the pairs of dark atoms is also 2π ($\equiv$ zero). However, the phase difference between adjacent rows of dark and light atoms is $2\pi hx$ ($x = \chi/a$) leading to some cancellation and reduced intensity of the scattered wave. More generally, in three dimensions the phase of a wave scattered by a dark atom relative to a wave scattered by a light atom at the origin is

$$\phi = 2\pi\left(hx + ky + lz\right) \tag{2.29}$$

where (x, y, z) is the fractional co-ordinate of the atom within a unit cell of dimensions a, b, c and h, k, and l are the Miller indices of the diffracting plane.

In addition to these phases, amplitude differences are introduced when atoms of different scattering length co-exist in the structure, for example, the light and dark atoms in Fig. 2.23. The wave scattered by a particular atom may then be expressed as

$$A\mathrm{e}^{i\phi} = b\mathrm{e}^{2\pi i(hx+ky+lz)} \tag{2.30}$$

and the total resultant wave or s*tructure factor* (F) is

$$F_{hkl} = \sum_n b_n \mathrm{e}^{2\pi i(hx_n+ky_n+lz_n)} \tag{2.31}$$

The intensity of the diffracted beam is given by $|F_{hkl}|^2$. The structure factor is a key quantity in diffraction analysis and will be referred to many times in the succeeding chapters.

We can make an obvious connection with the previous section by writing the position vector of the nth atom as $\boldsymbol{r}_n$ whereupon eqn (2.31) becomes

$$F_{hkl} = \sum_n b_n e^{2\pi i(\boldsymbol{H}_{hkl}\cdot\boldsymbol{r}_n)} \tag{2.32}$$

Equations (2.31) and (2.32) are nothing more than the Fourier transforms of the crystal structure sampled at the reciprocal lattice points. So if we weight the reciprocal lattice points with the diffracted intensity, a mathematically accurate model of the diffraction from a single crystal is obtained. This is intuitively correct since both the real to reciprocal space transformation and the diffraction process produce a geometrical representation of the crystal structure within which infinite stacks of planes of atoms appear as individual points or spots. If a Fourier transform took us from real space to reciprocal space it is evident that an inverse transform might take us in the reverse direction to recover the distribution of scattering density in the unit cell. This process will be addressed in more detail in Chapters 5 and 6. Here we content ourselves with noting that in attempting to compute the reverse transform mentioned earlier, we encounter a serious impediment. The structure factor F is a complex number comprising both amplitude and phase. The measured quantities, however are intensities which as just noted, are real quantities proportional to $|F|^2$. The phase of the diffracted beam is therefore lost. This so-called 'phase problem' has tormented crystallographers since early last century. It has led to very creative experimental and analytical methods for circumventing it to solve unknown crystal structures. These methods will be dealt with in more detail in Chapter 6.

In the discussion so far, we have noted that the diffracted intensity is *proportional* to $|F_{hkl}|^2$. There are quite a number of physical and geometrical factors that modify the intensity observed for a particular set of diffracting planes (hkl) during a powder diffraction experiment.

Atomic displacement parameters (temperature factors)

In §2.2.2, the effect of thermal and static atom displacements in reducing the perfection of a crystal structure was introduced. The scattering factor (or length) of the jth atom now comprises a 'stationary' part (b_j, say) and a dynamic or displacement part (T_j). In the following we take $\boldsymbol{\kappa}$ as the scattering vector, $\boldsymbol{u}$ as the total displacement from the summation of all vibrational modes at the time of measurement, and the brackets $\langle\,\rangle$ denote the time average. The probability density function (p.d.f.) $p_j(\boldsymbol{u})$ represents the probability of finding the atom at a certain position with respect to the mean position described in the ideal stationary structure. If the neutron scattering density of an atom $\rho_j(\boldsymbol{u})$ is represented as the convolution of the scattering density of a stationary atom $\rho_{jo}(\boldsymbol{u})$ with the probability density function $p_j(\boldsymbol{u})$:

$$\rho_j(\boldsymbol{u}) = \rho_{jo}(\boldsymbol{u}) * p_j(\boldsymbol{u}) \tag{2.33}$$

We can apply the convolution theorem and multiply the Fourier transforms of $\rho_{jo}(\boldsymbol{u})$ and $p(\boldsymbol{u})$. Recognizing that the Fourier transform of the stationary scattering density is just the atomic scattering length b_j, it can be seen that the Fourier transform of the vibrating atom scattering density $\rho_j(\boldsymbol{u})$ is nothing more than $b_j T_j$. It follows that the temperature factor T_j of an atom is the Fourier transform of its p.d.f.:

$$T_j(\boldsymbol{\kappa}) = \int p_j(\boldsymbol{u}) \exp(i\boldsymbol{\kappa} \cdot \boldsymbol{u})\, d^3u \tag{2.34}$$

where d^3u signifies that the integral is three-dimensional. The inverse Fourier transform of the temperature factor recovers the p.d.f.:

$$p_j(\boldsymbol{u}) = \frac{1}{(2\pi)^3} \int T_j(\boldsymbol{\kappa}) \exp(-i\boldsymbol{\kappa} \cdot \boldsymbol{u})\, d^3\kappa \tag{2.35}$$

The p.d.f. and temperature factors are Gaussian for harmonic oscillators and the transforms are readily conducted. A more compact form for the temperature factor of the jth atom to be used in intensity calculations is given by

$$T_j(\boldsymbol{\kappa}) = \exp\left[-\frac{1}{2}\left\langle(\boldsymbol{\kappa} \cdot \boldsymbol{u})^2\right\rangle\right] \tag{2.36}$$

The dot product represents the projection of the atom displacement onto the scattering vector[20] which gives rise to phase differences that reduce the diffracted intensity. More information concerning the use of displacement (or temperature) parameters in crystal structure refinement and the extraction of meaningful estimates of atom displacements from them is reserved for §5.5.2.

Lorentz factor

Readers familiar with X-ray diffraction will be aware of the corrections to integrated intensities made for the Lorentz factor and partial polarization of the X-rays by the diffraction geometry. These are usually combined into the Lorentz-polarization factor. Neutron beams do not suffer partial polarization on scattering and so only the Lorentz factor is appropriate. The Lorentz factor in powder diffraction is really a combination of three effects. First, it is found that the maximum height of diffraction peaks depends on the angular range over which some finite contribution is made to the diffracted beam at the exact Bragg angle θ_B (Cullity 1978). This quantity is proportional to $1/\sin\theta_B$. At the same time, the width of the diffraction peaks is proportional to $1/\cos\theta_B$. When combined, it is found that the integrated intensity of a Bragg reflection (I) is proportional to $(1/\sin\theta_B)(1/\cos\theta_B) = 1/\sin 2\theta_B$, other things being equal. Therefore peaks at very low and very high values of $2\theta_B$ are larger than those in the centre of the

[20] This is the only part of $\boldsymbol{u}$ that is relevant to the intensity of a given Bragg reflection with scattering vector $\boldsymbol{\kappa}$.

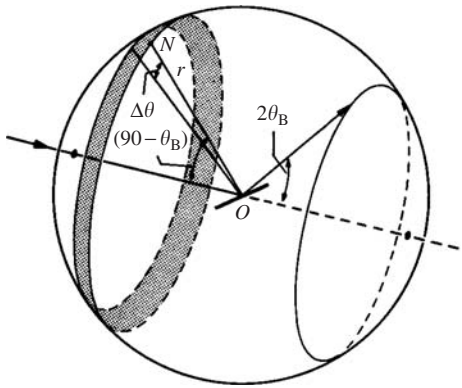

Fig. 2.24 Distribution of plane normals on a reference sphere as a function of 2θ (Cullity 1978).

pattern. This effect is quite general, that is, it is equally true of powder and single crystal diffraction peaks.

When only powder diffraction intensities are being considered, the relative populations of plane normals at different values of θ_B must also be accounted for. With reference to Fig. 2.24, it can be seen that the crystallites contributing exist in a narrow band (shaded) of width $r\Delta\theta$. The proportion of the total crystallite population (n/N) contained in such a band is the ratio of the shaded area to the total surface area of the sphere.

$$\frac{n}{N} = \frac{r\Delta\theta \cdot 2\pi r \sin(90 - \theta_B)}{4\pi r^2} = \frac{\Delta\theta \cos\theta_B}{2} \tag{2.37}$$

or a quantity proportional to $\cos\theta_B$ (since it is the dependence on the Bragg angle θ_B that is of primary concern here).

Finally, in most diffraction geometries, a detector of constant width (height) intercepts the Debye–Scherrer cones (or referring to Fig. 2.25, the bands of diffracting crystallites). Clearly the detection system receives a far greater proportion of the complete diffraction cone at low and high values of $2\theta_B$ than close to $2\theta_B = 90°$. This leads to a further dependence on $1/\sin 2\theta_B$.

When all three effects are combined, the Lorentz factor for powder diffraction becomes

$$L = \left(\frac{1}{\sin 2\theta}\right) \cdot \cos\theta \left(\frac{1}{\sin 2\theta}\right) = \frac{1}{4\sin^2\theta\cos\theta} \tag{2.38}$$

This function is illustrated in Fig. 2.26. The Lorentz factor for TOF diffractometers, with a fixed diffraction angle for each data point in the diffraction pattern (see §3.3), is given by

$$L = d^4 \sin\theta \tag{2.39}$$

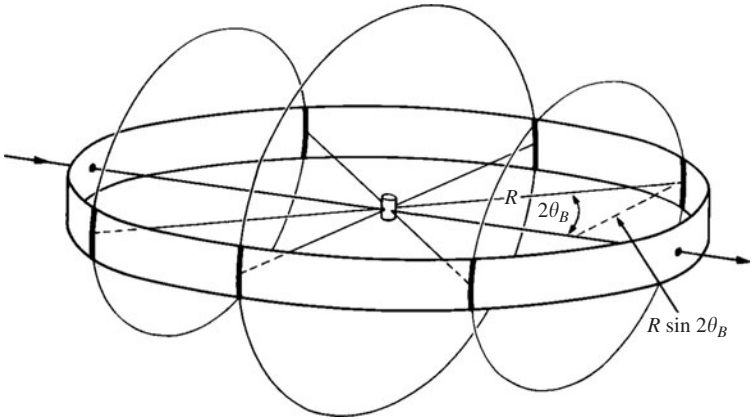

Fig. 2.25 Variation with 2θ of the proportion of a Debye–Scherrer cone that intercepts a detection aperture of fixed height for a conventional diffractometer (Cullity 1978).

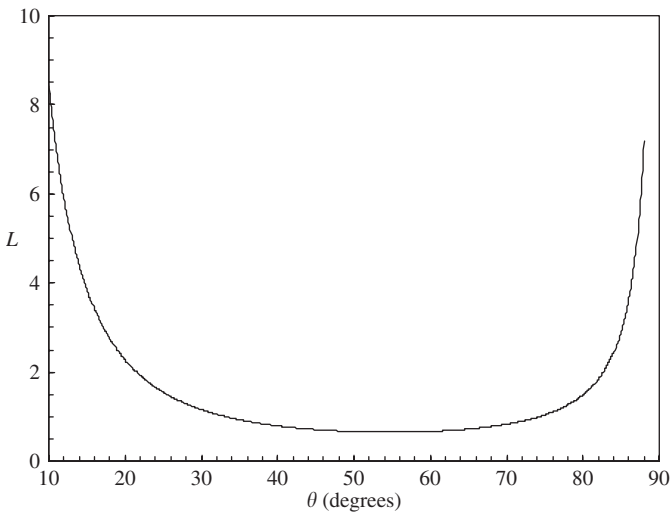

Fig. 2.26 Lorentz factor for powder diffraction as a function of θ.

Multiplicity

Due to the symmetry of crystal structures, all structures contain variants of diffracting planes that are to all intents identical. For example, the {111} planes of a cubic structure are all the same (see §2.2.1) and, having the same interplanar spacing, will all diffract at the same Bragg angle. There are eight cubic {111} planes. Other planes may be either less or more populous, for example, there are only 6 {100} type planes and 12 {110} planes. It follows that in a perfectly random collection

of crystallites, the intensity recorded from a more populous type of crystal plane will be proportionally greater than that from less populous planes. The number of equivalent (or identical) planes for a given (hkl) is termed the *multiplicity* of the plane type and here will be given the symbol J. As the crystal symmetry changes so too does the multiplicity. This coupled with small changes in d-spacing allow ready identification of the symmetry changes during some kinds of phase transition. For example, in the tetragonal crystal system, the $\{h00\}$ and $\{00l\}$ planes are different and have a multiplicity of 4 and 2, respectively. In the rhombohedral system, the $h00$ reflection remains unaltered ($J = 6$) whereas the $l\,l\,l$ reflection divides because the $l\,l\,l$-type reflections ($J = 2$) and the $\bar{l}\,l\,l$-type reflections ($J = 6$) have different d-spacings. If a powder diffraction study of a phase derived from a parent cubic phase shows splitting of the 200 reflection into two reflections with approximately 2:1 intensity ratio, the product is most likely tetragonal whereas if the 111 is split with a 3:1 intensity ratio then the product phase is likely to have rhombohedral symmetry. It is sometimes the case that planes that are unrelated have the same d-spacing (e.g. 333 and 511 or 330 and 411 in cubic structures). They will superimpose in the diffraction pattern – each with their own multiplicity and may complicate the simple relationships referred to earlier. A table of multiplicities for the different crystal systems is given in Appendix 2.

Attenuation (absorption)

The final factor that modifies the diffracted intensities considered here is absorption. An assumption of the treatment of intensities so far is that the whole sample is bathed uniformly in the neutron beam, that is, that the neutron beam is not attenuated by its passage through the sample. In our discussion of absorption cross sections in §2.3.3, we noted that most nuclei absorb neutrons only very weakly. Therefore in a majority of cases, only minor errors are introduced by neglecting absorption. There are however many situations in which it is necessary to understand and model absorption such as when highly absorbing nuclei are present, when very large samples are studied in transmission geometry, or when data over a very large wavelength range are obtained (e.g. in a TOF experiment). Furthermore, other processes contribute to attenuation of the neutron beam – primarily scattering – and these must be taken into consideration in all careful work.

We begin with a rather general treatment of attenuation in the two commonest geometries; Debye–Scherrer transmission through a cylinder and Bragg–Brentano reflection geometry. The differential equation governing all attenuation is

$$\frac{dI}{dx} = -\mu x \tag{2.40}$$

where I is the intensity, x the depth within the attenuating substance, and μ the linear attenuation (absorption) coefficient. Solution with the boundary condition $I = I_0$ at $x = 0$ has the familiar form of an exponentially decaying function:

$$I = I_0 \mathrm{e}^{-\mu x} \tag{2.41}$$

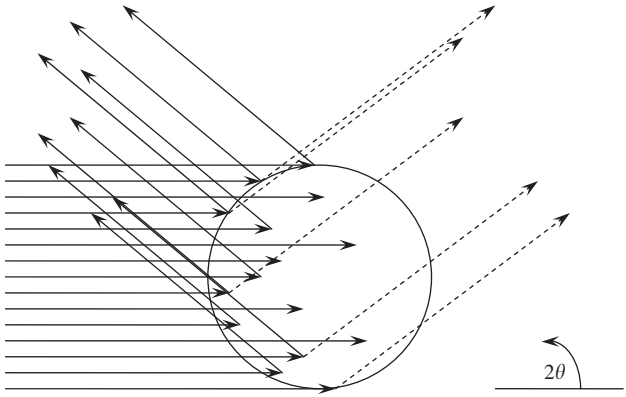

Fig. 2.27 Effect of attenuation in the sample on the diffracted intensity. At small 2θ neutrons must traverse large distances through the sample. In highly absorbing (attenuating) samples, the low angle peaks are greatly reduced in intensity compared with the high angle peaks.

In transmission geometry with a cylindrical sample and a fixed wavelength diffractometer, the situation is illustrated in Fig. 2.27.

Neutrons diffracted in different parts of the sample through different scattering angles travel quite different path lengths. The overall attenuation is obtained by numerically integrating over the sample cross section. In samples where the attenuation is appreciable, the end result is that diffraction peaks at low angles are attenuated far more strongly than those at high Bragg angles. This has the undesirable effect of distorting refined parameters during modelling of the diffracted intensities – especially the displacement parameters as discussed in §5.5. Values for the attenuation factor $A(\theta)$ are given in standard reference works such as the *International Tables for Crystallography*. Given that powder diffraction samples are often new materials, they may contain multiple phases and vary greatly in their packing density, the value of μ is not easily computed. As discussed in §3.5, μ should be measured routinely for each sample as a matter of course. If a measured value of μ is not available, then it can be computed in the following way.

The total attenuation will be the total of the true absorption, the incoherent scattering, and coherent scattering combined for each element. In powder diffraction, attenuation by coherent scattering (extinction) is usually small because it takes place only in those few crystals oriented for Bragg diffraction. Attenuation by incoherent scattering on the other hand can be appreciable because all crystallites are involved. For each element, the attenuation coefficient due to true absorption and incoherent scattering may be written as

$$\mu_i = \mu_{ai} + \mu_{si} \tag{2.42}$$

The *linear absorption coefficient* μ_{ai} is available in standard tabulations, for example, Koester *et al.* (1991), and the value of μ_{si} may be calculated from:

$$\mu_{si} = \left(\sigma_s - 4\pi b_{\text{coh}}^2\right) \times \frac{n}{V_{\text{c}}} \tag{2.43}$$

where σ_{s} is the total scattering cross section, b_{coh} is the coherent scattering length as before, n is the number of atoms per unit cell, and V_{c} the unit cell volume for the pure solid element. When the material under study contains more than one kind of atom, as is usual, it is common to work initially with the *mass absorption coefficient* (μ/ρ), where ρ is the solid density of the pure element, rather than the linear coefficient. The mass absorption coefficient for each phase or compound in the sample may then be obtained by summation in the usual manner as for X-ray diffraction:

$$\left(\frac{\mu}{\rho}\right)_j = \sum_i w_i \left(\frac{\mu}{\rho}\right)_i \tag{2.44}$$

where w_i is the weight fraction of element i in phase j and ρ_j is its solid density.

In cases where the powder sample contains multiple phases, the mass absorption coefficient is obtained by summation over all phases present:

$$\left(\frac{\mu}{\rho}\right) = \sum_j w_j \left(\frac{\mu}{\rho}\right)_j \tag{2.45}$$

where w_j is the weight fraction of phase j in the sample. The linear absorption coefficient of the powder sample, μ_{powder} is then found from

$$\mu_{\text{powder}} = \left(\frac{\mu}{\rho}\right) \times \rho_{\text{powder}} \tag{2.46}$$

This procedure is very accurate if applied to a solid polycrystalline sample, but rather less so with powders as ρ_{powder} under the same conditions of compaction as during the neutron diffraction experiment, may not be known to great precision. Where practical, the value should be verified experimentally as discussed in §3.5.3.

When faced with a relatively absorbing sample, it is often advantageous to use a flat plate reflection geometry as in X-ray powder diffractometers and outlined in §3.5. In this case, regardless of the sample attenuation coefficient, there is no systematic effect on the diffracted intensities and the absorption factor is given by $A = 1/2\mu$. This arises through fortuitous cancellation of the influence of beam spread and penetration depth as discussed in the standard X-ray texts, for example, Cullity (1978). There are however some practical difficulties such as surface roughness and beam spread at low angles which if neglected can lead to absorption-like effects in reflection geometry. This simple treatment has also neglected the influence of phases with widely differing attenuation (due to attenuation coefficient or particle size differences) on the apparent phase quantities in quantitative analysis. This is dealt with in Chapter 8. Finally, that form of attenuation, known

as extinction, can in a limited number of cases, influence the intensities recorded in a powder diffraction experiment (Sabine 1988, 1993).

The stage is now set for us to write down the complete equation for the diffracted intensity including the various experimental constants (Sabine 1980) as

$$I_{hkl} = \left(\frac{\Phi_0 \lambda^3 h}{8\pi r}\right)\left(\frac{\rho' V N_c^2}{\rho}\right)|F_{hkl}|^2\, TLJAP \tag{2.47}$$

where Φ_0 is the incident flux (neutrons $m^{-2}s^{-1}$), λ is the neutron wavelength, r and h are the distance from sample to detector and detector height (more strictly the length of the Debye–Scherrer cone intercepted by the detector), respectively, V is the sample volume, ρ and ρ' are the theoretical and actual sample densities, and N_c the (theoretical) number of unit cells per volume, T is the displacement factor, L is the Lorentz factor, J is multiplicity, A represents the attenuation correction, and P is a correction for preferred orientation.

Equation (2.47) describes the integrated intensity (peak area) for a neutron powder diffraction peak collected from an idealized sample. The observed data have this intensity spread over a profile of finite width and characteristic shape. Equations and methodologies for modelling peak shapes (diffraction profiles) are reserved for Chapters 4 and 5 (specifically §4.5 and §5.5). These techniques have assumed tremendous importance in modern powder diffraction and allow powder diffraction patterns to be used to reveal a wide range of structural and microstructural information about the sample. In powder diffraction it is often the case that we are forced to work with samples that are very poor approximations to our idealized powder or solid polycrystal. There are departures from randomness due either to too few crystallites in the beam (poor powder averaging) or a non-uniform distribution of crystallite orientations (preferred orientation). Departures from crystalline perfection lead to a wide range of peak shape effects (Chapter 9). Multiple phases within the sample have a profound effect which may be put to good use in quantitative phase analysis (Chapter 8). Finally, the diffracted intensities are superimposed on background radiation from incoherent and diffuse scattering which in some instances has a definite structure (Chapter 10). All of these are beyond an introductory chapter on the theory of neutron powder diffraction and will be dealt with in subsequent chapters.

3

Basic instrumentation and experimental techniques

In order to conduct a successful neutron powder diffraction experiment, the user should have a basic familiarity with the instrumentation to be used and the methodology of the experiments. This chapter is intended for users with little formal instruction in neutron powder diffraction and little first-hand experience. It begins by identifying the types and locations of neutron sources (§3.1) followed by a description of the two most common types of instruments for powder diffraction – constant wavelength diffractometers at reactor sources (§3.2) and time-of-flight (TOF) diffractometers at spallation sources (§3.3). Both are briefly compared in §3.4 followed by an analysis of the design of a successful neutron diffraction experiment (§3.5). The final section (§3.6) deals with the preparation of samples. Researchers with greater experience of powder diffraction may wish to dip only lightly into this chapter as required.

3.1 WHERE TO FIND NEUTRON POWDER DIFFRACTION FACILITIES

In Chapter 1, we saw that neutrons in sufficient quantity to observe diffraction effects can be generated by a number of types of sources. However, a sufficient flux of neutrons to conduct modern structural analyses is only available at a relatively small number of large-scale facilities. Neutron scattering sources may be categorized according to the means of generating neutrons (i.e. reactor or accelerator sources). We prefer however to categorize them according to their mode of operation – continuous or pulsed – because this usually determines the mode of operation of the associated diffractometers; that is, constant wavelength or time of flight, respectively.[21] A listing is given in Table 3.1 of most of the world's neutron sources where diffraction experiments may be undertaken. It should be noted that not all sources will be operational at any given time.

Continuous neutron sources are almost all small nuclear reactors dedicated to scientific research. They range in size from 2 MW (McMaster University) to 125 MW (Chalk River). The available neutron flux in the reactor core lies in the range 5×10^{12} to 1.5×10^{15} neutrons $cm^{-2}\,s^{-1}$, the latter belonging to

[21] TOF neutron scattering instruments may be readily constructed at continuous sources; however, this has no specific advantages for neutron powder diffraction.

Table 3.1 Location of neutron sources for diffraction (http://www.neutron.anl.gov/facilities.html).

Location	Source type
Asia and Australia	
OPAL reactor, Bragg Institute, Australian Nuclear Science and Technology Organisation (ANSTO), Lucas Heights, Australia	Continuous
High-flux Advanced Neutron Application Reactor (HANARO), Korea	Continuous
Japan Atomic Energy Research Institute (JAERI), Tokai, Japan	Continuous
Kyoto University Research Reactor Institute (KURRI), Kyoto, Japan	Continuous
Malaysian Institute for Nuclear Technology Research (MINT), Malaysia	Continuous
Europe	
Budapest Neutron Centre, AEKI, Budapest, Hungary	Continuous
Berlin Neutron Scattering Center, Hahn-Meitner-Institut, Berlin, Germany	Continuous
Center for Fundamental and Applied Neutron Research (CFANR), Rez nr Prague, Czech Republic	Continuous
Frank Laboratory of Neutron Physics, Joint Institute of Nuclear Research, Dubna, Russia	Pulsed (reactor)
FRJ-2 Reactor, Forschungzentrum Jülich, Germany	Continuous
FRM-II Research Reactor, Garching, Germany	Continuous
GKSS Research Center, Geesthacht, Germany	Continuous
Institut Laue Langevin, Grenoble, France	Continuous
Interfacultair Reactor Instituut, Delft University of Technology, The Netherlands	Continuous
ISIS Pulsed Neutron and Muon Facility, Rutherford-Appleton Laboratory, Oxfordshire, UK	Pulsed (spallation)
JEEP-II Reactor, IFE, Kjeller, Norway	Continuous
Laboratoire Léon Brillouin, Saclay, France	Continuous
Ljubljana TRIGA MARK II Research Reactor, J. Stefan Institute, Slovenia	Continuous
St. Petersburg Nuclear Physics Institute, Gatchina, Russia	Continuous
Studsvik Neutron Research Laboratory (NFL), Studsvik, Sweden	Continuous
Swiss Spallation Neutron Source (SINQ), Villigen Switzerland	Continuous (spallation)
North and South America	
Centro Atomico Bariloche, Rio Negro, Argentina	Continuous
Chalk River Neutron Program for Material Research, Chalk River, Ontario, Canada	Continuous
High Flux Isotope Reactor (HFIR), Oak Ridge National Laboratory, Tennessee, USA	Continuous

Table 3.1 (Continued)

Location	Source type
Intense Pulsed Neutron Source (IPNS), Argonne National Laboratory, Illinois, USA	Pulsed
Los Alamos Neutron Science Center (LANSCE), New Mexico, USA	Pulsed
Low Energy Neutron Source (LENS), Indiana University Cyclotron Facility, USA	Pulsed
McMaster Nuclear Reactor, Hamilton, Ontario, Canada	Continuous
MIT Nuclear Reactor Laboratory, Massachusetts, USA	Continuous
NIST Center for Neutron Research, Gaithersburg, Maryland, USA	Continuous
Peruvian Institute of Nuclear Energy (IPEN), Lima, Peru	Continuous
Spallation Neutron Source, Oak Ridge National Laboratory, Tennessee, USA	Pulsed
University of Missouri Research Reactor, Columbia, Missouri, USA	Continuous
University of Illinois Triga Reactor, Urbana-Champaign, Illinois, USA	Continuous
New projects	
Austron Spallation Neutron Source, Vienna, Austria	Pulsed
Canadian Neutron Facility, Chalk River, Ontario, Canada	Continuous
China Advanced Research Reactor (CARR), Beijing, China	Continuous
Chinese Spallation Neutron Source (CSNS), Dongwan, Guangdong, China	Pulsed
European Spallation Source (ESS)	Pulsed
Japan Proton Accelerator Research Complex (J-PARC), Tokai, Japan	Pulsed

the High Flux Reactor (HFR) at the Institut Max Von Laue – Paul Langevin in Grenoble, France. An exception is the continuous accelerator source at the Paul Scherrer Institute (PSI) in Switzerland. In reactor sources, the reactor core is relatively large and there is usually ample space for the insertion of beam tubes to extract neutrons for use in scattering experiments. As discussed in §2.1, the neutrons have a wavelength/energy distribution governed by eqn (2.1). Since eqn (2.1) is highly dependent on the temperature of the moderating medium, reactor sources are often used to provide 'cold' and 'hot' neutrons in addition to the 'thermal' neutrons that abound in the reactor core. This is achieved by the insertion of a liquid H_2 (or D_2) cold source and a graphite block heated to ~2000 K to provide a hot source. Neutrons exit from the reactor core through beam tubes and are either utilized at instruments mounted directly against the reactor shell or conveyed to more remote instruments through neutron guides A

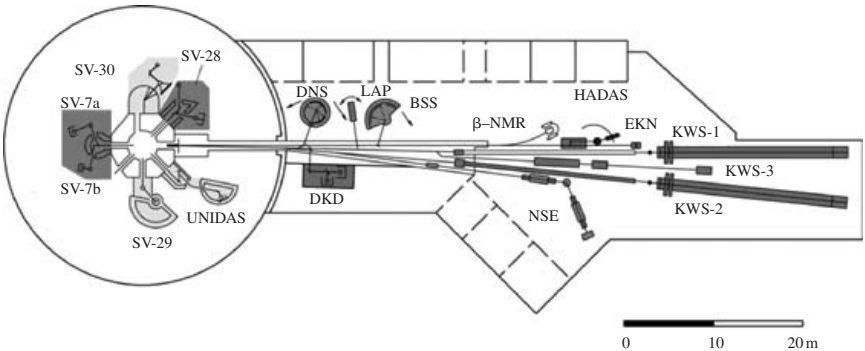

Fig. 3.1 A typical reactor-based neutron scattering facility (FRJ-2) showing instruments situated both within the reactor containment building and in a guide hall.

Table 3.2 Critical angles for common neutron guide materials at $\lambda = 1.5$ Å.

Guide material	Critical angle (°)
Ni (natural isotopic mixture)	0.1
Ni^{58}	0.12
Supermirror	0.3–0.4

typical reactor and guide hall layout is shown in Fig. 3.1. The operating principle of neutron guides is total internal reflection. All neutrons, whose angle of incidence on the wall of the guide is below some wavelength-dependent critical angle, θ_c, will be reflected. Neutrons making greater angles with the walls of the guide are absorbed. Critical angles for important neutron guide materials are shown in Table 3.2.

Until recently, the most commonly used material was Ni^{58}. Most new neutron scattering instrumentation is now designed to use super-mirror guides. A very important aspect of neutron guides is that they can be gently curved to remove the sample from direct line-of-sight to the reactor core. This greatly reduces unwanted γ-ray and fast neutron radiation. Instruments situated on curved neutron guides have intrinsically lower background radiation levels which is beneficial in improving signal to noise ratios and reducing the amount of shielding required around instruments. Guide halls also provide a comfortable, spacious low-radiation zone for experimenters to work in. The characteristics of the neutron beams delivered to the diffractometer depend on the characteristics of the guide. The acceptance angle of the guide (e.g. 0°–0.4° for supermirror guides) is fairly wide and so although there is a degree of collimation, the beam still has considerable divergence. The beam will adopt the full spatial extent of the guide (often 15 cm wide × 30 cm

high) but the curvature leads to a concentration of neutrons against the outer wall of the guide. The wavelength distribution of neutrons exiting the guide is different from that entering the guide. This occurs because the critical angle of reflection depends on the wavelength (λ) according to

$$\theta_c = \lambda \left(\frac{\sigma \bar{b}}{\pi} \right)^{1/2} \tag{3.1}$$

where σ is the number density of atoms in the material and $\bar{b}$ is its mean scattering length. Typically thermal neutrons from the reactor core or cold neutrons from a cold source are readily guided large distances. For example, at the Institut Laue-Langevin, Ni^{58} guides delivering neutrons of mean wavelength $\lambda = 2.8$ Å have a radius of curvature of 2700 m and service instruments 90 m from the reactor face. Neutron guides are ineffective for hot neutrons because of the very low critical angles involved.

The major disadvantage of diffractometers situated on neutron guides is that there is some loss of intensity compared to instruments close to the reactor face. In powder diffraction, a great deal of the background scattering arises within the sample and the sample environment. In high-resolution instruments, externally generated background is further reduced by Soller collimators (see §3.2) and so the advantages of a guide hall position may not be as great. Indeed, arguably the world's best high-intensity and high-resolution constant wavelength diffractometers (D20 and D2B at ILL) are situated at reactor-face positions.

Pulsed neutron sources are almost all accelerator-based.[22] The most prominent are the ISIS facility in the UK, IPNS and LANSCE in the USA, and until recently KENS in Japan. New, more intense sources are under construction in the USA and Japan and a further one is planned for Europe. These are all spallation sources that produce neutrons by colliding high-energy protons (typically 500–800 MeV) with heavy metal targets. Neutrons are 'spalled' or stripped from nuclei in the target, pass into a moderator for partial thermalization before emerging into beam tubes leading to various neutron scattering instruments. Extremely high intensities are generated within each pulse (e.g. $\sim 10^{19}$ cm^{-2} s^{-1} at ISIS) and there are typically $\sim$50 pulses per second although some pulses may need to be discarded for practical reasons. The wavelength distribution of the neutrons emerging from the moderator is not governed by eqn (2.1). The neutrons are deliberately under moderated to avoid the pulses merging into a continuum within the guide tubes. A typical wavelength spectrum is shown in Fig. 3.2. As the pulse travels from the source towards the diffractometer, it spreads out because the shorter wavelength neutrons are travelling at much higher velocities than those with longer wavelength [see eqn (2.2) and subsequent text]. This spreading is used to good advantage since the arrival time of the neutron immediately

[22] A pulsed reactor source operates at Dubna in Russia.

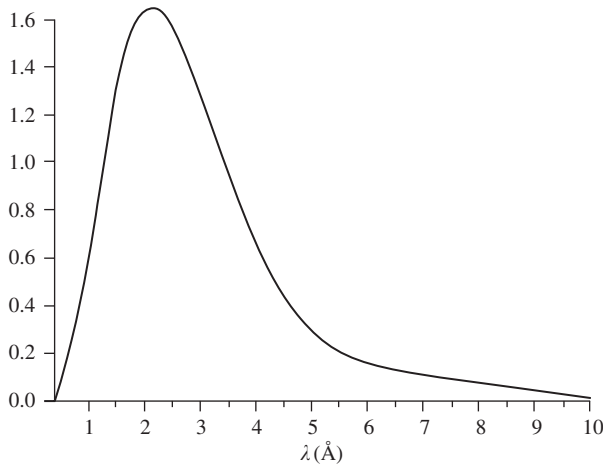

Fig. 3.2 Typical neutron wavelength distribution for a diffractometer situated on a neutron guide at a spallation source (http://www.isis.rl.ac.uk).

identifies its wavelength. The overall system (pulse frequency, pulse duration, moderator thickness, and source to instrument distance) is optimized to maximize the incident flux without frame overlap of pulses. This method of operation allows the entire spectrum of wavelengths to be used for diffraction and other neutron scattering experiments. A comparison of constant wavelength and TOF sources is reserved for §3.4, after we discuss the diffractometer designs used for powder diffraction.

3.2 CONSTANT WAVELENGTH NEUTRON DIFFRACTOMETERS

Constant wavelength neutron diffractometers operate by selecting a narrow wavelength band from the wavelength spectrum produced at the source [e.g. eqn (2.1) for a reactor source]. As shown in Fig. 2.2, the maximum intensity from a thermal source (i.e. ~300 K) occurs at a wavelength of ~0.9 Å, but appreciable intensity occurs at wavelengths in the range 0.8–2 Å. A diagram of the most common generic design is shown in Fig. 3.3. Neutrons emerging from the source through an in-pile collimator and primary flight tube or collimator are incident on a large single crystal monochromator. Neutrons diffracted from the monochromator travel through a secondary collimation system to the sample. Scattered neutrons emerge from the sample over 4π steradians of solid angle comprising the intense Debye–Scherrer cones and weaker background between them. The detection system is often placed so as to intercept the scattered neutrons in a horizontal arc and may incorporate additional collimators. Each element of the diffractometer is dealt with in a separate section.

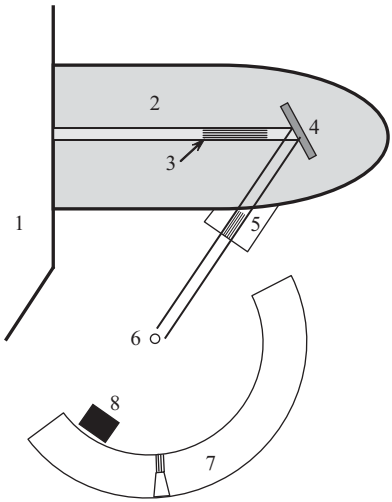

Fig. 3.3 Generic constant wavelength neutron powder diffractometer. Neutrons emerge from the reactor (1) along a heavily shielded flight path (2) through a primary collimator (3). They are incident on a monochromating crystal (4), pass through the flight tube and secondary collimator (5) to be incident on the sample (6). Detectors are arranged in an arc (7) (only one detector and tertiary collimator shown) and scanned to record the pattern. The direct beam is absorbed by a beam stop (8).

3.2.1 Monochromators

The most widely used method of selecting a monochromatic (single wavelength) beam of neutrons from the source spectrum is a monochromating crystal. A crystal monochromator is a simple application of Bragg's law (eqn (2.21)) wherein the crystal is oriented at a fixed angle (θ_M) such that a strongly diffracting set of crystal planes diffracts neutrons on to the sample.

Monochromating crystals must be carefully matched to the other elements of the diffractometer and the desired characteristics of the neutron beam. A systemic problem with early monochromators was contamination of the beam by a small number of neutrons of wavelength λ/n ($n = 2, 3, \ldots$). How this happens can be seen by noting that when planes (hkl) are oriented for diffraction, so are the planes $n(hkl)$ (see §2.2.1). The planes $n(hkl)$ have spacing d_{hkl}/n (see §2.2.1) and at a fixed angle, θ_m, diffract neutrons of wavelength λ/n. As shown in Fig. 2.2, the neutron intensity of a thermal source falls rapidly below about 0.9 Å. This means that the λ/n contamination is weak compared to the primary wavelength λ, and is rarely detectable beyond $\lambda/2$ except for very long primary wavelengths (see later). Some typical monochromator materials and their characteristics are given in Table 3.3.

A useful method for eliminating λ/n contamination for even values of n is to choose a monochromating crystal with the diamond structure (diamond, silicon, or

Table 3.3 Characteristics of some common monochromator materials.

Material	Coherent scattering length (10^{-12} cm)	Incoherent scattering cross section (10^{-24} cm^2)	Absorption cross section (10^{-24} cm^2)	Crystal structure
Graphite	0.66484(13)	0.001(4)	0.00350(7)	Hexagonal, a = 2.461 Å c = 6.708 Å
Copper	0.7718(4)	0.55(3)	3.78(2)	fcc, a = 3.6147 Å
Silicon	0.41491(10)	0.004(8)	0.171(3)	Diamond cubic a = 5.4309 Å
Germanium	0.81929(7)	0.18(7)	2.3(2)	Diamond cubic a = 5.6575 Å

germanium) since, for this structure, the structure factor of the $n(hkl)$ set of planes is in most cases zero for even values of n. The crystal is mounted so that a highly populated zone axis forms the axis of rotation for wavelength selection. Rotation about this zone axis gives rise to a sequence of diffracted beams from odd index planes, each with a distinct wavelength. As will be discussed later in §3.2.2 and §3.2.4, because the angular resolution of constant wavelength diffractometers is fixed, the d-spacing resolution ($\Delta d/d$) is dependent on the wavelength. In cases where extreme resolution is required, wavelengths as long as 5 Å may be used to split strongly overlapping diffraction peaks. In going to such long wavelengths, reflections of order higher than $n = 2$ also have appreciable intensity because they lie in the intense part of the source spectrum [e.g. compare the intensity of 5 Å and $\lambda/3 = 1.667$ Å neutrons in a reactor spectrum at 300 K in Fig. 2.2].

Contaminant neutron wavelengths may be removed by the use of a neutron filter. A majority of neutron filters make use of the so-called Bragg cut-off. By examining Bragg's law (eqn (2.21)), it is apparent that diffraction cannot occur for wavelengths equal to or greater than twice the largest d-spacing in the material. By placing a sufficient thickness of a suitable filter material in the primary neutron beam, all wavelengths below the Bragg cut-off are removed by elastic scattering (diffraction). Suitable filter materials should have very low absorption and incoherent scattering cross sections so that very few of the desired long-wavelength neutrons are removed. An example is Be which has a very low absorption cross section. It also has only one isotope and hence has zero isotope incoherent scattering. The largest d-spacing is 1.98 Å and so only neutrons with $\lambda > 3.96$ Å are transmitted.

A perfect crystal monochromator produces a diffracted beam over a very narrow range of angles, typically only a few minutes of arc. The selected band of wavelengths is hence correspondingly narrow ($\Delta\lambda/\lambda \approx 10^{-4}$). Such crystals are

invaluable in the design of extremely high-resolution synchrotron X-ray diffractometers; however, the neutron flux at neutron sources is too low to select only such a tiny fraction of the available neutrons. In general, monochromators for neutron diffractometers are deliberately plastically deformed to create imperfections[23] which ensure that a greater band of neutron wavelengths is diffracted. The exact wavelength spread utilized is determined by whether intensity or resolution is the most important design criterion for the diffractometer in question. High-resolution instruments have narrow collimators (see §3.2.2) and little is gained by increasing the mosaic spread of the monochromator beyond the angular acceptance of the collimators. High-intensity diffractometers on the other hand are designed to utilize every available neutron.

A strategy for further increasing the intensity of the neutron beam incident on the sample is to utilize vertical focusing. Analysis of the resolution of a powder diffractometer shows that the vertical divergence has little influence over a range of many degrees. This means that very tall primary neutron beams can be focussed onto the sample by the use of tall curved monochromators. The simplest design involves cutting the monochromator crystal into slabs and mounting them on a flexible backing plate. By mechanically bending the backing plate, vertical focussing is achieved. This method is somewhat crude in that the curved surface of the monochromator is made up from many straight segments. Nonetheless, provided that sufficient segments are used, a continuous incident beam profile is obtained. A more difficult approach is to elastically bend the crystals themselves. The crystals (typically Ge or Si) are very brittle and there is a very real danger of fracturing them. Some further gains in intensity and simultaneous gains in resolution can be obtained with simultaneous vertical and horizontal focussing. This is best achieved by combining crystal strips arranged in a vertical stack on a flexible backing that are individually elastically bent in the horizontal plane. This method, perfected for the high-resolution powder diffractometer at Brookhaven National Laboratory, has now been transferred to the new high-resolution powder diffractometer ECHIDNA at Lucas Heights, Australia.

3.2.2 Collimation

Collimation of the neutron beam is achieved by absorption of neutrons on paths more divergent than required for the diffractometer. Neutron guides perform a degree of collimation however for most powder diffraction applications, further collimation is required. The additional collimation is usually provided by a Soller collimator which allows fine collimation over short distances by dividing the beam into parallel segments. Formerly assembled from evenly spaced absorbing metal plates, these are now predominantly made from stretched polymer sheets, each covered with absorbing paint. For the most part, only the collimation in the plane of

[23] The degree of perfection is described by the 'mosaic spread' and is characterized by the mean deviation of the orientation of the lattice planes.

the diffractometer is critical – the out-of-plane divergence is often several degrees. In contrast, the in-plane collimation may be as fine as 5 min of arc and has a profound influence on the resolution and intensity of the instruments.

The optics of collimators has been widely studied (Caglioti *et al.* 1958, 1960; Caglioti and Ricci 1962; Caglioti 1970; Cussen 2000a,b; and others). Here we give only sufficient detail for users of neutron diffractometers to grasp the important concepts. Referring to Fig. 3.3 our generic constant wavelength diffractometer, the key parameters are the collimator half angles for the primary, monochromatic, and diffracted beams (α_1, α_2, and α_3) and the mosaic spread β of the monochromator crystal (here β is defined as the half width at half-maximum height of the beam diffracted by the monochromator). The transmission function of collimators is considered to be triangular, but in most analyses has been assumed Gaussian, that is, conforming to a normal distribution. The mosaic distribution of the monochromator likewise has been assumed to be Gaussian. Departures from this do not affect the general conclusions as outlined below. For powder diffractometers, Caglioti *et al.* (1958) have shown that using the Gaussian assumption, the influence of collimation on the intensity of a neutron beam is proportional to the luminosity L given by

$$L = \frac{\alpha_1\alpha_2\alpha_3\beta}{\left(\alpha_1^2 + \alpha_2^2 + 4\beta^2\right)^{\frac{1}{2}}} \tag{3.2}$$

In the absence of sample-induced broadening (see Chapter 9), the angular width of the diffracted beams measured at half their height (FWHM) will be given by:

$$\mathrm{FWHM} = \left[\frac{\left\{\begin{array}{l}\alpha_1^2\alpha_2^2 + \alpha_1^2\alpha_3^2 + \alpha_2^2\alpha_3^2 + 4\beta^2\left(\alpha_2^2 + \alpha_3^2\right) - \\ 4a\alpha_2^2\left(\alpha_1^2 + 2\beta^2\right) + 4a^2\left(\alpha_1^2\alpha_2^2 + \alpha_1^2\beta^2 + \alpha_2^2\beta^2\right)\end{array}\right\}}{\left(\alpha_1^2 + \alpha_2^2 + 4\beta^2\right)}\right]^{\frac{1}{2}} \tag{3.3}$$

The parameter a describes the dispersion effect (i.e. the diffraction peaks broaden at larger diffraction angle) and is given by

$$a = \frac{\tan\theta_\mathrm{s}}{\tan\theta_\mathrm{M}} \tag{3.4}$$

where θ_s and θ_M are the diffraction angles for the sample and monochromator, respectively. It has been pointed out (Bacon 1975; Hewat 1975) that despite the complexity of eqn (3.3), some simple generalizations can be made. For example, allowing $\alpha = \alpha_1 = \alpha_2 = \alpha_3 = \beta$ we find (Bacon 1975):

$$\mathrm{FWHM} = \alpha\left(\frac{11 - 12a + 12a^2}{6}\right)^{\frac{1}{2}} \tag{3.5}$$

and

$$L = \frac{\alpha^3}{\sqrt{6}} \tag{3.6}$$

We see from eqns (3.5) and (3.6) that resolution is gained at quite a heavy cost in intensity.

All of the previous discussion has assumed a diffractometer very much like Fig. 3.3. In particular, when the detector arrangement is such that $2\theta_s = 2\theta_M$, neutrons diffracted by the sample travel parallel to the primary beam leaving the source. It is possible to place the detection system on the other side such that the diffracted beam (at $2\theta_s = 2\theta_M$) travels antiparallel to the primary beam. The reason why constant wavelength diffractometers are not constructed in this way is apparent when the collimator analysis is considered. The expression for luminosity is the same as eqn (3.6), however the breadth becomes

$$\text{FWHM} = \alpha \left(\frac{11 + 12a + 12a^2}{6} \right)^{\frac{1}{2}} \tag{3.7}$$

and the resolution is greatly inferior.

The recent work by Cussen (2000a,b) is interesting in that rectangular rather than Gaussian functions are assumed for collimator transmission functions and the monochromator mosaic spread. With this assumption, the results can be presented visually, as polygonal regions of complete transmission in a series of phase-space diagrams. The effects of different optical elements can be quite readily explored and the main features of the Gaussian-based analysis [e.g. performance in the parallel configuration] reproduced. The methodology has been extended to three-axis spectrometers and other more complex instrumentation (Cussen 2002).

3.2.3 Detection

The design and manufacture of detectors is a science in itself and we only cover the basic aspects in this volume. Low-energy neutrons such as those used for powder diffraction are most often detected by variations of the Geiger counter comprising a gas filled tube with a fine anode wire running along the axis of the tube. Detection occurs by ionization of a gas atom which drifts towards the centre electrode. As it does so, it induces a cascade of further ionization that greatly amplifies the signal. The amplification is noiseless and directly proportional to the number of primary ionizations (Oed 2001). Thermal neutrons, being uncharged, do not cause primary ionizations directly. Instead, the filling gas is chosen to contain an isotope that strongly absorbs neutrons and emits charged particles capable of inducing ionization. An early detector that was widely used for more than four decades contained BF_3 gas at one atmosphere pressure and ambient temperature (Korff and Danforth 1939). The absorption reaction is

$$^{10}_{5}\text{B} + ^{1}_{0}\text{n} = ^{7}_{3}\text{Li} + ^{4}_{2}\text{He} + 2.8\ \text{MeV}$$

More recently the 'helium-3' detector has largely replaced BF_3 because the efficiency (per unit gas pressure and length) is higher and the detectors can be operated at lower voltages (~1250 V compared with 2500 V for BF_3). The reaction is ${}^{3}_{2}He + {}^{1}_{0}n = {}^{1}_{1}H + {}^{3}_{1}H + 0.76$ MeV (Cocking and Webb 1965). Modern ^{3}He detectors are compact and offer a large active area as a proportion of the external dimensions. Both are factors that make them suitable for powder diffraction instruments.

Our remarks thus far have concerned only single detectors. Few if any powder diffraction instruments remain where a single tube detector is used. Quite some time ago (Caglioti *et al.* 1958; Hewat 1975), it was realized that great gains in resolution (and hence the complexity of the problems that may be solved) could be had from careful attention to the neutron optics (see §3.2.2), but at a cost in intensity. Initially, more intense sources were used to make up the deficit; however, it was soon realized that far greater gains could be made by increasing the detection solid angle. An early example was the PANDA diffractometer at Harwell (Glazer *et al.* 1978) with a monochromator take-off angle of 90° and nine single detectors in three rows of three. Later designs have incorporated greater numbers of detectors. For example, the instrument D2B at the ILL used 64 detectors at 2.5° 2θ separation to cover the entire diffraction pattern (0°–160° 2θ) by scanning the detector bank just 2.5°. This has caused a blurring of the distinction between high-resolution and high-intensity diffractometers (see §3.2.4 and Chapter 12).

An alternative method for increasing the detection solid angle is the use of position sensitive detectors. An early instrument incorporating such a detector was D1B at the ILL which was able to simultaneously record a diffraction pattern spanning 80° in 2θ. This capability was found to be invaluable in the study of phase transitions and transient phenomena (see, e.g. Moisy-Maurice *et al.* 1982). The instrument has been responsible for more than 1090 publications since 1978. The latest constant wavelength diffractometer designs [e.g. Super-D2B at ILL and ECHIDNA at Lucas Heights] have incorporated 128 linear detectors aligned vertically so as to intersect a greater proportion of the Debye–Scherrer rings. This gives the diffractometer a two-dimensional detection capability that not only increases the count rate or sample throughput, but also allows examination of the Debye-Scherrer rings for sample-induced effects such as poor powder averaging and preferred orientation (see §3.5).

Even greater gains in intensity may be obtained by using a multi-wire proportional chamber (Charpak 1968). These gains are made at quite some cost in resolution and so these detectors are more appropriate for use on high-intensity diffractometers [e.g. HIPD at Lucas Heights]. In addition, multi-wire detectors have rather low local saturation limits that make them sub-optimal for the most rapid types of kinetic experiment. The microstrip detector (Oed 1988) has the potential to revolutionize rapid neutron detection with a factor of 20 improvement in the local saturation limit.

3.2.4 Resolution versus intensity

In the previous sections it has become apparent that in constant wavelength powder diffractometers, there is a reciprocal relationship between resolution (the ability to resolve diffraction peaks from sets of planes with closely similar d-spacing) and intensity. Indeed, eqns (3.5) and (3.6) suggest that intensity is proportional to the inverse cube of the angular resolution. This is an oversimplification based not only on equality of $\alpha_1, \alpha_2, \alpha_3$, and β but also on a single monochromator and single detector arrangement, ignoring the importance of wavelength on the d-spacing resolution and sample size on the intensity. Hewat (1975) produced a design for a high-resolution powder diffractometer taking all these factors, as well as density of reflections as a function of unit cell size and symmetry, into account.

In reality, with large detection areas, focussing monochromators and convergent primary beam optics, the distinction between high-resolution and high-intensity diffractometers has become blurred. There are several high-resolution diffractometers capable of recording a diffraction pattern in a matter of 10 minutes or less – comparable to or faster than many low- to medium-resolution diffractometers considered to have high intensity. The extremes of intensity are typified by the instrument D20 at ILL where diffraction patterns have been continuously recorded at as little as 200 ms or in as little as 30 μs in stroboscopic mode. Furthermore, the instrument has recently been upgraded to include 'high-resolution mode' in which diffraction patterns comparable to many high-resolution diffractometers can be recorded in a matter of tens of seconds. A more complete discussion of the latest high-resolution and high-intensity diffractometers is reserved for Chapter 12.

3.3 TOF NEUTRON DIFFRACTOMETERS

Constant wavelength diffractometers are by far the most common kind at continuous neutron sources [e.g. reactors]. However, it is possible to construct a completely different type of diffractometer that seeks to work simultaneously with all of the available wavelengths. If we examine Bragg's law (eqn 2.21) it becomes apparent that, in a sample where many d_{hkl} will be oriented for diffraction simultaneously, a fixed detector is required to make sense of the diffraction pattern. We can re-write eqn (2.21) as

$$\lambda_{hkl} = 2d_{hkl} \sin\theta \tag{3.8}$$

where θ is the fixed detector angle and each interplanar spacing, d_{hkl} is explored by a discrete wavelength λ_{hkl}. This necessitates a wavelength-selective detection system. Recalling eqn (2.1) relating neutron wavelength to velocity, the velocity distribution of the source spectrum provides the mechanism for wavelength discrimination – the 'time of flight' of the neutrons from source to detector. In order to implement the technique, it is necessary to have discrete bursts of neutrons entering the diffractometer. At continuous sources, this may be achieved with the use of

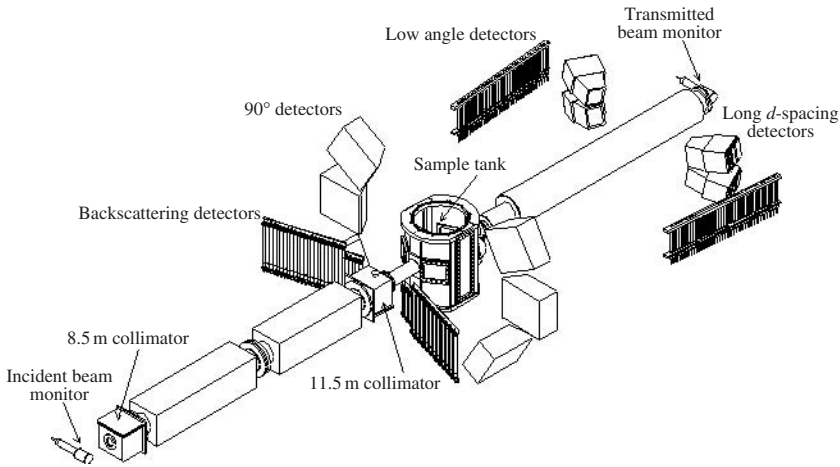

Fig. 3.4 Layout of a typical TOF powder diffractometer (the original POLARIS at the ISIS facility) showing how banks of detectors are used to record patterns in three primary areas: (i) the high intensity low angle region, (ii) the 90° region, and (iii) the high-resolution backscattering region (http://www.isis.rl.ac.uk).

a chopper[24]; however, this has seldom been implemented for powder diffraction instruments. By far the greatest use of TOF methods in powder diffraction has been at pulsed sources (see §3.1) where there is an intrinsic time signature associated with the incident neutrons.

The layout of a generic TOF powder diffractometer, the original POLARIS instrument at the ISIS facility of the Rutherford Appleton Laboratory, is shown in Fig. 3.4. In the case of ISIS, proton pulses of duration ~400 ns are used to generate intense neutron pulses that enter the neutron guides at a rate of 50 Hz. Each pulse contains neutrons with a considerable range of wavelengths and hence velocities. Neutrons whose propagation direction coincides with the transmission function of the neutron guide and any intermediate choppers are incident on the sample. Scattered neutrons are detected by large banks of individual detectors positioned around the sample position. Data are recorded as the number of neutrons as a function of the time-of-flight in microseconds. The wavelength is related to TOF (t) by a modified de Broglie equation

$$\lambda = \frac{ht}{mL} \tag{3.9}$$

where h is Planck's constant, t is the TOF, m is the neutron mass, and L is the total neutron flight path. Substituting eqn (3.9) into (3.8) and rearranging, we have the

[24] A rotating drum perforated by helical holes through which discrete bursts of neutrons are allowed to pass.

inter-planar spacing for a given set of diffracting planes given by

$$d_{hkl} = \frac{ht}{2mL\sin\theta} = \frac{t}{505.554\,L\sin\theta} \tag{3.10}$$

when the conventional units of t in microseconds, d in Å, and L in metres are used.

3.3.1 Collimation and resolution

From the discussion in §3.2.2, it was apparent that the resolution of a constant wavelength diffractometer is determined by the collimation of the incident and diffracted beams (α_1, α_2, and α_3) and the width of the wavelength band selected by the monochromator mosaic spread β (eqn (3.3)). In the TOF arrangement, the resolution is given by:

$$\frac{\Delta d}{d} = \left[\Delta\theta^2\cot^2\theta + \frac{\Delta t^2}{t^2} + \frac{\Delta L^2}{L^2}\right]^{\frac{1}{2}} \tag{3.11}$$

There are three important consequences of eqn (3.11):

(i) The contribution of uncertainties in θ to the uncertainty in d-spacing ranges from infinite at $\theta = 0°$ to zero at $\theta = 90°$ ($2\theta = 180°$). Therefore greater resolution is always obtained by placing detectors at as great a 2θ value as is practical. High-resolution diffractometers usually have backscattering detector banks ($2\theta > 90°$).

(ii) The resolution of the diffraction pattern is essentially constant across the entire diffraction pattern because $\Delta\theta\ \cot\theta$ is constant once a detector angle is chosen; the pulse and detection timing is so precise that the term $\Delta t/t$ is insignificant. The term in $\Delta L/L$ is also constant (see (iii) below).

(iii) Neutrons arriving at the detectors could arise at any position within the effective thickness of the moderator, ΔL. The uncertainty in the path length is then given by $\Delta L/L$. This has the important consequence of giving a linear improvement in resolution as L is increased. In extreme cases (HRPD at ISIS), the neutron flight path is nearly 100 m.

3.3.2 Detection

In principle, all of the kinds of detectors discussed in §3.2.3 can be used on TOF instruments. In addition, detectors based on ^{6}Li (reaction $^6_3\mathrm{Li} + ^1_0\mathrm{n} = ^3_1\mathrm{H} + ^4_2\mathrm{He} +$ 4.8 MeV) incorporated in ZnS scintillators are in common use. The γ-sensitivity of these detectors that prevents their use in CW diffractometers is not a problem in the TOF technique due to the different arrival times of γ-rays and the neutrons of interest. Given the electronic complexity of disentangling time of detection and positional information, large position sensitive detectors are seldom used on TOF

powder diffractometers. Instead, large banks of individual detectors are arranged around the sample position. Referring to Fig. 3.4, we see that detectors may be positioned to record forward scattering, back scattering, or scattering at 90°. Each bank has a quite different purpose. The forward scattering banks give very high-intensity diffraction patterns at low resolution and hence may be used for kinetic studies. The individual detectors are arranged so as to keep $\Delta\theta \cot \theta$ constant which allows the diffraction patterns recorded by each detector to be added ('focussed') into one composite pattern at constant resolution.

The backscattering banks give the best resolution (*cet.par.*) and are used to resolve overlapping peaks from samples with complex crystal structures or multiple phases. Detectors set at $2\theta = 90°$ are extremely useful for recording diffraction patterns from samples contained within complex sample environments. By suitably masking the incident and diffracted beams with neutron absorbing materials, neutrons scattered by the sample environment can be completely excluded from the detectors.

The newest TOF powder diffractometers have been designed to have extremely high detector coverage [e.g. GEM at ISIS and POWGEN3 at SNS – see Chapter 12] and associated very high intensity or short data collection times.

3.4 COMPARISON OF CW AND TOF DIFFRACTOMETERS

Newcomers to neutron powder diffraction are often uncertain about whether to use a constant wavelength or TOF instrument and ask 'which is better'? There is no global answer to this question. Each kind of instrument has certain advantages and disadvantages that might be matched to the problem under study (see §3.5.3) though it should be said here that most problems are amenable to study by either instrument. We have compiled a comparison table (Table 3.4) highlighting the advantages of each based solely on our personal experiences using both kinds of instrument.

3.5 EXPERIMENT DESIGN

The design of a neutron powder diffraction experiment is a lengthy process spanning from the realization that one's problem could be solved using the technique, through the preparation of an experiment proposal, preliminary work in the home laboratory, and the final detailed design with the instrument scientist responsible for the neutron diffractometer to be used. It is a process that ranges in complexity from the trivial (a single medium resolution diffraction pattern under ambient conditions) to the complex (*in situ* experiments in two or more environmental variables). Whatever the level of complexity, there are no experiments that could not benefit (nor are there any practitioners too experienced to benefit) from careful consideration of the experiment design.

3.5.1 Preliminary design

Preliminary design begins immediately that it is decided to study a problem with neutron powder diffraction. The first and most obvious decision is whether to work at high resolution or high intensity. This choice will rest heavily on preliminary work, usually conducted by X-ray powder diffraction, and on consideration of the problem under study. The parameters of interest are the resolution $\Delta d/d$ and the time-averaged neutron flux at the sample position. Table 3.5 gives some guidance to the suitability of one or other type of instrument. Given that neutron diffractometers are not standard laboratory equipment and one may not always have ready access to one's instrument of choice, some compromises may need to be made. These can include the use of high-resolution X-ray diffraction (lab or synchrotron) combined with neutron diffraction.

For those fortunate enough to have a choice, the next decision is whether to use a constant wavelength or TOF instrument. The comparison in Table 3.4 may be useful in making this choice. A majority of powder diffraction experiments can be conducted with equal facility on either kind of instrument. Those involving subtle phase transitions in pseudo-symmetric structures benefit greatly from the very high resolution attainable across the entire diffraction pattern from some TOF instruments [e.g. HRPD at ISIS in the UK]. Experiments requiring detailed diffraction peak broadening studies can benefit greatly from the simplicity of CW peak shapes.

Table 3.4 Advantages of CW and TOF Instruments.

CW	TOF
1. Peak shapes are far simpler to model	1. The whole incident spectrum is utilized
2. Incident beam spectrum is better characterized	2. Data are collected to very large Q-values (small d-spacings)
3. Large d-spacings are easily accessible	3. Very high resolution is readily attained by using long flight paths
4. Data storage and reduction is simple	4. Resolution is constant across the whole pattern
5. Absorption and extinction corrections are relatively straightforward	5. Complex sample environments are very readily used if 90° detector banks are available
6. Can fine tune the resolution during an experiment	6. Simpler to intersect a large proportion of the Debye–Scherrer cones.
7. More common	

Table 3.5 Suitability of problems to high-resolution or high-intensity diffractometers.

Problem	High resolution	High intensity (medium resolution)
Solve a complex crystal structure	Essential, especially in the presence of pseudo-symmetry	Not usually suitable*+
Refine a complex crystal structure	Essential, will benefit from a high Q range if available	Not usually suitable*+
Solve or refine small inorganic structures	Beneficial, but not usually essential unless pseudo-symmetry is present	Usually adequate
Quantitative phase analysis	Only required when peaks from the different phases are heavily overlapped	Usually adequate. Allows phase quantities to be tracked in fine environmental variable steps (T, P, E, H, etc.) during *in situ* experiments
Phase transitions	Depends on the nature of the transition and complexity of the structures. Essential for transitions involving subtle unit cell distortions and pseudo-symmetry	Often adequate for small inorganic structure transitions and order–disorder transitions. Allows fine steps in an environmental variable (T, P, E, H, etc.)
Line broadening analysis	Essential for complex line broadening such as from a combination of strain and particle size, dislocations, stacking faults, etc.	Adequate for tracking changes in severe line broadening as a function of an environmental variable (T, P, etc.) especially if the pure instrumental peak shape is well characterized
Rapid kinetic Studies	Not appropriate	Essential

* In some cases the symmetry and lattice parameters are such that the diffraction peaks are well spaced and not severely overlapped even at modest resolution.
+ May be necessary to supplement high-resolution data to observe weak superlattice reflections in the presence of very subtle or incomplete order–disorder transitions.

In assessing and comparing different instruments, it is useful to obtain a diffraction pattern recorded from a known mass of a standard sample (Si, Fe, CeO_2, etc.) under similar conditions to those that may be required. This allows the resolution (absolute and its distribution within the pattern) and intensity (and hence the time required to record a diffraction pattern) to be compared directly. Once a type of instrument is chosen, the sample environment needs to be considered; since for some experiments, the availability of a suitable sample environment can be more important than the choice of diffractometer.

3.5.2 Sample environment

An early (and persistent) advantage of neutron diffractometers over their X-ray counterparts was the ability to accommodate (and transmit neutrons through) large sample environment chambers. A great variety of sample environments have been used for *in situ* neutron diffraction experiments. These have included high and low temperatures, hydrostatic and uniaxial pressures (stress), high pressure reactive gases, electrochemical cells, magnetic fields, electric fields, and appropriate combinations. Means for creating such environments are discussed briefly later. The relative prominence given to the different environments partially reflects their frequency of use in neutron powder diffraction experiments and partially the authors' own experience.

A critical factor in non-ambient experiments is the desire for the diffraction patterns recorded to NOT include diffraction peaks from the sample environment. There are two strategies for achieving this. The first, relevant to CW diffractometers only, is to maintain all elements of the environment chamber outside the 'critical radius'. Figure 3.5 depicts a collimated beam of neutrons entering a sample environment and exiting to the detectors through a Soller collimator. Scattering and Bragg peaks from the sample cell are excluded from the detection system by the tertiary collimator in front of the detector except at very low and very high Bragg angles. The cut-off angle for exclusion of parasitic diffraction is a function of the inner radius of the environment cell and the wavelength. To ensure complete exclusion, the environment cell inner radius must be such that the lowest angle (i.e. largest d-spacing) Bragg peak of any of the environment cell materials is just absorbed by the tertiary collimator.

The second method involves TOF diffractometers. A very convenient situation arises in TOF diffraction if the detectors of interest are close to 90° to the incident and transmitted beams. In that case, simply masking the incident and diffracted beams as illustrated in Fig. 3.6 results in almost total exclusion of diffraction from the environment cell from the experimental diffraction pattern. For other detector configurations, masking is more difficult although suitable exclusion of scattering from the sample environment can usually be achieved by a judicious combination of sample cell materials selection [e.g. V, TiZr null-matrix alloys, etc.] and masking.

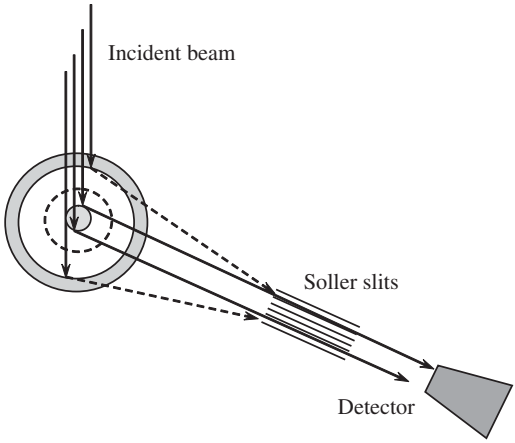

Fig. 3.5 The concept of a critical radius (dashed circle) for a CW neutron diffractometer outside which parasitic scattering from the sample environment (shaded anulus) cannot enter the neutron detection system within the useful 2θ range and angular acceptance of the Soller slits.

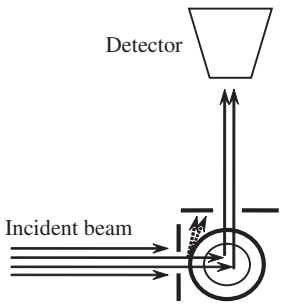

Fig. 3.6 Parasitic scattering (dashed arrows) from the sample environment (dark circle) is excluded from the detector using masking and the fixed 90° detector bank arrangement of a TOF diffractometer.

High temperature

There are many ways to obtain temperatures above ambient. Their suitability for neutron powder diffraction experiments has historically been shaped by

(i) the need for large samples and hence a large and uniform hot zone:
(ii) the temperature range required (hot to a polymer scientist may be 100°C whereas to a ceramist it may be 1600°C):
(iii) rigorous temperature control (furnaces are difficult to control at temperatures well below their maximum operating temperature).

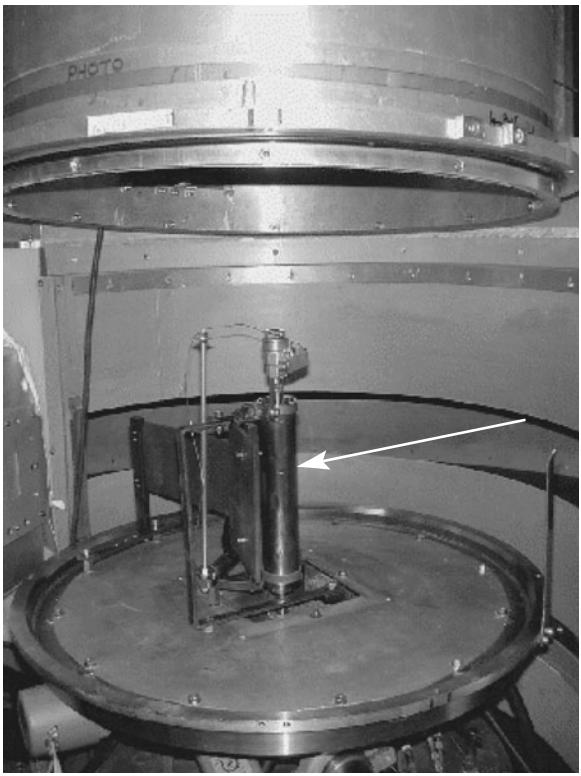

Fig. 3.7 Large vacuum furnace showing the metal foil heating element (arrowed) surrounding the sample position and connected to a copper busbar (http://www.ill.fr).

A versatile neutron diffraction furnace that is widely used is the foil element resistance furnace. A generic design is illustrated in Fig. 3.7. The heating element is a metal foil cylinder attached to Cu busbars and concentric with the sample. A large electric current is passed through the element to heat the sample within. Surrounding the heating element are a number of heat shields to reduce radiant heat losses to the furnace exterior. The entire chamber is evacuated to $\sim 10^{-5}$ mbar before heating to avoid convective heat loss and degradation of the elements. Obviously such a furnace can only be used with samples that do not sublime, decompose, or disproportionate under vacuum, but are otherwise versatile, stable, and very reliable. The temperature range is determined by the choice of heating element. Most popular is vanadium which has such a small coherent scattering length (Table 2.2) that it contributes essentially nothing to the diffraction pattern. Heat shields are likewise preferably V. V element furnaces are restricted to $< 900°C$ for long-term operation and $< 1000°C$ for short-term operation due to excessive V sublimation. Higher temperatures may be attained by replacing the heating element

and inner heat shield(s) with Nb (<1500°C), Ta (<2200°C), or W (<2600°C). These alternative materials will give a small contribution to the diffraction pattern. This contribution is readily characterized by first recording a diffraction pattern from the empty furnace or it may be avoided entirely in a TOF diffractometer using 90° detectors and judicious masking as described earlier.

A major problem with the metal foil resistance furnace is that a proportion of samples will not survive under vacuum and need to be heated in air or some other gaseous environment (N, Ar, etc.). A cost-effective solution is to use relatively standard laboratory tube furnace designs as illustrated in Fig. 3.8. The furnace in Fig. 3.8(a) has Kanthal® windings and can operate to 1100°C in air, vacuum, or a variety of gases. It has a split winding and insulation so that absorption of the neutron beam by the furnace is minimized. The central Al_2O_3 tube is outside the critical radius for the diffractometer and so no diffraction peaks are produced; however, it does contribute to the background count. The furnace in Fig. 3.8(b) has $MoSi_2$ heating elements and can attain 1600°C in air, vacuum, or gas environment. Although the three heating elements are spaced at 120°, the window for recording a diffraction pattern is reduced to $\sim$110° 2θ. If a wider diffraction pattern is required, then the furnace is simply rotated appropriately during the experiment [e.g. a θ–2θ rotation in a CW experiment].

A negative aspect of the laboratory style furnaces is that they introduce extraneous matter into the neutron beam. This partly attenuates the beam (up to 50%) and also increases the background counts – effectively the signal to noise ratio is degraded by a factor of 1.5–3. To attain very high temperatures in air without extraneous matter in the neutron beam, it is possible to use a thermal imaging or mirror furnace (Mursic *et al.* 1992). The furnace consists of two elliptical Al mirrors each with a high-power electric bulb at one focus. The mirrors are positioned such that the sample is at the second focus of both ellipses and an intense localized heating is rapidly produced. Temperatures in excess of 2000°C can be attained in this way.

As mentioned earlier, high-temperature devices are often difficult to control near room temperature. This arises from an imbalance between the heating power and thermal mass of the furnace and the cooling power of the ambient air. This may be overcome by introducing additional cooling and limiting the power output of the heater. A versatile example is the cryo-furnace. Here a He cryostat capable of cooling samples to 4 K (see succeeding section) is equipped with a heater capable of raising the sample temperature to 450–500 K. This offers great versatility as experiments can be conducted from below to above ambient without change of sample environment. Another approach is to use Peltier effect devices to pump heat into the sample space from an external source [e.g. hot water heat-exchanger outside the neutron beam]. A low-cost solution can also be constructed using a hot air blower whose output is ducted to flow over the sample under controlled conditions. The sample temperature is controlled by regulating the power to the heating element of the blower and/or by controlling a mixing valve that admits ambient air.

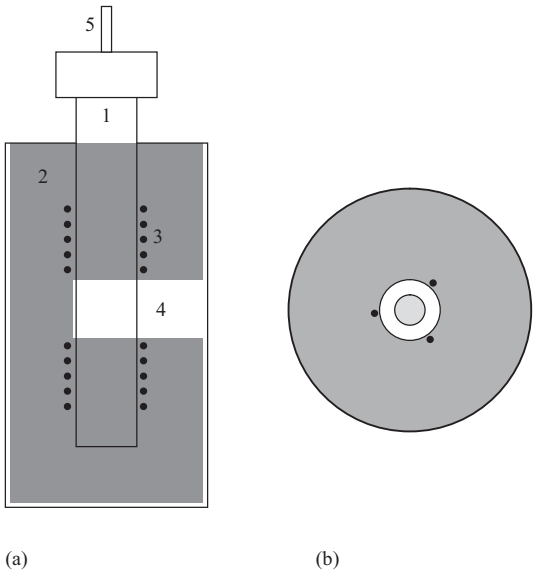

Fig. 3.8 (a) Schematic view through a conventional wire-wound furnace adapted for powder diffraction experiments from the perspective of the neutron beam. A thin-walled closed-end Al_2O_3 tube (1) is mounted within an insulated box (2). The furnace winding (3) is split to allow the beam to pass and the thermal insulation is removed entirely along the beam path and in an arc on the detector side of the furnace (4). The sample is suspended from a sample stick (5) or supported from below. (b) A top view of a high-temperature-controlled atmosphere furnace. Three $MoSi_2$ elements (•) positioned at 120° intervals allow the incident beam to enter unhindered and there is a window of 110° for scattered neutrons to enter the detection system.

Low temperature

The choices of low-temperature sample environment are fewer because two extremely effective and versatile options are available. The first is the cryostat, an example of which is shown in Fig. 3.9. Cryostats use a cryogenic liquid (nitrogen or helium) to cool a sample that is thermally isolated from its surroundings by a vacuum. Heat conduction is avoided by having the sample mount pass through a space cooled by the cryogenic bath. Heat shields, also cooled by the cryogen, avoid excessive warming of the sample by radiation from the outer skin of the device. The tail of the cryostat is usually V to avoid parasitic diffraction peaks in the data. Temperatures of 1.9 K (pumped He cryostat) or 77 K (liquid N) are routinely obtained using these devices. An electric heater is used to accurately raise the sample temperature above the base temperature. The second kind of device is the multi-cycle refrigerator (or Displex™). These operate on the same principle as the domestic refrigerator except that the He working fluid and multiple stages (2 or 3) allow temperatures as low as 4 K to be routinely attained. Again a small electric heater is used to elevate the temperature above the minimum.

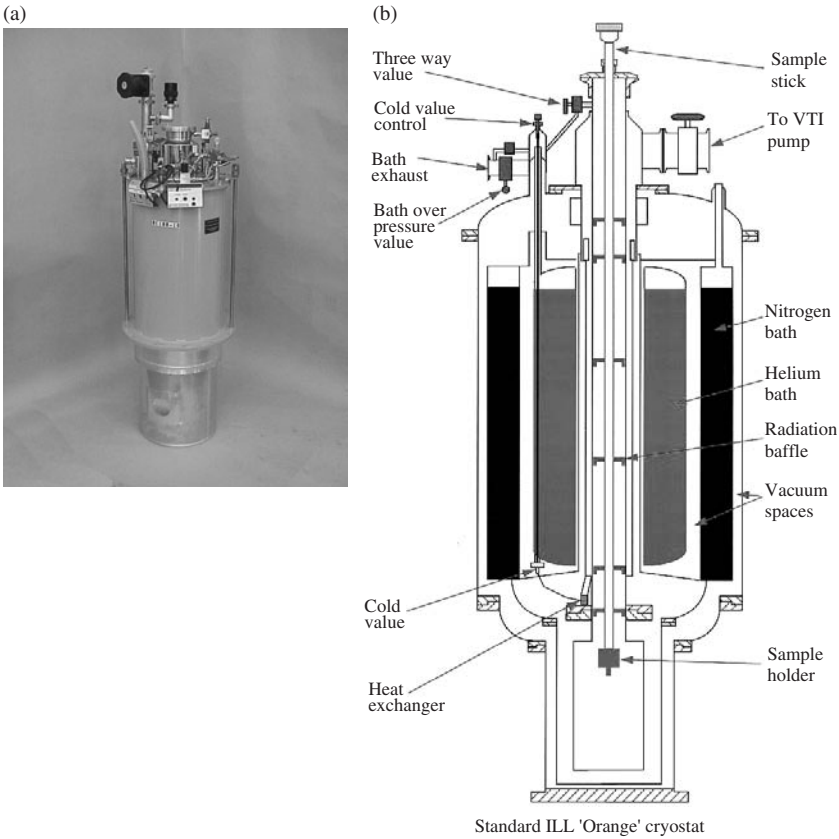

Fig. 3.9 (a) Exterior and (b) interior of the standard ILL liquid helium cryostat for cooling samples in the range 1.8–295 K. An internal heater allows samples to be studied without interruption from 1.8 to 430 K (http://www.ill.fr).

Hydrostatic pressure

A number of devices for attaining high pressures have been successfully used for neutron diffraction studies. High-pressure neutron diffraction experiments are a relatively specialized activity and expertise is localized to a small number of groups around the world. Here we will restrict ourselves to a discussion of only two devices spanning the available pressure range. As with furnaces, it is best to select a high-pressure apparatus based on the pressure range of interest. That is because ultra-high pressure apparatus is so bulky that it attenuates an unneccessarily large proportion of the neutron beam if only moderate pressures are required.

A versatile apparatus for low pressures up to 7 kbar (700 MPa) can be constructed using He gas pressure and a null-matrix alloy sample holder. A null-matrix cell is shown in Fig. 3.10 and is simple to operate, has low attenuation, and preserves a good signal to noise ratio.

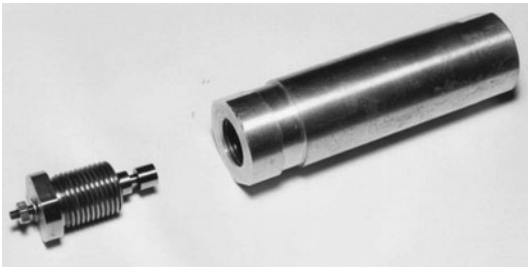

Fig. 3.10 He gas pressure cell for isostatic pressures between ambient and 0.7 GPa (http://www.isis.rl.ac.uk). The cell is coupled to a hydraulic accumulator which acts as a pressure reservoir and pressurizes the He gas within the system.

At higher pressures, the problems associated with the long-term use of high gas pressures have necessitated the development of clamped cells. Here a uniaxial pressure is converted into a hydrostatic pressure by compressing a small quantity of pressure-transmitting fluid contained by a plastically deformable annular metal ring. To date the ultimate clamped cell for neutron diffraction has been the Paris-Edinburgh cell shown in Fig. 3.11, capable of generating sample pressures up to 100 kbar. Significantly higher pressures can be generated using diamond anvil cells (up to 300 kbar). These have been difficult to adapt to neutron diffraction because sufficiently large diamonds are not affordable and are as yet restricted to X-ray diffraction.

Uniaxial stress (pressure)

By comparison with hydrostatic pressure, the generation of a uniaxial stress is much simpler. This is in part because most materials fail at far lower pressures under uniaxial loading than under hydrostatic loading and so more commonly available materials and far less robust designs can be used. Uniaxial stress can usually be accommodated using commercial laboratory scale universal testing machines or adaptations therefrom. They can operate in either tension (for metallic, polymeric, or composite samples) or compression (for ceramic samples) and have an open structure to give ready access for the neutron beam. An example is shown in Fig. 3.12 mounted horizontally. A particular advantage of TOF diffractometers is that, if the 90° detector banks are used, it is possible to simultaneously record diffraction patterns with the scattering vector parallel and perpendicular to the applied stress. This facility is critical in certain residual stress and elastic constants measurements (Chapter 11).

Controlled gaseous environments

There is a growing emphasis on *in situ* neutron diffraction experiments. Within this field, the study of gas–solid interactions is an important area. A field in which *in situ* neutron diffraction has long played an important role is that of metal hydrides.

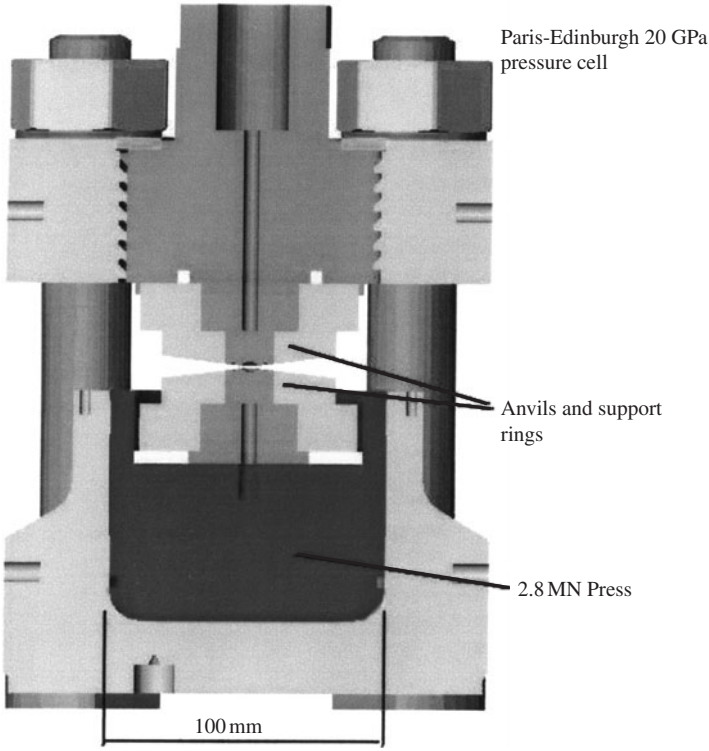

Fig. 3.11 The Paris-Edinburgh high-pressure cell for use in the range 0–25 GPa (http://www.isis.rl.ac.uk).

Hydrogen is not the easiest of gases to contain and since the H or D concentration in the sample is usually measured from the pressure decrease, even extremely minor leaks are disastrous. Deuterium is usually used to avoid the large incoherent scattering cross section of H. Apparatus for this kind of experiment is usually user-supplied although some neutron sources [e.g. ANSTO and ISIS] have generic gas storage and control apparatus on to which a user-supplied environmental cell can be attached. The apparatus controls the sample temperature as well as the D concentration and gas pressure.

Electric field

Devices for the application of an electric field to samples during a diffraction experiment are generally custom made for a particular experiment. The principles are simple involving merely plating silver, gold, or platinum electrodes onto opposing faces of the samples and attaching fine wires to them with a suitably conductive adhesive. However, there are many practical difficulties due to the large samples

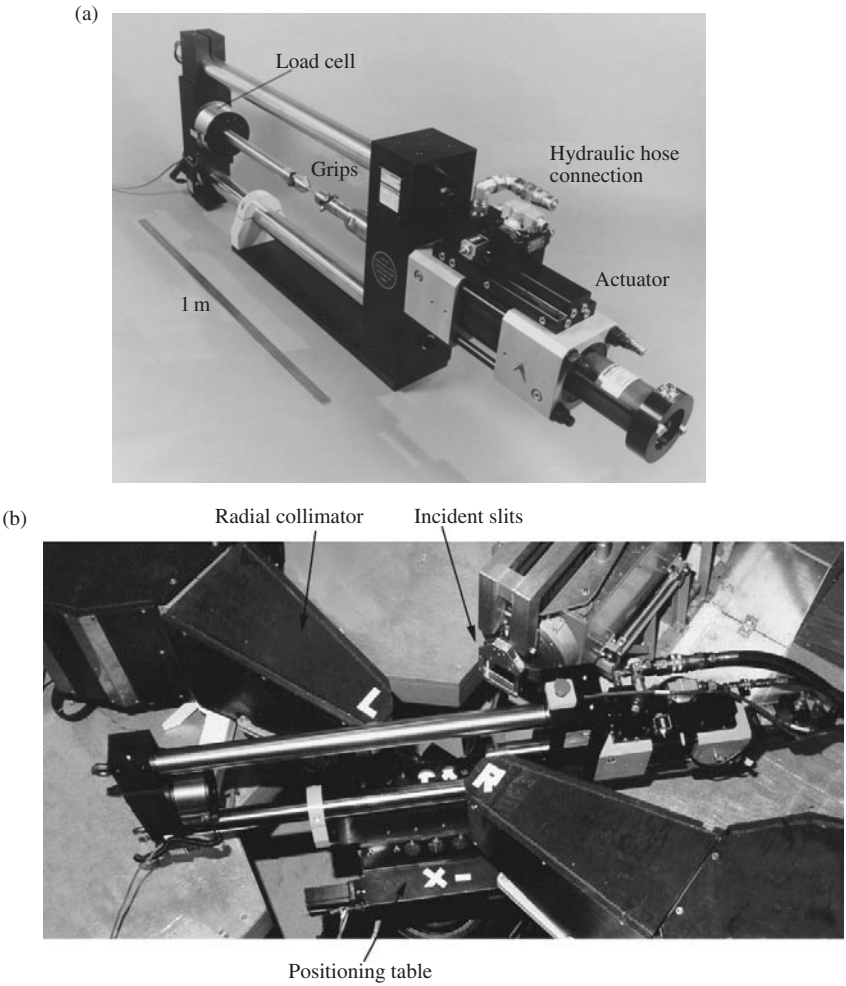

Fig. 3.12 (a) Elements of the uniaxial stress (pressure) device from the instrument ENGIN-X at the ISIS facility and (b) the device mounted in the 'bisecting position'. The incident beam enters through the flight tube at the top and the left (L) and right (R) 90° detector banks simultaneously record patterns with the scattering vector perpendicular and parallel to the applied stress, respectively (http://www.isis.rl.ac.uk).

used and consequent high voltages required. The electrical breakdown strength of dry air at ambient pressure is ~30 kV/cm.

The true electrical breakdown strength of the sample material should be a fixed quantity; however, the observed breakdown voltage will depend considerably on the surface condition, cleanliness, absorbed gases, and so on. For operation in air, coating the sides of the sample with a fine layer of vacuum grease, silicone

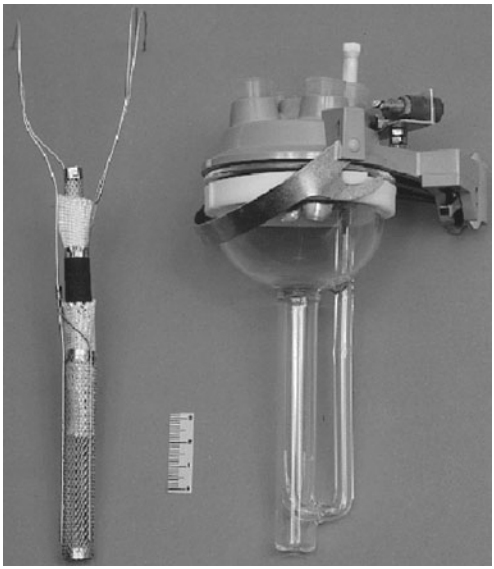

Fig. 3.13 Electrochemical cell used at ILL for *in situ* studies of batteries and fast ion conduction (www.ill.fr).

sealant, or transformer oil is recommended although any hydrogenous material will contribute substantially to the neutron background. A versatile alternative is to encapsulate the sample within an insulating sample holder such as SiO_2 glass filled with a high breakdown strength liquid. Fluorinert has been used successfully in this way. The sample cell will contribute an amorphous background pattern superimposed on the diffraction pattern; however, in most cases this is tolerable and does not invalidate the results.

A final note of caution must be made concerning flashover protection for personnel and equipment. With a high dielectric constant [e.g. ferroelectric or piezoelectric] sample in place, the current flow is negligible and the system is quite safe. The high-voltage power supply and measurement system may be protected from current surge during flashover by the installation of several MΩ of suitably chosen high-voltage resistors in series with the cell.

Electrochemical cells

A number of *in situ* experiments have been conducted using electrochemical cells (e.g. Berg *et al.* 2001) (Fig. 3.13). These are not standard equipment at neutron sources and are tailored to the experiment of interest. The sample forms one of the electrodes and diffraction data are recorded during charge–discharge cycling. The design minimizes the amount of electrolyte in the neutron beam to minimize

incoherent background. The use of heavy water is recommended to further reduce incoherent scattering although this is not always possible as in some systems the two H isotopes have different thermodynamic (I–V) and kinetic characteristics.

3.5.3 Detailed design

Neutron diffraction experiments are conducted at large and expensive facilities after considerable preliminary work and a sometimes lengthy proposal and review process. It is essential that the experiment be designed well to avoid any ambiguity in the results or the necessity for a follow-up experiment before reaching a conclusion. This requires a thorough consideration of the d-spacings required [wavelength (CW) or detector bank TOF], the required counting statistics and sampling interval, and the sequencing and timing of changes to any environmental variable (T, P, E, etc.).

The d-spacing range

The range of inter-planar spacings covered by a powder diffraction experiment is determined by the wavelength and angular range (CW) or the instrument and detector bank chosen (TOF). The choice is between information content (a large number of reflections) and resolution, depending on the type of problem under study. In Table 3.6, we have attempted to summarize experimental situations where the different choices are appropriate and why. The table is written for CW diffractometers on the understanding that there is *some* equivalence between short wavelength (CW) and low angle detector bank (TOF), and long wavelength (CW) and high angle detector bank (TOF).

For TOF however, $d = \lambda/(2\sin\theta) \approx \lambda/2$ for the high angle detector banks, so the d-spacing range will be determined by the wavelengths delivered in the incident beam. High-resolution measurements at large d-spacings require long wavelengths such as are available from a liquid hydrogen cold neutron source.

Counting statistics

The distribution of the number of counts recorded by a single fixed detector in a fixed time is governed by Poisson statistics. Hence, for an observed count N, the standard deviation σ from the true mean is approximated by

$$\sigma = \sqrt{N} \tag{3.12}$$

Strictly, N should be replaced by N_o, the true mean; however, eqn (3.12) is a good approximation for moderate to large N. It can be readily seen that greater precision $\left(\sigma/N = N^{-0.5}\right)$ requires a quadratically increasing counting time (*cet. par.*). For example to improve the precision 10-fold from 10% to 1% requires increasing the raw count 100-fold from 100 to 10,000. Clearly one rapidly approaches

Table 3.6 Guidance on choice of wavelength/detector bank.

Problem	Choice	Reasons
Solve complex or low-symmetry structures	Longer wavelength	Increase d-spacing resolution to allow correct symmetry and space group to be assigned
Refine a large or complex crystal structure	Shorter wavelength	Ensure that the number of peaks greatly exceeds the number of parameters. Improve determination of site occupancies and thermal parameters
Solve or refine magnetic structures	Longer wavelength	Ensure that large d-spacing peaks are observed. Spread the magnetic form factor over the entire diffraction pattern
Quantitative phase analysis	Usually shorter wavelength	Improve the accuracy of the determination. Longer wavelengths only required if peak overlap is severe
Phase transition	Shorter wavelength	Ensures adequate data for order–disorder or other unit cell enlarging transitions
	Longer wavelength	Subtle unit cell distortion or pseudo symmetric structures

practical limits such as the available beam time and the underlying accuracy[25] of crystallographic models. In some cases, the data required are the integrated intensities of some diffraction peaks. If these are measured by scanning a detector across the peak and accumulating the total count, then the precision of the result is still governed by eqn (3.12) (subject to a consideration of the background counts – see later). This method of data recording is little used in modern powder

[25] The term accuracy includes systematic and modelling errors such as defects, impurities, and peak shape inadequacies whereas precision includes only a consideration of random errors.

diffraction. Usually data are recorded over the entire accessible d-spacing range in discrete intervals. For diffraction patterns recorded at constant wavelength, this means that either the detectors are stepped through a 2θ range, pausing at each interval to record the intensity, or a position sensitive detector is broken up into discrete intervals by its own internal architecture or in some cases by the counting electronics. TOF diffractometers receive a pulse of neutrons in a continuous burst which is divided up into segments (bins) by the counting electronics according to pre-determined rules (see Sampling interval). In either case, it is often necessary to combine several individual or raw counts. This occurs when integrated intensities (peak areas) are of interest, but far more commonly when multiple detectors are used. The precision of the resulting individual or step intensities (from elementary statistics) is given by

$$\sigma_k = \sqrt{\sum_i \sigma_{ki}^2} \tag{3.13}$$

where σ_k is the standard deviation in the kth point of the pattern and the σ_{ki} are the individual standard deviations of the intensities being summed. Substituting for σ_{ki} from eqn (3.12) shows that (*cet. par.*) eqn (3.13) reduces to $\sigma_k = \sqrt{\sum_i N_i}$ or the same dependence on $\sqrt{N}$ for the total as is appropriate for individual detector counts. In reality small differences in detector efficiencies need to be taken into account as discussed further in §4.1.

In most cases, the background counts are small compared with the intensities recorded for the major reflections. In this case, the standard deviation in the step count is a relatively good indicator of the precision to which the diffraction at a particular d-spacing step (2θ or TOF) has been measured. However, in cases where the background counts are large with respect to the peak counts, this is not true. Whereas eqn (3.12) continues to give the precision of the total count, the precision of the diffraction peak is influenced by the precision to which the background is known (Klug and Alexander 1974). Take the example of the data point at the top of a strong reflection in a fairly high-intensity diffraction pattern – say 5000 counts. If the background count is essentially zero, then the relative precision of the peak count is quite good at $\sqrt{5000}/5000$ or 1.4%. Now introduce an independently measured background count of 5000. The total count becomes 10,000 and its relative precision is also good at 1%. But the relative precision of the peak count obtained by subtracting the background is given by $\sqrt{15,000}/5000$ or 2.4% – significantly worse than the low background case. The situation is far more serious for low-intensity peaks. Using the same background counts and taking a peak count of just 200, the relative precision of the peak count is 7% in the low background case and 36% in the high background case.

In modern neutron powder diffraction experiments, individual integrated intensities are useful in preliminary data analysis (see Chapter 4), but the bulk of quantitative work is now completed using 'whole pattern' techniques. Just as the

veracity of statistical estimates of precision based only on random errors becomes inadequate at very large values of N (see later), so too does the validity of the error estimates for fitted parameters and the values of agreement indices derived from whole pattern fitting. An analysis of CW X-ray powder diffraction patterns collected at different step counting times conducted by Hill and Madsen (1984) is instructive and equally valid for neutron patterns.[26] At first, the results showed the expected improvement in the agreement between the observed and calculated patterns approximately proportional to $\sqrt{t_s}$, where t_s is the counting time per step. There was however *no* improvement in the agreement, nor in the precision of the refined parameters, beyond values of t_s that yielded 2000–5000 counts at the peak of the strongest reflection. Further, at long counting times, since the expected values of the agreement indices continue to fall proportional to $t_s^{-0.5}$, whereas their actual values plateau,[27] statistical χ^2 gets larger. As a consequence, the precision of crystal structure and other parameters determined from the counting statistics does not reflect the accuracy to which the parameter is known.

The salient results relating to experiment design are:

(i) Accumulating intensity beyond the point where the top of the strongest reflection exceeds 2000–5000 counts does not improve the quality of subsequent crystallographic (or phase quantification) analysis and may invalidate the parameter error estimates from subsequent analyses (Chapters 5 and 8).
(ii) Quite reasonable crystal structure parameters were able to be derived from weak patterns with only 200–500 counts at the top of the most intense peak.

As with all of the decisions associated with experiment design, decisions relating to acceptable statistical precision in the data are dependent on the problem under study. The recommendations of Hill and Madsen (1984) are applicable in many cases. However, there are some experiments where the key information lies in weak super-lattice reflections or in the behaviour of a minority phase in an engineering or geological material. In those cases, longer counting times are required. At the other end of the scale, during *in situ* studies it is often important to use fine steps in an environmental variable (*T, P, E*, etc.) or to follow a rapid process in kinetic studies. In these cases, point (ii) above is an extremely useful guide in fitting the experiment into the beam time allocated.

Sampling interval

The choice of sampling interval is somewhat correlated with the choice of individual step intensities (counting time) since each contributes to the total number

[26] Neutron diffraction patterns are often 'timed' by a fixed number of counts in a low-efficiency detector that monitors the incident intensity.

[27] The plateau arises when $(y_{obs} - y_{calc}) \propto t$, then the agreement index (see Table 5.11) $R_{wp} \approx [(t^2/t)/t]^{1/2}$.

of counts in the diffraction pattern. In fact once the sampling interval is small enough to provide an adequate sampling of each peak (see later), the inclusion of more steps is entirely equivalent to an increase in counting time at the original step interval. Thus, the agreement between the observed and calculated integrated intensities is expected to improve in proportion to the square root of the number of steps (i.e. $\Delta 2\theta^{-1/2}$ where $\Delta 2\theta$ is the step size in the CW case), and the statistical precision in the determination of crystal structure parameters improve (i.e. estimated standard deviations (esd) decrease) in similar fashion. Hill and Madsen (1986) recorded such improvements in the X-ray case, but only so long as the counting statistics dominated the errors. Beyond this there was no improvement in agreement, and the precision of parameters determined from counting statistics became meaningless. It is thus an artifice to employ very long counting times, or very small sampling intervals, to decrease the esds, because these then do not reflect the true accuracy of the parameters refined (Hill and Madsen 1984).

It can be wasteful of neutron instrument time to sample at smaller than necessary intervals in CW experiments (TOF sampling intervals are imposed electronically and hence do not affect the experiment duration, though they do affect the size of the data files produced). We would recommend a sampling interval $\Delta 2\theta$ (or Δ TOF) in the range between about 0.2 and 0.5 FWHM, that is, giving between 2 and 5 data points in the top half of the peak. The larger step size might be adequate, other things being equal, for the refinement of structures of moderate complexity and experiments not expected to involve phase transitions with subtle symmetry changes. There are many instances, however, when finer sampling intervals would be beneficial:

(i) In attempting to resolve subtle symmetry changes where the changes may be revealed in the detailed shape of the diffraction peaks well before any definite peak splitting is visible.
(ii) In tracking the evolution of a new phase during an *in situ* experiment.
(iii) In peak broadening and peak shape analyses (Chapter 9).

An important point to remember is that with modern computing convenience, diffraction patterns recorded with a very fine sampling interval can be easily converted (by summation of adjacent points) into a more intense pattern at a slightly coarser sampling interval, but the reverse is not easily possible. The decision to re-bin the pattern on a coarser sampling interval will usually be motivated by a desire to reduce 'serial correlations' during profile refinement (Hill and Madsen 1986; see §5.5).

Environmental variables

The choice of which environmental variables to scan will have been made during the preliminary experiment design. Here we will restrict ourselves to some very simple guidelines on the sequencing of and control of environmental variables.

Naturally the broad spectrum of available sample environments means that there will be no rigorous or universal rules. The considerations include

(i) There should *always* be one pattern recorded under ambient conditions with the sample installed within the environmental cell and preferably one of the sample alone.

(ii) The range to be covered will be governed by what is known from preliminary work and the literature. It is good experimental practice to exceed the range of environmental variable that is thought to be of interest by a fair margin above and below. This allows a margin for errors in calibration and sensing equipment [e.g. thermocouples]; ensures that unexpected behaviour at the margins of the experimental range is also captured; and allows for ready integration of the diffraction results with data from other techniques and theoretical work. An example is the study of phase transitions in perovskites during heating where the experiment has often been terminated once the sample has undergone the transition to the cubic phase, whereas analysis of the transition(s) using Landau theory is greatly improved by the collection of data several hundred degrees into the cubic region (Carpenter 2002).

(iii) The *interval* in environmental variable should be as fine as is allowed by the beam time allowed. It is critical to note the interplay of this parameter with the choice of counting statistics, the diffraction range, and diffraction sampling interval. For a CW experiment using a scanned detector bank, the total experiment time, T(per sample) scales as

$$T \propto \left[\left(t_{\mathrm{s}} \times \frac{\Delta 2\theta}{(\Delta 2\theta)_{\mathrm{s}}}\right) + t_{\mathrm{d}}\right] \frac{\Delta V}{(\Delta V)_{\mathrm{s}}} \tag{3.14}$$

where t_{s} is the time per detector step, $\Delta 2\theta$ is the angular range that the detector bank is scanned, $(\Delta 2\theta)_{\mathrm{s}}$ is the angular step used, t_{d} is the dead time spent allowing the sample to equilibrate after changing an environment variable, ΔV is the range over which the environment variable is scanned, and $(\Delta V)_{\mathrm{s}}$ is the sampling interval used for the environmental variable. Similar expressions may be readily written down for other diffractometer types. It should be noted that eqn (3.14) is only valid for experiments in which a uniform $(\Delta 2\theta)_{\mathrm{s}}$ and $(\Delta V)_{\mathrm{s}}$ are used throughout and one diffraction pattern only is recorded per interval in the environmental variable. It nonetheless serves to illustrate the means at hand to control the flow of the experiment.

Just as with the diffraction sampling interval, if surplus capacity to record data exists, it is better to limit the counting statistics as previously indicated and reduce the size of the step in environmental variable lest some interesting phenomena are missed. Studies of the high-temperature phase transitions of WO_3 are a case in point. The occurrence of an intermediate monoclinic phase, missed by the use of coarse temperature steps (100 K, Vogt *et al.* 1999) and only subsequently established by data recorded using fine temperature steps (10 K; Howard *et al.* 2002), resolved several outstanding questions about the high-temperature behaviour of

this interesting material. If greater precision is required for detailed structural analysis, an occasional diffraction pattern with larger t_s can be included. Alternatively, with care several patterns can be summed to represent a larger data collection provided that the structural changes are relatively slow, linear, and continuous in the range summed.

Standard samples

A critical part of any neutron diffraction experiment is the recording of diffraction pattern(s) from suitable standard materials. Depending on the etiquette of the neutron scattering facility to be visited, this is likely to have already been conducted by the instrument scientist for the conditions to be used. However, at some facilities or in some circumstances it will be necessary for the user to record standard patterns. In CW experiments these are used for wavelength calibration,[28] that is, a material with very precisely determined lattice constants is used. From the known d-spacings, the mean neutron wavelength can be readily computed. TOF experiments also require standard samples to determine the relationship between d-spacing and time of flight. In addition, although the detectors of a TOF instrument record the full spectrum of available wavelengths, the incident spectrum needs to be precisely known. These and other uses for diffraction patterns from standard samples are discussed further in §4.1 in the context of data reduction from multiple detectors. Table 3.7 shows some useful standard materials, their characteristics, and their uses.

Attenuation coefficient

The computation of a linear attenuation coefficient for a polycrystalline sample is described in §2.4.2. However, as noted in the section, it is often desirable to measure the attenuation directly.

On a constant wavelength instrument, the procedure is to use a pinhole in a neutron absorber (Cd, B_4C, etc.) to define the neutron beam. Then, with one of the neutron detectors (or multi-detector cells) centred on $0°\ 2\theta$, the transmitted intensity is recorded without any sample (I_0) and with the sample in place (I_1). If the beam passes through a sample of thickness t, then $I_1/I_0 = e^{-\mu t}$, where μ is the effective linear attenuation coefficient. This procedure should be adequate for a beam of solely thermal neutrons such as would be delivered to an instrument situated on a neutron guide, but should be modified if fast or epithermal neutrons are expected in the beam as would be the case for instruments situated at a reactor face position. In this case, the measurements are made with and without the sample as before and then the measurements are repeated with and without a thermal neutron absorber [e.g. Cd] in the beam; four measurements in all. The thermal neutron intensities (I_0 without sample and I_1 with sample) are then given

[28] The monochromator angle and tilt cannot be positioned identically.

Table 3.7 Useful standard materials.

Material	Structure type and lattice parameters (Å)	Used for
Y_2O_3	Cubic, $a = 10.6039$	**CW** Wavelength*, detector relative efficiency
Al_2O_3	Trigonal (hex) $a = 4.757$, $c = 12.988$	**CW** Wavelength, detector relative efficiency
TiO_2	Tetragonal, $a = 4.594$, $c = 2.959$	**CW** Wavelength, detector relative efficiency
Si	Diamond cubic, $a = 5.4309$	**CW** Wavelength, detector relative efficiency
		TOF Diffractometer constants DIFA, DIFC
Cd	n/a	Neutron absorption by the sample
V	BCC, $a = 3.0232$	**TOF** incident neutron spectrum, detector relative efficiency
H_2O	n/a	**TOF** incident neutron spectrum, detector relative efficiency

* On constant wavelength instruments, there is no guarantee that the monochromator angle and tilt can be positioned identically each time the wavelength is changed. This leads to minor shifts in the mean wavelength that need to be monitored.

in each case by the reduction in intensity when the thermal neutron absorber is introduced.

The experimental measurement of attenuation may be less common on TOF instruments. The measurement would require a comparison of intensities recorded post- and pre-sample (with and without sample) over every TOF (wavelength) value in the spectrum. Matched detectors of the beam-monitor type positioned before and after the sample could accomplish this simultaneously.

3.6 SAMPLE PREPARATION

We refer here not to the preparation (i.e. synthesis) of the compound or material for study but rather to its preparation for a successful neutron powder diffraction experiment. The amount of preparation required varies depending on the sample type and the nature of the experiment.

3.6.1 Overview

The ideal sample for neutron powder diffraction is a fine, free-flowing powder with roughly spherical, strain-free crystals having no relationship between their external form and the underlying crystal structure. Samples approximating this ideal are quite commonly available in chemistry (fine precipitates), geology and environmental sciences (silts, soils, smokes, and dusts), and the materials sciences (ceramic pre-cursor powders, atomized metal powders, and corrosion deposits). Unfortunately various departures from perfection are also quite common.

Perhaps the most common imperfection is that the sample in its raw form is not a powder. Examples include rocks and minerals, ceramics, metals and alloys, and organic materials. Brittle materials such as rocks, minerals, ceramics, and intermetallic components may be finely ground in a variety of devices. Some materials that are not able to be ground at room temperature, for example polymers and inorganic crystals, become quite brittle at cryogenic temperatures and may be prepared in this way. Ductile materials such as metals and most alloys are largely immune to grinding. They can be rendered into fine powders by filing with a very fine file if the preparation of a powder is absolutely essential. However it should be noted that in many instances, a polycrystalline solid also makes a good powder diffraction sample adequate for most purposes.[29] In fact, there are many instances in which grinding of the sample either destroys the point of the experiment or degrades the quality of the diffraction patterns. An example of the former is work on zirconia ceramics where the martensitic transformation of the tetragonal phase to the monoclinic phase is readily triggered by grinding. Phase proportions and structural parameters derived from powdered samples produced by grinding therefore give no information about the constitution of the monolithic ceramic. Examples of the latter, that is degradation of the diffraction pattern due to sample preparation, include particle size problems, grinding induced strains, and disproportionation of multi-component samples.

3.6.2 Particle size

Particle size[30] problems occur at either end of an optimum range. If a collection of large crystals (say 2 mm diameter) was used as a powder diffraction sample, the resulting diffraction pattern would be compromised. In this case the continuum approximation used in Chapter 2 to derive a powder diffraction pattern from the single crystal patterns is not valid. In X-ray film or imaging plate techniques this problem is referred to as 'spottiness' because instead of continuous Debye–Scherrer rings, the resulting diffraction pattern has a series of spots loosely collected in bands. In (counter) diffractometer measurements, the spottiness manifests as extreme fluctuations in the observed intensity of the diffraction peaks because the number of crystals contributing to a peak is determined by chance and is not the same for each peak. The experimenter may not even be aware of this during the experiment as the peak intensity variations may be mistaken for preferred orientation (see later) until serious modelling is attempted. It should be noted that this problem does not always occur with large particles, for example from rock samples, since each particle may contain many smaller crystallites. Klug and Alexander (1974) have given the conditions under which spottiness is absent

[29] Other things such as crystallite size and preferred orientation being equal, it is only freedom from inter-crystalline stresses that makes a powdered sample superior.

[30] Here particle size is taken to mean the mean diameter of powder particles and is not to be confused with the crystallite size. In many cases, the powder particles may be agglomerates of many crystallites.

from X-ray powder photographs. In summary, the problem is avoided in almost all cases by having particles of $< 5\ \mu m$. Larger crystallites (15–50 μm) are acceptable for higher symmetry structures (with higher multiplicities for each peak) especially if the sample is rotated. Neutron powder diffraction samples have historically been quite large compared with an X-ray capillary sample (typically 12 mm diameter compared with 0.3 mm) and so spottiness has been a far less frequent problem.[31] The low attenuation of thermal neutrons by most samples also helps as absorption shadowing accentuates the spottiness of X-ray patterns at large crystallite sizes. With a typical large sample, crystallite sizes $\leq 53\ \mu m$ (i.e. passing through a 325 mesh sieve) are adequate for neutron powder diffraction experiments.

At the other end of the crystallite size spectrum, very small crystallites give rise to particle size broadening of the diffraction peaks which degrades the resolution. In a small number of cases, this broadening may be quantified to yield important information about the material under study (see §9.2); however, in most cases it is undesirable. The limiting particle size, below which broadening will be observed, depends on the resolution of the diffractometer. At the highest resolution so far attained with neutrons $(\Delta d/d) = 4 \times 10^{-4}$ and assuming a detection limit for particle size broadening of FWHM/4, crystallite size broadening should be just detectable from 2 μm crystallites. As a general rule, the sample should not contain a significant fraction of particles below 1–2 μm if crystallite size broadening is to be avoided.

3.6.3 Grinding strains

A second category of problem can occur when materials are ground into powders. Grinding is often accompanied by the production of strains – usually surrounding grinding induced defects. Although worst in ductile materials such as metals and alloys, organic materials, and some intermetallic compounds, grinding strains can also be observed in samples of minerals, ceramics, and inorganic compounds. As some of the induced strains are dilational (increasing the interplanar spacings) and others are compressive (decreasing the interplanar spacings), the result is strain-broadened diffraction peaks. Whereas the study of strain broadening can yield important information about solid polycrystals (§9.3 and §9.4) and crystal defects (§9.6 and §9.7), in most cases it is undesirable as it degrades the resolution of the diffraction pattern. Grinding strains can be readily removed by annealing the ground powder at an appropriate temperature. Usually heating for 1–2 h to the temperature at which creep deformation becomes appreciable for the class of material under study is sufficient. For example, most metallic samples need only be heated to 30–40% of the melting temperature (in Kelvin). Ceramics and minerals often need to be heated to 50% of the melting temperature to remove grinding damage. Care must be exercized that such heating is conducted in an

[31] In modern high-intensity diffractometers, there is a greater capacity to study very small samples with neutrons and care is required.

inert environment appropriate to the sample under study and that the heating does not cause other undesirable structural changes to the samples.

3.6.4 Disproportionation

Another category of sample preparation induced artefact is the disproportionation of multi-component samples [e.g. rocks, multi-phase engineering materials]. This is likely to occur when phases of different hardness are associated in the same monolithic sample. Upon grinding, the softer phases are more rapidly reduced in size and during subsequent sieving or sedimentation to select the desired particle size, the powder used for diffraction may not represent the raw sample. This is particularly serious if the diffraction data were to be used for quantitative analysis of the phase composition of the sample (Chapter 8).

3.6.5 Preferred orientation

A condition that may occur in powdered or polycrystalline solid samples is preferred orientation.[32] Preferred orientation is a breakdown of the randomness condition required for a perfect powder diffraction pattern. Preferred orientation leads to intensity modulations around the Debye–Scherrer cones which, unlike spottiness due to large particles, are systematic in *hkl*. In powders, preferred orientation requires two conditions:

(i) the powder particles or crystallites must be non-spherical,
(ii) there must be a rigid relationship between the external shape of the crystals and their crystal structure.

For example, chemically precipitated or mechanically cleaved hexagonal crystals are often either needle- or disk-shaped with the crystallographic *c*-axis along the needle axis or perpendicular to the disk, respectively. Taking the disk-shaped particles, it is simple to visualize how in a sample canister they preferentially settle with the *c*-axis vertical or nearly vertical. Consequently, depending on the diffraction geometry, the diffraction pattern has greatly enhanced or depleted 00*l* reflections and the converse for *hk0* reflections. In most instances, preferred orientation of this kind is a great nuisance and is to be avoided if possible. Rotating the sample during the recording of diffraction patterns is effective in reducing some forms of preferred orientation. Other methods involve diluting the sample powder with an inert powder until the particles settle more randomly. Suitable diluents are any material with small σ_a and σ_{incoh} that will not interact with the sample under the prevailing experimental conditions, nor cause any artefacts. The diluent may act as a useful internal quantitative analysis or wavelength standard. Another approach is to accept the preferred orientation in the data and then model it or 'correct' for it in subsequent analyses of the data [e.g. §5.5]. Preferred

[32] Also known as texture – see §9.8.

orientation in solid polycrystals is usually due to plastic deformation at some time during the history of the sample (material synthesis or fabrication, plate tectonics, plutonic instrusions, etc.). During plastic deformation, crystals shear and rotate which can lead to severe and sometimes complex preferred orientation. Short of a pseudo-random gyroscopic action similar to the Gandolfi camera used to record X-ray powder patterns from single crystal samples; there are no means available for removing preferred orientation in solid polycrystals. Instead one is forced to model the preferred orientation during data analysis. In fact, the deliberate study of crystallographic texture using powder diffraction is an emerging field (see §9.8).

3.6.6 Mounting the sample

Powder samples for study under ambient conditions are most easily mounted by filling them into a cylindrical, thin-walled vanadium can. The reader will recall that vanadium has a negligible coherent scattering cross section and hence does not contribute observable peaks to the diffraction pattern. Vanadium cans may be used at temperatures in the range 0–1200 K under vacuum; however, they should not be heated above 500 K in oxidizing atmospheres. Complex *in situ* experiments may require highly specialized sample containers [e.g. ZrTi null matrix alloys, stainless steels, SiO_2 glass vials, etc.] obtained from or developed in consultation with the instrument scientist.

Solid samples are usually cemented or lightly adhered to a rotating table in the centre of the incident neutron beam. Almost all neutron powder diffraction experiments are conducted using Debye–Scherrer (transmission) geometry, a requirement of which is that the sample is uniformly bathed in the incident beam. This places limitations on the size of solid samples that may be mounted (often 20 mm wide $\times$ 40–50 mm high). Larger samples may be studied but for careful work at CW instruments, an additional angle-dependent term may be required in the intensity equation.

One important case when Debye–Scherrer geometry is not appropriate is for highly absorbing samples. These are rare for ND but still represent an important group of materials for study. If studied in transmission geometry, CW diffraction patterns from absorbing samples become strongly distorted, that is, the low-angle peaks are relatively much weaker than the high-angle peaks (see §2.4.2). This problem can be reduced by using a flat plate sample and reflection geometry, analogous to a conventional laboratory X-ray powder diffractometer. To ensure that the same para-focussing principle[33] operates, the sample must scan at half the detector angle and must extend beyond the incident neutron beam at all values of 2θ recorded. If the beam spreads beyond the edges of the sample at low angles, any reflections appearing there will be artificially diminished as in laboratory X-ray patterns with very large slit sizes (see, e.g. Klug and Alexander 1974). This can lead to negative thermal parameters and other unphysical results (see §5.4) during

[33] Leading to essentially a constant irradiated sample volume at all values of 2θ.

structural analysis and is to be avoided. For very highly absorbing samples, the diffracting layer becomes so thin that surface roughness may influence the pattern as is the case in laboratory X-ray diffraction using flat plate samples.

The only remaining factors to consider are centring and masking. In general the sample position is well defined and centring presents little difficulty. The exception is when specialized or non-standard sample environments are used. In many such cases it is wise to record a transmission photograph (or imaging plate image) of the incident beam with and without the sample in place to ensure that it is centred in the most intense part of the incident beam. During *in situ* experiments, parts of the sample environment that may scatter (or diffract) into the detectors are often masked with neutron absorbing materials. These include cadmium sheet and foil, Boroflex (boron impregnated polymer), sintered B_4C sheet, or gadolinium paint (polymer resin impregnated with Gd_2O_3 powder). The use of cadmium is not recommended as it absorbs neutrons through an $n \rightarrow \gamma$ nuclear reaction and is a toxic heavy metal therefore causing both radiological and chemical safety hazards. When possible, beam photographs with and without masking are useful to ensure that the masking has been correctly positioned. Careful attention to all of the forgoing will ensure that optimum use is made of the available beam time and useful results are obtained.

4

Elements of data analysis

4.1 PRELIMINARIES

As most readers will be aware, electronically recorded data from a laboratory X-ray diffractometer is ready to use immediately. This is also usually the case for a constant wavelength neutron powder diffractometer fitted with a single detector (including position sensitive detectors). However, most diffractometers are fitted with multiple detectors to increase the count rate and hence the sample throughput (see Fig. 3.3). The detectors of constant wavelength (CW) instruments are usually fixed in position in a large bank and scanned over a region of 2θ as a single unit. Therefore each detector scans a 2θ range that is offset from its neighbours by the inter-detector angle (typically 2.5°–8° 2θ). For a bank of n detectors, the raw data contains in effect n diffraction patterns as illustrated in Fig. 4.1.

There are several obstacles to be overcome in reducing the data into a single diffraction pattern (i.e. a single $2\theta - y_{\text{obs}}$ list).

(i) The same number of detectors will have not have contributed to all parts of the (composite) pattern.
(ii) The detectors and their collimators will not all be identically efficient.
(iii) The effective centre of each detector (and hence its position relative to its neighbours) may drift over time due to changes in the intensity distribution across the incident beam and minor mechanical movement.

Hewat and Bailey (1976) proposed the procedure that is almost universally used to condense multi-detector CW powder diffraction patterns into a single pattern. First a diffraction pattern is recorded from a well-characterized standard material with sufficient density of diffraction peaks to ensure that each detector records several peaks. Next the raw data are analysed with the assistance of a computer program. The diffraction pattern from one detector is selected to act as a reference and the position and intensity of all the other patterns are compared to it. This is done by fitting each pattern to the reference pattern by adjusting a multiplicative intensity scaling factor and an additive 2θ offset by the method of least squares. In instruments with large numbers of detectors at small angular separation, it may not be possible to scan the detectors far enough for patterns recorded by the first and last detectors to overlap. In this case either secondary reference detectors are

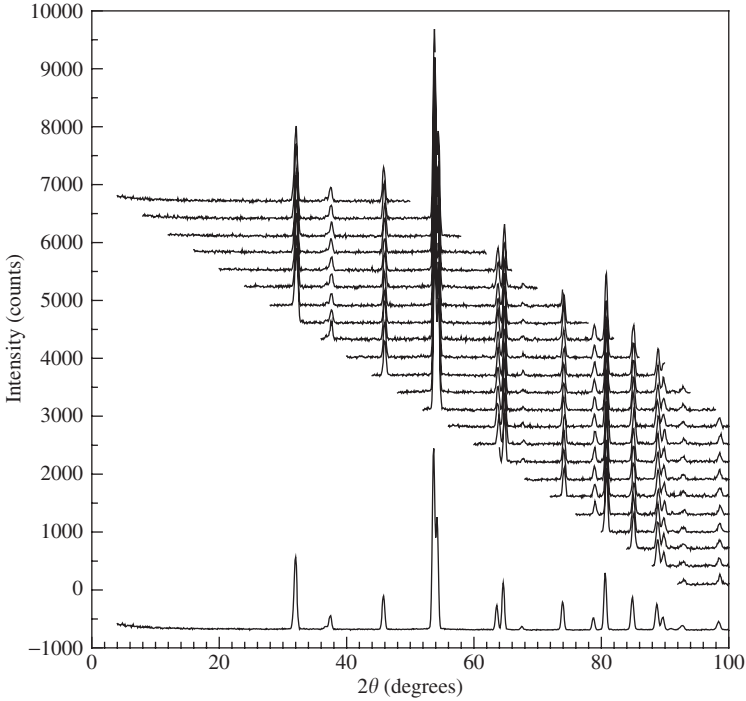

Fig. 4.1 A portion of the raw CW data recorded from a Ce-stabilized tetragonal zirconia polycrystal (TZP) on the medium-resolution powder diffractometer (MRPD) at the HIFAR reactor in Sydney. Patterns from 23 individual detectors are shown at their nominal offset (4° 2θ) along with the aligned and scaled pattern below.

assigned with respect to the primary reference or each pattern is aligned with reference to the preceding one.[34] The least squares fitting procedure gives as output, the position, and efficiency of each detector relative to the primary reference detector. These are used as data in the processing of experimental diffraction patterns by a data reduction program. The data reduction program typically takes the raw experimental data, matches up data points from the different detectors that occurred at the same 2θ value, applies the detector efficiency correction, plots graphical output (Fig. 4.1), and finds the *average* count at each step in the diffraction pattern. It will be obvious to readers that data points recorded near the centre of the diffraction pattern have contributions from more detectors than at the ends of the pattern (Fig. 4.1). The averaged pattern is plotted at the bottom of Fig. 4.1 where the statistical fluctuations may be seen to be largest at the ends of the pattern. These points should therefore receive a different weighting in any subsequent detailed analyses

[34] This has potential for the propagation of errors and should be avoided if possible.

(e.g. Rietveld refinements). One common method of handling this is to record the number of detectors contributing, alongside the neutron count in the data file. Another common method is to compute the standard deviation of each point in the pattern [eqn (3.13)] and record it alongside the neutron count. There are many data storage formats specific to one or more data analysis packages. Many data analysis packages can read (or interconvert) many data formats. Alternatively, it is not difficult to re-format data using a small computer program. Since analysis programs are frequently updated, the reader should consult the appropriate manual for guidance. A useful resource is the CCP14 web site (http://www.ccp14.ac.uk).

Data recorded on time-of-flight (TOF) diffractometers require reduction as well. In TOF diffractometry, the impediments to merely summing all of the detectors are

(i) The incident neutron intensity varies greatly as a function of wavelength giving large differences in both diffracted and background intensity across the diffraction pattern.
(ii) Although the detectors are fixed in position at some notional 2θ value, in reality they are usually spread over some tens of degrees in constant resolution banks (see §3.3.2). In addition they may have different flight paths L in eqn (3.10).
(iii) There are variations in detector efficiency.

Data from individual detectors are 'focussed' into a single diffraction pattern representing the mean detector angle in an analogous but somewhat distinct way to the procedure for CW patterns. Using a standard sample with known d-spacings, the appropriate value of θ for each detector can be computed absolutely using eqn (3.10). The experimental data are generally converted from TOF into d-spacings, summed for all detectors, and corrected for detector efficiency. Correction for the incident spectrum is usually conducted by subtracting the instrument background (with no sample in place) and dividing by a pattern recorded using a reference material that causes primarily incoherent scattering. Water and vanadium have been used for this purpose. Vanadium is preferred because water has such a large incoherent cross section that it partially moderates the incident spectrum and slightly perturbs the normalization. If a crystalline material such as vanadium is used, the normalization pattern must itself first be corrected for attenuation and multiple scattering before use. At each stage, the statistical significance of each point is retained, usually by recording the standard deviation alongside each neutron count. At most neutron sources where TOF powder patterns are recorded, these data reduction procedures are handled routinely by in-house software. At some sources or for some experiments, a degree of user intervention may be required. An example would be the use of an electrochemical cell sample environment. Even if D_2O is substituted for H_2O, the incoherent cross section is substantial and for very careful

work may require the use of a normalization pattern recorded using D_2O rather than vanadium.

4.2 VISUAL INSPECTION

Crystallography grew from mineralogy – an intensely observational discipline. Crystallography and diffraction remain beautifully visual sciences today, in spite of (or perhaps because of) more than a century of growth in mathematical and technical complexity. Powder diffraction retains particularly strong links between the appearance of the diffraction pattern and its information content. The benefits of intense scrutiny of the diffraction pattern(s), especially if an *in situ* experiment is being/has been conducted, cannot be overstated. A large proportion of the ground breaking work conducted using powder diffraction contains very subtle effects such as weak superlattice reflections, shoulders and unresolved splitting of reflections, subtle changes in the peak shape, and minor re-distributions of intensity between peaks. Such changes may be readily overlooked if the data are reduced to a set of integrated intensities or sophisticated computer modelling techniques are used too early. This process of close visual inspection should also be re-visited numerous times during subsequent analyses.

Visual inspection of diffraction patterns is greatly enhanced by appropriate software. We are fortunate to work in an age when graphical software is abundant and inexpensive. By zooming in and out on all parts of the diffraction pattern(s), the following questions may be answered and used to guide subsequent analyses.

Do the counting statistics appear adequate?

The peaks should be relatively smooth with uniform shapes. For general crystal structure refinement work, Hill and Madsen (1984) suggest that the highest data point in the largest diffraction peak needs to be several thousand counts[35] before statistical fluctuations cease to have a significant influence on derived crystal structure parameters (see also §3.5.3). Lesser statistics may be adequate for some *in situ* work, however the quality of derived physical parameters will be reduced somewhat.

Is the resolution adequate?

Methods such as profile analysis mean that it is no longer necessary to have every diffraction peak clearly resolved.[36] If the intention is to solve unknown structures, indexing[37] of the diffraction pattern will be greatly facilitated if the first (i.e. largest d-spacing) peaks are resolved or partially resolved. Figure 4.2 shows a sequence of diffraction patterns representing the different phases formed during the

[35] Allowance must be made for the number of contributing detectors.
[36] In fact, in some systems the symmetry imposes complete overlap, for example, 330/411 and 333/511 in cubic crystals.
[37] Assigning indices *hkl* to each reflection thus defining the unit cell size and shape.

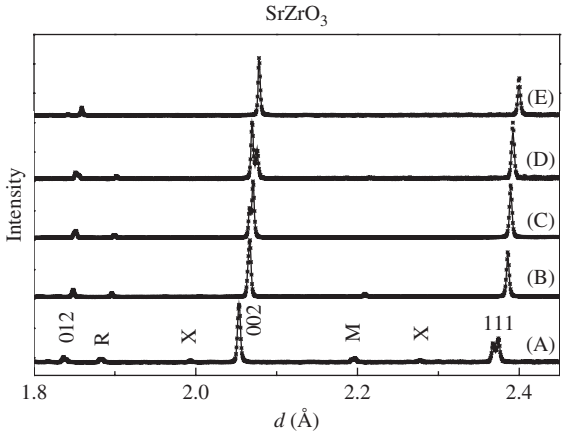

Fig. 4.2 A segment from the observed diffraction patterns (indicated by crosses) from $SrZrO_3$ showing the fundamental perovskite reflections, and the superlattice reflections arising from octahedral tilting (Howard *et al.* 2000). The patterns were recorded at room temperature (A), 660°C (B), 780°C (C), 880°C (D), and 1130°C (E). The continuous lines are fits obtained by the Rietveld method assuming structures in *Pnma* (A,B), *Imma* (C), *I*4/*mcm* (D), and $Pm\bar{3}m$. The significance of the splitting of fundamental peaks and the presence or absence of superlattice reflections is explained in the text.

heating of the perovskite $SrZrO_3$. In order to detect the intermediate phase shown at 1053 K, and solve its structure, resolution adequate to display the reversal of the tetragonal splitting of the pseudo-cubic 002 peak at $d \sim 2.08$ Å, between pattern C and pattern D, was required. This amounts to $\Delta d/d \approx 0.0017$ and the data shown are more than adequate. On most instruments the data can be viewed during data collection and these preliminary checks should be made as early as possible. Some instruments allow the resolution to be adjusted. For example in CW diffraction, the wavelength can be increased to move groups of overlapping reflections to angles having the highest angular resolution. In TOF experiments, some instruments (e.g. HRPD at ISIS) have two sample positions. Moving to the more remote sample position improves the resolution in the backscattering detectors by altering the $\cot\theta$ term in eqn (3.11).[38] For example HRPD has sample positions 1 and 2 m from the backscattering detectors, the latter giving approximately twice the instrument resolution. It should be noted from §3.6.2 and §3.6.3 that the sample sometimes limits the attainable resolution to be considerably less than what the instrument can record using a near-perfect sample. Before halting the experiment and altering the conditions, it is important to ascertain by comparison with a pattern recorded from a standard material, that these effects are not present.

[38] There is a small second order effect in the $\Delta L/L$ term because the overall flight path is also marginally longer.

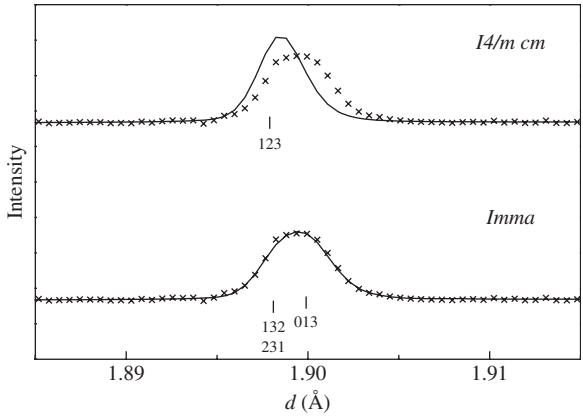

Fig. 4.3 The *R*-point reflection near $d = 0.5$ Å in the $SrZrO_3$ pattern recorded at 780°C (Howard *et al.* 2000). The continuous lines show the best Le Bail fits obtained assuming space groups *Imma* and *I*4/*mcm*. The positions of allowed reflections are indicated.

Are the peak shapes reasonable?

The issue of peak shape correlates with resolution. An occasional odd-shaped peak may, on closer inspection, be seen to be the result of an unresolved splitting. An example is the 123 peak in the *Imma* phase of $SrZrO_3$ (Fig. 4.3). Close inspection reveals a pair of peaks that were instrumental in determining the new structure and distinguishing it from the tetragonal structure that exists at higher temperature (Howard *et al.* 2000). In general, the peaks should be smoothly varying functions without step discontinuities that may indicate problems with the detection system or normalization routine (see §4.1). Powder diffraction peaks are often slightly asymmetric. In TOF diffraction, the asymmetry arises mostly from different rise time and decay characteristics in the spallation pulse. Asymmetry of this kind should distort (broaden) all of the peaks on the same (long d-spacing) side. In CW diffraction patterns, the asymmetry arises from intersecting a Debye-Scherrer cone with a detector slit of finite extent (Fig. 4.4). The asymmetry is worst at low and high diffraction angles and falls to zero at 90° 2θ, although it is often negligible for much of the diffraction pattern. The sense of the asymmetry switches at 90°, that is, at low 2θ, peaks are skewed to the low angle side and at $2\theta > 90°$, they are skewed to the high angle side. Departures from these purely instrumental asymmetries indicate imperfections in the sample that in some cases have only nuisance value, but in others can be meaningfully interpreted to quantify the microstructure of the material (see Chapter 9).

Is the background smooth and monotonic?

The background of the diffraction pattern is the best place to check for not only certain problems, but also a variety of interesting sample-related phenomena. First

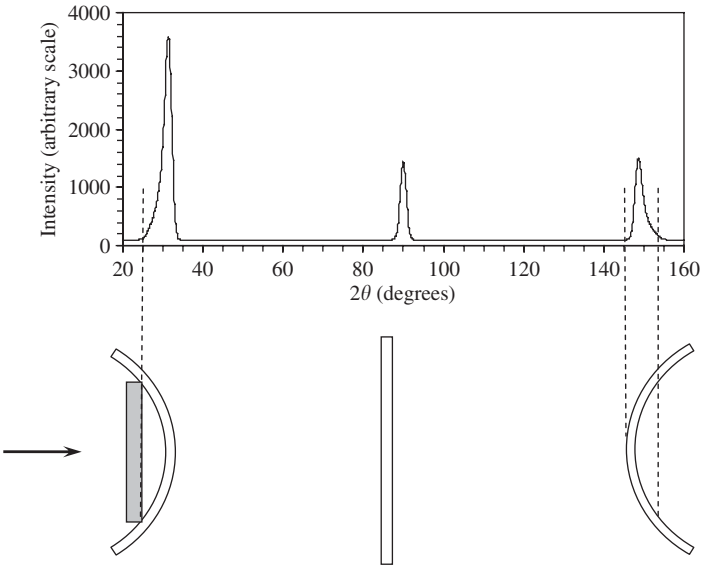

Fig. 4.4 Origin of peak asymmetry in CW neutron powder diffraction patterns. A detector slit of finite height sweeps across Debye–Scherrer rings of diffracted intensity which have different curvature depending on 2θ. The corresponding asymmetric peaks are shown schematically.

and foremost, the background is a good place to check for 'spikes' or unusually large counts at a single point. These can arise due to electronic effects in the detection system or from radiation bursts caused by other users of the neutron source. A useful technique is to plot the entire pattern with error bars at each point. Any points lying significantly outside the error bars of adjacent points must be investigated – especially if only present in one data channel. Spikes should be removed from the raw data (detector by detector) and the data reduction (see §4.1) conducted again. Although it is unusual for the background to be constant, it should vary only slowly across the diffraction pattern. Broad modulations of the background indicate short-range order in the sample either due to the presence of an amorphous phase or due to some partially completed atomic ordering process (see §2.2.2). An important part of examining the background is the search for very weak peaks. These may indicate crystal structure changes (superlattice reflections) or be the peaks from a phase present in the sample in only minor quantities. Superlattice peaks (and their d-spacings) have a geometric relationship to the larger peaks and are essential for solving the crystal structure. This may be observed in the case of $SrZrO_3$ in Fig. 4.2 where the superlattice peaks labelled R indicate out-of-phase tilting and those labelled M indicate in-phase tilting of ZrO_6 octahedral units about one or more of the parent cubic axes. The peaks labelled X confirm the simultaneous presence of R and M type tilting along

different axes. In contrast, peaks from minor phases have no connection to those from the major phase(s). They may highlight (and may be used to quantify) the presence of an impurity phase or be from a deliberate minor constituent crucial to the properties of the material under study. Our example here is the structural ceramic MgO partially stabilized zirconia (Mg-PSZ) which typically has a neutron powder diffraction pattern as in Fig. 4.5. In Fig. 4.5(b), the vertical bars under the figure show the positions of peaks from the various phases that coexist in Mg-PSZ (cubic, tetragonal, and monoclinic zirconia – *c*, *t*, and *m*, respectively, and an anion ordered version of the cubic phase, $Mg_2Zr_5O_{12}$ – the δ-phase). From XRD studies, the ceramic was thought to contain only the *c*, *t*, and *m* phases. Figure 4.5(a) shows a Rietveld refinement fit (§5.5) to the observed neutron diffraction pattern on the assumption of only those three phases. Note the relatively small peak at $\sim$46.5° which is poorly fitted. The fit is otherwise reasonable given that the constituent phases are highly strained and have very small crystallites. Later analysis with the correct four-phase mixture revealed that the δ-phase constitutes $\sim$30% of the sample (Hannink *et al.* 1994). The Rietveld fit, shown in Fig. 4.5(b), now accounts for the small peak at 46.5°. This example is dealt with in more detail in Chapter 8.

Is there any obvious preferred orientation?

The positive identification of preferred orientation requires modelling and comparison with the diffraction pattern of a random powder. However, if the preferred orientation is severe it will be obvious on visual inspection. Diffraction patterns in which there are only a few very intense lines well spaced in the pattern and many more weaker reflections should be checked closely for preferred orientation (or spottiness – see §3.6.2) during subsequent analysis. Whereas this situation is occasionally encountered with XRD, such extremes of preferred orientation are rare in neutron powder diffraction except for severely plastically deformed metals.

4.3 PHASE IDENTIFICATION

Phase identification is the most common use for laboratory X-ray diffraction patterns and it is always preferable if the phases present can be identified using XRD before the neutron experiment. There are of course instances when this is not possible, mainly involving phases that form transiently during an *in situ* experiment or are located deep within a monolithic sample, beyond the reach of laboratory X-rays. The popularity of XRD for phase analysis stems in part from the availability of large compilations of X-ray data in computer searchable databases. The most common example is the Powder Diffraction File available from the International Centre for Diffraction Data (ICDD). Primary data are in the form of a list of the *d*-spacings and (for historical reasons) the relative maximum height of the 20 or so highest *d*-spacing peaks as a measure of their relative intensity. A sample record (PDF 40-1132 ICDD, 2001) is shown in Fig. 4.6. The search

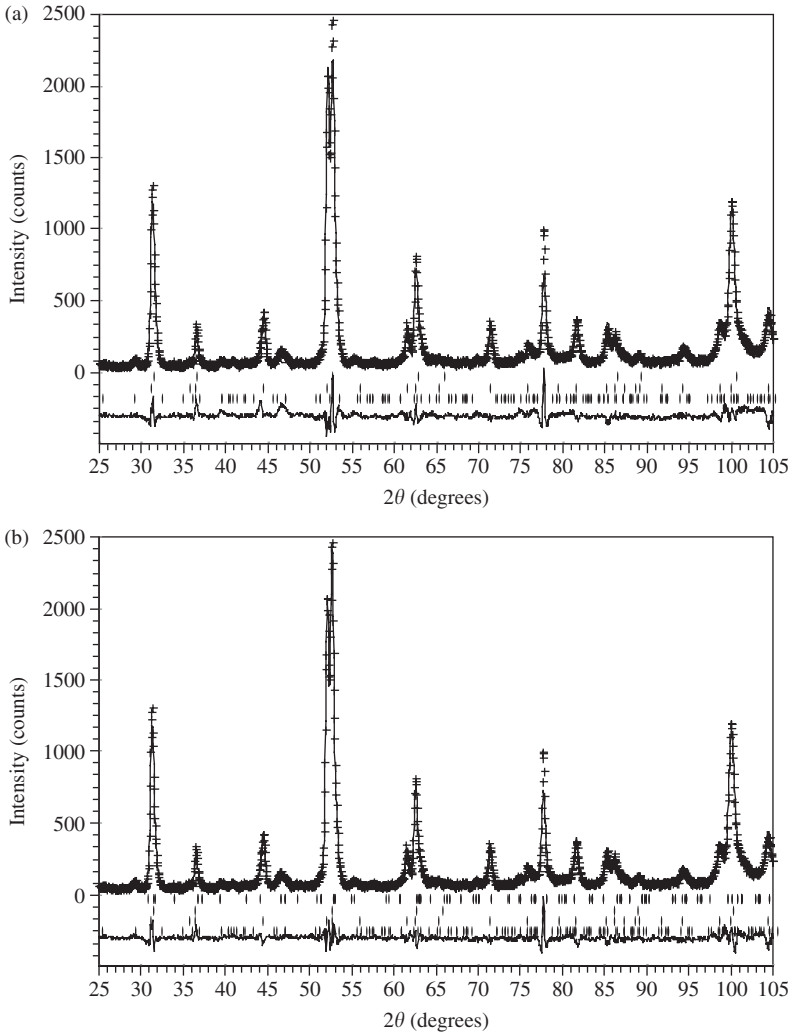

Fig. 4.5 CW neutron powder diffraction pattern from Mg-PSZ recorded at $\lambda = 1.594$ Å. Shown are Rietveld refinement fits based on the assumption of (a) the three standard zirconia phases *c*, *t*, and *m* and (b) including 28 wt% of the defect fluorite phase $Mg_2Zr_5O_{12}$. Only the latter accounts for the small peaks around 46.5° which are readily overlooked by a casual inspection of the refinement output.

algorithm seeks to match the strongest reflections first as these are deemed to be both statistically and structurally more significant. Peak heights in this context are only precise if the diffraction data were recorded under identical conditions (slits, wavelength, monochromator, etc.) from an identically prepared sample (particle

40–1132 Wavelength = 1.5418 i

Ti3SiC2

Titanium Silicon Carbide

Rad.: CuKa λ: 1.5418 Filter: Ni Beta d–sp: Diff.
Cut off: Int.: Diffract. I/Icor.:
Ref: Goto, T., Hirai, T., Mater. Res. Bull., 22, 1195 (1987)

Sys.: Hexagonal S.G.: $P6_3/mmc$ (194)
a: 3.062 b: c: 17.637 A: C: 5.7600
α: β: γ: Z: 2 mp:
Ref: Ibid.

Dx: 4.541 Dm: 4.530 SS/FOM: F_{20} = 12(0.043, 38)

Prepared using Si Cl4, TiCl, C Cl4 and H2 as source gases, the compound was prepared by chemical vapor deposition at a deposition rate of 200 μm per hour on a heated graphite substrate. Cell parameters generated by least squares refinement. Reference reports: a = 3.064, c = 17.650. C Mo type.
~Not permitted by space group.
Silicon used as an internal stand. PSC: hP12. Mwt: 195.81.
Volume[CD]: 143.21.

d(A)	Int	h	k	l
8.7232	22	0	0	2
4.3909	11	0	0	4
2.9336	13	0	0	6
2.6184	16	1	0	1
2.5355	2	1	0	2
2.4144	4	1	0	3
2.2703	75	1	0	4
2.2030	100	0	0	8
2.1184	37	1	0	5
1.8264	2	1	0	7
1.7636	3	0	0	10
1.6950	5	1	0	8
1.5766	19	1	0	9
1.5315	13	1	1	0
1.4694	5	0	0	12
1.4056	1	1	1	5 *
1.2864	1	1	0	12
1.2595	13	0	0	14
1.2420	3	2	0	5
1.2069	10 [	1	0	13]
1.1030	8	0	0	16

ICDD ® 2001 JCPDS–International Centre for Diffraction Data. All rights reserved

Fig. 4.6 One of the ICDD records for Ti_3SiC_2 (PDF 40-1132 ICDD, 2001).

size, strain, preferred orientation). However for rapidly searching and matching observed diffraction patterns, they have proved adequate for more than 70 years (Hanawalt *et al.* 1936, 1938).

To obtain the required d-spacing list, it is first necessary to determine the positions of the diffraction peaks in 2θ (CW) or TOF. In determining peak positions, we must first define what it is that we are measuring. At first glance, it might appear that the point (in either 2θ or TOF) at which the maximum count is recorded would give an accurate peak location. In reality this is the case only for completely symmetrical peaks that are not affected by any offsets and that have been sampled at very small intervals. Nonetheless, the maximum count can give an approximate peak position for rapid data checking and phase identification. Locating the peak maxima in a data file of many thousands of points is an onerous task for a person but a trivial one for a computer. The simplest and least accurate method is to search for local maxima in the entire data file. A more sophisticated method is to examine the first derivative of the diffraction pattern as illustrated in Fig. 4.7. A simple forward difference method can be implemented in a spreadsheet environment where the derivative is approximated by the unweighted difference between the observed step intensity (y_{obs}) at the point of interest and the preceding step intensity, divided by the 2θ or TOF interval. In patterns that contain weak reflections or have low counting statistics, some degree of smoothing may be necessary. Simultaneous smoothing and differentiation can be efficiently performed using the method of Savitky and Golay (1964). Irrespective of the numerical method used, the peak positions are given by the zeros of the derivative. The use of

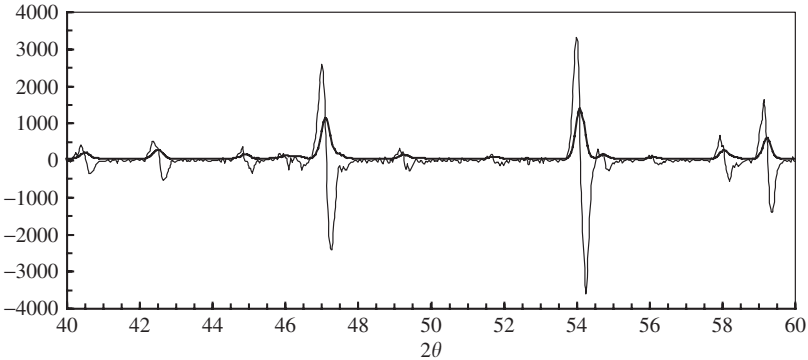

Fig. 4.7 Part of the room temperature neutron diffraction pattern of $Ca_3Ti_2O_7$ (bold) overlaid by its first derivative (scaled down).

derivatives has the advantage that the zero need not (seldom does) lie exactly on one of the sampled points (i.e. there is an implicit interpolation). Another approach is to fit an inverted parabola to the three most intense points. This too can be readily automated and both approaches are incorporated in commercial software distributed by major manufacturers of laboratory X-ray diffraction equipment. Software for neutron diffraction is usually customized to the host laboratory (e.g. CCSL, GSAS, etc.), although a range of free software is distributed through the Crystallographic Computing Project #14 (http://www.ccp14.ac.uk). Occasionally, d-spacings with greater precision are needed when two phases with similar structures are to be distinguished. Methods for determining the accurate peak positions and d-spacings needed for purposes such as unit cell determination are discussed in §4.4.

Once a set of peak positions has been determined, they need to be converted into d-spacings using Bragg's law for CW patterns [eqn (2.21)] or the TOF – d relationship [eqn (3.10)]. As discussed in §2.3.3, the relative coherent neutron scattering lengths for the elements in their natural abundances are quite different from the relative X-ray form factors. Therefore, whilst the d-spacing measured using neutron diffraction will, in the absence of systematic errors, be the same as those measured using XRD, the intensities can be completely different. Figures 4.8 and 4.9 show some examples. In Fig. 4.8 the difference between the neutron diffraction pattern [Fig. 4.8(a)] and the XRD pattern [Fig. 4.8(b)] is so great because Ti scatters neutrons out of phase with most other elements (i.e. has a negative scattering length). The patterns in Fig. 4.9 are slightly more similar because all elements are scattering with the same sign. The differences are confined to (i) peaks where the structure factor [eqn (2.31)] is primarily determined by the lighter elements and (ii) those at higher angles influenced by the X-ray form factor.

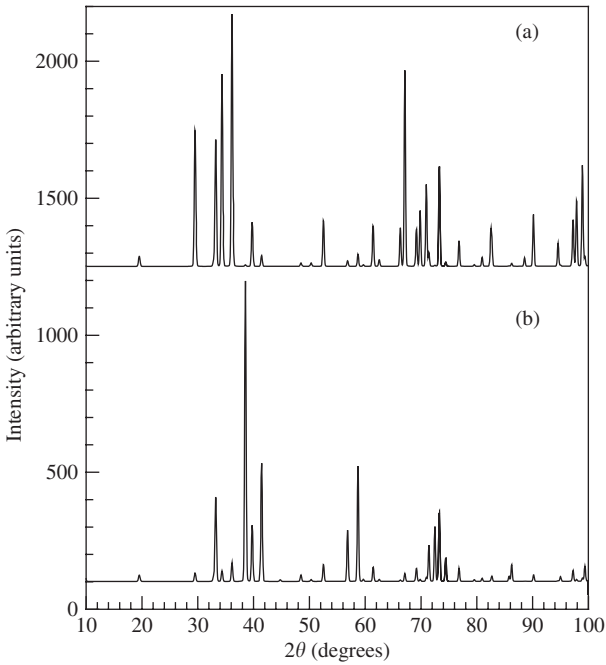

Fig. 4.8 Calculated (a) neutron and (b) X-ray powder diffraction patterns from the layered ternary carbide Ti_3SiC_2. A common wavelength of 1.5 Å and identical peak widths were used.

The ICDD database may still be used for neutron diffraction patterns. There are several strategies that may be applied. First, one may begin with the observed relative neutron diffraction intensities to see whether they return a credible solution. Second, it is possible to assign the same intensity to all reflections thereby placing greater emphasis on the d-spacings or select to search on d-spacing alone which is an option in some search programs. This strategy is immediately successful for even the difficult case of Ti_3SiC_2 shown in Fig. 4.8. Third, for simple diffraction patterns (few lines) when it is suspected that an element with negative scattering length is involved, a useful strategy *may* be to invert the observed neutron intensities (i.e. strong become weak and *vice versa*) although the other strategies should be attempted first.

If there are only a limited number of possible phases, an additional strategy for phase identification is to export a Crystallographic Information File (CIF) from sources such as the Inorganic Structure Database (http://icsdweb.fiz-karlsruhe.de/index.php) for each compound or phase potentially present. The CIF can then be directly imported into a whole-pattern refinement program (see §4.6 and §5.5.2) and a calculated diffraction pattern created for comparison with the observed pattern. Several whole pattern fitting programs now read CIFs directly (e.g. GSAS

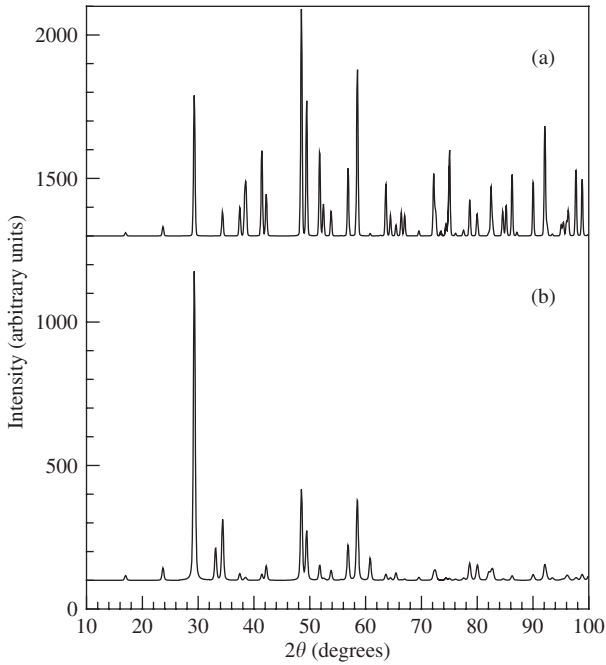

Fig. 4.9 Calculated (a) neutron and (b) X-ray powder diffraction patterns from the orthorhombic phase found in Mg-PSZ ceramics (Kisi *et al.* 1989). A common wavelength of 1.5 Å and identical peak widths were used.

through EXPGUI) which makes this method much faster than manual entry of coordinates and lattice parameters.

4.4 UNIT CELL PARAMETERS

Whereas approximate d-spacings are adequate for most phase analyses, the determination of unit cell parameters requires more accurate d-spacings. The accurate measurement of d-spacings and subsequent analysis to provide accurate unit cell parameters are at the root of almost all downstream analyses of powder diffraction data. Examples include the study of structural variations as a function of external variables such as composition, temperature, pressure, and so on (Chapter 5); the determination of unknown crystal structures (Chapters 5 and 6); and the study of residual stresses and elastic constants (Chapter 11). Although the mathematical relationship between the measured peak position (in 2θ or TOF) and the d-spacing is quite straightforward, the determination of very accurate peak positions and their conversion into accurate unit cell parameters is not.

4.4.1 Systematic errors in peak positions

Unit cell parameters may be determined by powder diffraction methods to great precision, one part in 100,000 or so in special circumstances. However, as with all measurements, there are some instrumental and experimental conditions that introduce systematic errors. To bring the accuracy of the determination in line with the precision, systematic errors need to be taken into account. It has been known for more than half a century that X-ray powder diffractometer peaks may be successfully represented as the convolution of the natural spectral distribution in the source (e.g. Cu Kα_1 spectral line) with several instrumental factors and any sample-dependent effects such as particle size or strain broadening (Alexander 1950, 1954). In flat-plate or Bragg–Brentano geometry with a conventional tube X-ray source, the components along the optical path and their peak shapes are

(i) Spectral width (Lorentzian)
(ii) Finite size of the source as viewed by the sample (Gaussian)
(iii) Flat specimen ($|(2\theta - 2\theta_i)|^{-1/2}$
(iv) Axial divergence ($|2\,(2\theta - 2\theta_i)\cot\theta|^{-1/2}$)
(v) Receiving slit (rectangular)
(vi) Specimen transparency ($\exp|k\,(2\theta - 2\theta_i)|$)
(vii) Misalignment (complex)

These are dealt with in some detail in X-ray texts (e.g. Klug and Alexander 1974) and have recently been incorporated into whole-pattern fitting programs such as TOPAS (http://members.optusnet.com.au/alancoehlo/#input). The convolution approach to diffraction line shapes from the instrument is known as the 'fundamental parameters' approach (Cheary and Coehlo 1992). Additional effects occur due to the sample microstructure such as particle size, strain, and lattice defects to which we devote a later chapter (Chapter 9). The key factor for this section is to note that from this list (iii), (iv), and (vi) are strongly asymmetric on the low 2θ (high d) side leading to peak shifts and systematic errors in the measured d-spacings.

As noted in §3.2 and §3.3, neutron diffractometers are constructed to operate in transmission or Debye–Scherrer geometry. This and their great size tend to make some of these systematic errors inoperative [e.g. (vi)] or less pronounced. The corresponding components of a CW neutron diffraction peak are

(i) Wavelength distribution of the monochromator (symmetric Gaussian)
(ii) Receiving slits (usually vertical Soller collimators) (symmetric triangular or Gaussian)
(iii) Sample height and axial divergence (asymmetric)

Three further systematic errors, unrelated to peak shape are

(iv) Misalignment of the sample (i.e. not in the centre of the diffractometer)
(v) The diffractometer (detector) zero error
(vi) Uncertainty in the neutron wavelength

In TOF neutron diffractometers, the exponential rise and decay of neutron flux associated with each pulse within the target is imprinted on the peak shapes. As the rise and decay time constants are unlikely to be matched, the peaks are asymmetric on the long d-spacing side. This makes the apparent peak position (e.g. maximum count) different from the peak centroid.

The most objective[39] method of correcting systematic peak position errors is to use an internal standard incorporated with the sample material. This is however not always practical (e.g. a monolithic solid sample) or it is not always known in advance that it will be required (e.g. an unknown phase forms during an *in situ* experiment). Next best is data from an external standard, recorded under identical conditions. The most precise set of d-spacings practicable should be determined from all major peaks of the phase of interest *and* the standard material. Then a plot of the observed d-spacings for the standard plotted against the correct d-spacings gives a calibration curve from which the experimental d-spacings may be corrected. For accurate results to be obtained, it is essential that the peak positions of the standard and the unknown phase be determined in the same way – preferably by peak fitting with an appropriate function as will be described in §4.5. The great advantage is that peak fitting will take care of many of the systematic errors associated with peak shapes [(i)–(iii)]. A further advance in computer-aided diffraction analysis, whole-pattern fitting, can also correct for alignment and diffractometer zero errors[40] [(iv) and (v)]. These methods will be discussed in greater detail in §4.5, §4.6, and §5.5.

4.4.2 Indexing (assignment of reflection indices)

Even when the crystal structure and approximate lattice parameters of a substance are known, the assignment of Miller Indices, known in diffraction circles as indexing, can be far from straightforward. For cubic materials, there is only one lattice parameter, a, in the expression relating the d-spacing to Miller indices and lattice parameters [eqn (2.26)]. As the symmetry is reduced, the number of parameters increases (Appendix 1) and an element of ambiguity enters the process; especially if there is some uncertainty in the starting values of the lattice parameters. Historically, elegant graphical methods were developed, for example, Bunn charts and Hull–Davey charts (Klug and Alexander 1974). In these days of easy access to computing power, it is convenient to simply calculate d-spacings for all possible permutations of *hkl* and index the pattern accordingly. It should be stressed at this point that correct pattern indexing requires accurate d-spacings (see §4.5.1). To illustrate, consider the example in Table 4.1. On the left are the raw d-spacings determined from peak maxima for a primitive cubic material (Cu_9Al_4) with a deliberate 2θ zero error of 0.2°. The trial indexing takes the first peak as 100 and

[39] Free from any assumptions concerning peak shapes, and so on.

[40] This is especially true if an internal standard is used so that the neutron wavelength may be determined independently during the analysis.

Table 4.1 Effect of a systematic error on a simple powder pattern indexing.

Raw d-spacing	*hkl*	Corrected d-spacing	*hkl*
8.6040	100	8.7184	100
6.1079	110	6.1648	110
4.9959	111	5.0336	111
4.3312	200	4.3592	200
3.8768	210	3.8990	210
3.5409	211	3.5593	211
3.0689	220	3.0824	220
2.8942	300	2.9061	300
2.7464	310	2.7570	310
2.6192	311	2.6287	311
2.5081	222	2.5168	222
2.4101	320	2.4180	320
2.3228	321	2.3301	321
2.1734	400	2.1796	400
2.1087	410	2.1145	410
2.0496	330/411	2.0549	330/411
1.9951	331	2.0001	331
1.9448	420	1.9495	420
1.8981	421	1.9025	421
1.8546	332	1.8588	332
1.7759	422?	1.7796	422
1.7401	422 or 500/430?	1.7437	500/430
1.7065	500/430 or 510/431?	1.7098	510/431
1.6747	510/431 or 511/333?	1.6779	511/333
1.6161	511/333?	1.6190	520/432
1.5890	520/432 or 521?	1.5918	521
1.5387	521?	1.5412	440
1.5153	440	1.5177	522/441
1.4930	522/441	1.4952	530/433
1.4716	530/433	1.4737	531
1.4510	531	1.4531	600/442
1.4314	600/442	1.4333	610
1.4125	610	1.4143	611/532
1.3768	611/532	1.3785	620
1.3600	620	1.3616	621/540/443
1.3438	621/540/443	1.3453	541
1.3281	541	1.3295	533
1.3130	533	1.3143	622
1.2984	622	1.2997	630/542
1.2843	630/542	1.2855	631
1.2573	631	1.2584	444
1.2445	444	1.2455	700/632
1.2321	700/632	1.2330	710/550/543

Table 4.1 (Continued.)

Raw d-spacing	hkl	Corrected d-spacing	hkl
1.2200	710/550/543	1.2208	711/551
1.2083	711/551	1.2090	640
1.1969	640	1.1976	720/641
1.1858	720/641	1.1864	721/633/552
1.1646	721/633/552	1.1650	642
1.1544	642	1.1548	722/544
1.1445	722/544	1.1448	730
1.1350	722/544 or 730?	1.1350	731/553

uses the trial lattice parameter determined from that peak (8.6040 Å) to attempt an indexing of the entire pattern. Note that the indexing becomes ambiguous after the first 20 peaks and incorrectly indexed peaks occur from about the middle of the list onwards. The corrected list on the right was determined by whole-pattern fitting and the refinement of a zero point error correction (see §4.5 and §4.6). When dealing with a known structure, as is the case here, this is a minor problem generally only of nuisance value. However, when the crystal structure and unit cell parameters of the substance are unknown, errors of this magnitude will prevent the solution being found.

The indexing of a powder diffraction pattern from a completely *unknown* crystal structure is a relatively daunting task. Before the widespread availability of computers, the crystal structures solved from powder diffraction patterns were of three kinds:

(i) Relatively small unit cells ≤ 200 Å^3
(ii) Relatively high symmetry (cubic, tetragonal, hexagonal)
(iii) Closely related to a high symmetry structure (e.g. Ruddlesden–Popper phases)

Indexing was conducted by trial and error methods using intuition and a knowledge of simple relationships that must exist in the d-spacings from a particular symmetry. For example, in the tetragonal system, from eqn (2.27) we see that the d-spacing of $hk0$ peaks only depends on the value of $\left(h^2 + k^2\right)/a^2$. Since $h^2 + k^2$ can only take certain values (1, 2, 4, 5, 8, etc.), searching a list of d-spacings for peaks in these ratios will reveal whether the material is tetragonal or not. If it is, the peaks that fit the ratios are $hk0$ and may be easily indexed. Similarly, $00l$ peaks depend only on the value of l^2/c^2 and as l^2 can only take certain values (1, 4, 9, 16, 25, etc.), the $00l$ peaks are readily identified and the value of c determined. Similar methodologies also apply to hexagonal and trigonal materials. It becomes increasingly difficult to obtain the correct indexing as the unit cell size increases and/or the symmetry decreases to below orthorhombic.

It is here that automated searching becomes necessary if a solution is to be found in reasonable time. There are many search strategies employed and automated indexing has become an important sub-branch of the field of powder diffraction.

Since the determination of completely unknown unit cells is more correctly a part of *ab initio* crystal structure solution, a more detailed discussion is reserved for §6.2.

4.4.3 Unit cell parameter refinement

In §4.4.1, the causes of systematic errors in measured peak positions and hence d-spacings were briefly discussed. With careful instrument alignment (and design), systematic errors can be minimized, however they are rarely eliminated. If the only information required from the neutron diffraction pattern is a list of d-spacings (very rare), then the compilation of a correction curve from the known d-spacings of an internal standard material will give very good answers.

In the absence of an internal standard, other methods must be used. A feature of all of the systematic errors in peak position is that they diminish as d becomes smaller (i.e. at large values of 2θ for CW). Historically this was used to devise extrapolation methods for the correction of systematic errors in X-ray peak positions. An example is the Nelson–Riley function, the bracketed term in eqn (4.1):

$$\frac{\Delta d}{d} = K\left(\frac{\cos^2\theta}{\sin^2\theta} + \frac{\cos^2\theta}{\theta}\right) \tag{4.1}$$

A plot of the lattice parameter inferred from each d-spacing against the N–R function will extrapolate to a very precise value at $\theta = 90°$ for some types of systematic error.

The applicability of a particular extrapolation function depends on the nature of the systematic error to be corrected. Some recommendations for X-ray powder diffraction patterns may be found in the International Tables for X-ray Crystallography Volume 2 (Kasper and Lonsdale 1959). The Nelson–Riley (N–R) function yields relatively linear plots for conventional CW diffractometers; however, plotting against $\sin^2\theta$ (or $\cos^2\theta$) alone should also be trialled for comparison. An example is shown in Fig. 4.10 using the data from Table 4.1. It may be seen that, although the fit is good over most of the range, the data points deviate from the fitted straight line as N–R approaches zero for this particular type of systematic error (CW diffractometer zero error). The extrapolated lattice parameter is 8.7134 Å compared with the true value of 8.7184 Å, a residual relative error ($\Delta a/a$) of 5.7×10^{-4} which is acceptable for many applications.

Extrapolation functions such as the N–R function are of greatest use for high symmetry materials. For example, the γ-brass in Fig. 4.10 has a cubic structure and so every measured d-spacing gives directly an estimate for the lattice parameter a. Reducing the symmetry to tetragonal immediately limits the number of reflections that can be used in the extrapolation; estimates for a being obtained from $hk0$ peaks and estimates for c from $00l$ peaks. Peaks with mixed indices (i.e. $h0l$, hhl, hkl, etc.) are not useful for this method. Cohen (1935, 1936) made the extrapolation process objective by applying the method of least squares. The method is summarized in books such as those by Warren (1969, 1990) and Cullity (1978). The least squares

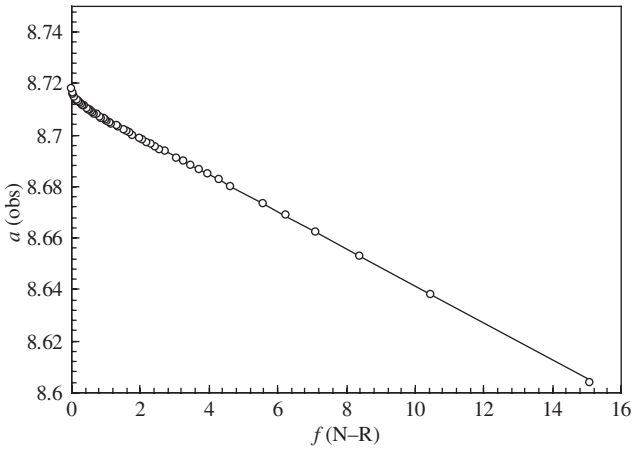

Fig. 4.10 Plot against the Nelson and Riley function, of the apparent lattice parameter a, determined from individual peaks in the calculated CW neutron diffraction pattern of the intermetallic compound γ-brass (Cu_5Zn_8) with a deliberately introduced 0.2° 2θ zero error.

procedure has the added advantages that peaks with any *hkl* can be incorporated into the calculation and it may be readily automated. As several systematic errors may be present at one time, it is not usually profitable to use extrapolation methods when very accurate lattice parameters are required. In those cases, the use of an internal standard material and/or the more powerful methods outlined later, are recommended.

As noted earlier, neutron diffraction patterns are only rarely recorded for the sole purpose of lattice parameter refinement. In a majority of cases, integrated intensities, peak widths, and peak shapes will also be put to good use. Consequently, it is rare that some form of peak fitting is also not conducted. For example, the data used for lattice parameter refinement may have been originally generated by fitting individual peaks to reduce the influence of systematic peak shape errors (§4.3 and §4.4.1). For those equipped with the necessary computer software, unit cell refinement from individual d-spacings has been largely replaced by whole-pattern fitting techniques that simultaneously optimize the fit of a calculated pattern to the observed data. An introduction to whole-pattern fitting (for lattice parameter determination) is reserved for §4.6, however it is first necessary to explore the basic shape and breadth of neutron powder diffraction peaks.

4.5 PEAK SHAPES AND WIDTHS

It is apparent from §4.3 and §4.4 that there are many stages in the analysis of powder diffraction patterns in which it may be advantageous to fit computed peaks to observed peaks. Carefully conducted peak fitting gives precise peak positions for

unit cell determination, indexing, residual stress studies, and so on. The integrated intensities so determined can be useful in *ab initio* structure solution (Chapter 6) and the peak widths for obtaining microstructural data (Chapter 9). We begin from the perspective of fitting individual peaks with simple functions, and then (§4.6) extend this concept to whole pattern fitting. Whole pattern fitting is explored in far greater detail in Chapter 5, especially as it relates to crystal structure analysis. In this chapter, we present sufficient detail that the method may be applied to the many *non-crystallographic* uses of neutron powder diffraction data as well as in the preliminary analysis of data recorded for crystal structure determination.

4.5.1 Constant wavelength diffractometer peak shapes

The peaks recorded by a low-medium resolution CW diffractometer are often very well described by a Gaussian function which may be written (Rietveld 1969):

$$y_i = \frac{2\sqrt{\ln 2}}{H_k\sqrt{\pi}}\exp\left[-4\ln 2\left\{\frac{(2\theta_i - 2\theta_k)}{H_k}\right\}^2\right] \tag{4.2}$$

where y_i is the intensity of step i, H_k is the full width at half maximum height of the kth peak, $2\theta_i$ is the position of the ith point, and $2\theta_k$ is the (true) position of the kth peak.[41] Fitting is conducted by optimizing the values of $2\theta_k$ and H_k by the method of least squares or other suitable optimization algorithm (see §5.5.3). Figure 4.11 shows a CW neutron diffraction peak fitted by eqn (4.2) with an additive linear background term. If desired, the integrated intensity can be readily derived from the refined parameters.

Higher resolution CW patterns develop 'tails' to the reflections that are broader than predicted by eqn (4.2). The peak shown in Fig. 4.12, from the work of Hill and Howard (1985), illustrates this effect. Peaks with wide tails are common in many forms of spectroscopy and in X-ray diffraction where they are modelled using a Lorentzian function:

$$y_i = \frac{2}{\pi H_k}\frac{1}{1 + 4\,(2\theta_i - 2\theta_k)^2/H_k^2} \tag{4.3}$$

Purely Lorentzian peak shapes are not observed in neutron powder diffraction patterns, however peaks with a mixed character are common (e.g. Fig. 4.12). These usually can be described using a convolution of Gaussian and Lorentzian peaks known as the Voigt function (Table 5.9 and §5.5.2). The same peaks can be equally well described using the pseudo-Voigt function, which is a mixing of the two peak

[41] The peak shape functions given in this section are normalized to have integrated area equal to 1 and must be appropriately scaled to fit actual data.

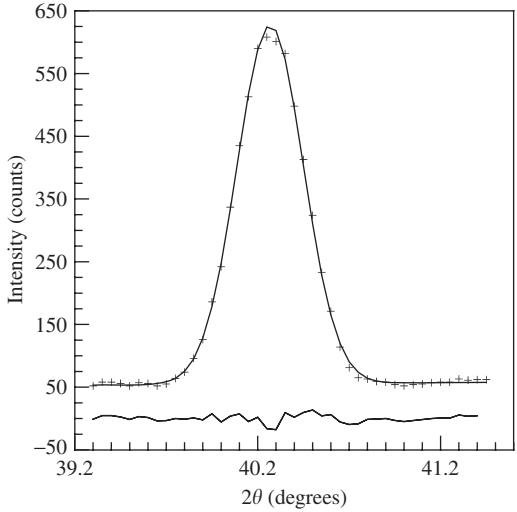

Fig. 4.11 Fit of a simple Gaussian function (eqn (4.2)) to a medium-resolution CW neutron diffraction peak. The data are shown as (+), the fitted Gaussian as a solid line and the difference ($y_{obs} - y_{calc}$) below.

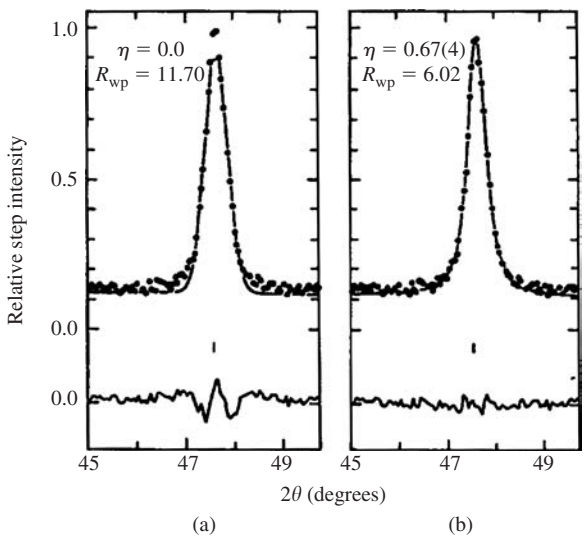

Fig. 4.12 Comparison of the fit to (a) Gaussian and (b) pseudo-Voigt functions of a CW neutron diffraction peak from electroformed β-PbO_2 recorded on the high-resolution powder diffractometer at the HIFAR reactor in Sydney (Hill and Howard 1985). The data points are given as circles and the fitted functions as lines. Below are shown a difference plot on the same scale and a marker giving the peak position. Also shown are the agreement index R_{wp} (see §5.5.3) and the pseudo-Voigt mixing parameter η.

shapes by simple addition:

$$y_i = (1-\eta)\frac{2\sqrt{\ln 2}}{H_k\sqrt{\pi}}\exp\left[-4\ln 2\left\{\frac{(2\theta_i - 2\theta_k)}{H_k}\right\}^2\right] + \eta\frac{2}{\pi H_k}\frac{1}{1+4\,(2\theta_i - 2\theta_k)^2/H_k^2} \tag{4.4}$$

where η is the Lorentzian fraction, or 'mixing parameter'.

The pseudo-Voigt function is widely used in laboratory X-ray powder diffraction where it often gives a superior fit to the observed peaks. It is also often used for CW neutron patterns although here the full Voigt function is also quite frequently used. As shown by the line in Fig. 4.12, the pseudo-Voigt function gives a very satisfactory fit to the observed peak. Most modern powder diffraction peak fitting programs, pattern decomposition programs (see §4.6), and Rietveld refinement programs (see §4.6 and §5.5) incorporate pseudo-Voigt and/or Voigt functions among the peak shape options.

It has been mentioned previously (§4.2 and §4.4.1) that a degree of asymmetry occurs in the low and high angle reflections of CW patterns. There have been several attempts to determine the functional form of the asymmetry or to devise numerical methods for modelling it. Rietveld (1969), in his initial development of whole pattern fitting, applied to the Gaussian peak shape function of eqn (4.2) an empirical multiplicative correction factor (C say) of the form:

$$C = \left\{1 - \frac{P\,(2\theta_i - 2\theta_k)^2 \cdot s}{\tan\theta_k}\right\} \tag{4.5}$$

where P is the asymmetry parameter and s takes the value $+1$, 0, or -1 depending on whether $2\theta_i - 2\theta_k$ is positive, zero, or negative. This correction factor, however, was soon found to be wanting. Howard (1982) and Prince (1983) considered the response of a slit of height $2H$ at a distance R from the sample as it traversed an infinitely sharp Debye–Scherrer cone, then evaluated the convolution of this response with symmetric peak shape functions such as given in eqns (4.2), (4.3), and (4.4). They obtained different but essentially equivalent results, involving a single asymmetry parameter that was refinable but connected to the experimental arrangement through the factor $\frac{1}{2}(H/R)^2\cot 2\theta_k$. The analysis has been extended to account for a finite sample height $2S$ (van Laar and Yelon 1984; Finger *et al.* 1994), the convolutions now being completed by numerical integration.

4.5.2 TOF diffractometer peak shapes

Time-of-flight neutron powder diffraction peaks have quite complex shapes. This is largely because the rise and decay of the spallation pulse are superimposed onto the fundamental (e.g. Gaussian or Voigt) peak shape. An example is shown in

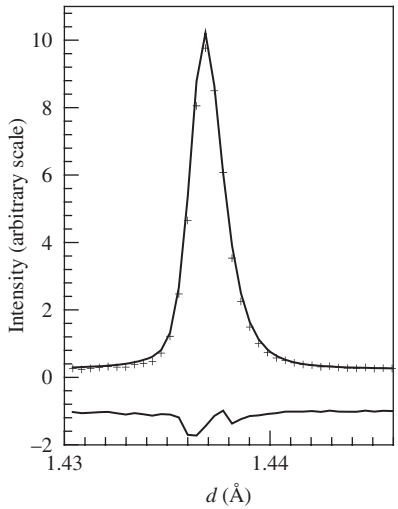

Fig. 4.13 Typical peak from a TOF neutron diffraction pattern fitted by eqn (4.6). Data are given as (+), the calculated pattern as a solid line and the difference below. Note that this peak was taken from a whole pattern fit not an individual peak fit.

Fig. 4.13. The exponential rise of the pulse and its exponential decay have different time constants leading to asymmetry across the entire pattern. To model the peak shapes, we form the convolution of an exponential rise followed by exponential decay with one of the simpler shapes. In the simplest case, that is convoluting the exponentials with a Gaussian, the result reads (Von Dreele *et al.* 1982):

$$y_i = A\left[\mathrm{e}^u \mathrm{erfc}\,(y) + \mathrm{e}^v \mathrm{erfc}\,(z)\right] \tag{4.6}$$

where
$u = \alpha/2(\alpha\sigma^2 + 2t_i - 2t_k)$, $v = \beta/2(\beta\sigma^2 - 2t_i + 2t_k)$, $y = (\alpha\sigma^2 + t_i - t_k)/\sigma\sqrt{2}$, $z = (\beta\sigma^2 - t_i + t_k)/\sigma\sqrt{2}$, $A = (\alpha\beta)/2(\alpha + \beta)$, $\sigma = H_k/\sqrt{8\ln 2}$, and erfc is the complementary error function. This is the result for a Gaussian peak of full width half maximum H_k located at time of flight t_k convoluted with a rising exponential, time constant α followed by a slower decaying exponential, time constant β. It should be noted that the peak shown in Fig. 4.13 was taken from a whole pattern fit to data from a slightly imperfect sample from which there is some sample-induced peak broadening that lessens the impact of asymmetry in the instrumental peak shape.

4.5.3 Peak widths

Close scrutiny of a powder diffraction pattern reveals that the peak characteristics vary considerably across the pattern. A simple CW example (low resolution) is shown in Fig. 4.14. The first thing of importance to note is the broadening or dispersion at large values of 2θ. As part of their pioneering work on collimators,

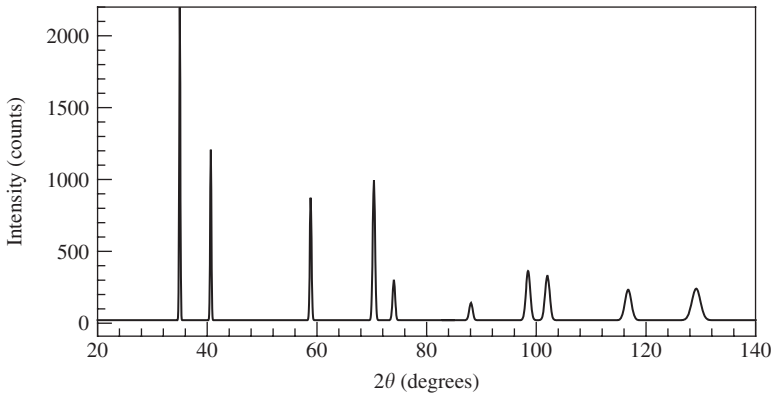

Fig. 4.14 CW neutron diffraction pattern showing line width changes with increasing diffraction angle.

Caglioti *et al.* (1958) determined that the widths of Bragg peaks in a CW neutron powder diffraction pattern usually vary according to a generic quadratic form:

$$\mathrm{FWHM}^2 = U \tan^2\theta + V \tan\theta + W \tag{4.7}$$

where U, V, and W are constants for a given diffractometer. The values of U, V, and W depend on the collimator half-angles $(\alpha_1, \alpha_2, \alpha_3)$ and mosaic spread (β) of the monochromator defined in §3.2.2 and may be computed by comparing eqn (4.7) with eqns (3.3) and (3.4). An example plot of eqn (4.7) for the original CW High Resolution Powder Diffractometer at Lucas Heights (Howard *et al.* 1983) is compared with a medium-resolution CW diffractometer in Fig. 4.15. Note that the value of V is usually negative for medium–high-resolution instruments leading to a pronounced minimum in the resolution curve at slightly less than the monochromator take-off angle $2\theta_{\mathrm{M}}$. In general, the peak shapes will also vary across the pattern. This would be reflected in the variation in any peak shape parameter, such as the Lorentzian fraction η in the pseudo-Voigt. This parameter might be expected to show a linear or quadratic variation with angle 2θ.

Already it should be evident (§4.5.2) that TOF diffractometer profiles from spallation sources are more complex. The time constants for the rise and fall of the neutron pulse, α and β, are in effect energy-dependent, and are found to vary (Von Dreele *et al.* 1982) according to

$$\alpha = \alpha_0 + \frac{\alpha_1}{d} \quad \text{and} \quad \beta = \beta_0 + \frac{\beta_1}{d^4} \tag{4.8}$$

where the energy dependence is included as a dependence on the d-spacing in the diffraction pattern, and α_0, α_1, β_0, β_1 are constants. The width of the Gaussian sample contribution, σ can be considered to vary as d or d^2, corresponding to strain broadening or crystallite size broadening, respectively. Despite this complexity, it is found that in the absence of the sample-induced effects dealt with in Chapter 9, the d-spacing resolution in TOF patterns (i.e. FWHM/d) is essentially constant

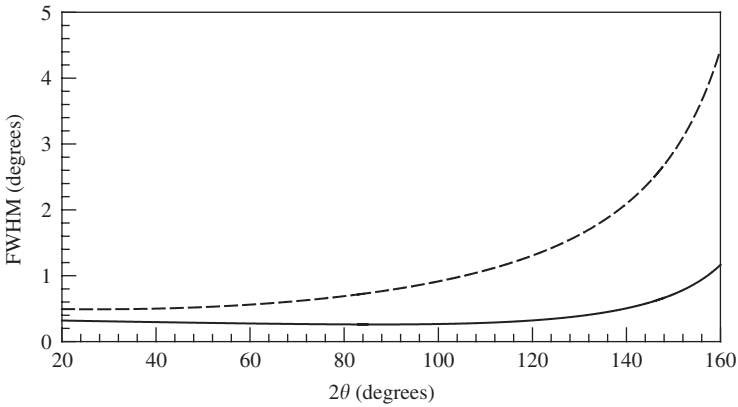

Fig. 4.15 Resolution curves for CW neutron diffractometers with notionally high resolution (solid line) and medium resolution (dashed line).

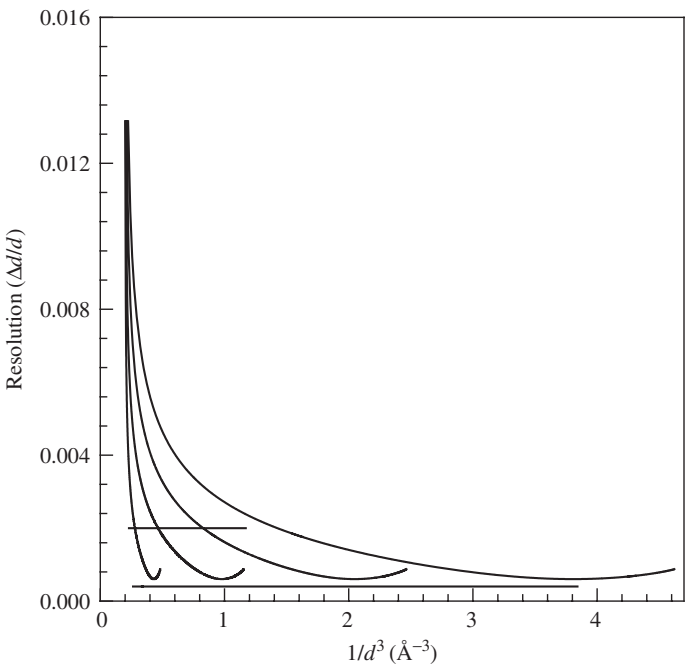

Fig. 4.16 Comparison of four resolution curves from a very high-resolution CW diffractometer with the constant resolution of the backscattering and 90° detector banks of a very high-resolution TOF diffractometer. The x-axis used is $1/d^3$ as, against this function, the distribution of reflections in a powder pattern is uniform (*cet. par.*).

across the whole pattern. Figure 4.16 illustrates this for a very high-resolution TOF powder diffractometer. The data are plotted against $1/d^3$ across which *cet. par.* the density of diffraction peaks is uniform. Also plotted are the equivalent curves for a very high-resolution CW diffractometer at four wavelengths. Note that both are capable of exceptional resolution – CW at the cost of d-spacing range and TOF at the cost of the larger d-spacing peaks, which though few in number, can be essential for some kinds of problems such as magnetic structures (Chapter 7) or long-period structures. At these extremes of resolution, sample-induced broadening is often more important in determining the resolution than instrumental effects (see Chapter 9).

4.6 WHOLE PATTERN FITTING

In the modern context, given that we can obtain peak position estimates using the methods in §4.4 and that we have excellent mathematical functions for modelling peak shapes (§4.5), combining them into whole pattern fitting methods seems like an obvious step! This approach requires, however, a computing capacity that has not always been readily available, and indeed not until 1967 (Rietveld 1967) did the first report on such a method appear in the literature. Whole pattern fitting methods have been in a state of continual development ever since (see §1.3).

In the wider context of the other chapters in this book, whole pattern fitting has advantages in accounting for overlapping reflections, locating minor symmetry changes (peak splittings), locating peaks from superlattices or minor phases, phase quantification, and diffraction peak shape analysis. These will be dealt with in detail in the following chapters.

The philosophy of whole pattern fitting in the context of this chapter (preliminary analysis) is that:

(i) Peak fitting corrects the observed peak positions for the effects of peak shape (§4.3 and §4.5).
(ii) Fitting the whole pattern at once also corrects for diffractometer zero and sample misalignment errors.

Thereby, most systematic errors in peak positions or d-spacings are properly accounted for.

The remaining systematic error is the uncertainty in the neutron wavelength emerging from the monochromator. This may be overcome with the use of an internal standard reference material.

There are two kinds of whole pattern fitting techniques. The original Rietveld refinement method (Rietveld 1969) is structurally based, that is a model for the crystal structure, including the atom locations within the unit cell, is required before starting. This method hardly constitutes a preliminary analysis and hence is dealt with in §5.5. Several non-structural whole-pattern fitting methods have however been subsequently developed (Schäfer and Will 1979; Pawley 1981; Will *et al.*

1982, 1983; Le Bail *et al.* 1988). The methods differ little in their basic philosophy, however there are slight differences in the methodology employed.

A Pawley fit starts with unit cell parameter estimates derived in other ways (§4.4) and the peak shape functions described in §4.5 to individually fit calculated peaks to the observed intensity at d-spacings (2θ's) corresponding to every *hkl* below the Bragg cut-off. If the space group is known, it can be used to limit the number of peaks calculated. Otherwise, the most general space group for the relevant crystal class must be used ($P1$, $P2$, $P222$, $P4$, $P3$, $P6$, $P23$).

Part of the fitting is constrained, that is all peaks have the same diffractometer zero offset and all peak positions are calculated from the same unit cell parameter set. Both the zero offset and the unit cell parameters are refined (optimized) by the method of least squares. The intensities of the peaks are however unconstrained, that is each is fitted by refinement of an *individual* scale factor. The peak width and shape parameters of the appropriate peak shape function are also able to be refined. Alternatively they may be constrained at values appropriate for the diffractometer used (on the assumption of no sample-induced effects) which is invaluable in identifying minor peak splittings. The output is a refined set of unit cell parameters, and for each *hkl*, an objectively determined integrated intensity (except in cases of complete or near-complete overlap). The results from a Pawley refinement can often be useful in the identification of space groups (see §5.3). Integrated intensities determined in the refinement may be used directly in *ab initio* structure solutions (§5.3 and Chapter 6), or for texture analyses (Chapter 9).

The two stage method of Jansen *et al.* (1988) is very similar except for two points. First, one of the fitting programs described, PROFIN, allows a whole-pattern fit

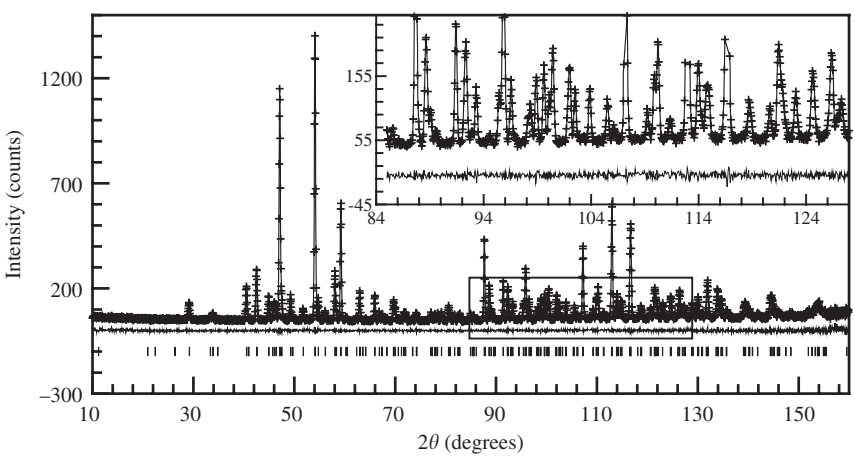

Fig. 4.17 Plotted output from a whole-pattern fit (Le Bail method) to the neutron diffraction pattern of $Ca_3Ti_2O_7$ recorded using 1.893 Å neutrons. The inset shows a close-up view of the region enclosed in the small rectangular box.

to be made without reference to any crystallographic information (including estimated unit cell parameters). This extra degree of versatility would be invaluable for the early stages of data analysis (§4.3 and §4.4). The data delivered (d-spacings and intensities) are then available for phase identification (§4.3) or peak indexing (§4.4.2). Once indexed, a more constrained whole-pattern fit, using the unit cell derived from the initial run, can yield precise cell parameters and intensities. It has the additional advantage of being able to handle diffraction patterns from incommensurately modulated or quasi-crystalline structures where the relationships between peaks are irrational. The second difference from Pawley's method is a minor one concerning the handling of complete or near-complete overlap of reflections. Pawley's method assigns equal weight to very nearly overlapped reflections whereas Jansen, Schäffer, and Wills programs treat unresolved peaks as a single unit (Jansen *et al.* 1988).

The Le Bail method (Le Bail *et al.* 1988) is a variation of the Rietveld method that does not however require crystal structure input. A description of this method appears (§5.6) after the detailed account of the Rietveld method in Chapter 5. An example of a whole pattern fit (Le Bail method in this case) is shown in Fig. 4.17.

5

Crystal structures

5.1 NEUTRON POWDER DIFFRACTION AND CRYSTAL STRUCTURES

The most frequent applications of neutron powder diffraction have been and still are applied to the solution and refinement of crystal and magnetic structures. The early applications at Oak Ridge were of this kind, and the Rietveld method, which helped spark a renaissance in neutron powder diffraction was developed for exactly such applications. Despite increasing the use of neutron powder diffraction for purposes such as phase quantification (Chapter 8), scanning of internal strains in engineering components (Chapter 11), and microstructural characterization (Chapter 9), these applications do not seem set to outnumber those in crystal and magnetic structure determination. In particular, it seems unlikely that neutron powder diffraction will find the same widespread use in phase identification as the corresponding X-ray technique.

The development of new compounds and materials is proceeding apace, and with each new compound or material comes the question of its crystal and molecular structure. Many properties of interest depend on crystal structure, and additionally on other factors such as the microstructure of the material. For example, the polarization in a ferroelectric (e.g. $BaTiO_3$) should be calculable from precise data on the positions of ions of known ionic charge. Attempts to understand the superconducting properties of oxide superconductors or the magnetic field-dependent resistivity in the case of materials displaying colossal magneto-resistive effects often start from detailed knowledge or assumptions about the atomic arrangement in these materials. The efficacy of a newly developed drug may depend on the details of its geometry in relation to that of the target system. In many cases of course, single crystals are available and structure solution and refinement can be completed by the standard methods of X-ray crystallography. In other cases, the material is by its nature polycrystalline, or attempts to grow even small single crystals result in 'twinning' (the product is an aggregate of two or more crystals in different but related orientations), or are otherwise doomed. X-ray and neutron powder diffraction may then provide the means to a structure solution. In such cases, the X-ray data would be important in establishing the unit cell and the positions of the heavier atoms, whereas the neutron data could be used to locate light atoms.

Crystal structure determination can be considered a two-step process. The first step is structure solution, in the sense of determining the unit cell, space group symmetry (see later), and approximate atomic positions. The elements of this first step are considered in more detail in Chapter 6. These provide a starting

model for the second step, structure refinement, in which the atomic positions are adjusted so as to optimize, in a least squares sense, the fit of the calculated to the observed diffracted intensities. By this means atomic positions may be precisely determined. In structure solution as just described, neutron powder diffraction plays a supporting role, being useful in instances that single crystals cannot be obtained. The technique is invaluable, however, at the structure refinement step, since it tends to give more precise information on atomic positions (and vibrations), most especially on light atoms in the presence of heavy ones. We note that in many instances, a starting model has been developed on the basis of analogy with chemically similar compounds, or obtained for a lower symmetry structure from the expected close relationship with the higher symmetry structure on the other side of a structural phase transition. This circumvents the need for the formal step of structure solution, and if refinement is successful then structure determination is complete. The determination of the structures of MoF_6 and WF_6 using the analogy with UF_6 (Levy *et al.* 1975a,b) are examples of the first approach to a starting model, whereas the determination of the low-temperature structure of NaOD (Bastow *et al.* 1986b) starting from the known room temperature structure is an example of the second.

Basics of the crystalline state, such as the space lattices, Miller indices, directions, and atomic position coordinates have been outlined in §2.2.1. The discourse on the crystalline state is extended to cover such concepts as space group symmetry in §5.2. In the subsequent sections we show how these concepts are applied to the determination of crystal structures, including the simple methods of obtaining trial structures, and subsequent structure refinement. The chapter concludes with a number of illustrative examples of structure determination and its applications.

5.2 MORE CRYSTALLOGRAPHY – DESCRIPTION OF CRYSTAL STRUCTURES

The tools presented in §2.2.1 are sufficient to describe the structure of a periodic array of atoms such as occurs in the crystalline state. The structure can be fully described by specifying the lattice, by means of the lattice translation vectors, $\boldsymbol{a}$, $\boldsymbol{b}$, and $\boldsymbol{c}$ that form the edges of the parallelepiped known as the unit cell, and the basis, comprising all the atoms that lie within that unit cell. The position of the nth atom in the unit cell is given by the vector $\boldsymbol{r}_n$ or fractional coordinates x_n, y_n, and z_n [eqn (2.4)]. Although the specification of the lattice together with a listing of the types and positions of all the atoms in the unit cell does indeed represent a crystal structure description, it neither reveals nor uses the symmetry that is present in most cases. Such symmetry is of interest, particularly to crystallographers, and provides the means for a more concise description of the structure.

In practice, crystal structures are described as having the symmetry of one of 230 distinct space groups. The crystal is then fully described by giving the space group symmetry, the lattice parameters appropriate to the given space group, and the types and positions of a minimal number of atoms such that all the remaining atoms are

generated by the symmetry operations of the space group. The *International Tables for Crystallography Volume A: Space Group Symmetry* (Th. Hahn ed.) is an indispensable reference. The Bilbao Crystallographic server (http://www.cryst.ehu.es) is another rich crystallographic resource. This section will include a description of the various symmetry operators that appear in the different space groups, how these operators combine to form groups (space groups), and importantly advice that may help in reading the entries that appear in the above-mentioned *International Tables*. Section 5.3 will provide advice on how to determine the space group experimentally, again with the aid of the *International Tables*.

5.2.1 Symmetry operators

Every lattice vector is a symmetry operator for the crystal, because the lattice is defined so that the translation of the crystal by such a vector carries the crystal into coincidence with itself. But as just indicated, the symmetry of a crystal structure is often higher, in that there are additional symmetry operations that will carry the crystal into itself. The complete set of symmetry operators, including those resulting from the successive application of other operators, forms a group,[42] known as the space group.

To start, we consider just the lattice, or equivalently the crystal structure formed by associating a symmetric basis (e.g. a single atom) with each of the lattice points. This already has additional symmetry – the negative of every lattice vector being also a lattice vector, there is an inversion centre (reversal of the sense of all vectors carries the lattice into itself) at every lattice point. We emphasize that inversion symmetry is a universal property of lattices, but not of crystals, since it is destroyed unless the basis also shows inversion symmetry around the same point. The lattice may also show rotational symmetry about certain axes, that is rotation about such an axis by an angle $2\pi/n$ may carry the lattice into itself. The value of n is restricted to the values 1, 2, 3, 4, and 6, as is most easily understood by consideration of the possible rotations of a two-dimensional net.

We make use of Cartesian axes in the plane, the unit vectors being denoted $\boldsymbol{i}$ and $\boldsymbol{j}$. The rotation is taken to be around an axis through a lattice point and perpendicular to the net. Let us suppose $\boldsymbol{a} = a\boldsymbol{i}$ is the shortest vector in the two-dimensional net (Fig. 5.1). A rotation through an angle $2\pi/n$ carries this to $\boldsymbol{b} = a(\boldsymbol{i}\cos 2\pi/n + \boldsymbol{j}\sin 2\pi/n)$. Since $\boldsymbol{a}$ and $\boldsymbol{b}$ are non-collinear vectors of shortest length, they generate the entire net. A second rotation produces a vector making an angle $4\pi/n$ with $\boldsymbol{a}$, that is the vector $a(\boldsymbol{i}\cos 4\pi/n + \boldsymbol{j}\sin 4\pi/n)$ – this also must be a lattice vector and hence expressible as a sum of the form $M\boldsymbol{a} + N\boldsymbol{b}$ where M and N are integers. A necessary condition is that $\sin 4\pi/n = N \sin 2\pi/n$ or $\sin 2\pi/n\,(2\cos 2\pi/n - N) = 0$, that is $\sin 2\pi/n = 0$ or $\cos 2\pi/n = N/2$, where

[42] A group is a set of elements (here symmetry operators) such that (i) the operation of any two elements produces another element in the group (ii) the successive operation of any three elements obeys the associative rule (written $(a \cdot b) \cdot c = a \cdot (b \cdot c)$), (iii) there is an identity element such that its combination with any other element leaves that other element unchanged, and (iv) for every element there is an inverse, such that its combination with the original element gives the identity.

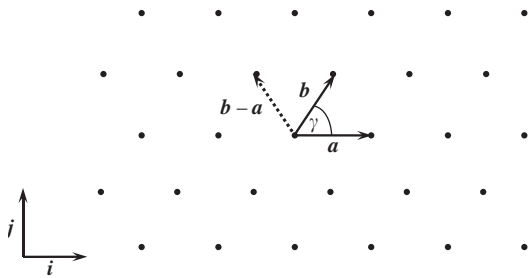

Fig. 5.1 A two-dimensional net of points with rotational symmetry. The unit vectors $\boldsymbol{a}$ and $\boldsymbol{b}$ are related by rotation through the angle γ ($2\pi/6$ in this case). Further rotation through the same angle merely produces other lattice vectors. Cartesian unit vectors $\boldsymbol{i}$ and $\boldsymbol{j}$ used in the derivation are also shown.

N is an integer. The first condition gives the (trivial) solution $n = 1$, and the second gives $n = 2, 3, 4, 6$ for $N = -2, -1, 0, 1$, respectively. It can be shown that these conditions are also sufficient to ensure that the vector produced by two successive rotations is a lattice vector. The axes are described as two-, three-, four-, and sixfold rotation axes.

The extension of these results to space lattices is relatively straightforward. Rotation of a lattice (or crystal structure) by 2π around any axis carries the object into itself. The two-, three-, four-, and sixfold rotation axes for a net are preserved in the three-dimensional lattice if and only if the translations reproducing this net in three dimensions are perpendicular to the net itself – that is, the fundamental translation vector $\boldsymbol{c}$ is perpendicular to both $\boldsymbol{a}$ and $\boldsymbol{b}$. The reader will appreciate that when the net is reproduced above and below the starting net, not only is the n-fold rotation axis preserved, but also additional symmetries are introduced. In particular, the lattice will be carried into itself by mirror reflection in a plane coinciding with the starting net, and therefore perpendicular to the rotation axis, or indeed by a mirror plane situated midway between the starting and a neighbouring net.

The group of symmetry operators (excluding translations) operating at or through a lattice point that carry the lattice into itself is called the *crystallographic point group*. The point group includes elements such as the inversion centre, two-, three-, four-, and sixfold rotation axes, and mirror planes. Another element encountered is the n-fold rotation–inversion or, more simply, n-fold inversion axis. The operation comprises a rotation about this axis through angle $2\pi/n$ followed by inversion through a centre located on this axis. Again n is restricted to take the values 1, 2, 3, 4, and 6. With $n = 1$, the result is simply an inversion. The results obtained for $n = 2$, 3, and 6 can be obtained also as combinations of rotation axes with centres or mirror planes. For $n = 4$, the result is an inversion tetrad that cannot be reproduced by any combination of other elements. The written and graphical symbols for the centre of symmetry, mirror planes, and the n-fold rotation and inversion axes ($n = 2, 3, 4, 6$) are shown in Table 5.1.

Table 5.1 Written and graphical symbols for symmetry operators (from Woolfson 1970).

Type of symmetry element	Written symbol	Graphic symbol	
Centre of symmetry	$\bar{1}$		
		Perpendicular to paper	In plane of paper
Mirror plane	m		
Glide planes	$a\ b\ c$	Glide in plane of paper	Arrow shows glide direction
		Glide out of plane of paper	
	n		
Rotation	2		
	3		
	4		
	6		
Screw axes	2_1		
	3_1, 3_2		
	4_1, 4_2, 4_3		
	6_1, 6_2, 6_3, 6_4, 6_5		
Inversion axes	$\bar{3}$		
	$\bar{4}$		
	$\bar{6}$		

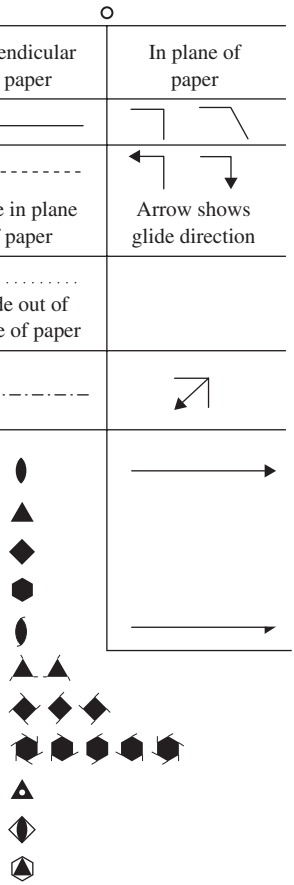

The last of the symmetry operators arise only in three dimensions, and only when there is more than one atom (or lattice point) in the unit cell. These are glide operations, and operations associated with screw axes.

The glide operation involves a glide plane, and this must contain two of the unit cell vectors or must be parallel to a plane defined by two such vectors. The operation is the reflection of the lattice or crystal structure in that plane combined with translation parallel to that plane of one-half or one-quarter of a lattice vector. In the event that the reflection is combined with translation by one-half the lattice vector, two successive applications will carry the lattice or crystal structure into

itself. The glide plane and the translation vector in that plane are needed to specify a glide operation – the first is implicit in the space group symbol (see §5.2.4), and the second is indicated by a, b, c, for glide translations $\boldsymbol{a}/2$, $\boldsymbol{b}/2$, $\boldsymbol{c}/2$, respectively, n for translation by the sum of two of these (the two that correspond to the vectors defining the glide plane), and d for the translation by the sum of two (depending again on the glide plane) of $\boldsymbol{a}/4$, $\boldsymbol{b}/4$, $\boldsymbol{c}/4$.

A screw operation combines a rotation through angle $2\pi/n$ about an axis in the structure accompanied by a displacement m/n ($m < n$) times the unit cell vector in the direction of this axis. A screw axis is denoted by n_m. If m is a submultiple of n, the n_m screw axis is also an m-fold rotation axis. The written and graphical symbols for glide and screw operations are shown in Table 5.1.

We have in this section described the various symmetry operators encountered in the 230 space groups, and shown the symbols representing them, as are used in the *International Tables*. An alternative algebraic description for each operator can be given by showing the result produced by its operation on an object (atom) at the general point x, y, z. For example, a mirror plane at $z = 0$ will operate on the object at x, y, z to produce another equivalent object at $x, y, -z$. For a more comprehensive listing of operators described in this manner, we refer the reader elsewhere (Megaw 1973; §8.14).

5.2.2 Seven crystal systems

We are now in a position to examine further the different geometrical forms of the unit cell, corresponding to the seven distinct crystal systems (Table 2.1). We recall that the unit cell (not necessarily primitive) is defined by translation vectors $\boldsymbol{a}$, $\boldsymbol{b}$, $\boldsymbol{c}$, or lattice parameters $a, b, c, \alpha, \beta, \gamma$. The possibility that the lattice generated by $\boldsymbol{a}$, $\boldsymbol{b}$, $\boldsymbol{c}$ may contain n-fold rotation axes with $n = 3, 4, 6$ imparts special significance to angles 120°, 90°, and 60°, in that the occurrence of these angles in the unit cell may lead to a lattice containing the corresponding symmetry element. The symmetry can also be affected by the equality or otherwise of the unit cell edges a, b and c. For example, for $\alpha = \beta = \gamma = 90°$, the symmetry is orthorhombic, tetragonal, or cubic according to whether $a \neq b \neq c, a = b \neq c$, or $a = b = c$. The seven different crystal systems are ultimately distinguished by different symmetries of the lattices generated by the translation vectors $\boldsymbol{a}$, $\boldsymbol{b}$, $\boldsymbol{c}$; that is by the fact that the group of symmetry operators that carries the lattice into itself is a characteristic of a particular crystal system, and unique to that system.

5.2.3 Fourteen Bravais lattices

The unit cell as discussed in the previous paragraph was not assumed to be primitive (that is, of minimum volume), since such a cell might not display the full symmetry of the crystal system. This leaves open the possibility of constructing lattices that contain more lattice points than are generated by the translation vectors defining the unit cell.

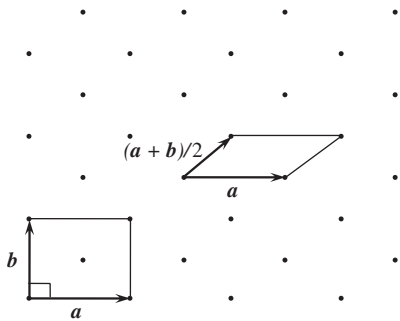

Fig. 5.2 Part of an infinite two-dimensional face-centred rectangular net. Lines of mirror symmetry run through each of the vertical and horizontal rows of points. Two possible unit cells are illustrated. The mirror symmetry is conveyed if the centred rectangular cell is chosen.

To illustrate this point, again we revert to two dimensions, and consider a rectangular net as shown in Fig. 5.2. This is characterized by $\gamma = 90°, a \neq b$, and by twofold rotation axes and mirror lines. Now if we add a point at the centre of the rectangle, that is at $(\boldsymbol{a} + \boldsymbol{b})/2$, and apply the lattice translations, we produce a centred rectangular net. This net could be generated from a smaller (primitive) unit cell, using vectors $\boldsymbol{a}$ and $(\boldsymbol{a} + \boldsymbol{b})/2$, but this choice of vectors gives no indication of the special angle 90°, by virtue of which the mirror lines are retained. This centred rectangular net is a new net, distinct from both the (non-centred) rectangular net, and also from the oblique net generated by two non-collinear vectors at arbitrary angle, since this latter has no mirror lines.

In three dimensions, there are several means to add lattice points (see, e.g. Megaw 1973). Lattice points might be added at the centre of one face (A face-centred, B face-centred, C face-centred, where A, B, C refer to faces defined by $\boldsymbol{b}$ and $\boldsymbol{c}$, $\boldsymbol{c}$ and $\boldsymbol{a}$, and $\boldsymbol{a}$ and $\boldsymbol{b}$, respectively), at the body centre (I centred), or at the centres of all the faces (F-centred). These new points do not always satisfy the condition for a lattice, and when they do, they do not always produce a new lattice type. By way of illustration, we consider a cell in the monoclinic system, where $\boldsymbol{b}$ is perpendicular to both $\boldsymbol{a}$ and $\boldsymbol{c}$. Vectors $\boldsymbol{a}$ and $\boldsymbol{b}$ generate a rectangular net and adding points in the centre of this net (i.e. C-centring) produces a new lattice type, much as the analogous operation in two dimensions. On the other hand, B-centring adds points at the centre of the parallelogram defined by $\boldsymbol{a}$ and $\boldsymbol{c}$, resulting simply in a net based on a smaller parallelogram, and the new lattice is of the same type as before. By detailed examination of the effects of the different kinds of centring in each of the seven crystal systems (Megaw 1973), 14 distinct lattices are found. These are the Bravais lattices of Fig. 2.5.

5.2.4 Two hundred and thirty space groups

Taking into account the 14 Bravais lattices and the different possible point group symmetries of the basis, 230 distinct space groups can be constructed

(Schoenflies 1891; Federov 1895). These are all listed in the *International Tables for Crystallography, Volume A*. The aim in this section is to offer some explanation.

To start, the space group symbols. Among several different symbols for space groups, we shall explain only the Hermann–Mauguin symbols as favoured in the *International Tables*. These tables also show the Schoenflies symbol for each space group, and the connection is made (*International Tables*, Chapter 12, Table 12.5) to the Shubnikov symbols.

We consider first the full Hermann–Mauguin symbols. In the general case, for example, for space group #12, $C2/m$, the full symbol comprises four parts (as indicated here by underlining):

$$\underline{C}\ \underline{1}\ \underline{2/m}\ \underline{1}$$

The first place shows a letter, the centring symbol:

- P – primitive
- C – centred on the (001) face
- A – centred on the (100) face
- B – centred on the (010) face
- I – body-centred
- F – centred on all faces
- R – rhombohedral (trigonal symmetry only)

R referring to lattices that can be described as primitive on a rhombohedral cell, or with three lattice points at (0, 0, 0) and (2/3, 1/3, 1/3) and (1/3, 2/3, 2/3) in a hexagonal unit cell.

There follows a list of symmetry operators (generally three), as defined in §5.2.1, the directions of these symmetry elements being indicated according to the conventions summarized in Table 5.2.

Trailing entries of '1', indicating no symmetry around the corresponding directions, are usually omitted from the space group symbol, for example, $P611$ is abbreviated to $P6$.

The space groups are more commonly referred to by the short Hermann–Mauguin symbols. These may involve abbreviation of the symbols for symmetry elements, along with the omission of '1' for directions of no symmetry. The symbol for our example space group, $C1\,2/m\ 1$, where the full Hermann–Mauguin symbol could be written (but is not) $C1\,2/m$, the short Hermann–Mauguin symbol is $C2/m$. This symbol is unambiguous in its reference to space group #12, but no longer carries unambiguous implication on the direction of the twofold axis. We emphasize at this point that even though the full Hermann–Mauguin symbol is sufficient to identify the space group, it does not convey all the symmetry elements in the space group. In our example, the space group includes the identity operation as it must, and (from successive operation of twofold rotation and mirror reflection) inversion, along with the translation operations associated with C face-centring.

Table 5.2 Conventions on symmetry directions referenced by the symmetry elements appearing in the full Hermann-Mauguin space group symbol.

Crystal system	Direction referenced in		
	First place	Second place	Third place
Triclinic	None	–	–
	There is no symmetry direction.		
	Symbol 1 used to indicate no symmetry, $\bar{1}$ to indicate inversion symmetry.		
Monoclinic	x-direction	y-direction	z-direction
	There is only one symmetry direction in a monoclinic structure. In our example, the symbol $C\ 1\ 2/m\ 1$ indicates this is the y-axis, and the symmetry element is a twofold axis perpendicular to a mirror plane.		
Orthorhombic	x-direction	y-direction	z-direction
Tetragonal	z-direction [001]	x-direction [100]	Bisector between x-and y-directions [110]
	The fourfold axis parallel to z ensures that the symmetry element in x-direction is reproduced in y-direction.		
Hexagonal	z-direction	x-direction	In x–$y$plane, at 30° to x-direction
	The sixfold axis parallel to z ensures symmetry element in the x-direction is reproduced at 60° intervals around the x–y plane.		
Rhombohedral (hexagonal axes)	z-direction	x-direction	–
	Only two kinds of symmetry direction occur in rhombohedral lattices.		
Cubic	z-direction (edge) [001]	body diagonal [111]	Face diagonal [110]

The directions referenced in the different places depend on the crystal system under consideration. Note that the symbol does not carry information on the positions of these operators within the unit cell. Crystal directions referred to in the Hermann-Mauguin Space Group Symbols, adapted from Table 2.4.1 in the *International Tables for Crystallography Volume A*.

The main entries for the 230 space groups, in Chapter 7 of the *International Tables*, show most space groups in 'standard setting' only. However, different permutations of the unit cell vectors are possible, and for monoclinic structures different cell choices, too. The full range of possibilities is recorded in the *International Tables*, Table 4.3.1. In fact for our example space group #12, six entries are recorded, corresponding to two different choices for the symmetry direction each with three different cell choices. The full Hermann–Mauguin symbols for these different settings (and cell choices) are $C\ 1\ 2/m\ 1$, $A\ 1\ 2/m\ 1$, $I\ 1\ 2/m\ 1$, $A\ 1\ 1\ 2/m$, $B\ 1\ 1\ 2/m$, and $I\ 1\ 1\ 2/m$. The lattice in the first setting (and cell choice #1) is C-centred, implying a lattice point in the centre of the face defined by unit vectors $\boldsymbol{a}$ and $\boldsymbol{b}$, hence at $(\boldsymbol{a} + \boldsymbol{b})/2$ (Fig. 5.3). On cell choice #3, the unit vectors in the x–z plane are effectively the original unit vector $\boldsymbol{c}$ and the diagonal $-(\boldsymbol{a} + \boldsymbol{c})$ of the original unit cell. The lattice point at $(\boldsymbol{a} + \boldsymbol{b})/2 = ((\boldsymbol{a} + \boldsymbol{c})/2 - \boldsymbol{c}/2 + \boldsymbol{b}/2)$ is evidently

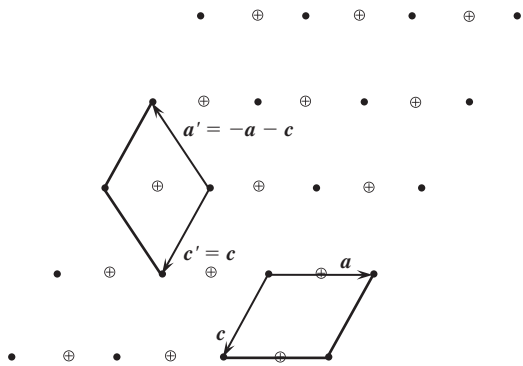

Fig. 5.3 Projection perpendicular to $\boldsymbol{b}$ of a C-centred monoclinic lattice. Lattice points in the plane are shown as filled circles and those in the C-centring positions in the centre of the x–y face, as $\oplus$. Both the C-face centred and body-centred cells are shown.

at the body centre of a unit cell of the new lattice, hence the lattice is I-centred with this cell choice. It often proves very convenient to use a non-standard space group setting or cell choice. The subtle, continuous transition from the orthorhombic structure in *Imma* to the monoclinic structure in $C2/m$ that occurs in perovskite crystallography (Howard and Stokes 1998) provides a pertinent illustration. The relationship between the two very similar structures is much more easily visualized using the $I2/m$ monoclinic setting, with unit cell only slightly distorted from that in *Imma*, than when using the standard $C2/m$ with its very different unit cell.

In working with different settings and on different cells, it may be necessary to connect the lattice parameters, fractional atomic coordinates, and so on, describing the structure in one setting with those needed for its description in another. This is the business of transformations in crystallography. Consider a crystal structure described on a unit cell defined by $\boldsymbol{a}$, $\boldsymbol{b}$, and $\boldsymbol{c}$, and suppose that we want to find its description on the unit cell defined by $\boldsymbol{a}'$, $\boldsymbol{b}'$, and $\boldsymbol{c}'$. The relationship of the new unit vectors to the old ones:

$$(\boldsymbol{a}',\boldsymbol{b}',\boldsymbol{c}') = (\boldsymbol{a},\boldsymbol{b},\boldsymbol{c}) \begin{pmatrix} P_{11} & P_{12} & P_{13} \\ P_{21} & P_{22} & P_{23} \\ P_{31} & P_{32} & P_{33} \end{pmatrix} = (\boldsymbol{a},\boldsymbol{b},\boldsymbol{c})\boldsymbol{P} \tag{5.1}$$

defines the matrix $\boldsymbol{P}$ which is fundamental to all the transformations. The matrix $\boldsymbol{P}$ is used for transforming the coordinates of points in reciprocal space (§2.4.1) and the Miller indices for planes (§2.1.1), while its inverse $\boldsymbol{Q} = \boldsymbol{P}^{-1}$ serves to transform the basis vectors of reciprocal space, and indices of direction in real space. The inverse matrix also serves to transform coordinates in real space, but particular care is needed here if a change of origin is involved. The reader who needs to carry out transformations of this kind is referred to Chapter 5 in the *International Tables* for detail on how these matrices are applied, as well as to the convenient tabulation there (Table 5.1) of the matrices $\boldsymbol{P}$ and $\boldsymbol{Q}$ for many of the transformations required.

5.2.5 Atomic coordinates – general and special positions

We are now in a position to see how a crystal structure can be fully described by giving, along with the lattice parameters, the space group and the types and positions of a minimal number of atoms. The symmetry operators of the space group generate the remaining atoms. We have already mentioned, by way of example, that a mirror plane at $z = 0$ operates on an atom at x, y, z to produce another similar atom at $x, y, -z$. If in fact the atom lies on the mirror plane, that is at $x, y, 0$, then nothing additional is produced by this mirror plane. The atom is then said to be at a *special* rather than *general* position.

By way of further illustration, we consider our example space group #12, $C\,2/m$, in standard setting (unique axis b, cell choice 1). The entry in the *International Tables* lists (among other things) equivalent positions generated by the symmetry operators in this space group (see Table 5.3).

The columns in Table 5.3 show the following:

- The first column gives the number of symmetry equivalent positions in the unit cell (multiplicity).
- The second column shows the Wyckoff letter – the lettering starts with a at the site with highest symmetry (bottom of table) and continues upwards as symmetry decreases and multiplicity increases.
- The third column gives the site symmetry, an indication of the point symmetry at the site in question. For example the 'm' under site symmetry for $4i$ reminds us that the point $x, 0, z$ is on the $y = 0$ mirror plane.
- And the fourth column records the coordinates of the symmetry equivalent positions.

Table 5.3 List of equivalent positions and related data for space group $C2/m$ (standard setting) obtained from the *International Tables for Crystallography Volume A*.

Number of positions (multiplicity)	Wyckoff letter	Site symmetry	Coordinates of equivalent positions
			(0, 0, 0)+ (1/2, 1/2, 0)+
8	j	1	x, y, z $-x, y, -z$
			$-x, -y, -z$ $x, -y, z$
4	i	m	$x, 0, z$ $-x, 0, -z$
4	h	2	$0, y, 1/2$ $0, -y, 1/2$
4	g	2	$0, y, 0$ $0, -y, 0$
4	f	$\bar{1}$	1/4,1/4,1/2 3/4,1/4,1/2
4	e	$\bar{1}$	1/4,1/4,0 3/4,1/4,0
2	d	$2/m$	0,1/2,1/2
2	c	$2/m$	0,0,1/2
2	b	$2/m$	0,1/2,0
2	a	$2/m$	0,0,0

The first row lists the coordinates of the symmetry equivalent points generated when the symmetry operators of $C\,2/m$ operate on a point at general position x, y, z. The subsequent rows list the results for different special points. The fact of C face-centring is indicated by $(1/2, 1/2, 0)+$, which means that (1/2,1/2,0) can be added to the listed coordinates in every case.

It may be instructive to examine the entries for $8j$, the symmetry equivalent set for the general point x, y, z, since the effects of the different symmetry operators can be recognized in the list. For example $x, -y, z$ is the point generated from x, y, z by the mirror plane at $y = 0$, while $-x, y, -z$ is the point generated from x, y, z by the twofold rotation about the y-axis. The point $-x, -y, -z$ is obtained most directly by inversion through the origin. The remaining rows refer to special positions, such that at least one of the symmetry operators maps the point onto itself – there are then fewer points in the symmetry equivalent set. As an example, the position $4g$ lies on the twofold axis, so only the mirror plane is effective in generating additional points from it. In the extreme, the points $2a$ (and similar) lie on both the twofold axis and the mirror plane, so only this point and that related by the C face-centring result.

We conclude this section with the description of an example crystal structure. The example we choose is the structure of the perovskite $PrAlO_3$ at 140 K. The crystal structure data are adapted[43] from Carpenter *et al.* (2005), and the space group is our example space group $C2/m$.

By showing just one of each symmetry equivalent set in Table 5.4, and adding symmetry equivalent atoms as specified in Table 5.3, we generate a structure

Table 5.4 Description of crystal structure of $PrAlO_3$ at 140 K (adapted from Carpenter *et al.* 2005).

Space group $C2/m$ (#12) – monoclinic				
Lattice parameters	a = 7.5037 Å	b = 7.4907 Å	c = 5.3109 Å	β = 134.64° $\alpha = \gamma$ = 90°
Atom	Site (multiplicity, Wyckoff)	x	y	z
Pr	$4i$	0.2517	0	0.5015
Al	$4e$	1/4	1/4	0
O(1)	$4i$	0.8021	0	0.0372
O(2)	$4g$	0	0.2849	0
O(3)	$4h$	0	0.2696	$^1/_2$

[43] Specifically, transformed from $I2/m$ to the standard setting in $C2/m$ used here.

with four formula units (20 atoms in all) in each unit cell.[44] The same minimum information is acceptable to most computer programs, whether they may be for drawing crystal structures (e.g. ATOMS, Dowty 1999) or for further calculation such as the simulation of diffraction patterns.

5.3 REFLECTION CONDITIONS AND SPACE GROUP DETERMINATION

The determination of the space group depends largely on an examination of the diffraction pattern (X-ray, neutron, or electron) from a crystal or from a polycrystalline material. The *International Tables for Crystallography Volume A* gives in Chapter 3, some detail on the procedures for determining space groups from the characteristics of the diffraction patterns, and includes extensive tables (Table 3.2) to assist in this task.

The first step is to determine the unit cell, and the crystal system. If single crystal diffraction data are available, these define the reciprocal lattice [eqn (2.23)], and from the reciprocal lattice vectors the vectors of the crystal lattice can be deduced [eqn (2.22)]. If however only powder data are available, then information on directions in the reciprocal lattice is lost, and the recognition of the unit cell can be very difficult. The problem of determining the unit cell from a powder pattern, and indexing the diffraction peaks on the basis of this unit cell (the 'indexing problem') is a very challenging one. It is considered to be the bottleneck in the process of the crystal structure determination from powder diffraction data only (David *et al.* 2002). This 'indexing problem' will be discussed further in §6.2.

If the unit cell can be determined, the structure assigned to one of the seven crystal systems, and the observed reflections indexed (i.e. assigned indices *hkl*, see §4.4.2), then the possibilities for the space group can be restricted by the recognition of systematic absences from the reflections observed. These systematic absences occur when the calculated structure factor F_{hkl} [eqn (2.31)] is necessarily zero. To illustrate how this occurs,[45] we recall the definition of F_{hkl}:

$$F_{hkl} = \sum_n b_n \exp[2\pi i(hx_n + ky_n + lz_n)] \tag{2.31}$$

then return to our example space group $C2/m$. The sum in eqn (2.31) is over all the atoms in the unit cell. We can however separate this sum into sums for the different atom types, each of these sums running over a set of symmetry related sites. Finally, we can pair the terms, so as to consider just the sum for the atom at x, y, z and the symmetry equivalent atom resulting from C-centring, at $x + 1/2, y + 1/2, z$.

[44] The coordinates, depending on the particular values of x, y, z, might not all lie within the unit cell. If not, equivalent points can be found that do lie within the unit cell, and the arguments (e.g. reckoning of site multiplicity) are unchanged.

[45] The structure factor here is written for neutron diffraction. That the same reflections should be systematically absent in X-ray and electron diffraction patterns is seen by replacing neutron scattering length b by the appropriate form factor.

The sum is

$$\begin{aligned} & b\{\exp[2\pi i(hx+ky+lz)]+\exp[2\pi i(h(x+1/2)+k(y+1/2)+lz)]\} \\ & \quad = b\exp[2\pi i(hx+ky+lz)]\{1+\exp[\pi i(h+k)]\} \\ & \quad = 2b\exp[2\pi i(hx+ky+lz)] \quad \text{for } h+k \text{ even} \\ & \quad = 0 \quad \text{for } h+k \text{ odd} \end{aligned} \tag{5.2}$$

This means that reflections hkl with $h+k$ odd are systematically absent from the diffraction pattern. In the *International Tables*, this is written as a reflection condition:

$$hkl\colon h+k=2n \tag{5.3}$$

expressing the necessary requirement that $h+k$ be even for the structure factor to be non-zero. Also seen in the *International Tables* are conditions for special classes of reflections, $h0l, 0kl$, and so on, but these represent nothing more than the application of the more general condition [eqn (5.3)] just shown.

It turns out that the only symmetry operators leading to necessarily zero structure factors are those involving translations, that is, centring operations, glide planes, and screw axes. The only such operation in our example space group is the C face-centring, just discussed. So, as a further illustration, we shall examine the effect in space group $P2/c$ (#13) of the c-glide on plane $y=0$. This generates from an atom at x, y, z a symmetry equivalent atom at $x, -y, z+1/2$, and summing the relevant pair of terms in the structure factor (2.31) leads to

$$\begin{aligned} & b\{\exp[2\pi i(hx+ky+lz)]+\exp[2\pi i(hx-ky+l(z+1/2))]\} \\ & \quad = b\exp[2\pi i(hx+ky+lz)]\{1+\exp[2\pi i(-2ky+l/2)]\} \\ & \quad = b\exp[2\pi i(hx+ky+lz)]\{1+\exp[\pi il]\} \quad \text{for } k=0 \end{aligned} \tag{5.4}$$

It is clear that this is zero unless l is even, a condition written in the *International Tables* as

$$h0l\colon l=2n \tag{5.5}$$

In space group $C2/c$ (#15), with both C face-centring and a c-glide plane, the condition on $h0l$ is written as

$$h0l\colon h, l=2n \tag{5.6}$$

where $l=2n$ by virtue of the glide plane and $h=2n$ through application of the C face-centring condition [eqn (5.3)]. The reflection conditions for other glide operations, and for screw operations (e.g. z-axis 4_1 taking x, y, z to $-y, x, z+1/4$), are derived in a similar manner. Results from such analyses are summarized in Table 5.5.

Table 5.5 Reflection conditions implied by different symmetry operators.

Symmetry operator	Reflection conditions
Centring operations	
C-face centring	$h + k = 2n$
A-face centring	$k + l = 2n$
B-face centring	$h + l = 2n$
F – all face centring	$h + k = 2n$, $k + l = 2n$, $h + l = 2n$ (implies h,k,l all even, or all odd)
I – body centring	$h + k + l = 2n$
R – rhombohedral (on hexagonal cell)	$hkil$: $-h + k + l = 3n$
Glide planes	
c-glide (on x–z plane)	$h0l$: $l = 2n$
(on y–z plane)	$0kl$: $l = 2n$
a-glide (on x–y plane)	$hk0$: $h = 2n$
(on x–z plane)	$h0l$: $h = 2n$
b-glide (on x–y plane)	$hk0$: $k = 2n$
(on y–z plane)	$0kl$: $k = 2n$
n-glide (on x–y plane)	$hk0$: $h + k = 2n$
(on y–z plane)	$0kl$: $k + l = 2n$
(on $x - z$ plane)	$h0l$: $h + l = 2n$
d-glide (on x–y plane)	$hk0$: $h + k = 4n$
(on y–z plane)	$0kl$: $k + l = 4n$
(on x–z plane)	$h0l$: $h + l = 4n$
Screw axes	
2_1 or 4_2 (x-direction)	$h00$: $h = 2n$
(y-direction)	$0k0$: $k = 2n$
(z-direction)	$00l$: $l = 2n$
4_1 or 4_3 (x-direction)	$h00$: $h = 4n$
(y-direction)	$0k0$: $k = 4n$
(z-direction)	$00l$: $l = 4n$
6_3 (z-direction, hexagonal)	$000l$: $l = 2n$
3_1, 3_2, 6_2, 6_4 (z-direction, hexagonal)	$000l$: $l = 3n$
6_1, 6_5 (z-direction, hexagonal)	$000l$: $l = 6n$

More detail can be found in Tables 2.13.1 and 2.13.2 in the *International Tables for Crystallography Volume A*.

The systematic absences establish the corresponding symmetry element in the space group as per the conditions tabulated above. The application to space group determination is laid out in Table 3.2 in the *International Tables* which, given the crystal system and reflection conditions, can be consulted to find the possible space groups. For a monoclinic structure showing (only) reflection conditions hkl: $h + k = 2n$, for example, the possible space groups are listed in that table as $C\,2$ (#5), Cm (#8), and $C\,2/m$ (#12). Evidently, because only centring, glide, and screw operations lead to systematic absences, it is generally not possible to obtain

from these absences an unequivocal determination of the space group. In fact, only 39 of the 230 space groups can be determined unambiguously from knowledge of the crystal system and systematic absences alone.

The determination of space group can be advanced by any means that will identify additional symmetry operators, that is, those operations that do not involve translations. It will be recalled that these are the elements of the crystallographic point group. The study of physical properties can assist in this regard. According to 'Neumann's principle', no physical property can show a symmetry lower than that of the crystallographic point group. In particular, phenomena such as pyroelectricity, ferroelectricity, or optical activity are not symmetric under inversion, so by Neumann's principle their observation means there can be no inversion operator in the pertinent point or space group. In our example system (hkl: $h+k = 2n$), the established lack of inversion symmetry would rule out $C\,2/m$ (#12). In this case there remain two possibilities, $C2$ (#5) and Cm (#8). There are, however, some 25 space groups (in addition to the 39 mentioned earlier) that can be determined unambiguously from the crystal system and systematic absences when the absence of inversion symmetry has also been demonstrated. Neumann's principle can be used only to establish the absence of symmetry operators, and the above application to inversion symmetry is by far its most common use. On the other hand, in favourable circumstances, it may be possible to infer the presence of additional symmetry elements such as rotation axes and mirror planes, from the morphology of well-formed crystals, or the symmetry apparent in the optical properties of transparent ones.

Though physical properties may provide some information, particularly as regards inversion symmetry, determination of the space group depends primarily on a closer inspection and analysis of (ideally single crystal) diffraction data. For crystal systems of tetragonal and higher symmetries, the diffraction patterns (seen as intensity distributions in reciprocal space) may show one or more mirror symmetries, and on this basis show different *Laue* symmetries. In total, 192 space groups are uniquely characterized by crystal system, Laue class, systematic absences, and presence/absence of a centre of inversion. But eventually there may come a point at which, either to resolve remaining ambiguities, or to confirm a proposed space group, a model of the crystal structure should be developed (with the space group symmetry proposed), intensities calculated, and a comparison made with the intensities observed.

The advantages of single crystals for the structure solution step should be becoming clear. It has already been stated that single crystal diffraction data provide a map of intensities in reciprocal space, and lattice vectors can be deduced. In addition, the data carry unambiguous indexing of all the diffraction peaks, so the systematic absences are readily discerned. The loss of directional information, as occurs in the powder diffraction pattern, makes the problem of unit cell determination from powder patterns very challenging. And even when the unit cell is known, reflections may overlap (appear at very similar values of 2θ), so that both the unambiguous assignment of indices hkl and the recognition of systematic absences are also very difficult. There seems little doubt that for structure solution, if single crystals are

available, they should be used. In summary, powder diffraction is used for structure solution only when single crystals of suitable size and quality are unavailable. If size is the issue, then high-intensity sources such as synchrotron X-ray sources now allow the use of smaller crystals than could previously be measured – it is said that under suitable conditions crystals as small as 5 μm can be examined in this way. Electron microscope techniques offer another route to obtaining single crystal diffraction in the absence of reasonably sized crystals. Here, by directing a small enough electron spot onto a sufficiently thin sample, it may be possible to illuminate a volume so small that the diffraction pattern from a single domain is obtained. For example, electron micro-diffraction, using a 0.05–0.1 μm spot, has been used to obtain a single crystal pattern from a sample of $Ca_{0.5}Sr_{0.5}TiO_3$ (Howard *et al.* 2001), and to resolve questions on its space group on the basis of the systematic absences observed.[46] Convergent beam electron diffraction (CBED) can achieve spot sizes 10 nm or less (Muddle 1985), so even smaller crystallites can be sought.

We remark that the CBED technique, under suitable conditions, can be a very powerful aid to the determination of symmetry elements and space groups (Morniroli 2004). Convergent beam patterns carry information on the reflection conditions[47] and, when recorded with the electron beam along a low index direction and normal to a plane, parallel-sided foil, they can by virtue of dynamical diffraction effects exhibit the projected symmetry of the potential, and therefore of the crystal structure itself. If more than one such projection is accessible, then it should be possible (using for example data in Table 10.2.2 in the *International Tables for Crystallography Volume A*) to establish the point group symmetry of the crystal.

5.4 SOLVING STRUCTURES

The determination of the low-temperature crystal structure of sodium deuteroxide, NaOD, serves to provide a relatively simple but non-trivial illustration of some aspects of the structure solution process. This is an instance where the solution of the low-temperature structure depends on its close relationship to the higher temperature structure.

At room temperature, NaOD adopts the same structure as NaOH, and that structure had been determined and reported previously (Ernst 1946; Stehr 1967; Bleif and Dachs 1982). The room temperature structure (of NaOD) is illustrated in Fig. 5.4, from the description recorded in Table 5.6.[48]

A neutron diffraction study of NaOD at 77 K was undertaken after indications of a new structure from infrared (Busing 1955) and nuclear quadrupole

[46] Even with this 0.05–0.1 μm spot size, it took some time and effort to locate a single crystal domain.

[47] The identification of absences can be made difficult because of additional intensity due to multiple scattering.

[48] The description here (in contrast to earlier reports) relates to space group #63 in its standard setting.

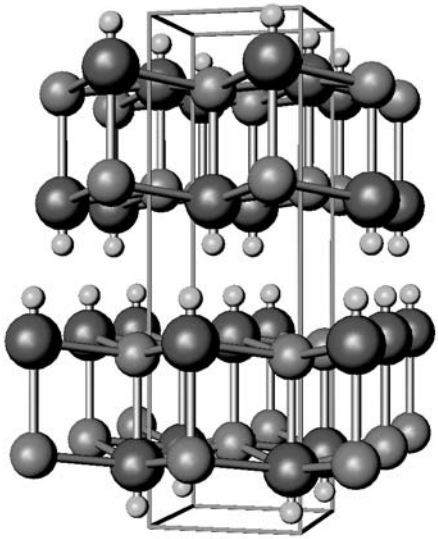

Fig. 5.4 Room temperature structure of NaOD (See plate 1).

Table 5.6 Crystal structure of NaOD at 293 K (Bastow *et al.* unpublished).

Space group *Cmcm* (#63) – orthorhombic				
Lattice parameters	a = 3.405 Å	b = 11.30 Å	c = 3.397 Å	$\alpha = \beta = \gamma = 90°$
Atom	Site (multiplicity, Wyckoff)	x	y	z
Na	4c	0	0.34	1/4
O	4c	0	0.13	1/4
D	4c	0	0.05	1/4

resonance (NQR) measurements (Bastow *et al.* 1986a) and confirmation from differential thermal analysis (DTA) of the occurrence of a phase transition in NaOD at ~150 K, not found in NaOH.

The neutron diffraction patterns, recorded at neutron wavelength 1.377 Å, are shown in part in Fig. 5.5. Evidently there are similarities and differences. In particular, the pattern recorded at low temperature shows additional peaks, as marked, that are not seen at room temperature and indeed cannot be indexed on the C-centred orthorhombic cell. The unmarked peaks can be satisfactorily indexed on the centred orthorhombic cell with dimensions adjusted to $a = 3.419, b = 10.80, c = 3.366$ Å (note the very significant reduction in the b dimension from 11.30 Å). The marked peaks can be indexed only by using half-integral values for the index h – this implies a period in the direction of a twice that indicated just earlier. The situation

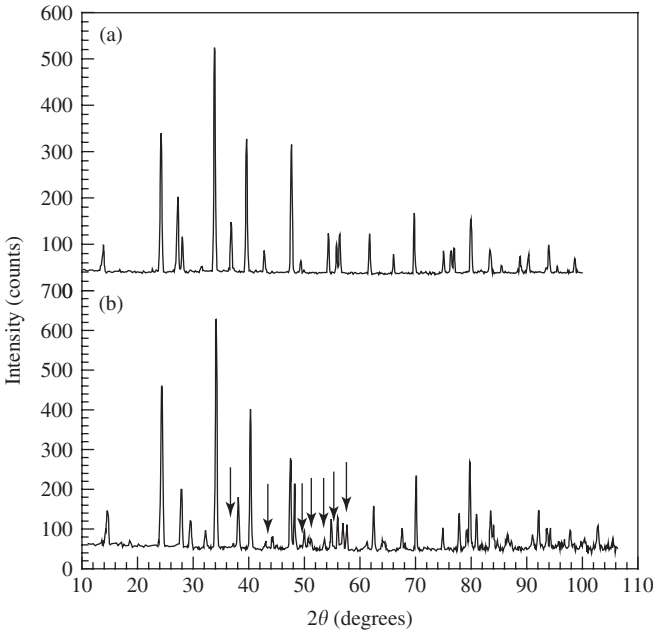

Fig. 5.5 Comparison of neutron diffraction patterns of NaOD at room temperature (a) and at 77 K (b) (Bastow *et al.* unpublished). Visible additional peaks due to the phase transition are arrowed.

is illustrated schematically in Fig. 5.6, which shows first the lattice points of the C-centred orthorhombic structure on the a–b plane. If we now double the period along the a-direction, that is make alternate lattice points in this direction distinct (circles), then the lattice is defined by the distinguished points only. The lattice is no longer centred orthorhombic, but rather a primitive monoclinic, as outlined in the figure. The vectors defining the unit cell of the monoclinic lattice, $\boldsymbol{a}', \boldsymbol{b}', \boldsymbol{c}'$ are related to those defining the centred orthorhombic, $\boldsymbol{a}, \boldsymbol{b}, \boldsymbol{c}$, by $\boldsymbol{a}' = 2\boldsymbol{a}$, $\boldsymbol{b}' = -\boldsymbol{c}$,[49] and $\boldsymbol{c}' = -\boldsymbol{a}/2 + \boldsymbol{b}/2$, whence the matrices $\boldsymbol{P}$ and $\boldsymbol{Q}$ (of §5.2.4) are determined. The indexing and monoclinic unit cell were confirmed using an automatic indexing program. Examining the final indexing of the observed peaks, it was apparent that certain peaks were missing, corresponding to the reflection conditions $h0l$: $h = 2n$ and $0k0$: $k = 2n$. If these are indeed the reflection conditions, then using Table 3.2 in the *International Tables* it can be deduced[50] that the space group is $P2_1/a$.

[49] Using conventional settings of the space groups, the vector $\boldsymbol{c}$ perpendicular to the centred plane becomes the unique axis $\boldsymbol{b}'$ of the monoclinic.

[50] Although this sounds simple enough, it is hard to be completely confident in the determination of reflection conditions from powder diffraction patterns, and our records show that it took some 5 weeks after indexing the pattern to convince ourselves of this result.

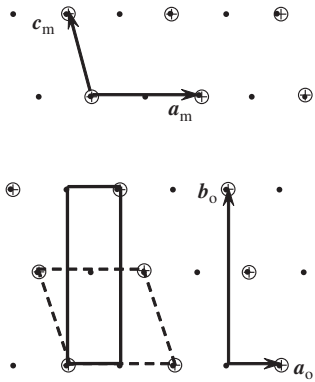

Fig. 5.6 Relationship of the low-temperature monoclinic lattice for NaOD to the room temperature C-face centred orthorhombic lattice.

The structure solution proceeded from the premise that the structure in the low-temperature $P2_1/a$ would be closely related to the room temperature structure in *Cmcm*. In the room temperature structure, the NaOD units are linear, parallel to the b-axis. The aim then, is to correctly position these in space group $P2_1/a$ to provide a starting model for the structural refinements. Now the relationship between the unit cell vectors of the two different space groups is given in the paragraph earlier, apart from a possible shift of origin. Comparing the [001] projection of space group *Cmcm* with the [010] projection of $P2_1/a$, we find that the twofold screw axes with centre of symmetry appearing in *Cmcm* become in $P2_1/a$ alternately centres of symmetry and twofold screw axes. The alternation of screw axes and centres of symmetry means in effect there are two possible choices for the origin of $P2_1/a$ with respect to *Cmcm* $-(0,0,0)$ and (1/4, 1/4, 0). To anticipate the solution, we will find that the NaOD units, which were linear in the room temperature structure, are no longer linear, the atoms moving (the D atoms more than the others) in alternate senses along what was the c-direction in *Cmcm* and is now the unique axis, b, in the $P2_1/a$ structure. These alternating displacements out of the former *Cmcm* mirror plane reduces this to the glide plane in $P2_1/a$. Careful inspection of the possible structures reveals that the choice (1/4, 1/4, 0) for the origin (inversion centre) of $P2_1/a$ permits the same sense of displacement for all the D-atoms lying along the same atomic row (parallel to the unique axis), whereas the choice (0, 0, 0) would require adjacent D atoms to be displaced in opposite senses. We consider the first arrangement rather more likely, and on this basis have made our origin choice. So, to set the room temperature structure into the low-temperature cell, the coordinates x_O, y_O, z_O in *Cmcm* (as recorded in Table 5.6) are first amended to $x_O - 1/4, y_O - 1/4, z_O$ to account for the origin shift, then the relevant matrix $\boldsymbol{Q}$ is applied to give the coordinates in $P2_1/a$ as $x_M = 1/4 - x_O/2 - y_O/2, y_M = z_O, z_M = 2(1/4 - y_O)$. The structure in space group $P2_1/a$, on cell $a = 6.838, b = 3.366, c = 5.664$ Å, $\alpha = \gamma = 90°, \beta = 107.57°$,

obtained by first setting the atoms as in the room temperature structure according to the recipe just given, then moving y_M (D) from 1/4 to ~0.3 to break the mirror symmetry, is in effect the structure solution, and provides a very suitable starting model for subsequent refinement.

Starting from values obtained as just described, the coordinates were varied, and determined so as to produce an optimum fit between a calculated diffraction pattern and that observed – this is the Rietveld method, introduced in §4.6, and to be described in detail in §5.5. The final results for the coordinates at 77 K are however recorded in Table 5.7 – the reader who cares to write down the starting coordinates according to the prescription above will see that the final values of the coordinates are not very different from these. The structure of NaOD at 77 K is illustrated in Fig. 5.7.

Table 5.7 Crystal structure of NaOD at 77 K (Bastow *et al.* unpublished).

Space group $P2_1/a$ (#14) – monoclinic				
Lattice parameters	a = 6.838 Å	b = 3.366 Å	c = 5.664 Å	$\alpha = \gamma = 90°$ $\beta = 107.57°$
Atom	Site (multiplicity, Wyckoff)	x	y	z
Na	4e	0.08	0.25	−0.18
O	4e	0.19	0.23	0.24
D	4e	0.23	0.33	0.41

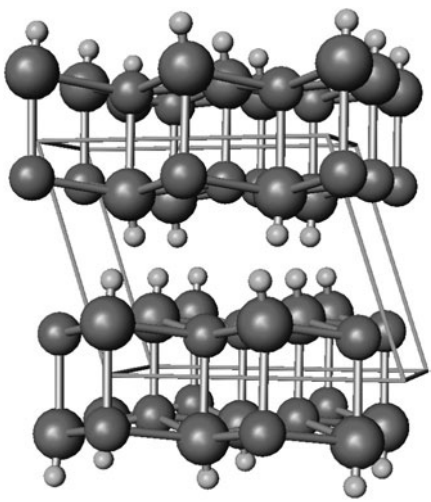

Fig. 5.7 Structure of NaOD at 77 K. (See Plate 2)

5.5 STRUCTURE REFINEMENT – THE RIETVELD METHOD

In the earlier days of neutron (and X-ray) powder diffraction, structure refinements followed the methods used in single crystal work. The integrated intensities (areas under peaks) were extracted by whatever means was possible – sometimes by simply cutting out peaks from a chart record and weighing them – then corrected for such factors as absorption, Lorentz factor, and multiplicity (§2.4.2) so as to reduce them to a set of 'observed' structure factors $|F_{hkl}|^2_{\text{obs}}$. These were then compared with suitably scaled calculated structure factors, $S\,|F_{hkl}|^2_{\text{calc}}$, obtained from the atomic coordinates of the starting model by applying eqn (2.31).[51] To complete the refinements, the scale S and those coordinates not constrained by symmetry were varied to give the best least-squares fit between the calculated structure factors and those observed. That is, these coordinates were determined by the conditions that $\overline{S}$, the sum of squared differences:

$$\overline{S} = \sum_{hkl} w_{hkl}(|F_{hkl}|^2_{\text{obs}} - S\,|F_{hkl}|^2_{\text{calc}})^2 \tag{5.7}$$

be a minimum. $\overline{S}$ should not be confused with the scale factor S. The quantity w_{hkl} represents the weight to be applied to fitting the *hkl* reflection, estimated from statistics on the measurement of the *hkl* reflection, or otherwise. This was the method used for structure refinements from the earliest days of neutron powder diffraction through to the 1970s. However, the difficulty of extracting integrated intensities in the case of overlapping reflections limited the applicability to relatively simple structures (§1.3).

Rietveld (1967, 1969) developed an alternative method for structure refinement, now very commonly employed. This method deals rather effectively with the problem of overlapping reflections in powder diffraction patterns. The key is the inclusion of appropriate model descriptions of peak widths and shapes such as already presented in §4.5. Using these, along with peak positions calculated from lattice parameters (and wavelength), and integrated intensities based on the usual model for crystal structure, permits a model-based calculation of the step-by-step intensities y_i (calc) corresponding to those y_i(obs) actually recorded in the powder diffraction pattern. The comparison then made is of the calculated diffraction pattern with that observed, and the quantity to be minimized is now:

$$\overline{S} = \sum_{i} w_i(\,y_i(\text{obs}) - y_i(\text{calc}))^2 \tag{5.8}$$

where the sum here is over all the points of the powder diffraction pattern. The scale factor S as appeared in eqn (5.7) has now been incorporated into the y_i(calc). The parameters determined in the least squares process now include those relevant

[51] In fact the displacement parameters (temperature factors), §2.4.2, are usually incorporated into the calculation of $|F_{hkl}|^2_{\text{calc}}$ at this stage.

to the description of peak widths and shapes, as well as lattice parameters, scale factor, and atomic coordinates as required.

The form of eqn (5.8) is deceptively simple, but each term, as well as the least-squares minimization itself, requires careful attention.

5.5.1 The observed pattern

The observed pattern comprises a set of intensities/counts y_i(obs) measured at different angles $2\theta_i$ when recorded using constant wavelength diffractometers (§3.2), or at different times t_i (proportional to d-spacing) if a time-of-flight (TOF) diffractometer is employed (§3.3). Measurements should be made according to the general recommendations on experimental design and practice given in Chapter 3. The intensity–resolution compromise should be appropriate to the problem under consideration (see Table 3.5), as should the range of d-spacings encompassed. Samples should be prepared (when practicable) in such a way as to minimize problems associated with excessively large or small crystallites, or preferred orientation (§3.6). Step sizes (in angle or time) should provide adequate sampling having regard to the peak widths, and accumulated counts should also be sufficient to ensure statistical errors are not excessive. Hill and Madsen (1987) suggest a step width of, say, one-fifth of the peak width (full-width at half-maximum), and counting to obtain at the maximum of the pattern a few thousand counts in the step. The reason for this is that the models usually employed in the Rietveld method are not quite adequate for fitting patterns that are recorded to a better statistical accuracy. As has already been pointed out in Chapter 3, there may be occasions when very weak features are of interest and longer counting times leading to higher accumulated counts should be employed.

The weight w_i used in fitting the observation y_i(obs) is usually based on the observation y_i itself. To be specific, the weight is taken to be the inverse of the variance in the determination of y_i(obs), and if y_i(obs) is simply a count then:

$$w_i = \frac{1}{\sigma^2(y_i)} = \frac{1}{y_i(\text{true})} \approx \frac{1}{y_i(\text{obs})} \tag{5.9}$$

the variance being estimated with the help of eqn (3.12). In the case that we record several counts at the same angle (or time), as is common when multiple detectors are employed, then we use the mean count $y_i(\text{obs}) = \sum_{k=1}^{n} y_{ki}/n$, where the y_{ki} are the counts recorded in the kth of n detectors, with variance $y_i(\text{obs})/n$. The weight to be ascribed in this case is $w_i \approx n/y_i(\text{obs})$.

5.5.2 The calculated pattern

The Rietveld method depends on the calculation of intensities y_i(calc) at the positions (angles $2\theta_i$ or times t_i) at which the intensities y_i(obs) have been recorded. To illustrate the steps we return to our example (§5.4) of the low-temperature (77 K) structure of NaOD.

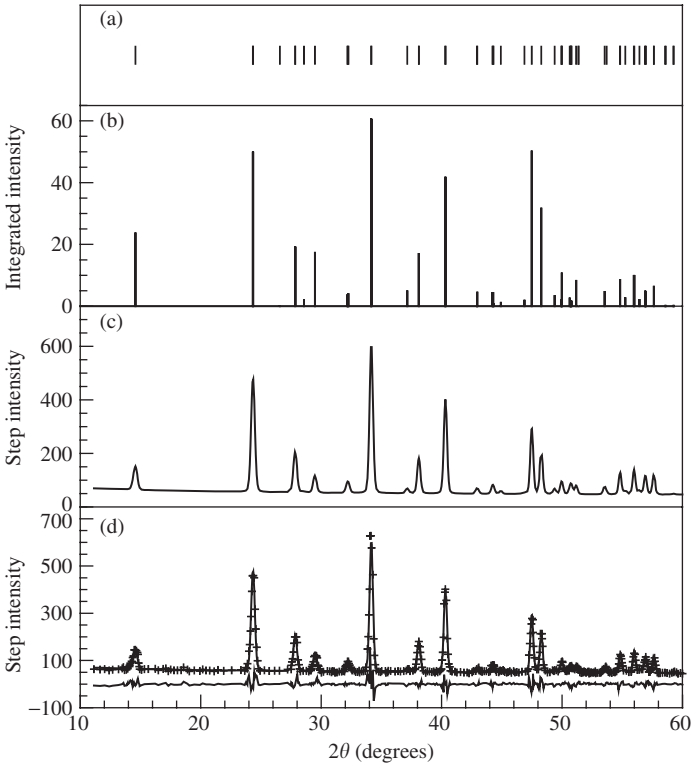

Fig. 5.8 Steps in the Rietveld refinement process using NaOD at 77 K as an example: (a) the calculated peak positions from the unit cell parameters, (b) integrated intensities calculated at each peak position, (c) intensity is distributed over the appropriate peak shapes to give a complete calculated pattern, and (d) the calculated pattern is matched to the observed pattern by the least squares refinement of variable parameters.

The first step is to calculate the expected locations of the diffraction peaks from wavelength,[52] lattice parameters, and the space group symmetry. The calculated peak positions, for a structure (NaOD) in space group $P2_1/a$, on cell $a = 6.838$, $b = 3.366, c = 5.664$ Å, $\alpha = \gamma = 90°, \beta = 107.57°$, using 1.377 Å neutrons, are shown by the set of markers (Fig. 5.8(a)).

Next is the calculation of the structure factors $|F_{hkl}|^2_{\text{calc}}$ for each of these peaks, as per the integrated intensity approach described at the beginning of §5.5, and based on the starting model of the crystal structure. The integrated intensity in each of the peaks is calculated, applying the multiplicity, Lorentz, absorption, and extinction factors (corrections) mentioned in §2.4.2. This is just the reverse of the reduction of integrated intensities to structure factors, used before the Rietveld

[52] This is for the constant wavelength instrument. The calculation in the TOF case involves instead the instrument constant appearing in eqn (3.10).

method, and described at the beginning of §5.5. The integrated intensity is thus:

$$I_{hkl} = S\,|F_{hkl}|^2_{\text{calc}}\,TLJAP \tag{5.10}$$

where T is an overall temperature or rather Debye–Waller factor, L is the Lorentz factor, J is multipicity, A represents an attenuation correction (which we will take to encompass 'extinction'), P is a correction for preferred orientation, and S is a scale factor, for the moment taken to be arbitrary. Apart from S which is constant,[53] the different factors in eqn (5.10) are either well defined for a given *hkl* or else change little over the range of a particular reflection, so each can be taken as a function of indices *hkl* only. For our example structure, we have calculated the structure factors from the starting model described in §5.4: the atomic coordinates in the $P2_1/a$ monoclinic structure are then just as transformed from their values in the room temperature orthorhombic phase, except that y_M (D) is shifted slightly from 1/4 as calculated to 0.3. The scattering from each nucleus has been reduced by a temperature factor, calculated as in eqn (2.36), using isotropic temperature/displacement parameters (see later) $U_{\text{iso}} = 0.0075, 0.0075$, and 0.0225 Å^2 for the Na, O, and D, respectively. The overall temperature factor has been set to 1. For the rest, the scale factor has been taken as $S = 0.01$, the Lorentz and multiplicity are reckoned in the usual way (see §2.4.2), and no correction has been made for absorption or preferred orientation, that is A and P have been left at unity. The results are summarized by showing in Fig. 5.8(b) at calculated angle $2\theta_{hkl}$ a vertical line representing the integrated intensity I_{hkl}.

It is convenient at this point to denote the reflection with indices *hkl* as the kth reflection, its location by $2\theta_k$ or t_k, and its integrated intensity from eqn (5.10) as I_k. This is no longer the k of *hkl* but simply a serial number for this reflection (or set of J equivalent reflections). A combination of instrumental factors (Chapter 3) and sample broadening (Chapter 9) means that the intensity I_k will appear not just at the location $2\theta_k$ or t_k, but will be distributed around this value. The distribution in angle or time is conveniently described by some *normalized* profile function, $G(2\theta - 2\theta_k)$ or $G(t - t_k)$. In the constant wavelength case, the contribution from a peak of *unit* integrated intensity into a counter with angular acceptance $\Delta(2\theta_i)$ located at angle $2\theta_i$ is just $\Delta(2\theta_i)G(2\theta_i - 2\theta_k)$. For a TOF instrument, the contribution into a bin of width Δt_i at time t_i from a peak of unit integrated intensity is $\Delta t_i G(t_i - t_k)$. The calculation of the intensity at a particular point (step) i of the diffraction pattern can now been carried out by adding the contributions from reflections k with integrated intensities I_k near enough to contribute at this point, then adding to these the background at this point. The result for a constant wavelength diffractometer is

$$y_i(\text{calc}) = \sum_k I_k G(2\theta_i - 2\theta_k)\Delta(2\theta_i) + y_{ib} \tag{5.11}$$

[53] That is, independent of angle. However S does involve wavelength, and to this extent is far from constant in the TOF case.

where y_{ib} is the background (measured or modelled) to be expected at $2\theta_i$, and the sum is over all of the reflections k making a significant contribution to the intensity at this point. The corresponding result for the pattern on a TOF instrument is

$$y_i(\text{calc}) = \sum_k I_k G(t_i - t_k)\Delta t_i + y_{ib} \tag{5.12}$$

In his original analysis, of patterns collected using a constant wavelength neutron diffractometer, Rietveld (1967, 1969) assumed that peak shapes were essentially Gaussian:

$$G(2\theta - 2\theta_k) = \frac{\sqrt{C_0}}{H_k\sqrt{\pi}} \exp\left[\frac{-C_0(2\theta - 2\theta_k)^2}{H_k^2}\right] \tag{5.13}$$

where H_k is the peak full width at half maximum (FWHM), and $C_0 = 4\ln 2$, though he did add a correction for peak asymmetry. He assumed the FWHM to vary with angle according to the formula from Caglioti *et al.* (1958):

$$H_k^2 = U\tan^2\theta_k + V\tan\theta_k + W \tag{5.14}$$

where the constants U, V, W can be related [by comparing with eqn (3.3)] to the instrumental parameters (see §4.5.3), or determined experimentally. Though Caglioti *et al.* (1958) analysed for instrumental factors only, Rietveld found that eqn (5.14) with suitably amended constants gave a good description of the variation of half-width with angle even when sample broadening was significant. Rietveld completed his pattern calculation using eqn (5.11), a background y_{ib} obtained by inspection and interpolation, and for the case (common for constant wavelength powder diffractometers) that the angular acceptance of the counter $\Delta(2\theta_i) = \Delta$, is independent of the angle $2\theta_i$. A constant angular acceptance can for most purposes be incorporated into the scale factor S (at eqn (5.10)), and does not in practice need to be known.

For NaOD at 77 K, the example considered here, the calculation has been completed using eqn (5.11), setting the background at each point $y_{ib} = 1$, and with Gaussian profiles as described by eqns (5.13) and (5.14) with $U = 0.06$, $V = -0.19$, $W = 0.19$.[54] The final calculated pattern for this example is shown in Fig. 5.8(c).

The reader with a more general interest in the method can proceed directly to §5.5.3, wherein the calculated pattern is matched in a least-squares sense to that observed. But we will pause here to consider in some detail certain of the quantities appearing in eqns (5.10) to (5.14).

[54] These values are given in $(^\circ\ 2\theta)^2$, so as to give the FWHM H_k in $(^\circ\ 2\theta)$.

Scale factor

The scale factor S for constant wavelength powder diffraction (see, e.g. Sabine 1980) is given by

$$S = \left(\frac{\Phi_0 \lambda^3 h}{8\pi r}\right)\left(\frac{\rho' V N_c^2}{\rho}\right) \tag{5.15}$$

where Φ_0 is the incident flux (neutrons $m^{-2}s^{-1}$), λ is the neutron wavelength, r and h are, respectively, the distance from sample to detector, and detector height (more strictly the length of the Debye–Scherrer cone intercepted by the detector), respectively, V is the sample volume, ρ and ρ' are the theoretical and actual sample densities, and N_c the (theoretical) number of unit cells per unit volume. Note that we have bracketed the terms, showing first the instrument-dependent terms, then the sample-dependent ones. Careful consideration of the scale factor, and particularly of the sample-dependent terms, underlies the use of the Rietveld method for the quantitative analysis of multi-phase samples. This forms the subject of Chapter 8.

Debye–Waller factors

Temperature and displacement effects have been shown explicitly in eqn (5.10) through an overall multiplicative Debye–Waller factor T. However, as was apparent in §2.4.2, the situation is rather more complex than this. In fact to good approximation the scattering from each nucleus is reduced by its own individual factor, and the effects are included in the structure factor itself. That is, the structure factor written in eqn (2.31) as $F_{hkl} = \sum_n b_n \exp[2\pi i(hx_n + ky_n + lz_n)]$ is amended to read

$$F_{hkl} = \Sigma_n b_n T_n(\boldsymbol{\kappa}) \exp[2\pi i(hx_n + ky_n + lz_n)] \tag{5.16}$$

where $T_n(\boldsymbol{\kappa})$, a function of the scattering vector $\boldsymbol{\kappa}$, is the Debye–Waller factor to be applied to the scattering from the nth atom. The analysis usually assumes the Gaussian approximation, which supposes that the combined effect of thermal vibrations and static displacements on the time and spatial averages is to produce a Gaussian distribution of each atom around its mean position. In this approximation, the atomic Debye–Waller factor is given by (see §2.4.2)

$$T(\boldsymbol{\kappa}) = \exp\left[-\frac{1}{2}\left\langle(\boldsymbol{\kappa}.\boldsymbol{u})^2\right\rangle\right] \tag{5.17}$$

where $\boldsymbol{u}$ is the displacement of an atom from its mean position and the brackets $\langle\,\rangle$ indicate time and spatial average. Expressing $\boldsymbol{u}$ in terms of the vectors defining the unit cell, and $\boldsymbol{\kappa}/2\pi$ in terms of those defining the unit cell of the reciprocal lattice, leads to the form:

$$T(\boldsymbol{\kappa}) = \exp[-(\beta^{11}h^2 + \beta^{22}k^2 + \beta^{33}l^2 + 2\beta^{12}hk + 2\beta^{23}kl + 2\beta^{13}hl)] \tag{5.18}$$

where the *hkl* are the reflection indices as usual and the $\beta^{ij} = 2\pi^2 \langle \Delta x^i \Delta x^j \rangle$ since Δx^i and Δx^j are expressed as fractions of the relevant unit cell vectors, are dimensionless versions of what are now termed the *anisotropic displacement parameters* (Trueblood *et al.* 1996). This is the form that has most commonly been incorporated into Rietveld computer calculations.

For atoms on general positions, six-independent β^{ij} are required. However, for atoms at sites where there is twofold symmetry or higher, the number of independent parameters is reduced. As an example, we consider an atom on a fourfold axis, which we take to lie along the z-axis. The probability distribution function will be an ellipsoid with axis of symmetry along the z-axis, and we will have $\beta^{11} = \beta^{22} \neq \beta^{33}$ and other $\beta^{ij} = 0$. We proceed to put this argument on a more formal basis. Rotation of an object around the z-axis through an angle φ takes the point at x, y, z to a new position x', y', z' given by

$$\begin{pmatrix} x' \\ y' \\ x' \end{pmatrix} = \boldsymbol{Q} \begin{pmatrix} x \\ y \\ z \end{pmatrix} \quad \text{where } \boldsymbol{Q} = \begin{pmatrix} \cos\varphi & -\sin\varphi & 0 \\ \sin\varphi & \cos\varphi & 0 \\ 0 & 0 & 1 \end{pmatrix} \tag{5.19}$$

and effects a transformation of the matrix (tensor) β to

$$\boldsymbol{\beta}' = \boldsymbol{Q}^{\mathrm{T}} \boldsymbol{\beta} \boldsymbol{Q} \tag{5.20}$$

$\boldsymbol{Q}^{\mathrm{T}}$ being the transpose of $\boldsymbol{Q}$. Since the atom is taken to be on a fourfold axis, application of rotation $\varphi = \pi/2$ must lead to a matrix $\boldsymbol{\beta'}$ identical with $\boldsymbol{\beta}$. After applying this rotation, then writing down the transformed matrix $\boldsymbol{\beta'}$, the condition reads

$$\begin{pmatrix} \beta^{22} & -\beta^{12} & \beta^{23} \\ -\beta^{12} & \beta^{11} & -\beta^{13} \\ \beta^{23} & -\beta^{13} & \beta^{33} \end{pmatrix} = \begin{pmatrix} \beta^{11} & \beta^{12} & \beta^{13} \\ \beta^{12} & \beta^{22} & \beta^{23} \\ \beta^{13} & \beta^{23} & \beta^{33} \end{pmatrix} \tag{5.21}$$

whence $\beta^{11} = \beta^{22} \neq \beta^{33}$, and $\beta^{12} = \beta^{13} = \beta^{23} = 0$. Symmetry conditions on the β^{ij} have been worked out for every site symmetry encountered in crystals, and have been tabulated by Johnson and Levy (1974). The incorporation of these symmetry conditions varies from one computer program to another – they are computed in some programs such as GSAS (Larson and Von Dreele 2004), in others they must be entered for one atom of each symmetry equivalent set. Peterse and Palm (1966) have tabulated the conditions to be applied, for every space group and every symmetry equivalent (Wyckoff) set, to the first listed position in the *International Tables for Crystallography Volume 1* (the predecessor of Volume A). This table can be used in conjunction with computer programs that require input of the symmetry conditions on β^{ij}.

Although the dimensionless $\beta^{ij} = 2\pi^2 \langle \Delta x^i \Delta x^j \rangle$ may provide a convenient form for computation, their interpretation can be aided by conversion to physical units. The simplest approach is to multiply the fractional displacements by the lengths of the unit cell vectors. The displacement distribution is then described by

quantities having dimensions of (length)^2:

$$U^{ij} = \left\langle \Delta x^i a_i \Delta x^j a_j \right\rangle = \frac{a_i a_j \beta^{ij}}{(2\pi^2)} \tag{5.22}$$

These quantities are useful in orthogonal crystal systems, but less so when the unit cell vectors are oblique.[55] For oblique axes, it may be necessary to define a convenient rectangular Cartesian system with unit vectors related to vectors of the crystallographic unit cell by

$$(\boldsymbol{e}_1, \boldsymbol{e}_2, \boldsymbol{e}_3) = (\boldsymbol{a}, \boldsymbol{b}, \boldsymbol{c})\boldsymbol{P} \tag{5.23}$$

referred to which the mean square vibrations are given in the matrix:

$$\boldsymbol{U}_C = (2\pi^2)^{-1}\boldsymbol{Q}^T \boldsymbol{\beta} \boldsymbol{Q} \tag{5.24}$$

where $\boldsymbol{Q} = \boldsymbol{P}^{-1}$ as before. If the crystallographic axes are orthogonal, and the Cartesian axes coincide with these, then U_C is identical with the matrix defined by eqn (5.22). The interpretation is particularly simple if matrix U_C is diagonal, for then unit vectors $\boldsymbol{e}_1, \boldsymbol{e}_2, \boldsymbol{e}_3$ represent the principal axes of the distribution and the diagonal elements U_C^{ii} the mean square displacements along these axes. More generally, matrix $\boldsymbol{U_C}$ can be combined with the displacement vector $\boldsymbol{u}$ (now referred to the unit vectors of the Cartesian system) to define constant probability surfaces $\boldsymbol{u^T U_C^{-1} u} = c^2, c$ being constant. In illustrations of structures, the displacement parameters are often represented by 'thermal' ellipsoids, these being constant probability surfaces for some particular value of c. A common choice is $c = 1.538$, for which the ellipsoid contains the atom centre with 50% probability. Virtually all structure drawing computer programs have incorporated the original code by Johnson (1965). For further details, the interested reader is referred to Willis and Pryor (1975), Stout and Jensen (1968), Prince (1982), or other crystallographic texts.

In certain circumstances, such as for site symmetry $m3m$, the displacement in the Gaussian approximation is necessarily *isotropic*. The atomic Debye–Waller factor from eqn (5.17) is then:

$$T(\kappa) = \exp\left[\frac{-8\pi^2 \langle u^2 \rangle \sin^2\theta}{\lambda^2}\right] \tag{5.25}$$

with $\langle u^2 \rangle$ in physical units. The matrices $\boldsymbol{\beta}$ and $\boldsymbol{U}$ are both diagonal, with all diagonal elements equal; for the latter $U^{11} = U^{22} = U^{33} = U_{\text{iso}} = \langle u^2 \rangle$. The isotropic displacement parameter is very often given or refined as a B-factor, $B_{\text{iso}} = 8\pi^2 U_{\text{iso}}$. In other circumstances, displacements may be nearly isotropic, or the data will not support refinement of all the anisotropic displacement parameters, so an isotropic approximation is used. If a full refinement has been completed,

[55] In fact the accepted definition of U^{ij} (Trueblood *et al.* 1996) shows the lengths of the unit vectors of the reciprocal cell in the denominator rather than the lengths of unit cell vectors in the numerator as we show in eqn (5.22). For orthogonal systems, the definitions are equivalent.

then an equivalent isotropic displacement parameter can be defined as $U_{\mathrm{eq}} = 1/3(U_C^{11} + U_C^{22} + U_C^{33})$. On the other hand, if we have an approximate value for the equivalent isotropic displacement parameter, and seek starting values for a full refinement of anisotropic parameters, then these are obtained from a diagonal $\boldsymbol{U}_C$ matrix with $U_C^{11} = U_C^{22} = U_C^{33} = U_{\mathrm{eq}}$ and using eqn (5.24). Some crystal structure analysis computer programs, such as GSAS, have an inbuilt facility for conversion between anisotropic and equivalent isotropic displacement parameters. Values for equivalent isotropic displacement parameters (or at least the thermal vibration contribution to these) range from about 0.003 Å^2 in harder materials at about room temperature up to about 0.025 Å^2 for light atoms such as hydrogen, or in materials at high temperature.

Lorentz factor

The Lorentz factor has been discussed in §2.4.2. For constant wavelength powder diffraction this is usually shown as:

$$L = \frac{1}{\sin\theta \sin 2\theta} \tag{5.26}$$

with wavelength-dependent terms being incorporated into the scale factor [eqn (5.15)]. For TOF neutron scattering, the Lorentz factor is usually written:

$$L = d^4 \sin\theta \tag{5.27}$$

implying a λ^4 wavelength dependence in this case.

Multiplicity

J refers to the number of reflections in a symmetry equivalent set. For details see §2.4.2 and the tabulation in Appendix 2.

Attenuation factor

Attenuation has been discussed in §2.4.2, with particular reference to its geometrical aspects. In that section we focussed on attenuation that could be described by a linear attenuation coefficient, μ, and tabulations of attenuation factors $A(\theta)$ were cited. These may be adequate for the constant wavelength case but, importantly for the TOF diffractometer, the attenuation coefficient μ itself is expected to show a strong dependence on wavelength, becoming $A(\theta, \lambda)$. In fact there are basically two mechanisms by which intensity is removed from the beam. Neutrons can either be truly absorbed (cross section σ_{a}, §2.3.1), or removed from the beam by scattering (cross section σ_{s}). Incoherent scattering removes neutrons from the beam and simply distributes them in the background. Coherent scattering gives rise to diffracted beams (these are the Debye–Scherrer cones of powder diffraction), these being formed at the expense of incident beam intensity. The diffracted beams may themselves be attenuated, and indeed may give rise to secondary Debye–Scherrer cones in a process known as multiple diffraction. The effect of multiple diffraction (Sabine 1993) is to remove intensity from the Bragg peaks and to redistribute it

more or less uniformly into the background. When it comes to the processes occurring within a single crystallite in the powder, the phenomenon of extinction[56] may also need to be considered. This occurs because the Bragg-reflected neutrons within this crystallite will be incident on planes at exactly the angle to be Bragg reflected a second time, so returning them to the incident beam, when of course they might be reflected again. The net effect is an augmentation of the incident beam, the intensity of the diffracted beam being below what might otherwise be expected. The effect is more significant at longer wavelengths and for stronger reflections, but at constant wavelength the angular dependence is usually not severe (Sabine 1988). The effect is, therefore, typically more important in TOF than in constant wavelength diffraction. Sabine (1988, 1993) has advanced complex analytical formulae to account for this effect.

Preferred orientation

The integrated intensities are calculated in the first instance assuming an ideal powder sample, comprising a large collection of crystallites in perfectly random orientation (eqn (5.10)). The crystallites however may not be randomly oriented, but rather show preference for some orientations over others. The effect on diffraction is to produce intensity variation around the Debye–Scherrer cone.[57] We discussed in §3.6.5 various causes of preferred orientation, and the experimental means to reduce it. If, however, preferred orientation cannot be eliminated, it may be possible to model its effects on the measured intensities, and include them through the factor P in eqn (5.10) for integrated intensities.

Three angular coordinates are needed to give the orientation of any particular crystallite relative to some fixed axes in space (or in the sample), making the complete description of preferred orientation (or 'texture') a task of considerable complexity. The more general problem will be addressed in §9.8. For the moment we suppose that the sample has rotational symmetry about some axis, and that the orientation distribution is adequately described by the distribution of some prominent (reciprocal lattice) vector[58] $[HKL]$ relative to this symmetry axis. The first condition may be inherent in the sample form, or can be imposed by spinning the sample during data collection. The second condition represents the assumption that any vector $[H'K'L']$ not collinear with $[HKL]$ is distributed uniformly in azimuth around $[HKL]$, which means that the distribution of $[HKL]$ poles completely determines the orientation distribution. Due to the rotational symmetry, the density of $[HKL]$ poles can depend only the angle ϕ from the rotation axis, so the distribution is now fully described by a function $P_{HKL}(\phi)$ of a single angular coordinate. This kind of distribution has been considered by Dollase (1986), who

[56] The single crystallite corresponds to the 'mosaic block', and the process described here to the 'primary extinction' of single crystal parlance. The 'secondary extinction' encountered in single crystal work reduces in powders to multiple diffraction.

[57] An ideal sample has no variation of intensity around this cone.

[58] We mean, for example, a vector along the axis of rod or disc-shaped crystallites.

showed that it gives a correction factor for the intensity of the reflection *hkl*, in a direction [*hkl*] making an acute angle α with [*HKL*], that is

- simply $P_{hkl} = P_{HKL}(\alpha)$ when the rotational axis is parallel to the scattering vector (Bragg–Brentano geometry)
- and

$$P_{hkl} = \hat{P}_{HKL}(\alpha) = (2\pi)^{-1} \oint P_{HKL}(\phi) d\beta = (2/\pi) \int_0^{\pi/2} P_{HKL}[\phi(\alpha, \beta)] d\beta \tag{5.28}$$

when the rotational axis is perpendicular to the scattering vector (the usual Debye–Scherrer geometry). The β here is an azimuthal angle, and the average, $\hat{P}_{HKL}$, is computed with the aid of the relationship $\phi(\alpha, \beta) = \cos^{-1}(\sin\alpha \sin\beta)$.

In this context, it is a little unfortunate that most neutron powder diffractometers employ Debye–Scherrer geometry with rotational axis perpendicular to the scattering vector, since the correction factor at eqn (5.28) inevitably involves numerical integration from the pole density profile $P_{HKL}(\phi)$. However, as suggested by Dollase, and confirmed for the March function, the form of the averaged quantity $\hat{P}_{HKL}(\alpha)$ may be similar to that of its parent distribution $P_{HKL}(\phi)$, except that the locations of maxima and minima are interchanged and the range between maximum and minimum values is reduced.

There are three forms of the pole-density profile $P_{HKL}(\phi)$, or (almost) equivalently the correction factor $\hat{P}_{HKL}(\alpha)$, in common use:

(i) Rietveld (1969) applied an intensity correction factor $P_{hkl} = \exp[R\alpha^2]$, R being refinable. This evidently ranges from 1 at $\alpha = 0$ to $\exp(R\pi^2/4)$ at $\alpha = \pi/2$. This function shows a cusp at $\alpha = \pi/2$, and consequently is less than ideal as an intensity correction factor, or indeed as a pole-density profile. The correction is either always greater than or less than 1 depending on the sign of R, leading to an undesirable correlation between the preferred orientation parameter R and the overall scale factor S. Nevertheless, this form of the correction factor is still quite often used.

(ii) Among the one-parameter functions proposed for describing pole-density profiles, the March function:

$$P_{HKL}(\phi) = (R^2 \cos^2\phi + R^{-1} \sin^2\phi)^{-\frac{3}{2}} \tag{5.29}$$

is arguably the best (Dollase 1986). This function gives a pole-density that varies smoothly with ϕ, and has its maximum value at $\phi = 0$ or $\phi = \pi/2$ according as $R<1$ or $R>1$. Evidently, for $R = 1$ it gives a uniform pole-density. Since the integral of this function over a sphere is always 4π independent of the value of R, application of the March function conserves the number of poles. This matter-conserving feature suggests there will be minimal correlation between the March preferred orientation parameter R and the scale factor S, an important consideration in quantitative phase analysis

(Chapter 8). It has been shown that, for the March function, the integral (5.28) to be applied in the usual Debye–Scherrer geometry can itself be well-matched by a March function with parameter $R_{DS} = R^{-1/2}$ (Howard and Kisi 2000). Finally, the March function has a physical basis, to the extent that it represents the pole-density profile produced in a cylindrically symmetric specimen, initially comprising randomly oriented platy or rod-shaped grains, by a volume-conserving compression or extension along its cylindrical axis (March 1932).

(iii) A pole-density profile $P_{HKL}(\phi)$ depending on a single angular coordinate, and symmetric about $\phi = \pi/2$, can be expanded in terms of Legendre polynomials:

$$P_{HKL}(\phi) = \sum_n c_{2n} P_{2n}(\cos\phi) \tag{5.30}$$

where $P_0(\cos\phi) = 1, P_2(\cos\phi) = (3\cos^2\phi - 1)/2, P_4(\cos\phi) = (35\cos^4\phi - 15\cos^2\phi + 3)/8$, and so on, and the c_{2n} are constants to be determined in the refinement. To contrast with the March function, this is a description of the function of a single variable in terms of several parameters. A similar expansion, in terms of symmetrized spherical harmonics, can be employed when symmetry around the pole [*HKL*] cannot be assumed (Ahtee *et al.* 1989). It is our experience that such multiparameter descriptions can allow pole-density profiles that are physically unrealistic.

Further contributions on the matter of preferred orientation range from a specific consideration for equivalent directions [*hkl*] making unequal angles with the pole direction [*HKL*] (Čapková *et al.* 1993) to methods for a complete determination (from many diffraction patterns) of texture (Von Dreele 1997).

Peak shapes

Critical to the success of the Rietveld method is the specification of the peak shapes, through the normalized profile functions, $G(2\theta - 2\theta_k)$ or $G(t - t_k)$, as appear in eqns (5.11) and (5.12). In general, the peak shapes $h(x)$ (x being the appropriate variable) result from the convolution of a sample contribution $f(x)$ with an instrumental profile $g(x)$,

$$h(x) = \int f(x')g(x - x')dx' \quad (\text{written } h(x) = f(x) * g(x)) \tag{5.31}$$

The peak shapes, either contributing or final, are described using a number of different functional forms, all including a width parameter, and some also involving one or more parameters providing for variation of shape.

We have already mentioned that in Rietveld's (1967, 1969) original application to constant wavelength neutron diffraction he found that peak profiles could be adequately described by Gaussians. The normalized Gaussian, eqn (5.13), involves only one width parameter H_k, and Rietveld took this to vary with angle according to eqn (5.14). Gaussian peak shapes were also assumed in the analysis of patterns

of modest resolution recorded using a chopper-based TOF diffractometer at the Argonne National Laboratory's CP-5 research reactor (Worlton *et al.* 1976). In this case the peak widths were taken to vary with time (proportional to d-spacing) according to:

$$\frac{\Delta d}{d} = (A + Bd^{-2})^{\frac{1}{2}} \tag{5.32}$$

where parameters A and B were determined in the refinement.

The development of higher resolution diffractometers and spallation neutron sources has necessitated the development of more complex peak shapes. A selection of commonly used profile functions is shown in Table 5.8 – these functions, and others, are described in greater detail in the manuals of the computer codes that employ them.

The specification of the peak shapes is complete only when the width and any shape parameters appearing in the relevant profile function are also prescribed. For the widths, the simplest prescriptions are those provided for a constant wavelength powder diffractometer in eqn (5.14) and for the chopper-based TOF instrument in eqn (5.32). For the Voigt function it is sometimes assumed that the width of the Gaussian component varies as prescribed by Caglioti *et al.* (1958), eqn (5.14), whereas the Lorentzian component arises from crystallite size broadening[59] and hence (Scherrer 1918) varies as $\sec\theta$. For the pseudo-Voigt function, the shape parameter might be taken to depend quadratically on angle. Alternatively, the connection of the pseudo-Voigt parameters H and η to the parameters H_G and H_L of the corresponding Voigt function (Thompson *et al.* 1987a) makes it possible to reflect in the pseudo-Voigt any desired variation in the widths of the Gaussian and Lorentzian components of the Voigt. For TOF diffraction at spallation neutron sources, it has been found that the time constants for the rise and fall of the neutron pulse, α and β vary (Von Dreele *et al.* 1982) according to

$$\alpha = \alpha_0 + \frac{\alpha_1}{d} \quad \text{and} \quad \beta = \beta_0 + \frac{\beta_1}{d^4} \tag{5.33}$$

where $\alpha_0, \alpha_1, \beta_0,\ \beta_1$ are constants. The double exponential is convoluted with either a Gaussian or pseudo-Voigt function representing other, mainly sample, contributions. The width of the sample contribution can be coded to vary as d or d^2, to represent strain broadening or crystallite size broadening, respectively. Peak widths and shapes can be coded in ever more complex variations to account for such effects as anisotropy in crystallite size and strain broadening, as may occur when small crystallites are needle- or disc-like in character. Then peak widths depend not only on d or θ, but may depend also on the relationship between the scattering vector for the hkl reflection and some crystallographic direction $[HKL]$

[59] Isotropic strain broadening leads to widths $\Delta d \propto d$, whereas isotropic crystallite size broadening leads to a constant reflection width in reciprocal space. These imply reflection widths varying, on an angle scale, as $\tan\theta$ or $\sec\theta$, respectively, or on a d-spacing scale, as d and d^2, respectively.

Table 5.8 Selection of normalized peak profile functions.

Function	Mathematical form
Gaussian	$G(x) = \frac{\sqrt{C_0}}{H\sqrt{\pi}} \exp\left(\frac{-C_0 x^2}{H^2}\right)$ where $C_0 = 4 \ln 2$
A commonly occurring symmetric peak shape. As well as being used by Rietveld (1967, 1969), employed by Worlton *et al.* (1976) in the first Rietveld type analysis of TOF diffraction patterns.	
Lorentzian	$L(x) = \frac{\sqrt{C_1}}{\pi H} \frac{1}{1+C_1 x^2/H^2}$ where $C_1 = 4$
Another simple symmetric function. Longer tails than the Gaussian and might better represent diffraction from small crystallites.	
Voigt	$V(x) = G(x) * L(x)$ $= \frac{\sqrt{C_0}}{H_G\sqrt{\pi}} \mathrm{Re}[\omega(\sqrt{C_0}x/H_G + i\sqrt{C_0}H_L/2H_G)]$ where $C_0 = 4 \ln 2$.
The Voigt function is the convolution of a Gaussian of width (FWHM) H_G and a Lorentzian of width H_L. The shape is flexible, varying from pure Gaussian to pure Lorentzian according to the ratio H_L/H_G, and the total width is given by $H \approx (H_\mathrm{G}^5 + AH_\mathrm{G}^4 H_\mathrm{L} + BH_\mathrm{G}^3 H_\mathrm{L}^2 + CH_\mathrm{G}^2 H_\mathrm{L}^3 + DH_\mathrm{G} H_\mathrm{L}^4 + H_\mathrm{L}^5)^{1/5}$ with $A = 2.69269, B = 2.42843, C = 4.47163, D = 0.07842$ (Thompson *et al.* 1987a). The Voigt shape could occur in practice, for example, through the convolution of a Lorentzian sample peak and an instrumental Gaussian. Some authors consider the sample peak itself to result from the convolution of a Lorentzian crystallite size contribution with Gaussian strain broadening effects. Whatever the rationale, the Voigt function is often used to describe sample peaks or, in the case of constant wavelength diffraction, the final profiles observed.	
Pseudo-Voigt	$pV(x) = (1-\eta)G(x) + \eta L(x)$ where $G(x)$ and $L(x)$ have the common width H, and η the shape or mixing parameter.
Clearly this is a flexible peak shape, ranging from Gaussian ($\eta = 0$) to Lorentzian ($\eta = 1$) and even beyond ($\eta > 1$). Explicit Gaussian and Lorentzian options have been dropped from a number of Rietveld computer codes, because they can be invoked as special cases of the pseudo-Voigt. The pseudo-Voigt is so named because it has been found to give a very good approximation to a Voigt function (Wertheim *et al.* 1974). The widths of the Gaussian and Lorentzian profiles forming this Voigt function, H_G and H_L, can be found from the width H and shape η of the pseudo-Voigt using the graphs provided by Wertheim *et al.* (1974) or the equivalent numerical relationships (Hastings *et al.* 1984). $H_\mathrm{G}/H = (1 - 1.10424\eta + 0.05803\eta^2 + 0.04622\eta^3)^{1/2}$ and $H_\mathrm{L}/H = 1.07348\eta - 0.06275\eta^2 - 0.01073\eta^3$.	
'Jorgensen' (pulsed source, TOF)	$F(x) = A\left[\mathrm{e}^u \mathrm{erfc}(y) + \mathrm{e}^v \mathrm{erfc}(z)\right]$ where erfc is the complementary error function, $A = \frac{\alpha\beta}{2(\alpha+\beta)}$, $u = \frac{\alpha}{2}(\alpha\sigma^2 + 2x), \quad v = \frac{\beta}{2}(\beta\sigma^2 - 2x)$, $y = \frac{\alpha\sigma^2 + x}{\sigma\sqrt{2}}, \quad z = \frac{\beta\sigma^2 - x}{\sigma\sqrt{2}}$, $\sigma = \frac{H}{\sqrt{8 \ln 2}}$, H being the FWHM of a Gaussian.

(Table 5.8 continues)

Table 5.8 (Continued)

Function	Mathematical form
This function (Von Dreele *et al.* 1982) is formed by considering the neutron pulse as comprising a rapidly rising exponential with time constant α, followed by a slower decaying exponential of time constant β, then convoluting this pulse with a Gaussian of FWHM H.	
Extended 'Jorgensen' functions	$F(x) = (1-\eta)A\left[e^{u}\text{erfc}\,(y) + e^{v}\text{erfc}\,(z)\right] + \eta\ldots$ where η is the Lorentzian fraction in the pseudo-Voigt. The reader is referred to the GSAS technical manual for detail.
These functions are the result of convoluting the pulse just described with pseudo-Voigt (rather than Gaussian) functions. They include additional terms (not shown here) from the convolution of the pulse with the Lorentzian part of the pseudo-Voigt. See GSAS technical manual (Larson and Von Dreele 2004) TOF profile functions #3 and #4.	

The quantity H represents a FWHM, and the variable x is taken to represent the angular distance or difference in time from the calculated peak position for CW and TOF diffraction, respectively.

particular to the crystal. For the purposes of the present chapter (crystal structure determination), these more complex variations in peak width and shape may be invoked in the Rietveld refinement simply to improve the overall fit to the pattern, and so to improve the confidence in the structural parameters obtained. However, it may be possible to interpret the parameters describing the width and shape of the diffraction peaks as providing information on the microstructure of the sample under study as discussed at length in Chapter 9.

That peak shapes obtained from constant wavelength instruments are afflicted by an asymmetry of instrumental origins has been indicated already in Chapter 4 (§4.2 and §4.5.1). This asymmetry can be considered to be the result of a straight slit of finite height traversing the (curved) Debye–Scherrer cone (Fig. 4.4) or, more generally, of axial divergence in the diffractometer. Rietveld (1969) tried to correct for this effect by the application of a multiplicative angle-dependent correction factor (eqn (4.5)). Howard (1982) and Prince (1983) considered the response of a slit of height $2H$ at a distance R from the sample as it traversed an infinitely sharp Debye–Scherrer cone, and considered the convolution of this response with a peak-broadening function. Prince (1983) expressed the result as an Edgeworth expansion, valid for peak shapes close to Gaussian. Howard (1982) used Simpson's rule to approximate the convolution and so obtained a sum of peak profile functions, valid (as an approximation) for a peak-broadening function of any form. Both solutions incorporated a single asymmetry parameter, refinable, but in principle connected to the experimental arrangement through the factor $1/2(H/R)^2 \cot 2\theta$. The analysis has been extended by van Laar and Yelon (1984) and subsequently by Finger *et al.* (1994) to account for a finite sample height $2S$, giving diffraction as a band of height $2S$ of Debye–Scherrer cones. We note at this point that vertical (axial) divergence of the beam incident onto the sample will also lead to a band of Debye–Scherrer cones, and so its effect is somewhat equivalent to sample size (Finger *et al.* 1994). The convolutions in this treatment are performed by numerical

integration, and the results depend on the two combinations of parameters, H/R and S/R. However, it may be necessary again to treat these parameters as refinable. This approach yields an excellent fit to the low angle peaks recorded from a zeolite on the High Resolution Neutron Powder Diffractometer at the Brookhaven Laboratory (Finger *et al.* 1994).

Background

The background term y_{ib} can be specified or modelled in a number of different ways (Young 1993). The background can be given point by point, as might be the case if it is taken from an independent run without the sample. The background can be interpolated between estimates made at locations where no peaks appear to contribute. The background is more commonly modelled by some function of

Table 5.9 Selection of functions used to describe background.

Function	Mathematical form
Simple polynomial	$y_{ib} = \sum_{n=-1}^{m} B_n (2\theta_i)^n$
Number of terms needs to be restricted (say $m < 5$) for stable refinement. Term with $n = -1$ useful for modelling a background rising at low angle.	
Cosine Fourier series	$y_{ib} = \sum_{n=0}^{m} B_n \cos 2n\theta_i$
The term $n = 0$ gives a flat contribution, the other terms are orthogonal over the interval from 0 to 2π.	
Chebyshev polynomials	$y_{ib} = \sum_{n=0}^{m} B_n T_n \left(\frac{2(t_i - t_{\min})}{(t_{\max} - t_{\min})} - 1 \right)$
The polynomials $T_n(x)$ are closely related to the cosines just shown, and with suitable weighting are orthogonal over the interval from -1 to 1. This has been written for a TOF pattern recorded from $t_{\min}$ to $t_{\max}$, but background in CW patterns can be described in an analogous way.	
Increasing background	$y_{ib} = \sum_{n=0}^{m} \frac{B_n Q^{2n}}{n!}$ where $Q = \frac{4\pi \sin\theta_i}{\lambda} = 2\pi / d_i$
Thermal vibrations reduce the intensities in the Bragg peaks, and this intensity appears as thermal diffuse scattering (TDS) in the background. It can be seen from eqn (5.25) that scattered intensities in the Bragg peaks are reduced by factors $\sim \exp(-Q^2 \langle u^2 \rangle)$, so the TDS increases roughly as $1 - \exp(-Q^2 < u^2 >)$.	
Amorphous contribution	$y_{ib} = B_0 + B_1 Q + \sum_{n=1}^{m} B_{2n} \frac{\sin(QB_{2n+1})}{QB_{2n+1}}$
The summation is intended to represent a contribution to the background from an amorphous component. The first two terms comprise a linear contribution, though this is written variously as linear in Q (as here), t in TOF patterns, and θ in CW patterns.	

angle or TOF, either phenomenological or physically based, and incorporating parameters to be determined in the refinement. A selection from the different functions employed is shown in Table 5.9 – for further detail on these and other background functions we once again refer the reader to the relevant computer codes and their manuals.

5.5.3 Matching of calculated pattern to that observed

Given the observed intensities y_i(obs) with estimates of the associated weights w_i (§5.5.1), and a set of calculated intensities y_i(calc) (§5.5.2), the task is to vary parameters involved in y_i(calc) so as to obtain the best possible match of the calculated pattern to that observed. This provides a determination of the parameters of interest, as well as of others of perhaps lesser interest. The matching is normally carried out using the mathematical method of least squares, that is, parameters are varied so as to minimize the 'weighted sum of squared residuals':

$$\overline{S} = \sum_i w_i(y_i(\text{obs}) - y_i(\text{calc}))^2 \tag{5.8}$$

or in an abbreviated notation:

$$\overline{S} = \sum_i w_i(y_i - y_{ic})^2 \tag{5.34}$$

Were the calculated intensities y_i(calc) to depend linearly on the variable parameters, then the minimization of the expression (5.8) could be applied with confidence. However, since the dependence of y_i(calc) on the parameters is highly non-linear (§5.5.2), the minimization of (5.8) can proceed only through iterative processes, and there are no guarantees that such processes will lead to a correct solution. It is therefore imperative that the match be judged not solely on the values of $\overline{S}$ and related measures of fit, but is checked by visual examination of the way the calculated pattern fits that observed. It is also important to check the plausibility of the parameters obtained.

Least squares mathematics

To proceed with the mathematics of the least squares method, we suppose that y_{ic} is considered to be a function of P independent parameters, $x_1, x_2, \ldots, x_P$. A necessary condition that $\overline{S}$ be minimum with respect to variations of these parameters is that for every parameter x_j the partial derivative $\partial\overline{S}/\partial x_j = 0$. Starting from eqn (5.34), we obtain the *normal equations*:

$$\frac{\partial \overline{S}}{\partial x_j} = -\sum_{i=1}^{N} 2w_i(y_i - y_{ic})\frac{\partial y_{ic}}{\partial x_j} = 0 \tag{5.35}$$

where j runs from 1 to P and N is the number of observations. The expressions for the P partial derivatives can be presented in matrix form:

$$\begin{pmatrix} \dfrac{\partial \overline{S}}{\partial x_1} \\ \dfrac{\partial \overline{S}}{\partial x_2} \\ \cdots \\ \dfrac{\partial \overline{S}}{\partial x_P} \end{pmatrix} = -2 \begin{pmatrix} \dfrac{\partial y_{1c}}{\partial x_1} & \dfrac{\partial y_{2c}}{\partial x_1} & \dfrac{\partial y_{3c}}{\partial x_1} & \dfrac{\partial y_{4c}}{\partial x_1} & \cdots & \dfrac{\partial y_{Nc}}{\partial x_1} \\ \dfrac{\partial y_{1c}}{\partial x_2} & \dfrac{\partial y_{2c}}{\partial x_2} & \dfrac{\partial y_{3c}}{\partial x_2} & \dfrac{\partial y_{4c}}{\partial x_2} & \cdots & \dfrac{\partial y_{Nc}}{\partial x_2} \\ \cdots & \cdots & \cdots & \cdots & \cdots & \cdots \\ \dfrac{\partial y_{1c}}{\partial x_P} & \dfrac{\partial y_{2c}}{\partial x_P} & \dfrac{\partial y_{3c}}{\partial x_P} & \dfrac{\partial y_{4c}}{\partial x_P} & \cdots & \dfrac{\partial y_{Nc}}{\partial x_P} \end{pmatrix}$$

$$\times \begin{pmatrix} w_1 & & & & & \\ & w_2 & & & & \\ & & w_3 & & & \\ & & & w_4 & & \\ & & & & \cdots & \\ & & & & & w_N \end{pmatrix} \begin{pmatrix} y_1 - y_{1c} \\ y_2 - y_{2c} \\ y_3 - y_{3c} \\ y_4 - y_{4c} \\ \cdots \\ y_N - y_{Nc} \end{pmatrix} \tag{5.36}$$

We see that the matrices in this expression have dimensions (rows $\times$ columns) $P \times 1, P \times N, N \times N$, and $N \times 1$, respectively. The differences between observations and calculations appear in a column vector, and the weights in a diagonal matrix. Note that the matrix of derivatives is in effect the transpose of the matrix $\left(\partial y_{ic}/\partial x_j\right)$.

We assume for the moment that we have good initial estimates of the parameters, such as we have obtained already for the example case of NaOD at 77 K, and denote these $x_1^0, x_2^0, \ldots, x_j^0, \ldots, x_P^0$. Since these initial estimates are assumed to be good, then the value of y_{ic} at the required values $x_1, x_2, \ldots, x_j, \ldots, x_P$ can be obtained by the linear terms in a Taylor expansion around the initial values x_j^0:

$$y_{ic}(x_1, x_2, \ldots, x_P) = y_{ic}(x_1^0, x_2^0, \ldots, x_P^0) + \sum_{j=1}^{P} \left.\frac{\partial y_{ic}}{\partial x_j}\right|_0 \Delta x_j \tag{5.37}$$

where $\Delta x_j = x_j - x_j^0$, and again the results can be presented in matrix form:

$$\begin{pmatrix} y_{1c}(x_1, x_2, \ldots, x_P) \\ y_{2c}(x_1, x_2, \ldots, x_P) \\ y_{3c}(x_1, x_2, \ldots, x_P) \\ y_{4c}(x_1, x_2, \ldots, x_P) \\ \vdots \\ y_{Nc}(x_1, x_2, \ldots, x_P) \end{pmatrix} = \begin{pmatrix} y_{1c}(x_1^0, x_2^0, \ldots, x_P^0) \\ y_{2c}(x_1^0, x_2^0, \ldots, x_P^0) \\ y_{3c}(x_1^0, x_2^0, \ldots, x_P^0) \\ y_{4c}(x_1^0, x_2^0, \ldots, x_P^0) \\ \vdots \\ y_{Nc}(x_1^0, x_2^0, \ldots, x_P^0) \end{pmatrix}$$

$$+\begin{pmatrix} \frac{\partial y_{1c}}{\partial x_1} & \frac{\partial y_{1c}}{\partial x_2} & \cdots & \frac{\partial y_{1c}}{\partial x_P} \\ \frac{\partial y_{2c}}{\partial x_1} & \frac{\partial y_{2c}}{\partial x_2} & \cdots & \frac{\partial y_{2c}}{\partial x_P} \\ \frac{\partial y_{3c}}{\partial x_1} & \frac{\partial y_{3c}}{\partial x_2} & \cdots & \frac{\partial y_{3c}}{\partial x_P} \\ \frac{\partial y_{4c}}{\partial x_1} & \frac{\partial y_{4c}}{\partial x_2} & \cdots & \frac{\partial y_{4c}}{\partial x_P} \\ \cdots & \cdots & \cdots & \cdots \\ \frac{\partial y_{Nc}}{\partial x_1} & \frac{\partial y_{Nc}}{\partial x_2} & \cdots & \frac{\partial y_{Nc}}{\partial x_P} \end{pmatrix} \begin{pmatrix} \Delta x_1 \\ \Delta x_2 \\ \cdots \\ \Delta x_P \end{pmatrix} \tag{5.38}$$

The matrices here are column vectors of calculations, a column vector of corrections to parameters, and the matrix $\left(\partial y_{ic}/\partial x_j\right)$. The elements of this matrix differ from those appearing in eqn (5.36) in that they are derivatives evaluated for the initial values of parameters x_j^0 [as indicated explicitly in eqn (5.37)], whereas those in (eqn (5.36)) are derivatives evaluated at solution values x_j. This difference can usually be ignored. Denoting the various matrices appearing in eqns (5.36)–(5.38) by $(\partial \overline{S}/\partial \boldsymbol{x})$, $(\partial \boldsymbol{y_c}/\partial \boldsymbol{x})$, $\boldsymbol{w}$, $\boldsymbol{y}-\boldsymbol{y_c}$, $\boldsymbol{y_c}(\boldsymbol{x})$, $\boldsymbol{y_c}(\boldsymbol{x}^0)$, $\Delta\boldsymbol{x} = \boldsymbol{x}-\boldsymbol{x}^0$, we can rewrite eqn (5.35) and make use of eqns (5.36) and (5.38) to give

$$\frac{\partial \boldsymbol{y_c}^{\boldsymbol{T}}}{\partial \boldsymbol{x}} \boldsymbol{w}(\boldsymbol{y}-\boldsymbol{y_c}) = \frac{\partial \boldsymbol{y_c}^{\boldsymbol{T}}}{\partial \boldsymbol{x}} \boldsymbol{w}\left(\boldsymbol{y}-\boldsymbol{y_c}(\boldsymbol{x}^0) - \frac{\partial \boldsymbol{y_c}}{\partial \boldsymbol{x}}\Delta\boldsymbol{x}\right) = \boldsymbol{0} \tag{5.39}$$

where superscript $\boldsymbol{T}$ indicates a transposed matrix, whence

$$\frac{\partial \boldsymbol{y_c}^{\boldsymbol{T}}}{\partial \boldsymbol{x}} \boldsymbol{w}(\boldsymbol{y}-\boldsymbol{y_c}(\boldsymbol{x}^0)) = \frac{\partial \boldsymbol{y_c}^{\boldsymbol{T}}}{\partial \boldsymbol{x}} \boldsymbol{w} \frac{\partial \boldsymbol{y_c}}{\partial \boldsymbol{x}}\Delta\boldsymbol{x} \tag{5.40}$$

and the solution to eqn (5.35) is given by $\boldsymbol{x} = \boldsymbol{x}^0 + \Delta\boldsymbol{x}$ where

$$\Delta\boldsymbol{x} = \left(\frac{\partial \boldsymbol{y_c}^{\boldsymbol{T}}}{\partial \boldsymbol{x}} \boldsymbol{w} \frac{\partial \boldsymbol{y_c}}{\partial \boldsymbol{x}}\right)^{-1} \frac{\partial \boldsymbol{y_c}^{\boldsymbol{T}}}{\partial \boldsymbol{x}} \boldsymbol{w}(\boldsymbol{y}-\boldsymbol{y_c}(\boldsymbol{x}^0)) \tag{5.41}$$

Evidently the evaluation of the parameter corrections $\Delta\boldsymbol{x}$ is relatively straightforward once the derivatives $(\partial \boldsymbol{y_c}/\partial \boldsymbol{x})$ are written out, apart from any problems that might be associated with the inversion of the $P \times P$ matrix $(\partial \boldsymbol{y_c}/\partial \boldsymbol{x}^{\boldsymbol{T}})\boldsymbol{w}(\partial \boldsymbol{y_c}/\partial \boldsymbol{x})$. Equation (5.41) would provide an exact solution were the calculations linearly dependent on the parameters, but given the highly non-linear nature of the crystallographic problem and the neglect of higher terms in the Taylor expansion, the new solution is taken as the starting solution for another cycle of iteration. In practice iterations are continued until the corrections to the parameters become very small (relative to estimated statistical errors) and likewise there is little improvement in the measures of fit.

The parameters $x_1, x_2, \ldots, x_P$ are often not independent, but related by constraints. For example, in tetragonal symmetry the equality of two of the lattice

parameters, $a = b$, can be considered a constraint. If there are C equations expressing constraints among the P parameters, it should be possible, at least in principle, to use these equations to eliminate C parameters, and recast the least squares problem in terms of just $P - C$ independent parameters. In practice this may not be the best way to handle constraints, but for purposes of estimating uncertainties and the like, we may suppose that such a reduction has been effected.

We emphasize again the importance of the initial estimates of parameters. Brandt (1970), for example, remarks that 'the art of using the least squares method with non-linear problems is to provide sufficiently good first approximations'. This is certainly the case in crystallography, and for the Rietveld method in particular. It is, for instance, a reasonably obvious requirement for the success of an iterative approach that the starting values for the lattice parameters should be close enough to the true values to ensure the calculated peaks overlap with the corresponding peaks in the observed pattern.

Parameter uncertainties

The iterative application of eqn (5.41) gives the required values for parameters, but we do not as yet have values for the uncertainties in them. Since we do not intend to pursue the mathematics of least squares any further, we will take the results from the literature. If the observations y_i are independent and correctly weighted, and the linear approximation at eqn (5.37) is good, then the $P \times P$ matrix $\left((\partial \boldsymbol{y_c}/\partial \boldsymbol{x}^{\boldsymbol{T}})\boldsymbol{w}(\partial \boldsymbol{y_c}/\partial \boldsymbol{x})\right)^{-1}$ is the variance–covariance matrix for the unknown parameters $\boldsymbol{x}$ (Prince 1993). This means that the jth diagonal element of this matrix is the square of the estimated standard deviation in the estimate of parameter x_j, while the off-diagonal element in the jth row and kth column is the product of the coefficient of correlation between variables x_j and x_k with the standard deviations $\sigma(x_j)$ and $\sigma(x_k)$ of these two variables. Most Rietveld computer programs list both the estimated standard deviations for the various parameters that are refined, along with the correlation matrix (the entries on this are 1 on the diagonal, and other entries can range between -1 and $+1$). The estimated standard deviations in the parameters provide the statistical basis (alluded to above) for terminating the refinement – for example, the process may be stopped when the parameter shifts in one cycle of iteration fall to less than a prescribed fraction (say 10%) of the estimated standard deviations.

Measures of fit

The value of $\overline{S}$, eqn (5.34), the quantity to be minimized is the most obvious numerical measure of fit of the calculated pattern to that observed. Its value can be monitored to indicate the progress of the refinement. With the correct weighting scheme $w_i = 1/\sigma^2(y_{ic})$ and a perfect refinement, the value of $\overline{S}$ reduces to $\sum_{i=1}^{N}(y_i - y_{ic})^2/\sigma^2(y_{ic})$, conforming to a χ^2 distribution with $N - P + C$ degrees of freedom (Brandt 1970). As such, its expectation value is $N - P + C$, with expected variance $2(N - P + C)$. A statistic often quoted, at least in a

crystallographic context (Prince 1993; Young, 1993), is the goodness of fit:

$$GoF = \left[\frac{1}{N - P + C} \sum_{i=1}^{N} w_i (y_i - y_{ic})^2 \right]^{\frac{1}{2}} \tag{5.42}$$

measuring in effect the ratio of weighted sum of squared residuals $\overline{S}$ to its ideal value. Deficiencies in the data or the crystallographic model usually result in values of GoF considerably greater than unity, and these same deficiencies cast doubt on the estimates of the parameters and their standard deviations. This situation is commonly addressed by reducing all weights w_i by the factor GoF^2, leaving the fit unchanged but increasing all entries in the variance–covariance matrix by the same factor GoF^2. To put this simply, the parameters are left unchanged, but their estimated standard deviations are all increased, somewhat arbitrarily, by the factor GoF. The correlation matrix is left unchanged.

There are a number of different measures of fit in use, some closely related to the quantity $\overline{S}$ that is minimized, some deriving from established usage in single crystal work. The most commonly used numerical measures of fit are summarized in Table 5.10.

The characteristics of these various measures of fit are extensively discussed in the literature (Hill and Flack 1987; Prince 1993; Young 1993). We refer the reader to these references for detail, and offer only a few comments here. Briefly, with a correct crystallographic model all the profile R-factors may be inflated by a poor description of peak shapes; on the other hand, they may appear satisfactory with an incorrect crystallographic model simply because the background is fitted well. If the counts recorded in a pattern are insufficient, then the statistics may not allow any meaningful test of the model – in these circumstances R_{wp} and R_{exp} would both be large, yet $GoF = R_{\mathrm{wp}}/R_{\mathrm{exp}}$ being close to unity might appear satisfactory. The Bragg R-factor, R_{B}, is the measure most sensitive to crystal structure, but depends on integrated intensities I_k ('obs') that are obtained not directly, but by apportioning each y_i(obs) between the contributing reflections and the background according to the refined model. This apportionment is always biased towards the assumed model, and can be dependent on the details of the refinement (e.g. in the manner of accounting for background). The values obtained for R_{B}, however obtained, are likely to be flattering. We conclude by again emphasizing the importance of a visual check of the way the calculated pattern fits the observed, as well as a check on the plausibility of the final parameters, no matter how many numerical measures of fit may be employed.

We return to the example of NaOD at 77 K. The final results recorded in Table 5.7, were obtained by the Rietveld method, that is by the least squares matching of the calculated pattern to that observed. For the refinements, the background assumed was a polynomial in 2θ (four variable parameters), and the peak shapes assumed were asymmetric pseudo-Voigts with an angle-independent Lorentzian fraction (one variable parameter), widths described by the Caglioti equation (three variable

Table 5.10 Common numerical measures of fit.

		Comment
Weighted sum of squared residuals	$\overline{S} = \sum_i w_i(y_i(\text{obs}) - y_i(\text{calc}))^2$	The quantity being minimized in the refinement. Main indicator of the progress of a refinement. Expected value under perfect conditions is $N - P + C$.
Weighted profile R-factor	$R_{\text{wp}} = \left\{ \frac{\sum_i w_i(y_i(\text{obs}) - y_i(\text{calc}))^2}{\sum_i w_i(y_i(\text{obs}))^2} \right\}^{1/2}$	Closely related to the weighted sum of squared residuals.
Expected profile R-factor	$R_{\text{exp}} = \left\{ \frac{N-P+C}{\sum_i w_i(y_i(\text{obs}))^2} \right\}^{1/2}$	Obtained by assuming numerator above takes its expected value.
Goodness of fit	$GoF = \frac{R_{\text{wp}}}{R_{\text{exp}}}$	Consistent with the definition given at eqn (5.42).
Profile R-factor	$R_{\text{p}} = \frac{\sum \lvert y_i(\text{obs}) - y_i(\text{calc}) \rvert}{\sum y_i(\text{obs})}$	Another perspective on the overall fit. It lacks the weighting factor, $w_i \approx 1/y_i(\text{obs})$, and so gives more weight (relative to R_{wp}) where counts are greater.
Bragg R-factor	$R_{\text{B}} = \frac{\sum \lvert I_k(\text{'obs'}) - I_k(\text{calc}) \rvert}{\sum I_k(\text{'obs'})}$	Based on integrated intensities of reflections, and thus sensitive to the fits at the reflections themselves. The 'observed' intensities, however, are not experimentally measured quantities – rather they are obtained by an apportioning of each $y_i(\text{obs})$ between the contributing reflections and the background. The closest equivalent to the R-factor quoted in single crystal studies.
Durbin–Watson statistic	'd' $= \frac{\sum (\Delta y_i - \Delta y_{i-1})^2}{\sum \Delta y_i^2}$ where $\Delta y_i = y_i(\text{obs}) - y_i(\text{calc})$	This is not in fact a measure of fit, but a measure of correlation between residuals at successive points of the pattern. It assumes values between 0 (perfect correlation) and 2 (uncorrelated residuals).

parameters), and the Howard description of asymmetry (one variable parameter). As to the structure, cell constants (four variable parameters), and for each atom the fractional coordinates x, y, z and the isotropic displacement parameter U_{iso} were varied (3×4 parameters). It was of course necessary to refine the scale factor (one variable parameter), and a single preferred orientation parameter (Rietveld model) was also allowed to vary. In all, 27 parameters were determined, the fit of calculated pattern to observed is shown in Fig. 5.8(d), and the measures of fit were $R_{\text{p}} = 4.8\%, R_{\text{wp}} = 5.7\% (R_{\text{exp}} = 4.3\%), R_{\text{B}} = 1.8\%$. The crystal structure itself is described by just the 13 parameters recorded in Table 5.7.

5.6 LE BAIL EXTRACTION

The Le Bail extraction (Le Bail *et al.* 1988) is one method to fit a diffraction pattern when the crystal system and perhaps the space group symmetry are known, but without recourse to a model of the structure. The primary application of such a method is to extract a set of integrated intensities that can be used towards the solution of unknown structures (Chapter 6). There are however other applications in the analysis of powder diffraction pattern, in particular to provide superior unit cell, zero, and peak width/shape parameters in the event that the structural model incorporated in the Rietveld analysis gives a less than satisfactory fit to the observations.

It is appropriate to discuss Le Bail extraction at this point because of its close connection with the Rietveld method. It is also sometimes used as a preliminary to the Rietveld analysis to provide good values for the various parameters mentioned just earlier, in effect reducing the number of parameters that the Rietveld method must determine. A successful Le Bail fit will also represent the best fit that can be achieved in any subsequent application of the Rietveld method (under the same assumptions of peak shapes, etc.).

The Le Bail extraction relates specifically to the determination of I_k('obs') within the Rietveld code, so we start with a more detailed account of how this is done. The intensity observed at the ith step in the diffraction pattern, y_i(obs) is first apportioned among the different reflections contributing at that point (and the background), the amount being given to the kth reflection being:

$$y_{ik}(\text{'obs'}) = \frac{y_i(\text{obs}) y_{ik}(\text{calc})}{y_i(\text{calc})} \tag{5.43}$$

These y_{ik} ('obs') are then summed, over those steps in the pattern close enough to the kth reflection that this reflection is taken to contribute, to provide a total 'observed' integrated intensity:

$$I_k(\text{'obs'}) = \sum_i y_{ik}(\text{'obs'}) \tag{5.44}$$

In the Rietveld method, this calculation of the 'observed' integrated intensities I_k ('obs'), and the related measure of fit R_B, is carried out after the last cycle of refinement is complete.

Le Bail extraction represents a variation of the Rietveld method, making use of the intensity decomposition eqns (5.43) and (5.44), but differing from the Rietveld method in the following respects:

- The intensity decomposition calculations are carried out after each cycle of refinement.
- The initial values of y_i(calc) are obtained using eqn (5.11) with a more or less arbitrary set of starting values for the intensities I_k. These may be calculated from eqn (5.10) on the basis of some approximate structural model, but more usually would be set all to unity.
- The I_k('obs') extracted using eqns (5.43) and (5.44) are used for the I_k in eqn (5.11) to provide the y_i(calc) for use in the next iteration of intensity decomposition.
- The final results from a Le Bail extraction are refined values for unit cell, peak width, and shape parameters, along with a set of 'observed' integrated intensities I_k('obs').

An interesting aspect of this procedure is that only unit cell and peak width/shape parameters are varied in the least squares minimization – the intensities I_k albeit initially unknown are not counted among the parameters to be determined by least squares. The course of a Le Bail extraction depends on the starting point – convergence is expedited when starting from reasonable unit cell and peak width and shape parameters and an approximate crystal structure model giving reasonable starting values for the I_k. If unit cell, peak width, and shape parameters are well known, but the structure is not, then there is a case for running several cycles of the Le Bail iteration [i.e. iterations through eqns (5.11), (5.43), (5.44)] with all the Rietveld parameters left fixed. The Le Bail extraction typically needs more cycles of iteration than a well-behaved application of the Rietveld method.

5.7 PRACTICAL CONSIDERATIONS IN STRUCTURE REFINEMENT

Most aspects of data collection, pattern calculation based on a crystal structure model, and the least squares matching of the calculated pattern to that observed, have been addressed in §5.5 and §5.6 or in earlier chapters. However, for the reader undertaking structure refinement by the Rietveld method, there remain a number of practicalities to be considered. The article by Kisi (1994) may well be useful to the beginning user of the Rietveld method, and the articles by Young (1993) and McCusker *et al.* (1999) also incorporate much useful advice.

With diffraction patterns in hand, and a starting model for the crystal structure, the question is how to proceed in practice with the least squares refinement. That is, what computer program should be employed? The authors' view is that there is no

Rietveld computer program that covers all possibilities so there is no single answer to this question. The different programs are certainly not all equal in terms of their capacities to cope with magnetic or incommensurate structures, to deal with multiphase mixtures, to describe peak shapes from TOF instruments or associated with anisotropic peak broadening, to permit X-ray patterns to be fitted simultaneously with the neutron data, to describe constraints, or to incorporate restraints on bond lengths, to list just a few examples. Thus, the choice of program will depend on the problem on hand, as well as on such factors as the reservoir of local experience with one program or another. Most of the available Rietveld programs, along with a number of pertinent tutorials, can be downloaded from the web site of the UK's Collaborative Computational Project Number 14, http://www.ccp14.ac.uk/. The authors tend to use the Australian developed LHPM (Hill and Howard 1986) with RIETICA interface (Hunter 1998) or the widely used program GSAS (Larson and Von Dreele 2004), with or without the EXPGUI interface (Toby 2001).

The Rietveld method requires the entry of a starting model for the crystal structure, often entered manually, or sometimes read in from a file. It is a useful feature of programs such as GSAS and RIETICA that they can read the data directly from a crystallographic information file (CIF) as can be obtained, for example, from the Inorganic Crystal Structure Database. Various choices must be made as to the peak shapes and form of the background function, and the suitable starting values given for the associated parameters. Choices may be guided by the discussion around Tables 5.8 and 5.9, and approximate values for the parameters obtained from inspection of the diffraction pattern to be fitted. Alternatively, it is often sufficient to start with choices and parameters based on previous experience, perhaps from measurements on standard samples, with the same diffractometer. In particular, the GSAS program takes such information from an 'instrument parameter file' constructed from measurements on a standard sample.

The sensitivity of the least-squares method to initial estimates of parameters was emphasized in §5.5.3. Not all initial estimates, however, need be equally good. For example, if the peak positions are correctly calculated, and the peak widths and shapes well described, then a very large error in the scale factor, by a factor of 10 or more, can be quickly corrected. If on the other hand the lattice parameters are in error, by say 1%, so that there is no overlap of the calculated peaks with those observed, then the refinement will not work. Such considerations lead to the conclusion that any attempt to refine all the parameters at the outset is almost certainly doomed, and to suggested strategies for 'turning on' parameters to enhance the prospects of success (Young 1993; Kisi 1994).

Given good starting values for lattice parameters and zero, so that calculated peak positions are in accord with those observed, and with reasonable initial descriptions of peak widths and shapes, then it should be possible to start with refinements of scale factor and background. This is in fact the default initial setup in the GSAS program. Success can be judged quite readily from the graphic output. If the calculated peaks (see position markers in graphics) do not overlap with

the observed peaks there is no point running further cycles of refinement – better starting values of lattice parameters and zero are needed. If there is reasonable overlap between the calculated peaks and those observed, some intensity will appear in the calculated peaks. Then an examination of the graphic output may well suggest the next step – examples of graphic output under different error conditions appear in publications already cited (Young 1993; Kisi 1994; McCusker *et al.* 1999). If the offset between calculated and observed peaks appears still to be significant, then lattice parameters and zero should be refined next. If problems of peak widths appear to be more serious, then peak width parameters should be corrected as necessary and perhaps refined ahead of the lattice parameters and zero. The refinements so far are the initial refinements (Kisi 1994), and in favourable circumstances should result in reasonable estimates of lattice parameters, zero, peak widths, scale, and background.

The fit of the calculated pattern to the observed after the initial refinements will depend on the adequacy of the structural model. If the fit is already reasonably good, then it should be possible to turn on refinements of atomic position parameters, displacement parameters, site occupancies (as appropriate), preferred orientation parameters (if required), in quick succession.[60] It should be possible to support refinements of additional peak width and peak shape parameters at the same time. Examination of the graphical output at the various stages of refinement again may be helpful. If on the other hand the fit to the intensities after the initial refinements is poor, then structure refinement may well prove difficult, and it could be prudent to complete a Le Bail extraction at this point. This will fit the intensities (§5.6), and in so doing it will provide excellent estimates of lattice parameters, zero, peak widths and shapes, and background, as well as an indication of the R-factors that could be achievable with the data in hand. Further attempts at structure refinement then can be stabilized, at least to some extent, by keeping lattice parameters, zero, peak widths and shapes, and perhaps background fixed at the values obtained from the Le Bail extraction. If these further attempts lead to a satisfactory structural model then it should be possible, though it may not be necessary, to release these fixed parameters at a later stage of refinement (McCusker *et al.* 1999). If the further attempts are unsuccessful, then the starting model may need a substantial revision. One approach, available in most computer programs, is to construct a difference Fourier map from the differences between the I_k('obs') estimated after the final cycle of Rietveld refinement, and the I_k(cal) based on the model assumed. Though the I_k('obs') are always biased towards the model [by virtue of eqn (5.43)] so features in the difference map are somewhat attenuated, it should still be possible to obtain some indication of model deficiencies and thus a means to correct for them. If this approach is unsuccessful then perhaps the structure should be considered unknown, and the *ab initio* methods described in Chapter 6 employed in its solution.

[60] This was the case for the refinement of the structure of NaOD at 77 K, the example referred to earlier in this chapter.

There are various circumstances in which, even with a reasonable starting model, refinements can become unstable. It is suggested that the most common cause of such problems is an inadvertent error in the input file, particularly when all the detail has been entered manually. The need for accurate initial estimates of lattice parameters has already been mentioned. In addition, instabilities can often arise from unworkable initial values for peak width and shape parameters. Refinements often fail when too many parameters are 'turned on' too soon. For example, if peak widths and shapes are refined while there remains serious intensity mismatch, instability may result. Problems will also be encountered if attempts are made to refine too many parameters. In this context, it is necessary to distinguish the number of steps in the pattern from the number of peaks observed. The individual step intensities help to determine parameters such as cell constants, peak width and shape parameters, and background. However, the atomic coordinates and displacement parameters, as well as preferred orientation, impact on the pattern only through the integrated intensities I_k [eqn (5.10)], so the number of such parameters that can be determined in a refinement depends on the number of peaks in the pattern rather than the number of steps. For practical reasons, such as severe peak overlap, the number of observations relating to atomic coordinates and related parameters is less than the number of peaks. It is said that for successful refinement that the ratio of the number of (relevant) observations to the number of parameters should be at least 3, preferably 5 (McCusker *et al.* 1999). Refinements will not converge if attempts are made to refine highly or completely correlated parameters – an inadvertent attempt to refine simultaneously wavelength and lattice parameters would be an example of the latter. A problem can also arise with a high-symmetry starting model in a lower symmetry space group. The symmetry may be such that moving an atom or atoms in opposite directions by equal amounts may lead to equivalent structures, and therefore to the same calculated pattern. This implies $\partial y_{ic}/\partial x_j\big|_0 = 0$ for the pertinent atomic position parameter x_j, and the matrix inversion within the least squares fails because of these zero derivatives. In our example problem, the structure of NaOD at 77 K (§5.4), we shifted an atom to remove mirror symmetry from our starting model to avoid just this problem.

Problems arising from too few data relative to parameters can be addressed by adding more data. These may comprise other measurements on the same material, most obviously X-ray diffraction data, or information of a more general kind, such as the accumulated wisdom on pertinent bond lengths and bond angles. Data of the latter kind are used to impose geometrical restraints. The quantity to be minimized might then be

$$w_{\mathrm{N}}\bar{S}_{\mathrm{N}} + w_{\mathrm{X}}\bar{S}_{\mathrm{X}} + w_{\mathrm{G}}\bar{S}_{\mathrm{G}} \tag{5.45}$$

where the weighted sum of squared residuals for the neutron diffraction pattern [eqn (5.8)] is now indicated by $\bar{S}_{\mathrm{N}}$, the corresponding sum for the X-ray diffraction pattern by $\bar{S}_{\mathrm{X}}$, and the geometrical restraints represented by perhaps a sum involving differences between actual (calculated from the model) and expected

bond lengths:

$$\overline{S}_{\mathrm{G}} = \sum w_n (d_n - d_{n\,\mathrm{exp}})^2 \tag{5.46}$$

The quantities $w_{\mathrm{N}}, w_{\mathrm{X}}, w_{\mathrm{G}}$ are weighting factors applied by the user to the different kinds of data. It is imperative that the final model fits the experimental data well, and not just the restraints.

Results from the Rietveld method should seldom be accepted without critical review. The possibility that the refinement may have found a local rather than global minimum of the residual sum of squares should not be forgotten. Kisi (1994) has outlined the final review as a series of questions, as follows. Are the *R*-factors acceptable? Is the plot acceptable? (This refers especially to the difference plot). Did the last parameters introduced make a significant difference to the fit? (It may be possible to apply tests of statistical significance). Are there any unexpected correlations between parameters? Are all the refined parameters physically reasonable? (Check bond lengths, bond angles, displacement parameters should be positive, peak widths remain positive). Has the refinement converged to a global or only to a local minimum[61]? This last question is an important one, and can be answered to some degree by using variations on the starting model and seeing whether the same solution is obtained. The reader must be referred to previously cited articles for further detail (Young 1993; Kisi 1994; McCusker *et al.* 1999).

5.8 STRUCTURE SOLUTION AND REFINEMENT – EXAMPLES

In the previous sections we have made frequent reference to the solution and refinement of the structure of NaOD at 77 K as our running example. In this section we outline other examples illustrating the solution and/or refinement of crystal structures from neutron powder diffraction data. These illustrations have been selected, as a matter of convenience, from the authors' own experience in this field.

5.8.1 The Ruddlesden–Popper compound $Ca_3Ti_2O_7$

The structure of the orthorhombic Ruddlesden–Popper phase $Ca_3Ti_2O_7$ has been solved by a combination of neutron diffraction, model building, and convergent beam electron diffraction (Elcombe *et al.* 1991). The neutron powder diffraction data were used for structure refinement.

[61] The inadvertent exchange of Sb and Bi atoms in the starting model for the ordered double perovskite Ba_2SbBiO_6 led the refinement to a well-defined local but not global minimum, from which the refinement program (Larson and Von Dreele 2004) could not escape. The problem was identified by a check on the bond lengths. Only by swapping the atoms back again could the required global minimum be found.

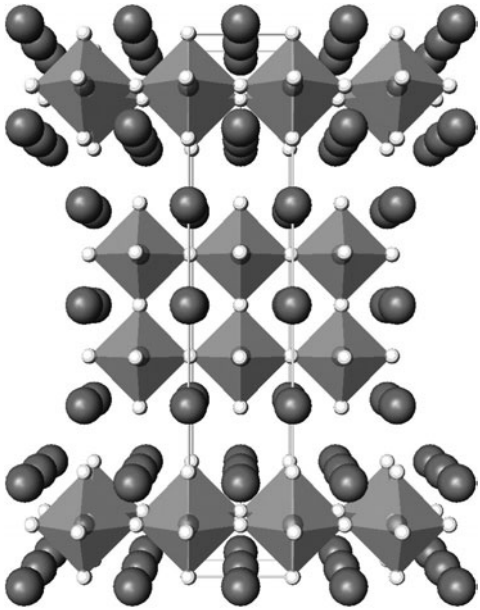

Fig. 5.9 The crystal structure of $Sr_3Ti_2O_7$ (Elcombe *et al.* 1991). Titanium is shown in blue at the centre of the blue octahedra of oxygen ions (white), separated by the A cation, Sr shown in red. (See Plate 3)

The model building made use of analogy with the strontium compound, $Sr_3Ti_2O_7$. The structure of this compound is illustrated in Fig. 5.9. The structure is tetragonal, in space group $I4/mmm$, with $a = 3.90$ (the edge of the unit cell in $SrTiO_3$) and $c = 20.37$ Å. It comprises two layers of the ideal perovskite structure of $SrTiO_3$ alternating with layers of SrO in a rock-salt arrangement. The model of $Ca_3Ti_2O_7$ was built by alternating two layers of the distorted perovskite structure of $CaTiO_3$, with layers of CaO in a rock-salt arrangement. This model structure was seen to be orthorhombic, in space group $Ccm2_1$, with a and c close to the corresponding (shorter two) lattice parameters in $CaTiO_3$, and b here as c in $Sr_3Ti_2O_7$ something near 20 Å.

The peaks in the neutron diffraction were indexed in a manner consistent with this model, on an orthorhombic cell with $a = 5.417, b = 19.517, c = 5.423$ Å. Reflection conditions appeared to be consistent with space group symmetry $Ccm2_1$. It will be shown in Chapter 6 that automatic indexing of the peak position data leads to the same conclusion. The same space group was favoured by the reflection conditions observed in electron diffraction, and the projected symmetries onto (100) and (001) of CBED patterns from the corresponding zones.

Structure refinement was undertaken by the Rietveld method, starting from the lattice parameters determined during indexing, and atomic coordinates obtained from the model described earlier. The refinements converged without difficulty

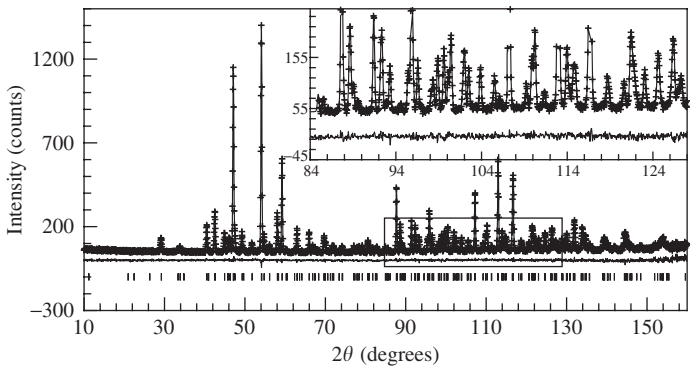

Fig. 5.10 Plotted output from Rietveld refinement of the $Ca_3Ti_2O_7$ structure (Elcombe *et al.* 1991). Data points are shown as (+) and the pattern calculated using the Rietveld method as a solid line. A difference profile and reflection markers are given below and the inset shows an expanded view of the boxed region. The figure is very like Fig. 4.17 except that the calculation now includes a crystal structure model rather than arbitrary integrated intensities as in the Le Bail method.

and an excellent fit to the neutron diffraction pattern obtained (Fig. 5.10). The refined structure is illustrated in Fig. 5.11.

We remark on the current availability of methods that could assist in identification of the space group symmetry of the starting model. The structure of $CaTiO_3$ is a distorted perovskite mainly on account of the tilting of the practically rigid corner-linked TiO_6 octahedral units. This particular pattern of tilting is described as $a^-a^-c^+$ in a notation due to Glazer (1972), or in the notation of Aleksandrov and co-workers as $\phi\phi\psi$. Aleksandrov and Bartolomé (2001) have recorded the space group symmetries corresponding to different tilting patterns in the perovskite layers of Ruddlesden–Popper phases, so now it would be merely a matter of looking up the entry for the two-layer Ruddleson–Popper structure with the matching tilt system $\phi\phi\psi_z$. The space group symmetry can also be obtained by application of group theory through computer program ISOTROPY (http://stokes.byu.edu/isotropy.html; Howard and Stokes 2005).

5.8.2 Phase transitions in strontium zirconate $SrZrO_3$

Strontium zirconate adopts at room temperature the same distorted perovskite structure as $CaTiO_3$, orthorhombic with space group symmetry *Pnma*. On heating, it undergoes three phase transitions according to the following schematic (Carlsson 1967):

$$\text{Orthorhombic} \xrightarrow[\text{Continuous}]{700^\circ\text{C}} \underset{c/a<1}{\text{Pseudo-tetragonal}} \xrightarrow[\text{Discontinuous}]{830^\circ\text{C}}$$

$$\underset{c/a>1}{\text{Tetragonal}} \xrightarrow[\text{Continuous}]{1170^\circ\text{C}} \text{Cubic.}$$

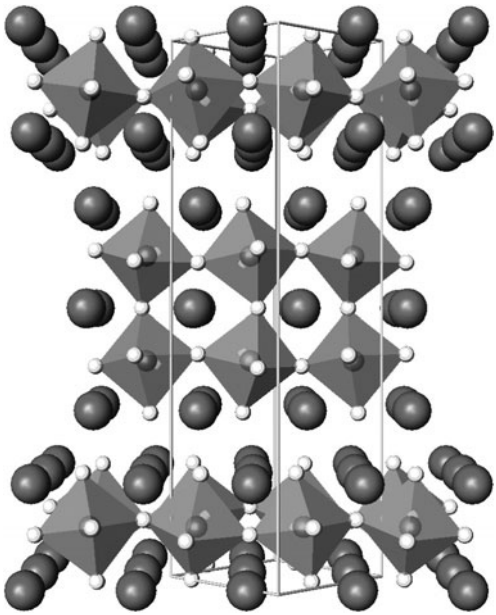

Fig. 5.11 The refined crystal structure of $Ca_3Ti_2O_7$ viewed along [101] for ready comparison to Fig. 5.9 (Elcombe *et al.* 1991). Titanium is again shown in blue at the centres of the oxygen octahedra. Oxygen ions are shown in white and Ca in red. (See Plate 4)

There is little doubt that at high-temperature $SrZrO_3$ achieves the ideal perovskite structure, in space group $Pm\bar{3}m$, like room temperature $SrTiO_3$, and the different phases are thought to correspond to different patterns of tilting of the corner-linked ZrO_6 octahedral units. The most recent work on this material (Howard *et al.* 2000) led to a revision of the structure and space group symmetry of the pseudo-tetragonal phase.

In re-examining the phase transitions in $SrZrO_3$, Howard *et al.* (2000) used very high-resolution neutron powder diffraction and worked in fine temperature steps (as small as 5 K) from room temperature to 1503 K. The solution was secured by reference to the scheme of possible structures developed by Howard and Stokes (1998). Though the group theoretical methods used are outside the scope of this book, the results can be summarized in Fig. 5.12 taken from that work. The figure shows the structures possible for an ABX_3 perovskite when the only distortion is simple BX_6 octahedral tilting. It shows the space-group symmetry for each possible structure, along with the Glazer (1972) symbol for the pattern of tilts – further detail on each of these structures can be found in the original paper (Howard and Stokes 1998). The lines indicate group–subgroup relationships, and a dashed line joining a group with its subgroup means that the corresponding phase transition is in Landau theory (Landau and Lifshitz 1980) required to be first order. This

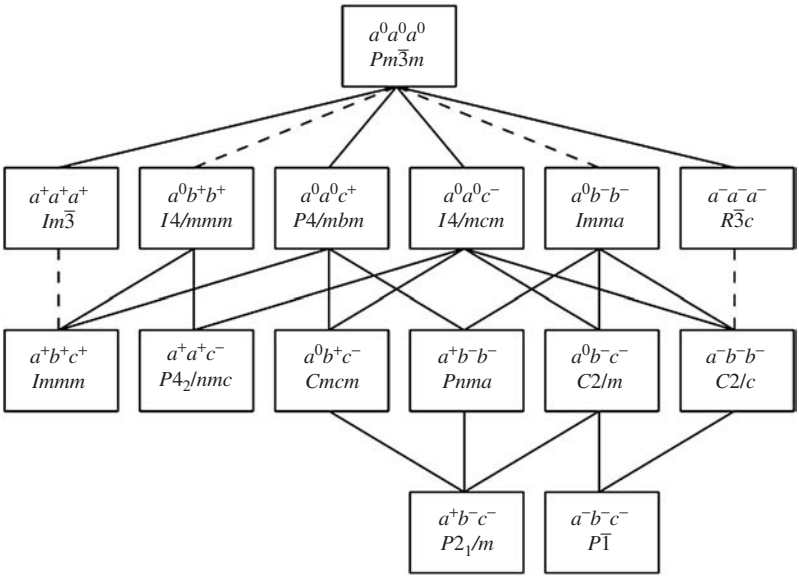

Fig. 5.12 The relationship between the archetypal perovskite structure in space group $Pm\bar{3}m$ and all of the subgroups that can form by combinations of in-phase or out-of-phase tilting of octahedral structural units (Howard and Stokes 1998, 2005). Structures are identified by their space group symbol and the Glazer (1972) symbol for the tilts. Lines indicate group–subgroup relationships that are of interest in the study of phase transitions. Transitions indicated by a solid line are allowed to be second order under Landau theory whereas those shown dashed must be first order.

means that only where a continuous line connects a group with its subgroup is the corresponding phase transition allowed to be continuous.

Ahtee and co-workers (Ahtee *et al.* 1976, 1978) used neutron powder diffraction to establish the room temperature orthorhombic structure as tilt system $a^+b^-b^-$, in space group *Pnma*. Then they recorded two diffraction patterns at elevated temperatures in an effort to establish the structures of the higher temperature forms. They found the tetragonal phase to be tilt system $a^0a^0c^-$, space group $I4/mcm$, and for Carlsson's 'pseudo-tetragonal' phase proposed the (orthorhombic) structure corresponding to tilt system $a^0b^+c^-$ in space group *Cmcm*. There are problems, however, with the structural sequence that these identifications imply. It can be seen in Fig. 5.12 that a transition from the *Pnma* orthorhombic to a 'pseudo-tetragonal' in *Cmcm* could not be continuous, whereas the transition from *Cmcm* to tetragonal $I4/mcm$ could and most likely would be continuous. This would conflict with Carlsson's observations at both transitions.

Howard *et al.* (2000), like Carlsson (1967) earlier, found three transitions, at temperatures 750°C, 840°C, and 1070°C. The resolution was sufficient, and the temperature steps fine enough, to confirm the sudden reversal of tetragonal splitting

Table 5.11 Crystal structure of $SrZrO_3$ at room temperature (unpublished data).

Space group *Pnma* (#62) – orthorhombic				
Lattice parameters	$a = 5.820$ Å	$b = 8.207$ Å	$c = 5.796$ Å	$\alpha = \beta = \gamma = 90°$
Atom	Site	x	y	z
Sr	4*c*	0.02	1/4	0.49
Zr	4*a*	0	0	0
O1	4*c*	−0.02	1/4	−0.07
O2	8*d*	0.28	0.04	0.22

Table 5.12 Crystal structure of $SrZrO_3$ at 800 K (unpublished data).

Space group *Imma* (#74) – orthorhombic				
Lattice parameters	$a = 5.857$ Å	$b = 8.268$ Å	$c = 5.858$ Å	$\alpha = \beta = \gamma = 90°$
Atom	Site	x	y	z
Sr	4*e*	0	1/4	0.50
Zr	4*a*	0	0	0
O1	4*e*	0	1/4	−0.05
O2	8*g*	1/4	0.03	1/4

at the second transition. It was noted that at the first, evidently continuous, transition, the weak superlattice reflections indicative of Glazer's (−) tilts persisted, but those indicative of (+) tilts disappeared. Starting from the *Pnma* ($a^+b^-b^-$) structure, and referring once more to Fig. 5.12, the only structure accessible by continuous transition and showing only (−) tilts is that in *Imma* ($a^0b^-b^-$). This structure was confirmed by a Rietveld analysis.

There are various means to find a suitable starting model for the *Imma* ($a^0b^-b^-$) structure, and computer program ISOTROPY can be used to assist. For present purposes it is sufficient to note the connection between the *Imma* structure and that in its subgroup *Pnma*. The simplest means to illustrate this connection is to record (Tables 5.11 and 5.12) the final results.

Evidently, both structures are described on the same orthorhombic unit cell, with approximate dimensions $\sqrt{2}$, 2, and $\sqrt{2}$ times the edge of the basic cubic perovskite. Taking the coordinates obtained in *Pnma*, then setting the values of x(Sr), x(O1), x(O2), and z(O2) to the values required at the special positions in the higher symmetry *Imma* structure, leads to a perfectly acceptable starting point for the Rietveld analysis.

The final results from the work can be summarized:

750ºC 840ºC 1070ºC

Orthorhombic ----------->Pseudo-tetragonal----------->Tetragonal----------->Cubic,

Pnma ($a^+b^-b^-$) *Imma* ($a^0b^-b^-$). *I*4/*mcm* ($a^0a^0c^-$) $Pm\overline{3}m$ ($a^0a^0a^0$)

Continuous $b < a\sqrt{2} \approx c\sqrt{2}$ Discontinuous $c > a\sqrt{2}$ Continuous

a sequence entirely consistent with both Carlsson's observations and the group theoretical analysis. The lattice parameter data obtained in this study are reproduced here in Fig. 5.13.

5.8.3 Crystal structure of an orthorhombic zirconia

The crystal structure of an orthorhombic zirconia was solved and refined (Kisi *et al.* 1989) in the context of a broad program of research on zirconia and zirconia ceramics. This was a challenging problem since the polymorph in question could not be isolated – in fact the structure was determined from neutron diffraction patterns recorded from a mixture of the orthorhombic zirconia with *four* other phases.

There had been several reports on orthorhombic polymorphs of zirconia ahead of the work outlined here. Such polymorphs were reported to occur under high-temperature high-pressure conditions, and after quenching from high pressure and temperature, and had also been seen by electron diffraction in studies of thin foils of zirconia engineering ceramics. Based on X-ray diffraction measurements on a crystal under pressures of 3.9 and 5.1 GPa, a structural model had been proposed (Kudoh *et al.* 1986). The work described here was undertaken following a study

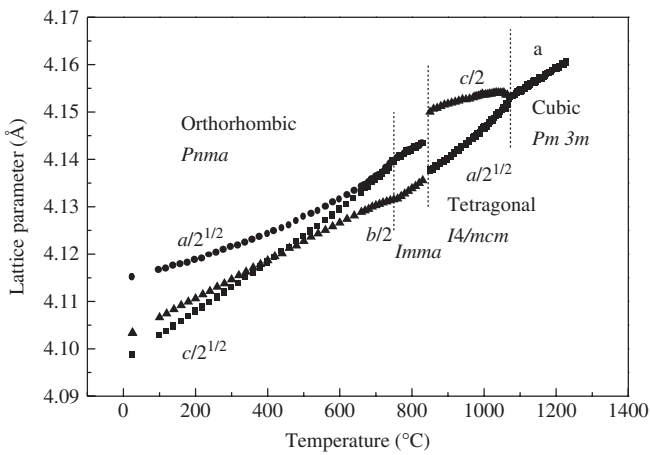

Fig. 5.13 Temperature dependence of the reduced lattice parameters for $SrZrO_3$. The first order transition at 830°C, and the second order transitions at about 780°C and 1100°C are indicated on this plot (Howard *et al.* 2000).

by Marshall *et al.* (1989) of high-toughness magnesia–partially stabilized zirconia (Mg-PSZ) engineering ceramic at low temperatures. They found that cooling this ceramic to liquid nitrogen temperatures induced a transformation from tetragonal zirconia to an orthorhombic phase, and estimated the fraction of orthorhombic zirconia after cooling as ~30%. Marshall, James, and Porter attributed peaks in X-ray diffraction patterns to this orthorhombic phase, and from the positions of these peaks the lattice parameters were estimated.

It was recognized by Kisi and co-workers that the possibility of producing substantial quantities of orthorhombic zirconia by cooling partially stabilized zirconia opened the way for crystal structure determination by neutron powder diffraction.

The work hinged on the general advantages of neutron diffraction for studying the polymorphs of zirconia and zirconia ceramics, which are:

(i) That the scattering by oxygen relative to zirconium is much greater for neutrons than for X-rays (Table 2.2). Scattering by oxygen is important since the structures of the different polymorphs of zirconia differ primarily in the disposition of the oxygen atoms about the heavier zirconium atoms.
(ii) The high transmission of neutrons through zirconia (Table 2.2). Neutron diffraction gives results representative of the bulk material, critical in the study of engineering ceramics, because the near-surface regions probed by X-rays are often affected by surface phase transitions and do not represent the bulk.
(iii) That the nuclear scattering of neutrons has no form factor (§2.3.1). Peaks are visible to high angles (short d-spacings), and the high angle data are sometimes the key to distinguishing the polymorphs.

Kisi *et al.* (1989) recorded room temperature neutron diffraction patterns from a high-toughness Mg-PSZ as received and after it had been cooled to 30 K. The patterns obtained are reproduced here in Fig. 5.14. Peaks appearing after the sample had been cooled were attributed to the orthorhombic phase, and all these additional peaks could be indexed assuming the lattice parameters due to Marshall *et al.* (1989). The pattern from the as-received sample could be fitted assuming a mixture of the cubic, tetragonal, and monoclinic polymorphs of zirconia with $Mg_2Zr_5O_{12}$, the so-called δ-phase. The amounts of the different phases were estimated from the Rietveld scale factors (Chapter 8). The sample as received contained about 60 wt.% tetragonal, 8 wt.% monoclinic, the balance being cubic and the δ-phase variant. The pattern obtained after cooling the sample was then analysed as a mixture of the cubic, tetragonal, and monoclinic polymorphs and the δ-phase with the orthorhombic polymorph, structure to be determined. Refinements were attempted from different starting models in several different space groups. The pattern was successfully fitted (Fig. 5.15) in a refinement starting from an adaptation into a different space group (maintaining the zirconium positions, but altering the disposition of oxygen atoms) of the structure proposed from their X-ray study by Kudoh *et al.* (1986). Table 5.13 records the final result for the structure obtained – the reader is referred to the original reference (Kisi *et al.*

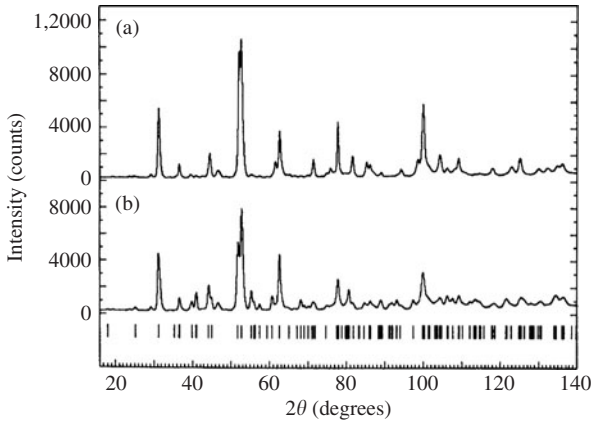

Fig. 5.14 Portion of the neutron diffraction patterns recorded at $\lambda = 1.594$ Å from an Mg-PSZ sample at room temperature (a) before and (b) following cooling to 30 K. Note the appearance of additional peaks most noticable near 40° and 56° 2θ (Kisi *et al.* 1989).

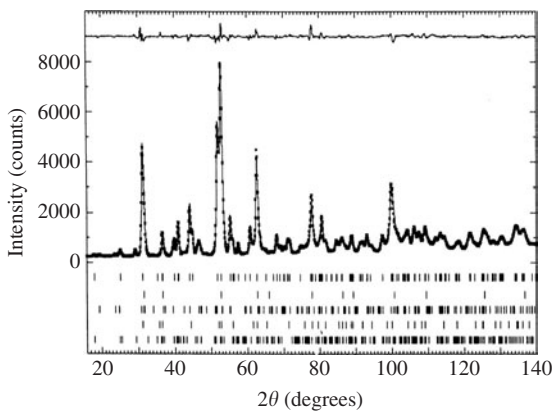

Fig. 5.15 Rietveld refinement fit to the Mg-PSZ pattern in Fig 5.14(b). Data are shown as (x), the calculated pattern as a line through the data and a difference profile on the same scale as a solid line above. Reflection markers are also given for the five phases within the sample: *c*, *t*, *m*, and *o* – ZrO_2 and the δ-phase (Kisi *et al.* 1989).

1989) for a more detailed description. The composition of the sample after cooling was consistent with the transformation of about 75% of the original tetragonal component to the orthorhombic form.

Neutron diffraction was also used to establish the structure of orthorhombic zirconia obtained by quenching from conditions of high temperature and pressure (Ohtaka *et al.* 1990). The structure of the orthorhombic zirconia obtained by quenching from high temperature and pressure is distinct from, yet closely related to, the orthorhombic structure given in Table 5.13 (Howard *et al.* 1991).

Table 5.13 Crystal structure o–ZrO_2 at room temperature (Kisi *et al.* 1989).

Space group $Pbc2_1$ (#29) – orthorhombic				
Lattice parameters	$a = 5.068$ Å	$b = 5.260$ Å	$c = 5.077$ Å	$\alpha = \beta = \gamma = 90°$
Atom	Site	x	y	z
Zr	4a	0.267	0.030	0.250
O1	4a	0.068	0.361	0.106
O2	4a	0.537	0.229	0

The origin, to some extent arbitrary in this non-centrosymmetric space group, has been defined by setting $z(O2) = 0$.

We hope that these limited examples go some way to illustrating the power and scope of crystal structure analysis using neutron powder diffraction.

6

Ab initio structure solution

6.1 INTRODUCTION

The motivation for solving a structure completely using powder diffraction data needs to be compelling; otherwise single crystal methods should be used to assist the process. Reasons for relying solely on powder diffraction can include the difficulty of growing or isolating single crystals in many systems, complex twinning problems, or because of extinction. In some instances, one begins from the outset to solve an unknown structure (e.g. a new compound, material, pharmaceutical or mineral). At other times, structure solution becomes necessary during the analysis of data recorded for another purpose. For example, an *in situ* heating or high-pressure experiment may disclose a previously unrecorded phase with a new crystal structure. Similarly a rock specimen may contain an unknown mineral or a functional material may contain a previously unknown contaminant phase(s). In each case, to complete the analysis by whole pattern fitting (e.g. Rietveld analysis), the crystal structure of each phase needs to be correctly described including the determination of any unknown structures.

Structure determination from powder diffraction has four basic elements that have been introduced separately elsewhere. These are (i) unit cell determination or indexing (§4.4.2), (ii) intensity extraction (§4.6, §5.6), (iii) structure solution (§5.4), and (iv) structure refinement (§5.5). Space group determination is also an important step but does not occur at a well-defined point in the sequence. Reflection conditions and systematic absences (§5.3) may be apparent from stage (i); however, sometimes it requires intensity extraction to find absences. In addition, only 39 space groups can be unambiguously found from these. Sometimes Fourier or Patterson methods can highlight the symmetry (or intuitive or group theoretical methods). Direct methods can, in principle, assign 215 of the 230 space groups, but sometimes ambiguity over space groups persists even until the refinement stage where exact intensity matches can usually distinguish the correct solution.

It is generally agreed that, of these four stages, unit cell determination and structure solution are frequently the most difficult and in many cases intractable. For example, a Structure Determination by Powder Diffraction (SDPD) *ab initio* structure solution round robin (http://www.cristal.org/SDPDRR/, http://www.iucr.org/iucr-top/comm/cpd/Newsletters/no25 jul2001/cpd25.pdf) was held in which the solution to step (i) was supplied. Even so, only 2 of 70 participants offered structure solutions for the pharmaceutical sample (∼30 non-hydrogen

atoms) and *none* for the inorganic sample (15 non-hydrogen atoms). A follow-up round robin conducted in two stages (i) indexing and (ii) structure solution (SDPD-2, Le Bail and Cranswick 2003) fared little better. Of eight samples, three had known but hidden structures and five were completely unsolved. One hundred participants downloaded the data, however only six returned solutions to the indexing problem and of these only one had any results for some of the previously unsolved samples. Only two participants sent structure solutions and then only for the first two samples.

Nonetheless, many important structures have been and continue to be solved using powder diffraction methods, and even small protein structures are now being addressed. This chapter deals with each of the four stages in turn and is meant to guide the unfamiliar reader through the process of solving a crystal structure using *only* neutron powder diffraction patterns. More details on each of the methods described are available in a recent monograph devoted solely to this topic (David *et al.* 2002).

6.2 UNIT CELL DETERMINATION (POWDER PATTERN INDEXING)

6.2.1 The problem

In §2.4.1 it was indicated that the unit cell size and shape, more particularly the six unit cell parameters a, b, c, α, β, and γ, determine the *positions* of the powder diffraction peaks through their connection to the d-spacings of planes (eqns (2.26) and (2.27), and Appendix 1), then Bragg's Law (eqn (2.21)). However, whereas the six unit cell parameters describe a three-dimensional space lattice, in the powder pattern this has been projected onto one dimension. This projection is readily accomplished in the forward direction using the equations in Appendix 1; however, it is very difficult to reverse the process. In many cases when smaller structures are being solved, the cell may be recognized by a simple relationship to a known structure (e.g. cell doubling, etc.) or a simple distortion of a known cell (e.g. tetragonal distortion of a cubic cell). In those cases, the diffraction pattern will strongly resemble that of the aristotype, and the experienced crystallographer may recognize it. Indexing under those circumstances can proceed by the simple methods described in §4.4. We are concerned here with cases where no clear relationship to a known structure has been found. The magnitude of the problem can be more fully appreciated by writing out the relationship between the square of the reciprocal d-spacing (d^{*2}),[62] the diffracting plane indices hkl and the reciprocal lattice constants for a general triclinic lattice:

$$d_{hkl}^{*2} = h^2a^{*2} + k^2b^{*2} + l^2c^{*2} + 2klb^*c^* \cos\alpha^* + 2hla^*c^* \cos\beta^* + 2hka^*b^* \cos\gamma^* \tag{6.1}$$

[62] Sometimes designated Q.

The reciprocal lattice expression is far more compact than the real space equivalent (Appendix 1) and may be further simplified for the purposes of indexing by using

$$\begin{aligned} A &= a^{*2} \\ B &= b^{*2} \\ C &= c^{*2} \\ D &= 2b^*c^* \cos\alpha^* \\ E &= 2a^*c^* \cos\beta^* \\ F &= 2a^*b^* \cos\gamma^* \end{aligned} \tag{6.2}$$

giving

$$d_{hkl}^{*2} = h^2A + k^2B + l^2C + klD + hlE + hkF \tag{6.3}$$

For a given diffraction peak, all nine parameters on the right hand side of eqn (6.3) (h, k, l, A, B, C, D, E, F) are unknown. To solve eqn (6.3) at least six completely independent indexed peaks (i.e. no higher orders, for example, 110, 220, etc.) must be used; otherwise the problem is algebraically indeterminant.

It is useful at this point to consider a simple illustration. Figure 6.1 shows a two-dimensional oblique lattice. Equation (6.3) is simplified to $d_{hk}^{*2} = h^2A + k^2B + hkF$ in this case. The first point to note in Fig. 6.1 is that an infinite number of unit cells can be constructed. Thankfully these are all simply related and procedures for finding the reduced (or smallest) cell are well established (*International Tables for Crystallography, V1*, p. 530). The second use for Fig. 6.1 is to illustrate how the higher dimensional (two-dimensional in this case) reciprocal lattice is collapsed in to the linear powder diffraction pattern. This is done by rotating the lines joining the reciprocal lattice points to the origin until they lie on the a^* axis. The lengths of these lines represent the d^* and it is clear how the diffraction pattern peak positions are determined. In three dimensions the situation is more complex; however, the

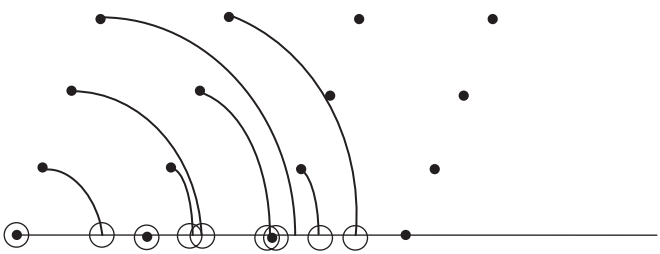

Fig. 6.1 Relationship between a two-dimensional oblique reciprocal lattice and the corresponding powder diffraction pattern represented as a rotation of reciprocal lattice points about the origin on to a diffraction line. Diffraction peaks will occur at positions along the line corresponding to the centres of the open circles.

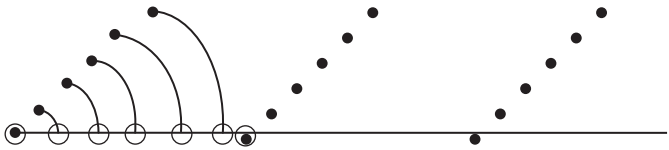

Fig. 6.2 Relationship between a two-dimensional oblique reciprocal lattice and the corresponding powder diffraction pattern to illustrate the dominant zone effect.

same result can be imagined from successive rotations about a^* (to collapse the third dimension on to the basal plane) and c^* (to project on to our chosen diffraction line as before). A third purpose for Fig. 6.1 is to illustrate that the pattern for a single zone is far simpler for a two-dimensional (or single-zone axis) powder pattern than for a three-dimensional pattern. Within the pattern in our two-dimensional example, certain relationships exist that assist in reconstructing the lattice. One of the major factors to note is that the first and second peaks, in this case, are from the fundamental reciprocal lattice points 01 and 10 and may be used directly to reconstruct the lattice dimensions (but not the interaxial angle). Often space-group absences cause one or more of these low index peaks to have zero intensity. However, a lattice reconstructed from the first few peaks can usually be easily related to the true unit cell. The exception is when there is a so-called dominant zone. Imagine that in our example, one unit cell parameter, b, was far larger than the other (i.e. b^* is much shorter). The result is shown in Fig. 6.2. For the example shown, all of the first six peaks are due to the dominant (b^*) zone and a lattice constructed from these will only index $0k0$ peaks.

The observations made using Fig. 6.1 are the basis of some of the most sophisticated powder pattern indexing techniques. Conducting the calculations manually is so time-consuming that the process has gone over almost completely to the computer assisted indexing that will be discussed below. This does not mean that human intervention and intuition are not called for – far from it. It is a combination of (i) the determination of high quality d-spacings corrected for systematic errors and (ii) the intelligent interpretation of the output of auto-indexing programs that solves unknown unit cells. A more in-depth discussion of precision, accuracy, figures of merit, and the interpretation of results is reserved for §6.2.6. Of the many auto-indexing programs (Shirley 1983) we present here only the three most commonly used (Werner 2002) and a few methods still under development.

6.2.2 Zone-indexing (ITO'S method) – ITO

This method of powder diffraction indexing is known variously as Ito's method, de Wolff's method, Visser's method, or Zone-indexing. As noted by Shirley (1984), the method was first proposed by Runge (1917) and re-discovered by Ito (1949, 1950). It was then further developed by de Wolff (1957, 1958, 1963) and

incorporated into a computer program by Visser (1969). It is an extremely effective method that relies on the observation made above that, in the absence of a dominant zone, the first few peaks are usually fundamental (i.e. 100, 010, or 001) or at least low order (200, etc.). Working in reverse, pairs of low d^* peaks are used to generate trial zones. For example, referring back to Fig. 6.1, we would select the 10 and 01 peaks. Note that this does not allow us to directly reconstruct the lattice since we do not know γ^*. The rest of the d^* values must be used to find this. If we consider Fig. 6.1 to be a zone within a three-dimensional system then 01 becomes 010 and 10 becomes 100. We may write the appropriate form of eqn (6.3) for this zone as

$$d_{hko}^{*2} = h^2A + k^2B + 2hk(AB)^{\frac{1}{2}} \cos\gamma^* \tag{6.4}$$

Trial values for A and B are determined by applying this equation to the selected reflections with the indexing as proposed. Then, setting[63]

$$P = 2(AB)^{\frac{1}{2}} \cos\gamma^* \tag{6.5}$$

gives via eqn (6.4)

$$P = \frac{-(h^2A + k^2B - d_{hk0}^{*2})}{hk} \tag{6.6}$$

The same value of P (within experimental error) is expected for peaks belonging to a common zone, provided that h and k take the appropriate values. In practice, eqn (6.6) is applied to each of the first 20 or 30 peaks, assuming various small values for h and k, and common values of P are sought in the output. Then eqn (6.5) is used to assign γ^* values to the possible zones. The axial lengths a^* and b^* are checked and reduced if necessary (i.e. one of the diffraction peaks used as the basis of a zone may have been 200 or 020 rather than 100 or 010). The values of a^*, b^* and γ^* are next optimized by least squares refinement for all prospective zones. A quality factor $1/C$ is assigned based on an estimated probability, C, that the zone accounts for the observed lines by accident:

$$C = \frac{N_C!}{N_0!(N_C - N_0)!} \cdot \rho^{N_0}(1-\rho)^{N_C - N_0} \tag{6.7}$$

where N_C is the number of calculated d^{*2} values in the zone, N_0 is the number of observed d^{*2} that fit the calculation, and $\rho = (\sum \Delta d^{*2} / d_{\max}^{*2})$.

A zone defined by a^*, b^* and γ^* will contain some peaks that rely on only one or other index (i.e. 100, 200, 300 or 010, 020, 030). If a pair of zones index the same set of peaks relying on just one Miller index, then they have a common 'row' or common axis and, provided they are not co-planar, can be combined[64] to make

[63] In earlier work, the parameter P was given the symbol R; however, we have chosen P to avoid confusion with the agreement indices in structure refinement.

[64] After the angle between these zones has also been determined.

a three-dimensional lattice. This lattice is then reduced to the standard form and used to try to calculate the first 20 or so d-spacings. Results for all of the solutions found are stored and ranked according to the quality index M_{20} (see §6.2.6).

6.2.3 The exhaustive method (successive dichotomy) (DICVOL)

With advances in computer speed during the 1970s and 1980s, it became apparent that solutions to eqn (6.3) could be found by exhaustively searching the available parameter space in small increments and looking for agreement between computed and observed d^{*2}. The development effort in this area was by Loüer and Loüer (1972), Loüer and Vargas (1982), and Boutif and Loüer (1991) leading to the program DICVOL91. The exhaustive search is made more efficient by scanning a succession of 400 $Å^3$ shells. The exhaustive approach is not affected by dominant zones, so the method is suitable for structures with one unit cell edge much larger than the others.

6.2.4 The semi-exhaustive or index space method (TREOR)

A semi-exhaustive method uses crystallographic rules of thumb to limit an otherwise exhaustive search. The program TREOR90 uses the notion, developed in §6.2.1, that the first few diffraction peaks often define the unit cell. Instead of using them in pairs to construct zones which are then combined into three-dimensional lattices, the approach taken (Werner 1964; Werner *et al.* 1985) is to propose complete unit cells based on trial indexing of the first few peaks. The unit cells so generated are then used to attempt to index the first 20 peaks and sorted for quality against the figure of merit M_{20} (see §6.2.6). Higher symmetry cells are tried first (cubic, hexagonal, etc.) and then successively lower symmetries. The program has a dominant zone search algorithm that assists with such problems. As with all auto-indexing programs, recognizing the correct unit cell from the ranked list supplied by the program and testing it for robustness is the responsibility of the user – not the program.

6.2.5 New methods under development

The programs mentioned here are not the only auto-indexing programs. They are the three most widely used and represent sufficiently different approaches that most problems are tractable by one or more of them. A slightly different and reportedly successful recent approach, due to Coelho (2003), involves the trialling of different lattice parameters, with, it would seem, a fast refinement of these parameters after every trial. Other indexing programs that fall within the range of approaches covered here are listed by Shirley (1983) and Werner (2002) and on the IUCr CCP14 site (http://www.ccp14.ac.uk).

As was demonstrated in §4.4.2 the success of powder pattern indexing depends heavily on the quality of the peak positions used as input. In some cases of very low symmetry or in cases of very small departures from a higher symmetry, the

peaks that are needed to determine the lattice symmetry are strongly overlapped. In such cases, the usual approach is to attempt to deconvolute them by fitting multiple peaks to the observed intensity, then using the fitted positions as input to the indexing program. One such problem is used as an example in §6.2.7. When the overlap is severe or several peaks are overlapped, the peak positions obtained using peak fitting methods are biased by the perception of the user concerning the number of overlapping peaks, etc. An argument can be made, analogous to that favouring the use of Rietveld refinement (§5.5), that the whole diffraction pattern should form the input data for auto-indexing, not just a list of 20 peak positions. One such approach is that of Kariuki *et al.* (1999), who combine the Le Bail fitting technique (§5.6) with a genetic algorithm to optimize the fit, as measured by the weighted *R*-factor R_{wp} (Table 5.10), to the entire pattern. Le Bail (2004) has also tried indexing by whole pattern fitting, using Monte Carlo methods to search for the lattice parameters that optimize the fit. However, the method was modified, when it was found that fitting the entire raw powder pattern is as yet too slow. Complex procedures such as these are time-wise a return to the early days of auto-indexing when indexing programs were run overnight on mainframe computers. Since the simpler methods used in ITO, DICVOL and TREOR only take a few seconds to a few minutes to run on a personal computer, it is worthwhile spending a day exhausting these options before proceeding to the next level.

6.2.6 Practical aspects of indexing

The first and most critical requirement for successful indexing is 'high quality' data. For the purposes of unit cell determination, high quality means

(i) having sufficient intensity that the peak positions are not significantly affected by random statistical errors,
(ii) having good d-spacing resolution,
(iii) free from systematic errors.

The first of these points is merely a sampling problem. The second depends on the choice of instrument and, for CW, on the choice of wavelength. It is common, when investigating unknown structures on high resolution CW diffractometers, to record indexing data using wavelengths in the range 2–5 Å, so as to displace the low angle (large d) peaks to the centre of the pattern or beyond, where the angular resolution is optimized and the influence of systematic errors reduced. It should be stressed here that one should never hesitate to use X-ray diffraction if the neutron diffractometer can not provide sufficient resolution. New generation laboratory powder diffractometers can easily provide resolutions of FWHM $\Delta d/d = 9 \times 10^{-4}$,[65] well beyond most neutron diffractometers and only a factor of 2 inferior to the highest resolution ever attained on a neutron powder diffractometer. Higher

[65] For example, Panalytical X'Pert PRO™ with X'Celerator™ at 50° 2θ, FWHM 0.05° 2θ, Cu Kα_2 digitally stripped.

resolutions still are routinely available at synchrotron X-ray sources. On the third point, systematic errors can be minimized by judicious choice of diffractometer and by the use of calibration standards. There is a slight difficulty in using calibration standards on CW instruments because of uncertainty in the neutron wavelength, which also is determined using a standard material. One (pragmatic) view is to accept that systematic errors of all kinds, including the wavelength, are adequately corrected in this way. Purists may wish to determine the wavelength independently using a precisely mounted analyzer crystal at the sample position.

Having obtained the best data practically available and extracted the d-spacings of (at least) the first 20 peaks, one is ready to begin indexing. If the structure under study is known to be related to another structure, then the simple methods outlined in §4.4 are worth attempting as much as an exercise in familiarizing oneself with the diffraction pattern as a means of indexing the pattern. Even if hand indexing appears successful, computer assisted indexing should be used as an objective test of the result and also to generate any alternative solutions that may also explain the observed peak positions. This latter point should not be taken too lightly. It has been shown, for example, that alternate to solutions in symmetries above orthorhombic, there are distinct solutions at lower symmetries – indexing just the same peaks – when certain special relationships among the lattice parameters of the lower symmetry structures pertain (Mighell and Santoro 1975). Deciding which solution is correct is then conducted based on a close examination of symmetry (the higher symmetry solution is usually correct) and chemical considerations such as molecular volume, etc.

Because of their accessibility and long history of successful use, the three programs described earlier, ITO, DICVOL, and TREOR, are usually used first. Computational time is no longer an issue for these programs although ITO does run faster than the others. The mathematical and scientific basis for ITO is also a little more sophisticated than for the others, so it is often the first choice. Failure of ITO often means that one is dealing with a dominant zone problem. It has been advised (e.g. Werner 2002) that this may be overcome by creating 'virtual' peaks with d-spacings that are multiples of the largest d-spacing peaks. Most careful scientists balk at the prospect of 'inventing' an observed point; however it is merely a means of forcing the program to not be fooled by a dominant zone, and these points are disregarded thereafter. This artifice succeeds in a surprising number of cases (see §6.2.7). Regardless of the success or failure of ITO, a second method should be used to check the solution and then perhaps a third method employed (especially if ITO was unsuccessful). But how is the success or otherwise of a given method to be judged? There are two primary means:

The number of peaks indexed

A correct solution using good quality data will index all of the observed peaks. Sometimes one or two weak peaks will not be indexed in the first iteration; however, these should be accounted for after unit cell refinement. No solution can be accepted

that cannot account for *all* of the peaks. In some cases, weak peaks may be omitted from the data supplied to the indexing program, however the solution, if correct, must account for them in subsequent analysis (e.g. whole pattern fitting). Unaccounted for peaks, especially weak peaks, may be due to one or more impurity phases. If their identity can be established then the peaks concerned may be safely ignored. Most indexing programs perform their operation on 19 or 20 peaks and some (e.g. ITO) then refine the unit cell using all of the data supplied.

Figures of merit

Figures of merit are statistical measures of the quality of the solution. The most widely used is M_{20} given by

$$M_{20} = \frac{d_{20}^{*2}}{2N_{20}\left\langle \Delta d^{*2} \right\rangle} \tag{6.8}$$

where d_{20}^{*2} is the square of the reciprocal d-spacing of the 20th peak in the data set, N_{20} is the number of calculated peaks for a given trial solution and $\left\langle \Delta d^{*2} \right\rangle$ is the mean deviation between observed and calculated (eqn (6.1)) values of d_{hkl}^{*2} for peaks considered to be successfully indexed by the trial solution. ITO, DICVOL, and TREOR all supply M_{20} as a figure of merit. Other figures of merit have been proposed, however it is generally agreed (e.g. Shirley (1983), Werner (2002)) that M_{20} is best for deciding how physically reasonable a given trial unit cell is.

There are many rules of thumb concerning the identification of the correct unit cell from those suggested by indexing programs. It is obvious that (see above) any solution that cannot explain all of the peaks in a pattern (unless a clearly identified impurity phase is present) can not be correct. If a solution appears to index all of the peaks in the indexing data set, a check should be made that it also indexes all of the peaks *not* included in the analysis, especially any weak peaks omitted because of unacceptably large random errors. It is generally agreed that any solution with a low M_{20} is unlikely to be correct. Opinions on exactly how low M_{20} needs to be for a solution to be rejected differ somewhat, from ≤ 4 (Visser 1969) to ≤ 10 (Shirley 1983). An important point is that M_{20} for an incorrect unit cell can usually not be improved, for example, by the inclusion of a zero offset correction[66] or by excluding a few weaker peaks and replacing them with stronger peaks from further up the pattern. Solutions that index all of the trial peaks (20–30) and have high M_{20} values are usually correct. Where to place the cut-off for successful indexing is also somewhat subjective, ranging from $M_{20} > 10$ (Visser 1969) to >20 (Shirley 1983). It is usually significant if there is only one solution that indexes all of the peaks and has an M_{20} far higher than others suggested by the programs. It is also significant if the same solution results from the use of different methods (e.g. ITO and DICVOL or TREOR) and from different starting states (Shirley 1983), for example, by omitting a few of the peaks or substituting

[66] Most programs include either a user supplied zero correction or compute their own internally.

others from elsewhere in the pattern. The final test for a correct solution is that it allows a sensible crystal structure to be constructed, that is, it can accommodate an integral number of formula units, is clearly related to the structures of related materials, and so on.

6.2.7 Examples

Let us first consider the example used to describe the elements of crystal structure solution in Chapter 5, NaOD at low temperature. Tables 6.1 and 6.2 summarize input to and output from the program ITO. Peak positions were determined by individual peak fitting and were corrected for zero offset and asymmetry effects. The first 20 peaks input are listed in the second column. The unit cell described in §5.4 was the most prominent suggestion; indexing all of the observed peaks and returning $M_{20} = 51.6$. The calculated peak position and errors are shown in columns 3 and 4. This solution was clearly correct, as it agreed with that from manual indexing, gave a whole number of formula units in the unit cell, and presented a cell related to that of the room temperature structure in a simple and logical way (§5.4). In fact, three of the first four cells suggested by ITO represented just different descriptions of the same lattice and a fourth was a doubled cell. Three other solutions with $M_{20} > 10$ and indexing all 20 peaks were rejected as they indicated far too many peaks where none were observed.

The second example is far less straight forward. It is the layered perovskite $Ca_3Ti_2O_7$, already considered briefly in §5.8.1. The neutron powder diffraction pattern, and the structure, were shown in that section. The structure was solved using neutron powder diffraction (Elcombe *et al.* 1991), although the unit cell parameters had previously been estimated using X-ray diffraction (Roth 1958). It nonetheless provides an excellent test of indexing programs because

(i) One unit cell edge is far larger than the other two.
(ii) The unit cell is pseudo-tetragonal (i.e. $a \approx c$).
(iii) The space group is centred ($Ccm2_1$) leading to numerous space group extinctions (absent peaks).
(iv) The structure is a perovskite derivative and hence has many accidentally absent peaks.

We will approach the indexing as though the unit cell is not known. An initial trial, using ITO13 and omitting two very weak peaks, returned the nine solutions shown in Table 6.3.

None of these solutions is convincing. Those with high figures of merit (#1–4) leave three or four peaks unindexed. One of the peaks not indexed is the strongest peak in the diffraction pattern. Solution #5 leaves only one peak unindexed, again the most intense peak in the pattern. Since one cell parameter is far larger than the other two, the main reason for the failure of ITO13 is the presence of a dominant zone. We will proceed as though this was not known.

Table 6.1 Indexing peaks in the neutron diffraction pattern (λ = 1.377 Å) from NaOD at 77 K, using ITO. The cell proposed by ITO was monoclinic, $a = 6.840$, $b = 3.368$, $c = 5.667$ Å, $\beta = 107.5°$, and all peaks were indexed as shown below. The 2θ are given in degrees.

Peak number	$2\theta_{obs}$	$2\theta_{calc}$	$\Delta 2\theta$	*hkl*
1	14.64	14.64	0.00	0 0 1
2	24.39	24.38	−0.01	2 0 0
		24.39	0.00	$2\,0\,\bar{1}$
3	27.87	27.88	0.01	0 1 1
4	29.52	29.52	0.00	0 0 2
5	32.23	32.22	−0.01	2 0 1
		32.24	0.01	$2\,0\,\bar{2}$
		32.28	0.05	1 1 1
6	34.17	34.18	0.01	2 1 0
		34.19	0.02	$2\,1\,\bar{1}$
7	37.21*w*[67]	37.19	−0.02	$1\,1\,\bar{2}$
8	38.14	38.13	−0.01	$0\,1\,\bar{2}$
9	40.32	40.32	0.00	2 1 1
		40.34	0.02	$2\,1\,\bar{2}$
10	42.96	42.95	−0.01	$3\,1\,\bar{1}$
				1 1 2
11	44.25	44.25	0.00	2 0 2
		44.28	0.03	$2\,0\,\bar{3}$
		44.29	0.04	3 1 0
12	47.48	47.48	0.00	$4\,0\,\bar{1}$
13	48.26	48.27	0.01	$0\,2\,0/2\,0\,\bar{1}$
14	49.41*w*	49.41	0.00	$1\,1\,\bar{3}$
15	49.95	49.95	0.00	4 0 0
		49.96	0.01	1 2 0
		49.97	0.02	$4\,0\,\bar{2}$
16	50.74	50.71	−0.03	0 2 1
		50.75	0.01	2 1 2
		50.78	0.04	$2\,1\,\bar{3}$
17	51.16	51.16	0.00	$1\,2\,\bar{1}$
18	53.51	53.51	0.00	1 2 1
19	54.81	54.79	−0.02	2 2 0
		54.80	−0.01	$2\,2\,\bar{1}$
20	55.96	55.95	−0.01	4 1 0
		55.97	0.01	$4\,1\,\bar{2}$

[67] *w* indicates a weak peak.

Table 6.2 The seven most probable solutions output from ITO13 for $\lambda = 1.377$ Å neutron diffraction pattern from NaOD at 77 K. Values for a, b, c are given in Å and α, β, γ in degrees.

Solution	A	B	C	D	E	F	M_{20}	$N^{\#}$
	a	b	c	α	β	γ		
1	235.02	881.54	342.34	0.0	170.67	0.0	51.6	20
	6.840	3.368	5.667	90	107.51	90		
2	58.73	881.48	315.66	0.0	32.09	0.0	51.6	20
	13.140	3.368	5.668	90	96.77	90		
3	234.94	881.50	342.27	0.0	170.80	0.0	49.0	20
	6.842	3.368	5.668	90	107.53	90		
4	235.04	881.48	342.21	0.0	171.24	0.0	45.9	20
	6.842	3.368	5.670	90	107.57	90		
5	213.61	21.38	881.44	0.0	0.0	0.0	34.9	20
	6.842	21.625	3.368	90	90	90		
6	213.67	21.38	220.33	0.0	0.0	0.0	19.6	20
	6.841	21.628	6.737	90	90	90		
7	213.68	21.40	881.72	0.0	0.0	0.0	17.5	20
	6.841	21.619	3.368	90	90	90		

Next the data were presented to DICVOL91. Two solutions are suggested, one tetragonal with $a = 5.4208(05)$, $c = 19.5155(25)$ Å and $M_{20} = 36.6$, the other orthorhombic with $a = 19.5151(14)$, $b = 5.4205(11)$, $c = 5.4214(6)$ Å, and $M_{20} = 26.3$. Both solutions index the first 20 peaks within acceptable limits as shown in Table 6.4, and they reveal the presence of a dominant zone. The fact that the tetragonal a parameter is the mean of the orthorhombic b and c highlights the pseudo-symmetry problem. Both solutions are worthy of further investigation.

TREOR90 was used to test the dominant zone hypotheses. It returned only one solution, the tetragonal cell found by DICVOL91 with $a = 5.4203(4)$, $c = 19.5163(26)$ Å, and $M_{20} = 35$. The output is very similar to Table 6.4(a) and is not reproduced here. At this stage the general nature of the unit cell is established; however, pseudo-symmetry has not yet been resolved. As a first step, we return to ITO13 recalling that the influence of a dominant zone can often be overcome by adding 'virtual' peaks at the high d-spacing (low 2θ) end of the pattern. In the DICVOL91 solutions, the third peak is associated with the long axis, and indexes as 006. The next move, therefore, was to include in the ITO run a virtual 002 peak at three times the d-spacing of this peak. The first *six* trial lattices (Table 6.5) all indexed all of the first 20 peaks with M_{20} in the range 38–75, and all gave orthorhombic unit cells with $a = 5.418$, $b = 19.54$, $c = 5.420$ Å, or with a and c reversed. All these lattices represented in effect the same solution. This is clearly the most likely solution as it meets all of the criteria for judging a successful indexing, including an obvious relationship to the basic perovskite cell (a and c are $\cong \sqrt{2} \times a_{\text{perov}}$). The solution is able to index all of the 38 peaks entered (not just the

Table 6.3 Trial indexing results for $Ca_3Ti_2O_7$ using ITO13 (Cell edge lengths in Å and angles in degrees).

A	B	C	D	E	F	a	b	c	α	β	γ	M_{20}	Indexed
445.66	367.5	761.16	210.39	260.62	−105.37	4.944	5.414	3.827	103.649	104.887	79.462	75.3	17
334.59	229.65	445.68	182.85	77.65	196.87	5.848	7.329	4.943	105.597	89.94	110.018	74.6	17
196.43	170.3	236.35	0	157.57	0	7.666	7.663	6.989	90	111.448	90	72.3	17
432.24	367.28	445.59	105.02	118.45	314.28	5.256	5.698	4.798	94.824	95.274	112.557	44.1	16
195.81	169.92	235.67	0	157.47	0	7.681	7.671	7.001	90	111.5	90	13.2	19
144.37	85.11	249.66	0	26.47	0	8.343	10.84	6.344	90	93.997	90	32.7	16
189.62	176.79	228.82	87.84	182.43	8.94	8.104	7.732	7.558	103.36	116.32	85.345	14.6	17
134.32	73.85	210.86	49.83	108.69	−31.55	9.392	12.234	7.554	105.569	111.498	76.095	8.8	17
65.48	170.69	163.08	0	52.13	0	12.771	7.654	8.092	90	104.609	90	7.2	16

Table 6.4(a) DICVOL91 solution 1, tetragonal $a = 5.4208$, $c = 19.5155$ Å.

Peak number	$2\theta_{obs}$	$2\theta_{calc}$	$\Delta 2\theta$	*hkl*
1	23.636	23.635	0	1 1 1
2	26.974	26.977	−0.003	1 1 3
3	27.395	27.399	−0.003	0 0 6
4	32.716	32.719	−0.003	1 1 5
5	34.307	34.31	−0.003	2 0 2
6	36.203	36.202	0.001	1 0 7
		36.190	0.013	1 1 6
7	37.057	37.053	0.005	2 1 0
8	37.332	37.348	−0.016	2 1 1
9	37.942	37.944	−0.002	2 0 4
10	38.244	38.222	0.021	2 1 2
11	39.631	39.643	−0.011	2 1 3
12	39.945	39.955	−0.01	1 1 7
13	41.584	41.563	0.021	2 1 4
14	43.422	43.424	−0.001	2 0 6
15	43.919	43.93	−0.012	2 1 5
16	44.99	44.99	0	1 0 9
17	46.507	46.496	0.012	0 0 10
18	47.400	47.396	0.005	2 2 0
19	50.277	50.279	−0.003	2 0 8
20	52.556	52.519	0.037	3 0 3
		52.581	−0.025	1 1 10

first 20). Whole pattern unit cell refinement gave $a = 5.4172(1)$, $b = 19.5469(4)$, and $c = 5.4234(1)$ Å.

It is interesting to note that creating a virtual peak by *doubling* the d-spacing of the third peak also leads to the same result. In fact doubling *any* of the first three d-spacings always leads to successful indexing. This suggests that the centred structure and accidentally absent reflections due to pseudo-symmetry were at least as important in the failure of the first attempt as was the dominant zone.

Having successfully indexed the pattern, it is in most cases necessary to extract integrated intensities for structure solution. The total absence of intensity at certain indexed reflection indices can, of course, be an indicator of centring operations, screw axes, and glide planes (§5.3, Table 5.5), and as such could assist in establishing the space group.

6.3 INTENSITY EXTRACTION

Since the intensities of diffraction peaks depend directly on the atom positions within the unit cell (§2.4.2), they are essential data in structure solution. The

Table 6.4(b) DICVOL91 solution 2, orthorhombic, $a = 19.5151$, $b = 5.4205$, $c = 5.4214$ Å.

Peak number	$2\theta_{obs}$	$2\theta_{calc}$	$\Delta 2\theta$	*hkl*
1	23.636	23.635	0.001	1 1 1
2	26.974	26.977	−0.003	3 1 1
3	27.395	27.399	−0.004	6 0 0
4	32.716	32.719	−0.003	5 1 1
5	34.307	34.307	0.000	2 0 2
6	36.203	36.191	0.013	6 1 1
		36.202	0.001	7 0 1
		36.204	0.000	7 1 0
7	37.057	37.050	0.007	0 1 2
		37.054	0.003	0 2 1
8	37.332	37.346	−0.014	1 1 2
		37.350	−0.018	1 2 1
9	37.942	37.942	0.000	4 0 2
10	38.244	38.220	0.024	2 1 2
		38.224	0.020	2 2 1
11	39.631	39.641	−0.009	3 1 2
		39.664	−0.013	3 2 1
12	39.945	39.955	−0.011	7 1 1
13	41.584	41.561	0.023	4 1 2
		41.565	0.019	4 2 1
		41.617	−0.033	9 0 0
14	43.422	43.422	0.001	6 0 2
15	43.919	43.929	−0.010	5 1 2
		43.939	−0.013	5 2 1
16	44.990	44.991	0.000	9 0 1
17	46.507	46.497	0.010	10 0 0
18	47.400	47.395	0.005	0 2 2
19	50.277	50.278	−0.001	8 0 2
20	52.556	52.514	0.042	3 0 3
		52.582	−0.026	10 1 1
		52.523	0.033	3 3 0

mechanics of intensity extraction using the Pawley or Le Bail methods have been covered in §4.6 and §5.6. We are concerned here with aspects that are important for the eventual solution of crystal structures. A major problem in intensity extraction is peak overlapping. Perusal of Table 6.4(b) reveals many examples where peaks almost exactly overlap. Routine fitting procedures are unlikely to detect multiple peaks unless their positions differ by more than 0.2–0.3 FWHM.[68] At smaller

[68] Careful Le Bail or Pawley fitting can sometimes separate peaks as close as 0.1 FWHM (David *et al*. 2002).

Table 6.5 ITO13 results for $Ca_3Ti_2O_7$ using a virtual peak at $3d_{006}$.

A	B	C	D	E	F	a	b	c	α	β	γ	M_{20}	Indexed
340.69	26.27	340.41	0	0	0	5.418	19.511	5.42	90	90	90	74.9	20
340.43	26.27	340.65	0	0	0	5.42	19.511	5.418	90	90	90	43.3	20
340.43	26.27	340.65	0	0	0	5.42	19.511	5.418	90	90	90	42.4	20
340.44	26.27	340.64	0	0	0	5.42	19.511	5.418	90	90	90	41.6	20
340.42	26.27	340.65	0	0	0	5.42	19.511	5.418	90	90	90	40.2	20
340.52	26.27	340.55	0	0	0	5.419	19.511	5.419	90	90	90	38.8	20
229.72	26.26	314.53	6.92	203.76	6.93	7.134	19.537	6.095	91.312	112.208	91.869	19.4	20
406.53	26.26	577.2	12.75	302.76	12.69	5.227	19.562	4.384	91.97	108.079	92.733	22.3	17
26.28	425.84	151.19	0	12.73	0	19.606	4.846	8.175	90	95.794	90	15.8	17

separations they are only apparent as peak broadening. It is therefore essential that not only the positions and intensities be recorded but also the *widths* of the peaks. In the first instance, peaks broadened beyond the general trend (a Williamson–Hall plot may be helpful here, see §9.4.1) should be omitted from indexing and used cautiously in structure solution unless anisotropic broadening has been clearly established (Chapter 9). If a trial structure can not be found using non-overlapped peaks, there are several approaches that may be taken. As two full chapters of a recent volume *Structure Determination from Powder Diffraction* (David *et al.* 2002) have been devoted to the subject of intensity extraction, we present here only the essential features.

6.3.1 Theoretical separation of overlapping reflections

The simplest method of extracting intensity estimates from completely overlapping or unresolvable peaks[69] is to partition them evenly over the allowed *hkl* following indexing. Care must be exercised to weight the partition according to the peak multiplicity (§2.4.2 and Appendix 2). For example, in the powder diffraction pattern from a cubic material, 330 and 411 coincide; however, because their respective multiplicities are 12 and 24, the observed intensity would initially be partitioned 1:2.

Several more sophisticated methods have been proposed (David *et al.* 2002), although none can guarantee the correct partitioning. What these methods offer is to shift the partitioning part way from equipartitioning towards the correct value. David (1987, 1990) has given two methods for incorporating the information contained within the non-overlapped reflections into the estimation of the intensities of overlapped reflections. Both methods rely on Patterson maps (see §6.4.1) and the physical constraints of positivity (in XRD the electron density is everywhere positive – this is not always the case for neutron scattering where the scattering length of some isotopes is negative) and atomicity (concentration of scattering density at atom locations within the unit cell). One method (David 1990) uses a maximum entropy Patterson map algorithm and is particularly suited to very high resolution data. The other, more generally applicable method is based on the work of Sayre (1952) on the interpretation of squared Patterson maps. It was proposed by David (1987) in the following form. Reducing observed intensities to $|F_{\boldsymbol{k}}|^2$ (corrected for Lorentz factor), the fraction of the observed intensity attributable to the mth of M overlapping peaks is expressed as

$$\frac{J_m\,|F_{\boldsymbol{h}m}|^2}{\Sigma_{l=1}^{M} J_l\,|F_{\boldsymbol{h}l}|^2} \cong \frac{J_m \Sigma_{\boldsymbol{k}}\,|F_{\boldsymbol{k}}|^2\,|F_{\boldsymbol{h}m-\boldsymbol{k}}|^2}{\Sigma_{l=1}^{M} J_l \left(\Sigma_{\boldsymbol{k}}\,|F_{\boldsymbol{k}}|^2\,\left|F_{\boldsymbol{h}l-\boldsymbol{k}}\right|^2\right)} \tag{6.9}$$

[69] Completely overlapping peaks have exactly the same d-spacing (e.g. 333 and 511 of a cubic structure) whereas unresolvable peaks are distinct but too close to separate with the diffractometer used.

where J_m and J_l are multiplicities, and the sum over $\boldsymbol{k}$ runs to all the reflections in the pattern.

The examples given by David (1987) show a clear advantage over equipartitioning, however for some peaks the shift is only a small proportion of the real difference from equipartition. More sophisticated partitioning may be attempted if part of the structure is known (e.g. a strongly scattering atom or a known configuration such as a benzene ring). These methods are dealt with by David and Sivia (2002).

6.3.2 Experimental separation of overlapping peaks

Two methods of experimentally separating overlapping peaks have been proposed (Wessels *et al.* 2002). The first is to record data over a range of temperatures and allow anisotropic thermal expansion to 'unmix' accidentally overlapped peaks. This method is of course not effective in separating symmetry overlapped peaks such as the 330 and 411 in cubic systems. It is nonetheless very useful in lower symmetry systems subject to certain conditions discussed below. First let us examine the sensitivity of the method. Although higher resolution instruments exist, a standard high resolution CW neutron powder diffractometer has a FWHM resolution $\Delta d/d$ in the range 10^{-2} to 10^{-3}, say $\Delta d/d = 5 \times 10^{-3}$. The minimum peak shift required for easy and accurate intensity extraction using the Pawley or Le Bail methods is approximately 0.3 FWHM (preferably >0.5 FWHM) leading to a required shift of $\Delta d/d = 0.15 \times 10^{-3}$. The thermal expansion coefficients of many solids are (within a factor 2) approximately 10^{-5} K^1; however, the thermal expansion anisotropy is often far lower, of order 2×10^{-6} K^{-1}, requiring a 75 K temperature change to effect the desired peak shifts. Since it is extremely unlikely that the anisotropic thermal expansion coefficients of a material with an unknown crystal structure will be known in advance, an experiment over a wider temperature range (say 200 K) is advisable. Clearly this requirement will be relaxed somewhat on the highest resolution instruments. The use of anisotropic thermal expansion to reveal 'hidden' peaks is based on the very important assumption that the crystal structure does not change significantly over the temperature range used. There will always be some atomic relaxation as a result of thermal expansion (otherwise the expansion would be isotropic); however, the effect on the intensities of peaks is usually quite small. Far more serious is the occurrence of a structural phase transition, which would invalidate the method (although it may well provide clues concerning the structure under study). In some structures, for example, perovskites, certain peaks begin to show relatively large systematic changes in intensity well in advance of an approaching phase transition. An additional systematic intensity change occurs as a result of changes to the thermal parameters. These too are unknown if the structure has yet to be solved. Perhaps the best practical solution is to record data at several temperatures. The extracted intensities may be plotted as a function of temperature and extrapolated back to the temperature of interest. This will simultaneously correct for thermal vibration

and minor structural changes. Major structural changes will become apparent as discontinuities in the plot.

The second method described by Wessels *et al.* (2002) involves deliberately introducing preferred orientation (texture) into the sample. As described in §9.8, when the randomness of a polycrystalline sample is not perfect, the diffraction pattern becomes more single-crystal like. The continuity of the Debye–Scherrer cones is broken and in extreme cases, overlapping peaks are separated and may be measured directly. Even peaks that are completely overlapped in the random powder pattern (e.g. cubic 330, 411) might become accessible. Thus the method is potentially an extremely powerful structure analysis tool. However, it involves a great deal of careful experimentation and analysis. First, the sample must be one amenable to inducing preferred orientation, that is, needle-like or plate-like crystals or a very ductile solid sample. Needle or plate-shaped crystals can be textured using sedimentation techniques, smear techniques, or in some circumstances using electric or magnetic field. Ductile materials may be textured using plastic deformation (rolling, wire drawing, etc.). Once prepared, the sample texture needs to be determined in a separate experiment on a single crystal diffractometer (see §9.8) or specially modified powder diffractometer. The data are used to generate an Orientation Distribution Function (ODF). Integration of the ODF along a specified path gives pole-figure values $P_{hkl}(\chi, \phi)$for a given sample tilt χ and rotation. Then the true or single crystal intensity I_{hkl} of the peak *hkl* can be extracted using the expression [cf. eqn (5.11)]:

$$y_i(2\theta_i, \chi, \phi) = \sum_{hkl} I_{hkl} P_{hkl}(\chi, \phi) G(2\theta_i - 2\theta_{hkl}) \Delta(2\theta_i) \qquad (6.10)$$

where $y_i(2\theta_i, \chi, \phi)$ is the step intensity at the angles $2\theta_i$, χ and ϕ, and $G(2\theta - 2\theta_{hkl})$ is the function used to describe the peak profile. Equation (6.10) can be used directly in a multi-pattern Pawley (or Will) type extraction to give the I_{hkl} values, or a more complex iterative procedure using Le Bail extraction can be used. The method has been successfully applied to some very large structures (see the example cited by Wessels 2002); however, it involves so much additional experimentation and analysis that it is best reserved as a last recourse when all other methods have failed (including synchrotron or electron microdiffraction from a single one of the needle- or plate-shaped crystals).

6.3.3 Example

Our example here and throughout the rest of the chapter is that already used in §6.2.7; $Ca_3Ti_2O_7$ (Elcombe *et al.* 1991). During the original structure solution, the peak fitting results used to extract the peak positions for indexing were scrutinized for absent peaks. Because the unit cell was known to be pseudo-symmetric ($a \approx c$), particular attention was paid to the width of the fitted peaks. Peaks that potentially contained overlaps associated with the interchange of *h* and *l* were particularly

targeted. From the 92 peaks fitted, the reflection conditions in Table 6.6 were compiled.

With reference to Table 5.5 in §5.3, we see that the structure is C-centred ($h+k$ even). There is a screw axis (2_1 or 4_2) in the z-direction (from $00l$ even). The most likely space groups are $Cmc2_1$, $Cmcm$, $Ccc2$, $Cccm$, and $C222_1$.

Now we will conduct an iterative Le Bail fit to the data using the C-centring to limit the number of peaks output. The first eight (of 200) lines of output are shown in Table 6.7.

Visual inspection of the data and the fit (Fig. 6.3) show that the 111, 311, and 600 type peaks are the only ones with any observable intensity. This suggests that a reasonable detection criterion for this example is $|F|^2 \geq 0.1$. This leads to a list of 184 peaks with their estimated squared structure amplitudes $|F|^2$. These intensities are available for use in the various structure solution methods to be described in the next section. We will content ourselves with applying equal weights to completely overlapping peaks.

Table 6.6 Reflection conditions for $Ca_3Ti_2O_7$.

Miller indices	Condition	Confidence level
hkl	$h+k$ even	high
$h00$	h even	high
$0k0$	k even	high
$00l$	l even	high
$0kl$	k or l or both even	fair
$hk0$	h and k can both be odd, no mixed ones	fair
$h0l$	probably h and l even. No definite odd indices or mixed indices	fair

Table 6.7 First eight integrated intensities (reduced to structure factor squared) extracted using the Le Bail method.

h	k	l	$\|F\|^2$
2	0	0	0.05
1	1	0	0.01
4	0	0	0.02
3	1	0	0.01
1	1	1	0.47
3	1	1	0.12
6	0	0	0.88
5	1	0	0.03

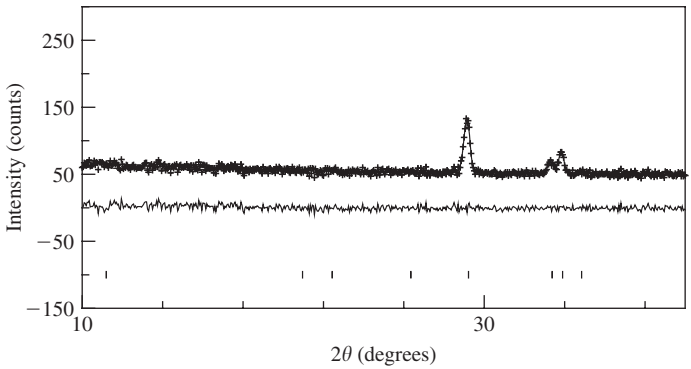

Fig. 6.3 First eight peak positions in the Le Bail fit to $Ca_3Ti_2O_7$ (see Fig. 4.17) used to determine the limiting intensity of 'observed' peaks for intensity extraction.

6.4 STRUCTURE SOLUTION

Having extracted what we believe to be a reliable set of integrated intensities, we are now faced with the same problem as any crystallographer trying to re-construct a crystal structure from diffraction data. As can be seen from eqn (2.32), the structure factors F, are the scattering length modified sum of the phase differences between all of the atoms in the unit cell. On the other hand, the intensities observed at the detector modified by various geometric factors (Lorentz factor, multiplicity, etc.) yield only the square of the structure amplitude $|F|^2$, thus the phase information is lost. So we can see that the so-called 'phase problem' in crystallography may be re-stated as: 'how do we convert our observed list of $|F_{hkl}|$ into F_{hkl}?'.

6.4.1 Fourier transform and Patterson methods

In developing an expression for the structure factor F [eqns (2.29)–(2.32)], it was assumed, without explanation, that the scattering density in the crystal could be represented by the appropriate mean atomic scattering lengths, b, located at the precise atom positions x, y, z within the unit cell. In reality, the scattering density is smeared by (i) the size of the nucleus (though this is always a negligible effect), (ii) thermal and other types of position disorder (see Chapter 2), and (iii) for magnetic scattering, the distribution of unpaired electrons within the outer shells of atoms.[70] The scattering density $\rho(x, y, z)$, although smeared, is nonetheless periodic and for a large crystal, may be written as an infinite Fourier series in which the Fourier coefficients are the structure factors from earlier discussion (§2.4.2):

$$\rho(xyz) = \frac{1}{V_c} \sum_{h=-\infty}^{\infty} \sum_{k=-\infty}^{\infty} \sum_{l=-\infty}^{\infty} F(hkl) \exp\{-2\pi i(hx + ky + lz)\} \qquad (6.11)$$

[70] In X-ray diffraction, it is the entire electron density of the crystal that scatters.

where x, y, and z are fractional coordinates within the unit cell, V_c is the unit cell volume and the structure factor, $F(hkl)$, is now given by:

$$F(hkl) = \int_0^1 \int_0^1 \int_0^1 \rho(xyz) \exp\{2\pi i(hx + ky + lz)\}\, dxdydz \tag{6.12}$$

For ease of visualization, it is often preferable to deal with either a two-dimensional section through the scattering density, for example, for an $x - y$ section at $z = 0$:

$$\rho(xy0) = \frac{1}{V_c} \sum_{h=-\infty}^{\infty} \sum_{k=-\infty}^{\infty} \sum_{l=-\infty}^{\infty} F(hkl) \exp\{-2\pi i(hx + ky)\} \tag{6.13}$$

or a projection of the whole three-dimensional density on to a plane, for example, for the basal plane:

$$\rho'(xy) = \frac{1}{A_{ab}} \sum_{h=-\infty}^{\infty} \sum_{k=-\infty}^{\infty} F(hk0) \exp\{-2\pi i(hx + ky)\} \tag{6.14}$$

where A_{ab} is the projected area of the unit cell on the $a - b$ plane. An important distinction between these two forms of the scattering density is that a two-dimensional section still requires all of the structure factors $F(hkl)$, whereas the projection requires only structure factors for $hk0$ peaks ($F(hk0)$).

The scattering density distribution $\rho(xyz)$ contains all of the information required to describe the average structure including the probability density function (p.d.f.) used to describe thermal motion and static disorder (see §2.4.2). Hence, once $\rho(xyz)$ is known, the structure has been solved. In order to compute$\rho(xyz)$, we must have good estimates of the structure factors $F(hkl)$. Our diffraction experiment however, provides only $F(hkl) \times F(hkl)^*$ (or $|F_{hkl}|^2$) and as discussed earlier, all of the phase information is lost. Even in centrosymmetric structures,[71] where the $F(hkl)$ are real, their sign is unknown. This is a re-statement of the 'phase problem' and all of the methods to be discussed here are concerned with circumventing it.

Several Fourier methods have been developed for single crystal X-ray diffraction. These are

(i) *Direct inversion*: In some very simple crystal structures (e.g. NaCl) the F_{hkl} are all positive so the scattering density may be re-constructed directly using eqn (6.11).
(ii) *Heavy atom methods*: If the position of a few strongly scattering atoms (by definition heavy atoms for X-ray scattering) are known, since the phases of most of the F_{hkl} will be dominated by the 'heavy' atoms, a trial scattering density can be obtained. Then by an iterative process, the phases of other F_{hkl}

[71] Crystal structures containing a centre of inversion symmetry.

can be determined. This is especially the case if only atoms with a positive scattering length are present (as is the case with X-ray diffraction).

(iii) *Isomorphous replacement*: If chemical means can be used to substitute atoms with others of quite different scattering length, the relative changes in the observed $|F_{hkl}|$ can indicate the signs of the F_{hkl}. In the case of a non-centrosymmetric structure, the structure solution may initially proceed as for a centrosymetric structure, that is, the 'phases' have only magnitude $+1$ or -1. Once the main features of the structure have been determined, it is possible that the details can be determined by an iterative process.

Although these techniques are applicable to X-ray or neutron diffraction, from single crystal or powdered samples, there are certain difficulties that have restricted their use in applying neutron powder diffraction to solving unknown crystal structures. First, the constraint in X-ray diffraction that $\rho(xyz)$ is positive does not always apply to neutron diffraction where several elements show negative mean scattering lengths (see §2.3.3). Second, heavy atom and isomorphous replacement techniques were developed primarily for chemical crystallography applications where the scattering entities are molecular and spectroscopy can establish the position of the heavy atoms or substituted atoms with respect to the other structural elements of the molecule (aromatic rings, side branches, etc.) and the symmetry of its local environment. Historically, powder diffraction has been used for solving non-molecular crystal structures. This tendency is slowly changing (even small proteins are now being investigated using powder diffraction); however, the complexity of the powder diffraction patterns from large molecular structures introduces a high degree of uncertainty into the integrated intensities extracted by the procedures described in §6.3. In general terms, the larger the structure, the less likely it is that simple Fourier techniques will yield a correct structure directly although they may provide very useful supplementary information.

There is an additional Fourier technique that does prove very useful in structure solution from powder diffraction known as Patterson synthesis. It relies on the Patterson function, a three-dimensional correlation function that may be derived directly from the experimentally determined $F_{hkl} \cdot F^*_{hkl}$ (i.e. intensities) without reliance on phase information. The following is a simple illustration of a one-dimensional Patterson function as found in elementary X-ray diffraction structure determination texts. We closely follow the account by Warren (1969, 1990). Consider a one-dimensional crystal structure containing three 'atoms' (A, B, C) per unit cell. The unit cell is shown in Fig. 6.4. The Patterson function in this case is defined as

$$P(X) = \int_o^1 \rho(x)\rho(x+X)\,dx \tag{6.15}$$

and this is also shown in Fig. 6.4. The Patterson function is only non-zero where $\rho(x)$ and $\rho(x+X)$ are non-zero. Therefore it contains peaks that represent all of

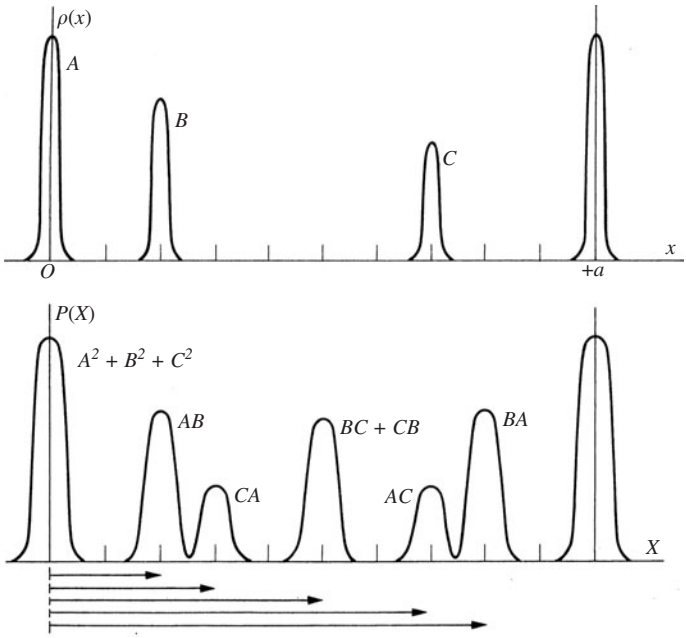

Fig. 6.4 The variation of scattering density in a simple three atom linear structure and the corresponding Patterson function (Warren 1969, 1990).

the interatomic distances measured in the positive direction. There is a peak at the origin representing the correlation of the three atoms with themselves (AA, BB, CC) and peaks for all of the other correlations (AB, AC, BA, BC, CA, CB). It should be noted that, although all of the interatomic distances are present, they all end up referred to the origin of the Patterson function, NOT the origin of the crystal structure. For example, the peak for the distance CA occurs at $x = 0.3$ representing the pure atomic separation situated on a vector from the origin of the Patterson function and not yielding any information concerning the actual location of atoms at this separation. Despite this limitation, the Patterson function (or Patterson maps as their pictorial representations are termed) is an extremely useful tool in crystal structure determination. The general three-dimensional form of the Patterson function is

$$P(UVW) = \int_0^1 \int_0^1 \int_0^1 \rho(xyz)\rho(x+U,\, y+V,\, z+W)\, dxdydz \tag{6.16}$$

which may be represented by the Fourier series:

$$P(UVW) = \frac{1}{V_c} \sum_{h=-\infty}^{\infty} \sum_{k=-\infty}^{\infty} \sum_{l=-\infty}^{\infty} |F_{hkl}|^2 \cos 2\pi(hU + kV + lW) \tag{6.17}$$

where $|F_{hkl}|^2 = F_{hkl} \cdot F^*_{hkl}$. Just as with the Fourier map or scattering density map [eqn (6.11)], it is often simpler to work in two dimensions through the use of sections; for example, parallel to the basal plane:

$$P(UV) = \frac{1}{V_c} \sum_{h=-\infty}^{\infty} \sum_{k=-\infty}^{\infty} \sum_{l=-\infty}^{\infty} |F_{hkl}|^2 \cos 2\pi(hU + kV) \tag{6.18}$$

or projections, for example, on to the basal plane:

$$P'(UV) = \frac{1}{A_{ab}} \sum_{h=-\infty}^{\infty} \sum_{k=-\infty}^{\infty} |F_{hk0}|^2 \cos 2\pi(hU + kV). \tag{6.19}$$

These concepts will be illustrated with reference to our example, the room temperature structure of $Ca_3Ti_2O_7$, which was indexed in §6.2.7 and intensities extracted in §6.3.3. Figure 6.5 summarizes the Patterson function for $Ca_3Ti_2O_7$ as a series of two-dimensional sections perpendicular to the long y-axis. Sections only where significant concentrations of density occur are shown for half of the unit cell, as the C-centring repeats the same pattern with an offset of (1/2, 1/2, 0). The first thing that is noticeable is that the Patterson map contains layers of density at ~0.1 in y (or ~1.95 Å) intervals, corresponding to the shortest (Ti–O) bond length in the perovskite $CaTiO_3$. In fact, the $Ca_3Ti_2O_7$ structure was actually solved by imposing the octahedral tilt pattern of $CaTiO_3$ on to the untilted aristotype $Sr_3Ti_2O_7$ (Elcombe *et al.* 1991), but we will continue as though the structure was unknown.

Examination of the $y = 0$ layer of the Patterson function shows strong concentrations of density at the origin due to self-correlation. This density does not indicate that a particular atom is located at the origin. All that we can derive from the zero layer Patterson slice is that along the x- and z-axis in this plane, the interatomic distances $\sim a/2$ and $\sim c/2$ are highly populated. In addition, the density near the cell centre indicates there are interatomic vectors distributed about $^1/_2$ [101]. The densities at $\sim a/2$ and $\sim c/2$ are also elongated, indicating probable structural distortions or a distribution of interatomic vectors about these positions. In building a trial crystal structure, we are faced with the problem of relating the Patterson cell (Fig. 6.5) to the crystallographic unit cell (of the same dimensions). In this case we begin with an empty unit cell and place 'atoms' at the origin, at (1/2, 0, 0), (0, 0, 1/2) and (1/2, 0, 1/2). Within perovskite derived $Ca_3Ti_2O_7$, Ca will take the role of the, fairly inactive, A-site cation. Therefore we can begin with Ca^{2+} ions fixed at the origin. In keeping with Pauling's rules for ionic structures, cations and anions should alternate so we place O^{2-} near (1/2, 0, 0) and (0, 0, 1/2). We have guidance from the Patterson section as to which way to displace the oxygen ions e.g. (1/2, 0, 0) becomes $(1/2, 0, 0 + \delta)$, (0, 0, 1/2) becomes $(0 + \eta, 0, 1/2)$ and $(1/2, 0, 1/2)$ becomes $(1/2 + \varepsilon, 0, 1/2)$. But the sense of the displacements is not known and somewhat arbitrary at this stage. We shall take the magnitudes of the displacements to be roughly equal and their senses to be positive (i.e. $\delta \approx \eta \approx \varepsilon \approx +0.05$) at

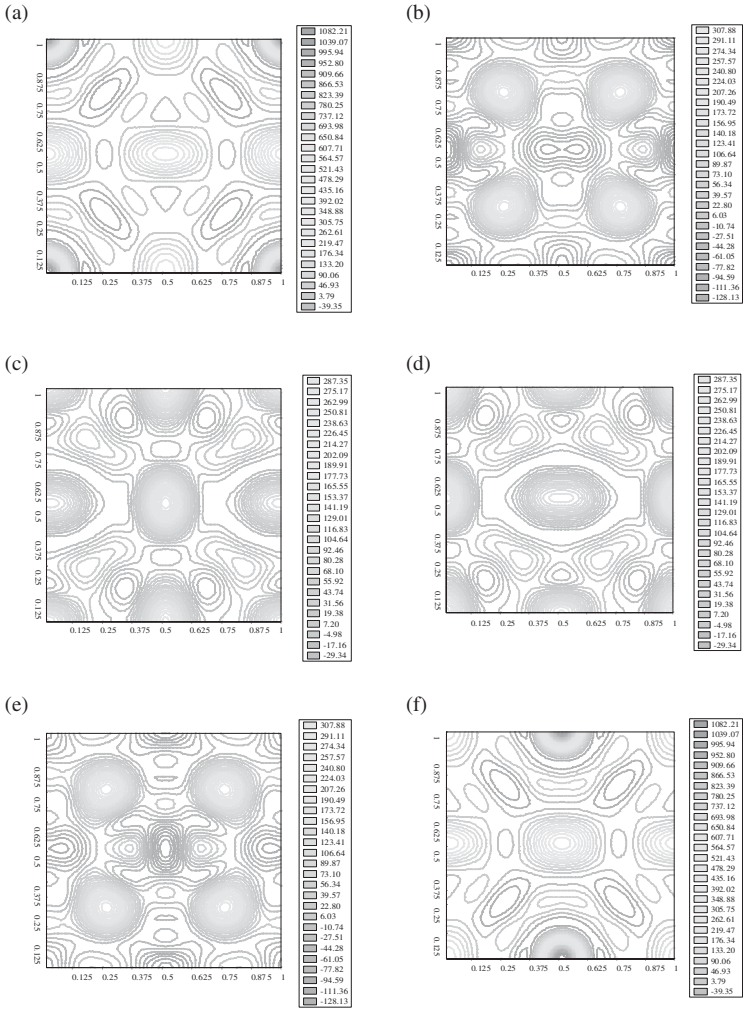

Fig. 6.5 Patterson functions for the lower half of the $Ca_3Ti_2O_7$ unit cell derived from intensities extracted during Le Bail fitting. Slices shown are for (a) $y = 0$, (b) $y = 0.0938$, (c) $y = 0.1875$, (d) $y = 0.3125$, (e) $y = 0.4063$, and (f) $y = 0.5$. (See Plate 5)

this stage. The next layer shows four strongly positive features around (1/4, 0.09, 1/4), etc., and significant negative density at (0, 0.09, 1/2). Close examination of the features like that at (1/4, 0.09, 1/4) shows them to be distorted and enlarged (compared with the self-correlating peaks at the origin of the zero layer slice). This suggests the existence of a distribution of interatomic vectors around positions like 1/4 [1, 0.36, 1], so we add to our model trial atoms (oxygen ions) at (1/4, 0.09, 1/4), (3/4, 0.09, 1/4), (1/4, 0, 3/4), and (3/4, 0, 3/4). The relatively

Table 6.8(a) Trial atom coordinates for $Ca_3Ti_2O_7$ from Patterson slices.

Atom name	Element	Coordinates
Ca1	Ca	(0, 0, 0); (0.55, 0, 1/2)
O1	O	(1/2, 0, 0.05); (0.05, 0, 1/2)
O2,3	O	(1/4, 0.09, 1/4); (3/4, 0.09, 1/4); (1/4, 0.09, 3/4); (3/4, 0.09, 3/4)
Ca2	Ca	(0, 0.1875, 0); (0.55, 0.1875, 1/2)
O4	O	(1/2, 0.1875, −0.05); (−0.05, 0.1875, 1/2)

Table 6.8(b) Trial atom coordinates for $Ca_3Ti_2O_7$ adapted to space group $Ccm2_1$[72].

Atom name	Element	Coordinates
Ca1	Ca	(1/4, 0, 0)
Ca2	Ca	(1/4, 0.1875, 0)
O1	O	(3/4, 0, 0.05)
O2	O	(1/2, 0.09, 1/4)
O3	O	(0, 0.09, 1/4)
O4	O	(3/4, 0.188, −0.05)

deep negative contours at (0, 0.09, 1/2) suggest a common distance involving Ti, which has a negative scattering length. Similar though less deep contours are found at the corners and centre of this section. We will not include these in our trial structure at this stage. The slice at $y = 0.1875$ has concentrations of density at the origin (i.e. 0, 0.1875, 0), indicating that an interatomic vector of [0, 0.18756, 0] is common in this structure. We can immediately position atoms above those in the zero layer. Again we face the problem of whether displacements should be positive or negative. Knowing that the structure is related to $CaTiO_3$ in which TiO_6 octahedra are corner linked in a three-dimensional tilt pattern (and indeed armed as we are with the already solved structure), we may choose to reverse the sense of the displacements compared with the zero layer. The trial atom coordinates as obtained from the first three slices are collected in Table 6.8(a). The layers at $y = 0.5$, 0.4063, and 0.3125 are the same as the lower layers but displaced by 1/2[100]. The order of the density also reverses at $y = 0.5$ indicating a mirror plane there.

The remainder of the trial structure is constructed by applying the C-centring and y-axis mirror plane observed in the Patterson slices (and required by the trial space group $Ccm2_1$). It is illustrated in Fig. 6.6. Next it is necessary to attempt to generate the trial structure using the space group $Ccm2_1$; beginning with the

[72] The symmetry equivalent positions are $(0,0,0)+$; $(\frac{1}{2},\frac{1}{2},0)+$; $x\,y\,z, \bar{x}\,\bar{y}\,z+\frac{1}{2}, \bar{x}\,y\,z+\frac{1}{2}$ and $x\,\bar{y}\,z$.

Table 6.8(c) Refined atom coordinates and thermal parameters for $Ca_3Ti_2O_7$.

		x	*y*	*z*	*B*
Ca1	Ca	0.2482(9)	0	0.0275(16)	0.55(11)
Ca2	Ca	0.2410(5)	0.1876(2)	−0.027(16)	0.55(7)
O1	O	0.6876(6)	0	−0.1625(17)	0.62(7)
O2	O	0.4621(4)	0.1100(1)	0.2105(14)	0.56(5)
O3	O	−0.0375(4)	0.0860(1)	0.2869(14)	0.54(4)
O4	O	0.8043(5)	0.1972(1)	0.1024(15)	0.81(5)
Ti	Ti	0.2507(9)	0.0989(2)	0.5	0.29(5)

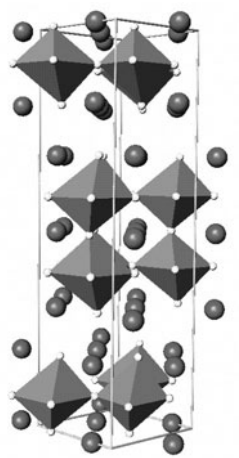

Fig. 6.6 The trial structure for $Ca_3Ti_2O_7$ from Patterson maps.

trial positions for Ca1(P) (Ca1 in the initial trial structure from the Patterson map) and comparing to the symmetry equivalent positions generated by the space group (Ca1(SG)).[73]

$$\begin{aligned} &\mathrm{Ca1(P)} \quad (0,0,0);\,(0.55,0,1/2);\,(1/2,1/2,0);\,(0.05,1/2,1/2) \\ &\mathrm{Ca1(SG)} \quad (0,0,0);\,(0,0,1/2);\,(1/2,1/2,0);\,(1/2,1/2,1/2) \end{aligned}$$

Clearly an origin shift of $^1/_4[100]$ will bring these into approximate agreement viz:

$$\begin{aligned} &\mathrm{Ca1(P')} \quad (1/4,0,0);\,(0.8,0,1/2);\,(3/4,1/2,0);\,(0.3,1/2,1/2) \\ &\mathrm{Ca1(SG')} \quad (1/4,0,0);\,(3/4,0,1/2);\,(3/4,1/2,0);\,(1/4,1/2,1/2) \end{aligned}$$

[73] Asymmetric unit only given.

Applying the same $^1/_4$[100] shift to the other trial atoms and dividing O2,3 between two individual positions O2, and O3, gives the coordinates shown in Table 6.8(b).

The trial structure was entered into the Rietveld analysis software RIETICA and without refinement returned the agreement indices $R_p = 29.7\%$, $R_{wp} = 52.2\%$ and $\chi^2 = 1462$; a less than convincing fit. Table 6.9 charts the course of the remainder of the structure solution (and refinement in this case) including the agreement indices at appropriate stages.

Refinement of the atom coordinates for the trial structure gave some improvement (steps 1 and 2); however, convergence occurred a long way from a good fit. This is largely because of the missing Ti and the powerful effect its negative scattering length has on the phases of the F_{hkl}. It would take considerable effort to locate the missing Ti by refinement and trial and error. Instead, either the refined model (step 2) or indeed the original model can be used to generate a special kind of Fourier map – a difference Fourier map in which the F_{hkl} in eqn (6.11) are replaced by $(F_{\text{obs}} - F_{\text{calc}})_{hkl}$. The slice at $y = 0.0938$ of the difference Fourier map generated at Step 5 is shown in Fig. 6.7. This map shows significant negative scattering density at ($^1/_4$, 0.09,$^1/_2$) in agreement with the siting of negative density in the Patterson function. After adding Ti at this position (step 6) and refining the oxygen coordinates (step 7), convergence to a good fit is rapidly achieved. It is important to note here that convergence was greatly assisted by reducing the angular range of data included in the calculation, from 10°–160° to 10°–90° 2θ, and damping the shifts applied to the refined parameters by a factor 0.3. Steps 6 and perhaps 7 complete the structure *solution.* The inclusion of the coordinates of Ca and Ti in a refinement over the full angular range (step 8) completes the essential elements of the structure *refinement*. Further discussion of the finer points of structure refinement including discussion on steps 9, 10, and 11 is reserved for §6.5.

The final structure has already been illustrated in Fig. 5.11. The coordinates shown here differ from those published by Elcombe *et al.* (1991) only in the absolute sense of the octahedral rotations.

Although this illustration of Fourier and Patterson methods has progressed relatively smoothly, it must be recalled that the structure was already known[74] and this knowledge may have biased the choices made when building a trial structure from the Patterson function. The $Ca_3Ti_2O_7$ structure is a difficult candidate for Patterson methods since, being only slightly distorted as compared with the aristotype $Sr_3Ti_2O_7$, it is highly pseudo-symmetric. It is also non-centrosymmetric. Molecular structures, especially if they are centrosymmetric, may in some instances be more readily solved using these methods, since prominent features (aromatic rings, etc.) will imprint themselves strongly on the Patterson function.

[74] The structure was originally solved by intuitive methods based on known structural relationships to $CaTiO_3$ and tetragonal $Sr_3Ti_2O_7$ (Elcombe *et al.* 1991). These methods were discussed briefly in Chapter 5.

Table 6.9 Stages in the Rietveld refinement of the $Ca_3Ti_2O_7$ structure.

Step	Action	R_p(%)	R_{wp}(%)	χ^2	R_B(%)	Comment
1	Refinement, 30 cycles all oxygen coordinates	16.6	24.8	330		Considerable improvement
2	A further 30 cycles	15.0	21.9	258		Convergence attained
3	Include Ca coordinates in refinement					A worse fit resulted. Restore Ca coordinates
4	Plot Fourier difference maps based on step 2 results					Significant negative density at (1/4, 0.09, 1/2)
5	Re-calculate difference Fourier based on the unrefined trial structure					Significant negative density at (1/4, 0.09, 1/2)
6	Add Ti at (1/4, 0.09, 1/2) to unrefined trial structure					
7	Refine (30 cycles) all free oxygen coordinates using the angle range 10°–90° and damping factor 0.3	6.4	8.8	43.4		Rapid convergence, good fit
8	Re-set angle range to 10°–160° 2θ, refine free Ca and Ti coordinates	5.3	6.1	20.2	4.1	Almost there!
9	Add all B's to refinement	5.2	5.95	19.2	3.8	B_{Ti} is very small and B_{Ca1}, B_{Ca2} are large
10	Add preferred orientation along [010] to the refinement	4.33	5.03	13.7	1.56	B_{Ca1}, B_{Ca2} still large
11	Add Ca site occupancy n_{Ca1}, n_{Ca2} to refinement	4.23	4.94	13.2	1.25	Finished

There are a number of special features associated with the use of neutron diffraction data, rather than X-ray data, in Patterson methods (Esterman and David 2002). The constant scattering length (i.e. lack of an appreciable form factor) makes it easier to attain 'atomic' resolution (~1 Å). The relatively small spread of neutron scattering lengths (most lie within a factor of 4 of each other) compared with X-ray scattering factors (which vary by a factor of up to 100) means that 'heavy atom' methods are far less effective – it is unlikely that one atom type will dominate the scattering to the extent it can be useful for phasing the reflections. However, the occurrence of atoms with *negative* scattering lengths means that the Patterson function contains negative as well as positive features. Negative

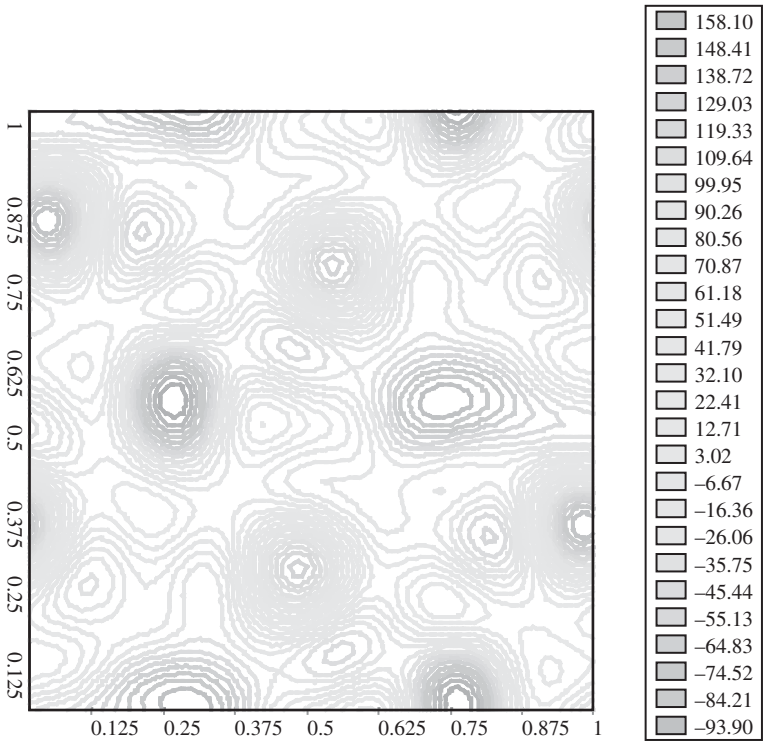

Fig. 6.7 Difference Fourier map for $Ca_3Ti_2O_7$ at $y = 0.0938$. (See Plate 6)

peaks in the Patterson function can occur for interatomic vectors that involve a negatively scattering atom. This may give a strong indication of the location of negative scatterers particularly if only one is present. Unfortunately for organic structures, hydrogen has a negative scattering length and the number of hydrogens in such structures makes this effect less useful. In addition, hydrogen has a very large incoherent scattering cross-section (see §2.3.3) which causes most of the incident beam to be scattered into the background. The different neutron scattering lengths for different isotopes of the same element can be a powerful tool in structure solution. The most widely used isotopic substitution is to mix hydrogen ($b = -3.74\,f\,\mathrm{m}$) and its heavy isotope deuterium ($b = 6.67\,f\,\mathrm{m}$). With H:D in the ratio 64:36 the mean scattering length is zero and the hydrogens make no contribution to the Bragg peaks. The scattering length can be adjusted over a wide range by mixing in different ratios and this may allow the phases of most or all peaks to be obtained directly. This is the neutron diffraction equivalent of the isomorphous substitution and multiple anomalous dispersion (MAD) techniques employed by X-ray crystallographers. Neutron diffraction is the only technique that can reliably locate the hydrogen atoms although distance least squares and

molecular simulation programs can place them approximately once the other atom positions have been determined. There is a popular perception that the hydrogen atom positions are not central to the properties of organic materials in a majority of cases. Consequently, neutron diffraction is generally only used to study organic crystals when hydrogen bonding is thought to contribute substantially to stability or to a property of interest.

As we have demonstrated with our example, relatively small structures can be solved by manual examination of Patterson maps constructed from good quality neutron powder diffraction data. In the case of much larger structures, an exhaustive manual search of the Patterson function is not practical. Automatic interpretation of the Patterson function is facilitated by the use of Harker vectors (Harker 1936) and Harker sections. The criterion often used to rank possible solutions is the symmetry minimum function (SMF). Its derivation and use have been discussed by Estermann and David (2002) and are available as part of the Xtal system of crystallographic software (http://xtal.crystal.uwa.edu.au). Similar Patterson search algorithms are available within suites of single crystal structure solution software (e.g. SHELX-95, Sheldrick 2007).

6.4.2 Direct methods

The phase problem in crystallography has been a strongly motivating factor for innovative solutions. Shortly before the middle of the last century, many ingenious methods for circumventing it were devised. A key historical perspective is given by Buerger (1959). Then Karle and Hauptmann (1956) demonstrated that, at least on statistical grounds, the amplitudes and phases of the reflections are NOT independent. They later demonstrated several methods to use this information in the direct phasing of reflections, for which they received the Nobel Prize for Chemistry in 1985. Subsequently new methods and improved algorithms for applying the older methods evolved. The field of direct methods is an entire branch of crystallography – far too diverse to be covered adequately in one section of one chapter. Thankfully there are several texts on the subject (e.g. Giacovazzo 1980; Ladd and Palmer 1980; Schenk H. ed. 1991) and several excellent computer programs to implement them in the general (usually single crystal) case. Direct methods have become the most commonly used approach to unknown crystal structures. They are now being routinely included in the software supplied by major single crystal X-ray diffraction equipment suppliers and their application to moderate-sized structures (20–60 atoms in the asymmetric unit) is considered routine in dedicated crystallography laboratories. Unfortunately this is not the case for powder diffraction. Giacovazzo (1996) has outlined pitfalls in the direct methods solution of structures from powder methods. These include the low information content of the powder pattern. Because they are statistically based, direct methods require a large 'sample' of reflections. It is recommended that approximately ten strong reflections per atom is required for successful application of these methods. This is routine with single crystal data, but in powder diffraction, symmetry-related, and

accidental overlaps restrict the number of observable reflections and also increase the uncertainty in the extracted intensities (see §6.3). Another uniquely powder diffraction problem is preferred orientation (see §5.5.2) which can severely influence the extracted $|F|^2$and render them meaningless for structure solution. The exception of course is when deliberate preferred orientation (texture) is used to extract single crystal-like intensities after a thorough texture analysis (§6.3.2). Despite the difficulty of adapting direct methods to powder diffraction, several successful structure solutions have been completed and research into better methods is continuing.

The basis of modern direct methods is the structure invariant. Structure invariants are quantities that do not depend on the choice of origin for the unit cell. We are already familiar with one class of structure invariant – the structure factor amplitude $|F|$. To see that this is so, we write the structure factor in vector notation[75]:

$$F(\mathbf{h}) = \sum_{j=1}^{N} \bar{b}_j \exp(2\pi i \mathbf{h} \cdot \mathbf{r}_j) = |F(\mathbf{h})| \exp\left[i\phi(\mathbf{h})\right] \tag{6.20}$$

Next imagine an origin shift by a vector $\boldsymbol{\delta}$. All of the atom position vectors $\mathbf{r}_j$ become $\mathbf{r}_j - \boldsymbol{\delta}$ and the structure factor becomes

$$\begin{aligned} F(\mathbf{h}) &= \sum_{j=1}^{N} \bar{b}_j \exp[2\pi i \mathbf{h} \cdot (\mathbf{r}_j - \boldsymbol{\delta})] = F(\mathbf{h}) \exp(-2\pi i \mathbf{h} \cdot \boldsymbol{\delta}) \\ &= |F(\mathbf{h})| \exp[i(\phi(\mathbf{h}) - 2\pi \mathbf{h} \cdot \boldsymbol{\delta})] \end{aligned} \tag{6.21}$$

where $\phi(\mathbf{h})$ is the phase of $F(\mathbf{h})$ at the original origin choice. Note that $|F(\mathbf{h})|$ remains unchanged but that the phase is shifted by an amount $-2\pi \mathbf{h} \cdot \boldsymbol{\delta}$. Since solving the structure relies on determining the phases of the reflections this would appear to make the problem intractable. However, there are other kinds of structure invariants formed by the products of structure factors. By considering the product $F(\mathbf{h}_1)\, F(\mathbf{h}_2) \ldots F(\mathbf{h}_n)$, it can be seen that the phase change of the product due to an origin shift $\boldsymbol{\delta}$ is given by $-2\pi \boldsymbol{\delta} \cdot \sum_j \mathbf{h}_j$. In the special case when $\mathbf{h}_1 + \mathbf{h}_2 + \cdots + \mathbf{h}_n = 0$, the structure factor product

$$\begin{aligned} &F(\mathbf{h}_1) F(\mathbf{h}_2) \cdots F(\mathbf{h}_n) \\ &\quad = |F(\mathbf{h}_1)| \cdot |F(\mathbf{h}_2)| \cdots |F(\mathbf{h}_n)| \exp\left[i\{\phi(\mathbf{h}_1) + \phi(\mathbf{h}_2) + \cdots + \phi(\mathbf{h}_n)\}\right] \end{aligned} \tag{6.22}$$

is invariant under origin shifts and, importantly, the phase sum $\sum_j \phi(\mathbf{h}_j)$ is also a structure invariant. The simplest product is $F(\mathbf{h})F(-\mathbf{h}) = |F(\mathbf{h})|^2$ the measured intensity (corrected for thermal, geometric, absorption, and multiplicity effects). The next simplest, known as a triplet, is the three-phase structure invariant,

[75] This treatment closely follows that of Allegra (1980) – in Ladd and Palmer (1980), pp. 1–22.

$F(-\mathbf{h})F(\mathbf{k})F(\mathbf{h}-\mathbf{k})$, leading to the triplet sum:

$$\psi_3 = \phi_{-\mathbf{h}} + \phi_{\mathbf{k}} + \phi_{-\mathbf{h}-\mathbf{k}} \tag{6.23}$$

It is generally possible to derive the individual phases if arbitrary phases are given to three (usually large) structure factors $F(\mathbf{h}_1)$, $F(\mathbf{h}_2)$, and $F(\mathbf{h}_3)$ and $\mathbf{h}_1$, $\mathbf{h}_2$, and $\mathbf{h}_3$ are not co-planar. This will result in an arbitrary origin choice to which all phases will be referred. If the space group has special origin choices as a result of symmetry (e.g. an inversion centre), it is useful to take one of these as the origin. The resulting phase sums are termed *semi-invariants* and it is these that are most often used in structure solution. Many methods have been developed for manipulating invariants and semi-invariants in order to extract the phases of all of the observed structure factors (see, e.g. Giacovazzo 1980). One prominent method (Karle and Hauptman 1958) is to assign the phases randomly and then to form a joint probability distribution with the atom coordinates (Peschar *et al.* 2002). Trial phase sets are assessed against a figure of merit and the most promising are used to refine the phases. This is most often conducted by iterative application of the tangent formula (Karle and Hauptman 1956; Karle and Karle 1966)

$$\tan\phi(\mathbf{h}) = \sum_k K(\mathbf{hk}) \sin\left[\phi(\mathbf{h}-\mathbf{k}) + \phi(\mathbf{k})\right] \Big/ \sum_k K(\mathbf{hk}) \cos\left[\phi(\mathbf{h}-\mathbf{k}) + \phi(\mathbf{k})\right] \tag{6.24}$$

where $K(\mathbf{hk}) = |F(-\mathbf{h})F(\mathbf{k})F(\mathbf{h}-\mathbf{k})|$.

It is quite common, in the application of direct methods to X-ray data, for the structure factors to be normalized for the effects of (i) scale factor (i.e. relationship between the scattering by one unit cell to scattering by the whole sample), (ii) form factor (f), and (iii) thermal vibration. The latter two give strong systemic variation to the intensities. With neutron data, the second correction is not necessary though the other corrections are advisable. For example, the *normalized* structure factor may be determined from (Peschar *et al.* 2002):

$$|E_{\mathbf{h}}|^2 = \frac{|F_{\mathbf{h}}|^2_{\text{obs}}}{K \exp(-2B \sin^2\theta/\lambda^2)\varepsilon(\mathbf{h}) \sum_{j=1}^{N} \bar{b}_j^2(\mathbf{h})} \tag{6.25}$$

where B is an overall thermal parameter, $\varepsilon(\boldsymbol{h})$ is a space group symmetry determined statistical weight, and K is a scaling factor defined by $|F_{\mathbf{h}}|^2_{\text{obs}} = K\langle|F_{\mathbf{h}}|^2_{\text{calc}}\rangle$ in the neutron diffraction case. The resulting unitary ($U(\mathbf{h})$) or normalized ($E(\mathbf{h})$) structure factors then replace $F(\mathbf{h})$ in all of the preceding discussion.

Care must be exercised as some forms of intensity extraction (e.g. Le Bail or Pawley) allow correction for thermal vibration to be simultaneously conducted. A value of $B = 0$ must then be used in direct methods calculations.

A test of our $Ca_3Ti_2O_7$ data in the single crystal structure solution package SHELX-97 was not successful. This highlights a particular problem with some neutron data – the presence of an element with a negative scattering length; in this case Ti. Even without the presence of Ti, it is unlikely that direct methods would

have produced a correct solution directly. To be successful with powder data, it is generally necessary to very closely scrutinize the extracted intensities and to partition them into 'single crystal-like' or well resolved (>0.5 FWHM) and 'poorly resolved' categories. Then direct methods can be applied to the single crystal-like intensities initially. An example of this approach is encapsulated in the POWSIM package as described by Pescher *et al.* (2002). Here the single crystal-like intensities are used to provide better estimates of the overlapped peaks via the program DOREES – and the results recycled into the direct methods solution. This is the powder equivalent of the phase expansion (extension) undertaken during direct methods solution from single crystal data except that the former interpolates the observed data whereas the latter extrapolates outside the observed data collection range. Extensive further discussion of direct methods applied to powder diffraction may be found in David *et al.* (2002), particularly Chapter 10 (Peschar *et al.* 2002), Chapter 11 (Giacovazzo *et al.* 2002), Chapter 13 (Ruis 2002) and Chapter 14 (Gilmore *et al.* 2002). Extensive lists of structures solved using neutron powder diffraction are given by Ibberson and David (2002) as well as Giacovazzo *et al.* (2002). Advanced and semi-automated application of Patterson function search methods via the symmetry minimum function, a kind of 'direct method' distinct from that of Karle and Hauptman, is described by Estermann and David (2002).

6.4.3 Global optimization methods

The solution of a crystal structure is one of many examples of multi-variable optimization problems in many branches of science and engineering. A persistent occurrence in such problems is the location of a solution which is locally optimum (i.e. small excursions take one to inferior solutions) but not the global optimum (i.e. *any* excursion takes one to inferior solutions). Without a global optimization strategy, the human mind is in some instances doomed to follow familiar paths (e.g. safe engineering paths are adhered to but may not be fully optimized). In other instances, it may be particularly gifted in plotting a path through a multi-dimensional space (e.g. the intuitive or 'trial and error' solution of structures – Chapter 5). One way to avoid local solutions to this kind of problem – including crystal structures – is to employ global optimization strategies.

In the context of *ab initio* structure solution, global optimization is a term that embraces a diverse range of strategies that have in common the use of modern computing power to (i) sample many possible solutions to a structure, (ii) judge them against the observed data using pseudo-energy or entropy functions, and (iii) to use pseudo-random changes in the model to move the system of atoms closer towards the global minimum or true structure. By analogy, global optimization is akin to the exhaustive strategies for auto-indexing (see §6.2), whereas Fourier and Patterson methods are more analogous to Ito's method.

Global optimization may begin from an assumed random starting state or may incorporate prior knowledge such as a known fragment of the structure (e.g. a molecular fragment determined by spectroscopy, Patterson or Direct Methods).

The principal advantage that global optimization strategies have is their ability to exit from a local minimum. Let us pause to consider the standard structure refinement algorithms (e.g. least squares as used in Rietveld refinements). These locate a minimum in the cost function $\bar{S}$, for example, $\bar{S} = \sum_i w_i(y_i(\text{obs}) - y_i(\text{calc}))^2$ [eqn (5.8)] by a gradient search using the derivatives of $\bar{S}$ with respect to the values adopted by all free parameters $(x_1, x_2, \ldots, x_n)$ as given in eqn (5.35). If there was only one minimum in the function $\bar{S}(x_1, x_2, x_3, \ldots, x_n)$ then we could proceed directly from a cell with atoms at random positions to the correct structure in a few refinement cycles. Unfortunately, crystal structure problems are typified by many local minima in $\bar{S}$. Once the system has settled within a local minimum, traditional refinements with parameter shifts based on the gradients fail because the gradients are zero at a local minimum. More robust methods are required to force the system to explore outside the local minimum.

In a recent review (Shankland and David 2002), global optimization methods have been categorized primarily according to the branch of science in which the phenomenon that the algorithm mimics originated; for example, simulated annealing from the physical sciences, genetic algorithms from the life sciences, and swarming behaviour from the social sciences. In contrast there has also been a strong tendency within the literature to classify methods according to the mathematical algorithm (e.g. Monte Carlo method) or the cost function used to judge success (e.g. Maximum Entropy methods) rather than the overarching strategy. This is rather confusing to the uninitiated and indeed unhelpful in comprehending the mechanics of the different methods so we will use the former categorization.

Simulated Annealing (SA)

The first application of global optimization methods to crystal structure solution was most likely the adaptation of a statistical mechanics approach by Khachaturyan and co-workers (Khachaturyan *et al.* 1979, 1981; Semenovskaya and Khachaturyan 1985; Semenovskaya *et al.* 1985). The asymmetric unit was regarded as a vessel containing a non-ideal gas of atoms and the *R*-factor was equated to the Hamiltonian to be minimized. The statistical sum, *Z* and free energy Φ were defined in the usual way:

$$\mathrm{Z} = \sum \exp\left(\frac{-R}{T}\right) \tag{6.26}$$

$$\Phi = -T\ln(\mathrm{Z}) \tag{6.27}$$

where T is the absolute temperature and the sum in §6.26 is over the unit cell contents. For a given T, the equilibrium state (i.e. structure + thermal disorder) was solved using the kinetic equations of Onsager (Khachaturyan *et al.* 1979, 1981). It was later determined that these solutions were not always free from local minima (metastable states in statistical mechanics), and the Monte Carlo method was adapted as a means to find the true global minimum (Semenovskaya and Khachaturyan 1985; Semenovskaya *et al.* 1985). Calculations were conducted

essentially by allowing atoms to take a random walk over a fine grid of points. The usual rules governing diffusive motion of atoms within solids are active, that is, the site to be jumped to must be vacant, if ΔR for the jump is negative the jump *must* occur and if ΔR is positive the jump may or may not occur with probability $\exp(-\Delta R/T)$. This acceptance of some positive ΔR values allows the system to exit from a local minimum and, for an infinite number of attempts, to locate the global minimum. This method of global optimization has become known as *simulated annealing* and is used in a very wide variety of thermodynamic, diffusion kinetics and molecular dynamics problems. The distinction between the structure solution algorithm and diffusion simulations is that in the former a very fine mesh is used whereas in the latter, atoms jump from one legitimate crystallographic atom position to another. The original form allowed the system to adopt any configurations (most of which are unphysical) on the way to a solution. It was tested on only a limited number of single crystal data. More sophisticated algorithms can be constructed that are constrained in terms of minimum distances of approach, however convergence to a solution is severely slowed if the system is heavily constrained. A typical program run is conducted in a series of steps at ever-decreasing temperatures to allow the system to 'condense' into the 'thermodynamically stable' (defined by agreement with the observed diffraction data) structure. Success is judged not on the basis of a single run but rather a solution is considered to be correct if runs from multiple random starting positions all converge to the same solution. It may also be tested by the success (or otherwise) of subsequent structure refinements judged by the usual statistical criteria.

The application of simulated annealing to powder diffraction data has the same problems with peak overlap as do the other structure solution methods. In common with Patterson and Direct Methods, one may elect to work with extracted integrated intensities or $|F|^2$ [see, e.g. Le Bail (2001)]. Then one is faced with the challenge of partitioning intensity between overlapping reflections (see §6.3). This is the most computationally efficient way to apply simulated annealing to powder diffraction data; however, it generally ignores a significant information resource – the absent or very weak reflections. Just as structure refinement by whole pattern methods is superior to refinements using extracted intensities because it *does not allow the model to generate spurious intensity where none was observed*, so too should absent or weak reflections be included in simulated annealing data. Best (though computationally costly) is to use the entire pattern – much as in a Rietveld refinement procedure. (see, e.g. Bruce and Andreev 2002). Many authors have now published accounts of successful structure solutions based on simulated annealing (see references in Shankland and David 2002; Le Bail 2001). The method appears to be particularly successful in solving molecular structures where the number of degrees of freedom can be greatly reduced by incorporating the known chemical connectivity of the molecule and bond distances and angles determined from other sources (spectroscopy, NMR, molecular simulations, etc.). The simulated annealing algorithm is then only required to permute the molecule through the available conformations within the unit cell. This strength has also been highlighted as a

weakness (Shankland and David 2002) not only of simulated annealing, but of all global optimization methods, because if the molecular data are incorrect outside small limits, no solution will be found because the system of atoms has been constrained to contain an error. On the other hand, completely unconstrained runs quickly become untenable for large structures due to the very large computational demand. These pitfalls are discussed further under the heading Cost Functions below.

Because of the organic nature of many of the structures solved, the majority of structure solutions by powder diffraction simulated annealing have used X-ray diffraction. With neutron diffraction, the H would need to be replaced by D to avoid unacceptably high background due to incoherent scattering. Structure solution from neutron powder diffraction data for non-hydrogen containing materials is just as effective as with X-rays, and in many cases should be more effective; for example, when the neutron scattering lengths are particularly advantageous (e.g. light elements in the presence of heavy elements), or when the magnetic structure is to be investigated simultaneously (Mellergård and McGreevy 2001). Although the number of reported powder diffraction simulated annealing programs exceeds 12, the field is sufficiently new that convergence to a reasonably small number of 'standard' programs has yet to occur (as thankfully it has with Rietveld refinement codes). Simulated annealing programs are also somewhat difficult to obtain in well documented user-friendly form (Le Bail 2001). Perhaps the DASH program comes closest to this ideal (David *et al.* 2001).

Genetic algorithms (GA)

Simulated annealing seeks to mimic the behaviour of a system of atoms (molecules, etc.) as it cools from vigorous thermal disorder into a more ordered state. Atomic motion occurs via a series of random thermal fluctuations. As the complexity of a system increases, the ability to self-assemble from merely random events is severely restricted. For example, the complex atom arrangements within biological macromolecules and the great diversity of life forms on Earth are considered unlikely to have occurred in the available time from purely random events. Instead, it is thought that evolution occurs in targeted ways that speed up convergence to an end point. Evolutionary strategies – the development of computer algorithms that mimic evolutionary behaviour – is a growing field of research in areas as diverse as engineering design and molecular docking (Michalewicz 1996). Genetic algorithms are a subset of evolutionary strategies that seek to mimic the way in which genetic mutations in individuals lead to the evolutionary change in a whole population over time. Instead of maintaining just one interim solution as is the case in simulated annealing, a genetic algorithm will maintain many potential solutions. Each individual 'solution' is characterized by a collection of atoms at defined coordinates (the genetic algorithm jargon of 'a chromosome of genes' may prove too remote an analogy for many readers). Just as in simulated annealing, random changes (mutations) are introduced to individual solutions and the agreement of a

computed diffraction pattern with the observed diffraction is assessed using a cost function (e.g. R_B). Favourable mutations usually have a high probability of survival and unfavourable mutations have low probability of survival (just as in simulated annealing). The non-vanishing probability of unfavourable mutations to survive allows the system to exit from local minima and to seek the global optimum. Surviving solutions are then allowed to 'breed' or to exchange genes to form the next generation of solutions. Mutations are allowed to occur and the process is repeated. Formally, it may appear that the process differs little from several parallel simulated annealing runs (even the 'breeding' may simply be viewed as another kind of random fluctuation in the solution) except that the changes introduced by breeding are not random but rather, part of another partially successful solution. In the general case, this leads to a great enhancement of convergence rates. Even greater convergence rates are achieved using several 'island' populations in parallel that only pass genetic material to each other periodically; or the use of a local optimizer (e.g. least squares refinement) on individual solutions that meet the fitness criteria after mutation and breeding.

Genetic algorithm programs may be influenced or fine-tuned using the probability of mutation, the breeding rate, and the types of changes allowed. A great deal of fine tuning (e.g. non-uniform probabilities) and system-specific information (e.g. refine only the torsion angles of an organic molecule) can be included in the program. However this limits the development of generic genetic algorithm software that can be applied to multiple problems without modifying source code, and we shall not consider it further here. A longer account is given by Shankland and David (2002) including many additional literature sources.

Several other approaches such as 'swarming' and downhill simplex methods are discussed by Shankland and David (2002) but will not be elaborated here as there is as yet no sign that they will be used extensively for solving structures from powder diffraction data.

Cost functions

A key factor in the success of any global optimization procedure is the evaluation of a particular solution against the observed data. In the field of global optimization, the most generally used cost-functions are akin to 'energy' functions, which need to be minimized to obtain the optimum agreement. These are usually based on an RMS deviation from observed behaviour. Programs which utilize the extracted single crystal-like intensities (e.g. Le Bail 2001) can operate using very simple single crystal-like R-factors [e.g. R_B (R_I), Table 5.10]. Programs which utilize the whole pattern may use the weighted profile R-factor, R_{wp} or χ^2 and are generally considered superior to extracted intensity programs. However, it has been shown by Shankland and David (2002) that a statistically equivalent approach is to use extracted intensities and cost function:

$$\chi^2 = \sum_h \sum_k \left[\left(I_h - S\,|F_h|^2 \right) \left(V^{-1} \right)_{hk} \left(I_k - S\,|F_k|^2 \right) \right] \tag{6.28}$$

where I's are extracted intensities from a Pawley refinement, V_{hk} is the co-variance matrix from the Pawley refinement, S is a scale factor, and Fs are the computed structure factors from the current trial structure. Intensities extracted by the Le Bail method may only be used if modifications have been made to output a co-variance matrix (David and Sivia 2002). Significant computational savings and increased speed can be obtained in this way (see Shankland and David 2002).

As we have stated earlier, the problem of solving structures from powder diffraction is one of lack of information. We are accustomed to assuming that additional information will always help in obtaining a solution to a given problem. Global optimization is no different and it seems at first as though the use of multiple cost functions (e.g. R_I or χ^2 *and* a potential energy function or bond-valence sum) would be of benefit in obtaining convergence. However several pitfalls associated with this approach have been highlighted by Putz (1999). The cost function may be visualized as a multi-dimensional hypersurface which the algorithm (simulated annealing, genetic algorithms, etc.) explores in search of the global minimum. Putz (1999) has shown that as additional cost functions are included in the solution, the total hypersurface (representing the sum of all the cost functions) is modified. The individual cost functions will have local minima in different positions to each other and because of model inadequacies and statistical factors, the global minimum slightly displaced for each cost function. The effect is that, as more and more cost functions are included, the local minima disappear and the global minimum is left isolated on a large flat hypersurface – the so-called 'golf course problem'. There is no longer any driving force for the solution to move about on the hypersurface and it becomes unable to converge. In addition, if the different cost functions displace the global minimum far enough, then adding them may cause it to disappear or be severely reduced in the overall cost function – making it ineffective.

Another means to include additional information, for molecular solids is to constrain molecular fragments (e.g. benzene rings) to act as rigid bodies. Again, the results can be counter-intuitive. First, the constraint needs to be accurate otherwise the system has been constrained to contain a mistake and can never converge to the correct solution. Second, because the motion of a large molecular fragment has such a profound effect on the diffraction pattern (and hence the primary cost function), the solution jumps about the hypersurface rather than smoothly exploring. If the algorithm is damped to apply only very small atom shifts, then it performs only a local optimization not a global one (Putz 1999). One strategy is to combine small local optimizations with large jumps to force convergence to a global minimum.

It can be seen from the preceding that global optimization methods have much to offer in structure solution from powder diffraction data. However they rely heavily on system-specific data from other techniques for the solution of large structures. At the time of writing, for most problems it is advisable to try the other methods before attempting a global optimization strategy. Improvements to methodology and software in this rapidly advancing field may change the situation in the not too distant future. It may eventuate that global optimization becomes as universal for powder diffraction as Direct Methods are for single crystal diffraction.

6.5 ADVANCED REFINEMENT TECHNIQUES

The mathematical basis and standard strategies for structure refinement using Rietveld's method (Rietveld 1967, 1969) are given in §5.5.3 and §5.7 respectively. Here we outline a few additional points that may assist in the attainment of smooth convergence, or in the refinement of structures with multiple occupancy of atom sites.

6.5.1 Ensuring convergence

In the solution/refinement of our example structure, $Ca_3Ti_2O_7$, (Table 6.9) several strategies to assist convergence were employed without explanation.

Staged introduction of parameters

It is found that, even from starting point parameters that are relatively close to their final values, the release of all of the available free variables in a single Rietveld refinement usually leads to divergence. Hence the recommendation (§5.7) of the release of parameters in stages. More details of this strategy can be found in Kisi (1994) wherein the details of the Rietveld refinement difference profile for different types of error are analysed. An example is shown in Fig. 6.8 for variables of interest in the latter stages of refinement. When the starting structure is relatively poorly determined, as is likely for a structure solved *ab initio* from neutron powder diffraction data, the likelihood of divergence is accentuated and even greater care is required. The problem is worse than in the single crystal case, since Rietveld refinements involve, in addition to the structural parameters, non-structural parameters describing the background, diffraction zero, lattice parameters, peak shapes, and widths.

If the strict sequence of structure solution outlined in this chapter has been followed (as it has been for the $Ca_3Ti_2O_7$ example), then all non-structural parameters can be held constant at the values obtained during whole-pattern intensity extraction (Le Bail fitting in this case). This was the strategy adopted in the refinements of $Ca_3Ti_2O_7$ outlined in Table 6.9. The structural parameters were added in a staged fashion as well. Initially (Step 7 of Table 6.9) only the free oxygen coordinates were refined. These were chosen because O is the strongest scatterer of neutrons present, and coordinated O atom shifts due to the tilting of TiO_6 octahedra are the basis of this perovskite-related structure. The coordinates of the metal atoms (Ca, Ti) were added next (Step 8) and finally the displacement parameters (B's, Step 9). At this stage, the structure was well determined, however the value of the agreement for integrated intensities, R_B was still 3.8% and seemed to be systematic in *hkl*. Since the material was known to have a strong cleavage, a preferred orientation correction was added (Step 10) and most of the residual errors were removed. There was no associated change in the structural parameters. The only remaining matter was the slightly puzzling observation of large values for the displacement parameters (B_{Ca1} and B_{Ca2}) of the Ca ions. In Step 11, the occupancy of

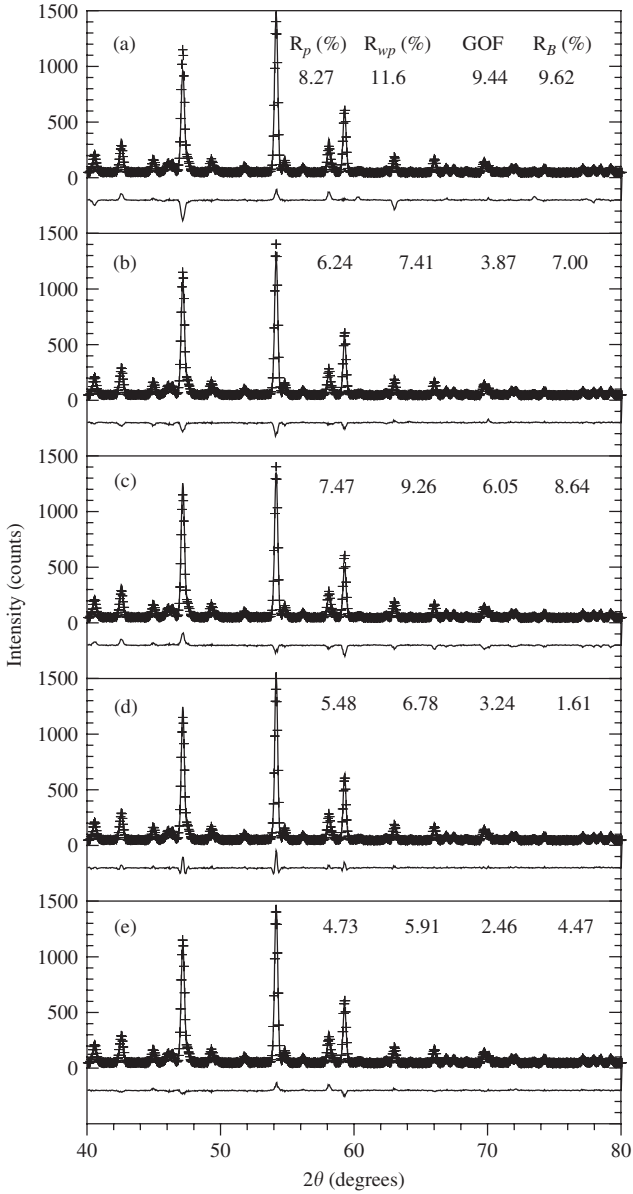

Fig. 6.8 The effect of differing kinds of errors common to the latter stages of structure refinement on the difference profile for part of the neutron diffraction pattern from $Ca_3Ti_2O_7$ (Kisi 1994). Illustrated are (a) atom positional errors, (b) occupancy errors, (c) displacement parameter errors, (d) peak width errors, and (e) preferred orientation. Agreement indices are given for each for comparison with the final values $R_p = 4.27\%$, $R_{wp} = 4.99\%$, $GOF = 1.34$, and $R_B = 1.37\%$ for the published structure (Elcombe *et al.* 2001).

the Ca sites was included in the refinement. More acceptable values were obtained (see §6.5.3) and a small improvement in R_B resulted (Table 6.9). The occupancies had changed by identical amounts. Similar observations had been made on other Ca-containing compounds and further investigation revealed that the then current scattering length for Ca was slightly incorrect.

Restricting the data range

In Table 6.9, the critical first refinement stage (Step 7) was conducted using only data in the angle range 10°–90° 2θ (d-spacings 11–1.3 Å). This is because the high-angle (low d) data is heavily overlapped. This strategy has also been reported to be effective in *ab initio* structure solution (see, e.g., Shankland and David 2002, p. 270). Once the structure is essentially established, the full data set may be added (Step 8). The extent to which this strategy is effective will vary from structure to structure and also depends on the resolving power of the diffractometer used.

Damping

For some key parameters with a highly non-linear effect on R_{wp}, the parameter shifts computed by a simple least-squares algorithm may be large enough to push the entire refinement out of the region of the global minimum, into the realm of incorrect local minima. This may also set up highly oscillatory behaviour if allowed to continue. One simple solution is to 'damp' or reduce the computed parameter shifts by a constant factor before they are applied. In our example, a factor 0.3 was chosen after some problems were encountered using a factor 0.9. It is difficult to comment on the individual effects of these strategies as all were applied simultaneously. In any event, their effects are highly structure-, model-, and data-specific. All can be effective and have no deleterious effect other than to slightly lengthen the time to convergence.

6.5.2 Constraints

During structure refinements, parameters that have equal values for reasons of symmetry, must be constrained in some way. For example, Wyckoff position 12i in space group $P\bar{4}3m$ (No. 215) must have coordinates x, x, z. Most refinement programs either recognize symmetry required constraints or use sequential codewords that make it trivial to couple the x and y coordinates. Hexagonal space groups (e.g. $P6_3/mmc$ – No. 194) often have positions such as $x, 2x, z$. Again it is usually trivial to constrain the shifts in the y coordinate to be twice those in x by applying a weight to the codeword. More complex situations occur through the connectivity of structural elements and are not required by symmetry. An example occurred in the original solution and refinement of $Ca_3Ti_2O_7$. High correlations (or anti-correlations) were observed between non-symmetry-related oxygen ions on opposite sides of tilting TiO_6 octahedra (see Fig. 5.11). By applying the constraints $x_{02} = x_{03}, z_{02} = \frac{1}{2} - z_{03}$ and $\Delta z_{01} = -\Delta z_{04}$ an equally good fit to the

observed data was obtained and high correlation coefficients were removed from the correlation matrix. The correlation matrix is an important tool in monitoring structure refinements for this very purpose – the identification of essentially non-independent parameters.

More complex constraints can be applied to undertake targeted refinements. For example the torsion angle of a molecular group (e.g. methyl group) about a crystal vector does not change the shape of the group to any great degree. Therefore it is often beneficial to reduce the degrees of freedom available to the refinement algorithm by not allowing the shape of the molecular grouping to change, that is, constraining it to rotate as a unit. Many other kinds of constraints can be applied. A solid discussion is given by Baerlocher (1993).

6.5.3 Displacement parameters

In §2.4.2 the phenomenon of the reduced intensity in Bragg peaks at higher angles (smaller d) due to thermal motion was introduced. Its influence on the observed diffraction pattern was further discussed in §5.5.2. We will use this section to detail the physical significance of displacement parameters, their correlation with other parameters and how in some instances useful data on the local environment of atoms can be obtained from them.

Reasonable values of the displacement parameters

From the simple Debye theory of monatomic solids, the effect due purely to thermal motion is given by

$$F = F_0 e^{-M} \tag{6.29}$$

Here F is the structure factor, F_0 is the structure factor in the absence of any atom displacements (i.e. a perfect frozen crystal) and M is given by (Cullity 1978)

$$M = B\left(\frac{\sin\theta}{\lambda}\right)^2 \tag{6.30}$$

$$B = 8\pi^2\left\langle u^2\right\rangle = \frac{6h^2T}{mk\theta_D^2}\left[\phi(x) + \frac{x}{4}\right] \tag{6.31}$$

where $\langle u^2\rangle$ is the time-averaged displacement of the atoms from their mean positions, h is Planck's constant, k is Boltzmann's constant, θ_D is the Debye characteristic temperature (usually in the range 200–1000 K), m is the mass of the vibrating atom, T is the absolute temperature, $x = \theta_D/T$, and $\phi(x)$ is the Debye function:

$$\phi(x) = \frac{1}{x}\int_0^x \frac{\xi}{e^{\xi} - 1}\,d\xi \tag{6.32}$$

The computed B values for the metallic elements from Na to Pb, are, despite a wide range of θ_D and m, in the range 0.2–1.0 Å^2 at room temperature. The simple theory is not strictly valid for more complex solids; however, the B values observed in non-protein crystal structures at room temperature usually fall in this same range. It is also apparent from eqn (6.31) that heavier atoms should have smaller B (*cet. par.*) and that if B is due to thermal motion alone (and if at higher temperatures where the Debye function approaches unity) a linear dependence on absolute temperature should be observed.

Artifacts

When a particular aspect of the diffraction is not adequately modelled, the least squares refinement algorithm will distort the *available* parameters to unrealistic values in order to improve the fit to the data. Displacement parameters are often affected by this phenomenon. The simplest case is when the background at high angle (short d-spacing) is incorrectly described. Because the peaks here are broad (CW) and closely spaced (CW and TOF), the profile R_{wp} can be improved if the peak intensities are shifted in the opposite direction to the background misfit (i.e. if the background is underestimated, the peak intensities will be increased by decreasing Bs to compensate). Close scrutiny of the numerical values of refined Bs and the plotted output is required to avoid this. If a relatively 'flat' background model is being used, then a rapid test is to increase the order of the background polynominal by one. A systematic shift on Bs confirms the diagnosis whereas no change in Bs and a near zero coefficient for the new parameter is a strong contra-indication.

Absorption and extinction (see §2.4.2, §5.5.2) are phenomena that correlate (or anti-correlate) with displacement parameters. This is particularly evident when substantial absorption is present in a CW pattern recorded in Debye–Scherrer geometry. In this instance, the low angle peaks will be reduced in comparison to higher angle peaks. If not corrected, the scale factor will decrease during refinement leaving the high angle peaks from the model underestimated. Intensity will be transferred into the high angle peaks by making B smaller and often negative. Similar problems may arise in TOF refinements for even modestly attenuating samples because of the wavelength dependence of absorption (see §2.4.2). Very small or especially negative displacement parameters should not be accepted. The physical cause should be isolated and modelled or corrected.

A final occurrence that leads to negative thermal parameters (quite common in laboratory X-ray diffractometers using wide scatter and receiving slits) is beam spread beyond the sample at low angles. In neutron diffraction experiments, this is only a problem in some unusual experimental arrangements, for example, if a thin flat-plate sample is used in reflection geometry because of a highly absorbing sample (see §3.6.6).

Static displacements

A number of effects such as non-stoichiometry, point and line defects and solid solution effects can cause static displacements or relaxation of atoms from

their ideal positions. The correlation with thermal displacements here is strong because the averaging effect of recording the diffraction pattern makes the two indistinguishable in a single measurement (§2.4.2). The presence of significant static displacement is usually readily detected, however, as the observed B's will be unusually high. If we assume that thermal and static displacements are independent, then we can write $\langle u^2 \rangle$ as composed of two parts:

$$\left\langle u^2 \right\rangle = \left\langle u_T^2 \right\rangle + \left\langle u_S^2 \right\rangle \tag{6.33}$$

and from eqn (6.31)

$$B = B^T + B^S \tag{6.34}$$

For a new material where B^T is not known, it may be estimated from eqns (6.31, 6.32) if the Debye temperature θ_D is known. If θ_D is unknown, B^T, B^S and θ_D may be simultaneously determined from data recorded at many temperatures. This was the approach taken, for example, by Cheary (1991) for non-stoichiometric Ba-substituted Hollandites. Figure 6.9 (Cheary 1991) shows a fit to a combination of eqns (6.31) and (6.34), adjusted for a polyatomic structure by using the mass-weighted displacement parameter; $B_M = \frac{1}{M}\sum_i m_i B_i$

$$B_M = B_M^S + \frac{6h^2 T}{\bar{m} k \theta_D^2}\left[\phi(x) + \frac{x}{4}\right] \tag{6.35}$$

where $\bar{m}$ is the mean atom mass. For the example shown, the static component is approximately 0.5 Å^2 and the Debye temperature $\theta_D = 430$ K. Over the temperature range studied, the material seems to adhere to the Debye model relatively well. However, data concerning the behaviour of the individual ions is lacking. Two approaches have been used to overcome this.

The first, due to Housley and Hess (1966) is based on the inequality

$$B_i^2(0) \leq \frac{h^2 B_i(T)}{2 m_i k T} \tag{6.36}$$

where $B_i(T)$ here refers to B^T for atom i at the designated temperature T and the other symbols are as before. Equation (6.36) provides a means to estimate the *maximum* thermal contribution $B_i^T(0)_{\max}$ from measurement at any given temperature. In the limit $T \to \infty$, the two sides of eqn (6.36) become equal (Cheary 1991). Therefore a plot of $B_i^T(0)_{\max}$ estimated from data at a number of temperatures against $1/T$ allows, by extrapolation to $1/T = 0$, a very good estimate of $B_i^T(0)$. B_i^S can be obtained from a modified form of eqn (6.34):

$$B_i = B_i^T + B_i^S \tag{6.37}$$

or at 0 K $\quad B_i(0) = B_i^T(0) + B_i^S$.

In practice, $B_i(0)$ cannot be measured; however, generally any B measured below $\theta_D/10$ will suffice as B_i^T vary only very slowly in this temperature range. Cheary (1991) extended this approach to individual static components of the anisotropic

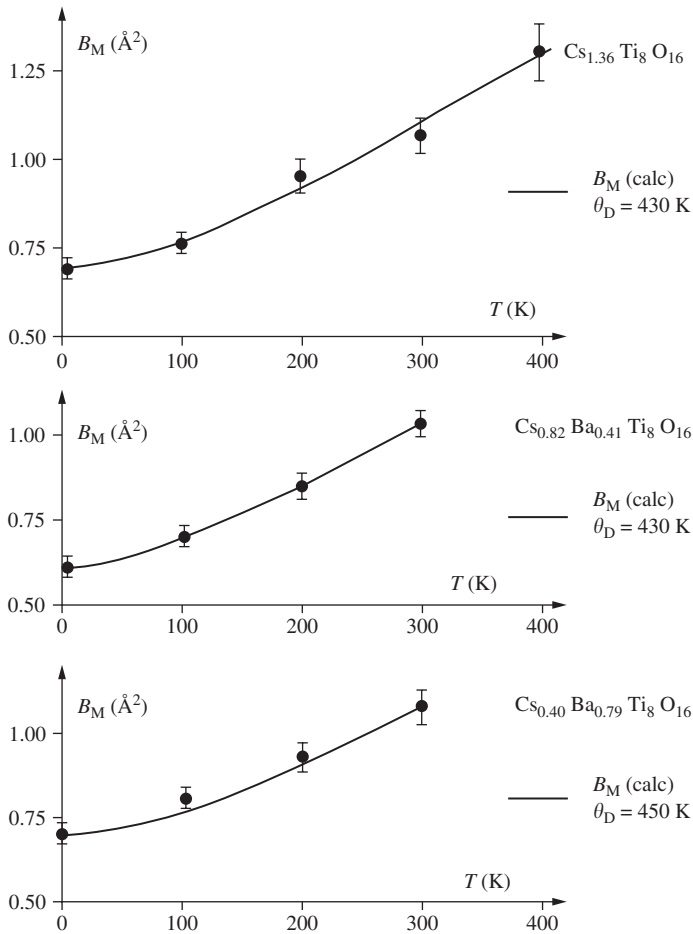

Fig. 6.9 The fit of the displacement parameter B to a combined thermal vibration and static displacement model as given by eqns (6.31) and (6.34) in order to extract mean static displacements from refined thermal parameters in a multi-atom structure (adapted with permission from Cheary 1991).

displacement tensor ($(U^{ij})^S$) and found that the static rms displacements of Cs and Ba parallel to the Hollandite tunnels were very large (≥ 0.16 Å), confirming that the Cs ions within the tunnels have only short range order.

A second way to access B^S for individual atoms (B_i^S) is to undertake the fitting procedure using eqn (6.35) not for a mass-weighted average but for individual atoms (Kisi and Ma 1998). This necessitates the estimation of a distinct θ_{Di} for each atom type. In some cases, for example, relatively simple binary oxides, some significance may be attached to the refined θ_{Di} as representing the distinct behaviour

of the cation and anion sub-lattices. In more complex structures, the refined θ_{Di} are less meaningful. It should be emphasized that regardless of the method used, success is contingent on thermal vibration within the sample conforming to a harmonic Debye model over a large range of temperature.

In a study of cubic zirconia in the range 295–1873 K (Kisi and Ma 1998), it was found that a significant isotropic fourth order anharmonic component was required in order to fit the high temperature data. In this circumstance eqn (6.37) becomes

$$B_i = B_i^S + B_i^T \left(1 + T\left[2\chi\gamma_G - \frac{20k_B\gamma_i}{\alpha_i^2}\right]\right) \tag{6.38}$$

where χ is the volume coefficient of thermal expansion and γ_G is the Grüneisen parameter. γ_i and α_i are force constants in the fourth order expansion of the isolated atom potential (Willis and Pryor 1975)

$$V = V_0 + \frac{1}{2}\alpha\,\langle u\rangle^2 + \gamma\,\langle u\rangle^4 \tag{6.39}$$

where $\langle u\rangle$ is the rms displacement. These relationships, though known for some time, are seldom used to maximize the information obtained from a powder diffraction experiment. With careful attention to the background fitting, choosing a neutron wavelength that minimizes structured thermal diffuse scattering under the Bragg peaks (§10.2) and paying careful attention to occupancies and substitutions (§6.5.4), information concerning the local structures around particular atom species of at least the same quality as from routine solid-state EXAFS could be readily obtained.

6.5.4 Atomic site occupancy

In the molecular structures familiar to single crystal diffractionists, the atomic site occupancy of the bulk of the positions within a molecule is one. Exceptions may occur when an H atom or small molecular side-group is disordered over two sites. The details are relatively routine to determine (using either single crystal or good powder data for smaller structures) by refinement of selected site occupancies. The H case is particularly well determined by neutron diffraction if isotopic substitution by deuterium has been conducted.

Site occupancy problems of a completely different magnitude occur in the non-molecular solids of interest in solid state physics, materials science, mineralogy, and solid-state chemistry. Two phenomena are of interest. First, non-stoichiometry is relatively straightforward to understand and to model during structure refinement. Certain simple compounds do not obey Dalton's law of definite proportions. For example, titanium carbide exists as a stable phase over a range of chemical composition from $TiC_{0.6}$ to $TiC_{0.995}$. $TiC_{0.995}$ has the NaCl structure which may be viewed as two interpenetrating cubic-close packed structures – one occupied by Ti and the other by C or alternatively as an FCC arrangement of Ti with C occupying the octahedral voids. The non-stoichiometry could be accommodated by the

structure in two ways – as vacant C sites or as interstitial Ti atoms. No additional diffraction peaks occur in either case so this question can only be decided by structure refinements based on diffracted intensities. Using a neutron powder diffraction pattern (Fig. 6.10) it is relatively simple to demonstrate that the non-stoichiometry is accommodated as C vacancies. This kind of refinement opens the door to elemental[76] chemical analysis by diffraction. In addition to phases that can naturally support non-stoichiometry, are phases made non-stoichiometric by doping. Our example here is again (cf §5.8.3) ZrO_2, which has three pure ambient pressure polymorphic structures: monoclinic (<1205°C), tetragonal (1205°C–2377°C), and cubic (2377°C–2710°C) (Baker 1992). The high temperature structures may be 'stabilized' at room temperature by suitable ternary additions (doping). This stabilization forms the basis for the ZrO_2-based solid electrolytes used in fuel cells and for zirconia structural ceramics such as Partially Stabilized Zirconia (PSZ) and Tetragonal Zirconia Polycrystal (TZP) (Green *et al.* 1989). Common dopant oxides include MgO, Y_2O_3, and Ce_2O_3. There is complete solid solubility between the dopant oxides and the fluorite-related ZrO_2 structure. Because the cations in these oxides have a lower charge than Zr^{4+} (e.g. Mg^{2+}, Y^{3+}, Ce^{3+}) the structure must adjust the O^{2-} content to maintain charge balance. Another way of viewing the phenomenon is that Mg, for example, will 'bring' less O to the ceramic than Zr will bring. For example, the addition of 10 mol% of MgO to ZrO_2 will result in $Zr_{0.9}Mg_{0.1}O_{1.9}$. Again the non-stoichiometry could be accommodated as either oxygen vacancies or interstitial cations. The comparable (though distinct) scattering lengths of Zr, O, and Mg allow precise refinement of the oxygen content. Faber, Seitz, and Mueller used neutron powder diffraction at 900°C to prove that the charge compensating defects are oxygen vacancies (Faber *et al.* 1976). They also concluded that the dopant cations substituted randomly on the Zr site and that the oxygen ions tend to drift away from the perfect fluorite site at (1/4, 1/4, 1/4) along [111] directions. Howard *et al.* (1988a) were also able to demonstrate excellent agreement in Rietveld refinements for cubic $Zr_{0.78}\ Y_{0.22}\ O_{1.89}$ and $Zr_{0.88}\ Mg_{0.12}\ O_{1.88}$ using models based on random substitution of dopant cations for Zr and random charge compensating vacancies in the O site. There has been some suggestion that the oxygen vacancy content increases when the temperature is raised (Kisi and Ma 1998). This would have a profound influence on our understanding of high temperature ionic conduction in ZrO_2 materials and is worthy of further study.

A second kind of occupancy problem occurs when different atoms share the same site (e.g. Zr/Y, Zr/Mg in the examples above). In binary cases, this situation is just as easy to resolve as the vacancy problem (provided that the scattering lengths are not too similar). However, it is increasingly common in materials science (and a long-standing problem in mineralogy) for many atoms to be doped on to the same site (or indeed multiple sites). Two key materials science examples

[76] As distinct from phase analysis (see Chapter 8).

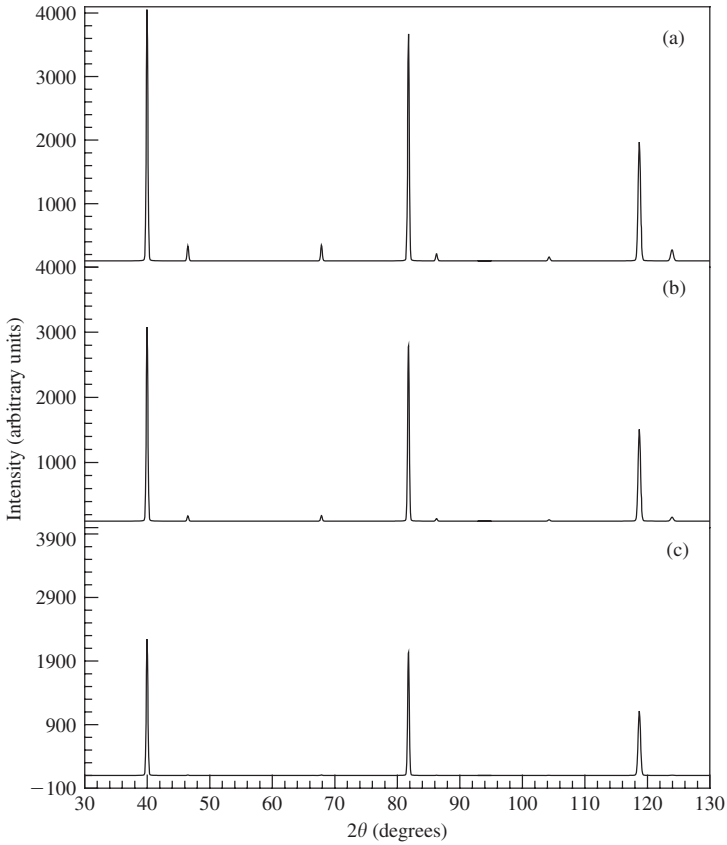

Fig. 6.10 Calculated CW neutron diffraction patterns from (a) TiC, (b) $TiC_{0.8}$ and $TiC_{0.6}$ to illustrate the effect of non-stoichiometry on the peak intensities.

are the oxide superconductors and the hydrideable metal alloys for hydride battery applications. In these cases, the important function of occupancy refinements – for confirming the correct siting of dopants or determining their partition across multiple sites – becomes increasingly difficult. To illustrate the problem, consider an abstract archetypal crystal structure that has two sites A and B. In the undoped condition, atoms of type 1 occupy the A site and atoms of type 2 occupy the B site. Now consider that two kinds of dopant atom (types 3 and 4) are added to the material. The usual approach is to refine the occupancies of the archetypal (2 atom) model. This is equivalent to refining the mean scattering length of each site $\bar{b}$. For our hypothetical example we may write

$$\begin{aligned} \bar{b}_A &= n_1^A b_1 + n_3^A b_3 + n_4^A b_4 \\ \bar{b}_B &= n_2^B b_2 + n_3^B b_3 + n_4^B b_4 \end{aligned} \tag{6.40}$$

where $n_1 - n_4$ are the fractional occupancies of each site by atoms of types 1–4 and $b_1 - b_4$ are the scattering lengths of atom types 1–4. If we ignore momentarily the possibility of vacancies, then both sites are fully occupied,

$$\begin{aligned} n_1^A + n_3^A + n_4^A &= 1 \\ n_2^B + n_3^B + n_4^B &= 1 \end{aligned} \tag{6.41}$$

Now $b_1 - b_4$ are known so we have at this point, for a single diffraction pattern, six unknowns ($n_1^A, n_3^A, n_4^A, n_2^B, n_3^B, n_4^B$) and only four equations.

Given independently measured chemical compositions C_1, C_2, C_3, and C_4, we also have

$$\begin{aligned} C_1 &= \frac{n_1^A N_A}{N_A + N_B} \\ C_2 &= \frac{n_2^B N_B}{N_A + N_B} \\ C_3 &= \frac{n_3^A N_A + n_3^B N_B}{N_A + N_B} \\ C_4 &= \frac{n_4^A N_A + n_4^B N_B}{N_A + N_B} \end{aligned} \tag{6.42}$$

and using eqns (6.41)

$$C_1 + C_2 + C_3 + C_4 = 1$$

where N_A and N_B are the site multiplicities for the A and B sites respectively (see §5.2.5 and International Tables for Crystallography, Volume A).

Now we have eight independent equations in six unknowns and the problem is overdetermined. In principle, this problem is always tractable if the site selectivity for the original atoms is maintained. If however there are j sites (each starting with different species) and n dopant species, and if *any* atom is allowed to occupy *any* site, then there are $j(j+n)$ unknown occupancies to be determined. In comparison, there are j equations of the kind shown in eqn (6.40), j like eqn (6.41), and $j + n$ like eqn (6.42), $3j + n$ equations in all. This problem should be tractable when $3j+n \geq j(j+n)$, that is for 2 sites and 1 or 2 dopant atoms, but not when 3 or more distinct sites are involved. Difficult examples are found among the intermetallic compounds, for example, $Cu_{10}Al_4$ is a rhombohedrally distorted gamma brass with 18 occupied atom sites. Approximately three of the Cu sites accommodate substituent Al atoms and approximately 2.5 structural vacancies per (nominally 52 atom) unit cell (Kisi and Browne 1991).

Another important problem with occupancy refinements is parameter correlation. Two major cases arise. First, when all of the occupancies are refined in conjunction with the scale factor, the total scattering is not constrained. In extreme cases the occupancies and scale factor can drift to mutually compensating unphysical values (e.g. a miniscule scale factor and huge occupancies or vice versa). At

least one occupancy or the scale factor must be fixed. The second major category of parameter correlation is between occupancies and thermal parameters. This will be discussed separately in a later section.

Despite the significant difficulties outlined in the treatment above, extremely useful data on atomic substitution and doping is routinely obtained from neutron powder diffraction data. There are several approaches to overcoming the limitations indicated by eqns (6.40)–(6.42), and these will be outlined below.

Chemical data and site selectivity

In order for a collection of atoms to settle into an ordered state, there must be a degree of site selectivity, that is, the system is optimized with respect to free energy by certain atoms occupying certain sites. Without such selectivity there would be no crystals. The strength of the site selectivity varies greatly. It is easiest to comprehend in ionic crystals where we find that cations *never* have cation nearest neighbours and anions *never* have anion nearest neighbours. We can apply equations like (6.40)–(6.42) (suitably modified for the number of sites and dopant species) to the cations and anions separately. This allows much larger structures to be tackled. In addition to the sign of the ionic charge, the size of the ion also has a strong part to play. Take for example the family of structures known as perovskites (Fig. 6.11(a)). Many materials with perovskite structures have useful electrical, magnetic, and hydrogen storage properties. The archetypal perovskite (space group $Pm\bar{3}m$) has a chemical composition ABO_3 with the A cation at the origin of a cubic unit cell and the B cation at the cell centre. The oxygen ions are in the face centres [e.g. (1/2, 1/2, 0), (1/2, 0, 1/2) and (0, 1/2, 1/2)].[77] The larger cation always occupies the A site. If the A cation is small the structure distorts [Fig. 6.11(b)] and if it becomes too small, the structure is de-stabilized in favour of another [e.g. $MgTiO_3$ adopts the ilmenite structure (Megaw 1973)]. It is usually possible to predict which site (A or B) a given cation dopant will occupy within a perovskite structure.

The site selectivity of covalent structures is also very strong and again significant reductions in the number of degrees of freedom in equations like (6.40)–(6.42) can be made by applying the appropriate rules.

In metallic structures (e.g. intermetallic compounds) the site selectivity is far less pronounced. Not only is the energy difference between the occupation of one site type or another far more subtle, there are often kinetic barriers such that the ordered structure only forms after prolonged annealing. Subtle influences such as atomic size and electro-negativity do come into play; however, there are many exceptions to any rule yet devised.

For any structure type containing dopants, it is wise to first fully analyse the undoped structure to try to determine the governing influences of its ordering

[77] An alternative origin choice may be used with the B cation at (0, 0, 0), the A cation at (1/2, 1/2, 1/2) and O at (1/2, 0, 0), (0, 1/2, 0) and (0, 0, 1/2).

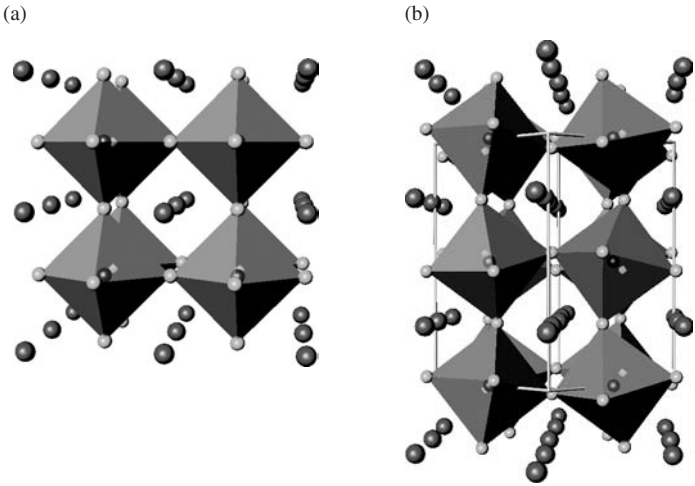

Fig. 6.11 (a) The cubic archetypal structure of perovskite ($CaTiO_3$) in space group P$m\bar{3}m$. (b) the room temperature $CaTiO_3$ structure in space group P*bnm* which has the TiO_6 octahedra tilted about each of the three cube axes in (a). The ions are in each case plotted as red (Ca^{2+}), maroon (Ti^{4+}) and pale blue (O^{2-}). (See Plate 7)

scheme. Then the principles learned may be safely applied to the problem of correctly locating substitutional (dopant) atoms.

Combined neutron and X-ray diffraction investigations

Even with the use of all available chemical and site selectivity data, there will be cases where a single diffraction measurement cannot resolve an ambiguity. In such cases, it is often extremely valuable to use both neutron and X-ray diffraction data. There are relatively few cases of atoms with neutron scattering lengths in the same ratio as their X-ray form factors. Therefore it is usually possible to set up a second set of equations like (6.40) with the neutron scattering lengths replaced by the X-ray form factors (see, e.g. Kisi 1988).

Rather than refine the neutron and X-ray models independently and then interpret the refined occupancies in terms of substitutions, many Rietveld refinement programs now allow the refinement of a model from multiple diffraction patterns (often referred to as histograms) including both neutron and X-ray diffraction patterns.

A persistent difficulty in such joint refinements is the question of how to weight the two data types given the different sample sizes, scattering cross sections, and detection efficiencies. If both patterns are recorded according to the guidelines given in Chapter 3, then little advantage is likely to be gained by using other than equal weights. Both approaches, interpreting independently refined occupancies

using a set of simultaneous equations or conducting joint refinements, should yield essentially the same result.

Isotopic substitution

Another, less accessible, method of obtaining extra scattering length contrast is by using isotopic substitution. It was demonstrated in Chapter 2 that, because neutron scattering depends on the state of the nucleus, different isotopes of the same element have different coherent neutron scattering lengths.[78] Therefore, in principle, the average scattering length from a particular site can be substantially altered by changing the isotopic mix of one or more elements occupying it. Assuming the same chemical and site selectivity for different isotopes of the same element, neutron diffraction patterns recorded from samples containing two or more distinct isotopic mixtures on one or more sites yield additional equations like (6.40)–(6.42) allowing more unknown quantities to be determined. This is the neutron equivalent of anomalous dispersion methods in X-ray diffraction except that the samples must be specially prepared, usually at some expense. A similar though distinct use of isotopic substitution is to 'tune-out' one element by reducing its average scattering length. A good example is the hydride of the intermetallic compound $LaNi_5H_7$ which has six distinct sites where it would be possible for H to reside and a great deal of controversy over which sites are occupied and the resulting space group symmetry. Thompson *et al.* (1987a) studied the H distribution by using the Ni isotope ^{60}Ni such that Ni, previously responsible for the bulk of the scattering power of the unit cell $\left(\bar{b} = 10.3\,f\,\mathrm{m}\right)$, became insignificant $\left(\bar{b} = 2.8\,f\,\mathrm{m}\right)$. A second substitution of deuterium for hydrogen to avoid the large incoherent scattering cross section of the former (see Table 2.2) resulted in the bulk of the diffraction pattern being due to the atoms of interest –D. In other systems where the H positions are of less interest, similar strategies are readily employed using partial hydrogen–deuterium substitution. The great mobility of H/D at room temperature means that in some H-containing systems it is sometimes enough to merely allow exchanges of H with D from a D-rich environment (D_2O/H_2O mixture for solution grown materials, H_2/D_2 gas for interstitial solids, etc.). This methodology is widely used in small angle neutron scattering (SANS) and in neutron single crystal diffraction studies of organic crystal structures but it has yet to achieve widespread acceptance in powder diffraction.

Occupancy defining peaks

Before attempting to solve occupancy-related structural problems, it is wise to examine the general form of the structure factors or, for large structures, conduct some pattern calculations to search for what we shall term *occupancy defining peaks*. To convey the concept of occupancy defining peaks, consider substoichiometric TiC_x (see earlier discussion). There are only two types of structure factor

[78] They also have different incoherent scattering and absorption cross-sections.

for TiC_x:

$$\text{for } h+k+l \text{ even}, \quad F_{hkl} = 16(b_{\mathrm{Ti}} + xb_{\mathrm{C}})$$
$$\text{for } h+k+l \text{ odd}, \quad F_{hkl} = 16(b_{\mathrm{Ti}} - xb_{\mathrm{C}}) \tag{6.43}$$

where x is the fractional occupancy of the C site. Since $b_{Ti} = -3.438 fm$ and $b_C = 6.648 fm$, peaks with $h+k+l$ even are extremely sensitive to x. In particular, F for these peaks will be exactly zero at $x = 0.5171$. To more readily visualize how this comes about, consider the 200 peak that arises from scattering density in the basal planes (and equivalents) at a spacing $a/2$. In the stoichiometric structure there are two alternating layers, both equally populated by Ti and C. When approximately half of the C sites are empty, the mean scattering density in each of these layers is zero and hence the intensity of 200 becomes zero [see Fig. 6.10(c) with $x = 0.6$].

Similar effects can occur, not by the mean scattering going to zero because of negative scattering length, but because of phase differences between the layers. Our example here is the intermetallic compound Ti_5Si_3 which has been of interest because of its interesting high-temperature properties. Under certain conditions, Ti_5Si_3 absorbs interstitial C to form $Ti_5Si_3C_x$ up to a maximum of $x = 1$. This C absorption is particularly important when the compound forms as an intermediate phase in the production of the layered ternary carbide Ti_3SiC_2. The C is absorbed into face-sharing Ti octahedra that zig-zag up the c-axis. As a result, the 110 peak is extremely sensitive to the C content (Fig. 6.12), its intensity decreasing by more than a factor 10 at $x = 1$ (from $> 26\%$ of the strongest peak to just 2.5% in a 1.5 Å CW neutron powder diffraction pattern).

Interpreting displacement parameters for occupancy data

As mentioned earlier, correlations between occupancies and thermal or displacement parameters can be a problem in structure refinements. How this occurs can be understood by considering Fig. 6.13. For the simple FeAl structure used to calculate the diffraction patterns in Fig. 6.13, it can be seen that a reduction in site occupancy [Fig. 6.13(b)] reduces the peak intensities as expected, whereas an increase in B has a similar, though not identical effect [Fig 6.13(c)]. It is quite common for occupancies to drift to unphysical values when refined simultaneously with displacement parameters because the mean observed scattering can be approximately conserved when n and B are strongly anti-correlated. The situation is far worse for X-rays since the effects of B are angle (d) dependent in a manner that makes them difficult to distinguish from the X-ray form factor. In more complex structures, because the structure factors (F) for the peaks will have very different phases, the effect of a change in occupancy will be oppositely directed in some peaks and so the ability to de-couple from displacement parameters is greater. Nonetheless, the structures of many materials of interest in mineralogy, metallurgy, and materials science are susceptible to occupancy-thermal parameter correlations. When the correlation is so severe that it undermines confidence

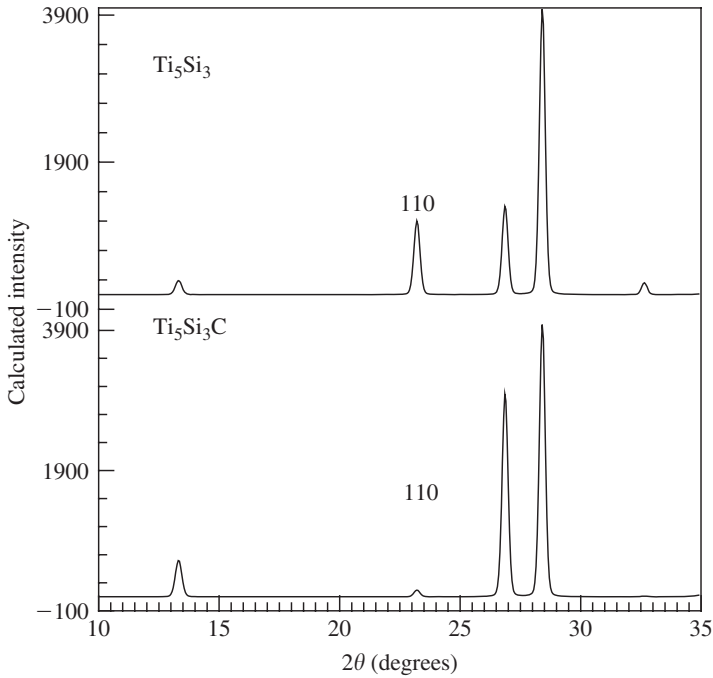

Fig. 6.12 Calculated neutron powder diffraction patterns ($\lambda = 1.5$ Å) from the intermetallic compound $Ti_5Si_3C_x$ with $x = 0$ and $x = 1$ illustrating quenching of the 110 peak at ~23°.

in the refined parameters, independent refinement of occupancies and displacement parameters should not be undertaken. One approach is to adopt a stepwise approach, that is, nominal *B*s are held constant while occupancies are refined. These are then held constant while the *B*s are refined and so on. There is no guarantee that such an approach will find the optimal structure and the system may still drift to unphysical values albeit far more slowly than in a full-matrix refinement.

An alternative approach (Kisi 1988) is to refine *B* for each site and then attempt to interpret it in terms of a combination of substituent species and thermal displacement. If the occupancies are fixed, then for each site the refinement will (to good a approximation) optimize:

$$b = b_0 \exp\left[-B_{ref}\left(\frac{\sin^2\theta}{\lambda^2}\right)\right] \tag{6.44}$$

where b is the equivalent scattering length from the site, b_0 is the coherent scattering length of the element located on the site in the refinement input, and B_{ref} is the refined displacement parameter. The real situation, for one substituting

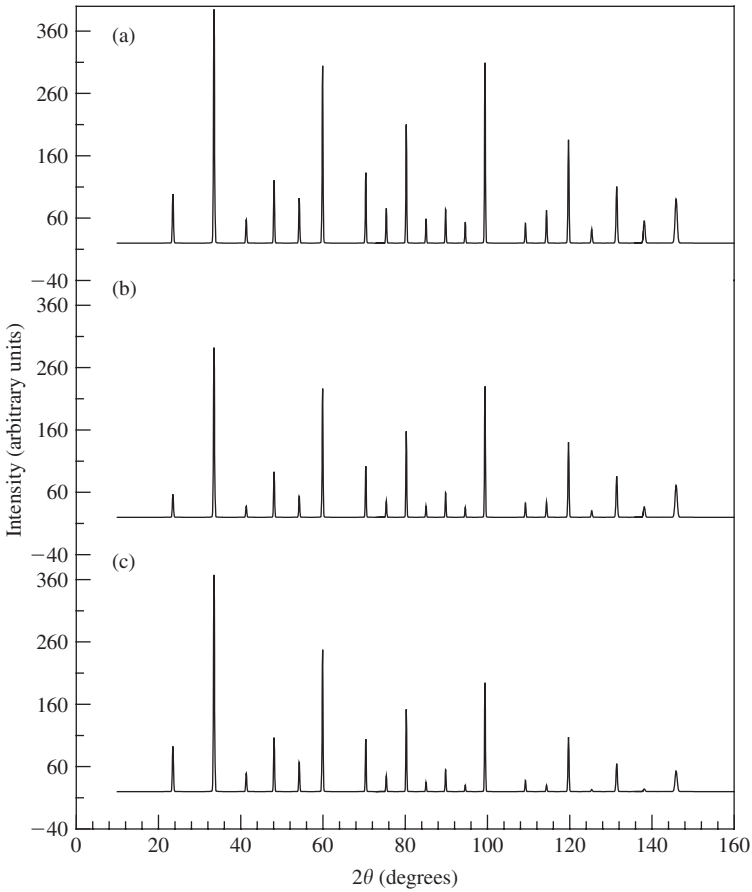

Fig. 6.13 Calculated CW neutron diffraction patterns for the intermetallic compound FeAl which adopts the CsCl structure (a) fully stoichiometric at room temperature and illustrating (b) how the effect of partial disordering of the Fe and Al gives intensity changes similar to those (c) caused by an increase in the displacement parameter of the Fe**.**

species, is

$$b = (x_0 b_0 + x_1 b_1) \exp\left[-B\left(\frac{\sin^2\theta}{\lambda^2}\right)\right] \tag{6.45}$$

where x_0 and x_1 are the fractions of host and substituting elements and B is the true displacement parameter, assumed to be the same for both host and substituent, which may be purely thermal (B^T) or may contain a contribution from static disorder (B^S). Equating eqn (6.44) and (6.45), and writing $B_{\text{ref}} - B = \Delta B$

gives

$$x_0 b_0 + x_1 b_1 = b_0 \exp\left[-\Delta B\left(\frac{\sin^2\theta}{\lambda^2}\right)\right] \tag{6.46}$$

substituting $x_0 = 1 - x_1$ and rearranging gives

$$x_1 = \frac{b_0}{b_1 - b_0}\left\{\exp\left[-\Delta B\left(\frac{\sin^2\theta}{\lambda^2}\right)\right] - 1\right\} \tag{6.47}$$

To remove the dependence on θ, a weighted mean is obtained by integrating eqn (6.47) and dividing by the $\sin^2\theta$ range of the experiment:

$$\bar{x}_1 = \frac{\frac{b_0}{b_1-b_0}\int_{\theta_{\min}}^{\theta_{\max}}\left\{\exp\left[-\Delta B\left(\frac{\sin^2\theta}{\lambda^2}\right)\right] - 1\right\}\sin 2\theta d\theta}{\sin^2\theta_{\max} - \sin^2\theta_{\min}} \tag{6.48}$$

As an example of how to use eqn (6.48), we examine an example from Kisi (1988) (see also Kisi and Browne 1991). Cu_9Al_4 has a cubic γ-brass structure with eight occupied point sets in space group $P\bar{4}3m$ (Kisi and Browne 1991). There are two concentric clusters A and B centred on (0, 0, 0) and (1/2, 1/2, 1/2). Each cluster contains an inner tetrahedron (IT), an outer tetrahedron (OT), an octahedron (OH), and a cubo-octahedron (CO). Al occupies IT(A) and CO(B). Cu_9Al_4 can take additional Al into solid solution and it is of interest to consider where this Al is located. Table 6.10 shows the displacement parameters refined using a perfect Cu_9Al_4 model for a near stoichiometric sample and one containing ~1.7 excess Al atoms per 52 atom unit cell. The sites IT(B) and OH(B) show the greatest systematic change (intermediate compositions also support this trend, Kisi (1988)). Choosing IT(B) as having the greatest change, we substitute $\Delta B = 0.57$, $b_0 = 0.7718$, $b_1 = 0.3447$, $\theta_{\max} = 80°$, $\theta_{\min} = 10°$, and $\lambda = 1.5$ Å into eqn (6.48) and evaluate numerically.[79]

The result is a value of $x_1 = 0.211$ for the IT(B) site. This compares well with $x_1 = 0.25$ determined by combined occupancy (IT(B), OH(B) only) and displacement parameter refinements. Displacement parameter-occupancy correlations were a serious problem in these refinements until at least half of the occupancies were held constant. Thereafter, occupancies and displacement parameters (B's) could be co-refined; however, the displacement parameter analysis (eqns (6.44)–(6.48)) gives us greater confidence that the results of Kisi and Browne (1991) are correct.

6.6 LOOKING AHEAD

Ab initio structure solution is an active and expanding field that we have not been able to do justice here. Further information can be found in David *et al.* (2002) and

[79] Using Mathematica™.

Table 6.10 Displacement parameters refined for stoichiometric Cu_9Al_4 Model (Å^2).

Site	$Cu_{8.92}Al_{4.08}$	$Cu_{8.57}Al_{4.43}$
IT(A)	0.39(12)	0.58(14)
OT(A)	0.57(07)	0.54(07)
OH(A)	0.62(05)	0.48(05)
CO(A)	1.03(03)	0.92(03)
IT(B)	0.91(05)	1.48(06)
OT(B)	0.33(06)	0.22(06)
OH(B)	0.72(06)	0.94(06)
CO(B)	0.55(05)	0.47(06)
R_{wp}(%)	5.35	7.63
R_B(%)	2.16	5.23

in the regular European Powder Diffraction Conference, EPDIC 1–7 published in Materials Science Forum as well as many individual contributions to IUCr (*Acta Crystallographica and Journal of Applied Crystallography*) and other journals. Watch this space!

7

Magnetic structures

7.1 INTRODUCTION

Materials may display, as a function of temperature and applied field, a great variety of magnetic responses ranging from diamagnetism and paramagnetism through the many anti-ferromagnetic states to ferro- and ferrimagnetism (Craik 1971; Crangle 1977). In Chapters 1 and 2, we have outlined how, in some circumstances the magnetic moments of atoms (due to unpaired electron spins or electron orbitals) can become ordered into a magnetic structure.

Here we are interested only in those forms of magnetism which, due to their ordered nature, lead to the diffraction of magnetically sensitive radiations – primarily thermal neutrons. In fact, as outlined in Chapter 1, our understanding of certain kinds of magnetism is due largely to the availability of neutron diffraction. Techniques such as anomalous scattering have been used to elevate magnetic X-ray diffraction from a mere curiosity in the 1980s to a very useful adjunct to magnetic neutron diffraction. It is nonetheless still the case (at the time of writing) that neutron diffraction is the workhorse of magnetic structure investigation. Many thousands of magnetic structures have been solved using neutron diffraction to reveal a bewildering range of complex and beautiful patterns (see, e.g. Otes *et al.* 1976). There are many reasons why a basic understanding of magnetic diffraction is important to practitioners of neutron powder diffraction.

(i) The magnetic state, arising as it does from the interplay of the electronic state of the atoms, the crystal field, and thermal excitations, is central to our understanding of the solid state itself.
(ii) Magnetism is of great technological importance in power conversion, data storage and retrieval, and a range of electronic applications. An understanding of magnetic structures and phase transitions is essential underlying knowledge for the further development of technical magnets. A detailed understanding of magnetic structures and magnetic phase transitions provides invaluable input and a stringent test-bed for theories of the solid state. Although as we will see later, it is sometimes inadequate for the complete determination of complex magnetic structures, powder diffraction is an invaluable first step along the path to a magnetic structure.
(iii) Other research fields also benefit from investigations into magnetic structure. For example, in geology, paleomagnetism assists with the dating of rocks

through the regular reversal of the earth's magnetic field[80] and also with establishing the temperature history of plutonic events.

(iv) Even when the magnetic structure does not form part of the problem under study, magnetic diffraction may nonetheless be present in the neutron powder diffraction pattern and needs to be modelled in order to obtain an adequate fit to the data.

In this chapter, we will begin by briefly reviewing what we mean by a 'magnetic structure' and how it may be described. This includes a discussion of the symmetry of magnetic structures and how this may assist in their solution. Next we outline those aspects of the magnetic scattering of neutrons essential for the interpretation of powder diffraction patterns. Following this, we outline the steps involved in the solution of a magnetic structure, focusing on those where neutron powder diffraction has a significant role to play. Various experimental strategies such as *in situ* magnetic fields that may be employed to assist are discussed, as well as the limitations facing powder diffraction in the study of complex (usually not collinear) magnetic structures. As with crystal structure solution, the final stage of structure refinement is also discussed. It is assumed here that Chapter 5 has been studied in detail or that the reader is already well versed in the study of crystal structures prior to commencing this chapter.

7.2 CRYSTALLOGRAPHY AND SYMMETRY OF MAGNETIC STRUCTURES

7.2.1 Overview

Just as the regular repeating nature of the atom motif in a crystal structure may be described by a collection of symmetry elements, so too can the regular arrangement of magnetic moments within a magnetic structure be characterized according to its symmetry. However, whereas the crystal structure is fully determined once the unit cell and the coordinates (and identity) of all the atoms within it are known, the magnetic structure is at once more complex *and* simpler. As we shall see later, the magnetic neutron scattering amplitude is a *vector* quantity that depends on the relative orientation of the scattering vector and the atomic magnetic moments. This means that in addition to the location of the magnetic atoms within the unit cell, it is necessary to know the orientation (and size) of the magnetic moments on the atoms. Additional levels of complexity, and indeterminancy above those present in crystal structure determination, accrue from this. However, there are some simplifying factors that come to our aid. First, the magnetic structure overlays the crystal structure which has usually already been determined. Second, the magnetic structure only involves the magnetic atoms (or ions), usually a subset of the atoms present. The problem of describing a magnetic structure is nonetheless a challenging one.

[80] Ferromagnetic crystals cooled through their Curie temperature in a magnetic field align their magnetic structures with the external field thus recording the field direction at a particular time in history.

7.2.2 Commensurate magnetic structures

Commensurate magnetic structures are those in which there is an integer relationship between the magnetic unit cell volume and the volume of the underlying crystallographic unit cell. Even with this restriction, a great variety of structure types exist. A selection is given in Fig. 7.1 (after Fig. 1, Izyumov and Ozerov 1970).

The simplest and most familiar because it gives rise to strong remanent magnetization in technical magnets is ferromagnetism [Fig. 7.1(a)] where all of the atomic magnetic moments are aligned and all have the same size. In this case, the basic repeating unit is the same as the crystallographic unit cell.

In antiferromagnets [Fig. 7.1(b)] adjacent spins are anti-parallel leading to no net magnetization in zero field. For the simple case shown (only one magnetic atom), the magnetic unit cell is doubled in the direction of the spins compared with the crystallographic unit cell. Anti-parallel arrangements are also possible for which the cell is doubled along two or three directions and also where, if more than one type of magnetic atom is present, the magnetic unit cell can be the same as the crystallographic unit cell for anti-parallel moments.

The third of the so-called collinear magnetic structures occurs in ferrimagnetic materials. Here two or more magnetic atoms with magnetic moments of different magnitudes are arranged anti-parallel. There is a net magnetization in zero field leading to important technical applications, for example, the 'ferrites'. Ferrimagnets have magnetic unit cells that may be either the same or larger than the crystallographic unit cell.

All of the remaining arrangements of moments in Fig. 7.1 are non-collinear but nonetheless are *commensurate* with the underlying crystal structure. Triangular arrangements such as that shown in Fig. 7.1(d) almost invariably lead to unit cell multiplication as does the 'weakly ferromagnetic' arrangement in Fig. 7.1(e). Whereas the former has no net moment, the arrangement in Fig. 7.1(e) does lead to weak ferromagnetism perpendicular to the layers containing the moments. These two-dimensional representations are coplanar, the next degree of complexity after collinear structures. There are more complex examples of triangular and weakly ferromagnetic structures that are non-coplanar, that is, three-dimensional (Izyumov and Ozerov 1970). Other non-coplanar structures include 'umbrella' structures [e.g. Fig. 7.1(f) and multi-axial structures Fig. 7.1(g)]. All of the examples shown in Fig. 7.1 may be described in terms of their symmetry.

We have seen in Chapter 5 the power of space groups in describing crystal structures in the most compact way and in interpreting diffraction patterns in order to solve the structure. In order to represent magnetic structures, it turns out that only one additional symmetry operator is required. All of the rotations, reflections, and complex symmetry elements (screw axes, glide planes, and inversion axes) are equally applicable to magnetic moments as they are to atomic coordinates. The additional operation that is required is the reversal operator $\boldsymbol{R}$, which reverses the direction of the magnetic moment. This seemingly innocent operation, when combined with the standard crystallographic operations (1, 2, 3, m, $\bar{2}$, etc.), forms

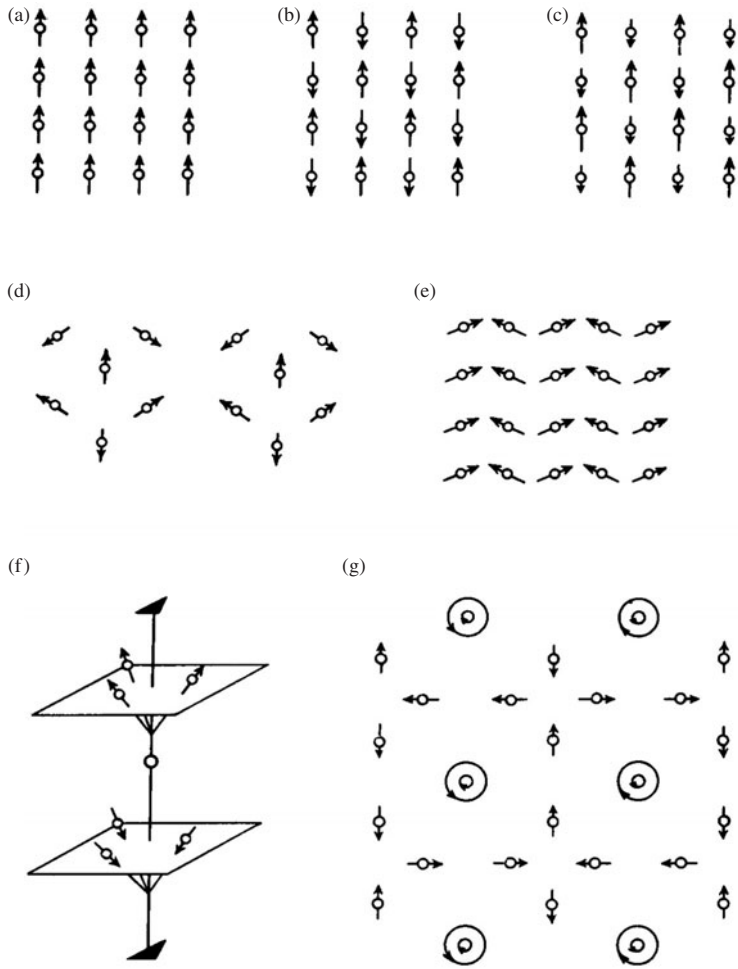

Fig. 7.1 Types of ordered magnetic structure: (a) ferromagnetic, (b) antiferromagnetic, (c) ferrimagnetic, (d) triangular, (e) weakly ferromagnetic, (f) umbrella, and (g) multiaxial (arrows perpendicular to the plane of the sketch are shown by corresponding circular currents). Reproduced with permission from Izyumov and Ozerov (1970).

a new set that includes moment reversals ($1'$, $2'$, $3'$, m', $\bar{2}'$, *etc.*). Some examples of the relationship between crystallographic and the corresponding magnetic operators are given in Fig. 7.2. These lead to 36 magnetic Bravais lattices and 1651 magnetic space groups (Shubnikov 1951; Shubnikov and Belov 1964).[81]

[81] Compared with 14 crystallographic Bravais lattices and 230 crystallographic space groups.

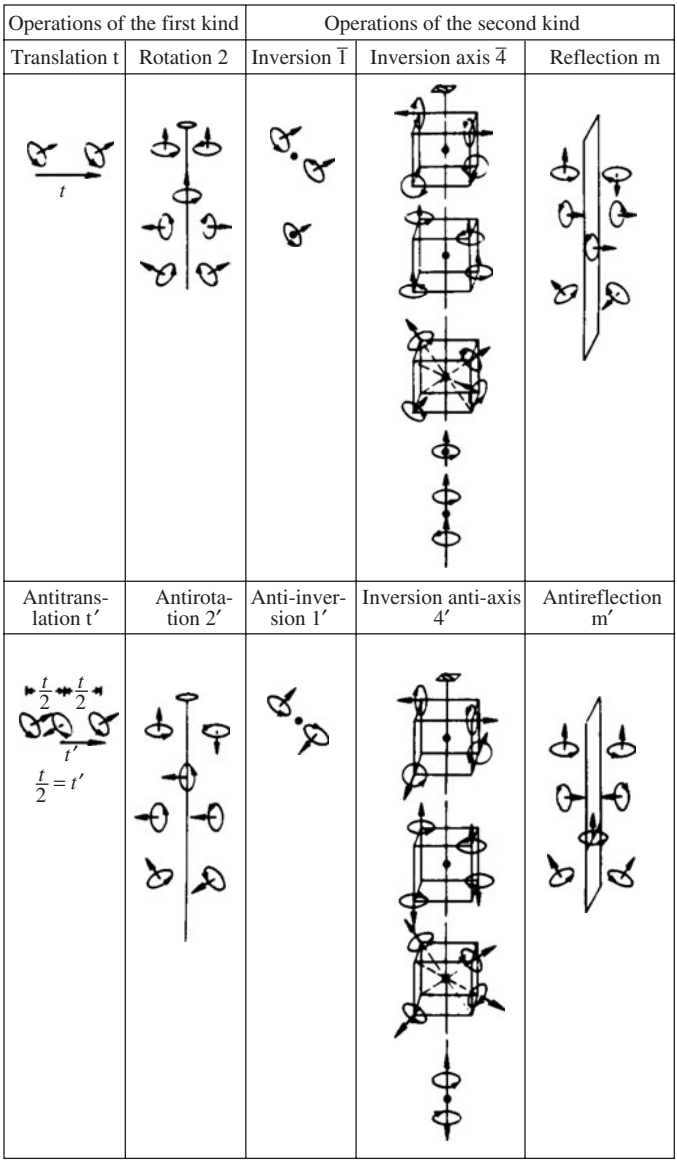

Fig. 7.2 Action of elements of symmetry and antisymmetry on magnetic moments. Reproduced with permission from Izyumov and Ozerov (1970).

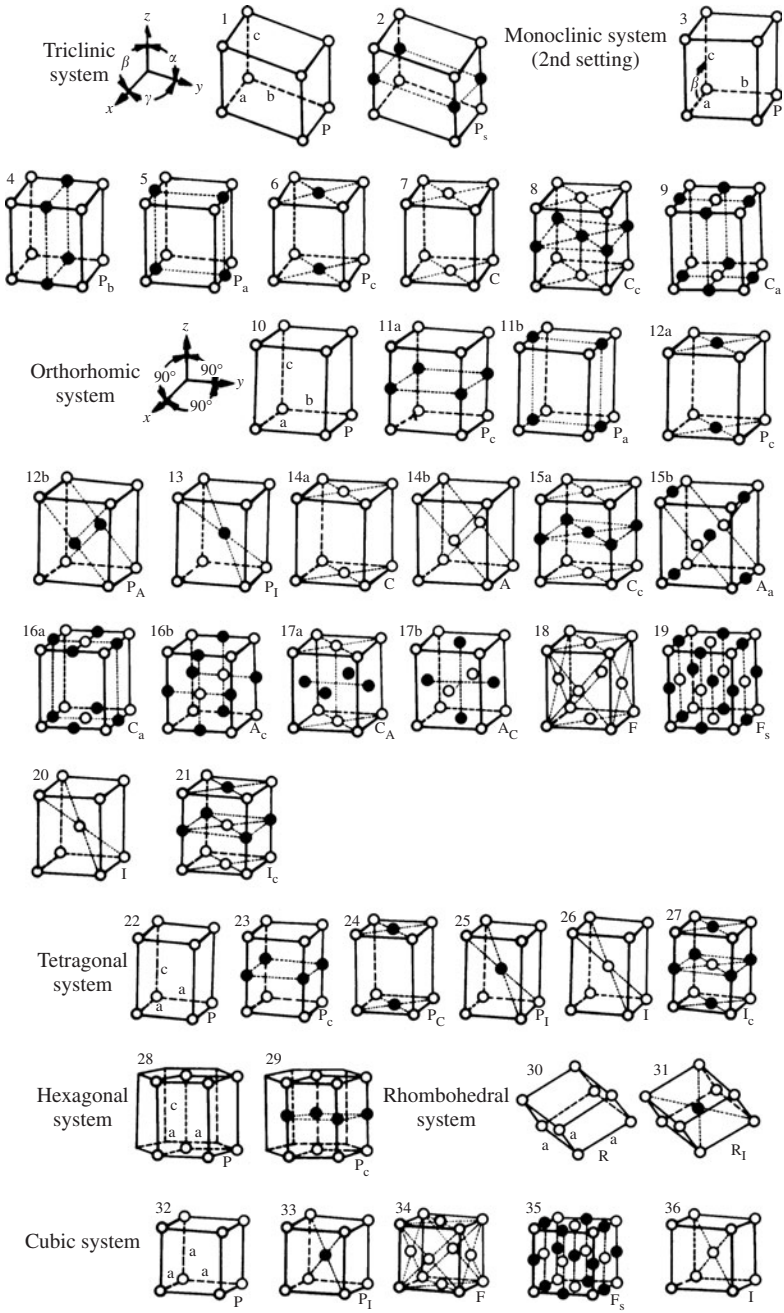

Fig. 7.3 The 36 magnetic Bravais lattices. Black and white circles refer to anti-parallel orientation of the magnetic moments (reproduced from Bacon 1975).

The 36 magnetic Bravais lattices are illustrated in Fig. 7.3 where the white and black circles are taken to have anti-parallel magnetic moments. The 14 crystallographic Bravais lattices form a subset with all-white circles. As with the crystallographic space groups, the symmetry operators lead to systematically absent diffraction peaks that are very useful in diagnosing possible structures from the diffraction pattern. For example, moment reversal (known as antitranslation) along one axis (x, say) leads to cancellation of $h00$ peaks with even values of h, that is, the magnetic reflection condition in standard nomenclature is $h00$: $h = 2n + 1$. Anti-translation along a face-diagonal (anti-face-centring), say the C-face or xy plane, leads to the reflection condition $hk0$: $h + k = 2n + 1$. Note that this is the *opposite* of the crystallographic C-face centring rule $hk0$: $h + k = 2n$ because of the moment reversal. Reflections $hk0$ with $h + k = 2n$ will in this case contain only diffraction from nuclear scattering, whereas those with $h + k = 2n + 1$ will be purely magnetic. A complete listing of the extinction[82] conditions can be found in Appendix 1 of Izyumov and Ozerov (1970). We will return to the calculation of magnetic structure factors in §7.3.

To illustrate the concepts of magnetic space groups we examine the effects of magnetic ordering in space group $C2/m$, which served as our example space group through §5.2 and §5.3. The symmetry operations in the crystallographic space group included a twofold axis perpendicular to a mirror plane, and (from successive operation of twofold rotation and mirror reflection) inversion, along with the translation operations associated with C face-centring. If we associate a magnetic moment (its direction given by a vector) with the point x, y, z then the effect of the twofold rotation around the y-axis is clear – the point is taken to $-x$, y, $-z$ and the vector changes such that its component parallel to the rotation axis is unchanged while the component perpendicular to this axis is reversed (Fig. 7.2). There is no change in the direction of this vector under the translations associated with C face-centring. The effect of the mirror plane is more subtle – the vector represents in effect the sense of a circulating charge, and it is the component of this vector parallel to the mirror plane that reverses on reflection, not the perpendicular component.[83] Inversion takes the point to $-x, -y, -z$ leaving the direction of the magnetic moment unchanged. The successive operation of twofold rotation and mirror reflection takes the point from x, y, z to $-x, -y, -z$ but reverses the direction of the magnetic moment – thus the result is no longer the inversion operation $\bar{1}$ but the 'anti-inversion' denoted $1'$. This point can be emphasized by writing the magnetic space group $C2/m1'$. The results from the additional operations $2'$ and m' are simply as for 2 and m, as described above, with the sense of the magnetic moment vector reversed. The inclusion of these operations leads to a total of four

[82] Whereas in crystallography, reflection conditions are commonly shown (e.g. *Volume A, International Tables for Crystallography*), Izyumov and Ozerov (1970) actually show extinction conditions, that is the conditions for the relevant reflections to be *absent*.

[83] A magnetic component perpendicular to the mirror plane represents circulation parallel to this plane and as such is not reversed by reflection.

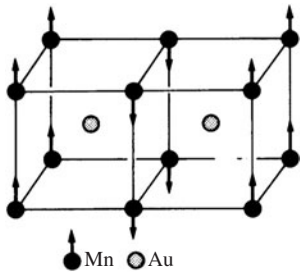

Fig. 7.4 The antiferromagnetic structure of AuMn. (From Bacon 1975).

magnetic space groups associated with crystallographic space group $C2/m$ and on the same size cell, written (in brief form) as $C2/m$ (as just described), $C2'/m'$, $C2/m'$, $C2'/m$.

By way of further illustration we consider the case of AuMn (Fig. 7.4). The chemical crystal structure is cubic (space group $Pm\bar{3}m$), with the Mn atom at the origin, and the Au at the body centre. The figure shows how the moments on the Mn atoms are ordered in the room temperature structure. It can be seen that the moments are aligned within sheets (vertical in this figure), but the moments in successive sheets are aligned in opposite directions. This reversal of magnetic moments leads to an apparently tetragonal structure, with the tetragonal axis horizontal and at double the cubic repeat. It can be seen from Fig. 7.3 that the appropriate Bravais lattice is tetragonal P_c (#23). This lattice, showing tetragonal symmetry, and a reversal of magnetic moments from one sheet to the next, represents the 'configurational symmetry' (Shirane 1959) of the structure. This is not the true symmetry however, since there is evidently only twofold symmetry of the magnetic arrangement around the apparent tetragonal axis (in the horizontal direction), and in principle the unit cell will be distorted to reflect this. The magnetic space group is found (using, for example, computer program ISOTROPY referenced in §5.8) to be P_amma, the true symmetry being orthorhombic as expected. The configurational symmetry is often a very useful simplifying assumption, in part because the determination of the direction of magnetic moments and detection of the corresponding reduction in symmetry are often very difficult.

Complete treatments of the application of magnetic symmetry groups to the solution of magnetic structures have been given by Izyumov and Ozerov (1970) and Izyumov *et al.* (1991).

Although methods based on magnetic space groups can be quite powerful in solving magnetic structures, a great many magnetic structures have been solved without making reference to symmetry groups, relying rather on intuition, experience, and trial and error methods. This is partly because the background of scientists studying magnetism is generally in physics rather than crystallography.

Another reason is the high degree of pseudo-symmetry encountered. It was recognized quite early (Shirane 1959; Cox 1972; Bacon 1975) that any ordered magnetic structure will inevitably distort the host cell thereby reducing the underlying crystallographic symmetry, but in the early days of neutron diffraction these distortions were too small to be detected. These days the actual symmetry due to the distortion can be detected using high resolution neutron diffraction or synchrotron X-ray diffraction, but for practical structure solution the configurational symmetry may still suffice.

7.2.3 Incommensurate magnetic structures

Incommensurately modulated crystal structures are relatively rare and most often occur in 'framework' structures or in complex alloys with many elements substituting on the crystallographic sites available in the underlying unit cell. One may expect the same to be true of magnetic structures, however this is not the case. Incommensurate magnetic structures are neither rare nor do they occur only in complex materials. Nowhere is the ability of the exchange interaction to override the crystal field more apparent than in the element chromium. The crystal structure of Cr is body-centred cubic leading to the expectation of either a ferromagnetic or anti-ferromagnetic arrangement (i.e. body-centre moment reversed). In fact the neutron diffraction pattern of Cr at low temperatures has a very intriguing form. Below 313 K, each nuclear diffraction peak is accompanied by magnetic 'satellite' peaks on either side. There was initially considerable controversy over the origin of these satellites (see, e.g. Bacon 1975 and references therein). Early models included a regular anti-phase domain structure with a domain size of 13 unit cells (repeat distance 26 unit cells – Fig. 7.5) and another structure in which the moments spiral about the [0 0 1] axis. The former model leads to higher order satellites, which are not observed, and the latter cannot account for a second phase transition at 153 K. Consequently, the model proposed by Shirane and Takei (1962) in which the moments are arranged antiferromagnetically but have magnitudes that vary sinusoidally with a period of 26 unit cells is now preferred. This model preserves the reversal of moments every ~13 unit cells leading to peaks in the correct *positions*, but generates only first order satellites. The phase transition at 153 K is thought to occur by rotation of the moments from perpendicular to the sinusoid axis above 153 K to parallel below 153 K. The rare-earth metals also show complex long range magnetic structures involving sinusoidal or helical variation of moments in successive layers. Alloys and compounds involving magnetic elements can also display spiral or helical magnetic structures that are usually incommensurate with the underlying crystallographic unit cell. An example is Au_2Mn (Bacon 1975) in which successive Mn containing sheets have their magnetic moments rotated by approximately 51° with respect to the previous sheet (Fig. 7.6). As we will demonstrate in §7.3.2, this kind of arrangement leads to satellite peaks at $hkl \pm \frac{2}{7}$. For example, 002 has $00\frac{12}{7}$ and $00\frac{16}{7}$, 101 has $10\frac{5}{7}$ and $10\frac{9}{7}$, etc. (Bacon 1975).

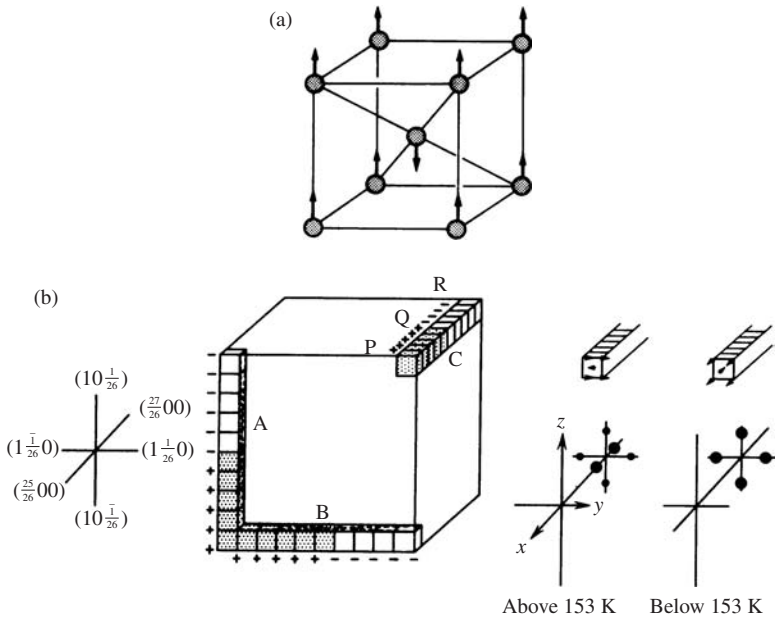

Fig. 7.5 Stages in the development of the magnetic structure of chromium (a) the basic antiferromagnetic structure and (b) the antiphase domain model indicating the arrangement of the magnetic moments and the distribution of satellite spots around the (100) position in reciprocal space, both above and below the spin-flip transition temperature of 153 K. In the final model, the size of the moments varies sinusoidally with the same period as the antiphase domain structure. From Bacon 1975.

7.3 MAGNETIC SCATTERING AND DIFFRACTION

7.3.1 Introduction

The theory of magnetic neutron scattering has been comprehensively covered in a number of monographs (Marshall and Lovesey (1971), Balcar and Lovesey (1989), and Squires (1978)). A brief overview of magnetic scattering was given in §2.3.4. We are interested here in coherent magnetic diffraction peaks in which the magnetic contribution to the differential scattering cross-section of an atom (eqn (2.18)) is p^2q^2 for an unpolarized incident beam. In the nuclear scattering case, the structure amplitude $\boldsymbol{F}_{hkl}^{\text{nuc}}$ was formed by summing the contributions from all atoms within the unit cell (eqn (2.31)). When coherent magnetic scattering occurs, the magnetic structure amplitude may likewise be written as

$$\boldsymbol{F}_{hkl}^{\text{mag}} = \sum_n p_n \boldsymbol{q}_n \exp\{2\pi i(hx_n + ky_n + lz_n)\} \tag{7.1}$$

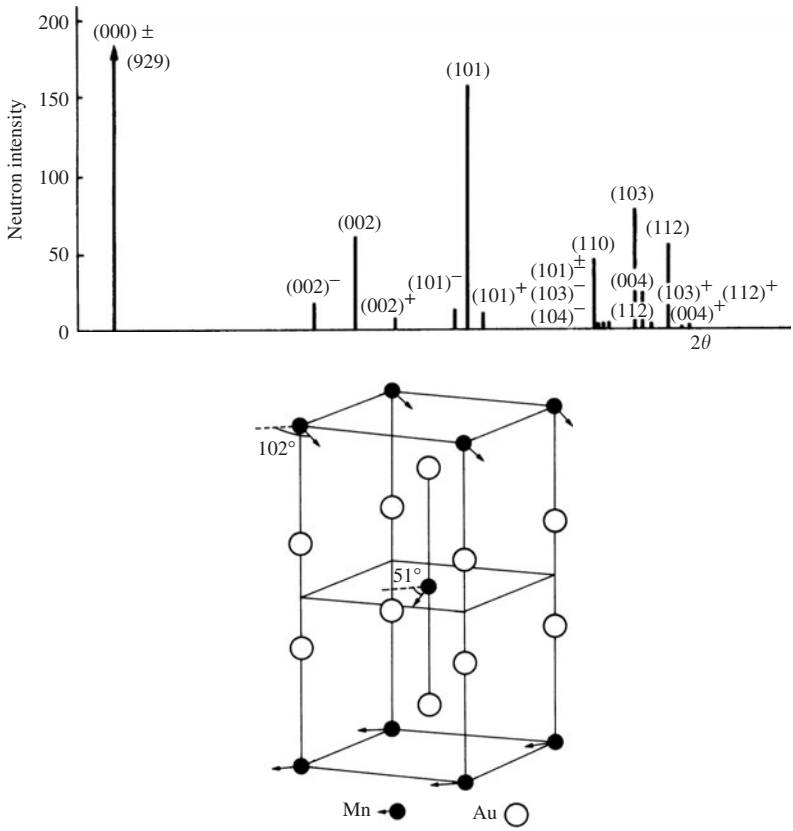

Fig. 7.6 A schematic neutron powder diffraction pattern from Au_2Mn illustrating how each nuclear reflection is flanked by a pair of satellite magnetic reflections. For example, (0 0 2) has satellites marked as (002^-) and (002^+), which index as $\left(00\frac{12}{7}\right)$ and $\left(00\frac{16}{7}\right)$. Likewise, (101) is paired by $\left(10\frac{5}{7}\right)$ and $\left(10\frac{9}{7}\right)$. Below the diffraction pattern, the structure is illustrated. The manganese moment spirals about the *c*-axis. From Bacon (1975).

where $\boldsymbol{q}_n$ is the magnetic interaction vector (defined in §2.3.4), p_n is the magnetic scattering length of *n*th atom (eqn (2.15)), and the other terms as before describe the positions of atoms within the unit cell. $\boldsymbol{F}_{hkl}^{\text{mag}}$ is a vector and the intensity of the magnetic contribution to the *hkl* peak (for unpolarized neutrons) is proportional to[84] $\left|\boldsymbol{F}_{hkl}^{\text{mag}}\right|^2$. The summation in eqn (7.1) need only be conducted over those atoms with non-zero magnetic moments. In cases where the magnetic and nuclear

[84] As with nuclear diffraction peaks, Lorentz, multiplicity and temperature factors apply.

diffraction peaks overlap, the intensity is given by simple addition:

$$\left|\sum_n b_n \exp\{2\pi i(hx_n + ky_n + lz_n)\}\right|^2 + \left|\sum_n p_n \boldsymbol{q}_n \exp\{2\pi i(hx_n + ky_n + lz_n)\}\right|^2 \tag{7.2}$$

A very important feature of magnetic diffraction is its strong angular (d-spacing) dependence. Because the magnetic scattering of neutrons is due to the electrons, the forward scattering is much stronger than the back-scattering. Interference effects within individual atoms, give rise to a form factor, f, analogous to the form factor in X-ray diffraction. In the notation used here, the form factor is introduced via the magnetic scattering length p and eqn (2.15). In general, the magnetic scattering form factor has a comparable magnitude to the nuclear scattering length (b_{coh}) at $2\theta = 0$, but it falls even more sharply than the X-ray scattering form factor. Hence the observable magnetic peaks are limited to a relatively restricted 2θ or d range. It is fortunate that as additional complexity occurs in the magnetic structure, the unit cell size increases and more peaks are generated in the long d-spacing region where the magnetic scattering length is appreciable.

7.3.2 Commensurate magnetic structures

The intensities of the magnetic peaks for commensurate structures can be computed in a straightforward manner using eqns (7.1) and (7.2). Take as an example, the antiferromagnetic structure of MnAu shown earlier in Fig. 7.4. The pseudo-tetragonal cell has dimensions $a \times 2a \times a$ where a is the edge of the cubic chemical cell, and relative to this cell the atom positions are: Mn↑ at (0, 0, 0), Mn↓ at (0, 1/2, 0), Au at (1/2, 1/4, 1/2), and (1/2, 3/4, 1/2), where the up and down arrows convey the magnetic moment directions. It is clear from its definition that $\boldsymbol{q}_n$ changes sign when the magnetic moment is reversed – it is here in fact zero for reflections like $00l$ ($\hat{\boldsymbol{\kappa}} \,//\, \hat{\boldsymbol{\mu}}$) and has magnitude 1 for reflections $h00$ and $0k0$ ($\hat{\boldsymbol{\kappa}} \perp \hat{\boldsymbol{\mu}}$). The scattering amplitude for the nuclear contribution is

$$\begin{aligned}
\boldsymbol{F}_{hkl}^{\text{nuc}} &= \sum_n b_n \exp\{2\pi i(hx_n + ky_n + lz_n)\} \\
&= \left[e^{2\pi i 0} + e^{2\pi i k/2}\right]\left[b_{\text{Mn}} + b_{\text{Au}} \exp\left\{2\pi i\left(\frac{h}{2} + \frac{k}{4} + \frac{l}{2}\right)\right\}\right] \\
&= 0 \quad \text{for } k \text{ odd} \\
&= 2\,(b_{\text{Mn}} + b_{\text{Au}}) \quad \text{for } h + \frac{k}{2} + l \text{ even} \\
&= 2\,(b_{\text{Mn}} - b_{\text{Au}}) \quad \text{for } h + \frac{k}{2} + l \text{ odd}
\end{aligned} \tag{7.3}$$

On the other hand, the magnetic scattering amplitude (taking into account the reversal of the sign of $\boldsymbol{q}$ between Mn at 0, 0, 0 and 0, 1/2, 0)) is

$$\boldsymbol{F}_{hkl}^{\text{mag}} = \sum_n p_n \boldsymbol{q}_n \exp\{2\pi i(hx_n + ky_n + lz_n)\} = \left[e^{2\pi i 0} - e^{2\pi i k/2}\right] p_{\text{Mn}} \boldsymbol{q}_{\text{Mn}}$$

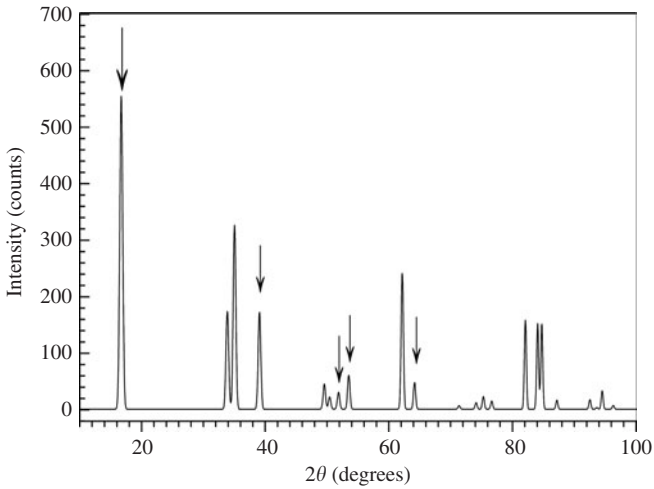

Fig. 7.7 Neutron powder diffraction pattern for AuMn calculated at wavelength $\lambda = 1.5$ Å. The major magnetic diffraction peaks are arrowed.

$$= 0 \quad \text{for } k \text{ even}$$
$$= 2p_{\mathrm{Mn}}\boldsymbol{q}_{\mathrm{Mn}} \quad \text{for } k \text{ odd} \tag{7.4}$$

As shown in Fig. 7.7, this is a case in which the peaks with k even are purely nuclear, and those with k odd purely magnetic, a circumstance which greatly assists in their separation. Several of the prominent powder diffraction Rietveld refinement codes can handle magnetic structures as well as crystal structures (e.g. GSAS, FULLPROF, RIETAN).

7.3.3 Incommensurate structures

The most common form of incommensurate magnetic structures are the helimagnetic structures. In these materials, the magnetic moments are uniform within planes and the direction of the moments is rotated a fixed amount between successive planes. This defines a spiral propagation direction perpendicular to the planes of magnetization such as in the Au_2Mn example depicted in Fig. 7.6. At first, it may seem as though the computation of the intensities of the magnetic peaks due to such a structure is intractable because the lack of a unit cell means the sums in eqn (7.1) must be over all magnetic atoms in the crystal. However, methods for handling this problem have been known for several decades. The treatment given here is an abbreviation of that given by Bacon (1975).

Consider the generalized helimagnetic structure with a spiral axis inclined to the diffraction plane (Fig. 7.8). By substituting eqns (2.15) into (7.1) we

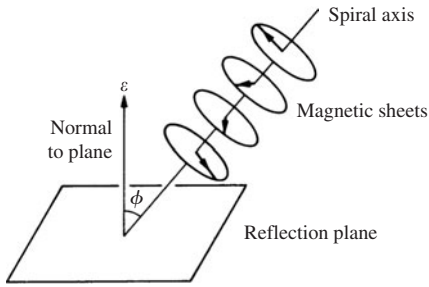

Fig. 7.8 General case of a helimagnetic structure in which the spiral axis is inclined with respect to the normal to the diffracting plane (ε) by an angle φ. From Bacon (1975).

obtain

$$\boldsymbol{F}_{hkl}^{\text{mag}} = \frac{e^2\gamma}{m_e c^2} \sum_n \boldsymbol{q}_n S_n f_n \exp\{2\pi i(hx_n + ky_n + lz_n)\} \tag{7.5}$$

Recall that the magnetic interaction vector may be written as

$$\boldsymbol{q}_n = \hat{\boldsymbol{\mu}}_n - \left(\hat{\boldsymbol{\kappa}} \cdot \hat{\boldsymbol{\mu}}_n\right) \hat{\boldsymbol{\kappa}} \tag{7.6}$$

where $\hat{\boldsymbol{\kappa}}$ and $\hat{\boldsymbol{\mu}}_n$ are unit vectors parallel to the scattering vector (thus perpendicular to the reflecting planes) and the magnetic moment of the atom respectively. Substituting into eqn (7.5) gives

$$\boldsymbol{F}_{hkl}^{\text{mag}} = \frac{e^2\gamma}{m_e c^2} \sum_n \{\hat{\boldsymbol{\mu}}_n - (\hat{\boldsymbol{\kappa}} \cdot \hat{\boldsymbol{\mu}}_n)\hat{\boldsymbol{\kappa}}\} S_n f_n \exp\{2\pi i(hx_n + ky_n + lz_n)\} \tag{7.7}$$

or, by replacing $\boldsymbol{\mu}_n S_n$ by $\boldsymbol{S}_n$ – the spin expressed as a vector:

$$\boldsymbol{F}_{hkl}^{\text{mag}} = \frac{e^2\gamma}{m_e c^2} \sum_n \{\boldsymbol{S}_n - (\hat{\boldsymbol{\kappa}} \cdot \boldsymbol{S}_n)\hat{\boldsymbol{\kappa}}\} f_n \exp\{2\pi i(hx_n + ky_n + lz_n)\} \tag{7.8}$$

Next the vector $\boldsymbol{S}_n$ is resolved into two components: $\boldsymbol{S}_\kappa$ parallel to the scattering vector and $\boldsymbol{S}_P$ in the plane of diffraction.[85] For the parallel component $\boldsymbol{S}_\kappa - \left(\hat{\boldsymbol{\kappa}} \cdot \boldsymbol{S}_\kappa\right) \hat{\boldsymbol{\kappa}}$ is zero, whereas for the component in the diffraction plane $\hat{\boldsymbol{\kappa}} \cdot \boldsymbol{S}_P$ is zero, hence eqn (7.8) becomes

$$\boldsymbol{F}_{hkl}^{\text{mag}} = \frac{e^2\gamma}{m_e c^2} \sum_n \boldsymbol{S}_P f_n \exp\{2\pi i(hx_n + ky_n + lz_n)\} \tag{7.9}$$

Now we must introduce the effect of the spiral axis, taking into account the angle ϕ it makes with the normal to the reflecting plane (scattering vector). The plane of magnetic moments makes the same angle ϕ with the reflecting planes (Fig. 7.9). We take the intersection of these planes to define a common axis OX, and we suppose the spin $\boldsymbol{S}_n$ (represented by OP) makes an angle $\alpha + \xi$ with this common

[85] That is, in the reflecting plane.

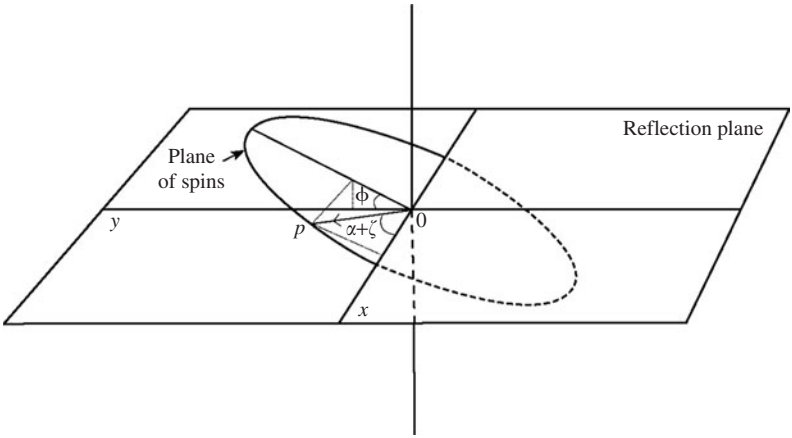

Fig. 7.9 Illustration of the geometry of diffraction from a spiral magnetic structure used in the discussion of eqns (7.10)–(7.15).

axis, where ξ is the angle that the moments are rotated between successive sheets in the spiral structure and α is an arbitrary angle. The magnitude of the component of $\boldsymbol{S}_n$ along OX is evidently:

$$S_x = S_n \cos(\alpha + \xi) \tag{7.10}$$

Within the plane of the spins, the component perpendicular to this is $S_n \sin(\alpha+\xi)$, and its projection onto the diffraction plane lies along OY and has magnitude

$$S_y = S_n \cos\phi \sin(\alpha + \xi) \tag{7.11}$$

Assuming that the magnetic atoms all have the same (magnitude of) spin and form factor, substituting into eqn (7.9), and squaring gives

$$\left|\boldsymbol{F}_{hkl}^{\text{mag}}\right|^2 = \left(\frac{e^2\gamma}{m_e c^2}\right)^2 \frac{S^2 f^2}{4} \times \left(\begin{array}{l} \left|\sum \exp\{i(\alpha+\xi) + 2\pi i(hx_n + ky_n + lz_n)\} \right. \\ \quad \left. + \exp\{-i(\alpha+\xi) + 2\pi i(hx_n + ky_n + lz_n)\}\right|^2 + \cos^2\phi \\ \left|\sum \exp\{i(\alpha+\xi) + 2\pi i(hx_n + ky_n + lz_n)\} \right. \\ \quad \left. - \exp\{-i(\alpha+\xi) + 2\pi i(hx_n + ky_n + lz_n)\}\right|^2 \end{array} \right) \tag{7.12}$$

Diffraction peaks will be observed for values *hkl* that lead to reinforcement of the scattered waves. Note that unlike the crystal Bragg peaks, *hkl* here need not be integers. Reinforcement will occur if either

$$(\alpha + \xi) + 2\pi(hx_n + ky_n + lz_n) \quad \text{or} \quad (\alpha + \xi) - 2\pi(hx_n + ky_n + lz_n) \tag{7.13}$$

has the same value for all the magnetic atoms in a sheet, *and* this value changes by an integer (or zero) from one sheet to the next. The first condition is satisfied for any *hkl* leading to reciprocal lattice positions displaced from the integer or crystallographic reciprocal lattice points in a direction perpendicular to the magnetic sheets (parallel to the spiral axis). The second condition is then satisfied if the magnetic diffraction reciprocal lattice points are displaced an amount dictated by the equality:

$$\Delta[2\pi(hx_n + ky_n + lz_n)] = \pm\xi \tag{7.14}$$

The simple example of Au_2Mn (Bacon 1975) shown in Fig. 7.6 is very instructive. Its underlying crystal structure is tetragonal with single Mn layers separated by double Au layers. The Mn repeat distance is $^1/_2c$ and the moments are confined to the *ab* plane. This leads to satellite peaks displaced from the crystallographic position by a reciprocal lattice vector $(00\Delta l)$.[86] The size of the displacement will be given by

$$\xi = 2\pi\Delta l \cdot \frac{1}{2} \tag{7.15}$$

$$\text{or} \quad \Delta l = \frac{\xi}{\pi}$$

Experimentally, the value of Δl is approximately 2/7, that is, the diffraction pattern contains magnetic peaks at $hkl\pm2/7$ (Fig. 7.6). Substituting $\Delta l = 2/7$ into eqn (7.15) gives $\xi = 51°$ as the rotation angle between the moments on successive Mn planes. It should be noted that commensurate spiral structures can occur as a special case when the rotation angle ξ divides 360 integrally, for example, Au_2MnAl. Here the rotation angle between moments on successive Mn planes is 45°, and the structure can be described by quadrupling of the *a*-axis.

A rapid method for estimating the intensity of satellite reflections predicted for a spiral structure is to note that they are related to the expected intensity for a ferromagnetic peak (i.e. $\Delta h = \Delta k = \Delta l = 0$) by a factor $1/4(1+\cos^2\phi)$(see eqn (7.12)). Therefore the $00l$ peak of the Au_2Mn example, with $\phi = 0$ is expected to have satellites with 50% of the ferromagnetic intensity expected if all the Mn moments were aligned. On the other hand, $hk0$ peaks with $\phi = 90°$ are expected to have satellites with 25% of the ferromagnetic intensity.

An important factor in magnetic diffraction from spiral structures is that the forward scattering peak 0 0 0 also develops satellites. Therefore for Au_2Mn, a peak indexing as approximately 0 0 2/7 occurs close to the straight through beam. Such very large *d*-spacing peaks are very important in determining magnetic structures.

[86] The first condition arising from eqn (7.13) compels the satellites to lie along the *c*-axis.

7.4 SOLVING MAGNETIC STRUCTURES

7.4.1 Overview

Just as the solution of an unknown crystal structure using powder diffraction data must proceed in stages (indexing, trial structures, refinement, etc.) and relies upon input from other techniques; so too does the solution of a magnetic structure. The four stages in this case have been outlined by Izyumov and Ozerov (1970) as

(i) Determination of magnetic properties
(ii) Observation of magnetic ordering
(iii) Determination of the orientation of magnetic moments
(iv) Determination of the magnitude of magnetic moments

The first stage is not sensibly undertaken with diffraction measurements but rather with sensitive magnetization and susceptibility measurements as a function of state variables – principally temperature. From this it should be apparent whether the material is paramagnetic, ferromagnetic, ferrimagnetic, anti-ferromagnetic, or has more complex behaviour. The latter three stages are all usually undertaken using neutron diffraction, in some cases assisted by high resolution synchrotron X-ray diffraction. Neutron powder diffraction has a contribution to make to all three. It should be understood, however, that because of the loss of orientational information using polycrystalline samples, many magnetic structures cannot be uniquely solved without single crystal data. Nonetheless, a great deal of information can be obtained using powder diffraction as will be briefly outlined below.

7.4.2 Magnetic ordering

In §7.2 we briefly reviewed the types of magnetic structures and their symmetry. The determination of the magnetic ordering type makes use of the principles outlined in §7.2 applied to the observed diffraction pattern. As noted in §7.2.2, ferromagnetic materials have identically sized magnetic and crystallographic unit cells, meaning that the magnetic powder diffraction peaks lie directly over those due to nuclear scattering. If a diffractometer of sufficient resolution is used, the distortion of the unit cell due to the onset of magnetization may be resolvable. The presence of magnetic diffraction can be established by

(a) recording data at several temperatures above and below the Curie temperature or
(b) applying an external magnetic field

In the first method, the data recorded just above the Curie temperature may be subtracted from the patterns recorded below after suitable correction for thermal expansion and, if the temperature interval is great, the thermal vibration factor. Care must be exercised because diffuse magnetic scattering may persist for more than 100 K above the Curie temperature leading to errors if the data are recorded at low resolution. Fortunately most modern diffractometers can readily distinguish

Bragg peaks from diffuse scattering. In the second method, a large magnetic field parallel to the scattering vector suppresses the magnetic diffraction peaks allowing their magnitude to be determined by subtraction.

The presence of magnetic diffraction peaks at only the same positions as peaks due to the underlying crystal structure, however, does *not* confirm ferromagnetism. This situation can also occur in anti-ferromagnetic and ferrimagnetic materials either because the magnetic ordering does not lead to any new peaks, or because of systematic or accidental absences. There will, however, be intensity differences between the diffraction patterns of these and genuine ferromagnets as well as distinct differences in the magnetic properties determined in stage (i).

In a majority of magnetically ordered materials other than ferromagnets (anti-ferromagnets, ferrimagnets, etc.) the magnetic unit cell is larger than the crystallographic cell leading to additional peaks in the powder diffraction pattern. As with any structure solution from powder data, we must begin by indexing the peaks (see §4.4 and §6.2). The indexing problem is often far simpler for magnetic peaks since they must have some relationship to the crystallographic peaks. For example cell-doubling along the c-axis of a tetragonal material will lead to magnetic peaks that index with $l = 1/2$, 3/2, 5/2, etc. Doubling along all three axes is revealed by peaks that index as $h/2$, $k/2$, $l/2$. Therefore, once indexed, it is possible to define a magnetic unit cell and its relationship to the underlying crystallographic cell. If the magnetic structure is incommensurate with the crystal structure (§7.2.3) the magnetic peaks will be arranged as satellites around the non-magnetic Bragg peaks (§7.3.3). Indexing should then be attempted on the basis of small departures from the crystal Bragg peaks – first along a particular crystal axis, then in oblique directions if necessary. Clearly single crystal data mapping the positions of the magnetic reflections in three-dimensional reciprocal space is extremely advantageous here; however, good progress may be made with powder diffraction if the structure is not too complex.

Next it is advantageous to examine which of the magnetic reflections allowed by the trial magnetic unit cell are present and which are absent. As noted in §7.2.2, the systematically absent magnetic reflections can substantially reduce the number of possible magnetic (Shubnikov) space groups to be considered for commensurate structures in the configuration symmetry approximation (i.e. assuming that the underlying crystallographic unit cell remains undisturbed).

An example from the early literature (Abrahams and Williams 1963) widely used in texts (e.g. Izyumov and Ozerov 1972; Bacon 1975) is $LiCuCl_3 \cdot 2H_2O$ which has the crystallographic space group $P2_1/c$. This structure is antiferromagnetic below 6.5 K, as witnessed by the appearance of intensities indexing as $00l$ with $l = 2n + 1$, such reflections being otherwise absent on account of the c-glide (see Table 5.5). The most promising Shubnikov subgroups are $P_a2_1/c, P_b2_1/c$, P_C2_1/c, $P2_1'/c$, $P2_1/c'$, and $P2_1'/c'$. Those belonging to magnetic Bravais lattices P_a, P_b, and P_C were discarded because they either gave no magnetic scattering at all (P_a) or because they would imply magnetic superlattice reflections, when no such reflections were seen. This leaves the four Shubnikov groups $P2_1/c$, $P2_1'/c$,

$P2_1/c'$, and $P2'_1/c'$ which were then used to generate trial structures.[87] In most cases, the final structure is only able to be solved following detailed structure factor calculations (§7.3).

7.4.3 The orientation of the magnetic moments

The analysis so far has produced a set of possible Shubnikov groups within which there is considerable freedom in the orientation of the basis moment to which all the other moments are related by symmetry. Three methods are used in powder diffraction to determine the orientation of the basis moment(s). First, as noted by Izyumov and Ozerov (1970), in some magnetic structures there may be accidental or non-systematically absent peaks allowed by the space group but which have a structure factor near zero. Such reflections are very powerful in highlighting the orientation of the moments. Examples include the situation when all of the moments are perpendicular to the diffracting planes (i.e. parallel to the scattering vector) then $\boldsymbol{q}_n$ is zero so there is no magnetic diffraction peak.

The second method is through matching the calculated intensities with observation. Recalling that $\boldsymbol{q}_n$ has magnitude 1 for moments within the diffracting planes, and given enough magnetic peaks of measurable intensity, the orientation of the moments can be readily deduced from a single-domain single crystal. This is also generally the case for low-symmetry structures using powder diffraction. However, as the symmetry increases, the problem of determining the moments using powder diffraction becomes indeterminate. This is because within the powder diffraction pattern, diffraction from all planes with the same d-spacing is superimposed. Since in general each type of plane will have differently oriented moments, the observed intensity is the average over all orientations. The situation is worst for cubic symmetry where the averaging leads to a scalar, 1/3. In this case no information concerning the directions of the moments is directly available from the intensities of the powder diffraction peaks although other methods may still provide the answer (see above and below). For tetragonal and hexagonal structures with a strong symmetry axis, the averaged intensity depends on the angle of the moments to the c-axis and so this angle (but not the absolute orientation) may be determined. For rhombohedral and lower symmetries, if there are enough observable magnetic peaks, the complete orientation of the moments can be derived.

The third method of finding the orientation of the moments is through the use of a magnetic field. Within a powder or polycrystalline sample, only a small proportion of the crystallites, those with planes of the appropriate d-spacing oriented perpendicular to the scattering vector, contribute to a given diffraction peak. These crystallites are, however, randomly distributed with respect to rotation about the scattering vector. Superimposed on this is the magnetic structure and so the magnetic moments are randomly distributed over all equivalent directions of easy

[87] These days, the solution might be facilitated by making use of a computer program such as ISOTROPY.

magnetization. For example, in Ni metal the easy magnetization direction (i.e. direction of spontaneous magnetization) is [1 1 1] and so the 110 peak will contain overlapped diffraction (nuclear + magnetic) from the (1 1 0), (1 0 1) and (0 1 1) planes each of which has four possible ⟨1 1 1⟩ directions within it (e.g. (1 1 0) has $\pm[\bar{1}\,1\,1]$ and $\pm[1\,\bar{1}\,1]$. The effect of averaging over all of these orientations is that the magnetic contribution is smaller than for a single domain single crystal. A magnetic field applied along the scattering vector will begin to rotate moments that were initially unfavourably oriented with respect to the field, towards alignment with the field. Since moments aligned with the scattering vector do not contribute to magnetic diffraction, *all* of the magnetic diffraction will be reduced. However, because of the magneto-crystalline anisotropy energy, the peak corresponding to the scattering vector aligned with the easy magnetization direction (i.e. [1 1 1] for Ni) will decrease in intensity more rapidly with increasing external magnetic field. Therefore, in high symmetry materials with unknown moment orientations, diffraction patterns recorded at varying field strengths can highlight the orientation of the basis moment. By symmetry analysis and pattern simulation (or structure factor calculation) the entire magnetic structure can be solved. An example is shown in Fig. 7.10 where it may be seen that in HoN, the moments lie along [1 0 0] and in TbN the moments are along [1 1 1].

It should be noted that some practical difficulties may occur in attempting to apply method three. The first is that a loose magnetic powder in a magnetic field will suffer *physical* rotation of the powder particles at far lower fields than that required to rotate the magnetic moments within the powder particles. To avoid this, a polycrystalline solid is preferred to a powder. If powders are used they should be tightly packed into a sealed container or compressed into a pellet using

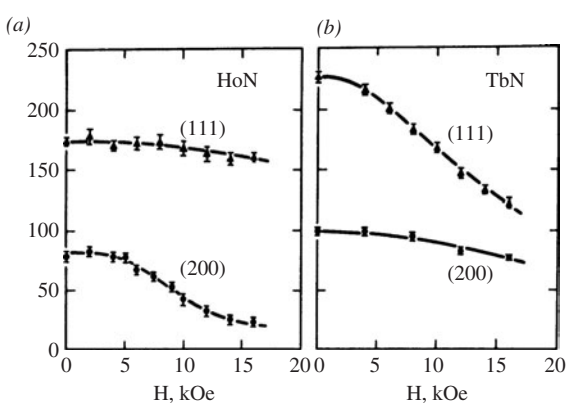

Fig. 7.10 Intensity of the magnetic maxima in the powder neutron diffraction patterns of (a) HoN and (b) TbN as a function of magnetic field parallel to the scattering vector (Child *et al.* 1963).

a die. It might be argued that physical rotation of the powder particles is independent confirmation of the direction of the moments. This is the case for very simple structures such as Ni; however, the rotation of the powder causes such severe preferred orientation in the diffraction pattern that quantitative analysis of the data is compromised.[88] Therefore, whereas it can provide useful diagnostic information, careful work requires that the powder particles remain in the same orientation throughout the experiment. The second difficulty relates to the diffractometer configuration. The application of a magnetic field parallel to the scattering vector on a modern multi-detector CW diffractometer is not very practical. Most of the detection capability of the instrument has to be discarded and a single detector used either to scan individual peaks with the magnet re-positioned for each or in a θ–2θ scanning arrangement.[89] Time-of-flight instruments have distinct advantages as the scattering vector direction is the same for all diffraction peaks and the use of, say, 90° detector banks allows plenty of space for the installation of magnets. Unfortunately, many TOF instruments are designed for crystallographic applications and have very low flux at large d-spacing, OSIRIS at the ISIS facility being an exception.

The special case of incommensurate structures deserves some mention here. Structures involving modulation of the size of the magnetic moments (e.g. Cr metal) or both their size and direction (e.g. some rare-earth metals) are generally intractable using powder diffraction. Spiral structures are difficult but in some cases solvable with polycrystalline samples. The major method for determining the orientation of the moments is by computing intensities for various models (i.e. method 2). First, the underlying order type is examined, that is, do the satellites occur adjacent to crystallographic diffraction peaks (underlying ferromagnetic order) or absent peaks (underlying anti-ferromagnetic order). Then the rotation angle ξ may be determined using eqns (7.12)–(7.15) or equivalent. If the moments are canted with respect to the spiral axis, they may be resolved into a component perpendicular to the spiral leading to satellites and a component parallel leading to a ferromagnetic contribution to the crystallographic peaks. Method three – an applied magnetic field, must then be used to isolate the ferromagnetic contribution for inclusion in the intensity calculations. Clues as to the orientation of the spiral axis are present in the diffraction pattern as noted in the discussion after eqn (7.15). The satellites will be most intense (after correction for the form factor f) around that diffraction peak (or direction) for which the scattering vector is closest to parallel to the spiral axis.

Two final cautionary notes are required to complete this section. First, in most magnetic structure types, the multiplicity factor used in crystallographic powder diffraction calculations is invalid because not all of the planes that are equivalent

[88] Especially the separation of nuclear and magnetic scattering and the determination of the magnitude of the moments which relies upon it.

[89] That is to say the sample and magnet are scanned simultaneously with the 2θ detector scan, but through half the angle.

in the crystal structure remain equivalent in the magnetic structure. It is advisable to compute the contribution of each plane rather than rely on a multiplicity, at least in the early stages of a structure solution, unless one is confident that profile simulation or other software being used has been correctly coded to take this into account. The second note is that the absolute direction of the moments (i.e. [1 1 1] vs. $\left[\bar{1}\,\bar{1}\,\bar{1}\right]$) cannot be determined with the unpolarized neutrons commonly used for powder diffraction.[90]

7.4.4 The magnitude of the magnetic moments

The magnetic moment of an atom $\boldsymbol{\mu}$ enters the intensity equation (7.2) through both the geometric factor $\boldsymbol{q} = \hat{\boldsymbol{\mu}} - \left(\hat{\boldsymbol{\kappa}} \cdot \hat{\boldsymbol{\mu}}\right)\hat{\boldsymbol{\kappa}}$ and the magnetic scattering length p. Its magnitude varies from material to material because of variations in the exchange interaction. Hence, in the computation of intensities, the magnitude of $\boldsymbol{\mu}$ remains a variable until quite late in the structure solution. This problem can be circumvented in the earlier stages by using an arbitrary value for μ based on previous values obtained for the same element or ion in a similar crystallographic environment. Trial structures may then be evaluated on the basis of relative intensities either as individual peaks or by whole-pattern fitting using an arbitrary scale-factor. Once the basic details of the magnetic structure have been established though, the magnitudes of the atomic moments are important in the overall study of magnetism and should be computed. This is done by an absolute scaling against the nuclear (or crystallographic) peaks. The connection is made via the magnetic scattering length defined in eqn (2.15).

$$p = \left(\frac{e^2\gamma}{2m_e c^2}\right) gJf \tag{2.15}$$

which, after substitution of fundamental constants, becomes

$$p = 5.4gJf \text{ fm} \tag{7.16}$$

Values for g and J (or S) are available from the theory of magnetism (see, e.g. Crangle 1977). The form factor, f, in the spherical approximation to magnetization, is available in compilations (*International Tables for Crystallography*, Volume C, 2006, E. Prince (ed.)). There has been considerable effort to determine more detailed (non-spherical) forms of f and the corresponding magnetization density (e.g. Shull and Yamada 1962); however, there is no currently implemented method to readily use this data in the computation of powder diffraction intensities and given the averaged nature of powder diffraction, it is doubtful that any additional insight into magnetic structures would be obtained thereby.

[90] The use of polarized incident neutrons for powder diffraction is certainly less common, but could be helpful in addressing this problem.

7.5 RECENT EXAMPLES

Despite the several cautionary notes made within the preceding sections, a large number of magnetic structures determined using neutron powder diffraction are published each year. The advent of higher resolution diffractometers (e.g. HRPD at ISIS and D2B at ILL) and especially the complementary use of synchrotron X-ray powder diffraction to determine the subtle distortions of the underlying crystal structure due to the phase transition to the magnetic state have revived the field. The following examples represent a small sample of the kinds of problems recently published.

7.5.1 Intermetallic compounds

Intermetallic compounds, representing the next level of complexity from the simple ferromagnetic metals, have had their magnetic structures studied intensively for more than half a century. Nonetheless, with over 80 metallic elements, there is a bewildering range of compounds for study. An example is the Laves phase $TbCo_2$ which undergoes a paramagnetic–ferromagnetic transition on cooling below ~240 K (Ouyang *et al.* 2005). The transition is accompanied by a slight rhombohedral distortion that makes the two Co atoms non-equivalent. The direction of the magnetization [1 1 1] was revealed by the rhombohedral distortion and the strategy for magnetic structure refinement was to obtain the nuclear structure by using only data recorded between 100 and 160° 2θ ($\lambda = 2.4699$ Å) in the initial refinements. This strategy has universal applicability since the magnetic contribution is negligible above 100° 2θ for this wavelength. The diffraction patterns above and below the transition are illustrated in Fig. 7.11. Despite becoming non-equivalent, the two Co atoms nonetheless retain approximately the same magnitude moment. The Co and Tb are antiferromagnetically coupled (Fig. 7.12) with [1 1 1] moments drawn.[91]

Intermetallic compounds are capable of being modified by the absorption of interstitial solutes (H, C, O, N, B). Hydrides in particular have received much attention due to their potential for energy storage and H storage in renewable energy cycles. The absorption of H into an intermetallic compound causes considerable lattice expansion and hence interacts strongly with the magnetic structure.

However, intermetallics, which absorb large quantities of H, fracture into fine powders which must therefore be studied using powder diffraction. Recent work (Paul–Bancour *et al.* 2004) on the Laves phase system $YFe_2(D_{1-x}H_x)_{4.2}$ has revealed that, following the rhombohedral distortion (similar to $TbCo_2$) there is a monoclinic distortion. A useful strategy was to use a value of $x = 0.64$ at which the D ($b = 6.671$ fm) and H ($b = -3.741$ fm) coherent nuclear scattering lengths

[91] Ouyang *et al.* (2005) assume that the moments on all atoms are parallel to [1 1 1]. Our own analysis, using ISOTROPY, suggests that for one of the two Co atoms, this is not necessarily the case.

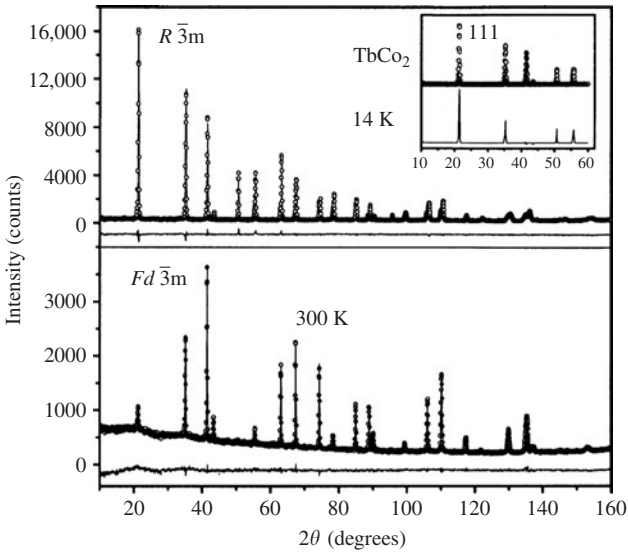

Fig. 7.11 Neutron powder diffraction patterns from $TbCo_2$ above and below the magnetic phase transition. From Ouyang *et al.* (2005).

average to zero. Among the many interesting structures observed is a helimagnetic structure with a rotation angle of $\pi/4$ leading to a strong magnetic reflection at $d = 23.5$ Å as illustrated in Fig. 7.13.

Many other studies of the magnetic structure of intermetallics using neutron powder diffraction are available in the literature. There is such a large body of established magnetic structures for intermetallics that starting structures appear to be most often determined by analogy with a known structure rather than an analysis of the magnetic symmetry groups.

7.5.2 Silicides and germanides

There has been considerable recent interest in the magnetic structures of intermetallic compounds containing the semi-metals Si and Ge: here termed silicides and germanides to differentiate them from wholly metallic compounds (e.g. Eriksson *et al.* 2004; Schobinger-Papamantellos *et al.* 2004; Gil *et al.* 2004). These materials adopt a variety of magnetic structures (some of which are still controversial) including: collinear structures with moments along the c-axis in $HoCu_{33}Ge_2$ and moments parallel to the a-axis in $ErCu_{25}Ge_2$ (Gil *et al.* 2004); in Mn_3IrGe non-collinear Mn moments in somewhat arbitrary directions (e.g. $[1.4\ 2.4\ \bar{2}]$), the moment directions on equivalents being determined by the action of the three- and twofold rotation axes of the crystallographic space group $P2_13$ (Eriksson *et al.*

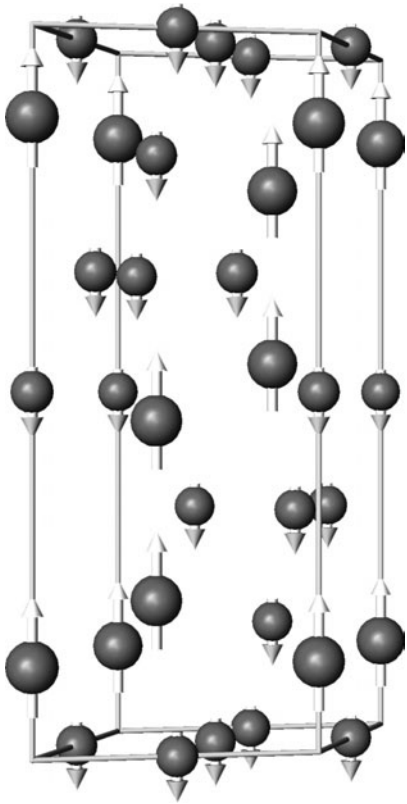

Fig. 7.12 Magnetic structure of $TbCo_2$ as determined by Ouyang *et al.* (2005).

2004); and most demanding for powder diffraction, incommensurately modulated structures in DyCuSi and HoCuSi (Schobinger-Papamantellos *et al.* 2004). The structure of these latter compounds and the related phases TbCuSi and TmCuSi has been the subject of some disagreement. The latest data from Schobinger–Papamantellos *et al.* (2004) suggest the existence of at least two independent wave-vectors. This was established using the very important peaks within the first Brillouin zone, that is, satellites around the 000 peak (Fig. 7.14). The complexity of the structure is confirmed by the number and distribution of the satellites within the main body of the diffraction pattern as illustrated by Fig. 7.14 for HoCuSi. Both compounds (HoCuSi and DyCuSi) appear to have magnetic structures with a combination of a uniaxial structure with propagation vector along the *c*-axis of the hexagonal crystal structure, and an amplitude modulated structure with moments parallel to the *c*-axis. The former has moments directed perpendicular to the *c*-axis (deduced from the strength of the zero order satellites) but a flat

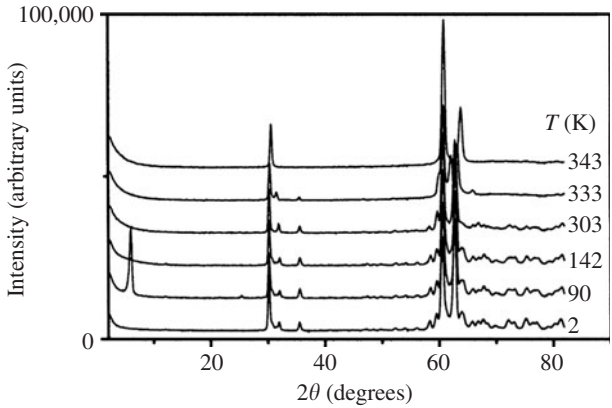

Fig. 7.13 Neutron powder diffraction pattern from $YFe_2(D_{1-x}H_x)_{4.2}$. Note that the helimagnetic structure with $\xi = \pi/4$ at 90 K gives a strong diffraction peak at $d = 23.5$ Å (Paul-Bancour *et al.* 2004).

spiral and a transverse amplitude modulated structure cannot be distinguished on the basis of powder diffraction for hexagonal crystallographic symmetry. This serves to highlight the limitations imposed by the averaging that occurs in powder diffraction. Single crystal experiments preferably with polarized neutrons, will be required to fully resolve these structures.

7.5.3 Oxides

Many oxide ceramics (or minerals) are known to exhibit magnetic ordering. Probably the first known technical magnet was the mineral magnetite (Fe_3O_4), or lodestone used for early navigational instruments. The first known antiferromagnet was the oxide MnO (see Chapter 1) and these classes of simple oxides have been studied extensively over the last five decades.

Recent work on oxides has been more closely associated with compounds crystallizing in the ubiquitous ABX_3 perovskite structure and its many derivatives. Work on perovskite phases has progressed in several directions. Relaxor ferroelectrics are of great technological interest because of their interesting piezoelectric and dielectric properties. The relaxor state is one in which some ferroelectric-like behaviour is maintained well above the transition to the nominally paraelectric cubic phase. This is achieved through local atom displacements because of shared occupancy of the *B*-site. An example is $PbFe_{2/3}W_{1/3}O_3$ (it is assumed that Fe and W are distributed randomly over the perovskite *B*-sites) which is of relevance here because the Fe moments order below 340 K.

Recent neutron powder diffraction work (Ivanov *et al.* 2004) has shown that the ordering is of the simple antiferromagnetic type in which the magnetic unit

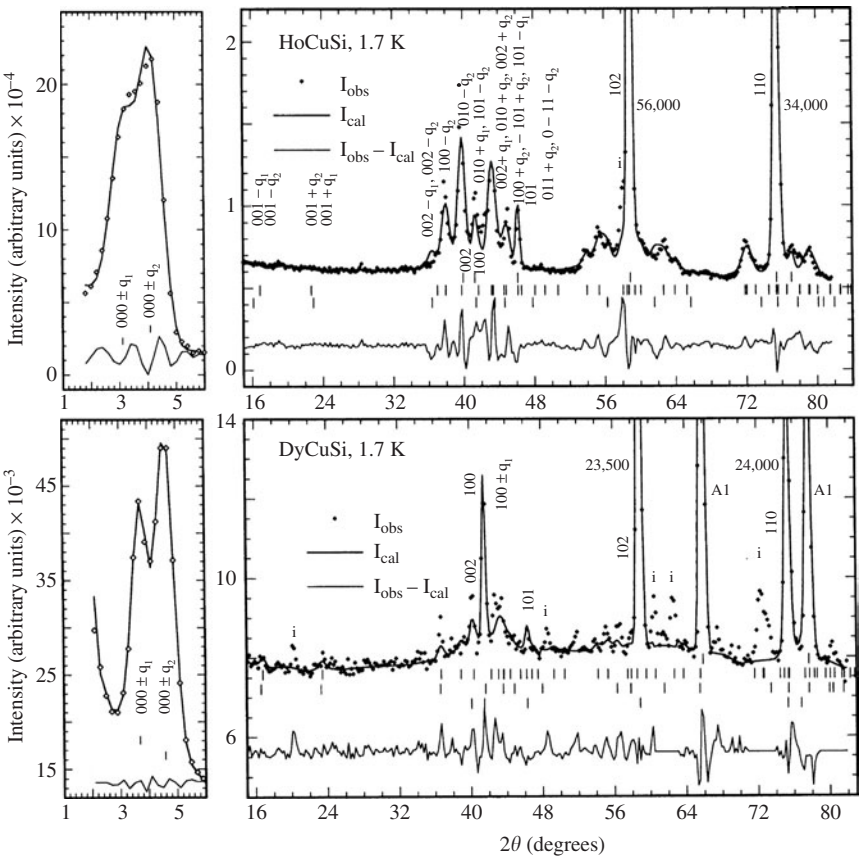

Fig. 7.14 Neutron powder diffraction pattern from HoCuSi and DyCuSi at 1.7 K and the associated Rietveld fit (Schobinger-Papamantellos *et al.* 2004).

cell is the crystallographic cell doubled in all three directions. The moments of all six closest Fe neighbours are anti-ferromagnetically coupled (Fig. 7.15). The moment determined, 3.63(4) μ_B[92] is smaller than the $5\mu_B$ expected for Fe, most likely due to disruption of the exchange interaction due to 1/3 occupancy of the *B* site by W.

The ceramics known as manganites rose to prominence because of their magnetostrictive properties culminating in the colossal magnetoresistive materials (CMR). Since the magnetic order must be related to the CMR behaviour, and they are produced primarily by solid state sintering methods, neutron powder

[92] The unit of electromagnetic moment, The Bohr Magneton (μ_B) is given by $\mu_B = \frac{he}{4\pi m_e c}$.

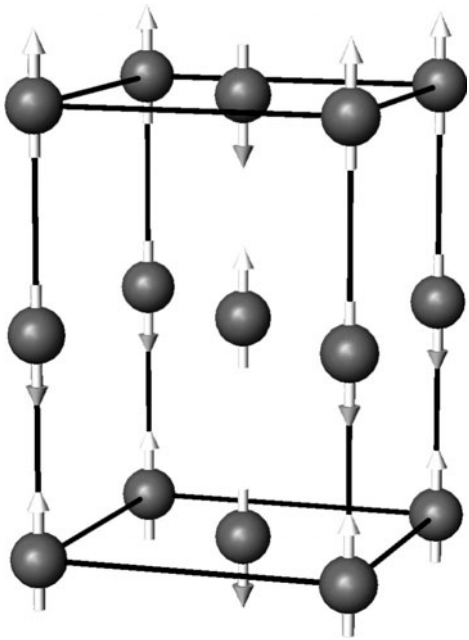

Fig. 7.15 Magnetic structure of the perovskite $PbFe_{2/3}W_{1/3}O_3$ (Ivanov *et al.* 2004).

diffraction has been used to study the magnetic structure. An example is the compound $Nd_{92}Ca_{0.08}MnO_3$ (Gamari–Seale *et al.* 2004) in which both ferromagnetic order (at 195 K) and a canted antiferromagnetic order (150–50 K) are observed.

The complexity of perovskite crystal structures can be increased by compositional variations from simple ABX_3 stoichiometry that lead to layering (e.g. Ruddlesden–Popper phases (Elcombe *et al.* 1991), the creation of oxygen vacancies (e.g. $YBa_2Cu_3O_{7-\delta}$ superconductors) and the multiple occupancy of sites due to solid solution formation. Such compounds, if they contain magnetic ions, often also undergo magnetic ordering that may be profitably studied using neutron powder diffraction. In some cases, for example the oxy-halide $Sr_3Fe_2O_5Cl_2$ (Knee *et al.* 2004), the magnetic structure is relatively simple in relation to the crystal structure (Fig. 7.16). The magnetic unit cell is $a_{mag} = b_{mag} = \sqrt{2}a_{nuc}$, $c_{mag} = c_{nuc}$ and the Fe moments are anti-ferromagnetically coupled. However, more complex arrangements are also possible (Khalyavin *et al.* 2004), for example in $TbBaCo_{2-x}Fe_xO_{5+\gamma}$ in which both the Fe and Co are statistically distributed over octahedral and pyramidal sites each with different moments (i.e. 2 Fe moments and 2 Co moments). The Fe/Co is antiferromagnetically ordered along all three crystallographic axes.

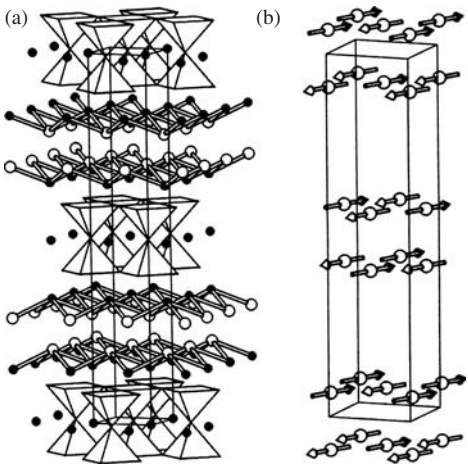

Fig. 7.16 The crystal structure (a) and magnetic structure (b) of the complex perovskite derivative $Sr_3Fe_2O_5Cl_2$ (Knee *et al.* 2004).

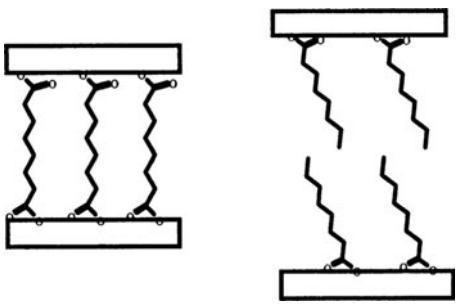

Fig. 7.17 Two views of the Co^{II} hydroxide terephtalate (Feyerherm *et al.* 2003).

7.5.4 Organic–inorganic compounds

There has been recent interest in the synthesis and study of organic-inorganic compounds assembled from regularly stacked organic and inorganic units. They are being studied due to the opportunity to tailor properties by altering the sequencing of the different structural units. An example is Co^{II} hydroxide terephtalate, shown in two different views in Fig. 7.17 (Feyerherm *et al.* 2003). Despite the large Co–Co separation along a, magnetic ordering develops below 48 K. The zero field cooled magnetic structure as determined using neutron powder diffraction is illustrated in Fig. 7.18(a). The difference pattern (10–50 K) is shown in Fig. 7.19 along with the refinement results. The presence of $h0l$ peaks with h, l odd indicates antiferromagnetic coupling between crystallographically non-equivalent Co1 and Co2 sites within the bc planes (Fig. 7.18). The presence of $h00$ peaks with h odd

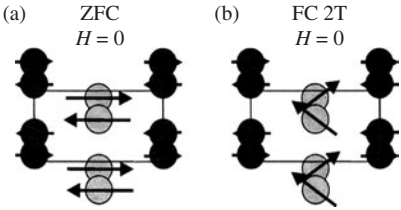

Fig. 7.18 (a) Zero field-cooled (ZFC) and (b) field-cooled (FC) structures for Co^{II} hydroxide terephtalate (Feyerherm *et al.* 2003).

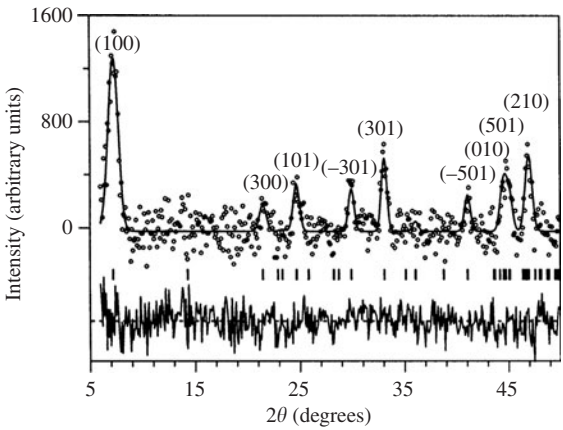

Fig. 7.19 Rietveld refinement fit to the difference pattern obtained by subtracting a pattern recorded at 50 K from one recorded at 10 K from a zero field-cooled sample of Co^{II} hydroxide terephtalate (Feyerherm *et al.* 2003).

indicates that the moments of Co1 and Co2 are different, that is, the in-phase structure is ferromagnetic and the magnetic planes are anti-ferromagnetically coupled along the *a*-axis. Rietveld refinements indicate that the moments lie within the *ac* plane perpendicular to the *a*-axis and thus canted approximately 6° with respect to the *c*-axis. The refined moments are 2.3(1) μ_B and 3.8(1) μ_B for Co1 and Co2, respectively. Owing to the use of powder diffraction data, a non-collinear structure with different canting angles for Co1 and Co2 could not be ruled out, nor could a small ferromagnetic component parallel to the *b*-axis.

When cooled in magnetic fields >0.3T, Co^{II} hydroxy terephtalate develops a large remanent magnetization that is not explained by the zero field cooled structure. Further studies on a sample cooled in a 2T field revealed that the field cooled structure is quite different, leading to a quite different diffraction pattern

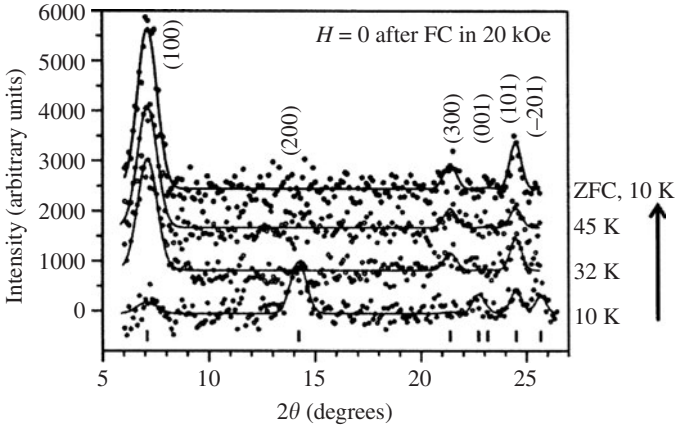

Fig. 7.20 Neutron diffraction pattern recorded from Co^{II} hydroxide terephtalate cooled to 10 K in a 20 kOe field and its reversion to the zero field cooled pattern on heating. The ZFC pattern is shown for comparison (Feyerherm *et al.* 2003).

at 10 K (Fig. 7.20). The postulated structure is shown in Fig. 7.18(b) to contain canted moments on the Co2 site only. The canting is 37° towards the *b*-axis and the ferromagnetic component of the moment is 1.8(1) μ_B. Fig. 7.20 also demonstrates that heating to above 32 K restores the zero-field cooled state.

7.5.5 Concluding remarks

The preceding examples have demonstrated the diversity and complexity of magnetic structures able to be attempted with modern powder diffraction methods. They have included a wide variety of material types and many types of magnetism. They highlight many of the methods outlined in §7.4 being applied in practice. We note, however, that despite improvements in diffractometer resolution that allow ambiguities in the crystal system due to magnetic distortions to be readily identified in many cases, most practitioners do not make use of magnetic space groups in either their structure solution or in describing the refined structure. A counter example is provided by a recent study of the perovskite $BaPrO_3$ (Goossens *et al.* 2004). The crystal structure is orthorhombic in space group *Pbnm* with $a = 6.2015$, $b = 6.1719$ and $c = 8.7157$ Å (Popova *et al.* 1996) differing at most by $\sim 1/2\%$ from cubic. The antiferromagnetic part of the magnetic structure was solved by examining models derived from the two Shubnikov groups $Pb'n'm$ and $Pbn'm'$ that are consistent with the observation of a small ferromagnetic component and the systematic absences. Calculations based on these are shown in Fig. 7.21 for the four possible models giving clear agreement with $Pb'n'm$ with the anti-ferromagnetic component of the moments directed along the *a*-axis. The

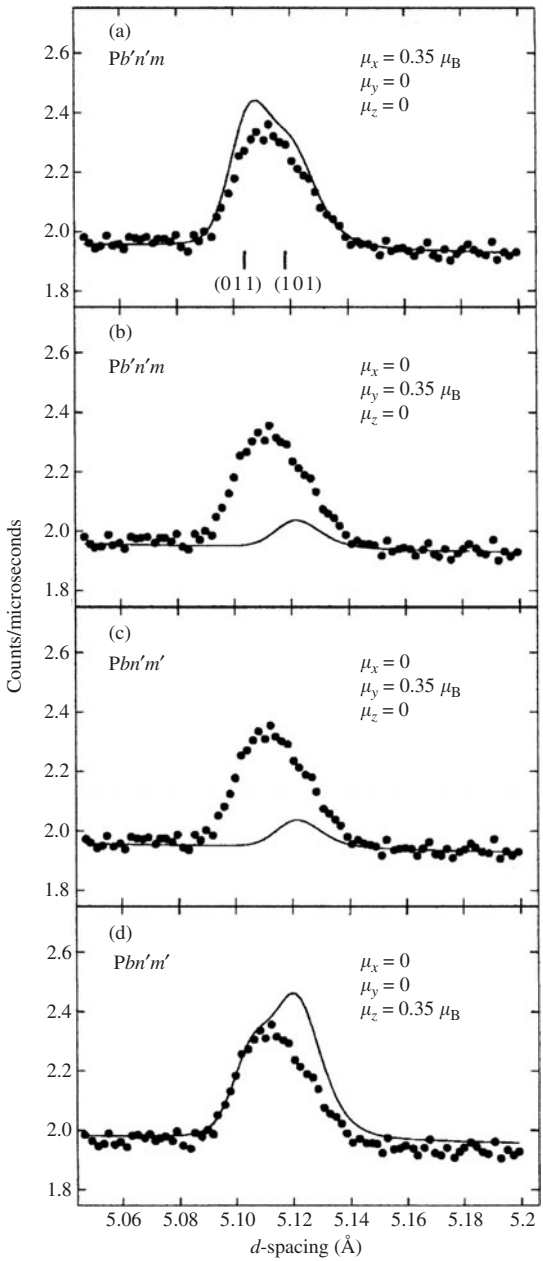

Fig. 7.21 Fits to the observed neutron powder diffraction intensity in the 011 and 101 pair of peaks from $BaPrO_3$ using models with space group P$b'n'm'$ with non-zero moments along (a) the x-axis and (b) the y-axis and space group P$bn'm'$ with non-zero moments along (c) the y-axis and (d) the z-axis (Goossens *et al.* 2004).

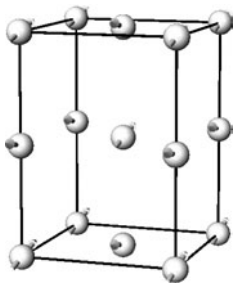

Fig. 7.22 The magnetic structure of $BaPrO_3$ (Goossens *et al.* 2004).

magnetic structure is illustrated in Fig. 7.22. The ferromagnetic component was too small to be determined due to the small magnetic intensity superimposed on strong nuclear peaks.

Although many of the examples in §7.5 could have benefited greatly from single crystal neutron diffraction, this is not possible in a large number of cases. Consequently neutron powder diffraction was used to obtain partial or complete magnetic structures as dictated by symmetry and the experimental conditions. We are certain that the rich diversity of magnetic structures will continue to provide stimulating problems for study using neutron powder diffraction.

8

Quantitative phase analysis

8.1 INTRODUCTION

The properties of all solid materials depend not only on the chemical composition but also, equally importantly, on the distribution of compounds or phases within the solid. An example is a steel comprising Fe containing 0.8 wt% C. Above 727°C, the C is uniformly distributed as an interstitial solid solution (§2.2.2) within the face-centred cubic (fcc) structure. Below 727°C, the Fe transforms into the bcc crystal structure where it can only contain ~0.02 wt% C in solution. The remainder of the C forms a hard brittle phase Fe_3C that acts to considerably strengthen the otherwise soft Fe.[93] Chemical analysis of either material would reveal the same answer, that is, on average the sample contains 0.8 wt% C. Therefore, it is desirable to undertake *phase analysis* in conjunction with chemical analysis.

Situations in which phase analysis is important include the study of first-order phase transitions, materials synthesis, petrology, corrosion, and forensic science. Whereas there are many techniques for undertaking chemical analysis to quantify the elements and/or molecules present in a sample, there are relatively few techniques for phase analysis. Historically, optical microscopy has been widely used in the earth sciences and materials sciences. This was generally conducted by manually measuring and counting grains or crystallites within a polished specimen. Identification of the phases relies upon differences in optical reflectivity enhanced or modified by chemical etchants (materials science) or optical transmission (earth sciences). Most laboratories now have automatic image analysis systems that can remove the tedium from optical phase analysis. The method is, however, sensitive to crystallite shape and in particular great care needs to be exercised when studying severely anisotropic microstructures. Phase identification is also problematic when studying new materials. Scanning electron microscopy can be used in a manner similar to optical microscopy. It has the added advantage that phase identification is easier due to simultaneous elemental chemical analysis via the characteristic X-rays emitted by the sample. Automated systems that can in principle identify and quantify phases are available. There are however many examples that are unsuitable for this type of analysis. Zirconia ceramics present one such example, since the properties depend critically on the phase quantities

[93] The distribution of the Fe_3C within the microstructure also plays an important role however that is not within the scope of this chapter.

and distribution but the elemental analysis of the different phases is the same or very similar (see §8.6.2). X-ray powder diffraction is an excellent tool for phase identification (i.e., qualitative phase analysis) because it simultaneously samples many thousands of crystallites if samples are optimally prepared (2–5 μm) and because an excellent database and software is available (PDF, §4.3). Difficulties do arise because of preferred orientation and extinction when large grained solid polycrystalline samples are studied. Quantitative analysis using laboratory XRD is also possible; however, the results are only representative of the first 1–20 μm of the surface depending on the sample and the X-rays chosen. Accurate results usually require corrections for micro-absorption and extinction.

Neutron powder diffraction provides a useful alternative to these methods. Thermal neutrons penetrate very large samples thereby giving results with good statistical relevance that are free from the effect of surface gradients. The results are not generally influenced by the distribution of phases or the grain shape. Coexisting phases with very similar optical properties and chemistry (e.g., tetragonal and monoclinic zirconia) can be quantitatively analysed. Lastly, quantitative analysis is available throughout an *in situ* diffraction experiment. The major shortcoming of Neutron Diffraction Quantitative Phase Analysis (ND-QPA) is that the distribution of the phases is not determined. This relies on the microscopes which should be used qualitatively to support diffraction-based measurements.

8.2 THEORY

Two relatively simple principles underlie the ND-QPA technique:

1. That the total number of neutrons per unit time, I_{hkl} diffracted into a length h of the Debye–Scherrer ring (the height of the detector opening)[94] is

$$I_{hkl} = \frac{\Phi_0 \lambda^3 h V \rho' J N_c^2 F_{hkl}^2 \exp(-2M)}{8\pi r \rho \sin\theta \sin 2\theta}, \tag{8.1}$$

   where Φ_0 is the incident neutron flux, λ the neutron wavelength, V the sample irradiated volume, J the multiplicity, N_c the number of unit cells per unit volume, F the structure factor, $\exp(-2M)$ is the thermal displacement (Debye–Waller) factor, r is the sample-to-detector distance, ρ' is the measured density and ρ the theoretical density (Bacon 1975; Sabine 1980, §5.5.2).
2. That there is no coherence between neutrons scattered from the different phases in a multi-phase sample.

As we will see below, the first principle allows us to demonstrate proportionality between the observed intensities and the mass of a single phase. The second principle means that the diffraction peaks generated by each phase in a multi-phase sample are completely independent. Where they overlap the intensity is simply the

[94] Not to be confused with h from the Miller indices hkl.

sum of the intensities from the contributing phases. This means that the proportionality between intensity and the irradiated mass of a phase persists no matter how many or which types of additional phases are present.

Taking eqn (8.1), including attenuation and preferred orientation factors and re-arranging, we obtain eqn (5.10):

$$I_{hkl} = S\,|F_{hkl}|^2\,TLJAP \tag{5.10}$$

and by equating coefficients [noting that since A and P did not appear in eqn (8.1) they were implicitly taken to be unity] we arrive at eqn (5.15) for the scale factor obtained in structure refinements S:

$$S = \left(\frac{\Phi_0 \lambda^3 h}{8\pi r}\right)\left(\frac{\rho' V N_c^2}{\rho}\right). \tag{5.15}$$

By substituting $N_c = 1/V_c$, $m_c = \rho V_c$, and $m = \rho' V$, where m is the mass of the phase, V_c is the unit cell volume and m_c is the mass of one unit cell, we obtain

$$S = \left(\frac{\Phi_0 \lambda^3 h}{8\pi r}\right)\left(\frac{m}{m_c V_c}\right). \tag{8.2}$$

The mass of the unit cell m_c is given by the product of the mass of one formula unit (M) and the number of formula units per unit cell (Z) giving

$$S = \left(\frac{\Phi_0 \lambda^3 h}{8\pi r}\right)\left(\frac{m}{ZMV_c}\right). \tag{8.3}$$

Or for each phase p

$$m_p \propto S_p Z_p M_p V_p \tag{8.4}$$

since Φ_0, λ^3, h, and r are invariant for a given experimental arrangement. Assuming a 100% crystalline sample, the total sample mass is represented by

$$m = \sum\nolimits_i m_i \propto \sum_i S_i Z_i M_i V_i \tag{8.5}$$

with the same constant of proportionality and the mass (weight) fraction of phase p by

$$w_p = \frac{S_p Z_p M_p V_p}{\sum_i S_i Z_i M_i V_i}. \tag{8.6}$$

The specific forms of the expressions given here were developed for ND-QPA based upon Rietveld refinement scale factors by Hill and Howard (1987). The analogous expression for X-ray diffraction was given a short time later by Bish and Howard (1988). Although developed specifically for QPA based on Rietveld refinement scale factors, the equations are equally valid for, and analogous to expressions used in the older form of QPA (see, e.g. Cullity 1979) to be discussed in §8.3. Due to the penetrating nature of neutrons we have, except in eqn (5.10), ignored the effect of absorption. It should be noted that for highly absorbing samples (and for

XRD) the absorption coefficient (or attenuation coefficient if we include the effect of incoherent scattering) may be different in the different phases and this must be accounted for in the derivation of eqn (8.6) (Taylor and Matulis 1991).

8.3 INDIVIDUAL PEAK METHODS

8.3.1 Overview

Individual peak methods for X-ray QPA have been used for many decades. However, before the advent of whole pattern profile analysis, the use of XRD-QPA was not common[95] as considerable calibration was required in order to obtain meaningful results (Cullity 1979; Klug and Alexander 1974): the results not always justifying the effort. There are however many cases where useful data can be extracted from relatively few diffraction peaks.

In individual peak analysis, we do not focus on the scale factor, S, but on the intensity of one peak, given by eqn (8.1), or by combining eqn (5.10) with eqn (8.3):

$$I_{hkl} = \frac{\Phi_0 \lambda^3 h}{8\pi r} \frac{m}{ZMV_c} |F_{hkl}|^2 \, TLJAP. \tag{8.7}$$

We see that the intensity of any chosen peak depends linearly on the mass[96] of the phase to which the peak belongs. The attenuation factor A, to the extent that it depends on composition, is the only other quantity on the right-hand side of eqn (8.7) that varies with the weight fraction of phase p.[97] All of the other terms may be replaced by a constant K_{pk} for the kth peak of the pth phase:

$$I_{pk} = K_{pk} m_p A_{pk}. \tag{8.8}$$

In cases where absorption (or attenuation by scattering) is appreciable and phases with quite different attenuation coefficients are mixed within the sample, the intensity of peaks due to phase p is quite non-linear in the mass fraction of phase p. This is common in X-ray QPA and a strength of ND-QPA is that such absorption problems are usually absent. In cases where this is not true, the procedures are the same as for X-ray QPA and are dealt with in detail by Klug and Alexander (1974) and Cullity (1979). Equation (8.8) may then be manipulated in various ways depending on the nature of the problem under study as outlined below.

8.3.2 The polymorph method

The polymorph or direct comparison method was first developed for use in determining the level of retained Austenite in quenched steels using XRD. When

[95] That is, only a tiny fraction of all XRD patterns recorded were used for QPA.
[96] Or to the volume (via the density) as was more common in XRD.
[97] This is distinct from the microabsorption effects that might impact on the validity of eqn (8.6).

quenched rapidly from the fcc Austenite phase, medium and high carbon (0.3–1.2% C) steels undergo a diffusionless first-order transition to body-centred tetragonal Martensite. The transition is usually incomplete and the amount of retained Austenite is critical to properties. Retained Austenite is very unstable and so the samples must remain as a solid polycrystal which cannot be mixed with an internal standard. However, since the absorption coefficients of the two phases are very similar, even with highly absorbed X-rays (e.g., Cu K_α) a reliable standardless analysis may be made.

We proceed by dividing the constant term K_{pk} in eqn (8.8) into factors that depend on the crystal structure of the phase and the position (or d-spacing) of the chosen peaks:

$$R_{pk} = \frac{|F_{hkl}|^2\, TLJP}{ZMV_c} \tag{8.9}$$

and those that are independent of the phase and its structure

$$K = \frac{\phi\lambda^3 h}{8\pi r} \tag{8.10}$$

to give

$$m_p = I_{pk}(KR_{pk}A_{pk})^{-1} \tag{8.11}$$

The weight fraction of phase p in a mixture of other phases is then given by

$$w_p = \frac{m_p}{\sum_i m_i} = \frac{I_{pk}(KR_{pk}A_{pk})^{-1}}{\sum_i I_{ik}(KR_{ik}A_{ik})^{-1}} \approx \frac{I_{pk}R_{pk}^{-1}}{\sum_i I_{ik}R_{ik}^{-1}} \tag{8.12}$$

as all attenuation coefficients are assumed to be similar.

The simplest example is a binary mixture, for example, the retained Austenite problem in steels. Using subscripts 'A' for Austenite and 'M' for Martensite and choosing the 200_A and $002/200_M$ the weight fraction of retained Austenite is given by

$$w_A = \frac{I_{A200}R_{A200}^{-1}}{I_{A200}R_{A200}^{-1} + I_{M200}R_{M200}^{-1}} \tag{8.13}$$

where the subscript 'M200' refers to the sum of the 002 and 200 peaks which due to strain and particle size broadening are often not resolved. The values of R, in eqn (8.9), must be calculated from the crystal structures.

The particular strength of the polymorph method for X-ray diffraction is that polymorphs or different crystalline modifications of the same material have approximately the same density and absorption coefficients thereby removing the need for standards. In neutron diffraction this is most often not an issue and so the polymorph or direct comparison method is not restricted to polymorphs of the

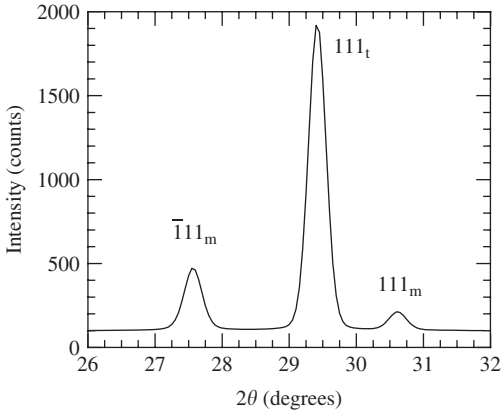

Fig. 8.1 Distribution of 111 peaks in the diffraction pattern calculated at $\lambda = 1.5$ Å for zirconia alloys containing just the tetragonal and monoclinic phases.

same material provided that attenuation[98] is low in all phases present. Although the retained Austenite example was only set out for one peak from each phase, the method may be readily extended for (i) more than one peak per phase and (ii) more than two phases.

As an example, consider magnesia partially stabilized zirconia (Mg-PSZ). This high strength, high toughness ceramic material usually contains at least four coexisting phases (Kisi *et al.* 1989): the cubic (c), tetragonal (t), and monoclinic (m) forms of zirconia, and the anion vacancy ordered (δ) phase $Mg_2Zr_5O_{12}$. All of the phases have crystal structures that derive from the cubic fluorite structure and apart from minor chemical differences, there are many similarities in their diffraction patterns that makes a complete phase analysis impossible by the polymorph method (see §8.6.2). However, a critical parameter in the study of Mg-PSZ is the fraction of the m phase under different circumstances (e.g. in the bulk, on a ground surface, on a fracture surface, etc.). It turns out that the fraction of m phase is very readily determined by the polymorph method even in the presence of the other phases.

Consider first the hypothetical case where the sample is composed entirely from t and m phases. The fluorite 111 peak is split in the m phase into 111 and $\bar{1}$ 1 1 which are situated on either side of the tetragonal peak (Fig. 8.1). Adapting eqn (8.12), the weight fraction of the monoclinic phase is given by

$$w_m = \frac{I_{(1\,1\,1)m}R^{-1}_{(1\,1\,1)m} + I_{(\bar{1}\,1\,1)m}R^{-1}_{(\bar{1}\,1\,1)m}}{I_{(1\,1\,1)m}R^{-1}_{(1\,1\,1)m} + I_{(\bar{1}\,1\,1)m}R^{-1}_{(\bar{1}\,1\,1)m} + I_{(1\,1\,1)t}R^{-1}_{(1\,1\,1)t}}, \tag{8.14}$$

[98] By both scattering and absorption.

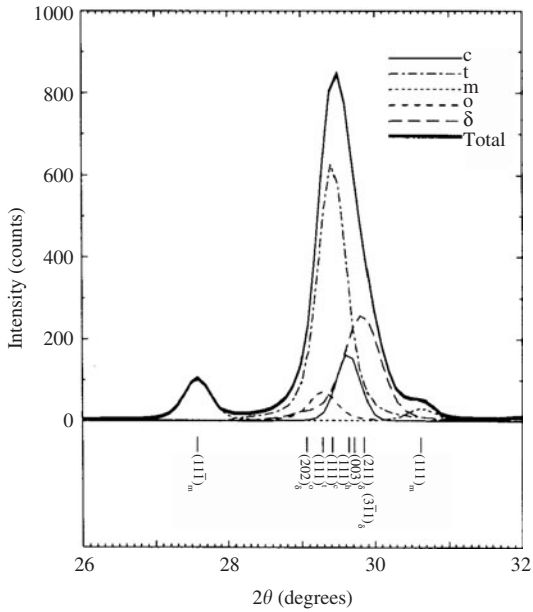

Fig. 8.2 Severely overlapping peaks from the five phases present in Mg-PSZ ceramics (Howard and Kisi 1990).

which may be simplified as

$$w_{\mathrm{m}} = \frac{P_{\mathrm{t}} X_{\mathrm{m}}}{1 + (P_{\mathrm{t}} - 1)\, X_{\mathrm{m}}} \tag{8.15}$$

where X_{m} is the intensity ratio,

$$X_{\mathrm{m}} = \frac{I_{(1\,1\,1)\mathrm{m}} + I_{(\bar{1}\,1\,1)\mathrm{m}}}{I_{(1\,1\,1)\mathrm{m}} + I_{(\bar{1}\,1\,1)\mathrm{m}} + I_{(1\,1\,1)\mathrm{t}}}$$

and

$$P_{\mathrm{t}} = \frac{R_{(1\,1\,1)\mathrm{t}}}{R_{(1\,1\,1)\mathrm{m}} + R_{(\bar{1}\,1\,1)\mathrm{m}}}$$

The actual situation is far more complex. As shown in Fig. 8.2 all of the non-monoclinic phases have peaks that overlap with $(1\,1\,1)_{\mathrm{t}}$. In eqn (8.15), the intensity ratio now contains the contributions from *all* of the phases in the denominator and in eqn (8.15) we replace P_{t} by

$$\bar{P} = \frac{w_{\mathrm{c}} P_{\mathrm{c}} + w_{\mathrm{t}} P_{\mathrm{t}} + w_{\delta} P_{\delta} + w_{\mathrm{o}} P_{\mathrm{o}}}{w_{\mathrm{c}} + w_{\mathrm{t}} + w_{\delta} + w_{\mathrm{o}}} \tag{8.16}$$

The orthorhombic zirconia phase (o) is included for completeness as it is sometimes observed in these materials (Hannink *et al.* 1994). Since generally w_c, w_t, and so on, are unknown $\bar{P}$ cannot be pre-determined. However, Howard and Kisi (1990) have shown that, because of the insensitivity of X-rays to variations in the oxygen ion positions within the structures, excellent estimates of the fraction of the amount of monoclinic phase in the top 5–10 μm of the sample surface, may be made by using a value of $\bar{P} = 1.1$. Because neutron diffraction is very sensitive to the oxygen ion positions, values of P for the different phases range from 1.08 to 1.46. Nonetheless, very reasonable estimates (±1%) may be obtained for the phase compositions commonly encountered, by taking $\bar{P} \approx P_t = 1.44$ (Howard and Kisi 1990).

8.3.3 The use of standard materials

Quantitative phase analysis by X-ray diffraction was until 1988, heavily dependent on the use of standards. This derives from the very different absorption coefficients that often apply to different phases within a mixture. Absorption is far less frequently a problem with neutron diffraction. Nonetheless, the use of standards does have its place. They are particularly useful if there is some doubt about the sample being 100% crystalline. This may be the case in some rapidly solidified minerals, fired ceramic bodies, dust samples, and fly ashes. Standards may also be useful when it has not been possible to identify all of the phases present or when one or more phases have unknown crystal structures and hence R_{pk} (e.g. during an *in situ* experiment). Standardless analysis will then give only phase fractions relative to the total mass of known crystalline phases rather than relative to the total sample mass.

Two kinds of standards may be used: external and internal. External standards are comprised from the pure phases and measured mixtures of the pure phases at intermediate compositions. They are only valid for cases where the diffraction pattern from the unknown sample is recorded under identical conditions to the standard samples; in addition corrections for different absorption by the sample and standard may be required. The penetrating nature of a neutron beam makes the external standard approach unreliable since minor differences in the powder packing density (especially of patterns recorded from the pure phases) will lead to incorrect results.[99] This is overcome by using an *internal* standard mixed in known proportion with the sample under study. This makes the method unsuitable for solid polycrystalline samples in most instances as it is not usually possible to ensure that the standard and the sample intercept the same neutron flux.

If a standard material is incorporated within a powder sample in a known weight fraction w_{std}, and R_{pk} is known for the standard (say R_{std}) and the phase of interest,

[99] This is not a problem with XRD because looser packing will merely allow the beam to penetrate deeper – the volume of material sampled will remain approximately unaltered. Particle size differences and micro absorption are far more crucial for XRD.

then by a straightforward application[100] of eqn (8.11), the weight fraction of phase p is given by

$$w_p = \frac{I_{pk} R_{pk}^{-1}}{I_{\text{std}} R_{\text{std}}^{-1}} w_{\text{std}} \tag{8.17}$$

Unknown values of R may be computed from eqn (8.9) or determined by experiment from one or more reference samples mixed in known ratios.

The major drawback of all of the individual peak methods is that they are extremely susceptible to preferred orientation or texture within the sample. As will be shown in §9.8, non-randomness or preferred orientation can occur by a number of mechanisms and can seriously perturb the intensities of individual peaks – in some cases leading to the complete absence of an otherwise moderately strong peak. Steps that can be taken to try to avoid preferred orientation effects in quantitative analysis include

(i) Sample preparation techniques including dilution (see §3.6.5).
(ii) Use of several peaks and a comparison of results for consistency.
(iii) Careful selection of peaks that are not very susceptible to preferred orientation effects [e.g., 111 in tetragonal systems with (0 0 1) cleavage].

However, even with these measures in place or in the absence of preferred orientation, the results of individual peak QPA are also susceptible to peak overlap and to errors in the value of R. These may occur due to minor changes in the crystal structure (e.g. approaching a phase transition), solid solutions, and thermal and static displacement effects. The likelihood of such changes is particularly high during *in situ* experiments. The preferred way to either avoid or successfully model such effects is to undertake whole pattern analysis (e.g. Rietveld analysis).

8.4 WHOLE PATTERN ANALYSIS

Whole pattern analysis techniques have been discussed briefly in Chapter 4 and at length in Chapter 5. There are two kinds depending on whether a crystal structure model is simultaneously refined (Rietveld analysis) or not (pattern decomposition methods). Both methods have been proposed for quantitative phase analysis although Rietveld analysis has become the preferred method. Quantitative phase analysis by Rietveld refinement was first developed for neutrons by Hill and Howard (1987) and soon after for X-rays by Bish and Howard (1988). QPA by pattern decomposition was developed concurrently by Toraya (1988).

The principles of both methods were developed in §8.2, eqns (8.1)–(8.6). In the Rietveld method, each phase has a scale factor S, defined in eqn (5.15). During the refinement, the scale factor is optimized alongside all of the free structural, peak shape, and global variables necessary to obtain a good fit to the observed pattern.

[100] Assuming here, for this composite sample, absorption does not affect the two peaks differently.

As shown in eqn (8.2), the scale factor of phase p is directly proportional to the mass of phase p in the neutron beam. Assuming that the sample only contains crystalline phases, the fraction of any one of those phases relative to the total is given by eqn (8.6).

In the circumstances outlined in §8.3.3, that is, in the presence of poorly crystalline samples, unknown phases, or unknown crystal structures, it is wise to incorporate a known weight fraction w_{std} of a suitable standard within the sample. Then, by direct application of eqn (8.4), the weight fraction of the phase of interest w_p is given by

$$w_p = \frac{(SZMV)_p}{(SZMV)_{\text{std}}} w_{\text{std}} \tag{8.18}$$

8.5 EVALUATION OF THE TECHNIQUES

Individual peak methods of QPA have been used successfully for XRD for many decades. As noted in §8.3.3 they are susceptible to a number of systematic errors due to a number of causes including preferred orientation, micro-absorption, and extinction. These may be accounted for by the selection of the correct method (polymorph, external standard, or internal standard) and careful experimental technique. To ensure a correct result by these methods often takes considerable effort in calibration and is only justified if the same method is to be used for many samples within the same system.

The whole pattern methods are, on the other hand, largely free from systematic errors that bias the integrated intensities because (i) these effects tend to average out if sufficiently large numbers of peaks are used and (ii) many of them can be modelled during the refinement. Whole pattern methods also have the advantage of simultaneously providing other data concerning the sample. Pattern decomposition methods provide lattice parameters for all of the phases and the Rietveld method also provides crystal structure data for the major phases. These can be used to supplement chemical analysis data. For example, if the lattice parameter versus chemical composition relationship is well known then precisely determined lattice parameters allow the chemical composition of one or more phases to be determined, for example, Y-doped ZrO_2 (Scott 1975), TiC_x (Pierson 1996), and Fe–C alloys (Cullity 1979). Refined occupancy factors can also provide chemical data as was discussed in §6.5.4. With the correct software[101] whole pattern neutron diffraction quantitative phase analysis can be very rapid provided that the crystal structure of all of the phases is known.

The availability of a relatively rapid standardless phase quantification method has greatly expanded the use of diffraction-based QPA using both X-rays and neutrons. Several different commercial software packages have been developed[102]

[101] A robust Rietveld refinement or pattern decomposition program.

[102] Usually underpinned by public domain Rietveld refinement software supplemented by a proprietary graphical user interface.

that implement the method. However, it should not be seen as a panacea. The Powder Diffraction Commission of the International Union of Crystallography conducted a quantitative phase analysis round-robin in which the same samples were analysed by different laboratories around the world (Madsen *et al.* 2001; Scarlett *et al.* 2002). The major results are (i) that neutron diffraction performed far better than X-ray diffraction; (ii) in general, determinations that included a standard material within the sample were considerably better than standardless analysis (especially with XRD); and (iii) considerable operator skill and care was required at all stages (sample preparation, data collection, analysis, and error estimation) for reasonable results to be obtained.

8.6 PRACTICAL EXAMPLES

The power of QPA methods in providing a deeper understanding of geological and engineering materials is best illustrated by example. The authors' personal experience of geological systems is limited and so the bias here is towards materials science. In addition, the ready availability of X-ray sources compared with neutron sources makes X-ray powder diffraction the method of choice for rock and mineral systems. Neutron powder diffraction, although more accurate, is usually reserved for special cases, for example, *in situ* diffraction during simulated service or material synthesis.

8.6.1 Rocks and ores

Our example here dates back to when Rietveld refinement based QPA was still being tested in various applications. In this case, the samples were synthetic mixtures of minerals aimed at mimicking Australian ore bodies (Howard *et al.* 1988b). The results from a five phase mixture of equal parts by weight of Galena (PbS), Pyrite (FeS_2), Sphalerite (ZnS), Chalcopyrite ($CuFeS_2$), and Quartz (SiO_2) are summarized in Fig. 8.3. An internal standard, 25 wt% Rutile (TiO_2) was added. Data were recorded on the High Resolution Powder Diffractometer at the Australian Nuclear Science and Technology Organisation reactor at Lucas Heights. The figure shows the analysis results in wt% compared with the as-weighed amounts. The results are quite good considering that the demanding six-phase Rietveld refinement required was the most complex to have been attempted at that time. Results for Galena, Pyrite, and Sphalerite are low compared with the as-weighed amounts which was attributed to poor crystallinity in these minerals.

8.6.2 Multi-phase engineering materials

As was briefly discussed in Chapter 2, many materials of practical importance are multi-phase. In §8.3.2 (and also in §5.8.3) we introduced magnesium partially stabilized zirconia (Mg-PSZ), one of several important zirconia-based ceramics.

	Rutile TiO_2	Galena PbS	Pyrite FeS_2	Sphalerite ZnS	Chalcopyrite $CuFeS_2$	Quartz SiO_2	Σ
As weighed (%)	25	15	15	15	15	15	100
Measured (%)	25.0(9)	13.3(12)	13.9(8)	13.8(11)	15.1(8)	14.4(6)	95.5

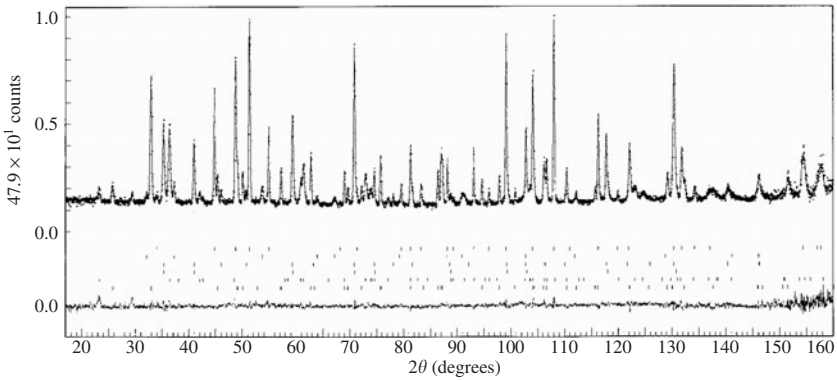

Fig. 8.3 Example of neutron diffraction QPA of a five phase simulated ore with 25% of rutile as an internal standard (Howard *et al.* 1988b).

It is widely accepted that zirconia ceramics rely for much of their toughness on the stress-induced Martensitic transformation of the tetragonal phase to the monoclinic phase (Green *et al.* 1989). This is achieved by a careful balance within the ceramic of the partition of chemical dopants between the various phases present together with various microstructural constraints. An early use of neutron powder diffraction QPA was in the study of the temperature-induced phase transition of the tetragonal phase in Mg-PSZ (Kisi *et al.* 1989; Howard *et al.* 1990). Unlike earlier partially stabilized zirconia ceramics (e.g. Ca-PSZ), cooling of Mg-PSZ was found not to induce the tetragonal to monoclinic transition but rather to cause the formation of a new orthorhombic phase (Marshall *et al.* 1989). The determination, from neutron diffraction studies, of the crystal structure of this orthorhombic phase has already been described in detail (Kisi *et al.* 1989, §5.8.3). The diffraction pattern of a cooled Mg-PSZ and the patterns from the constituent phases (orthorhombic, tetragonal, $Mg_2Zr_5O_{12}$, cubic, and monoclinic) are shown in Fig. 8.4. The composition of this cooled Mg-PSZ, estimated from the Rietveld scale factors, was 3.2% c, 16.9% t, 7.2% m, 26.3% δ, and 46.4% o. Neutron diffraction has been used in a subsequent more detailed study (Howard *et al.* 1990) of the transformation from tetragonal to orthorhombic zirconia upon cooling, and its reversion to the tetragonal form upon heating to about 300°C (Fig. 8.5). Changes in the physical dimensions of the ceramic were accounted for quite precisely by changes in composition as the temperature changed.

We digress at this point to discuss the estimation of errors in QPA – with particular attention to whole pattern analysis. We start by evaluating the 'estimated

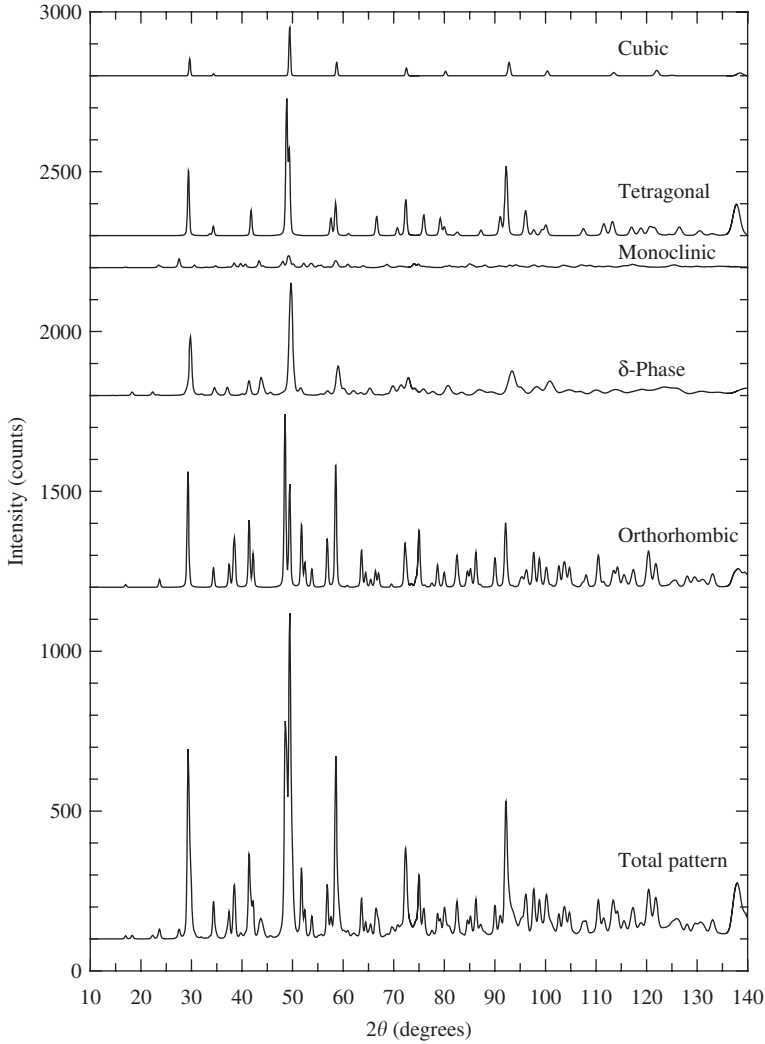

Fig. 8.4 Contributions from the cubic, tetragonal, monoclinic, and orthorhombic phases of zirconia and the intermediate phase $Mg_2Zr_5O_{12}$ to the neutron diffraction pattern observed from an Mg-PSZ sample cooled to 77 K and returned to room temperature.

standard deviation' or esd in each phase fraction from statistical data. In the computation of the weight fraction of phase p using Rietveld refinement scale factors and eqn (8.6), the quantities S, Z, M, and V for each phase are used. The number of formula units per unit cell, Z, is fixed by the crystal structure and

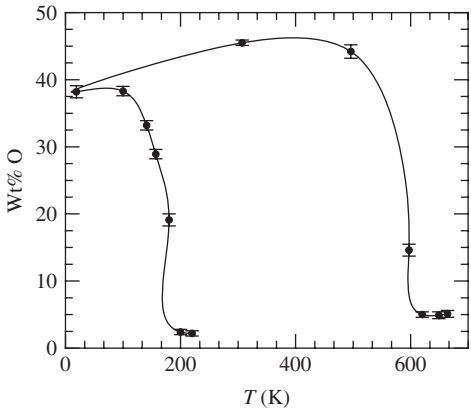

Fig. 8.5 Weight percentage of orthorhombic zirconia in Mg-PSZ around a thermal cycle from room temperature to 19 K and back up to 660 K as determined from Rietveld analysis based QPA (Howard *et al*. 1990).

provided it has been determined correctly, there is no associated uncertainty. The unit cell volume, V, is determined from the lattice parameters which are usually known to very good precision and so the error in V is usually negligibly small. The greatest uncertainty usually lies in the phase scale factors. If we take these scale factors to be the only sources of uncertainty, we find that the variance[103] in the estimate of the weight fraction as given by eqn (8.6) is related to the variances in the scale factor estimates by[104]

$$\sigma^2(w_p) = \sigma^2(S_p)\left[\frac{(ZMV)_p \sum_{i\neq p} S_i(ZMV)_i}{\left\{\sum_i S_i(ZMV)_i\right\}^2}\right]^2 + \sum_{k\neq p}\sigma^2(S_k)\left[\frac{S_p(ZMV)_p(ZMV)_k}{\left\{\sum_i S_i(ZMV)_i\right\}^2}\right]^2 \tag{8.19}$$

[103] This is the square of the estimated standard deviation.

[104] Generally, if $Y = f(X_1, X_2, X_3, \ldots, X_n)$, and there are no correlations between the various X_i, then $\sigma_Y^2 = \sum_{i=1}^{n}\left(\frac{\partial f}{\partial X_i}\right)^2 \sigma_{X_i}^2$.

It is common practice to approximate the numerator in the first term in this equation, and to ignore the second term, in which case we have simply

$$\sigma(w_p) = \frac{\sigma(S_p)(ZMV)_p}{\sum_i S_i(ZMV)_i} \tag{8.20}$$

The relationship given in eqn (8.19) ignores correlations between estimates of the different S_i. When reflections overlap (e.g. as they do in Mg-PSZ), intensities will be ascribed to one phase or another, so there is likely to be a considerably negative correlation between the different S_i. This could diminish the contribution from the second term in eqn (8.19),[105] and thereby improve the approximation inherent in eqn (8.20).

Unfortunately, all QPA techniques, including microscopy and image analysis, are susceptible to systematic errors that are quite difficult to quantify. If sufficient patterns are available, it is can be instructive to examine the scatter of data points. The detailed study of the tetragonal to orthorhombic transition in Mg-PSZ (Howard *et al.* 1990), mentioned just above, provides data (Table 8.1) that can be studied in this way.

Table 8.1 Phase analyses for the tetragonal to orthorhombic transition in Mg-PSZ (Howard *et al.* 1990). This transition was induced by cooling; the reverse transition by subsequent heating. The entries for the different phases are given in wt %.

T (K)	c	t	o	m	$Mg_2Zr_5O_{12}$
220	6.0 (5)	61.4 (4)	2.2 (4)	7.0 (5)	23.3 (4)
200	6.0 (4)	61.5 (4)	2.4 (4)	7.0 (5)	23.2 (4)
180	6.1 (4)	42.7 (10)	19.1 (9)	6.9 (4)	25.1 (6)
157	5.5 (4)	33.9 (8)	28.9 (7)	6.8 (4)	25.0 (6)
141	5.9 (4)	30.8 (8)	33.2 (7)	6.4 (4)	24.5 (6)
100	4.6 (3)	26.5 (7)	38.3 (7)	6.3 (1)	24.3 (6)
19	4.0 (4)	26.2 (10)	38.2 (9)	7.1 (4)	24.5 (9)
307	3.8 (2)	19.4 (3)	45.5 (4)	6.7 (2)	24.6 (3)
496	3.8 (7)	20.9 (7)	44.2 (10)	7.0 (9)	24.2 (7)
597	3.5 (5)	49.3 (11)	14.6 (9)	8.0 (5)	24.6 (10)
620	4.1 (4)	59.6 (10)	5.0 (4)	7.9 (5)	23.3 (10)
649	4.4 (4)	59.6 (10)	4.9 (5)	7.6 (5)	23.5 (11)
664	4.1 (4)	61.6 (11)	5.1 (5)	7.5 (5)	21.8 (10)

Number in parenthesis are in the last decimal(s).

[105] Some Rietveld computer programs output QPA results, and it may be that the calculation and the error estimates are done quite correctly (try checking by hand, because it cannot always be assumed).

During the thermal cycle, there are no known mechanisms that alter the fraction of the cubic or $Mg_2Zr_5O_{12}$ phases and yet there does appear to be some systematic drift in the values, presumably due to the large degree of peak overlap for all the phases (see Fig. 8.4). The total drift is of order 3–5 esd, so we can see that in this case, the esd's underestimate the real uncertainty by a small amount.

The final component of eqn (8.6), the mass of a formula unit, M, is fixed for all stoichiometric compounds. However, the zirconia examples raise the important question of non-stoichiometric phases, that is, those that do not conform to Dalton's law of definite proportions. The stabilizing oxides used to tailor the microstructure of zirconia ceramics usually have cations of lower valence than Zr^{4+}. Examples include Ca^{2+}, Y^{3+}, and Mg^{2+}. In order to maintain charge balance, oxygen vacancies are created. These vacancies are of critical importance in zirconia alloys because they allow the ceramic to become electrically conductive above about 800°C. This fast ion conduction is useful in fuel cells, oxygen sensors, and heating element technology. Take, for example, cubic zirconia with 18 mol% MgO in solution. The correct formula unit becomes $Zr_{0.82}Mg_{0.18}O_{1.82}$ and M changes from 123.33 to 108.3 amu. Even more extreme departures from ideal proportions are possible, for example, in titanium carbide, TiC_x, x can range from 0.6 to 0.98. To illustrate the effect of this on a QPA result, let us use a contrived example with 60 wt% tetragonal zirconia (assuming pure zirconia for simplicity) and 40 wt% cubic zirconia with 18 mol% MgO in solution. We have used these phase proportions to calculate the diffraction pattern. Next, using the calculated pattern as data, we have conducted a Rietveld refinement ignoring the non-stoichiometry, that is, assuming both phases are pure zirconia. Table 8.2 shows the QPA results for two cases – the first when M_{ZrO_2} is used and the second when $M_{Zr_{0.82}Mg_{0.18}O_{1.82}}$ is used in eqn (8.6). Next, the reverse experiment was conducted, that is, the calculated pattern was produced using pure cubic zirconia as input, and then the refinement was conducted using $Zr_{0.82}Mg_{0.18}O_{1.82}$ as the refined cubic phase. The QPA results for this example using M_{ZrO_2} and $M_{Zr_{0.82}Mg_{0.18}O_{1.82}}$ in eqn (8.6) are also compared in the table.

Table 8.2 Effect of unrecognized stoichiometry changes on QPA results for a simulated $(c + t)$ ZrO_2 mixture.

	wt % t	wt % c
Pattern calculated using $Zr_{0.82}Mg_{0.18}O_{1.82}$ and fitted using ZrO_2		
M_{ZrO_2}	59.7	40.3
$M_{Zr_{0.82}Mg_{0.18}O_{1.82}}$	62.8	37.2
Pattern calculated using ZrO_2 and fitted using $Zr_{0.82}Mg_{0.18}O_{1.82}$		
M_{ZrO_2}	56.7	43.3
$M_{Zr_{0.82}Mg_{0.18}O_{1.82}}$	59.8	40.2

It can be seen from these results, which are based on simulated 'data' free from systematic or random errors, that departures from stoichiometry of this order *in this case* have a serious effect on QPA results if and only if there is a mismatch between the formula unit used in the Rietveld analysis and that used in the QPA calculation. The results are very robust with respect to stoichiometry change as long as a consistent formula unit (even if it is the incorrect one) is used in the Rietveld analysis *and* the QPA calculation. This observation can be understood by examining eqns (5.10) and (8.4). In eqn (5.10), a change in the model to account for non-stoichiometry changes the computed value of $|F|^2$ and because the observed intensities are fixed, there is a compensating change in S. In eqn (8.3), this change in S is offset by the change in M due to non-stoichiometry. The effect is partly fortuitous in this case since the scattering length difference and atomic mass difference have the same sign (i.e. b_{Mg} and m_{Mg} are less than b_{Zr} and m_{Zr}). This is not always the case with neutrons (see §2.3.3); however, it is the case for X-rays where it is likely to be always observed. More generally, known cases of non-stoichiometry should not be ignored in Rietveld-based QPA, because the chemical composition of the phase in question is valuable additional information. What it does mean is that the 'error' introduced into the computed phase proportions by the uncertainty in M can usually be safely ignored.

Other ND-QPA work on Mg-PSZ led to a documentation of the influence of the phase $Mg_2Zr_5O_{12}$, formed during aging at 1100°C, on the propensity of the tetragonal phase to transform into the monoclinic phase (Hannink *et al.* 1994). The QPA results are summarized in Fig. 8.6. Also shown on the figure are the 'toughness increments' (0.6, 3, and 7.5 MPa $m^{-1/2}$ for 0, 2, and 8 h aging).

8.6.3 Materials in simulated service

Another important area where neutron diffraction QPA has been invaluable has been in the study of materials in simulated service. The zirconia ceramics that were used as examples in the previous section are the toughest known and can be plastically deformed slightly. They are used in high stress applications such as ball-valves for oil wells. Initially it was thought that sufficient data could be obtained from *ex situ* XRD and TEM studies for the mechanical behaviour of zirconia ceramics to be understood. However, the observation of room temperature creep in Mg-PSZ (Finlayson *et al.* 1994) and the apparent time dependence of QPA results conducted on tensile test samples after testing changed matters somewhat. It was suggested that transient states may exist in the material and that these cannot be reliably observed *ex situ*. There are three major types of structural zirconia ceramic: 9Mg-PSZ, 12Ce-TZP, and 3Y-TZP.[106] All three have been studied by ND-QPA during the application of compressive stresses of up to 2.3 GPa

[106] 9 mol% MgO – partially stabilized zirconia, 12 mol% CeO_2 – tetragonal zirconia polycrystal and 3 mol% Y_2O_3 – tetragonal zirconia polycrystal.

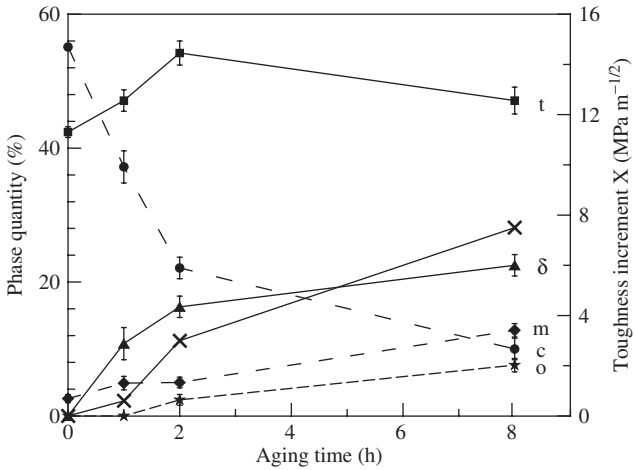

Fig. 8.6 Phase quantities estimated from Rietveld analysis QPA of neutron diffraction patterns from Mg-PSZ samples aged for various times at 1100°C. The identity of the phases is indicated at the right and the toughness increment due to these phase changes is indicated by (×) referred to the right-hand axis.

(Cain *et al.* 1994; Kisi *et al.* 1997; Ma *et al.* 2001, 2004, Ma and Kisi 2005). It transpires that two major microstructural mechanisms are at work: the Martensitic tetragonal to monoclinic phase transformation discussed earlier *and* ferroelastic domain switching within the tetragonal phase. The results are summarized in Fig. 8.7 as the wt% of monoclinic phase and the March–Dollase preferred orientation parameter R [eqn (5.29), §5.5.2] as a function of applied stress for 12Ce-TZP. It can be seen that Ce-TZP shows both t→m transformation and ferroelasticity, whereas Mg-PSZ shows only t→m transformation and Y-TZP shows ferroelasticity alone.

All three materials showed time-dependent behaviour. In Mg-PSZ, each (2 h) diffraction pattern was recorded at constant stress, and creep strain accumulated continuously during this time. The macroscopic creep strain was independently observed using strain gauges glued to the samples. After release of the stress, a proportion of the stress-induced monoclinic phase reverted back to the tetragonal phase on the scale of days to months. In Ce-TZP, most of the observed strain was due to t→m transformation which occurred in sharp bursts separated by slow creep even during holding of constant stress. The accompanying ferroelasticity was readily observed but was only a secondary deformation mechanism. The monoclinic phase was observed to revert to the tetragonal form on a time-scale of hours to days. Y-TZP in compression showed only ferroelastic switching. Reverse switching on release of the stress occurred within a few hours. Had the work been conducted using individual peak methods, ferroelasticity in the tetragonal phase could have been overlooked and, because ferroelasticity causes preferred orientation in the

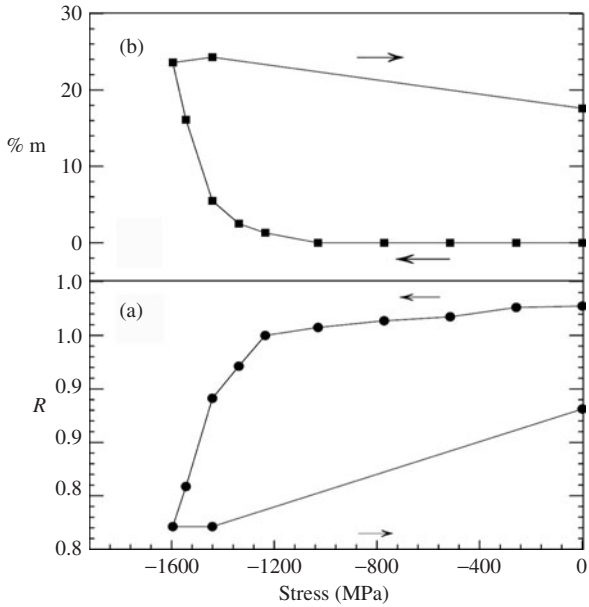

Fig. 8.7 Summary of (a) the wt% monoclinic phase and (b) preferred orientation in the majority tetragonal phase in a Ce-doped tetragonal zirconia polycrystal under applied compressive stress (Kisi *et al*. 1997).

monoclinic phase, it would have invalidated QPA results concerning the amount of that phase.

8.6.4 *In situ* synthesis

Perhaps the most powerful examples of ND-QPA relate to the *in situ* study of materials synthesis. The series of results chosen here represent, for the same reacting system, three levels of sophistication that may be obtained with different time-resolution instruments and differently designed experiments. The system chosen is the synthesis of Ti_3SiC_2 from $3Ti + SiC + C$ starting materials. Ti_3SiC_2 has a very unusual combination of properties both ceramic (heat, oxidation, and chemical resistance) and metallic (thermal and electrical conduction, machinability, and excellent thermal shock resistance). *Ex situ* studies had led to considerable debate in the literature concerning the identity and role (if any) of intermediate phases in the overall reaction:

$$3Ti + SiC + C \rightarrow Ti_3SiC_2$$

There are abundant potential intermediate phases in the Ti–Si–C system including TiC, $TiSi_2$, TiSi, Ti_5Si_4, Ti_5Si_3, and Ti_3Si, all of which had been observed in

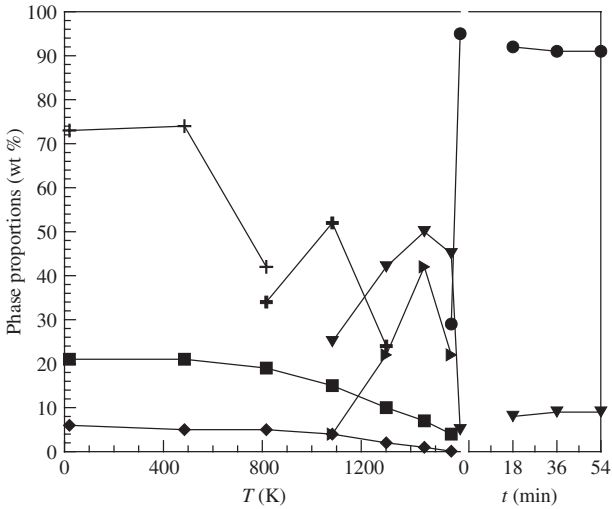

Fig. 8.8 Phase quantities estimated from Rietveld analysis QPA of neutron diffraction patterns recorded during the synthesis of Ti_3SiC_2 at 18 min time resolution (Wu *et al.* 2001). The phases shown are the reactants α-Ti (+), SiC (■), and C (♦); the intermediate phases β-Ti (heavier +), TiC_x (▼), and $Ti_5Si_3C_x$ (►); and the product Ti_3SiC_2 (●).

partially reacted samples cooled from the usual processing temperature (1600°C). Three stages in the solution of this problem follow.

Identity of intermediate phases

The first *in situ* ND-QPA study of this system used the CW medium resolution powder diffractometer at ANSTO (Wu *et al.* 2001). Neutron diffraction patterns were recorded from pellets made from stoichiometric mixtures of Ti, SiC, and C during heating at 10°C/min and holding at 1600°C. The time resolution of the experiment was approximately 19 min comprising 18 min to record a pattern with sufficient intensity to allow Rietveld refinement and 1 min for the detector bank to drive back to the starting position.

The QPA results are shown in Fig. 8.8. From these data it is clear that the α–β transition in Ti (hcp → bcc) begins before any other resolvable product is formed. Next two intermediate phases, TiC_x and $Ti_5Si_3C_x$ form during the heating ramp. These two phases then appear to react with each other to form Ti_3SiC_2. Even with these rudimentary data, it was possible to rule out all other intermediate phases and to postulate a reaction mechanism. A very small amount of the reactant phase SiC appears to persist at the same time as the intermediate phases; however at this time resolution, the exact sequence was still a little unclear. Either individual peak *or* whole pattern analysis would both have been able to give the QPA results in

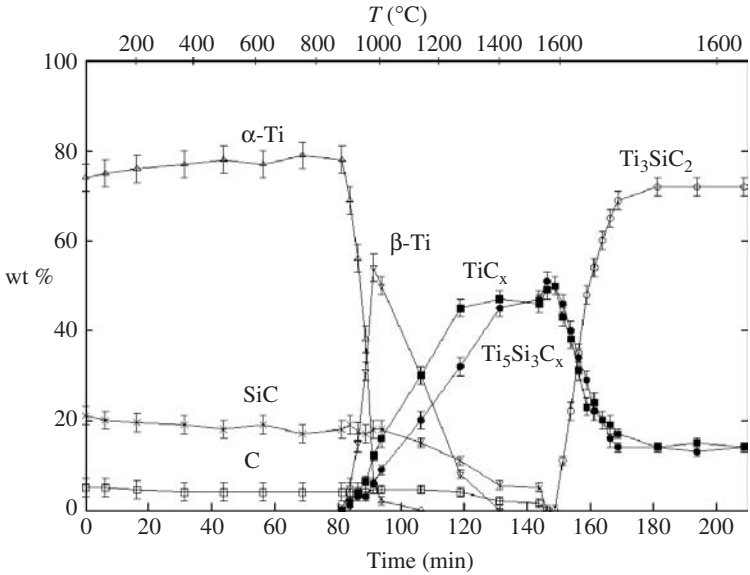

Fig. 8.9 Phase quantities estimated from Rietveld analysis QPA of neutron diffraction patterns recorded during the synthesis of Ti_3SiC_2 at 2.7-min time resolution (Wu *et al.* 2002).

Fig. 8.8; however, the Rietveld refinements were able to provide valuable additional information. This includes the value of x in TiC_x and $Ti_5Si_3C_x$ both of which begin close to their minimum values (0.5 and 0, respectively) and increase with temperature appearing to attain their stoichiometric states ($x \approx 1$) just prior to their disappearance. However this information too is a little clouded by insufficient time resolution.

Reaction mechanism

To clarify the reaction sequence a second experiment was conducted at 2.7 min time resolution[107] on the TOF diffractometer POLARIS at the ISIS facility, Rutherford Appleton Laboratory, UK (Wu *et al.* 2002). The QPA data are summarized in Fig. 8.9. A number of features are clarified. First, the α–β transition in Ti is definitely the first change in the samples and is well underway before any chemical change occurs. TiC_x and $Ti_5Si_3C_x$ are confirmed as the only intermediate phases and, for a period covering several diffraction patterns, are the *only* crystalline phases visible in the diffraction patterns. The decay in the fractions of intermediate phases mirrors the growth of Ti_3SiC_2. The reaction is incomplete in the example shown due to Si and Ti loss within the vacuum furnace used. The overall reaction

[107] Approximately 2 min per pattern and 30 seconds for data download.

may now be written as

$$3\beta\text{–Ti} + \text{SiC} + \text{C} \rightarrow \frac{4}{3}\text{TiC} + \frac{1}{3}\text{Ti}_5\text{Si}_3\text{C} + \frac{1}{3}\text{C}$$

$$\frac{4}{3}\text{TiC} + \frac{1}{3}\text{Ti}_5\text{Si}_3\text{C} + \frac{1}{3}\text{C} \rightarrow \text{Ti}_3\text{SiC}_2$$

the first half occurring during heating below 1200°C and the second half upon attaining temperatures above 1300°C.

Reaction kinetics

The next level of detail available was to study the reaction kinetics (Wu *et al.* 2005). During the same campaign at ISIS, data were recorded by heating at 10°/min and holding at 1450°C, 1500°C, 1550°C, and 1600°C while neutron diffraction patterns were recorded at 2.7-min time resolution. A small correction was applied to the time scale to account for part of the incubation period occurring on the heating ramp. The aim of the experiment was to study the kinetics of the high temperature reaction between the intermediate phases to form Ti_3SiC_2. QPA data for $f(t)$ the mol fraction of Ti_3SiC_2 as a function of time at each temperature were fitted to the Avrami kinetic equation (Avrami 1939, 1940):

$$f(t) = 1 - \exp\left[-K(t)^n\right] \tag{8.21}$$

where n is an exponent that gives some insight into the mechanism and K is the rate constant given by

$$K = K_0 \exp\left[\frac{-E}{RT}\right] \tag{8.22}$$

for a process with activation energy E. Taking logarithms of eqn (8.21) twice we obtain

$$\ln\left[-\ln\left(1-f\right)\right] = n\ln K + n\ln t \tag{8.23}$$

and a plot of $\ln[-\ln(1-f)]$ versus $\ln(t)$ will give n and K. Data at several temperatures allow the activation energy E to be determined. The plots for this system are given in Fig. 8.10. Note that the data recorded at 1600°C can only be processed as part of the same data set if a notional temperature of 1565°C is substituted for 1600°C because all of the incubation period and some of the reaction period had elapsed before reaching 1600°C (Wu *et al.* 2005). The activation energy determined is 380 kJ/mol; larger than the formation enthalpy of TiC (−185 kJ/mol) but smaller than the formation enthalpy of Ti_5Si_3 (−579 kJ/mol).

In Fig. 8.10, it can be seen that the data depart from the lines of best fit towards the end of the reaction. This is equivalent to a change in the exponent n from close to 3 to close to 1. According to Avrami (1941), this is most

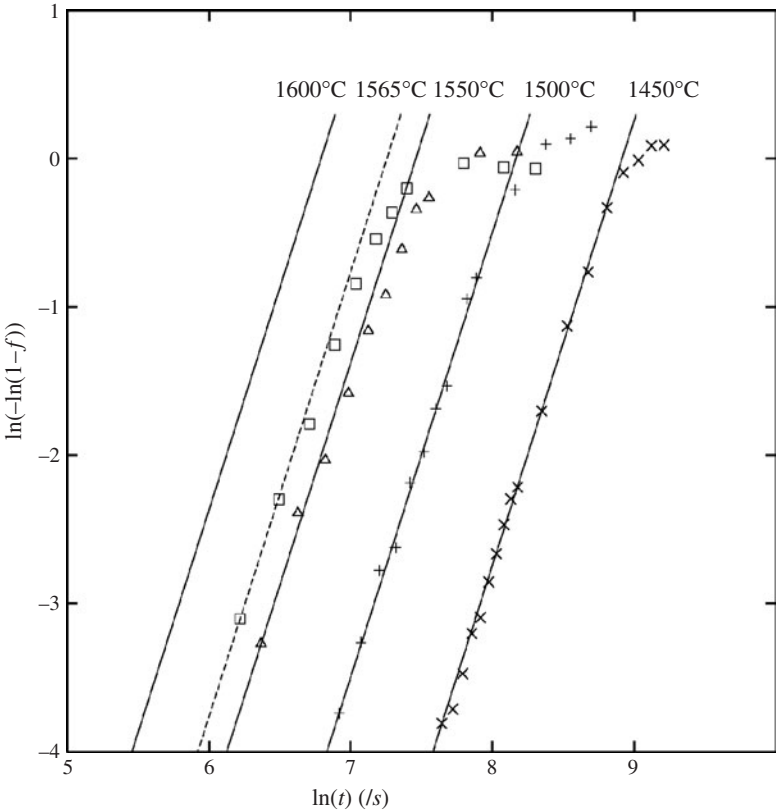

Fig. 8.10 Kinetics of the reaction between TiC_x and $Ti_5Si_3C_x$ to form Ti_3SiC_2 expressed as the function $\ln[-\ln(1-f)]$ versus $\ln(t)$ at different temperatures (Wu *et al.* 2005). The straight line at each temperature is drawn according to the fitted values of $k_0 = 4.45 \times 10^7$ s^{-1} and $E = 380 \pm 10$ kJ/mol. The symbol corresponding to each temperature is ×1450°C, + 1500°C, Δ 1550°C and □ 1600°C.

likely the result of a change from unrestricted three-dimensional growth (or nucleation plus two-dimensional growth) to one-dimensional growth. In this system, we have interpreted this as signifying when the sheet-like hexagonal crystals of Ti_3SiC_2 which grow preferentially in the *a–b* plane, impinge on one another. The crystal growth mechanism then changes to one-dimensional growth along the non-preferred *c*-axis. Pockets of intermediate phases are isolated between Ti_3SiC_2 crystals and if, after time, a given pocket is occupied by TiC or Ti_5Si_3C alone then these will remain as 'impurity' or remnant intermediate phases in the final product.

There is, in fact, a fourth episode to the *in situ* study of Ti_3SiC_2 synthesis. If the heating rate is increased from 10°/min to >30°/min, the reaction enters a self-propagating high-temperature (SHS) synthesis regime. In this mode, the heat of

reaction takes over from the external heat source and the sample temperature soars to >2000°C. This too has been studied using *in situ* neutron powder diffraction and QPA at extreme time resolutions (380 ms). However, a discussion of that work is reserved for Chapter 12 as one of the exciting new directions for neutron powder diffraction. The impatient reader may of course go directly there.

9

Microstructural data from powder patterns

9.1 INTRODUCTION

It was just two years after the discovery of X-ray diffraction in 1912 that the influence of the internal structure of crystals on the diffracted intensities (extinction) had been mathematically described (Darwin 1914). Similarly, it took only 2 years from the advent of the X-ray powder diffraction camera (Debye and Scherrer 1916) before the influence of the sample microstructure on powder diffraction peaks was realized (Scherrer 1918). Except in the case of texture (§9.8) the principal influence of microstructure is to alter the detailed *shapes* of the diffraction peaks. This varies from simple symmetric broadening of the peaks (small crystallite size, strain distributions) to very complex, sometimes asymmetric, broadening that differs from peak to peak (dislocations, stacking faults). The effects are the same in neutron as in X-ray powder diffraction so in this chapter distinction is rarely made between the two, although it is acknowledged that the techniques discussed were developed for the X-ray case.

In many kinds of research (e.g. phase analysis, crystal structure solution), these microstructural effects are largely of nuisance value and steps should be taken to avoid them (see §3.6). It was the Swiss physicist, Paul Scherrer, who first realized that line broadening could be used as a tool to investigate microstructure in the sample (Scherrer 1918). The simple relationship that he derived, between peak width and the particle size in the sample, remains in use today except for variations of a few percent to a constant term. From these insightful beginnings, a rich field of study with many outstanding contributions grew. There is easily sufficient material for an entire volume in this area (see indeed Snyder *et al.* 1999); however, we will limit ourselves here to covering the fundamental aspects of microstructural studies using powder diffraction and how to apply them in the modern context using neutron data.

One of the greatest difficulties in this area is that sample microstructures can be very complex. Several of the elements of a complex microstructure may each contribute to peak broadening or peak shape changes. How can we separate them? Two primary philosophies have arisen over time:

(i) Deconvolution of peak profiles into components due to the sample microstructure and the diffraction instrument used to record the data;
(ii) Peak profile simulation with or without direct fitting to the observed peaks.

A hybrid approach, known as the 'fundamental parameters approach' is a variant of the profile simulation method that assembles the peak profile by (forward) convolution from all of the elements along the optical path (including the sample).

In modern times, the availability of considerable computational power and the advent of whole pattern fitting methods has led to a preference on the part of most workers to adopt method (ii) – peak profile simulation. An advantage of this approach is that the microstructural data are extracted simultaneously with crystal structure and if desired, phase quantification data. The only disadvantage is that in some cases the available peak shape functions (§4.5) are not sufficiently flexible to fit the grossly distorted peaks that arise from chemical and physical gradients, line defects, or plane defects. In these cases, specialized methods are employed. We attempt here to provide a balanced mix of deconvolution and profile simulation methods.

This chapter is organized to begin with the simplest forms of broadening (small particle size (§9.2) and microstrains (§9.3)). Next we introduce methods of handling the combined effects of these two features, as is often necessary in solid polycrystalline samples (§9.4). There follow three sections concerned with peak shape changes associated with chemical and physical gradients (§9.5), line defects (§9.6), and plane defects (§9.7). A final section (§9.8) deals with a microstructural feature that leads to intensity rather than peak shape changes – namely texture or non-randomness of crystallite orientations.

9.2 PARTICLE SIZE

As a prelude to our discussion, it is important to have a feel for the magnitude of the line broadening due to small crystal size. Figure 9.1 shows an example for crystals 100 Å in diameter. The diffraction peak width due only to the crystallite size, is ~0.8–1.5° 2θ in this CW pattern calculated for 1.5 Å neutrons, compared with the instrumental breadth of ~0.25° 2θ.

9.2.1 Isotropic particle size broadening

To explore the physical origins of particle size broadening, we wish to examine more closely the intensity of diffracted beams. In our discussion of the intensity of the diffracted beams of neutrons in §2.4.2, we calculated the structure factor, F, scattered by one unit cell and applied various physical and geometric corrections to it. This treatment neglects the fact that for sharp diffraction peaks to occur, it is necessary for destructive interference to take place between a large number of adjacent unit cells, at all angles not satisfying Bragg's law. The missing link oft overlooked in elementary crystallographic texts, is the phase relationship that exists between *adjacent* unit cells. A readable account of how this may be incorporated into the intensity calculation is given by Azároff (1968) and we present the essential results below, adapted to neutron diffraction.

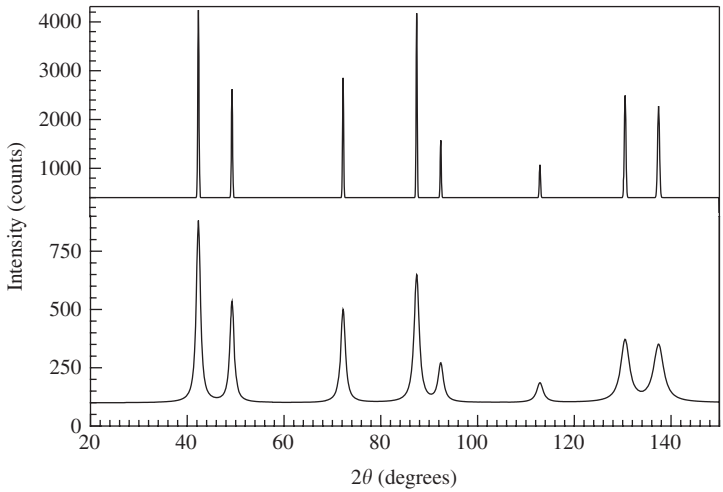

Fig. 9.1 Simulated 1.5 Å CW neutron diffraction pattern from Ni showing the influence of particle size broadening due to 100 Å crystallites (lower pattern) compared with the unbroadened pattern. Instrument characteristics match the instrument HRPD at the HIFAR reactor, ANSTO, Australia.

The wave scattered by the unit cell is represented by:

$$\psi = W \sum_n b_n \exp 2\pi i \, [\boldsymbol{H}_{hkl} \cdot \boldsymbol{r}_n] \tag{9.1}$$

where W is a collection of physical constants [see eqn. (2.47)] that remain unaltered throughout, and the summation is the usual structure factor F written in vector notation [eqn (2.32)]. To include the scattering from *all* of the unit cells and correctly account for phase relationships between them, we must sum over the whole volume of the crystal. The position vector of the atom within the unit cell, $\boldsymbol{r}_n$, must be replaced with the position vector within the crystal $\boldsymbol{R}_n = \boldsymbol{r}_n + m_1\boldsymbol{a} + m_2\boldsymbol{b} + m_3\boldsymbol{c}$ to give

$$\psi = W \sum_n \sum_{m_1} \sum_{m_2} \sum_{m_3} b_n \exp 2\pi i \left[\frac{\boldsymbol{s} - \boldsymbol{s}_0}{\lambda} \cdot (\boldsymbol{r}_n + m_1\boldsymbol{a} + m_2\boldsymbol{b} + m_3\boldsymbol{c}) \right] \tag{9.2}$$

Here $\boldsymbol{s}$ and $\boldsymbol{s}_0$ are unit vectors in the directions of $\boldsymbol{k}$ and $\boldsymbol{k}_0$ respectively. Assuming for simplicity that the crystallite is a parallelepiped of dimensions M_1 unit cells along the $\boldsymbol{a}$ crystallographic axis, M_2 along $\boldsymbol{b}$ and M_3 along $\boldsymbol{c}$, the scattered wave

becomes:

$$\psi = WF \frac{\left(\exp\left[\frac{2\pi i}{\lambda}(\boldsymbol{s}-\boldsymbol{s}_0)\cdot M_1\boldsymbol{a}\right]-1\right)}{\left(\exp\left[\frac{2\pi i}{\lambda}(\boldsymbol{s}-\boldsymbol{s}_0)\cdot \boldsymbol{a}\right]-1\right)} \frac{\left(\exp\left[\frac{2\pi i}{\lambda}(\boldsymbol{s}-\boldsymbol{s}_0)\cdot M_2\boldsymbol{b}\right]-1\right)}{\left(\exp\left[\frac{2\pi i}{\lambda}(\boldsymbol{s}-\boldsymbol{s}_0)\cdot \boldsymbol{b}\right]-1\right)}$$
$$\times \frac{\left(\exp\left[\frac{2\pi i}{\lambda}(\boldsymbol{s}-\boldsymbol{s}_0)\cdot M_3\boldsymbol{c}\right]-1\right)}{\left(\exp\left[\frac{2\pi i}{\lambda}(\boldsymbol{s}-\boldsymbol{s}_0)\cdot \boldsymbol{c}\right]-1\right)} \tag{9.3}$$

which, after further simplification and multiplication by the complex conjugate, represents the intensity of the diffracted beam as:

$$I = C\,|F|^2 \frac{\sin^2\left[\frac{\pi}{\lambda}(\boldsymbol{s}-\boldsymbol{s}_0)\cdot M_1\boldsymbol{a}\right]}{\sin^2\left[\frac{\pi}{\lambda}(\boldsymbol{s}-\boldsymbol{s}_0)\cdot \boldsymbol{a}\right]} \frac{\sin^2\left[\frac{\pi}{\lambda}(\boldsymbol{s}-\boldsymbol{s}_0)\cdot M_2\boldsymbol{b}\right]}{\sin^2\left[\frac{\pi}{\lambda}(\boldsymbol{s}-\boldsymbol{s}_0)\cdot \boldsymbol{b}\right]} \frac{\sin^2\left[\frac{\pi}{\lambda}(\boldsymbol{s}-\boldsymbol{s}_0)\cdot M_3\boldsymbol{c}\right]}{\sin^2\left[\frac{\pi}{\lambda}(\boldsymbol{s}-\boldsymbol{s}_0)\cdot \boldsymbol{c}\right]} \tag{9.4}$$

Each quotient may be expressed as a generalized interference function

$$\frac{\sin^2 Mx}{\sin^2 x} \tag{9.5}$$

which is a periodic function with maximum value M^2 at $x = n\pi$, where n is an integer. Thus, for the intensity at eqn (9.4) to be maximum the three conditions:

$$\begin{aligned}(\boldsymbol{s}-\boldsymbol{s}_0)\cdot\boldsymbol{a} &= h\lambda\\ (\boldsymbol{s}-\boldsymbol{s}_0)\cdot\boldsymbol{b} &= k\lambda\\ (\boldsymbol{s}-\boldsymbol{s}_0)\cdot\boldsymbol{c} &= l\lambda\end{aligned} \tag{9.6}$$

must be met simultaneously. This is in fact a re-statement of the diffraction conditions (eqn 2.25) in what is known as the Laue form.

Recalling that M is a measure of the crystallite size (e.g. $M \sim \frac{V^{1/3}}{a}$ for a cube crystal of volume V), it is instructive to see what happens as M varies. It is only necessary to examine one quotient (eqn (9.5)) since it is always possible to re-define the unit cell such that a given scattering vector forms one of the unit cell axes. Some examples are shown in Fig. 9.2 for M equal to 10, 20, 50, 500, respectively.[108] Several remarks can be made:

(i) The width of the central maximum is sensitive to the crystal size; in fact by numerical methods it is found that the function eqn (9.5) falls to half its maximum value at $x_{1/2}$ satisfying

$$Mx_{1/2} = 0.443\pi \tag{9.7}$$

practically independent of M.

[108] Here the functions have been normalized to have a maximum height of 1 by dividing through by M^2. See, for example, Klug and Alexander (1974).

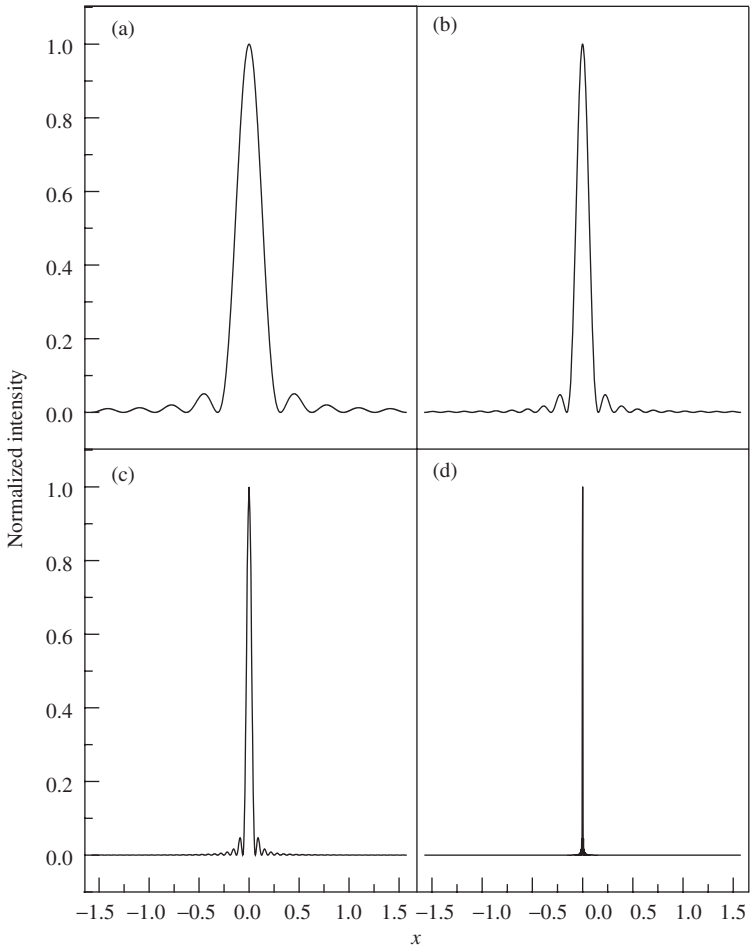

Fig. 9.2 Interference functions from summation over (a) 10, (b) 20, (c) 50, and (d) 500 unit cells.

(ii) The subsidiary maxima diminish into the background as M becomes larger. In practice these are rarely observed in powder diffraction because of the combined effects of the wavelength spread in the incident beam (CW), the incident beam divergence and the effect of the particle size distribution about the mean value. These lead to a blurring of the subsidiary maxima into relatively smooth peak 'tails'.

(iii) Since the maximum value of the interference function is M^2, and [from (i)] the width varies as $1/M$, we would expect the area under one period of the interference function to vary directly with M. In fact for positive integer M,

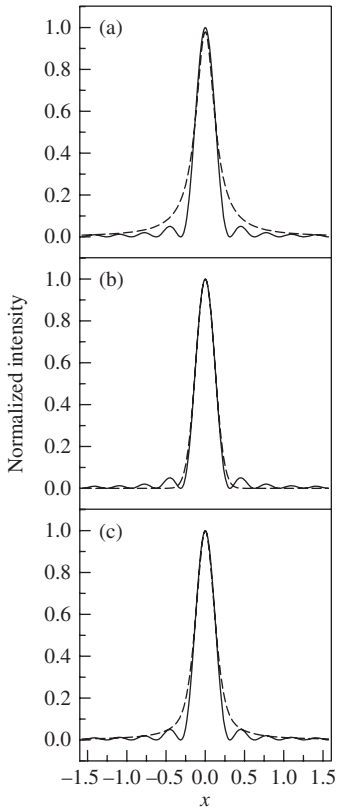

Fig. 9.3 Comparison of the interference function from Fig. 9.2(a) with (a) Lorentzian and (b) Gaussian peaks with the same height and FWHM. A comparison to a pseudo-Voigt function of arbitrary shape is given in (c).

we find[109]

$$\int_{-\pi/2}^{\pi/2} \frac{\sin^2 Mx}{\sin^2 x} dx = M\pi \tag{9.8}$$

(iv) Neither the Gaussian nor Lorentzian profile (Table 5.8, §4.5.1) provides an adequate description of the interference function. It is quite clear (Fig. 9.3) that the central peak is almost Gaussian but that the subsidiary maxima extend well beyond the Gaussian cut off. The tails, on the other hand, can be well represented by a Lorentzian profile but then the central peak is too narrow

[109] Based on Gradshteyn and Ryzhik (2007), eqn 3.624(6).

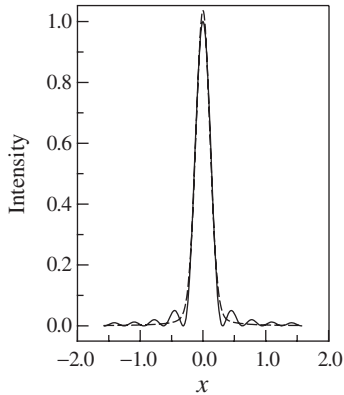

Fig. 9.4 Fit to the interference function from Fig. 9.2(a) of a pseudo-Voigt function with the same integrated intensity. The refined value of the mixing parameter η was 0.23, that is, the best fit peak has only 23% Lorentzian character.

and tall. We pause here to ask; '*is there a simple profile shape that does fit the envelope of an interference function?*' The answer is '*Yes, it is the Voigt function*'. This is demonstrated in Fig. 9.4 showing the function of Fig. 9.2(a) fitted by pseudo-Voigt, eqn (4.4), with Lorentzian fraction ~0.23. From this we can conclude that, for a collection of spherical crystals of identical size, the appropriate profile is a Voigt function with the characteristics indicated above. In practice, the peaks obtained from any real crystallites may be far closer to Lorentzian than this fitting would imply (§9.2.2).

Noting that the full width at half maximum (FWHM) in 2θ, H_P, is related to $x_{1/2}$ by $H_P = 2\lambda x_{1/2}/(\pi a \cos\theta)$ and taking $x_{1/2}$ from eqn (9.7), or by simple geometric arguments,[110] it is possible to derive a relationship between the mean particle diameter, D, and the particle size broadening in a CW diffraction pattern:

$$H_P = \frac{K\lambda}{D\cos\theta} \text{ (radians) or } H_P = \frac{180K\lambda}{\pi D\cos\theta} \text{ (degrees)} \tag{9.9}$$

a relationship known as Scherrer equation. K is a constant approximately equal to 0.9 depending on assumptions made during the derivation.

Now H_P refers only to the broadening caused by particle size effects and not to the width of the entire peak. As discussed in §4.5, the shape and width of diffraction peaks are influenced by several elements along the optical path. The situation is most conveniently described using the ideas of convolution [defined at eqn (5.31)]. Stated mathematically, the observed peak profile $h(x)$ is shaped by the convolution or folding of the source peak profile $g_1(x)$with the functional form of each element

[110] See, for example, Klug and Alexander (1974).

of the optical path $g_i(x)$ and with the pure peak profile of the sample $f(x)$, that is,

$$h(x) = g_1(x) * g_2(x) * g_3(x) * \ldots * g_n(x) * f(x) \tag{9.10}$$

Convolution is associative and so we can combine all of the profiles due to the source and instrumental factors giving the simplified form:

$$h(x) = g(x) * f(x) \tag{9.11}$$

where $g(x) = g_1(x) * g_2(x) * g_3(x) * \ldots * g_n(x)$.

A critical feature of particle size estimation using powder diffraction is therefore the problem of extracting the pure sample profile, $f(x)$, from the observed profile $h(x)$. Several methods have been proposed. We will begin with the Fourier transform method of Stokes (1948).

Fourier deconvolution

The method is based on a result of Fouriers' integral theorem (also known as the convolution theorem) that the Fourier transform of the convolution of two functions is given by the product of their individual Fourier transforms. The convolved function can be retrieved (from the Fourier space) by taking the inverse transform of the product. Symbolically, if we let $F(\xi)$ be the Fourier transform of $f(x)$:

$$F(\xi) = \int f(x) \exp(2\pi i x \xi) dx \text{ [111]} \tag{9.12}$$

and similarly $H(\xi)$ and $G(\xi)$ be the Fourier transforms of the observed and instrument profiles $h(x)$ and $g(x)$, respectively, then by the convolution theorem:

$$H(\xi) = G(\xi) F(\xi)$$

or

$$F(\xi) = \frac{H(\xi)}{G(\xi)} \tag{9.13}$$

Taking the inverse Fourier transform gives the required sample profile:

$$f(x) = \int \frac{H(\xi)}{G(\xi)} \exp(-2\pi i x \xi) d\xi \tag{9.14}$$

Therefore if we are in the possession of a carefully measured diffraction pattern from a standard material (i.e. unaffected by particle size or strain broadening), the pure sample profile $f(x)$ can be extracted as illustrated in Fig. 9.5. If the broadening is known to be purely from particle size, then a direct application of the Scherrer equation [eqn (9.9)] can be made. In the presence of other forms of broadening, extra computation is required (see §9.4).

[111] In practice the integration is from $-\frac{1}{2}x_m$ to $+\frac{1}{2}x_m$, these limits being set at values beyond which intensities $f(x)$, $g(x)$, $h(x)$ are judged to have fallen to background. In these circumstances, the Fourier transforms are reduced to Fourier series.

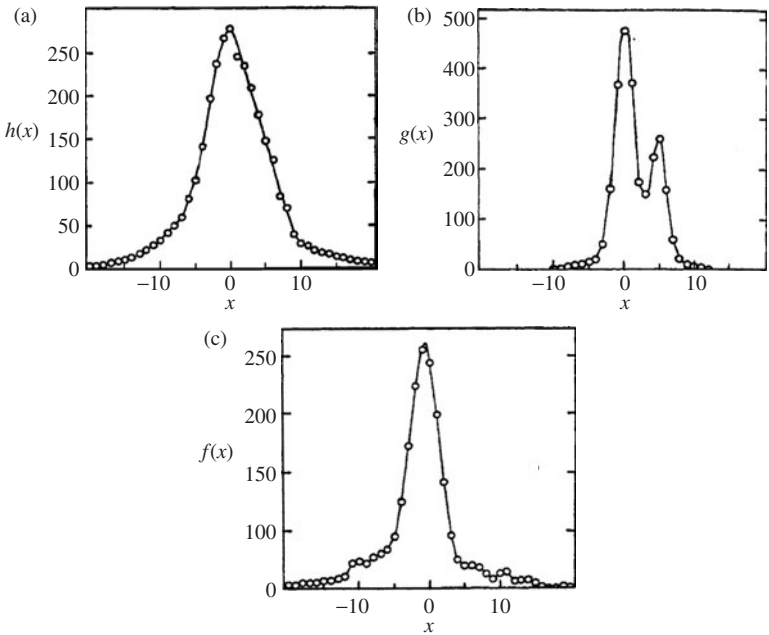

Fig. 9.5 Fourier deconvolution method of Stokes (1948).

An important feature of the deconvolution method is that it involves no assumptions about the functional form (or shape) of either the instrument contribution $g(x)$ or the sample profile $f(x)$. Though, at the time of its inception the method was computationally laborious, it was considered less laborious than most alternatives. Modern computing power has greatly facilitated the computations. There remain, however, certain other disadvantages:

(i) Only selected peaks are used and, depending on the complexity of the sample and its crystal structure, this may give misleading results (e.g. if there is unresolved splitting of the chosen peaks).
(ii) The results are sensitive to the choice of background level and the peak cut-off limits ($\pm\frac{1}{2}x_m$) assumed.
(iii) The results are sensitive to noise in the data and usually the raw profile must be smoothed. The convolution of the experimental profile with a Gaussian, or equivalently the application of damping to the high frequency components in Fourier space (Reefman 1999), can be employed for this purpose.
(iv) The method as usually implemented is not integrated with other diffraction-based analyses (structure refinements, etc.).

Fourier deconvolution links naturally with the Fourier methods for analysing the combination of size and strain broadening that will be described later, in

§9.4.2. There appear to be few instances, however, of the application of Fourier deconvolution to the analysis of neutron data.

Peak variance

A method based on the peak variance or reduced second moment, was developed by Wilson (1962a, 1962b). The special advantage of the method is that the variance of the measured peak is merely the sum of the variance of the instrument and sample profiles regardless of their shapes. A major disadvantage is an enhanced sensitivity to the background and the values used for the peak cut-off limits. The authors are not aware of any application of this method to neutron diffraction data and it seems to have been overtaken by developments in profile fitting and whole pattern analyses.

Peak shape functions

Simplified methods for estimating crystallite size (and strain) by assuming a particular functional form for $g(x)$ and $f(x)$, and then working only with the peak widths (FWHM or integral breadths) were developed for X-ray diffraction peaks in the 1940's. Gaussian [eqn (4.2)] and the Lorentzian [eqn (4.3)] (or Cauchy) functions were commonly employed. There was until recently no clear theoretical guidance on which (if either) one should expect for a sample profile $f(x)$ showing particle size broadening. The difference is very significant because the widths of Gaussian peaks add in quadrature, that is,

$$H_{\text{obs}}^2 = H_I^2 + H_P^2 \tag{9.15}$$

where H_{obs} and H_I are the width of $h(x)$ and $g(x)$ respectively. The widths of Lorentzians on the other hand, add linearly, that is,

$$H_{\text{obs}} = H_I + H_P \tag{9.16}$$

There was evidence in the early X-ray diffraction literature suggesting that the Gaussian function was appropriate for strain broadening (see §9.3) and the Lorentzian for particle size broadening (e.g. Klug and Alexander 1974; Delhez *et al.* 1993). Assuming a Lorentzian form for particle size broadening, however, would not solve the problem posed by eqns (9.15) and (9.16), because the instrumental peak shape in neutron powder diffraction is either nearly Gaussian (CW) or a complicated double exponential [time-of-flight (TOF)]. The observed peak profile, being the convolution of the instrument profile $g(x)$ with the sample profile $f(x)$ broadened by the small crystal effect, would be neither Gaussian nor Lorentzian in form. This renders simple procedures involving linear or quadratic sums of peak widths inadequate, suitable for preliminary analyses at best.

The problem can be partly resolved by peak fitting using one of the profile functions given in Table 5.8. The simplest example is the use of a Voigt function for peaks recorded on CW instruments where $g(x)$ is known to be close to Gaussian. The Voigt function given in Table 5.8 has been specifically set out in terms of

the FWHM of the contributing Gaussian and Lorentzian components, H_G and H_L. If one has faith in the assumption of a Lorentzian shape for the particle size broadening, then H_L may be used directly as H_P in Scherrer equation [eqn (9.9)], and the mean crystallite diameter, D, estimated. The more complex TOF peak shapes can be used in a similar way although it is common for there to be strong correlations between the parameters when single peaks are fitted. In the TOF case, it is necessary to fix instrument related parameters [e.g. see eqn (4.8)] from data recorded using a 'perfect' standard sample.

Individual peak fitting and FWHM techniques are attractive because of their simplicity. However, they too are not recommended for serious particle size analysis without a significant amount of calibration work. The assumptions that can lead to problems are that

(i) small crystallite size is the sole source of broadening;
(ii) the crystallites are equi-axed[112] leading to isotropic broadening;
(iii) the size broadening is Lorentzian.

Instead, the recommended approach is whole pattern fitting (§4.6). In whole pattern fitting software (e.g. Rietveld analysis programs) the particle size component of the peak width is made to vary as $1/\cos\theta$ in CW patterns and as d^2 in TOF patterns, in keeping with the Scherrer equation. The peak profile parameters relating to the instrument are determined from a standard sample and then not allowed to vary during the fitting procedure.[113] If another source of broadening is present, then the quality of the fit will deteriorate as a function of 2θ or TOF. The question of multiple sources of broadening is discussed in the later sections of this chapter. Similarly, if the crystallites are not equi-axed (e.g. needles or platelets) with a strong association between the crystallographic axes and the external dimensions; then the broadening will be anisotropic, that is, peaks with different *hkl* will be broadened to a different extent. This too is readily observable during whole pattern fitting as the calculated peaks will adopt an average width and the difference profile excursions under certain peaks will invert, that is, the difference profile under a peak that is calculated too narrow will be the inverse of that under a peak that is calculated too wide. Ways to fit anisotropically broadened diffraction patterns are dealt with in §9.2.3. An example of a particle size determination by whole pattern fitting is shown in Fig. 9.6.

9.2.2 Interpretation of particle size estimates

Only very rarely is the sample in a powder diffraction experiment composed from spherical, uniformly sized, strain free, non-interacting crystals. In those few rare cases, the crystal size measured using neutron (or X-ray) diffraction peak

[112] Uniform dimensions in all directions.
[113] In programs where these are not separate variables, the refined peak shape parameters may still be decomposed using peak shape parameters from a standard sample.

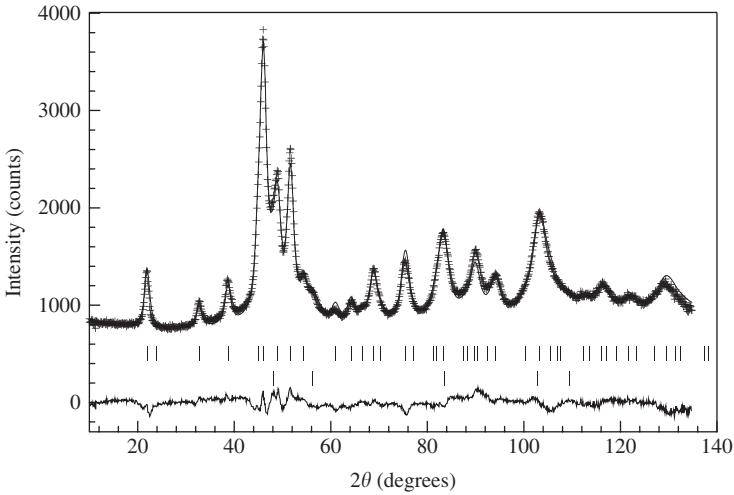

Fig. 9.6 Example of a Rietveld refinement fit to extract the mean particle size from a CW neutron diffraction pattern recorded from the hydrogen storage alloy $LaNi_5$ subjected to high energy ball milling for 5 h. Data are shown as (+) and the calculated pattern as a solid line through the data. A difference profile and peak markers are given below the pattern for $LaNi_5$ and Ni which begins to separate from the alloy due to milling induced damage. The estimated crystallite size is 83 Å.

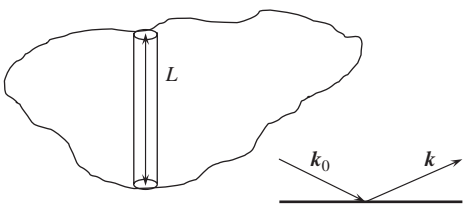

Fig. 9.7 Illustrating the characteristic dimension L parallel to the scattering vector. The refined crystallite size represents the volume average of L over the whole sample.

broadening can be regarded as a good approximation to the actual crystal size. The quantity measured is usually less clearly defined – for an individual crystallite, it may be the mean column length, L, parallel to the scattering vector as shown in Fig. 9.7. An attempt at a generalized definition for isotropic broadening might be: 'the radially averaged size of the coherently scattering domains within the sample, weighted by the particle size distribution'.

There are several key points to this definition that are worthy of discussion. First, crystals have long been known to contain substructure of various kinds. Metallic crystals that have been deformed contain small relatively perfect regions (sub-grains) bounded by dense tangles of dislocations. The unit cells within a

subgrain scatter coherently; however, they are largely incoherent with neighbouring subgrains. This is the same kind of definition as that for mosaic blocks given in the treatment of extinction (Darwin 1914). When lightly annealed, the dislocation tangles can assemble themselves into low angle or tilt boundaries that preserve the incoherency between neighbouring sub-grains. Mineral samples can display similar effects although less frequently. Other ways for crystals to be subdivided include twins, ferroelectric domains, anti-phase domain boundaries and stacking faults. When particle size estimates are attempted on samples containing them, the quantity measured is the mean distance (radially averaged and weighted, etc.) between twin/domain boundaries or faults. Complex features can arise in the diffraction pattern due to extensive twinning or stacking faulting and these are dealt with in a later section (§9.7). Happily, it is usually the dimensions of the substructure that are critical in determining the physical properties of materials and so these are just the features that we would wish to study.

Second, our definition above includes the 'radially averaged' diameter in an attempt to take into account crystallite shape. The radial average produces an 'equivalent' sphere and it is the diameter of this sphere that is measured. Implicit in this is an assumption of no relationship between the exterior topography of the crystal or domain and the crystallographic axes, that is, isotropic broadening (no *hkl* dependence). The equivalent sphere concept is the same as the radius of gyration $R_G = \langle r^2 \rangle^{1/2}$, where r is the distance from the centre of mass, used in the analysis of small angle scattering data (SANS, SAXS) as well as in classical mechanics. As with most quantities in diffraction, the radially averaged diameter is readily computed (numerically) for any given particle; however, it is difficult if not impossible to reverse the process uniquely. That is, to a good first approximation, all crystals with the same radially averaged diameter (or radius of gyration) will give an identical sample profile fit. We are therefore unable to determine any information about particle shape in the absence of anisotropic broadening (see §9.2.3).

Third, our definition includes the phrase 'weighted by the particle size distribution'. This is no trivial statement. Very narrow particle size distributions are extremely rare in both natural and man made materials. So in a majority of cases one expects a distribution of particle (crystallite) sizes in the sample.

Langford and Wilson (1978) have given equations for determining the influence of particle size distributions on the Scherrer constant applicable to various measures of peak breadth. They stated that 'qualitatively, the line profile resulting from a specimen containing a distribution of particle sizes will have a sharper maximum and longer tails than a specimen containing the same number of crystallites and the same total quantity of material but with the crystals all the same size'. The implication is that the shape becomes more Lorentzian as the breadth of the particle size distribution increases. This conclusion has been supported by the recent computation (Langford *et al.* 2000) of peak profiles for Gaussian and log-normal particle size distributions of different widths – the Lorentzian fraction increases systematically with the width of the distribution, and was reported as

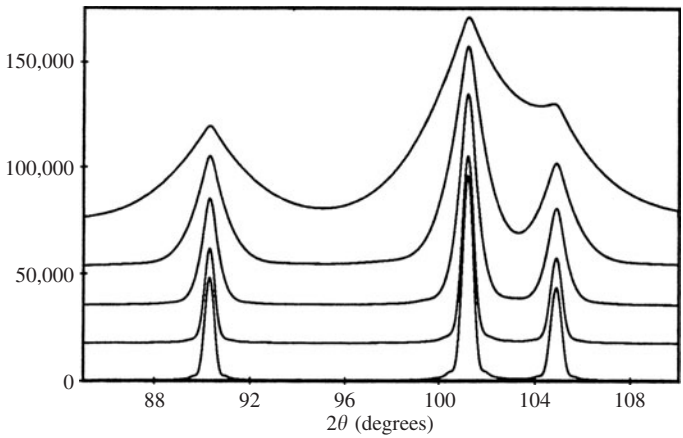

Fig. 9.8 The effects of crystallite size distributions on the apparent crystallite size as determined from *ab initio* calculations using a mean size of 300 Å and particle size distributions of width 280, 250, 200, 100, and 50 Å, respectively from top to bottom (Marciniak *et al.* 1996).

high as 0.67 for the widest Lognormal distribution considered in the work. Whilst the influence of particle size distributions on the peak *shape* was quite pronounced, the influence on the peak *breadth* was rather less significant.

On the contrary, there are certain *ab initio* calculations (Marciniak *et al.* 1996) of peak profiles from samples with the same mean particle size but widely differing size distributions that indicate the influence of particle size distribution on peak width is severe. The results are reproduced in Fig. 9.8. Taking the broadest distribution (280 Å) as a worst-case, routine application of the Scherrer equation to the peak near 90° yields a mean particle size of ~30 Å whereas the mean size used to calculate the peak was 300 Å. Despite the lack of detail concerning the nature of the distribution used, such disparities with the work of Langford *et al.* (2000) are cause for concern.

It is of interest to explore these effects in more detail. It is assumed that the crystallites are sufficiently small to satisfy the kinematic criterion that each crystallite is uniformly bathed in the incident radiation.[114] Consider the schematic *volume* distribution of crystallite sizes depicted in Fig. 9.9. Let the distribution be represented by the function $v(D)$ where D is the crystallite size. At any discrete value of the crystallite size, D_1 say, we invoke a normalized diffraction profile, $y(2\theta)$, with a *shape* defined by the interference function (eqn (9.5)) or some suitable approximation to it, then assign an *integrated intensity* given by $v(D_1)$. The peak shape function, $Y(2\theta)$, resulting from the entire distribution of sizes is obtained by

[114] This is a good approximation for most neutron and high energy synchrotron X-ray diffraction studies, but rather worse for standard laboratory based X-ray sources and larger particles.

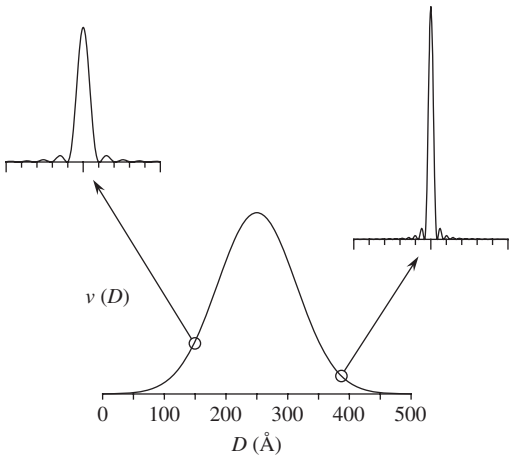

Fig. 9.9 Method used to investigate the influence of a volume distribution $v(D)$ of particle size on the peak shape. Each discrete particle size D contributes an interference function with width determined by D_i and area determined by $v(D_i)$ to the overall sum determined by integration in eqn (9.17).

performing the integration[115]:

$$Y(2\theta) = \int_0^\infty v(D)\, y(2\theta)\, dD \tag{9.17}$$

A simple illustration is the case when the crystallite size distribution is Gaussian. The crystallite size distribution may be represented as

$$v(D) = \frac{C_1}{H_s} \exp\left[-C_0 \left(\frac{D - D_0}{H_s}\right)^2\right] \tag{9.18}$$

where C_0 is $4\ln(2)$, C_1 is $\sqrt{C_0/\pi}$, H_s is the FWHM of the particle size distribution and D_0 is the mean crystallite size. For the diffraction profile due to each discrete particle size we take the normalized interference function[116] [from eqns (9.5) and (9.8)]:

$$y(2\theta) = \frac{1}{M\pi} \frac{\sin^2 M(2\theta - 2\theta_0)}{\sin^2(2\theta - 2\theta_0)} \tag{9.19}$$

[115] Multiplication of a normalized profile function by a volume fraction $v(D)\,dD$ depends on the assumption that the integrated intensity from any crystallite depends linearly on its volume.

[116] For simplicity, the scaling between x in eqn (9.5) and $(2\theta–2\theta_0)$ in eqn (9.19) has been omitted.

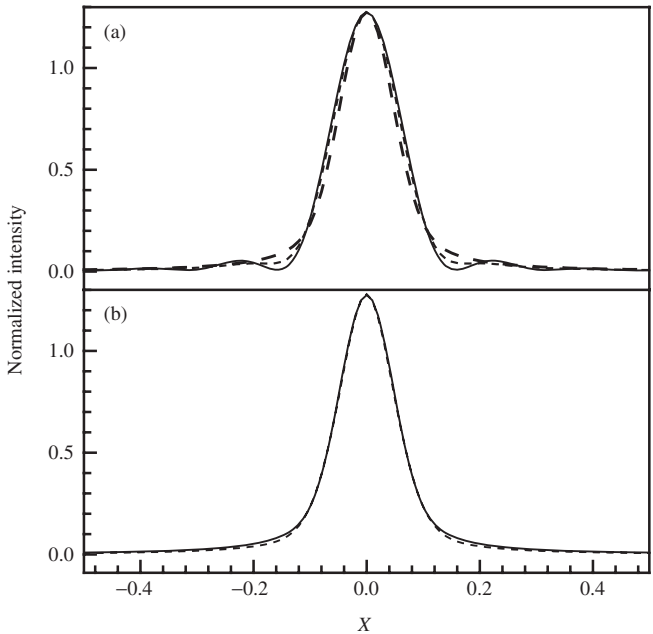

Fig. 9.10 (a) Comparison of the peak shape generated by eqn (9.20) for a mean particle size of 100 Å and particle size distributions with FWHM of 20 Å (solid), 50 Å (thin dashed), and 100 Å (heavy dashed). Note that in contrast with Fig. 9.8, the width changes very little until the distribution gets very wide and the changes are in the opposite direction to Fig. 9.8. (b) Least-squares fit of a pseudo-Voigt function to the widest distribution above. The refined value of η is 0.48.

where $2\theta_0$ is the peak position and M is the size of the crystal in units cells along the scattering vector, given by D/a for 'unit cell' dimension a.[117] Substituting eqns (9.19) and (9.18) into (9.17) we get:

$$Y(2\theta) = \frac{C_1}{H_s}\int_0^\infty \exp\left[-C_0\left(\frac{D-D_0}{H_s}\right)^2\right] \times \frac{\mathrm{a}}{D\pi} \times \frac{\sin^2\left(\frac{D}{a}(2\theta-2\theta_0)\right)}{\sin^2(2\theta-2\theta_0)}dD \tag{9.20}$$

The integral at eqn (9.20) may be evaluated numerically. Several examples for different values of H_s are shown in Fig. 9.10. The key results are

(i) As the breadth of the particle size distribution increases, it damps out the subsidiary maxima in the interference function.
(ii) The *shape* of the resulting profile is sensitive to the breadth of the particle size distribution as expected. It varies smoothly from the input intrinsic shape, the

[117] For convenience, the unit cell is assumed to have been chosen such that the peak under consideration is 00*l*.

interference function, to quite Lorentzian at very large values of H_s. The fitted curve is pseudo-Voigt with the characteristics shown on the figure.

(iii) The shape is the same for constant H_s/D_0.

(iv) The effect of increasing peak tails (i.e. a more Lorentzian shape) is greatly accentuated for a log-normal distribution of particle sizes (Langford *et al.* 2000) which is also the most commonly encountered distribution in practice.

(v) The presence of a symmetric Gaussian particle size distribution of credible width (i.e. $H_s \ll D_0$), does not invalidate particle size estimates determined by direct application of the Scherrer equation to peak breaths. These remain accurate to within a few percent.

Due to the periodic nature and oscillatory features of the interference function, its use in equations like eqn (9.17) (leading to eqn (9.20)), even with powerful numerical tools (e.g. Mathematica, Matlab, Maple, etc.) often leads to convergence problems. Since the presence of a wide distribution eliminates the subsidiary maxima, and we have already shown that the mean envelope of the interference function may be modelled by an approximating pseudo-Voigt function with $\eta = 0.23$, an equivalent result *may* be obtained in most circumstances by using this pseudo-Voigt in eqn (9.17) giving

$$Y(2\theta) = \frac{C_1}{H_s} \int_0^\infty \exp\left[-C_0 \left(\frac{D - D_0}{H_s}\right)^2\right] \left[(1-\eta)\frac{\sqrt{C_1}}{H_{PV}} \exp\left\{\frac{-C_0 (2\theta - 2\theta_0)^2}{H_{PV}^2}\right\} + \frac{2\eta}{\pi H_{PV}} \frac{1}{1 + 4(2\theta - 2\theta_0)^2 / H_{PV}^2}\right] dD \tag{9.21}$$

The FWHM of the pseudo-Voigt for this computation, H_{PV} is obtained from the Scherrer equation (eqn (9.9)). A variety of other peak shapes (Gaussian, Lorentzian, etc.) may be substituted for $y(2\theta)$ in eqn (9.17), however, the connection to a physical model for the sample is less clear than when either the interference function or its approximating pseudo-Voigt function is employed.

These analytical results are quite rigorous and yet are at odds with the *ab initio* results (Fig. 9.8). There is a need for substantial verification in this area by careful experimental work.

In summary, we may conclude that, despite considerable complexities, diffraction peak widths *can* provide a very useful measure of the crystallite size. The $\sec\theta$ angular dependence usually allows it to be separated from other types of broadening and several new insights have been made into the shape of the pure particle size broadened peak. Further, a method is available for investigating the influence of many other types of distribution on the peak shape.

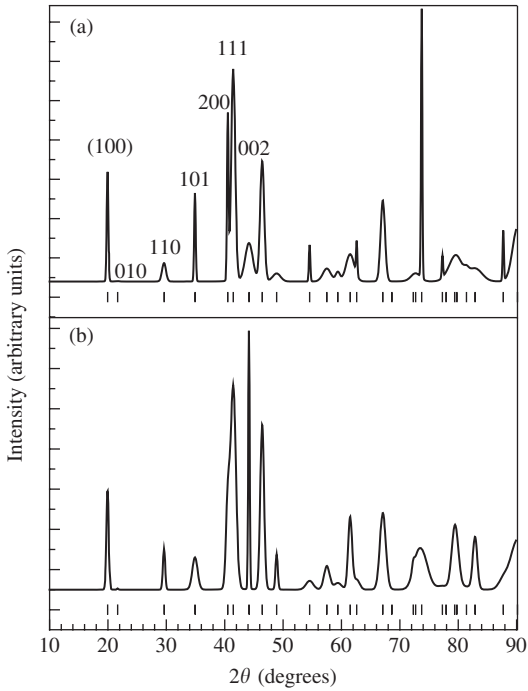

Fig. 9.11 Simulated diffraction patterns for $LaNi_5$ illustrating the expected effects of (a) needle-shaped crystals with the needle axis [00.1] and (b) disc-shaped crystals with [00.1] normal to the plane of the disc. Instrument characteristics match the former instrument HRPD at the HIFAR reactor, ANSTO, Australia.

9.2.3 Anisotropic particle size broadening

In principle, a mild anisotropy is introduced into the diffraction pattern due to the shape of the crystallites except in those rare cases when the crystals are spherical. It arises from the different mean path lengths travelled by diffracted beams forming the different peaks. The effect has been quantified by Langford and Wilson (1978) in terms of the effective Scherrer constant to be used for different peaks in diffraction patterns from regular three-dimensional shapes (cubes, tetrahedra, octahedra, etc.). In practice, the crystals of real samples scarcely if ever conform to such regular shapes. In addition, there is inevitably a distribution in both shape and size that tends to equalize the Scherrer constant for all values of *hkl* for regularly shaped (quasi-isotropic) crystals.

The anisotropic particle broadening of interest here is particle size broadening that arises from anisotropic particles where a strong association exists between the particle shape and the crystal structure. This is illustrated in Fig. 9.11 for both needle and disc-shaped crystals.

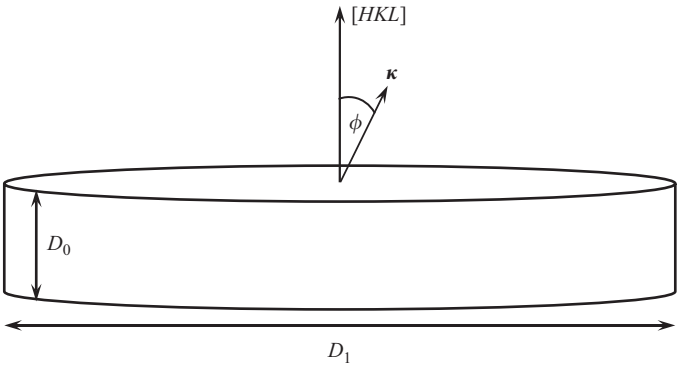

Fig. 9.12 Illustration of the nomenclature used in the discussion of eqn (9.22). A disc-shaped crystal has its short axis associated with the crystal direction [*HKL*]. The cosine of the angle (ϕ) between the scattering vector ($\boldsymbol{\kappa}$) and [*HKL*] gives the correct behaviour at the limiting values $\phi = 0$ and $\phi = 90°$.

Anisotropic particle size broadening and its origins have been known for some time. Disc-like $Ni(OH)_2$ crystals provided an early example (Klug and Alexander 1974). Analysis of the resulting diffraction patterns serves to illustrate valuable methods for the identification of and preliminary study of particle anisotropy. First, the peak breadths (widths) are determined by one of the methods discussed in Chapter 4 (preferably by peak fitting). These are then corrected for the instrumental width and assembled on a Williamson-Hall plot (see §9.4.1). If different classes of *hkl* peaks show systematically different widths, then particle anisotropy may be inferred, and the Scherrer equation applied to indicate dimensions parallel to the scattering vector (diffracting plane normal) associated with each class of reflection. Useful as they are for determining the type of anisotropic broadening and estimates for the particle shape, these methods do not give a sufficiently detailed description of the particle shape to predict the widths of all peaks in a diffraction pattern, hence allowing full profile refinement. A number of methods have been used to develop the required relationship with varying degrees of success.

The simplest method is illustrated in Fig. 9.12. It arises from a consideration of a crystallite[118] of very limited extent parallel to a well-defined crystal direction [*HKL*], and much larger extent perpendicular to [*HKL*]. By defining the angle that a particular scattering vector makes with [*HKL*], it can be seen that $\cos\phi$ has the correct behaviour at the limiting values of $\phi = 0$ ($\cos\phi = 1$, the maximum particle size effect) and $\phi = 90°$ ($\cos\phi = 0$, no particle size effect). Profile analysis of CW diffraction may then be conducted on the assumption that the peak FWHM

[118] This is in effect a disc-shaped crystal. Equation (9.22) applies equally to needle-shaped crystals, but for these, $K_1 < 0$.

(in degrees 2θ) due to particle size effects is given by

$$H_P = (K_0 + K_1 \cos\phi) \sec\theta \tag{9.22}$$

where $K_0 = \frac{180\lambda}{\pi D_1}$, $(K_0 + K_1) = \frac{180\lambda}{\pi D_0}$ and for convenience the Scherrer constant is taken as 1. D_0 is the crystallite size parallel to [*HKL*] and D_1 is the crystallite size perpendicular to [*HKL*]. For $K_0 = 0$ the disc becomes a slab of infinite extent – Greaves in early work (Greaves 1985) assumed this form for the Rietveld analysis of neutron data from $Ni(OD)_2$. Although the function at eqn (9.22) behaves correctly at the limits $\phi = 0$ and $\phi = 90°$ and has been implemented as an option in some popular Rietveld refinement programs (e.g. FULLPROF and GSAS), it has some major shortcomings. Not least is that it generates a rather unusual particle shape, which may be seen by substituting for K_0 and K_1 to give

$$H_P = \frac{180\lambda}{\pi}\left[\frac{1}{D_1} + \left(\frac{1}{D_0} - \frac{1}{D_1}\right)\cos\phi\right]\sec\theta \tag{9.23a}$$

or a direction dependent crystallite diameter

$$\frac{1}{D_{hkl}} = \frac{1}{D_1} + \left(\frac{1}{D_0} - \frac{1}{D_1}\right)\cos\phi \tag{9.23b}$$

The resulting particle shape is plotted in Fig. 9.13. Although such a shape is plausible for an individual crystallite, it is unlikely to be the shape of the ensemble average of a large collection of real crystallites. The latter is far more commonly

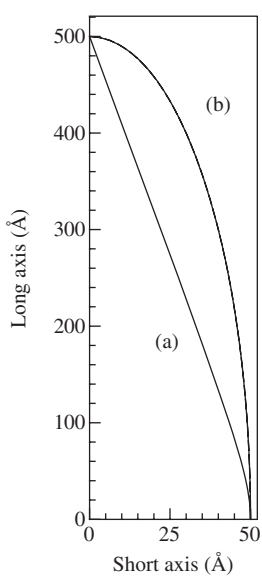

Fig. 9.13 Comparison of the particle shapes implicit in (a) eqn (9.23b) and (b) eqn (9.24).

an ellipsoid – usually an ellipsoid of revolution about a prominent crystallographic axis.

It is not difficult to construct a peak width function that corresponds to a genuine ellipsoid of revolution. An example is given by

$$H_P = \left(\sqrt{K_0^2 + \left(K_1^2 - K_0^2\right)\cos^2\phi}\right)\sec\theta \tag{9.24}$$

$$\left(\text{or } H_P = \left(\sqrt{K_0^2\sin^2\phi + K_1^2\cos^2\phi}\right)\sec\theta\right)$$

The next level of complexity is to abandon the requirement for cylindrical symmetry about the unique crystal axis [HKL]. This allows complex three-dimensional crystal shapes and one can imagine cases where this might arise. For example, chemically precipitated orthorhombic or lower symmetry crystals can be envisaged with three different mean crystallite sizes (and size distributions) along the three crystallographic axes. The first attempts to model this case used a second rank tensor description of the crystal shape [e.g. Lutterotti and Scardi (1990)] as shown as

$$M\left(h_1h_2h_3\right) = \left[\frac{\sum_{ij} M_{ij}^2 h_i h_j}{\sum_{ij} \delta_{ij}^2 h_i h_j}\right]^{1/2} \tag{9.25}$$

where M is the dimension (number of unit cells) in the direction of the scattering vector $h_1h_2h_3$, and $\delta_{ij} = 0$ or 1 according to whether $M_{ij} = 0$ or otherwise.

The particle shapes generated by eqn (9.25) no doubt depend on the coefficients. With a positive definite tensor, the shape may be ellipsoidal which appears plausible. However, a great variety of physically impossible particle shapes can arise during profile refinement. Intuitively, one can expect that the symmetry restrictions that apply to other second rank tensors (e.g. thermal ellipsoids, strain, stress, etc.) for the particular crystal system under study should also apply to this tensor. However, with symmetry restrictions imposed, this method has had rather limited success in fitting anisotropically broadened diffraction patterns as these symmetry restrictions are too limiting. The six independent parameters in eqn (9.25) are reduced to four (monoclinic), three (orthorhombic), two (hexagonal, trigonal, tetragonal), or one (cubic) for higher symmetry crystals. As a consequence, no anisotropic broadening is allowed for cubic crystals under this model, whereas in practice many cubic materials are known to exhibit anisotropic broadening. Similarly, tetragonal, trigonal, and hexagonal crystals are only allowed to adopt axially symmetric shapes (needles or oblate ellipsoids). In fact problems can arise whenever individual crystallites adopt shapes that have symmetry lower than the point group symmetry of the crystal structure itself.

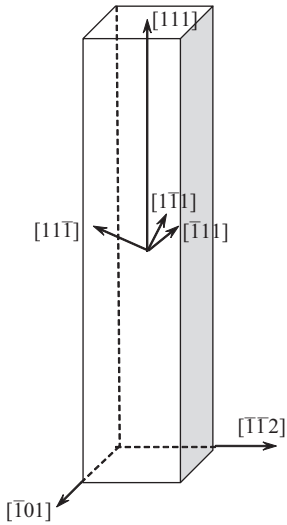

Fig. 9.14 Hypothetical crystal with cubic crystal structure but a pronounced [111] growth habit as might be expected for a close-packed structure. The non-equivalence of the crystallite radius along the crystallographically equivalent {111} directions is illustrated.

Popa (1998) has demonstrated the reason for this by considering the entire polycrystalline ensemble. We consider an ellipsoid crystal generated by eqn (9.24). The width of the diffraction peak due to this one crystal will be determined by the thickness of the crystal along the scattering vector $\boldsymbol{\kappa}_{hkl}$. However, in a polycrystalline sample, there will be other crystallites oriented for diffraction from crystallographically equivalent scattering vectors that trace out quite different thicknesses within the crystal. The situation is illustrated in Fig. 9.14 for cubic symmetry. The resultant diffraction peak will be the average over all equivalents. Popa's treatment makes use of a composite crystal that represents the aggregate of the individual crystallites, each of which may be ellipsoidal but lack the full point group symmetry. The composite crystal is constructed to be invariant under the operations of the Laue group, but generally is not ellipsoidal. The same argument applies to strain ellipsoids (see §9.3.3) although the solution is quite different. To model the composite crystal responsible for the observed diffraction pattern, Popa (1998) uses the symmetrical spherical harmonics such as

$$\begin{aligned} &P_{2l}^{m}(x)\cos m\phi \\ &P_{2l}^{m}(x)\sin m\phi \end{aligned} \tag{9.26}$$

where the $P_l^m(x)$ are normalized Legendre functions

$$P_l^m(x) = \left[\frac{(l+m)!}{(l-m)!}\right]^{\frac{1}{2}} \left(l+\frac{1}{2}\right)^{\frac{1}{2}} (-1)^{l-m} \left(2^l l!\right)^{-1} \times \left(1-x^2\right)^{-m/2} \frac{d^{l-m}\left(1-x^2\right)^l}{dx^{l-m}} \tag{9.27}$$

The argument x is given by $x = \cos\Phi$ where Φ is the polar angle of the scattering vector and ϕ is the azimuthal angle defined with respect to an orthogonal coordinate system $(\boldsymbol{x}_1, \boldsymbol{x}_2, \boldsymbol{x}_3)$ where $\boldsymbol{x}_3$ is a unit vector along the n-fold axis and $\boldsymbol{x}_1$ along a two-fold axis when possible.

The result is a convergent series for each of the Laue groups, for example, for hexagonal symmetry (point group 6/*mmm*):

$$\langle R_{\boldsymbol{\kappa}} \rangle = R_0 + R_1 P_2^0(x) + R_2 P_4^0(x) + R_3 P_6^0(x) + R_4 P_6^6(x)\cos 6\phi + \ldots \tag{9.28}$$

where $\langle R_{\boldsymbol{\kappa}} \rangle$ is the ensemble average radius for a scattering vector $\boldsymbol{\kappa}$. The full set of expressions for $\langle R_{\boldsymbol{\kappa}} \rangle$ is given by Popa (1998). The appropriate place for truncation of the series cannot be predicted. It must be determined iteratively by introducing more terms until no significant improvement in the fit occurs.

There are two reasons for attempting to fit anisotropically broadened diffraction peaks, during whole pattern fitting, (i) to improve the overall fit so that crystallographic parameters can be more accurately determined and (ii) in some cases so that the mean crystallite shape can be measured by diffraction. The spherical harmonics approach to anisotropic particle size is without a doubt the most powerful in terms of its ability to fit observed diffraction patterns and it is expected that it will eventually be implemented in all popular Rietveld analysis codes. What is less clear is how to interpret the 'composite crystal' represented by the spherical harmonic series in terms of the size and shape of individual crystallites. The interpretation becomes more challenging when it is remembered that there are other causes of peak broadening, such as line defects (e.g. dislocations, see §9.6) or planar defects (e.g. stacking faults, antiphase domain boundaries, see §9.7), with effects that may be difficult to distinguish from the broadening due to particle size effects.

9.3 MICROSTRAINS

In Chapter 2, it was established that the *positions* of the diffraction peaks are determined by the interplanar (hence interatomic) spacings within the crystals of the material under study. Consequently, anything that changes the mean interplanar spacings (phase transition, atomic substitutions, etc.) changes the peak positions. This is also true of factors such as externally applied stresses. These lead, via the elastic constants, to strains that are visible as peak shifts and are discussed further in Chapter 11.

Peak shifts due to strains represent the *average* response of a particular set of planes (*HKL*). In certain types of samples such as solid polycrystals where considerable intercrystalline stresses can accumulate due to thermal expansion mismatch and elastic anisotropy, or in ground powders where microscopically inhomogeneous internal strains (hence microstrains) are also present. These do not lead to peak shifts but, due to their inhomogeneous nature, to peak *broadening*.

9.3.1 Isotropic microstrains

Isotropic microstrains are those that, when averaged over the whole irradiated volume of the sample, have no dependence on *hkl*. That is not to say that the broadening is constant across the entire diffraction pattern. Just as particle size broadening was shown in §9.2 to have a secθ (d^2 in TOF) dependence, so too microstrain broadening has a distinct angular (or d in TOF) dependence. This is best understood by examining the effect of small perturbations in d-spacing on the peak position by differentiating Bragg's law [eqn (2.21)].

$$\lambda = 2d \sin\theta \tag{2.21}$$

$$0 = 2d \cos\theta \Delta\theta + 2 \sin\theta \Delta d \tag{9.2a}$$

whence

$$\Delta\theta = \frac{-\Delta d}{d} \tan\theta \quad \text{(radians)} \quad \text{or} \quad \Delta\theta = \frac{-180\Delta d}{\pi d} \tan\theta \text{ (degrees)} \tag{9.29b}$$

The peak is shifted by $\Delta(2\theta) = 2\Delta\theta$. Taking the strain, $\varepsilon = \Delta d/d$, as constant, we see that peak shifts vary with tan θ. The TOF pattern shows d and Δd directly, so in the case of constant strain we see $\Delta d \propto d$. A distribution of strains will lead to a distribution in $\Delta\theta$ or, for TOF Δd, that is observed as peak broadening. The tan θ dependence in CW (d dependence in TOF) is very useful in separating strain broadening from particle size broadening (see §9.4). A simulated strain-broadened CW diffraction pattern is shown in Fig. 9.15 for comparison with un-broadened and particle size broadened patterns in Fig. 9.1 simulated with otherwise identical conditions.

It is often assumed, with some experimental justification, that the distribution of strains is Gaussian leading to the strain-broadened component of the peak having a Gaussian profile. This has a number of advantages for whole pattern or profile refinement methods of analysis as discussed further below. The question of the validity of this assumption has been examined by Delhez *et al.* (1993) who concluded that whilst the underpinning theory does not demand that $f(x)$ is Gaussian for strain-broadened peaks, there is no compelling reason to abandon the use of a Gaussian for this purpose. Instead it should be used with caution and routine checking procedures adopted, for example, conducting single peak analyses on higher orders of the same peak[119] to check for consistent behaviour.

[119] For example, 200, 400 and 600 or 111, 222 and 333.

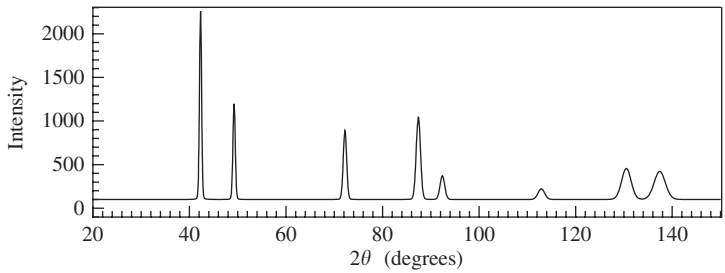

Fig. 9.15 Simulated 1.5 Å neutron diffraction pattern for Ni containing broadening due to a distribution of micro-strains (compare with Fig. 9.1). The value of ε_{rms} used in the calculation was 0.0037 and the un-broadened profile was that for HRPD at the HIFAR reactor, ANSTO, Australia.

Methods of analyzing microstrains parallel the methods used for particle size. Stokes' (1948) Fourier de-convolution method applied to individual peaks is often considered the most rigorous. The mathematics is identical to eqns (9.12)–(9.14), except that $f(x)$ and $F(\xi)$ now correspond to the strain-broadened profile rather than the particle size broadened profile. As before, it is necessary to determine the instrumental profile, $g(x)$, from a sample known to be free from small particle size, strain or other sample induced broadening. In CW neutron diffraction, in cases when the assumption of a Gaussian strain-broadening profile appears justified, then Fourier analyses are not necessary to extract $f(x)$. Provided that the instrumental profile $g(x)$ is known, then individual peak fitting will return good results for the width of the strain-broadened peak. For example, in the happy situation when $g(x)$ is also Gaussian (often a reasonable approximation for CW instruments), the FWHM of the total Gaussian peak, H_G is given by

$$H_G^2 = H_I^2 + H_S^2 \tag{9.30}$$

where H_I is again the FWHM characteristic of the instrument profile $g(x)$ and H_S is the FWHM of the strain-broadened sample profile ($f(x)$). Similarly for integral breadths:

$$\beta_G^2 = \beta_I^2 + \beta_S^2 \tag{9.31}$$

If a Voigt function is needed to fit the instrument profile of a CW diffractometer, then the isolation of the strain component is equally simple including only the additional step of isolating the width of the Gaussian component of the instrument Voigt function and then applying eqns (9.30) or (9.31) as appropriate. More complex instrumental profile functions, such as those appropriate to TOF diffractometers, give less concrete results for single peak analyses unless a large number of parameters are constrained during fitting. Far better results are obtained, with either type of data, by conducting whole pattern analyses such as Rietveld refinement or pattern decomposition.

Within whole pattern methods, the widths of the diffraction peaks are forced to vary according to known behaviours. For example the Gaussian component of the profile is usually made to vary according to the equation proposed by Caglioti *et al.* (1958) (eqn (4.7)):

$$H_G^2 = U \tan^2 \theta + V \tan \theta + W \tag{4.7}$$

where θ is the scattering angle and U, V, and W are refinable parameters. In TOF diffractometers, where patterns are presented as a function of d-spacing, the corresponding relationship is

$$H_G^2 = a + bd^2 + cd^4 \tag{9.32}$$

The parameterization is in terms of H_G^2 because Gaussians add in quadrature. This allows the strain contribution to be accessed by simply subtracting the known values of U or b for the diffractometer as determined from strain free samples, that is,

$$U = U_I + U_S$$

or

$$b = b_I + b_S \tag{9.33}$$

where U_S and b_S represent the contributions to H_G due to a distribution of strains in the sample. The meaning of H_S, U_S, β_S, b_S, and other measures of microstrains are discussed in §9.3.2.

9.3.2 Interpretation of strain parameters

Unlike particle size broadening, strain broadening of diffraction peaks is not due to an intrinsic quantity (e.g. the size of the crystallites) but due to the presence of a distribution of strains about a mean value. The mean value of the strain can only be determined by examining peak *positions* such as in residual stress determinations (see Chapter 11). The peak broadening only indicates the *width* of the distribution of strains about the mean. Except for the Fourier method, our measures of strain broadening are all in terms of peak widths. The interpretation of these as strains is relatively straightforward for the peak fitting techniques (single peak analysis and whole pattern analysis), provided that strain distributions can be assumed to be Gaussian. The relevant equations are obtained by using eqn (9.29) to establish a relationship between the root mean square (rms) variation of θ, hence 2θ, and the rms strain, then using the properties of the Gaussian[120] to connect this rms value with other measures of width. The results are presented in Table 9.1.

[120] The standard deviation (rms deviation from the mean) σ of a Gaussian is related to its FWHM, H, by $H = 2\sigma\sqrt{2 \ln 2}$, and to its integral breadth, β, by $\beta = \sigma\sqrt{2\pi}$.

Table 9.1 Relationship between width parameters and rms strain.

Parameter	$\varepsilon_{rms} = \left\langle \varepsilon^2 \right\rangle^{1/2}$
H_S (degrees)	$\frac{\pi H_S}{180 \times 4\sqrt{2\ln 2}\tan\theta}$
β_S (degrees)	$\frac{\sqrt{2\pi}\beta_S}{180 \times 4\tan\theta}$
U_S (degrees^2)	$\frac{\pi\sqrt{U_S}}{180 \times 4\sqrt{2\ln 2}}$
b_S	$\frac{\sqrt{b_S}}{2\sqrt{2\ln 2}}$

9.3.3 Anisotropic microstrains

There are two major ways in which anisotropic micro-strains can arise in polycrystalline samples. The first affects only solid polycrystals and is due to thermal expansion mismatch and elastic anisotropy in the constituent crystallites. Peaks arising from crystal directions with softer elastic constants are influenced to a greater extent by neighbouring crystals and so are broader than peaks arising from crystal planes perpendicular to a direction of high stiffness. The result is an *hkl* dependence to the microstrain broadening. A second way that anisotropic microstresses can arise is through the presence of lower dimensional (planar or linear) defects. The defects lead to highly localized strains that decay to zero in the unperturbed structure leading to a microstress distribution. Because the defects are crystallographic in nature, they have preferred orientations within the individual crystallites. This gives a very pronounced anisotropy to the microstrain distribution (e.g. the strain field around a dislocation core). As we will demonstrate below, in some cases these materials are able to be handled on a purely microstrain model without reference to specific defect types. However, it is more common that crystal defects also have the effect of subdividing the crystal into smaller parts, therefore leading also to particle size like effects. In addition, there are often coherent diffraction effects between neighbouring defects (e.g. twins) that lead to complex peak shapes and extra diffraction peaks that can only be accounted for using a proper physical model of the microstructure. Such cases are dealt with in §9.6 and §9.7.

Early attempts to model anisotropic microstrains to some extent parallel those for anisotropic particle size broadening (§9.2.3). It is possible by inspection or the use of a Williamson-Hall plot to isolate the crystal directions of lowest and highest microstrains. In many instances, these are orthogonal and one may write a simple cylindrically symmetric anisotropic form of eqn (9.29)[121]:

$$\Delta\theta = \frac{180}{\pi}\left[\left(\frac{\Delta d}{d}\right)_0 + \left(\frac{\Delta d}{d}\right)_1 \cos\phi\right]\tan\theta \tag{9.34}$$

[121] The $\Delta\theta$ and Δd are here taken to measure widths of distributions of the relevant quantities.

(in degrees) where $(\Delta d/d)_0$ is characteristic of the narrowest peaks and may be zero in some cases, $(\Delta d/d)_1 + (\Delta d/d)_0$ is characteristic of the microstrain in the broadest peaks and ϕ is the angle that the scattering vector makes to the direction of maximum microstrain. Although this model sometimes gives reasonable agreement with observed diffraction data, it is difficult to interpret the refined values of $(\Delta d/d)_0$ and $(\Delta d/d)_1$ in a meaningful way, particularly when $(\Delta d/d)_0 \neq 0$.

If $(\Delta d/d)_0$ and $(\Delta d/d)_1$ are to be interpreted as the integral breadths or the FWHM of strain distributions then they are unlikely to be simply additive. If the usual assumption is made, that the strain distribution is Gaussian, replacing eqn (9.29) with an equation of the form:

$$\Delta\theta = \frac{180}{\pi}\sqrt{\left[\left(\frac{\Delta d}{d}\right)_0^2 \cos^2\phi\right] + \left[\left(\frac{\Delta d}{d}\right)_1^2 \sin^2\phi\right]}\tan\theta \tag{9.35}$$

would allow $(\Delta d/d)_0$ and $(\Delta d/d)_1$ to be directly interpreted as rms microstrains (i.e. $\langle\varepsilon^2\rangle^{1/2}$) according to the relationships given in Table 9.1.

The next degree of sophistication is obtained by deriving an equation specific to the crystal structure of the phase or compound being studied. Two early examples studied by Elcombe and Howard (1988) were RbOD (i.e. RbOH where the hydrogen has been replaced by its heavy isotope deuterium) and α-PbO. RbOD is monoclinic and it was observed that the broadening was consistent with a model in which a, b and $c \sin\beta$ do not vary but in which distributions in β and c exist in such a way as to preserve $c \sin\beta$ unaltered. The corresponding broadening function is

$$\Delta\theta = \frac{h\,(Ah\cot\beta + El\,\mathrm{cosec}\,2\beta)\tan\theta\Delta\beta}{Ah^2 + Bk^2 + Cl^2 + Ehl} \tag{9.36}$$

abbreviated as $\Delta\theta = X\tan\theta\Delta\beta$, where A, B, and so on are coefficients in the expression for interplanar spacings:

$$\frac{1}{d^2} = Ah^2 + Bk^2 + Cl^2 + Dkl + Ehl + Fhk$$

and $\Delta\beta$ here is the FWHM of the distribution of the monoclinic angle β (in degrees). It is relatively simple to implement broadening given by equations such as (9.36) into whole pattern analyses, by recognizing the $\tan\theta$ dependence like the U term in the Caglioti eqn (4.7). It suffices to implement a modified Caglioti equation [refer also to eqn (9.33)]:

$$H_G^2 = (U_I + U_S)\tan^2\theta + V\tan\theta + W \tag{9.37}$$

where $U_S = (2X\,\Delta\beta)^2$ and U_I is characteristic of the instrument. The improvement to the Rietveld fit, illustrated in Fig. 9.16(A) is substantial.

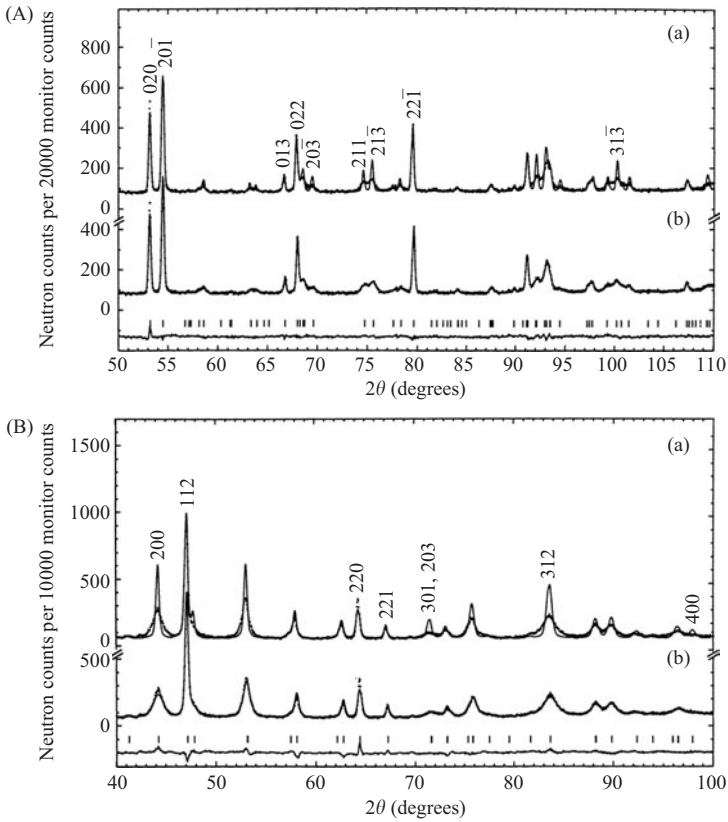

Fig. 9.16 Results of modelling anisotropic strain broadening using the method of Elcombe and Howard (1988) applied to (A) RbOD and (B) α-PbO. In each, pattern (a) indicates the Rietveld fit before correction for anisotropy and (b) the fit after correction.

Tetragonal α-PbO was found to conform to a model where there is no variation in the c parameter whereas a and b undergo area conserving fluctuations, that is, $a = a_o - \Delta a$ and $b = a_o + \Delta a$. The broadening function in this case is:

$$\Delta\theta = \frac{\left(h^2 - k^2\right)/a_0^2}{\left(h^2 - k^2\right)/a_0^2 + l^2/c^2} \tan\theta \frac{\Delta a}{a_0} \tag{9.38}$$

where Δa is the FWHM of the distribution of a cell parameters about their mean value a_0.[122] Again the Rietveld refinement is greatly improved as may be seen in Fig. 9.16(B).

A third example of this approach was used to model the anisotropic broadening that occurs as a result of hydrogen absorption in the hydridable intermetallic

[122] Equations (9.38) and (9.39) give $\Delta\theta$ in radian, so conversion to degrees will be necessary.

compound $LaNi_5$ (Kisi *et al.* 1992). There the broadening affects the basal plane uniformly and the c-axis is unaffected. The broadening function is:

$$\Delta\theta = \frac{\left(h^2 + hk + k^2\right)/a_0^2}{\left(h^2 + hk + k^2\right)/a_0^2 + \frac{3}{4}l^2\Big/c^2} \tan\theta \frac{\Delta a}{a_0} \tag{9.39}$$

where Δa is, as in eqn (9.38), the FWHM of the distribution of cell parameters.

As illustrated in Fig. 9.16 for two of these examples, these simple relationships were able to give excellent agreement to the severely anisotropic diffraction peak broadening observed. Despite the good agreement, these models may not give the full physical meaning of the broadening. For example, it has subsequently been shown that the broadening observed in $LaNi_5$ is mainly due to $a\langle\bar{2}110\rangle\{0\bar{1}10\}$ type edge dislocations (Wu *et al.* 1998a). Since the purpose of that investigation was to establish the link between lattice defects and the detailed hydrogenation behaviour of $LaNi_5$ (Kisi *et al.* 1992), the simple strain-based model was inadequate. On the other hand, when the aim of the investigation is to determine details of the average crystal structure as was the case for Elcombe and Howard (1988), a simplified approach is more than adequate.

A strength of this type of analysis is that very careful scrutiny of the diffraction pattern is required before the broadening function can be derived. That is, the user will be very well acquainted with their pattern before proceeding further, with an associated reduced probability of error. A weakness of the approach is that it lacks generality and so is only accessible to those with crystallographic training.

A more general approach is to express the lattice strain as a symmetric second rank tensor ε_{ij}. This rather intuitive approach mimics the real situation in an individual crystallite subject to an applied stress. It has been developed in parallel by several authors (Lartigue *et al.* 1987; Lutterotti and Scardi 1990; David and Jorgensen 1993; Le Bail and Jouanneaus 1997). The strain contribution in the Caglioti equation is written as

$$U_S = (180/\pi)^2 \Big(h^2\Delta\varepsilon_{11} + k^2\Delta\varepsilon_{22} + l^2\Delta\varepsilon_{33} + 2hk\Delta\varepsilon_{12} + 2hl\Delta\varepsilon_{13} + 2kl\Delta\varepsilon_{23}\Big)^2 / H^4 \tag{9.40}$$

where $\Delta\varepsilon_{11}$, $\Delta\varepsilon_{22}$, ... are not strains *per se*, but rather represent the FWHM of strain distributions along the crystallographic axes, and H is the magnitude of the scattering vector $\boldsymbol{H}$. Just as with anisotropic temperature factors, the result needs to be diagonalized to retrieve the distribution of microstrains.

Whilst this form of the tensor is correct for strains in a single crystal bathed in a uniform stress field, it is *not* correct for strain distributions, as are measured by peak broadening analysis. This point was realized by Thompson *et al.* (1987a) and a more rigorous general solution was given by two authors almost simultaneously (Popa 1998; Stephens 1999).

One of the major problems associated with using a simple strain tensor in line broadening analysis is that, being a macroscopic property of the crystal, the strain must conform to the appropriate Laue group (see, e.g. Nye 1957). This leads to only isotropic strains in cubic crystals and only axisymmetric strains in tetragonal, trigonal and hexagonal materials under this model. In practice, anisotropic peak broadening has been observed in cubic materials and, for example, non-axisymmetric strain broadening in tetragonal zirconias (Lutterotti and Scardi 1990).

In the treatment given by Popa (1998), the macroscopic strain (see Chapter 11) is given by[123]

$$\varepsilon_{hh} = \left(\varepsilon_{11}h^2 + \varepsilon_{22}k^2 + \varepsilon_{33}l^2 + 2\varepsilon_{12}hk + 2\varepsilon_{13}hl + 2\varepsilon_{23}kl\right) \times \left(E_H^2\right)^{-1} \quad (9.41)$$

where E_H is aH and H is the magnitude of the reciprocal lattice vector $\boldsymbol{H}$. In the absence of a macroscopic strain (i.e. a strain distribution centred on zero, $\langle\varepsilon_{hh}\rangle = 0$) the distribution of ε_{hh} is characterized by $\langle\varepsilon_{hh}^2\rangle$, that is, the average of ε_{hh}^2 over all equivalent directions, differently oriented crystallites and differing values of ε_{hh}. To obtain $\langle\varepsilon_{hh}^2\rangle$, eqn (9.41) is squared and then averaged. The result is

$$\begin{aligned}\left\langle\varepsilon_{hh}^2\right\rangle E_H^4 = {} & E_1h^4 + E_2k^4 + E_3l^4 + 2E_4h^2k^2 + 2E_5k^2l^2 + 2E_6h^2l^2 \\ & + 4E_7h^3k + 4E_8h^3l + 4E_9k^3h + 4E_{10}k^3l + 4E_{11}l^3h + 4E_{12}l^3k \\ & + 4E_{13}h^2kl + 4E_{14}k^2hl + 4E_{15}l^2hk \end{aligned} \quad (9.42)$$

where the fifteen coefficients E_n are linear combinations of terms such as $\langle\varepsilon_{ij}\varepsilon_{mn}\rangle$. The coefficients E_n are considered as parameters to be determined in refinement. The strain contribution in the Caglioti equation in this instance is given by

$$U_S = 4\left(\frac{180}{\pi}\right)^2 (8\ln 2)\left\langle\varepsilon_{hh}^2\right\rangle \quad (9.43)$$

Equation (9.42) is the 'worst case' in that it is the form required for triclinic symmetry. Considerable simplification is possible for higher symmetry structures as detailed by Popa (1998).

Stephens (1999) has used a different argument to obtain essentially the same result. He considers the interplanar spacing d defined by

$$\frac{1}{d^2} = \Psi_{hkl} = Ah^2 + Bk^2 + Cl^2 + Dhk + Ehl + Fhk \quad (9.44)$$

[123] This equation along with earlier eqns (9.25) and (9.40) are often thought to describe ellipsoids, but in general they do not.

where quantities A to F vary from one individual crystallite to the next, and expands the variance of Ψ_{hkl}

$$\sigma^2(\Psi_{hkl}) = \sum_{HKL} S_{HKL}\, h^H k^K l^L \tag{9.45}$$

where S_{HKL} are defined only for $H + K + L = 4$ and correspond to $E_1 - E_{15}$ above.[124] The FWHM attributed to strain is

$$\begin{aligned} H_S &= 2(2\ln 2)^{\frac{1}{2}} \frac{\sigma(\Psi_{hkl})}{\Psi_{hkl}} \tan\theta \\ &= 2(2\ln 2)^{\frac{1}{2}} \frac{\left[\sum_{HKL} S_{HKL}\, h^H k^K l^L\right]^{\frac{1}{2}}}{\Psi_{hkl}} \\ &\quad \times \tan\theta \text{ (radian)} \end{aligned} \tag{9.46}$$

so, if again the strain-broadening profile (CW) is assumed to be Gaussian:

$$U_S = \left(\frac{180}{\pi}\right)^2 (8\ln 2) \frac{\sigma^2(\Psi_{hkl})}{\Psi_{hkl}^2} = \frac{\left(\frac{180}{\pi}\right)^2 (8\ln 2) \sum_{HKL} S_{HKL}\, h^H k^K l^L}{\Psi_{hkl}^2} \tag{9.47}$$

Stephens simplifies eqns (9.46) and (9.47) by incorporating the factor (8ln2) into the definition of S_{HKL}. In addition, he relaxes the usual assumption that strain broadening is Gaussian, by apportioning the width given by eqn (9.46) between Gaussian and Lorentzian contributions. The coefficients S_{HKL} are subject to the same symmetry restrictions as E_n and likewise number 15 for a general triclinic structure. Symmetry restrictions for higher symmetries are given by Stephens (1999) and this method has been successfully implemented in at least one popular Rietveld refinement code – GSAS (Larson and Von Dreele 2004).

Leineweber (2007) has re-investigated the behaviour of anisotropic strain broadening in terms of the interaction of a *stimulus* (or field) with a *property tensor* to give as *response*, an anisotropically broadened powder diffraction pattern. The analysis reproduces all of the important results above (Popa 1998; Stephens 1999) as well as exploring some new ground. The specific examples studied are a stimulus of rank n (0 or 2) acting on a property tensor of rank $n + 2$ (2 or 4). The property rank $n + 2$ ensures a rank 2 response (the strain tensor). The use of a scalar stimulus to elicit an anisotropic response is particularly significant as few in the field have realized the potential for this to occur. Specific examples include a powder made from internally chemically homogeneous particles which have a particle-to-particle distribution in composition. In all but cubic materials, the lattice parameter–composition relationship (a rank 2 tensor) will be anisotropic and the result of the scalar chemical composition distribution is

[124] The connection is made via $4\left\langle\varepsilon^2\right\rangle = \sigma^2(\Psi_{hkl})/\Psi_{hkl}^2$.

anisotropic peak broadening. A similar result will occur for distributions of other scalars such as temperature (via the rank 2 thermal expansion tensor). Although Leineweber (2007) focussed on cases where the stimulus is isotropic, the work also highlights an important point concerning sources of anisotropic broadening, that is, the anisotropy may be due to an anisotropic stimulus *or* an anisotropic property tensor *or* both. This point is revisited in §9.6 when dislocation induced broadening is discussed.

9.4 COMBINED SIZE AND STRAIN BROADENING

We have proceeded thus far on the assumption that only one source of peak broadening is present in the sample, either small particle size (§9.2) or a distribution of strains (§9.3). In fact there are many instances in which the two occur together. These include cold worked metals, materials in which Martensitic phase transitions have occurred (e.g. Martensitic steels, partially stabilized zirconia ceramics) and petrological samples. In fact the true nature of peak broadening (size or strain) was a cause of great debate in the early X-ray diffraction literature.

9.4.1 Williamson–Hall plots

To this day, one of the clearest and most concise expositions of the individual and combined effects of (isotropic) particle size and strain broadening is that given in the first three sections of Williamson and Hall (1953).

We have seen in §9.2 that (in CW data) pure particle size broadening varies as $\sec\theta$ whereas in §9.3 we observed that pure strain broadening has a $\tan\theta$ dependence. Hall (1949) recognized that merely plotting peak breadths (β) against $\sec\theta$ or $\tan\theta$ could give misleading results. If, however, the broadening is considered in terms of the size of reciprocal lattice points (infinitely small for a perfect crystal) one obtains the relationships (Williamson and Hall 1953):

$$\beta_s^* = \varepsilon\, d^* \tag{9.48}$$

and

$$\beta_p^* = \frac{1}{t} \tag{9.49}$$

where β_s^* and β_p^* are the integral breadths of reciprocal lattice points due to strain and particle size, ε describes the strain distribution and t is the 'particle size'. This means that in reciprocal space, the broadening due to small particle size is constant and that due to strain increases linearly as we move away from the origin of reciprocal space (i.e. as d^* increases). Therefore a plot of $\beta^*(=\beta\cos\theta/\lambda$, with β in radians) versus d^* for pure particle size broadening is a horizontal line of intercept $1/t$ (Fig. 9.17(a)) and for pure strain broadening it is a straight line through the origin with slope ε (Fig. 9.17(b)). For combined particle size and strain broadening we encounter again the problem of the intrinsic shape of the

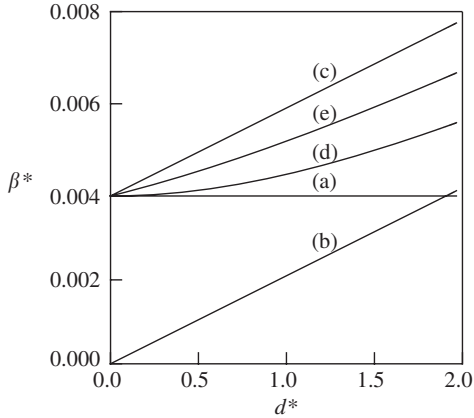

Fig. 9.17 Williamson-Hall plot illustrating the expected trends for (a) pure size broadening, (b) pure strain broadening, and combined size and strain broadening if the peaks are (c) Lorentzian, (d) Gaussian, and (e) intermediate (Voigt). A crystallite size of 250 Å and a strain distribution 0.2% wide were used to generate the figure. Units on both axes are $Å^{-1}$.

pure particle size and strain-broadening profiles [see discussion of eqns (9.15) and (9.16)]. If both profiles are Lorentzian, their integral breadths add linearly and the resulting plot shown in Fig. 9.17(c) (adapted from Williamson and Hall 1953) is a straight line with intercept $1/t$ and slope ε. If both profiles are Gaussian then the graph is curved [Fig. 9.17(d)], having a terminal slope at large d^* the same as the Lorentzian case and still intercepting at $1/t$. Intermediate peak shapes result in curves that lie between these two limiting cases [Fig. 9.17(e)].

The value of this method, known as the Williamson–Hall plot[125] is that regardless of the peak shapes, it provides:

(i) clear discrimination between particle size- and strain-like effects,[126]
(ii) an estimate of the mean particle size t,
(iii) an estimate of the integral breadth of the strain distribution ε,
(iv) a clear distinction between isotropic (monotonic curve) and anisotropic (scatter) broadening.

As such, a combination of individual peak fitting (§4.5), subtraction of the instrument profile, and a Williamson–Hall plot is the most rapid diagnostic tool for determining the kind(s) of broadening present and providing starting values for size and strain parameters. It also gives, from the curvature of the plot, an indication of whether the size and strain profiles are approximately Lorentzian, or Gaussian, or whether they adopt intermediate shapes.

[125] Perhaps a little unfairly as the idea was first published by Hall (1949).
[126] Lattice effects such as dislocations can cause very similar broadening to a combination of small particle size and lattice strains.

9.4.2 Fourier methods

A very elegant method for separating the effects of particle size broadening from those of strain broadening was devised by Warren and Averbach (1950, 1952). Here the lengthy and complex derivation is omitted because this method has not been extensively used with neutron diffraction data for the reasons discussed below. The definitive treatment is that due to Warren himself (Warren 1969, 1990) or adaptations such as that by Klug and Alexander (1974). At the core of the method is Warren's powder pattern power theorem whereby the total diffracted power is formulated by summing over all unit cells in the crystal based on their position from the origin and a distortion vector that represents lattice strains. In this way the expression retains contact with the size of the crystallite and its perfection (in terms of displacements or strain). The power may be expressed as a Fourier series.

$$P'(2\theta) = \frac{KNF^2}{\sin^2\theta} \sum_{n=-\infty}^{+\infty} \{A_n \cos 2\pi n h_3 + B_n \sin 2\pi n h_3\} \tag{9.50}$$

where K is a collection of physical constants [refer to Warren (1969, 1990) p. 24, for the X-ray case], N is the total number of unit cells in the sample, F is the structure factor for the reflection under consideration, and the Fourier coefficients are

$$\begin{aligned} A_n &= \frac{N_n}{N_3} \langle \cos 2\pi l Z_n \rangle \\ B_n &= -\frac{N_n}{N_3} \langle \sin 2\pi l Z_n \rangle \end{aligned} \tag{9.51}$$

The treatment in Warren (1969, 1990) is presented only in terms of a $00l$ reflection for an orthogonal unit cell but it has been shown to be completely general. It involves considering columns of unit cells perpendicular to the diffracting planes and within these columns, pairs of cells a fixed distance apart. The parameter Z_n is the component, perpendicular to the reflecting planes, of the relative displacement for a particular pair of cells that are n cells apart. Finally, N_3 is the average number of unit cells per column, N_n is the average number of pairs at separation n cells per column, and h_3 is given by

$$h_3 = \frac{2\,|\boldsymbol{a}_3|\sin\theta}{\lambda} \tag{9.52}$$

The cosine coefficient encompasses both a column length (crystallite size) coefficient $A_n^S = N_n/N_3$ and a distortion coefficient $A_n^D = \langle \cos 2\pi l Z_n \rangle$. In common with other methods, the peak profile due to the instrument needs to be taken into account. If the Fourier deconvolution method of Stokes (1948) is used [see eqns (9.12)–(9.14)] then the Fourier coefficients are directly available.[127] The method of separating A_n^S from A_n^D relies on the same observation as made by Hall (1949),

[127] The Fourier series should be evaluated for the same range as that implied by eqn (9.50).

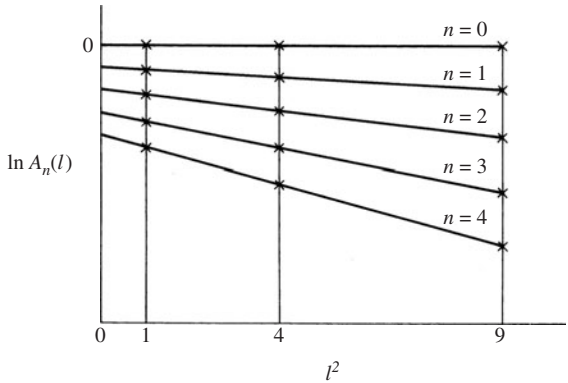

Fig. 9.18 The logarithmic plot which is used to separate particle size and distortion effects when multiple orders 00*l* are available (Warren 1969, 1990).

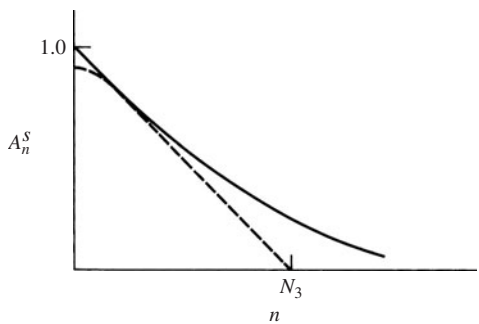

Fig. 9.19 Plot of the size coefficient A_n^S against the variable n. The intercept of the initial slope on the axis of abscissae is the mean column length number N_3. (Warren 1969, 1990).

that the size coefficient A_n^S is independent of the reflection order whereas the distortion coefficient depends linearly on it. Therefore by measuring several orders of reflection (e.g. 001, 002, 003, etc.) and plotting $\ln A_n(l)$ against l^2 for different values of the harmonic number n, a graph such as Fig. 9.18 is obtained. The intercepts at $l = 0$ give the size coefficients A_n^S and the slopes give $-2\pi^2 \langle Z_n^2 \rangle$, which may be re-written $-2\pi^2 n^2 \langle \varepsilon_n^2 \rangle$. Therefore the initial slopes of the lines in Fig. 9.18 give mean square values of an average component of strain. To interpret the A_n^S values, a plot is made of A_n^S versus n (e.g. Fig. 9.19). The initial slope of the curve, extrapolated to the n axis is the mean column length, N_3 or the 'particle size'.

Advantages of the Warren–Averbach method are that, by using Fourier coefficients of the experimental profile, no assumption about the functional form of the size or strain-broadened peaks is made. Disadvantages include the complexity of the method and high sensitivity to the background level assumed in the extraction of the data. It is also somewhat detached from other forms of powder diffraction

analysis (lattice parameter and structure refinements, etc.). There are relatively few examples of its use in neutron diffraction studies for two principal reasons. First, when the method was devised the resolution of neutron diffractometers was far too poor to conduct line broadening analysis. Second, by the time access to high resolution neutron powder diffractometers became more widespread (mid-1980s), whole pattern fitting methods such as Rietveld refinement had become the data analysis method of choice in neutron powder diffraction. Neutron diffraction peak shapes (especially from CW instruments) are amenable to either individual peak or whole pattern fitting methods, as we shall see below.

9.4.3 Peak and whole pattern fitting methods

As we have mentioned in §9.4.1, particle size broadening is independent of d^* and strain broadening is not [eqns (9.49) and (9.48)]. These observations are rigorous and provide the core of all methods for reliably separating crystallite size broadening and strain broadening including whole pattern fitting methods. In addition, it is generally accepted that the intrinsic profile shape due to the two types of broadening lies within the envelope defined by purely Lorentzian and purely Gaussian functions – in essence Voigt functions. Therefore the most general approach to modelling a combination of size and strain broadening is to use two Voigt functions, one that varies with d^* ($\tan\theta$ in CW determinations) and one that doesn't ($\sec\theta$ in CW patterns). Unfortunately, often the resolution and d-space range (Q range) covered in the experiment is insufficient to support the refinement of Gaussian strain and size half-width components $\left(H_G^S, H_G^D\right)$ and Lorentzian strain and size half-width components $\left(H_L^S, H_L^D\right)$ simultaneously. This leads to serious parameter correlations and no convergence to a unique solution during refinement.

To overcome these difficulties, it has been common practice to incorporate assumptions concerning the profile shapes into analysis programs, that is, the crystallite size broadening (§9.2) is Lorentzian and that the strain broadening (§9.3) is Gaussian. Although theoretical justification for these assumptions is not rigorous (see §9.2, §9.3 and Delhez *et al.* (1993) for discussion of this point), there is a significant body of experimental observations that conform to this model. Furthermore, it is a relatively straightforward assumption to test using a Williamson–Hall plot. Implementation of this basic model has been accomplished by very simple adaptations of the basic peak width equations (de Keijser *et al.* 1983; Hill and Howard 1986). Taking, for example, the constant wavelength case, it may be possible to describe the peaks using Voigt functions with Gaussian and Lorentzian component widths given by

$$H_G^2 = (U_I + U_S)\tan^2\theta + V\tan\theta + W \tag{9.37}$$

$$H_L = \frac{K\lambda}{D}\sec\theta \tag{9.9}$$

respectively. Such a description depends on the *assumption* that the total sample contribution can be represented by a convolution of the Gaussian strain and

Lorentzian particle size contributions, as well as that the instrumental peak shape is Gaussian.

More complex methods have been implemented. These include the inclusion (or allowance) of both the particle size and strain-broadening profiles to be Voigt functions, or G and L components within more complex peak functions such as those used for TOF patterns. For example the functions used within the CCSL and GSAS programs for modelling high resolution TOF patterns contain up to 16 parameters. To avoid parameter correlations, as many as possible of these are fixed by careful analysis of standard patterns. The four sample dependent terms (Gaussian size and strain terms and Lorentzian size and strain terms) can in favourable circumstances (high resolution and data spanning a large d-range) be refined independently. In the event that the Rietveld refinement codes provide for separation of instrument from sample contributions, care must then be taken to avoid refining these simultaneously – the instrument contributions should be held constant. If they are refined simultaneously then severe parameter correlations will occur resulting in either a divergent refinement or meaningless refined parameters.

As highlighted in §9.2.3 and §9.3.3, particle size and microstrain broadening can be anisotropic. In severe cases, both forms of anisotropic broadening can occur together. Although it is possible in principle to deconvolute these effects by careful fitting procedures using high Q range, high resolution data, the time and effort required to be certain that a unique and correct result has been obtained may be prohibitive. If the main aim of the experiment lies elsewhere (e.g. structure solution, quantitative analysis, etc.) then exhaustive testing of the uniqueness of the fit is not required providing that satisfactory convergence of the key parameters is observed and the overall fit accounts for the *integrated* intensity correctly. If the aim of the experiment is to extract microstructural data, then it is strongly recommended that where possible supplementary techniques such as SEM and TEM be used to provide additional information concerning particle size and shape.

In summary, we have shown (§9.2–§9.4) that a considerable amount of microstructural information is available within a powder diffraction pattern, but that it is entangled with other effects. Procedures for extracting microstructural data are available and are widely implemented in pattern fitting software; however, these must always be used with caution and having regard to other information sources (SEM, TEM). The powder diffraction techniques are at their most useful for tracking *changes* in the microstructure as a function of some external variable (e.g. during an *in situ* experiment). A far greater investment of time and effort is required to make the refined parameters take on an absolute physical meaning. The development of very high resolution instruments (e.g. HRPD at ISIS and D2B at ILL) has improved the potential for accurate neutron diffraction microstructural studies; however, extreme resolution can be a double-edged sword. It reduces the influence of the instrument on the result; however, the determination of the pure instrument profile becomes problematic because it is difficult to find samples free from particle size effects at extreme resolution. Even the NIST LaB_6 peak shape standard has been shown to have a small amount of particle size broadening

(Lynch 2003). In this case, the best approach is likely to be an adaptation of the fundamental parameters approach to whole pattern fitting – where the instrument's peak width is determined from the principles of neutron optics, perhaps assisted by Monte-Carlo or other appropriate simulation techniques.

9.5 CHEMICAL AND PHYSICAL GRADIENTS

Materials prepared for the purpose of crystal structure determination should, as far as possible, be chemically and physically homogenous. However, materials that are of interest in other fields (e.g. materials science, mineralogy, etc.) sometimes unavoidably contain chemical or physical gradients. Although methods for removing the gradients might be conceived, in some cases the gradient is an essential part of the phenomenon being studied, for example, chemical diffusion associated with the *in situ* study of a chemical reaction, in functionally graded materials, or in mineralogical and petrological samples. Chemical and physical gradients can have a profound influence on the appearance of the diffraction pattern, in particular the shape of the diffraction peaks. Typical effects are the development of a pronounced asymmetry (monotonic gradients) or saddles between twin-related reflections (strain gradients). In many cases, these greatly degrade the quality of single peak or whole pattern fits to the data and hence reduce the quality of the information that may be derived from the pattern.

Chemical and physical gradients may be of two kinds. The first are simply statistical distributions about a mean value. An example is the micro-strain discussed in §9.3. Another example is an imperfectly formed solid solution, where the chemical composition varies slightly on either side of the mean value. Provided that the distribution is nearly symmetrical, the effect of the gradient is merely to broaden the peaks. This kind of effect is readily handled with the methods already developed in §9.3 and requires no further comment here. The second type is in the form of a monotonic gradient of a chemical and/or physical variable within the crystallites of the sample. An example is Ti particles exposed to oxygen at 1200°C for a short time. The surface will have approached the solubility limit (30 at% O) whereas the centre remains pure Ti. In between lies a 'primary' chemical gradient that may take a variety of functional forms (e.g. linear, error function, etc.) depending on the atom transport mechanism. The chemical gradient in this case will have an associated 'atomic size effect' that produces a 'secondary' physical gradient of the same functional form. These monotonic gradients form the subject of this section.

Little attention has been paid in the literature to the problem of how to account for chemical and physical gradients in diffraction patterns except for two very specific cases. We begin by adapting methods developed to simulate the effect of a particle size distribution on particle size broadened peaks (§9.2.2) to the description of the effect of a generalized gradient in the sample on the diffraction pattern (§9.5.1). This approach is then applied to both chemical (§9.5.2) and physical (§9.5.3) gradients and the results of literature studies presented.

9.5.1 A generalized approach to gradients

Following the approach adopted for particle size distributions (§9.2.2), we consider a sample containing similar chemical or physical gradients within each crystallite. Let the sample be described by the function $g(c)$ where $g(c)$ represents the volume of the sample having composition (or physical property) c. At any single value of c, c_1 say, consider a small diffraction profile $y(2\theta)$ of instrumental width (unlike the particle size case) but with a *position* $2\theta_c$ defined by the functional relationship between the variable c and the d-spacing [$d(c)$ say] and an *area* given by $g(c_1)$. The resultant peak shape function, $Y(2\theta)$ may be found by integration:

$$Y(2\theta) = \int_{c_{\min}}^{c_{\max}} g(c) y(2\theta, 2\theta_c)\, dc \tag{9.53}$$

The specific form of $g(c)$ and $d(c)$ will be determined by the type of gradient and other factors such as the shape of the diffracting object (e.g. loose powder vs. solid polycrystal). These aspects will be expanded in §9.5.2 and §9.5.3.

9.5.2 Chemical gradients

A chemical gradient affects the diffraction peak shape in two ways. First, the mean interplanar spacing will vary as a function of chemical composition and the volume fraction of material with given d-spacing will be described by the function $d(c)$ in §9.5.1. The simplest case is when the volume distribution of d-spacings is linear.[128] This could arise as illustrated in Fig. 9.20, wherein the volume distribution g(c) varies linearly between two composition limits (Fig. 9.20(a)), $g(c) = g_0 + \Lambda c$. The composition gradient causes a gradient in both the d-spacing and the structure factor F (Fig. 9.20(b)). The diffraction peaks will be 'smeared' by these gradients and the effect on a CW diffraction peak is shown in Fig. 9.20(c). The relationship between the different parts of the figure is shown by the arrows. The integral in eqn (9.53) becomes

$$Y(2\theta) = \int_{c_{\min}}^{c_{\max}} \left(g_0 + \Lambda c\right) y(2\theta, 2\theta_c)\, dc \tag{9.54}$$

If we assume for purposes of illustration a simple Gaussian form for $y(2\theta, 2\theta_c)$ eqn (9.53) becomes

$$Y(2\theta) = \int_{c_{\min}}^{c_{\max}} \left(g_0 + \Lambda c\right) \frac{C_1}{H_I} \exp\left[-C_0 \left(\frac{2\theta - 2\theta_c}{H_I}\right)^2\right] dc \tag{9.55}$$

where $C_0 = 4 \ln 2$, $C_1 = \sqrt{C_0/\pi}$ as before (eqn (9.18)) and H_I is the FWHM of the peak shape due only to instrumental factors.

[128] It should be noted that a linear variation of d-spacing with composition, coupled with a distribution $g(c)$ that is constant (as could arise with a uniform concentration gradient in a tabular sample) or symmetric, leads only to peak broadening, not to peak shape changes.

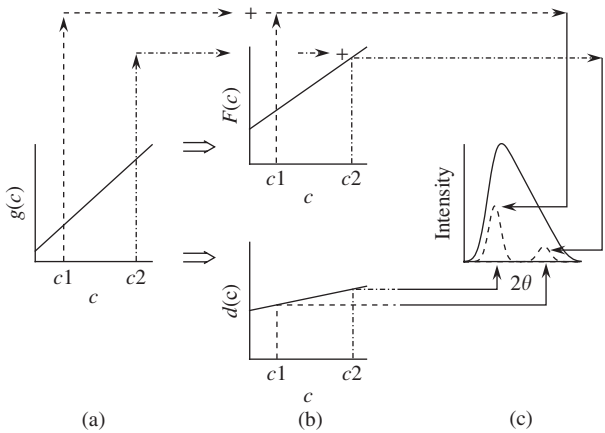

Fig. 9.20 Demonstration of the method used to investigate the effect of concentration gradients on peak shapes. At the left, a concentration distribution at (a) generally implies a distribution in both d-spacing $d(c)$ and structure factor $F(c)$ at (b). Taking two example concentrations $c1$ and $c2$, we see by following the arrows that each will generate a discrete diffraction peak at a *position* determined by the concentration dependence of the d-spacing and with *intensity* determined by the value of the concentration distribution $g(c)$ ***and*** the concentration dependence of the structure factor $F(c)$. The small peaks representing that part of the sample with compositions $c1 \pm \delta$ and $c2 \pm \delta$ are shown dashed in part (c) of the figure along with the composite peak obtained by summing all such peaks.

The quantity $2\theta_c$ can be obtained from known or measured lattice parameters (and hence d-spacing) vs. composition relationships. Again by way of example, we assume a linear relationship (i.e. Vegards' law is followed) giving for the d-spacing $d(c)$ at a given composition c:

$$d(c) = d_0 + \Gamma c \tag{9.56}$$

where Γ is the constant of proportionality. Since $2\theta = 2\sin^{-1}\frac{\lambda}{2d(c)}$, the expression for the peak shape becomes

$$Y(2\theta) = \int_{c_{\min}}^{c_{\max}} (g_0 + \Lambda c)\frac{C_1}{H_I}\exp\left[-C_0\left(\frac{2\theta - 2\sin^{-1}\frac{\lambda}{2(d_0+\Gamma c)}}{H_I}\right)^2\right]dc \tag{9.57}$$

The solution, shown schematically in Fig. 9.20(c), is a strongly asymmetric peak shape. Unlike instrumental sources of asymmetry in CW diffraction patterns, which are symmetric about $2\theta = 90°$, the composition effect occurs on the same side of every peak in the diffraction pattern. For pulsed neutron TOF patterns, where all peaks are generally asymmetric on the same side due to different rise

and decay times of the neutron pulse, asymmetry due to chemical gradients may increase or decrease this inherent asymmetry.

If the scattering lengths of the two species participating in the gradient are the same, then solution of eqn (9.57) for each peak will give an accurate peak shape.[129] It should be noted at this point that H_I will differ for each peak in a pattern; however, its value is easily determined from the instrument resolution function – perhaps given in the form of the Caglioti equation (4.7) or its TOF equivalent eqn (4.8).

If the scattering lengths of the two components forming the gradient are not equal, then an additional factor is introduced. The scattering length gradient may be quite a minor effect (e.g. a solid solution of Zr and Nb where $b_{\mathrm{Zr}} = 7.16$ fm and $b_{\mathrm{Nb}} = 7.054$ fm) or it may become the dominant effect (e.g. when an element with a negative scattering length such as Ti is involved). It is relatively straight forward to incorporate this effect within eqn (9.57) through the effect of the scattering length on the structure factor expansion, eqn (2.31). For solid solutions with very simple structures that have peaks arising from only one atom site, b_n may be simply replaced by $\bar{b}_n$, the weighted average of the scattering lengths of the elements co-occupying a particular site within the structure. Focussing on this example for simplicity, the integrated intensity of the peak is directly proportional to $\left(\bar{b}_n\right)^2$ and if all other factors are constant (e.g. instrumental peak shapes, etc.), eqn (9.57) should scale the same way. Therefore we may write

$$Y(2\theta) = \int_{c_{\min}}^{c_{\max}} \left(\bar{b}_n\right)^2 \left(g_0 + \Lambda c\right) \frac{C_1}{H_I} \exp\left[-C_0 \left(\frac{2\theta - 2\sin^{-1}\frac{\lambda}{2(d_0+\Gamma c)}}{H_I}\right)^2\right] dc \tag{9.58}$$

Since

$$\bar{b}_n = b_A + (b_B - b_A)\, c \tag{9.59}$$

where b_A is the scattering length of the solvent species and b_B is the scattering length of the solute species, we get

$$Y(2\theta) = \int_{c_{\min}}^{c_{\max}} \left[b_B c + b_A (1-c)\right]^2 \left(g_0 + \Lambda c\right) \frac{C_1}{H_I} \times \exp\left[-C_0 \left(\frac{2\theta - 2\sin^{-1}\frac{\lambda}{2(d_0+\Gamma c)}}{H_I}\right)^2\right] dc \tag{9.60}$$

in which ideally only the constants associated with the chemical gradient, g_0 and Λ are unknown. Figure 9.20(c) illustrates the effect associated with a linear chemical gradient coupled with a linear dependence of d-spacing on chemical composition

[129] Subject to our assumptions of a linear chemical composition distribution, a linear d-spacing composition relationship, and a Gaussian instrument peak shape.

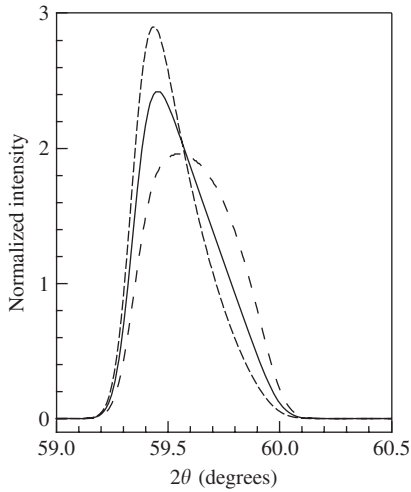

Fig. 9.21 Comparison of CW neutron diffraction peak shapes arising from application of eqn (9.60) to the same linear distribution of concentration with no structure factor effect (solid line), $b_A < b_B$ (short dash) and $b_B > b_A$ (long dash). The concentration distribution used was linear from 0 to 100% with a linear d-spacing effect of 0–1% over the full concentration range. Scattering lengths due to Si (4.2 fm) and Ge (8.2 fm) were used in conjunction with a neutron wavelength of 1 Å and a Gaussian instrumental peak 0.15° FWHM matching the best angular resolution on CW instruments.

(Vegard's Law) alone (i.e. no scattering length effect). Figure 9.21 compares this with the scattering length effect in a face centred cubic (diamond) structure. Two cases, $b_A < b_B$ and $b_A > b_B$ are explored. Oddly shaped peaks such as these are often observed in diffraction patterns from partially synthesized materials, for example, during *in situ* experiments, and it is clear that they contain untapped microstructural information about the sample.

Non-linear chemical gradients or non-linear d-spacing – composition relationships (or both) can be readily accommodated within the formalism outlined above by substituting the appropriate form of $g(c)$ or $d(c)$. Examples of 'typical' non-linear gradients include the chemical gradient resulting from diffusion of an element from a finite source through a planar boundary into a semi infinite substrate. The resulting composition profile is well described by

$$c(x,t) = \frac{M}{\sqrt{\pi D t}} \exp\left(\frac{-x^2}{4Dt}\right) \tag{9.61}$$

where x is the depth below the surface, t is the elapsed time, M is the mass per unit area of source material and D is the diffusion coefficient given by $D = D_0 \exp(-E/RT)$ in which D_0 is a material specific constant and E is the

activation energy for the diffusing species. The volume of sample with concentration between c and $c + dc$, $g(c)dc$, is in this circumstance proportional to the thickness of sample dx with concentrations in this range, that is,

$$g(c)dc \propto dx = \frac{dx}{dc}dc = \frac{dc}{\frac{\partial c}{\partial x}},$$

so we apply eqn (9.53) with $g(c) = (\partial c/\partial x)^{-1}$. More complex diffusing systems involving extended sources give rise to different solutions as described in detail by Crank (1975).

It is also possible that, in samples about which little is known, the form of $g(c)$ can be extracted from the data by suitable modelling and refinement. There are as yet no examples of the use of neutron powder diffraction for this purpose in the literature. However, there are a limited number of examples where a similar technique has been used to extract diffusivities from the shape of X-ray diffraction peaks (Fogelson 1968; Fogelson *et al.* 1971; Unman and Houska 1976) with reasonable accuracy. The samples conformed to the conditions outlined in the discussion of eqn (9.61), that is, a finite source evaporated on to the surface of a monolithic sample. The theoretical treatment is in essence the same as given above but considers only the d-spacing effect, not the structure factor effect. There are also severe limitations in the use of the method with conventional X-rays due to the effect of absorption which must be modelled very well. This limits its applicability to the case of a gradient in a planar surface which spans a distance comparable to the penetration depth of the X-rays. It is therefore useful for determining diffusion coefficients under carefully controlled conditions, but not for general use in the study of polycrystalline materials. Only one example of the study of more general chemical gradients in partially reacted polycrystalline materials was found, again using laboratory X-rays (Rafaja 2000). In that case a convolution approach was taken and various strategies (Stokes method, Fourier expansion and linear combinations of instrumental profiles) for deconvoluting the profile due to the diffusion couple were adopted. The latter approach is akin to a coarse grained version of the integral method given above.

The advantage of using neutron diffraction lies in the ability to examine very large samples and large gradients, for example, in the study of functionally graded materials (FGM). The low absorption of neutrons by most materials means that absorption can be ignored in the theoretical treatment and the process greatly simplified. Since chemical gradients are a feature of non-equilibrium systems, modern developments in rapid neutron diffractometers with quite high-resolution (see Chapter 12) will allow the technique to be used to monitor the development and decay of chemical gradients *in situ* as a function of processing variables (time, temperature, etc.).

In closing this section, it should be noted that the approach adopted here is not the only way of modelling the effect of chemical gradients on diffraction peaks. Rafaja (2000) has demonstrated that it is certainly possible to extract the sample

induced broadening using the Fourier de-convolution method of Stokes (1948) (see §9.2.1) or related procedures and then to apply various models to understand the nature of the gradient. An alternative approach would be to use the Debye equation [eqn (9.67)] and *ab initio* methods to calculate the peak shape from various models for comparison to the observed peak shapes. These authors favour the integral approach [eqns (9.53)–(9.61)] because it is rigorous, not susceptible to termination and background estimation problems, and lends itself readily to incorporation in whole pattern fitting methods such as Rietveld refinement. This latter point is important if the study of gradients is part of a larger study that also requires crystal structure and/or phase quantification.

9.5.3 Strain gradients

Several types of strain gradient have been dealt with in earlier sections. Most notably, the case of a more or less symmetric distribution of strains about some mean value was the subject of §9.3 and will not be considered further here. One particular kind of monotonic strain gradient, that due to lattice dilation associated with a chemical gradient, has also been considered (§9.5.2). Those remaining are the pure strain gradients and are the subject of this section.

Pure strain gradients can occur in a number of ways. Macroscopic gradients exist in any object subjected to a non uniform stress (point loading, etc.) and irregularly shaped objects subjected to any stress (localized or uniform). Microscopic strain gradients are developed between the layers of lamellar materials (e.g. surface coatings and multi layers) and, very importantly, between the differently oriented domains of ferroic materials (e.g. ferroelectrics). The characteristics of these domain wall boundaries are responsible for the resistance experienced when the polarization (electrical, magnetic, or mechanical) is reversed in ferroic materials, leading to hysteresis. They are therefore important in determining important properties such as the coercive field in ferroelectrics. We will use this latter example because it has received some attention in the literature and is amenable to analytic solution in some cases.

Darlington and Cernik (1991) demonstrated that the unusual synchrotron X-ray diffraction profiles observed from the 200/002 peaks of tetragonal $BaTiO_3$ arise from the strain gradient within domain walls. Similar peak profiles may be observed for all tetragonal ferroelectric phases – for example the tetragonal phase of $PbZn_{1/3}Nb_{2/3}O_3$–8%$PbTiO_3$ (PZN-8%PT) as shown by the neutron TOF peaks shown in Fig. 9.22.

To see how the gradients arise, one needs to consider the partitioning of a ferroelectric crystal into domains. For simplicity, consider a tetragonal crystallite containing 90° domains involving interchange of the a and c axes. The situation is depicted in Fig. 9.23. The change from one domain to the next is never instantaneous being always accompanied by a domain wall of finite extent. The domain wall accommodates the dimensional mismatch between the domains in the form of a gradient of lattice parameter (and hence d-spacing) from a to c, or an orientation gradient.

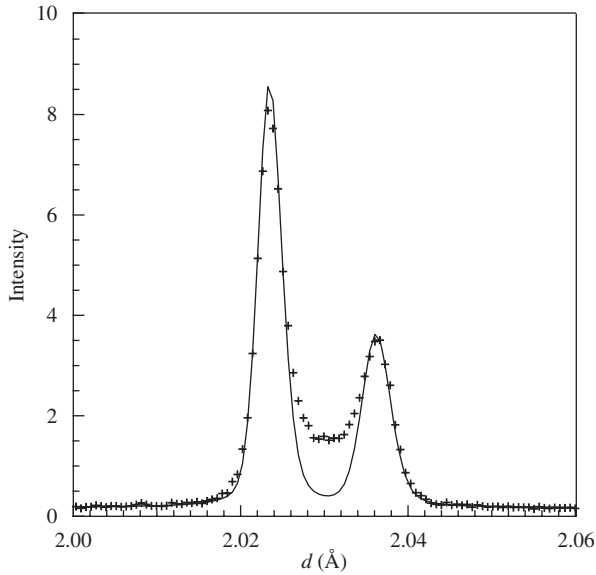

Fig. 9.22 Domain wall scattering between the tetragonal 200/002 doublet in the high resolution neutron diffraction pattern from a $PbZn_{1/3}Nb_{2/3}O_3$–8%$PbTiO_3$ sample at 400 K. Data, shown as (+) were recorded on the instrument HRPD at ISIS. The line is part of the corresponding Rietveld refinement fit on the assumption of no domain wall scattering.

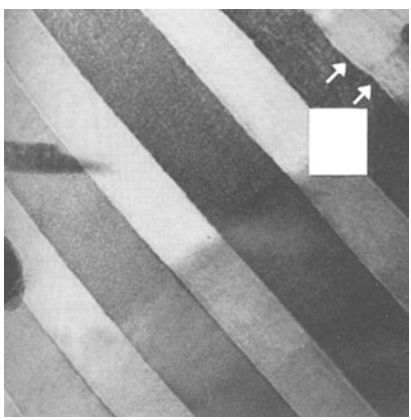

Fig. 9.23 Electron micrograph of 90° domains adapted from Salje (1990). The arrows indicate a domain wall boundary.

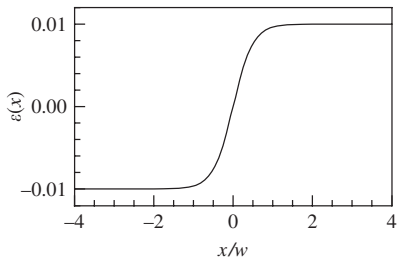

Fig. 9.24 Strain distribution across a ferroelectric domain wall as a function of the normalized width (x/w) according to eqn (9.62). Symmetric spontaneous strains of $\pm 1\%$ were assumed in the calculation. Note the approximately linear central section.

Recalling eqn (9.53), our generalized equation for the peak shape from a sample containing a gradient.

$$Y(2\theta) = \int_{c_{\min}}^{c_{\max}} g(c) y(2\theta, 2\theta_c)\, dc \tag{9.53}$$

We can see that $g(c)$ in this case will simply be the volume fraction of material with a particular lattice parameter and d-spacing, $V(d)$. Within the domain wall, the theoretically expected form of the strain gradient is given by

$$\varepsilon(x) = \varepsilon_0 \tanh \frac{x}{w} \tag{9.62}$$

(Barsch and Krumhansl 1984; Salje 1990) where $\varepsilon(x)$ is the value of the strain (referred to the parent cubic structure) at distance x from the domain wall centre position, ε_0 is the maximum strain remote from the domain wall, and w is the width of the domain wall in theory given by

$$w = \frac{\sqrt{2} c_0}{\sqrt{A\,|T - T_c|}} \tag{9.63}$$

where c_0 is a characteristic velocity for the wall, A is the first coefficient in the order parameter expansion, T is the absolute temperature and T_c is the critical temperature (Salje 1990). The strain evidently varies from $+\varepsilon_0$ in the c-domain to $-\varepsilon_0$ in the a-domain (Taylor and Swainson 1998). The shape of the function in eqn (9.62) is depicted in Fig. 9.24 in units of x/w. Although not strictly correct, a linear variation provides a reasonable first approximation for this kind of boundary. In terms of diffraction peaks derived from the whole crystal (or polycrystal), we must consider not only the domain wall but must take account of the relative volume fractions of:

(i) domain walls V_d
(ii) a-type domains V_a, and
(iii) c-type domains V_c

where $V_d + V_a + V_c = 1$.

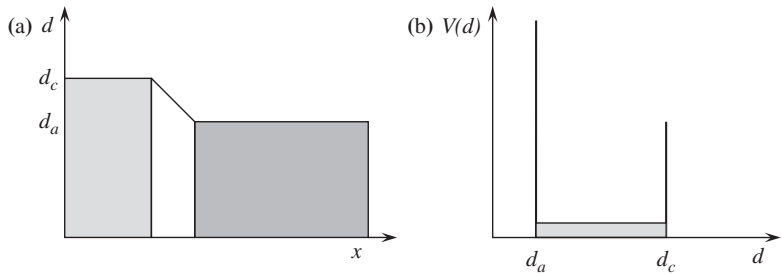

Fig. 9.25 (a) Distribution of d-spacing as a function of distance x for two domains and the associated domain wall in the linear approximation and (b) the resulting volume distribution $V(d)$ of the ensemble average (a domains, c domains, and domain walls) over the whole sample.

An important consequence of this is that the computed peak shape will reproduce not a single distorted peak, but twin related peaks and associated domain wall scattering for a particular domain ensemble and parent structure peak. Take for example the ferroelectric perovskite $BaTiO_3$. The structure is cubic above 400 K but becomes tetragonal below that temperature. Taking the cubic 200 peak as an example, it splits into 200 and 002 in the ratio 2:1, indicating that the domain populations are also in this ratio.[130] The distribution of d-spacings as a function of position (x) across a hypothetical ferroelectric domain wall is shown in Fig. 9.25(a). Although this figure is drawn for a single pair of domains and the associated domain boundary between them, it should for the purposes of this discussion, be considered as an ensemble average over the whole sample. The resulting volume distribution of d-spacings $V(d)$ is shown in Fig. 9.25(b) and the resulting diffraction is in effect the convolution of this distribution with the instrumental peak shape.

The total CW diffraction peak envelope $Y(2\theta)$ may be partitioned into three parts, due to a-type domains, c-type domains and domain walls:

$$Y(2\theta) = V_a\, y(2\theta, 2\theta_a) + V_c\, y(2\theta, 2\theta_c) + \int_{d_a}^{d_c} V(d)\, y(2\theta, 2\theta_0(d))\, dd \qquad (9.64)$$

As shown in Fig. 9.25(b), $V(d)$ for the domain wall region and a linear strain field is merely a constant. The dependence of $2\theta_0$ on d-spacing is obtained from Bragg's law:

$$2\theta_0(d) = 2\sin^{-1}\left(\frac{\lambda}{2d}\right) \qquad (9.65)$$

[130] In the absence of electric or mechanical poling or preferred orientation effects.

and assuming a Gaussian instrument peak shape, the observed peak function becomes

$$Y(2\theta) = V_a \frac{C_1}{H_I} \exp\left[-C_0\left(\frac{2\theta - 2\theta_a}{H_I}\right)^2\right] + V_c \frac{C_1}{H_I} \exp\left[-C_0\left(\frac{2\theta - 2\theta_c}{H_I}\right)^2\right] + \frac{V_d}{d_c - d_a}\int_{d_a}^{d_c} \frac{C_1}{H_I} \exp\left[-C_0\left(\frac{2\theta - 2\sin^{-1}\frac{\lambda}{2d}}{H_I}\right)^2\right] dd \tag{9.66}$$

where C_0, C_1, and H_I have been previously defined in §9.5.2. The third component of eqn (9.66) is directly proportional to V_d, the volume fraction of domain walls. If the mean domain size can be reliably determined, for example, by microscopy, then this quantity may be readily converted into a domain wall width – a quantity not easily accessed in other ways. The domain wall width is of interest in the study of certain types of phase transitions, ferroelasticity, the poling of ferroelectrics, and so on.

For a more precise analysis, the assumption of a linear strain gradient should be replaced by the theoretical domain wall strain profile eqn (9.62). This has been conducted by Taylor and Swainson (1998) in the course of an analysis for a tetragonal to orthorhombic transition. By considering a unit cell rotated 45° from the crystallographic cell, direct strains become shear strains and strain may be replaced by the shear angle, ψ which ranges from ψ_0 far from the domain wall to zero midway between the domains. They produced a diagram demonstrating 'lineshapes' or peak shapes for the domain wall scattering at two different (exaggerated) w/d ratios with d here being the total distance from the centre of a domain to the centre of the adjacent domain. These lineshapes [analogous to Fig. 9.25(b)] are reproduced in Fig. 9.26. They are plotted as the probability of a scattering event versus position across the domain wall between the centres of two adjacent domains expressed as a function of ψ/ψ_0. An attempt was made to compute the actual diffraction profile using convolution techniques but this could not be achieved for the entire doublet profile in the general case. These problems should be overcome using the piecewise integral method (eqn (9.64)). Taylor and Swainson (1998) did propose an alternative method based on the effect of the domain wall on the shape and position of the main peaks (i.e. due to the domains themselves) which was successfully applied to $YBa_2Cu_3O_{7-\delta}$ by Taylor (2000).

Many other kinds of domain structure, crystal symmetry, and instrument peak shape may be envisaged. The method developed above is equally valid for all of them and in favourable cases, will be able to distinguish between different gradient functions in both the domain wall scattering case and the other types of strain gradient mentioned in the introduction to this section. One disadvantage of the method is that, at present, it must be algebraically re-worked for each reflection of interest, that is, it has not yet been implemented as a general solution within a whole-pattern fitting environment.

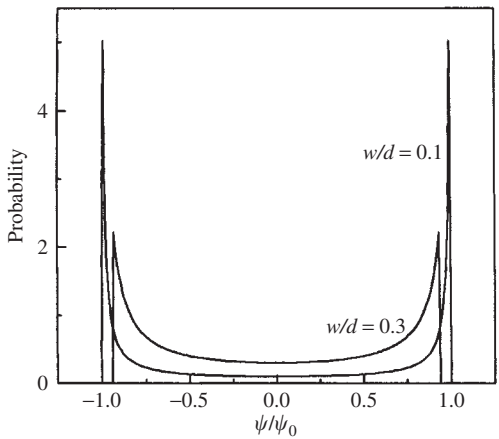

Fig. 9.26 Illustration from Taylor and Swainson (1998) of the intensity of diffraction, expressed as the probability of particular d-spacings, across domain walls with exaggerated w/d. The position within the domain wall (x-axis) is given as the shear strain expressed as the ratio of the shear angle ψ to its value within the domains and remote from the domain wall ψ_0.

An alternative approach to using a form of eqn (9.64) is to calculate the scattering *ab initio* using the generalized Debye scattering equation (Debye 1915):

$$Y(\theta) = \sum_m \sum_n b_m b_n \left[\frac{\sin\left(4\pi r_{mn} \sin\theta/\lambda\right)}{(4\pi r_{mn} \sin\theta/\lambda)} \right] \tag{9.67}$$

where b_n and b_m are the scattering lengths of atoms m and n, and r_{mn} is the distance between the pair of atoms (m, n). The calculated scattering is then modified with an instrument peak shape/width function to give the scattering to be expected from a particular model. In the domain wall case, the simplest tetragonal model would extend from mid-way through an a-type domain, across the domain wall, to midway through the adjacent c-type domain. This method is computationally intensive; however, it may be applied to any model for the scattering sample (see Andreev and Bruce 2001). Its strength in this case would be that it produces the entire powder diffraction pattern from a single computation.

Although materials such as ferroelectrics containing domain walls and domain wall scattering are widely studied in the literature, most authors have avoided a discussion of the domain wall scattering due to the difficulty of analysis and its absence from any standard powder diffraction analysis software. In a study of $BaTiO_3$, Darlington and Cernik (1991) estimated the fraction of domain walls from their X-ray diffraction peak profiles at 20%. No details of the method used were given, but presumably the integrated area not contained within the Bragg peaks was compared with the total integrated area of the 200 + 002 doublet. Valot *et al.* (1996) undertook analyses including subtracting the Bragg peaks to look

at the residual domain wall scattering. They concluded that it had a plateau-like form, for example, as shown for the linear approximation to the strain field in Fig. 9.25(b). They also demonstrated that, irrespective of the *hkl* of the peak doublet considered, the domain wall scattering (or intensity plateau as they expressed it) has approximately the same intensity relative to the total doublet intensity ($\sim$10% in their case). They also claimed without experimental proof, that the same approach may be used for triplets (Bragg peaks in the parent phase which split into three in the ferroelectric phase) in a pair-wise fashion. This has the consequence that when one pair of peaks within a triplet is more closely spaced than the other pair, the domain wall scattering is much higher so as to maintain the same integrated intensity for both pairs (see Valot *et al.* 1996, Fig. 8).

9.6 LINE DEFECTS – DISLOCATION BROADENING

A considerable amount of the foregoing discussion has concerned peak broadening due to 'strains'. The concept of a distribution of lattice strains giving rise to peak broadening is quite simple. However, the underlying crystal physics of elastic strains in a polycrystalline sample is more complex. If the sample is a solid polycrystal, then thermal expansion mismatch across grain boundaries and elastic anisotropy can lead to both residual stresses (and hence strains) that give peak shifts (see Chapter 11) and strain distributions that give peak broadening (see §9.3). However, this is not the only source of internal strains in polycrystals. In addition, there are very few genuine mechanisms for pure strains within loosely powdered samples. Nonetheless, many powder samples show 'strain-like' peak broadening (i.e. with $\tan\theta$ dispersion in CW experiments or d dispersion in TOF experiments). In these cases, and in a significant number of solid polycrystals as well, the 'strain' broadening is due to crystal defects – most often dislocations.

9.6.1 Dislocations

Dislocations are line defects that are responsible for the plasticity and toughness of metals; the high temperature creep of metals, ceramics and rocks; and the accommodation of lattice misfit strains across a wide range of semi coherent interfaces in materials science, and many other technologically important phenomena. The formal description of an edge dislocation is an extra half-plane (or part plane) of atoms 'inserted' into a crystal structure (Fig. 9.27(a)). Their actual formation mechanisms are far more complex; however, they are beyond the scope of this volume. Dislocations make plastic deformation easier because only one row of chemical bonds at a time must be broken to propagate a shear step, one atomic plane wide, across the entire crystal. This is illustrated in Fig. 9.27(b). The leading edge of the extra half plane defines an elastic singularity about which there is considerable strain: compressive above and tensile below. The displacement field about an edge dislocation lying along the z-axis and with the slip plane in the $x-z$

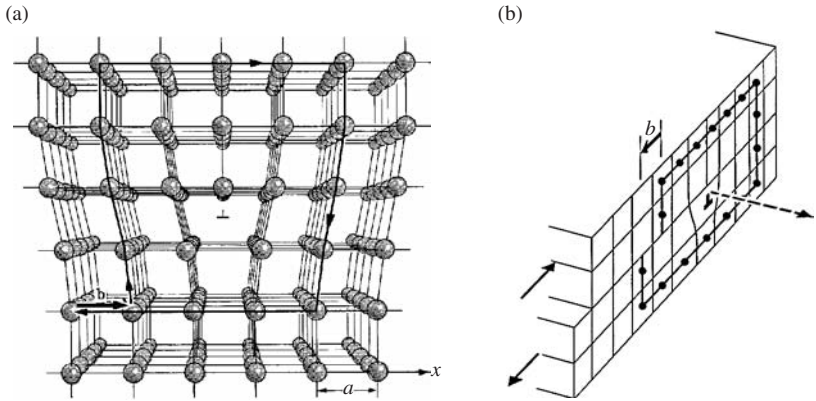

Fig. 9.27 Model of an edge dislocation illustrating (a) the strain field and (b) how dislocations propagate slip in crystals [adapted from Van Vlack (1975)].

plane in an elastically isotropic medium (continuum approximation) is given by

$$
\begin{aligned}
u &= \frac{b}{2\pi}\left[\tan^{-1}\left(\frac{y}{x}\right) + \frac{1}{2\,(1-\nu)}\frac{xy}{r^2}\right] \\
v &= \frac{b}{4\pi\,(1-\nu)}\left[(2\nu-1)\ln r + \frac{y^2}{r^2}\right] \\
w &= 0
\end{aligned}
\tag{9.68}
$$

where $r = \sqrt{x^2 + z^2}$, ν is Poisson's ratio and here b is the magnitude of the Burger's vector. Note that the displacements (or strains) decay quite slowly and so the strained region extends a long way from the dislocation core ~40–100 Å.

To maintain mechanical equilibrium, the strain energy within the two strain fields must balance. It might then be expected that the strain distribution about the dislocation would be symmetrical. This expectation is approximately true for simple materials such as face-centred cubic metals in the case of elastic isotropy (e.g. Al metal), whereas in complex materials it is rarely the case. The considerable variation in interatomic spacing (strain) caused by the dislocation is responsible for a substantial degree of diffraction peak broadening when the density of dislocations is high (10^9–10^{12} cm/cm^3).[131] A second type of dislocation, the screw dislocation, is also present in crystals. It propagates a shear step *parallel* to the line of the dislocation (Fig. 9.28) and the strain field is now one of pure shear deformation

[131] Dislocation density is defined as the length of dislocation line per unit volume of crystal.

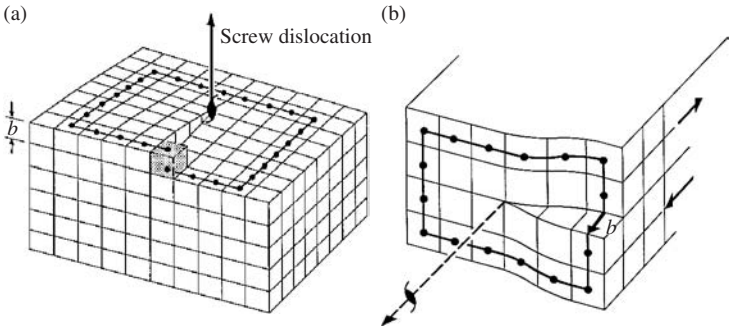

Fig. 9.28 (a) Model for and (b) motion of a screw dislocation [from Van Vlack (1975)].

and in an elastically isotropic medium is given by

$$\begin{aligned} u &= 0 \\ v &= 0 \\ w &= \frac{b}{2\pi}\tan^{-1}\left(\frac{y}{x}\right) \end{aligned} \tag{9.69}$$

where the screw dislocation too has been taken to lie along the z-axis. Note that the displacements in eqns (9.68) and (9.69) are ill-defined on the dislocation line itself, $x = y = 0$, and indeed continuum elasticity theory is not expected to apply closer than some inner cut-off radius from it.

Each type of crystal structure has particular slip planes and directions for easiest slip. The energy of the crystal is lowest if any dislocations present are straight and are aligned with these lowest energy directions. Although this situation can not be attained in most practical polycrystalline materials, there is a strong tendency within all materials for dislocations to align themselves strongly with the crystal structure. As such, dislocations are one of the primary causes of *anisotropic* strain broadening (§9.3.3). To fully appreciate the effect, consider the deformation field in Fig. 9.27(a), and eqn (9.68). For an edge dislocation lying along [001], the strain is zero along [001] and hence no broadening is observed in 00l type diffraction peaks whereas for perpendicular directions (such as [h00]) the strain is large and considerable broadening occurs in h00 type peaks. Similar orientation related broadening is also caused by screw dislocations. If, as is usually the case, the material is elastically anisotropic, there is a further contribution to the anisotropy of the peak broadening. In summary, the degree of *broadening* depends on the dislocation density whereas the kind and degree of *anisotropy* depends on other factors (crystal system, type of dislocation, elastic anisotropy). Two pure cases may be distinguished – (i) an elastically isotropic material will have anisotropic peak broadening where the anisotropy is governed only by the 'orientation factor',

and (ii) an elastically anisotropic material with a random distribution of dislocations will have the broadening anisotropy governed by the elastic constants. Unfortunately, most materials contain a mixture of both effects.

9.6.2 Theory of dislocation-induced peak broadening in brief

The dislocation sub-structure of a real material is very complex. At any reasonable dislocation density, the strain fields of neighbouring dislocations overlap. Dislocations with strain fields of like sign repel whereas strain fields of unlike sign attract; leading to complex arrangements including dipoles, slip bands, dislocation cell walls, and so on. In addition, during plastic deformation, the activation of multiple slip systems leads to pinning and entanglement of dislocations. The ensemble of dislocations will contain screw, edge, and mixed-type dislocations, and the ensemble of crystallites in the polycrystalline sample will randomize the orientation of them with respect to the scattering vector. It is extremely unlikely that any comprehensive theory will emerge that *uniquely* links the dislocation structure with the diffracted intensity distribution for such a complex structure. Nonetheless there are several important factors that still make the powder diffraction analysis of dislocations worthwhile. First, the degree of broadening must scale with the total strain and hence with the dislocation density. Second, the observed anisotropy of peak broadening confirms that orientation factor and elastic anisotropy effects dominate even at extremely high dislocation densities. Third, other means of dislocation density measurement such as TEM become extremely difficult and sometimes unreliable at high densities.

Compared with the real situation inside a deformed crystal, the models used to derive the scattering from a crystal containing dislocations have been substantially simplified to make them tractable. Perhaps the first theory of note was that of Krivoglaz and Ryaboshapka (1963), based on a completely random arrangement of dislocations in an elastically isotropic material. The result for this model was that the dislocation-induced peak broadening for both edge and screw dislocations is Gaussian and isotropic. The Gaussian peak shape arises from randomness in the placement of dislocations with respect to each other (i.e. no dislocation interaction), and the isotropy of the broadening arises from the assumption of random *orientation* and of elastic isotropy. In fact, there are arrangements of dislocations (dipoles for example) where the resulting profile is Lorentzian (e.g. Pototskaya and Ryaboshapka 1968). This fact introduces a key element of the analysis of dislocations using powder diffraction. Unlike strain or simple particle size broadening, the *shape* of the broadened peaks contains almost as much information as its breadth. Notwithstanding the many simplifying assumptions made, the theory of dislocation-induced broadening is quite complex, and only a brief account can be presented here. The interested reader is referred to the original literature for a more detailed account.

Two very similar theories were developed by Krivoglaz, Ryaboshapka, and co-workers; and by Wilkins. The basis of each is an equation for the scattering

from a crystal containing an ensemble of straight dislocations. The influence of the dislocation is accounted for by the static displacement field that surrounds the dislocation core (essentially eqns (9.68) and (9.69)). Adapting the notation of Krivoglaz and Ryaboshapka (1963),[132] the intensity I_{hkl} in the kinematic approximation, of the *hkl* peak from a crystal containing dislocations may be written as

$$I_{hkl} = F_{hkl}^2 \sum_{s,s'} \exp\left[i\boldsymbol{q} \cdot \boldsymbol{R}_{ss'}\right] \exp\left[T\left(\boldsymbol{R}_s, \boldsymbol{R}_{ss'}\right)\right] \tag{9.70}$$

where F_{hkl} is the structure factor, $\boldsymbol{q}$ is the position in reciprocal space relative to the Bragg reflection, $\boldsymbol{R}_{ss'} = \boldsymbol{R}_s - \boldsymbol{R}_{s'}$ is the difference between the position vectors of atoms at site s, and s' in the perfect crystal. The effect of the dislocation is contained within the factor

$$T\left(\boldsymbol{R}_s, \boldsymbol{R}_{ss'}\right) = \sum_{t,i} c_i \exp\left[i\boldsymbol{\kappa} \cdot \left(\boldsymbol{u}_{sti} - \boldsymbol{u}_{s'ti}\right) - 1\right] \tag{9.71}$$

where $\boldsymbol{u}_{sti}$ is the displacement of an atom from its ideal position at s due to a dislocation of type i located t lattice sites away measured perpendicular to the dislocation core. Here c_i is the concentration of dislocations of type i and $\boldsymbol{\kappa}$ is the scattering vector.

To obtain the intensity of diffraction from a polycrystalline material, I_p, the expression at eqn (9.70) needs to be averaged over all possible orientations (Krivoglaz *et al.* 1983)

$$I_p = \frac{I_{\text{int}}}{2\pi} \int_{-\infty}^{\infty} \exp\left(iqR\right) \exp\left[T\left(\boldsymbol{R}_s, \boldsymbol{R}\right)\right] dR \tag{9.72}$$

where I_{int} is the integrated intensity of the Bragg peak, q is the distance in reciprocal space to the centre of the peak, and $\boldsymbol{R}$ is taken parallel to the scattering vector.

The resulting peak profile may be anything from pure Gaussian for a high density of randomly oriented dislocations (Krivoglaz and Ryaboshapka 1963) to Lorentzian for dislocation dipoles (Pototskaya and Ryaboshapka 1968), but will generally be somewhere between these two limits. In the theories developed by Krivoglaz *et al.* (1983), Krivoglaz and Ryaboshapka (1963) and Wilkens (1970), the integral breadth of the broadening due to dislocations will be given by

$$\beta^2 = \rho_d \chi f(M) \tan^2\theta \tag{9.73}$$

where ρ_d is the dislocation density, and χ is the orientation/contrast factor (a function of *hkl*) that incorporates the anisotropic effects of a particular slip system *and* elastic anisotropy. The parameter M (Wilkens 1970)[133] models the effects

[132] The treatment given here follows closely the summary in Wu *et al.* 1998(a).

of different distributions of dislocations depending on the degree to which they interact (i.e. random and uniformly spaced *vs* dipole formation). $f(M)$ is a function to be considered further below in §9.6.3. A useful definition of M given by Wilkens (1970, 1976) is

$$M = r_c \rho_d^{1/2} \tag{9.74}$$

where r_c is the effective outer cut-off radius of the strain field due to the dislocation. Since the strain field decays asymptotically, it never truly reaches zero – however, it does become too small to meaningfully affect the peak broadening.[134] The model was derived for an assumed 'restrictedly random' dislocation distribution, that is, each crystal is divided into smaller sub areas within which the dislocation placement is random. The number of +ve and –ve dislocations in each sub-area balance. The cosine Fourier coefficients for this model were given by Wilkens (1970) as

$$A(L) = \exp\left[-PL^2 (Q - \ln L)\right] \tag{9.75}$$

with

$$P = \frac{\pi}{2}\kappa^2 b^2 \chi \rho_d$$

where L is the correlation length, b is the magnitude of the Burgers vector, and

$$Q = \ln(r_c) + 2\ln 2 - \frac{1}{3} - \ln(\sigma|\mu|) \tag{9.76}$$

Here $\sigma = |\sin\psi|$ where ψ is the angle between the dislocation line and the scattering vector, μ is the dot product of the scattering vector and the Burgers vector, κ is the length of the scattering vector, and χ is the orientation factor (contrast factor) as before. Computer simulations of the diffraction peak broadening for restrictedly random arrangements of dislocations have shown that the model works well for the restrictedly random arrangement, provided that $M \geq 3$ (Kamminga and Delhez 2001),[135] with the true dislocation density being underestimated by about 20% at $M = 1$. The model may be successfully used outside this limit by applying a linear correction factor presented by Kamminga and Delhez (2001). Application of the model to distributions of dislocations that don't conform to the restrictedly random model will lead to inaccuracies – however, the method may still be quite valuable for tracking *changes* in the dislocation density as a function of some sample processing variable (e.g. annealing temperature and or time).

[133] A related parameter P was used by Krivoglaz and Ryaboshapka (1963) and is given by $P \approx 3M$.

[134] As diffraction instruments attain higher resolution, it is possible to imagine the effective values of r_c being instrument dependent. A mitigating factor is that the far distant tails of the strain field at any appreciable dislocation density will tend to merge and largely cancel out.

[135] Wilkens (1976) had cautioned that the model would become inaccurate unless $M \geq 1$.

It should be noted here that the calculation of χ, the orientation (contrast) factor is non-trivial. It may be expanded in general form (Klimanek and Kužel 1988) as:

$$\chi = \sum_{K,L} b^2 \langle \boldsymbol{G}_{KL} \rangle \boldsymbol{E}_{KL} \quad (K, L = 1, 2, \ldots, 6) \tag{9.77}$$

where $\boldsymbol{G}$ is a symmetric matrix describing the orientational effects of a particular system and $\boldsymbol{E}$ is similar matrix describing the effects of elastic anisotropy on the displacement field of the dislocation. The specific cases of face-centred cubic and hexagonal structures have been given by Wilkens (1987) and Klimanek and Kužel (1988), respectively, and an empirical approach has been given by Ungar *et al.* (1999) whereas a new first principles method has been developed by Armstrong and Lynch (2004).

9.6.3 Practical determination of dislocation densities from powder diffraction

It may appear that ρ_d can be determined by straightforward application of eqn (9.73) to integral breadths determined by the methods outlined in §4.5. However, this requires a good understanding of the orientation (contrast) factors, χ, for different *hkl*,[136] a value for M, and a means for evaluating $f(M)$. Whilst it is relatively straightforward to simulate dislocation broadened profiles in the forward direction by numerical evaluation of the expression for $f(M)$ given by Wilkens (1970), this is of limited value in interpreting real diffraction results and so integral breadths are usually not directly applied to dislocation analysis. Another approach is to evaluate the Fourier coefficients of the observed diffraction peaks by the methods outlined in §9.3 and compare them with Fourier coefficients determined using eqn (9.75) for an assumed type, density and distribution of dislocations. Some convergence can be achieved with several iterations, especially if the predominant dislocation type has been determined beforehand using TEM. Again the approach is limited by sensitivity to how the background and peak tails are handled.

The fact that the dislocation profile is intermediate between Gaussian and Lorentzian shapes led to a realization of great practical potential, that the profile should be readily approximated by a Voigt function [Wu *et al.* 1998a]. This allowed the characteristic curve relating the shape of the dislocation broadened peak, defined by $y = \frac{C^{1/2}}{2}\frac{H_L}{H_G}$, to the dislocation distribution parameter M, shown in Fig. 9.29, to be constructed. In this expression, $C = 4\ln 2$ and H_L and H_G are Lorentzian and Gaussian FWHM. The value of M obtained using this curve may then be substituted into an analytical approximation to Wilkins $f(M)$:

$$f(M) \approx a\ln(M+1) + b(\ln(M+1))^2 + c(\ln(M+1))^3 + d(\ln(M+1))^4 \tag{9.78}$$

where $a = -0.173$, $b = 7.797$, $c = -4.818$ and $d = 0.911$ (Wu *et al.* 1998a).

[136] This analysis can not be applied to a single reflection since it is the form of χ as *hkl* vary that confirms the slip system assumed.

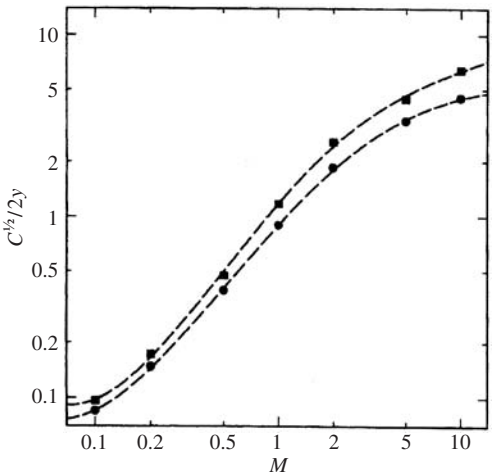

Fig. 9.29 The relationship between M in Wilkens' dislocation theory and the shape parameter, y, of the Voigt function, estimated by fitting the latter to the theoretical profile. Squares: fit using reciprocal intensity weighting scheme. Circles: fit using equal weighting scheme. Note that the ratio of the Gaussian and Lorentzian FWHMs, $H_G/H_L = C^{1/2}/2y$ behaves roughly like M [from Wu *et al.* (1998a)].

Equation (9.73) may now be evaluated using χ calculated for the slip system(s) expected. An analytical form for $f(M)$ allows for the ready incorporation of dislocation induced peak broadening into full pattern analysis techniques such as Rietveld refinement. The $\tan^2\theta$ term in eqn (9.73) means that a modified form of the Caglioti equation (eqn (4.7)) can be constructed for the Gaussian part of the Voigt function:

$$H_G^2 = \left(U + S_G^2\right)\tan^2\theta_k + V\tan\theta_k + W \tag{9.79}$$

where S_G is the Gaussian strain co-efficient due to dislocations. Similarly, a modified version of eqn (9.16) can be constructed for the Lorentzian FWHM:

$$H_L = K\sec\theta_k + S_L\tan\theta_k \tag{9.80}$$

Substituting

$$\beta_V = \frac{\beta_G}{\Omega(iy)} = \beta_G\frac{\exp\left(-y^2\right)}{1-\mathrm{erf}(y)} \tag{9.81}$$

into eqn (9.73), we obtain

$$\beta_G^2 = \rho_d\chi f(M)\Omega^2(iy)\tan^2\theta \tag{9.82}$$

and

$$S_G^2 = \frac{4\ln 2}{\pi}\rho_d f(M)\Omega^2(iy)\chi = T\chi \tag{9.83}$$

and, then using $\beta_L = \pi^{\frac{1}{2}} y\beta_G$, we get

$$S_L = \frac{2y}{\pi^{1/2}}\rho_d^{\frac{1}{2}}\,[f(M)]^{\frac{1}{2}}\,\Omega(iy)\chi^{\frac{1}{2}} = J\chi^{\frac{1}{2}} \tag{9.84}$$

Ω above is the complex error function.

To illustrate the procedure, we shall use the example of hydrogen activated $LaNi_5$. The following steps are involved:

(i) Determine (TEM) or assume the predominant slip system[137]

By scrutiny of Fig. 2(a) of Klimanek and Kužel (1988a) it was possible to see that $a\langle\bar{2}110\rangle/\{0\bar{1}10\}$ type dislocations gave qualitative agreement with observation, that is, $hk0$ peaks were the broadest and $00l$ peaks were the narrowest. Figure 9.30 was also re-calculated explicitly for $LaNi_5$ by Wu *et al.* (1998b). There is confirmation of the slip system of Wu *et al.* in the TEM literature (Kim *et al.* 1994, 1995; Inui *et al.* 2002) although the dislocation density is so high as to make TEM extremely difficult.

(ii) Determine the form of χ

Klimanek and Kužel (1988) have observed that in most cases, elastic anisotropy does not have a large effect on χ. Given that the elastic constants c_{ij} for $LaNi_5$ are not known, an assumption of elastic isotropy was made. We then have

$$\chi = \frac{1}{N}\sum_N b^2\left(\chi_e \sin^2\gamma + \chi_s\cos^2\gamma + \chi_i \sin\gamma\cos\gamma\right) \tag{9.85}$$

where γ is the angle between the Burgers vector and the dislocation line. The edge dislocation component χ_e is given by

$$\chi_e = E_{11}\gamma_1^4 + E_{55}\gamma_2^4 + \varepsilon\gamma_1^2\gamma_2^2 \tag{9.86}$$

where $E_{11} = \left(5/2 - 6\nu + 4\nu^2\right)/\mu$, $E_{55} = \left(1/2 - 2\nu + 4\nu^2\right)/\mu$, $\varepsilon = (3 - 8\nu + 8\nu^2)/\mu$, $\mu = 4(1-\nu)^2$ and ν is Poisson's ratio. The screw component is

$$\chi_s = \gamma_3^2\left(1 - \gamma_3^2\right) \tag{9.87}$$

and the interaction component is

$$\chi_i = L\gamma_1\gamma_3(1 - \gamma_3^2) \tag{9.88}$$

[137] Solutions are readily available for cubic and hexagonal materials.

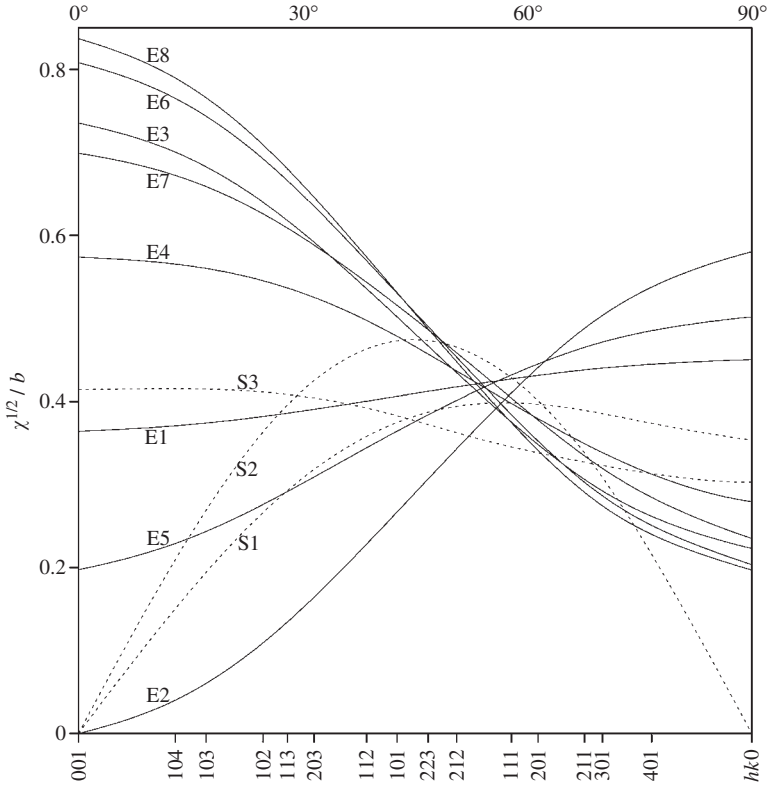

Fig. 9.30 The dislocation orientation/contrast factor χ calculated by Wu *et al.* (1998b) for the different potential slip systems in hexagonal $LaNi_5$. Curves are labelled E for edge dislocations and S for screw dislocations. The numbering corresponds to that used by Klimanek and Kužel (1988).

where $L = \left(6 - 14\nu + 8\nu^2\right)/\mu$. The quantities γ_1, γ_3, γ_2, are the direction cosines of the scattering vector, the edge and screw components of the Burgers vector, and the slip plane normal, respectively. A plot of χ for the possible slip systems in $LaNi_5$ is shown in Fig. 9.30. The curve labelled E2 applies to the observed slip system.

(iii) Undertake a Rietveld refinement using T and J [eqns (9.83) and (9.84)] as adjustable parameters.

The refinement result for $LaNi_5$ is summarized in Fig. 9.31 and clearly models the severe anisotropic broadening very well. The refined values are $T = 2.8(1)$ degree^2 Å^{-2} and $J = 0.68(3)$ degrees Å^{-1}.

(iv) Use the relationship $J^2 = y^2 T/\ln 2$ to obtain $y = 0.340$, and from Fig. 9.29, $M = 1.91$.

(v) Use eqn (9.78) to obtain $f(M)$ and use either eqn (9.83) or (9.84) to obtain $\rho_d = 4.8 \times 10^{12}$ cm^{-2}.

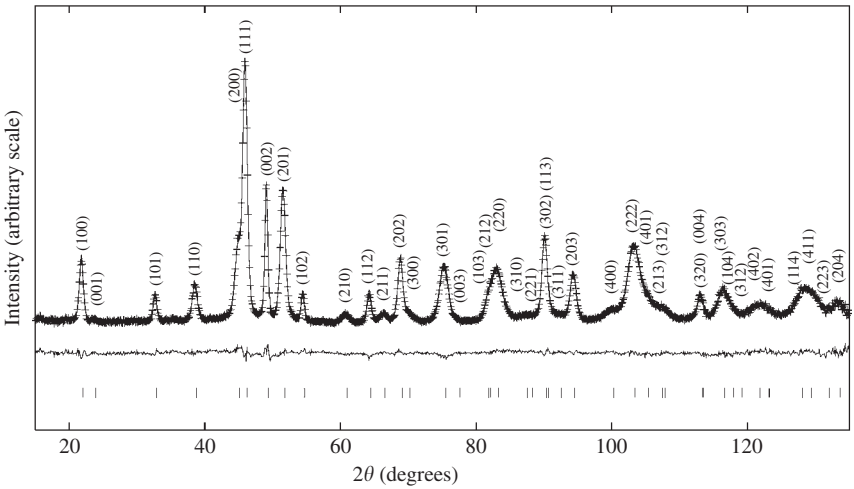

Fig. 9.31 Rietveld refinement result for $LaNi_5$ obtained by modelling the anisotropic broadening as due to $a\langle\bar{2}110\rangle / \{0\bar{1}10\}$ dislocations (Wu *et al.* 1998b). The data are shown as (+) and the fitted profile as a solid line through the data. A difference profile and reflection markers are shown below the main figure.

Subsequent to this work (Wu *et al.* 1998b) extensive TEM studies (e.g. Inui *et al.* 2002) have confirmed both the dislocation type and density determined by this method.[138]

Dislocation analysis using powder diffraction remains a very active field, for example, with new methods for determining dislocation contrast factors (Leoni *et al.* 2007). A very new approach that does not require the computation of contrast factors but rather computes the average effect of the dislocations using micromechanics shows some promise; however, it appears there are as yet no practical examples of its use to simulate neutron or X-ray diffraction patterns (Bougrab *et al.* 2002).

9.7 PLANE DEFECTS AND STACKING DISORDER

The nature of planar defects such as stacking faults, twin boundaries and antiphase domain (APD) boundaries is briefly outlined in §2.2.2. Further description of APDs is given in §10.3.4. As with dislocations, planar defects have associated strain fields which, in general,[139] are of far more restricted range than the strain

[138] Note that the value of ρ_d in the original work (Wu *et al.* 1998b) was affected by the use of the Burgers vector $\frac{a}{3}\langle 2110\rangle$ (for hexagonal close packed structures or a partial dislocation in $LaNi_5$) rather than $a\langle 2110\rangle$ for a complete dislocation in the ordered $LaNi_5$ structure.

[139] Except in ferroelectric crystals.

fields due to dislocations. There are, however, phase shifts between neutrons scattered on either side of stacking faults, twin boundaries or APD boundaries, additional to these associated with the base structure. When the faults are closely spaced, these phase shifts lead to interesting (and sometimes misleading) diffraction effects. Conversely, in favourable circumstances, diffraction patterns affected by planar defects can be analysed to give quantitative data concerning the average microstructure.

As an example antiphase domain boundaries commonly occur in perovskites and an account of their diffraction effects has been given for the layered perovskite $KAlF_4$ (Gibaud *et al*. 1986). $KAlF_4$ incorporates planes of corner-linked AlF_6 octahedra and the tilting of these octahedra around axes perpendicular to these planes gives rise to additional superlattice peaks (as compared with the situation without tilting). In the perfect structure, the sense of tilting is the same from one plane to the next. In real crystals, there are occasional reversals of the sense of tilting giving rise to anitphase domains. The analysis of Gibaud *et al*. (1986) shows that the antiphase domain structure leads to broadening of the superlattice peaks while the primary diffraction peaks are unaffected. The situation can be handled within some Rietveld refinement programs such as GSAS (Larson and Von Dreele 2004) by invoking the 'stacking fault' option.

Stacking faults, where occasional layers of a crystal have their layer origin displaced laterally with respect to the perfect sequence, have three main effects on the diffraction pattern, depending on the crystal structure and fault type. These are

(i) *hkl* dependent or anisotropic peak broadening
(ii) peak asymmetry
(iii) peak shifts

When there are more than occasional faults, additional effects are seen:

(iv) additional diffraction peaks and disappearance of others
(v) pseudo-symmetry.

And when there is ordering between faults, the result is

(vi) new crystal structures, that is, polytypes.

The problem of how to accurately model stacking faults has been the subject of intense study for over 70 years in the X-ray diffraction literature. There has been a far lesser contribution from the neutron diffraction community, largely because of generally inferior resolution and a relatively limited number of neutron sources for the greater part of this period. However, there are now a large number of neutron diffractometers with sufficient resolution that an understanding of this phenomenon may now be required.

Early attempts to model the X-ray scattering from faulted structures included explicit computation (Landau 1937; Lifshitz 1937, 1939), difference equations (Wilson 1942, 1943), correlation probability matrices (Hendricks and Teller 1942),

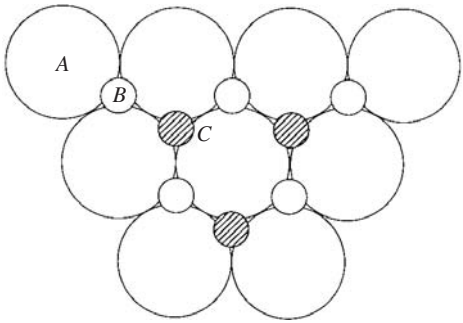

Fig. 9.32 [111] projection for a face-centred cubic (fcc) structure showing the three distinct positions A, B, and C for close-packed (111) planes (Warren 1969, 1990).

and the summation of convergent series (Cowley 1976a, 1976b, 1981; Cowley and Au 1978). The relationship between the latter three methods has been given by Kakinoki and Tomura (1965) and Kakinoki (1967). Except for Cowley's method, these techniques are generally only tractable for simple close-packed structures and relatively low faulting probabilities (<5%–10%).

Inspection of points (ii)–(vi) above reveals a deeper truth concerning faulted crystals, that is, they are merely transitional structures lying on a continuum between two perfect structures.[140] To illustrate, consider the trivial example of cubic close-packed (fcc) structures. As can be seen in Fig. 9.32, there are three kinds of layers A, B, and C when viewed down the [111] axis of the cube. The layers are identically close packed, however the origin is displaced. As highlighted by Warren (1969, 1990), we can conveniently use a 3-atom hexagonal unit cell to consider the layers. When viewed perpendicular to the *c*-axis, the stacking sequence is ABCAB-CABCABC, and so on. [Fig. 9.33(a)]. Errors in this sequence are historically known as 'deformation faults' (Fig. 9.33(b)) and 'twin faults'[141] (Fig. 9.33(c)).[142] At low fault densities, the former lead to peak broadening *and* peak shifts whereas the latter lead to peak asymmetry. The close-packed hexagonal structure (cph) contains exactly the same types of layers; however, the perfect stacking sequence is ABABABAB, etc. This represents the fcc structure with a faulting probability of 1 and conversely the fcc structure is cph with a faulting probability of 1. So we see that close packed metals containing stacking faults may be described as lying on a continuum of states between fcc and cph and having a certain degree of 'stacking disorder'. This fact concerning faulted structures has long been known; however, it was not explicitly catered for in the early analysis techniques which all apply to low faulting probabilities. Cowley's method is more general; however, it must

[140] One or other end member may not be observed in practical samples.
[141] Also known as growth faults.
[142] The distinction relates to the correlation length after the fault and the names relate to the circumstances in which they occur in simple metallic structures.

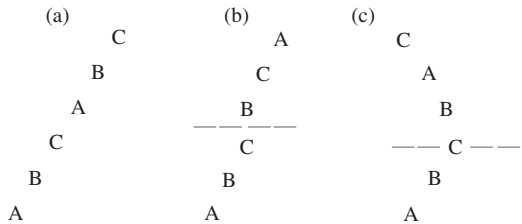

Fig. 9.33 Stacking sequence in close-packed crystals illustrating (a) perfect cubic close-packed (fcc) stacking, (b) deformation faults and (c) twin faults. Hexagonal close-packing (hcp) is an ordered sequence of twin faults to give the sequence ABABABABAB, etc. (Warren 1969, 1990).

be reformulated for each structure and becomes difficult as the complexity of the layers increases.

Perhaps the last word[143] on diffraction by faulted crystals is the general recursive method developed by Treacy *et al.* (1991)[144] and incorporated into the computer program DIFFaX. The basis of the method is that, within any infinite crystal (faulted or not) the number of unique layer sequences is relatively small. The example given by Treacy *et al.* (1991) is that of a simple structure constructed from two layer types, 1 and 2. The structural sequence in a faulted crystal can be readily represented in a simple probability tree diagram (Fig. 9.34) showing the two possible sequences, A beginning with a type 1 layer and B beginning with a type 2 layer. The recursive behaviour of the sequences is clear because each 'type' of sequence is embedded within the other.[145] This is true regardless of the complexity of the layers and the faulting probabilities, that is, it is equally true of perfect end members and heavily faulted structures.

As the full treatment of the recursive method is too lengthy to reproduce here, we will present only the results. Consider a crystal of N layers with M distinct types of layer and a probability α_{ij} that a layer of type i will be followed by a layer of type j. For such a crystal, the interference function from an N-layer statistically average crystal $\boldsymbol{\Psi}^{(N)}$ is given by the recursion equation:

$$\boldsymbol{\Psi}^{(N)} = \boldsymbol{F}' + \boldsymbol{T}\boldsymbol{\Psi}^{(N)} \tag{9.89}$$

Here $\boldsymbol{F}'$ is a modified layer form factor given by

$$\boldsymbol{F}' = \left(\frac{1}{N}\right)\left\{(N+1)\boldsymbol{I} - (\boldsymbol{I}-\boldsymbol{T})^{-1}\left(\boldsymbol{I}-\boldsymbol{T}^{N+1}\right)\right\}\boldsymbol{F} \tag{9.90}$$

[143] Despite the publication of the apparently comprehensive recursive algorithm (Treacy *et al.* 1991), there has been continued activity in the field of stacking disorder – see for example, the Proceedings of the European Powder Diffraction Conference published annually in Materials Science Forum.

[144] A less general recursive method was developed independently by Michalski (1988).

[145] They are also embedded within themselves leading to great computational simplification.

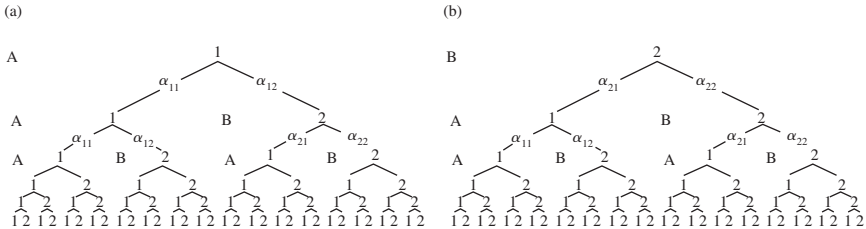

Fig. 9.34 From Treacy *et al.* (1991) 'Diagram illustrating the recursive relation between the ensemble average scattered wavefunctions from crystals which have layers of type 1 (left) and type 2 (right) at the origin. Note how the two distinct sequences, A and B, can be found embedded within one another'.

where $\boldsymbol{I}$ is the identity matrix, $\boldsymbol{T}$ is a two-dimensional stacking probability matrix $\left[\alpha_{ij} \exp\left(-2\pi i \boldsymbol{\kappa} \cdot \boldsymbol{R}_{ij}\right)\right]$, $\boldsymbol{F}$ is a one-dimensional matrix $[F_i(\boldsymbol{\kappa})]$ of the layer form factors $F_i(\boldsymbol{\kappa})$, $\boldsymbol{\kappa}$ is the scattering vector and $\boldsymbol{R}_{ij}$ is the vector joining the layer origins of type i and type j layers. The normalized diffracted intensity is then:

$$\frac{I(\boldsymbol{\kappa})}{N} = \boldsymbol{G}^{*T}\boldsymbol{\Psi}^{(N)} + \boldsymbol{G}^{T}\boldsymbol{\Psi}^{(N)*} - \boldsymbol{G}^{*T}\boldsymbol{F} \tag{9.91}$$

where $\boldsymbol{G} = [g_i F_i(\boldsymbol{\kappa})]$, g_i being the fraction of layers of the ith type.

The example here (Fig. 9.35) is one of the examples given by Treacy *et al.* (1991) calculated using their program DIFFaX. It concerns the transition between the cubic and hexagonal (Lonsdaleite) forms of diamond via an increasing probability of growth twins on $(111)_c \equiv (0001)_h$. Note that the problem is computationally simpler using hexagonal axes and so the faulting probabilities are defined as $\alpha = 0$ for Londsdaleite and $\alpha = 1$ for cubic diamond. All of the features of faulted structures (i)–(vi) can be seen here. Peak broadening and asymmetry are obvious. New peaks of hexagonal like positions appear with as little as 10% of faulting in the cubic structure whereas some peaks disappear at high faulting probabilities (e.g. at $\sim 125°\ 2\theta$) and re-appear at either end of the structural sequence. The pseudo-symmetry in this case is merely a corollary of the peak shifts, that is, the pattern at $\alpha = 0.1$ would probably no longer be indexed as hexagonal by auto indexing programs.

The recursive algorithm is comprehensive. It can calculate the diffraction from any kind of random fault, twin fault, ordered faults (polytypism) or perfect structure. With the incorporation of Cowley's method (Cowley and Au 1978) of allowing small perturbations to the layers, it is likely to become the method of choice for analysing faulted structures, and would have done so before now except it has, to the best of our knowledge, not yet been incorporated into full pattern refinement software.

In a small number of cases, for example where relatively *regularly spaced* micro twins occur, it may be simpler to use the method of Cowley and Au (1978) as for

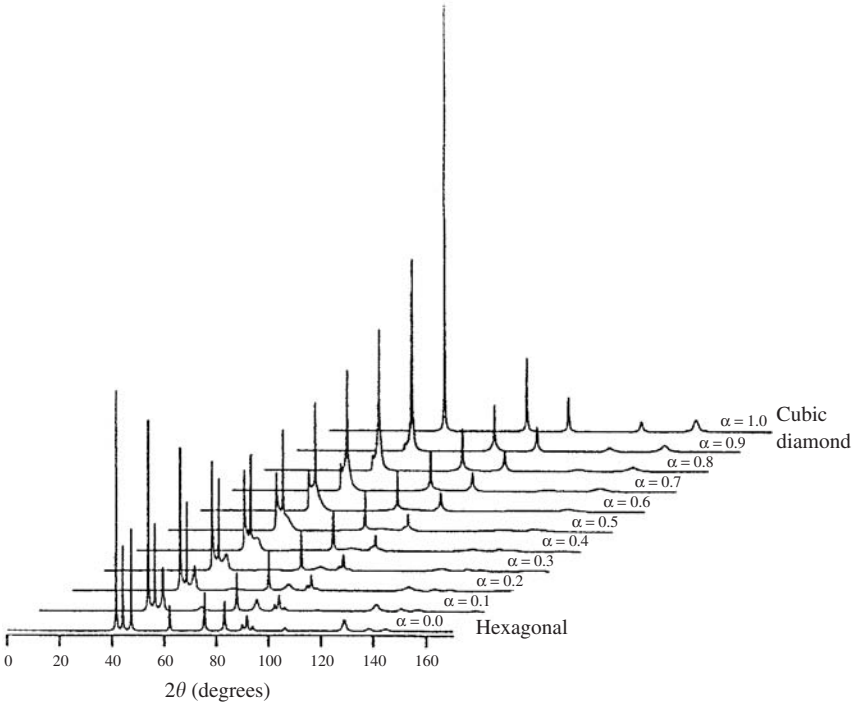

Fig. 9.35 From Treacy *et al.* (1991) 'Montage of powder X-ray diffraction patterns calculated as a function of the probability that layers in a diamond crystal will stack in the cubic diamond sequence. Thus $\alpha = 0$ corresponds to pure Lonsdaleite, and $\alpha = 1$ corresponds to pure diamond. Note the peak broadening and the disappearance of certain peaks as the stacking probability is varied between 0 and 1. The defects simulated in this sequence are analogous to growth twins. Instrumental peak broadening was simulated using a pseudo-Voigt function with $U = 0.89$, $V = -0.32$, $W = 0.08$ and $\eta = 0.6$. The step size was $\Delta\theta = 0.01°$'.

example in the beautiful case of monoclinic Mg_2NiH_4 analysed (using X-rays) by Zollicker *et al.* (1986). Microtwinning had in that case caused considerable confusion to X-ray and neutron diffractonists alike because it leads to pseudo-orthohombic diffraction patterns at sufficiently high twin densities and pseudo two-phase patterns at intermediate densities. The method of Cowley and Au was applied and yielded the calculated patterns shown in Fig. 9.36(a). Figure 9.36(b) illustrates the calculated effect of small distributions about the mean twin density which was able to simulate all of the observed kinds of diffractions patterns with different micro-twin densities. A least squares fit of one such simulated pattern to an observed pattern is reproduced in Fig. 9.36(c).

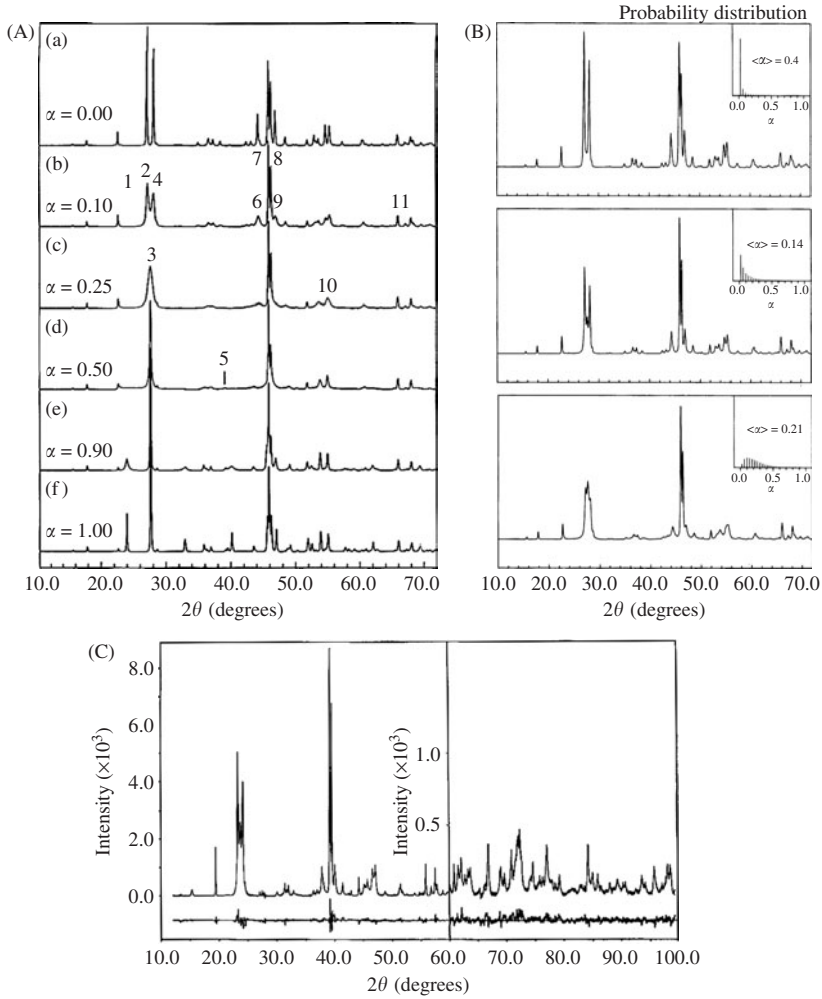

Fig. 9.36 X-ray diffraction patterns for the monoclinic structure of Mg_2NiH_4 containing micro-twinning showing the effect of (A) the twinning probability in the range $\alpha = 0$ (monoclinic) and $\alpha = 1$ (orthorhombic), (B) a distribution of twinning probabilities and (C) a least squares fit to data recorded on a high resolution lab diffractometer. Adapted from Zolliker *et al*. (1986).

9.8 TEXTURE

Texture and preferred orientation both refer to non randomness in a powder or polycrystal diffraction pattern. Their usage differs according to the problem under study. Preferred orientation is used to describe an unwanted non randomness in diffraction patterns collected for another purpose (structure refinement, QPA, microstructural

analysis, etc.). Texture is used to describe lack of randomness as a result of some material processing, geological or biological process. Texture is a very important factor in determining material properties. Most single crystal properties are anisotropic and so a textured polycrystal also develops anisotropic properties.

Comprehensive texture analysis is generally accomplished using diffractometers constructed similarly to single crystal diffractometers. The aim is to determine the relative intensity of a particular diffraction peak as a function of sample orientation over one hemisphere of real space. Often there is additional symmetry to the texture that allows a smaller region (say quadrant or octant) to be measured. However, to construct a complete knowledge of the texture, several peaks need to be surveyed. Given that, for highly textured samples, the intensity may be relatively weak within a large amount of the surveyed area,[146] to gain complete data to adequate statistical precision is a very lengthy process. Hence there has been some interest in obtaining texture data from powder diffraction patterns, where a (relatively coarse) one-dimensional slice through space is rapidly acquired.

Raw texture data are routinely plotted as a 'pole density' on a stereographic projection of the *sample* (not the crystal structure). An example is shown in Fig. 9.37. Data gathered from several *hkl* is then subjected to pole figure inversion to generate the Orientation Distribution Function (ODF). Once a satisfactory ODF is found, the pole density of any arbitrary plane can be calculated as projections of the ODF onto the sample coordinate system (see Kallend 1998; Kallend *et al.* 1991; Wenk 2006).

9.8.1 A single powder diffraction pattern

Methods for 'correcting' powder diffraction patterns for the effects of texture (preferred orientation) have been reviewed in §5.5.2 in the context of crystal structure refinement. The most popular method is based on the March function as applied by Dollase (1986). In the context of texture measurement by diffraction, this method is useful in only a limited number of cases. Specifically, the March function describes a one-dimensional pole density that, in the case of the flat plate geometry commonly employed for laboratory X-ray powder diffraction, exactly describes the pole density of the preferred orientation vector on the assumption of cylindrical symmetry (i.e. a sample spun about its axis) or only fibre texture present in the sample. In this case the texture *is* one-dimensional and so the density of planes is faithfully reproduced.

Neutron diffraction is more commonly conducted in Debye-Scherrer geometry using a cylindrical sample (see Chapter 3). In that case, the function used to correct the peak intensities for texturing does not *directly* represent the pole density function, however a March function now of opposite sense is still a relatively good approximation (Dollase 1986). Howard and Kisi (2000) noted that a March

[146] The limiting case of texturing is a single crystal where the coherent intensity drops to zero over most of the sphere.

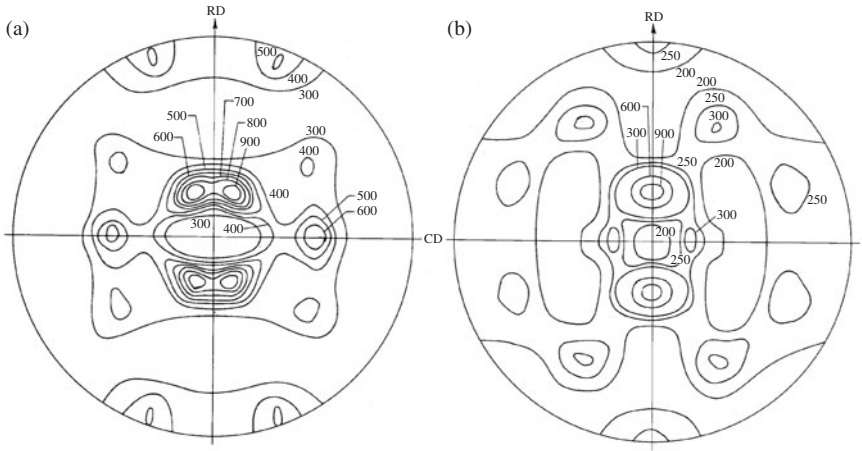

Fig. 9.37 Pole figures for (a) the 111 and (b) the 200 peaks of a rolled 70% Cu/30% Zn brass determined using X-ray diffraction (Beck and Hu 1952). Contours are drawn at particular count rates in arbitrary units. The rolling direction is annotated RD.

coefficient refined using data recorded in D-S geometry (with coefficient R_{DS}) is related to a March function representing the true one-dimensional pole density (with coefficient R) as follows:

$$R = R_{DS}^{-2} \tag{9.92}$$

An example diffraction pattern recorded from an Al_2O_3 cylinder on High Resolution Powder Diffractometer (HRPD) at ISIS is shown in Fig. 9.38. The refinement was conducted using GSAS and the refined March coefficient is $R_{DS} = 0.72$. Using eqn (9.92), we obtain $R = 1.93$ and the one-dimensional pole density in Fig. 9.39. Using eqn (9.92) it becomes possible for one-dimensional (i.e. fibre) textures to be measured using a single D–S diffraction pattern. Some advantages accrue through the use of neutrons, including the ability to conduct depth profiling because of generally low attenuation. Powder diffraction is particularly advantageous here since the texture measurement is based on relative intensities and so is internally consistent no matter where the 'gauge volume' is situated within the sample. This is not the case for conventional X-ray or single crystal neutron methods where the data would require very careful absorption correction to allow depth profiling.

An additional method of texture 'correction' used in structure refinements involves the use of symmetrized spherical harmonics (Ahtee *et al.* 1989; Popa 1992) in much the same way as they are used in describing ODFs in standard texture analysis (Bunge 1982). This method is, in principle, free from the restriction that the texture must have cylindrical symmetry about the sample axis. Therefore more complex textures can be modelled and in favourable circumstances it might be possible to determine the ODF from a single powder diffraction pattern. An

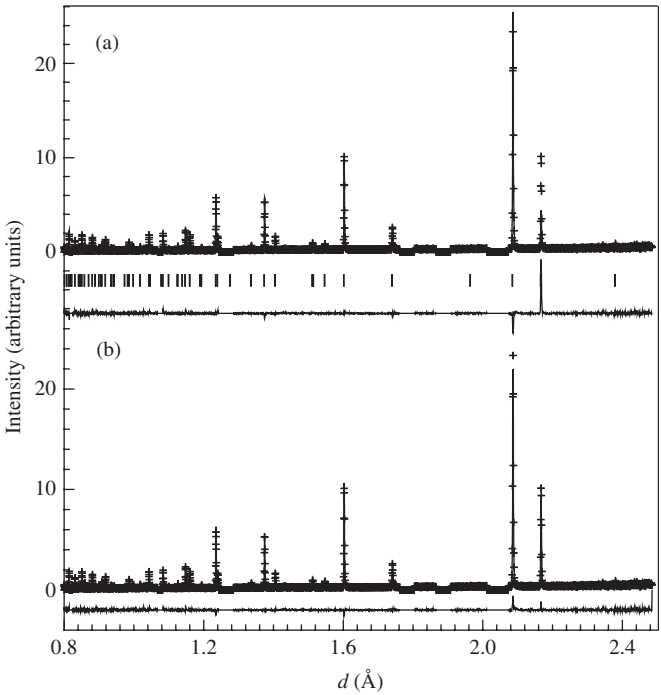

Fig. 9.38 (a) Effect of texture in an Al_2O_3 ceramic cylinder on the TOF neutron diffraction pattern and the corresponding Rietveld refinement fit ($R_{wp} = 14.4\%$, $\chi^2 = 2.58$) and (b) the result of Rietveld fitting using the March model for preferred orientation ($R_{wp} = 11.1\%$, $\chi^2 = 1.54$).

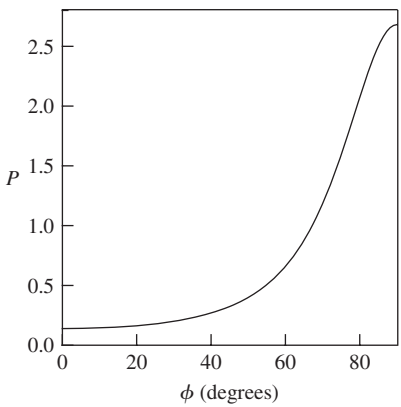

Fig. 9.39 One-dimensional pole density for the 111_R (0001_H) peak of Al_2O_3 determined from the refined March coefficient in the refinement illustrated in Fig. 9.38(b).

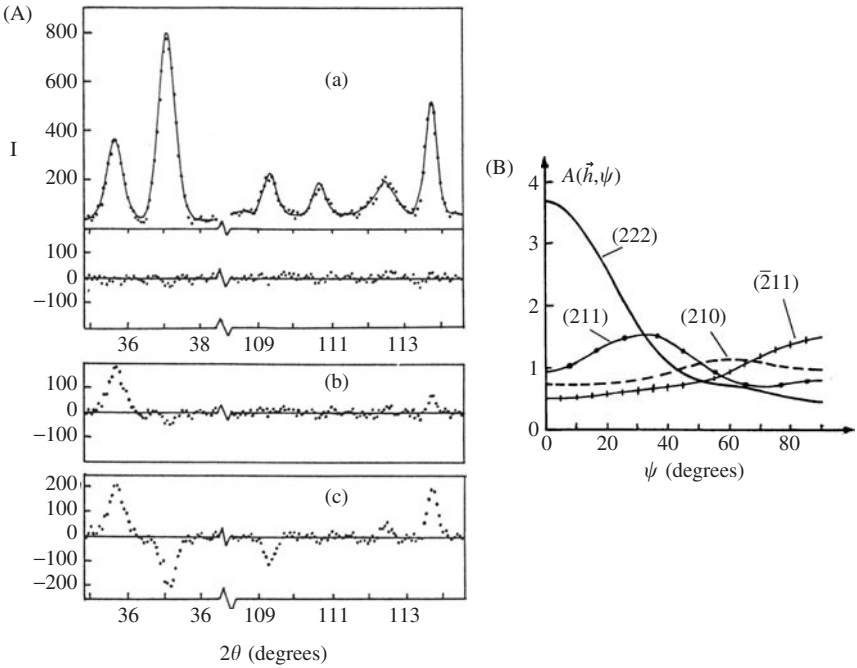

Fig. 9.40 (A) Modelling of the neutron diffraction pattern of a textured Al_2O_3 plate using spherical harmonics (Popa 1992). A(a) shows parts of the Rietveld fit using the spherical harmonics model, A(b) shows the difference plot for a Rietveld fit using the March–Dollase model and A(c) the difference plot with no texture model. (B) The pole distribution obtained in the refinement for four lattice planes in the Al_2O_3 plate sample (Popa 1992). Peak indices *hkl* are referred to rhombohedral axes.

example given by Popa (1992) is shown in Fig. 9.40 for an Al_2O_3 plate sample, however it fails to demonstrate generality for the technique, as cylindrical symmetry was assumed.

Unfortunately when spherical harmonics are used, the number of free variables in the profile refinement increases dramatically as the crystal symmetry is reduced and as the complexity of the texture increases. Two problems arise (i) the uniqueness of the refined parameters rapidly becomes questionable and (ii) non physical parameter values sometimes occur, for example, for the data shown in Fig. 9.38, refined in GSAS using spherical harmonics to sixth order. Although a slightly better fit was obtained (Fig. 9.41), negative pole density was implied in some directions.

9.8.2 Multiple diffraction patterns

To gain greater insight into the texture of a sample, several authors (Jansen *et al.* 1996; Ferrari and Lutterotti 1994) have suggested the use of multiple diffraction

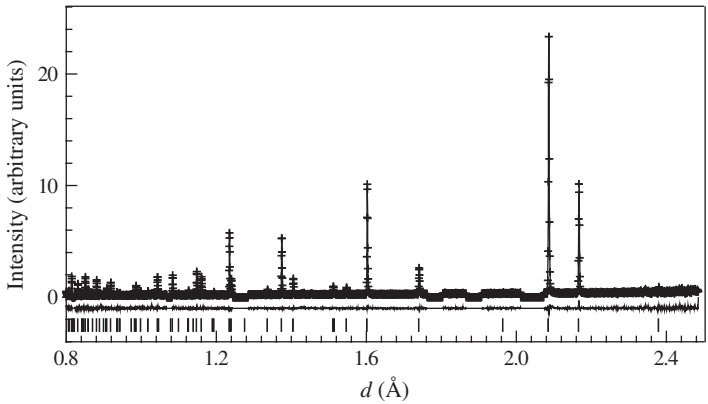

Fig. 9.41 Rietveld fit to the same data as in Fig. 9.38 using the spherical harmonics approach to texture modelling as implemented in GSAS (Larson and Von Dreele 2004). The agreement indices were $R_{wp} = 10.7\%$ and $\chi^2 = 1.42$.

patterns recorded at different sample declinations. This is a major departure from the speed and simplicity of a single pattern (see §9.8.1) however it holds the promise of allowing the study of quite complex textures.

Suitable experimental arrangements for such measurements are given below.

Theta: two theta scanning

If data are recorded at constant wavelength in a θ–2θ scan, then the scattering vector is fixed relative to the sample for all values of 2θ (see Fig. 9.42(a)). This means that each diffraction pattern represents the pole density of all the peaks contained in it, for the *same* real space direction in the sample. To sample the pole density in other parts of the sample, the sample must be rotated in angular increments ($\Delta\omega$) about its vertical axis and tilted about the horizontal (χ) in small increments, recording a θ–2θ scan at each position. This process may become almost as time consuming as using a single crystal diffractometer to establish the sample texture. The only advantage of the powder method is that many *hkl* are recorded simultaneously at each value of (ω) and (χ).

Position sensitive detection at constant wavelength

An alternative to the θ–2θ scan is to use constant wavelength and a large angular acceptance position sensitive detector. In that case the whole diffraction pattern may be recorded very rapidly, however each data point in it represents a slightly different *direction* in the sample. To a good approximation individual peaks can be regarded as arising from a well defined direction in the sample and the texture information must be extracted from the raw diffraction patterns by specialized software (e.g. RITA). This approach has been used by Wenk *et al.* (1994) with the

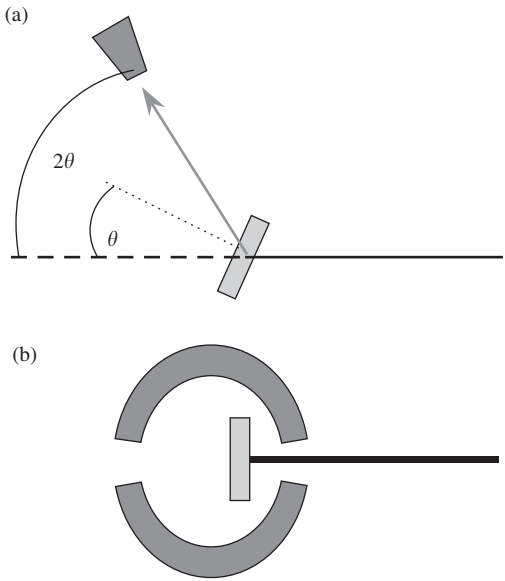

Fig. 9.42 Geometry of texture measurement using neutron powder diffraction. (a) The CW θ–2θ scanning method for a single pattern from a sample set at arbitrary angles ω in the plane of the diffractometer and azimuthal angle χ. The sample is re-positioned at new values of ω and χ (not shown) to record multiple patterns. (b) The TOF method in which, because each detector element samples a different direction through the sample, all of the required information for given ϕ and χ is recorded simultaneously.

rapid diffractometer D20, which can record sub-second diffraction patterns over a useful detection angle of $>140°$ 2θ. Therefore, data relating to a range of 70° of ω can be obtained by only scanning the sample in the azimuthal angle χ. To obtain a full quadrant, two ω positions would need to be used however this is a considerable saving over θ–2θ scans at some cost to the analysis complexity.

Time-of-flight

For a given detector of a TOF instrument, the scattering vector is fixed. Therefore diffraction patterns recorded by that detector relate wholly to one direction in the sample much as in θ–2θ scanning. The difference is that in a TOF diffractometer, the entire diffraction pattern is recorded simultaneously (see §3.3). If a sufficiently large number of detectors are positioned around the sample, each recording many diffraction peaks for a given real space sample vector, the entire data required to determine the ODF can be recorded simultaneously. An instrument that shows great promise for this purpose is GEM (General Materials Diffractometer) at the ISIS facility. This instrument is outlined in greater detail in Chapter 12.

10

Diffuse scattering – thermal, short-range order, gaseous, liquid, and amorphous scattering

10.1 INTRODUCTION

In §2.3.2 we saw that *random deviations* from the mean scattering length lead to scattering which, in the case of isotopic mixtures or mixed spin states, is referred to as *incoherent* scattering and when of chemical origin, as *diffuse* scattering. This scattering is completely unstructured, that is, it is uniform across the entire diffraction pattern forming the major part of the background in most powder diffraction patterns. The mean scattering length, on the other hand, is responsible for coherent diffraction effects such as the sharp Bragg peaks from perfectly ordered crystalline material. Also in Chapter 2 we saw that many types of order exist that do not have rigidly repeating crystallographic unit cells. These departures from crystallinity lead to other types of diffuse scattering not only because of deviations from the mean scattering length but also because of the lack of strict phase relationships between neutrons scattered in different parts of a particle of the material. Coherent diffuse scattering from a crystalline material (hereafter merely diffuse scattering) is often highly structured into intricate patterns throughout reciprocal space. It often peaks under the Bragg peaks thereby making accurate intensity determination difficult. Common sources of diffuse scattering include thermal vibration, static disorder in atomic positions, and short-range chemical order (or disorder). Special cases of short-range order (SRO) exist in the non-crystalline forms of condensed matter, liquids, and amorphous solids (glasses), as discussed briefly in §2.2.2–§2.2.5.

We note that the study of liquids and amorphous solids is not generally conducted using powder diffraction but rather purpose-built diffractometers (e.g. the liquids and amorphous diffractometer, D4 at the ILL). Further, the analysis of liquids and amorphous solids using neutron scattering is a distinct field of study that is covered in separate volumes in this series (Egelstaff 1994; Balucani and Zoppi 1995). Likewise, the study of diffuse scattering from crystalline solids using neutrons is also a distinct art covered in separate volumes concerned with structural or chemical SRO scattering (Nield and Keen 2000) and with neutron scattering from magnetic SRO/disorder (Hicks 1995).

In neutron powder diffraction experiments we are nonetheless sometimes confronted with significant diffuse intensity. Examples include the study of order–disorder phase transitions, the crystallization of glasses, freezing, and melting behaviour in alloys and the high-energy milling (mechanical alloying) of materials where amorphous phases are often observed. In some cases, the diffuse scattering in powder diffraction patterns can be removed by modifying the sample preparation or experimental conditions; however, in many situations it is an intrinsic part of the phenomenon under study. In these cases at the very least, we need to understand the influence that it may have on our data analysis and the reliability of derived quantities. Sometimes it may be possible to derive some useful information from the diffuse intensity that helps to illuminate the problem at hand although as noted above, this is usually better conducted using other more specialized techniques.

10.2 THERMAL DIFFUSE SCATTERING

As we have discussed before (§2.2.2), the atoms in a solid are not fixed but vibrate about their mean positions by amounts determined by temperature and in directions determined by the crystal structure and interatomic force constants. These vibrations are responsible for the observed decrease in the intensity of Bragg peaks as a function of $\sin\theta/\lambda$ as described by eqn (2.36 and 5.25). The vibrations also lead to diffuse scattering known as thermal (or temperature) diffuse scattering (TDS). If the atom displacements due to thermal effects were completely random and independent then the TDS would vary monotonically throughout reciprocal space. The dependence on Q ($= 4\pi \sin\theta/\lambda$) for the first-order (one-collision) TDS is given by (Willis and Pryor 1975)

$$I_1 \propto \left[Q \exp\left(-\tfrac{1}{2}Q^2 \left\langle u^2 \right\rangle\right)\right]^2 \tag{10.1}$$

where $\exp(-\frac{1}{2}Q^2 \langle u^2 \rangle) = \exp[-8\pi^2 \langle u^2 \rangle \sin^2\theta/\lambda^2]$ is the standard isotropic temperature factor for a monatomic solid [eqn (5.25)]. In addition to this dependence on Q, the intensity of the first-order TDS also depends on the vibrational frequency ω:

$$I_1 \propto \frac{1}{\omega^2} \tag{10.2}$$

because, far from being random, the vibrations are organized into the various acoustic and optical modes and are strongly imprinted with the periodicity of the lattice. By virtue of this factor the acoustic modes, being of low frequency, make a strong contribution – substituting $\omega = v_s q$ where v_s is the sound velocity and q is the wave number, we have

$$I_1 \propto \frac{1}{v_s^2 q^2} \tag{10.3}$$

As a reciprocal lattice point is approached, $q \to 0$, and the intensity rises sharply to a singularity at the Bragg peak position. Thankfully, the population at a given q-vector goes to zero as $q \to 0$. The overall effect is that the TDS rises to a (finite) maximum under the Bragg peaks.

There is an additional structure factor term (see Willis and Pryor 1975) that also modifies the intensity. The complete theory is rather more complex and must include second- and higher-order scattering which can account for up to 25% of the total TDS. The theory for X-ray diffraction has been presented by James (1945), and an abbreviated version by Warren (1969, 1990) and Willis and Pryor (1975). We will not delve further into the theory here for the reasons explained below, so the interested reader is referred to the literature for further details.

The theory of TDS for neutron diffraction is more complex than for X-ray scattering (Willis 1970; Willis and Pryor 1975). The results differ depending upon whether the neutron velocity is greater than or less than the speed of sound in the material under study. In the case of faster than sound neutrons [Fig. 10.1(a)], the TDS behaves as in the X-ray case. For slower than sound neutrons, the TDS forms a plateau that extends beyond the tails of the Bragg peak [Fig. 10.1(b)]. In single crystal diffraction experiments this is good news since the TDS contribution is avoided simply by setting the peak tail limits carefully. In general,[147] hard matter has $v_s \approx 3 \times 10^3$ m/s which means that the TDS correction for wavelengths[148] $\lambda < 1.3$ Å is as for X-rays. A complication arises in TOF experiments since a wide range of neutron velocities are sampled, both above and below the sound velocity in the material.

Powder diffraction (X-ray or neutron) introduces new complexities into the TDS calculation. As with the diffraction peaks, all scattering at the same 2θ or d-spacing superimposes at the same point on the diffraction pattern. The theory has been presented for cubic materials and the X-ray case (Warren 1969, 1990); however, a general solution for more complex crystal structures is, as far as we are aware, still lacking. Likewise, there does not appear to be a generally applicable theoretical solution for the neutron powder diffraction case.[149]

Thankfully, there are many situations in which the TDS does not cause any serious concerns. It does not prevent the correct determination and refinement of crystal structures. Similarly, quantitative phase analyses (QPA) are unaffected. However, because the TDS peaks under the Bragg peaks (faster than sound neutrons) or locally raises the background (slower than sound neutrons) there are some implications for the displacement parameters (U^{ij},U_{iso}) especially if whole pattern analyses are used. Consider the schematic slower than sound neutron diffraction peak in Fig. 10.1(b). In a powder pattern with widely spaced peaks, the peaks sit

[147] With the exception of tin- or lead-based alloys.

[148] Stiffer materials have even lower cut-off wavelengths (e.g. W, 0.77 Å).

[149] Some software such as GSAS (Larson and Von Dreele 2004) offers a background correction that follows the gross Q^2 dependence of the TDS.

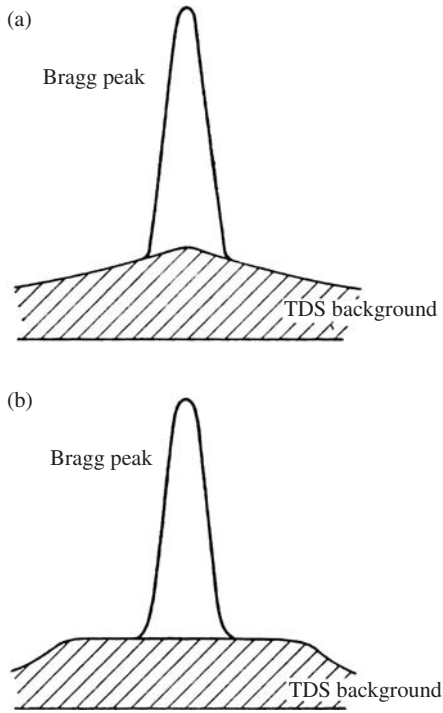

Fig. 10.1 Schematic illustration of the thermal diffuse scattering (TDS background) for (a) faster than sound neutrons and (b) slower than sound neutrons (Willis and Pryor 1975).

atop small TDS plateaux that are separated by intervals of true background plus the unstructured $Q^2 \exp\left(-Q^2 \langle u^2 \rangle\right)$ part of the TDS. When a simple polynomial background function (see §5.5.2, Table 5.9) is refined, it will fit neither the true background nor the TDS. The result is that the high 2θ (or low d) peaks are systematically ascribed a greater intensity than the true value. The situation is even worse for faster than sound neutrons [see Fig. 10.1(a)]. In both cases the reduction in the peak intensity at high angles (low d – TOF) will appear less than the true value and so the displacement parameters U_{iso} (or U^{ij}) will be underestimated. Two factors mitigate the seriousness of this effect in modern neutron powder diffraction:

(i) The more complex structures commonly studied today have a far greater density of peaks and so the TDS is expected to become a more slowly varying, continuous function.
(ii) For simple structures, the high resolution of modern diffractometers makes it easier to recognize the partition between peak and TDS background.

If very careful work on displacement parameters is to be undertaken there are several experimental and analytical steps that can be taken to minimize its effect:

(i) Slower than sound neutrons should be used.
(ii) Extracted intensities determined using manually fixed (or at least closely inspected) background levels should be used.
(iii) In extreme cases, a diffracted beam analyser crystal can be used to filter out all of the TDS leaving only the purely elastic Bragg peaks. This would have a detrimental effect on the recorded intensities but, depending on the characteristics of the analyser crystal, may improve the resolution.

10.3 SHORT-RANGE ORDER SCATTERING

10.3.1 Introduction to short-range order

In §2.2.2, we discussed the concept of a solid solution in which a completely physically ordered material (i.e. crystalline) has a number of chemical species occupying the same site. The most studied examples are the metallic alloys. The simplest and perhaps best known example is beta brass CuZn (Fig. 2.10). At temperatures well above the critical temperature, Cu and Zn atoms occupy both positions in the bcc unit cell with equal probability. Below the transition temperature, the alloy is capable of developing long-range order in which one element (Cu, say) occupies the cube-corner position and the other element (Zn) occupies the cube-centre position to form the CsCl structure. The approach to the ordered state as a function of time, temperature, or composition (i.e. non-stoichiometry) can be measured by the long-range order parameter S [eqn (2.6)], to be considered further in §10.3.4. Long-range ordered structures form due to a small free-energy advantage (arising from both chemical and strain energy components of the free energy) and favourable kinetic factors. However, in almost all solid solutions, even those that are not able to be made to order on observable time frames, the thermodynamic drive favouring certain local structures and pair interactions is still present. This leads to short range order (SRO). Returning to our β-CuZn example, SRO manifests as a slight preference for non-alike near-neighbours. More remote shells of neighbours are also affected (e.g. a preference for alike next-nearest neighbours, etc.) but to a decreasing extent. Therefore, in a system like a β-CuZn, even moderately above the transition temperature, occupancy of the cube corner and cube centre positions is not random. From our discussion of the basic neutron scattering equation (§2.3.2) we expect that this SRO will lead to interference or diffraction effects that, in favourable circumstances, will be observable. SRO leads to structured diffuse scattering which forms intricate and beautiful patterns in single crystal diffraction, particularly when using electrons or X-rays. In powder diffraction patterns, the SRO diffuse scattering appears as modulations in the background known as SRO peaks. SRO peaks have many times the breadth of the Bragg peaks and so are readily distinguishable from those whereas they persist visibly to much larger Q values (i.e. to larger 2θ or smaller d) than liquid or amorphous scattering

(see §10.4). When a clear link to a long-range ordered state exists, the SRO peaks are located at just those positions at which the superlattice peaks will form on ordering. In other cases we may speculate that the SRO peaks represent *possible* structures that, due to kinetic factors, are never realized.

10.3.2 Modelling and interpretation of SRO peaks

The study of SRO and SRO scattering is not our primary aim; however, many of the uses for powder diffraction that we have described involve samples with the potential to develop SRO peaks. If the primary aim of the experiment lies elsewhere, then the SRO has only nuisance value as it makes background fitting during whole pattern analyses difficult. One approach is to adopt a background fitting function that is capable of fitting modulated diffuse scattering without relying on a physical model of the scattering process. For example a high-order Chebyshev polynomial is available in some structure refinement packages, for example, GSAS (Larson and Von Dreele 2004). This approach, though perfectly adequate for many purposes, must be used with caution. An approximating polynomial of too high order can begin to model the bases of the Bragg peaks as diffuse or background intensity. This can have serious consequences for some refined parameters, particularly thermal (displacement) parameters and occupancies. If significant SRO scattering is present, it is far better to use a realistic physical model for it during data analysis.

A basic theory of SRO and SRO scattering in binary alloys was developed by Cowley (1950a) and extended and popularized by Warren (1969, 1990). The result presented here, without derivation, is from the expression for the intensity of the SRO scattering I(SRO) from a centrosymmetric single crystal (Warren 1969, 1990), adapted for neutrons:[150]

$$I\,(\mathrm{SRO}) = N x_{\mathrm{A}} x_{\mathrm{B}}\,(b_{\mathrm{B}} - b_{\mathrm{A}})^2 \sum_n \alpha\,(n) \cos\,(\boldsymbol{k} - \boldsymbol{k}_0) \cdot \boldsymbol{r}_n \tag{10.4}$$

where N is the number of atoms in the sample; x_{A} is the fraction of those of kind A; x_{B} is the fraction of atoms of type B; b_{A} and b_{B} are the appropriate coherent neutron scattering lengths; $\boldsymbol{k}_0$, $\boldsymbol{k}$, and $\boldsymbol{r}_n$ are the incident and diffracted wave vectors and the atom position vector as defined in Fig. 2.18 and eqn (2.4), respectively. The terms $\alpha(n)$ represent the SRO parameters (Cowley 1950a), defined as

$$\alpha(n) = 1 - \frac{p_{\mathrm{A}}(n)}{x_{\mathrm{A}}} = 1 - \frac{p_{\mathrm{B}}(n)}{x_{\mathrm{B}}} \tag{10.5}$$

in which $p_{\mathrm{A}}(n)$ represents the probability of finding an A atom at (vector) distance $\boldsymbol{r}_n$ from a B atom and $p_{\mathrm{B}}(n)$ represents the probability of finding a B atom at $\boldsymbol{r}_n$ from an A atom. Because the underlying structure is physically ordered (i.e., crystalline), the atom positions around a particular starting atom (origin) are arranged in

[150] The intensity here, commonly denoted by the symbol I, is akin to the ordinate y of a powder diffraction pattern and is not to be confused with the integrated intensity of a Bragg peak.

well-defined coordination shells. In the absence of long-range chemical order, atoms in very remote coordination shells are uncorrelated with the atom at the origin and so in most cases $\alpha(n) \to 0$ as n becomes large. Usually five or so SRO parameters are sufficient to explain the observed SRO scattering. Warren (1969, 1990) has highlighted that if ordering (long or short range) is totally absent, then $\alpha(n) = 0$ for all values of $n \neq 0$ and the diffuse contribution is

$$I(\text{random}) = Nx_\text{A}x_\text{B}\,(b_\text{B} - b_\text{A})^2 \tag{10.6}$$

representing incoherent scattering as we described it §2.3.2 [eqn (2.10)] and known in this context as Laue monotonic scattering.

In a powder diffraction experiment, the observed SRO intensity will be the spherical average of eqn (10.4). Letting $Q = 4\pi \sin\theta/\lambda$ and ϕ be the angle between $\boldsymbol{k} - \boldsymbol{k}_0$ and $\boldsymbol{r}_n$, we have

$$\begin{aligned} I\,(\text{SRO}) &= \frac{Nx_\text{A}x_\text{B}\,(b_\text{B} - b_\text{A})^2}{4\pi r^2} \sum_n \alpha\,(n) \int_0^\pi \cos\,(Qr\cos\phi)\,2\pi r^2 \sin\phi\; d\phi \\ &= Nx_\text{A}x_\text{B}\,(b_\text{B} - b_\text{A})^2 \sum_n \alpha\,(n)\,\frac{\sin Qr_n}{Qr_n} \end{aligned} \tag{10.7}$$

If the notation is changed to reflect the coordination shells each with a shell number i, a coordination number c_i (number of atoms in shell i) situated at radius r_i, eqn (10.7) becomes

$$I\,(\text{SRO}) = Nx_\text{A}x_\text{B}\,(b_\text{B} - b_\text{A})^2 \sum_{i=0}^{\infty} c_i\alpha_i \frac{\sin Qr_i}{Qr_i} \tag{10.8}$$

A problem in the modelling of SRO is the scaling, that is, eqn (10.8) is in absolute units. The recommended procedure is to work with the total SRO scattering as a ratio to the Laue monotonic scattering [eqn (10.6)]:

$$\frac{I\,(\text{SRO})}{Nx_\text{A}x_\text{B}\,(b_\text{B} - b_\text{A})^2} = 1 + c_1\alpha_1\frac{\sin Qr_1}{Qr_1} + c_2\alpha_2\frac{\sin Qr_2}{Qr_2} + c_3\alpha_3\frac{\sin Qr_3}{Qr_3} + \cdots \tag{10.9}$$

Equation (10.9) converges to 1 with increase in Q, or in terms of the observed diffraction pattern, the structured SRO scattering converges to the Laue monotonic scattering (i.e. the background intensity after other sources of incoherent scattering and TDS have been corrected for or shown to be negligible). For simple structures with one or two atoms per primitive unit cell, the SRO can be accurately modelled by adjusting the scaling according to the procedure above and then refining SRO parameters until an adequate fit to the observed data is obtained.

As with all scattering from solids, the SRO diffuse scattering is influenced by thermal motion of the atoms. The effect, however, is quite different from the effect of temperature on the Bragg peaks (e.g. §5.5.2). Thermal vibration reduces the intensity of Bragg peaks and has little influence on their shape. The intensity of SRO peaks on the other hand is insensitive to temperature increases and it is the *breadth* and *shape* of the SRO peaks that changes with temperature. The modifications to the widths are neither constant nor monotonic in reciprocal space. Further details of the influence of temperature on the SRO scattering may be found in Warren (1969, 1990) or in the original work of Walker and Keating (1961).

To this point we have ignored an important second-order phenomenon – the 'size effect'. In §6.5.3 we discussed the influence of static disorder on the intensity of the Bragg peaks. Static disorder also produces two kinds of diffuse intensity. The overall effect of many (mostly remote) neighbours being shifted slightly off their ideal positions gives rise to Huang scattering (Huang 1947) – somewhat akin to TDS. The second kind of static disorder scattering is the size effect. Accompanying the short-range chemical order that typifies successive shells of atoms in a solid solution is an effect due to the different atomic radii in the differently populated shells. The result is an additive modulation to the chemical SRO diffuse scattering [eqn (10.4)] leading to an overall equation for i shells:

$$I\,(\mathrm{SRO}) = Nx_\mathrm{A}x_\mathrm{B}\,(b_\mathrm{B} - b_\mathrm{A})^2 \sum_i \alpha(i) \cos\,(\boldsymbol{k} - \boldsymbol{k}_0)\cdot \boldsymbol{r}_i$$
$$+ Nx_\mathrm{A}x_\mathrm{B}\,(b_\mathrm{B} - b_\mathrm{A})^2 \sum_i \beta\,(i)\,(\boldsymbol{k} - \boldsymbol{k}_0)\cdot \boldsymbol{r}_i \sin\,(\boldsymbol{k} - \boldsymbol{k}_0)\cdot \boldsymbol{r}_i \qquad (10.10)$$

where

$$\beta(i) = \left(\frac{1}{\eta - 1}\right)\left\{\left(\frac{x_\mathrm{A}}{x_\mathrm{B}} + \alpha_i\right)\varepsilon^i_{\mathrm{AA}} - \left(\frac{x_\mathrm{B}}{x_\mathrm{A}} + \alpha_i\right)\eta\varepsilon^i_{\mathrm{BB}}\right\} \qquad (10.11)$$

is known as the size effect coefficient incorporating $\eta = b_\mathrm{B}/b_\mathrm{A}$, $\boldsymbol{r}_i = \boldsymbol{R}_m - \boldsymbol{R}_n$ and $\varepsilon^i_{\mathrm{AA}}$ and $\varepsilon^i_{\mathrm{BB}}$ are the strains (first order only) introduced by size differences among the close neighbours of an atom. The latter are defined, for neighbours separated by an overall mean distance r_i, by

$$r^i_{\mathrm{AA}} = r_i\left(1 + \varepsilon^i_{\mathrm{AA}}\right)$$
$$r^i_{\mathrm{BB}} = r_i\left(1 + \varepsilon^i_{\mathrm{BB}}\right) \qquad (10.12)$$

where r^i_{AA} is the mean distance for A–A pairs and r^i_{BB} is the mean distance for B–B pairs. Several approximations are used in the derivation of eqns (10.10)–(10.12) (Warren 1969, 1990) and a more complete theory has been given by Borie (1957, 1959, 1961) that includes both the size effect and Huang Scattering. Despite the simplifications underpinning eqn (10.10), it models the size-effect

modulations rather well. The size effect has the interesting outcome that the background *between* Bragg peaks is alternately higher and lower than if the effect is ignored (see Fig. 12.13 in Warren 1969, 1990). This is generally only observed with single crystals.

The treatments presented thus far were developed for simple binary alloys, often with cubic crystal structures. Whilst it is possible to generalize them for more complex crystal structures and binary or higher-order solid solutions the uniqueness of the interpretation is questionable. This is particularly apparent (Warren 1969, 1990) when it is realized that we have now discussed five major contributions to the background or diffuse intensity: incoherent scattering, thermal diffuse scattering (TDS), SRO scattering, size effect modulations, and Huang diffuse scattering. A more general approach, as compared with fitting the observed data with equations such as eqns (10.9) and (10.10), is to conduct a Fourier inversion of the diffuse intensity to obtain the pair-correlation function $g(r)$:

$$g(r) = \frac{2r}{\pi} \int_0^\infty Q\, j(Q) \sin Qr \, dQ \tag{10.13}$$

where

$$Q = 4\pi \frac{\sin\theta}{\lambda} \quad \text{and} \quad j(Q) = \frac{I(\text{SRO})}{N x_\text{A} x_\text{B} (b_\text{B} - b_\text{A})^2} - 1 = \sum_{i=1}^{\infty} c_i \alpha_i \frac{\sin Qr_i}{Qr_i}$$

from eqn (10.9). This is very similar to the method used for liquids and amorphous solids (§10.4); however, here the underlying structure still has strong positional periodicity. The SRO parameters are readily obtained from $g(r)$ because the peak areas in $g(r)$ are proportional to $c_i\alpha_i$. Features in the computed $g(r)$ that do not occur at known values of r_i for the crystal structure should be ignored. The method can be very powerfully applied if steps are taken to modify the scattering length contrast by (i) isotopic substitution, (ii) combined X-ray and neutron diffraction studies, or (iii) anomalous X-ray scattering (Wright and Wagner 1988). In that case, $g(r)$ (and hence α_i) may be obtained for each pair of atom types within a binary sample (§10.4).

The problem of using the SRO parameters α_i to investigate the atomic interactions – the so-called Effective Pair Potentials (EPP) – is more difficult. For atoms situated at the terminal ends of the vector r_n the effective pair interaction for near neighbours is defined as

$$V_n = \frac{1}{2}\left[V_n^{\text{AA}} + V_n^{\text{BB}} - 2V_n^{\text{AB}}\right] \tag{10.14}$$

The simplest relationship, originally derived by Cowley (1950b) and later also by Krivoglaz (1969), Clapp and Moss (1966, 1968), and Moss and Clapp (1968),

has become known as the Krivoglaz–Clapp–Moss approximation and is given by (Reinhard and Moss 1993)

$$\alpha(k) = \frac{D}{1 + 2x_{\mathrm{A}}x_{\mathrm{B}}\beta V(k)} \tag{10.15}$$

where $\alpha(k)$ and $V(k)$ are Fourier transforms of the SRO parameters α_n and the pair interactions V_n, respectively; $\beta = (k_{\mathrm{B}}T)^{-1}$; x_{A} and x_{B} describe the composition as before, and D is a normalization constant (commonly 1).

Another approach is the γ-expansion method (Tokar 1985) based on an Ising model with the assumption of exponentially decaying SRO parameters, $g_n = x_{\mathrm{A}}x_{\mathrm{B}}\alpha_n$. The final method is the Monte Carlo (sometimes Inverse Monte Carlo[151]) method (Gerold and Kim 1987) which is exact although more difficult to apply. The approximate methods by Cowley and Krivoglaz–Moss–Clapp have been shown to be relatively reliable at higher concentrations (i.e. x_A nearer to $1/2$ than 0) and less reliable at low concentrations[152] (Reinhard and Moss 1993). In contrast, the γ-expansion method has been shown to give results very close to exact Inverse Monte Carlo simulations (Reinhard and Moss, 1993) and can be used to model a wide range of SRO problems.

A distinct methodology is the reverse Monte Carlo (RMC) method where, rather than attempting to model and explain experimentally determined SRO parameters (α_i), the diffraction pattern is directly simulated from atom arrangements generated by a Metropolis algorithm (McGreevy 1994). The ensemble of atoms generated in this way may then be interrogated to obtain data concerning diffusion or fast-ion conduction pathways.

10.3.3 Applications to neutron powder diffraction

There are a number of applications in which the degree and propensity to SRO has a profound effect on the properties of materials. Some examples are explored below.

Among the common high-strength aerospace alloys are those based on Ti (e.g. Ti–6wt%Al and Ti–6wt%Al–4wt%V). These are often used at elevated temperatures due to their excellent oxidation resistance. Alloys subjected to stress at elevated temperatures suffer from time-dependent plastic deformation known as creep. It has recently been shown by neutron diffraction (Noeraj and Mills 2001) that these Ti alloys have a tendency to SRO, but also somewhat remarkably, to *room temperature* creep. Studies of the mechanical behaviour demonstrated that the creep strain was reduced by more than an order of magnitude (or slowed by 2–3 decades in time) when the alloy was deliberately given short-range ordering treatments.

[151] Not to be confused with Reverse Monte Carlo in which the diffracted intensities are directly simulated from randomly generated models (see below).

[152] An unexpected trend for mean-field theories.

An area where it is beneficial to use a combination of diffuse SRO and Bragg scattering within the neutron powder diffraction patterns is ionic conductivity. Examples include halides such as AgBr (McGreevy 1994) and CuBr (Nield *et al.* 1994); Mg–Zr–O–N (Lerch *et al.* 1997); and Y_2O_3–ZrO_2, Y_2O_3–ZrO_2–TiO_2 and Y_2O_3–ZrO_2–Nb_2O_5 (Irvine *et al.* 2000). In all cases diffuse intensity was observed and the local structures responsible were discussed; however, in only the halide cases was any serious attempt made to analyse the SRO (McGreevy 1994; Nield *et al.* 1994). Several interesting findings emerged from the work. First, the diffusion pathways, often the subject of considerable debate in the literature, were relatively clearly demonstrated to be via a jump to an interstitial site in the case of AgBr, with collinear jumps strongly preferred over non-collinear jumps (McGreevy 1994). Second, in the CuBr system where three crystalline phases (α, β, and γ) occur, the SRO changed relatively smoothly with temperature despite gross changes in the underlying ordered structure at the transition temperatures. Conduction was found to occur via Cu^+ ions hopping through interconnected octahedral and tetrahedral voids.

The third area where SRO diffuse scattering has an important contribution to make is in the metal hydrides. Our example here is α-$VD_{0.8}$[153] studied using neutron powder diffraction patterns for both average (Bragg peaks) and local structure (diffuse intensity). The SRO in hydrides is very important as it indicates the nature of the H–H (or D–D) interaction and the degree of screening provided by the metal atoms. Poor screening is expected to result in strong D–D repulsion and low capacity for the hydride (deuteride) (e.g. $PdD_{0.6}$) compared with well-screened systems (TiD_2). In previous examples, any modelling of the SRO was completed by in-house software in various institutions and not generally available. The $VD_{0.8}$ example allows us to introduce a generally available software suite RMCPOW purpose written for the combined analysis of SRO and Bragg peaks in powder patterns from crystalline solids (Mellergård and McGreevy 2000). It uses the Reverse Monte Carlo (RMC) method constrained by the average crystal structure and other user-imposed constraints (e.g. allowable interatomic distances, etc.). The results for $VD_{0.8}$ [Fig. 10.2(a); Sørby *et al.* 2004] demonstrate that the D–D repulsion is so strong that the first three shells of D sites around an occupied D position are essentially empty. This is strongly reinforced in Fig. 10.2(b), the difference between the observed D–D pair distribution function and the computed g_{D-D} for random occupation. The fourth nearest neighbour site is heavily occupied (three times the random structure prediction). Other structural details including positional disorder (i.e. the 'size effect') can also be obtained (Sørby *et al.* 2004). The availability of this software will no doubt increase the number of studies that include a consideration of the diffuse scattering in a powder diffraction experiment. Of course it must be remembered that the diffuse scattering in a powder pattern is inferior compared with the intricate patterns of diffuse intensity available with single crystals which

[153] Deuterium has been used instead of hydrogen because of the large incoherent scattering cross section of the latter.

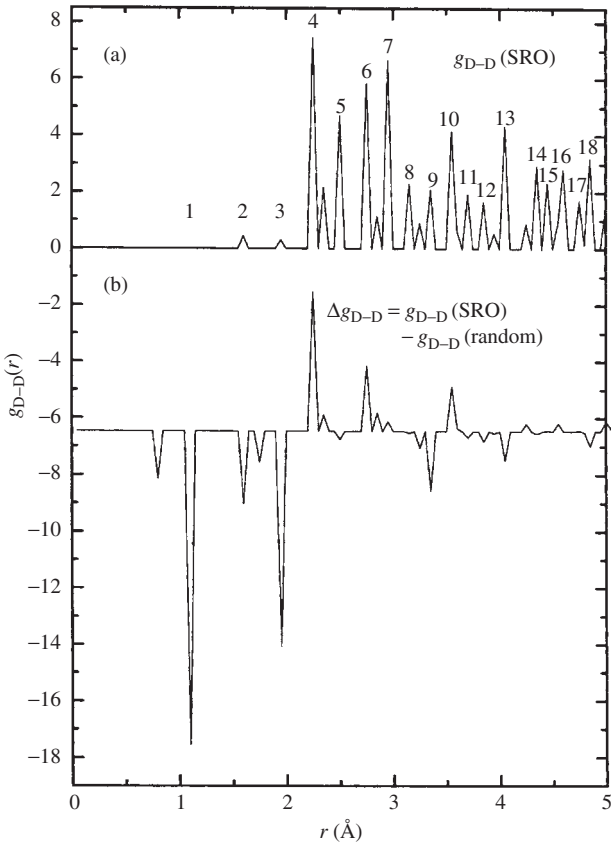

Fig. 10.2 "(a) D–D radial distribution functions in $VD_{0.8}$ for the configuration obtained by *swap-only* RMC simulations. Coordination sphere numbers for tetrahedral sites are given. Unnumbered peaks are due to deuterium in octahedral sites. (b) Difference between the D–D radial distribution function for the swap-only configuration and a configuration with D randomly distributed over the interstices. Hence, positive (negative) peaks are due to D–D distances that are (dis)favoured in the short-range ordering scheme" (Sørby *et al.* 2004).

are to be preferred if SRO is the prime purpose of the work and if crystals are available.

10.3.4 The approach to long-range order

At eqn (10.5) we introduced the Cowley SRO parameters which describe the probability of finding particular neighbours in shells around one type of atom. In many systems showing SRO, prolonged annealing in the correct temperature range allows sufficient atomic mobility for longer range ordered structures to form. In the β-brass (CuZn) example, the disordered structure has the body centred

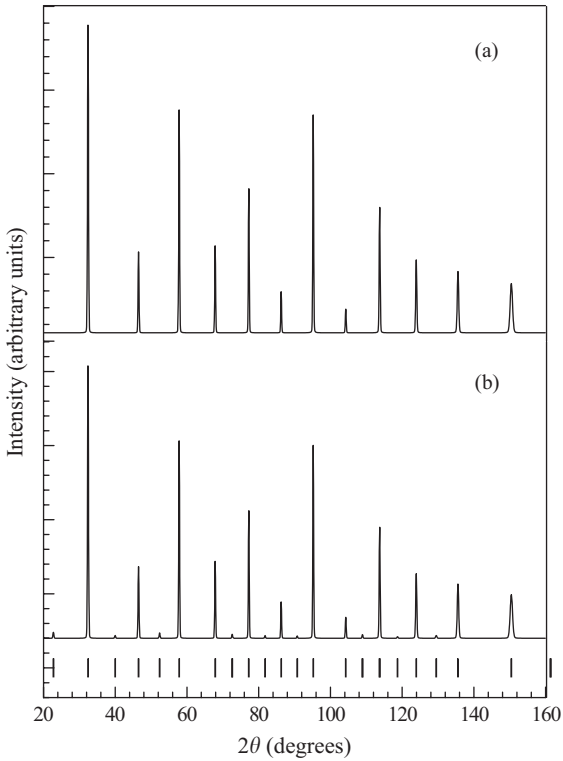

Fig. 10.3 Calculated neutron diffraction patterns for a disordered (a) and fully ordered (b) β-CuZn alloy illustrating the formation of superlattice peaks.

cubic structure above ~460°C. Below 460°C, long-range order begins to develop, resulting below ~100°C in a primitive cubic CsCl type structure. The perfect ordered state has additional peaks in the diffraction pattern, known as superlattice peaks. These are illustrated for β-CuZn in Fig. 10.3. The degree of long-range order is described by the long-range order parameter S defined as the fraction of atoms of type A that are on their 'correct' positions minus the fraction that are in the 'incorrect' position. The integrated intensity of the superlattice peaks scales directly with S, and so a ready means of determining the degree of long-range order is available.

As discussed by Warren (1969, 1990), ordered metallic alloys often exist over a range of composition, that is, they can be non-stoichiometric. Similar behaviour is also common in some ceramics and in many minerals. In these situations, a modified form of S is required. For a binary system, consider two atom types A and B which occupy sites α and β, respectively, in the ordered structure. We represent the fractions of α-sites by y_α and of β-sites be y_β, and the atom fractions of A and B by x_A and x_B, respectively. The fractions x_A, x_B, can differ from y_α,

y_β by virtue of non-stoichiometry. Writing the fraction of α sites occupied by an A atom as r_α and the fraction occupied by a B atom as w_α and likewise for the B atom site r_β, w_β, we can write the long-range order parameter as

$$S = r_\alpha - w_\beta \tag{10.16}$$

by recognizing that $r_\beta + w_\beta = 1$:

$$S = r_\alpha + r_\beta - 1 \tag{10.17}$$

or, noting also that $x_\mathrm{A} = y_\alpha r_\alpha + y_\beta w_\beta$, $x_\mathrm{B} = y_\beta r_\beta + y_\alpha w_\alpha$, and $y_\alpha + y_\beta = 1$:

$$S = \frac{(r_\alpha - x_\mathrm{A})}{y_\beta} = \frac{\left(r_\beta - x_\mathrm{B}\right)}{y_\alpha} \tag{2.6}$$

To provide a link to the intensity of superlattice reflections we may write the structure factor summation for the two sites α and β separately (Warren 1969, 1990):

$$\begin{aligned} F = &\sum_\alpha (r_\alpha b_\mathrm{A} + w_\alpha b_\mathrm{B}) \exp\left(2\pi i \left(hx_n + ky_n + lz_n\right)\right) \\ &+ \sum_\beta \left(r_\beta b_\mathrm{B} + w_\beta b_\mathrm{A}\right) \exp\left(2\pi i \left(hx_n + ky_n + lz_n\right)\right) \end{aligned} \tag{10.18}$$

For example in β-CuZn, letting the α-site be at (1/2, 1/2, 1/2) and the β-site at (0, 0, 0) and recognizing that $y_\alpha = y_\beta = \frac{1}{2}$ we obtain

$$F = (r_\alpha b_\mathrm{A} + w_\alpha b_\mathrm{B}) \exp(\pi i\,(h + k + l)) + \left(r_\beta b_\mathrm{B} + w_\beta b_\mathrm{A}\right) \tag{10.19}$$

Simplifying using eqn (10.16) along with the relationships between site and atom fractions presented above eqn (2.6) we obtain

$$F = (r_\alpha b_\mathrm{A} + w_\alpha b_\mathrm{B}) + \left(r_\beta b_\mathrm{B} + w_\beta b_\mathrm{A}\right) = 2\,(x_\mathrm{B} b_\mathrm{B} + x_\mathrm{A} b_\mathrm{A}) \tag{10.20a}$$

for peaks with $h + k + l$ even. These are fundamental peaks that are present in diffraction patterns from the (bcc) disordered structure and are clearly not affected by the value of S. For peaks with $h + k + l$ odd, we obtain

$$F = \left(r_\beta b_\mathrm{B} + w_\beta b_\mathrm{A}\right) - (r_\alpha b_\mathrm{A} + w_\alpha b_\mathrm{B}) = S\,(b_\mathrm{B} - b_\mathrm{A}) \tag{10.20b}$$

With careful corrections for multiplicity, Lorentz factor, temperature factor, and preferred orientation; individual peaks may be used to determine S. It is nowadays more convenient to conduct a whole pattern analysis (e.g. Rietveld refinement) in which the occupancies of the α and β sites are refined in such a way as to constrain the overall composition to be correct (see §6.5.4). The long-range order parameter is then easily calculated from eqn (2.6) by recalling that r_α is the fractional

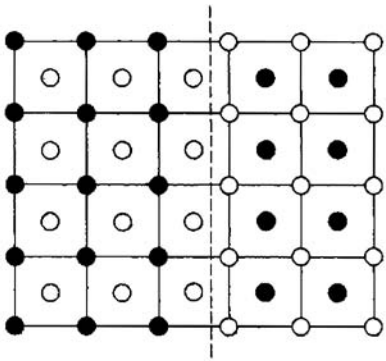

Fig. 10.4 Two-dimensional view of the β-CuZn structure illustrating the concept of an anti-phase domain boundary (dashed) from Warren (1969, 1990).

occupancy of the α-site by A atoms. Whilst this is a very powerful methodology, it is often the case that the whole pattern analysis of structures that have undergone order–disorder (or more accurately, disorder–order) transitions is not routine. This is because the spatial extent over which the chemical ordering is perfect is likely to be less than the spatial extent of the underlying physical order. That is, the crystallites will often contain domains, known in this context as anti-phase domains. An example is shown in Fig. 10.4 for the β-CuZn structure. This particular type of anti-phase domain boundary is energetically not favoured due to the large number of A–A atom pairs that it introduces. However, there are many other arrangements that do not disturb the order parameter. It has been shown (Warren 1969, 1990) that despite the fact that neutrons or X-rays diffracted by the two domains in Fig. 10.4 are out of phase with respect to the superlattice peaks, the effect does not alter the intensity of superlattice peaks but rather introduces *hkl*-dependent broadening due to the anti-phase domains.

10.4 SCATTERING FROM GASES, LIQUIDS, AND AMORPHOUS SOLIDS

10.4.1 The Debye scattering equation

In §9.5.3 we briefly introduced the Debye scattering equation [eqn (9.67)] as a means of simulating the powder diffraction pattern from large ensembles of atoms containing various types of defects. That approach is far more common in the study of non-crystalline (and non-quasicrystalline) forms of matter. The Debye scattering equation may be simply derived from the general structure factor of an ensemble of atoms multiplied by its complex conjugate:

$$I = \sum_m b_m \exp[i\,(\boldsymbol{k} - \boldsymbol{k}_0)\cdot \boldsymbol{r}_m] \times \sum_n b_n \exp[-i\,(\boldsymbol{k} - \boldsymbol{k}_0)\cdot \mathbf{r}_n] \qquad (10.21a)$$

Or expressed in terms of the difference vector $\boldsymbol{r}_{mn} = \boldsymbol{r}_m - \boldsymbol{r}_n$

$$I = \sum_m \sum_n b_m b_n \exp[i\,(\boldsymbol{k} - \boldsymbol{k}_0) \cdot r_{mn}] \tag{10.21b}$$

The ensemble average over all directions is computed as at eqn (10.7):

$$\begin{aligned}\langle \exp\,[i\,(\boldsymbol{k} - \boldsymbol{k}_0) \cdot \boldsymbol{r}_{mn}]\rangle &= \frac{1}{4\pi r_{mn}^2} \int_{\phi=0}^{\pi} \exp(iQr_{mn}\cos\phi)\, 2\pi r_{mn}^2 \sin\phi d\phi \\ &= \frac{\sin Qr_{mn}}{Qr_{mn}}\end{aligned} \tag{10.22}$$

where $Q = 4\pi \sin\theta/\lambda$.

Therefore the intensity is given by

$$I = \sum_m \sum_n b_m b_n \frac{\sin Qr_{mn}}{Qr_{mn}} \tag{10.23}$$

and this is the equation commonly referred to as the Debye scattering equation.

10.4.2 Gases

From the kinetic theory it is obvious that a monotonic gas has no structure at all and consequently its diffraction pattern will have no structure. Molecular polyatomic gases on the other hand have characteristic near neighbour distances *within* their molecules. The Debye scattering equation can be used to model this on the assumption that there is no coherence between scattering from different molecules. Consider methane gas, CH_4. Computing the double sum in eqn (10.23) by allowing each atom in turn to be the origin atom m we obtain for each of N molecules:

$$\frac{I}{N} = b_{\mathrm{C}}\left(b_{\mathrm{C}} + 8b_{\mathrm{H}}\frac{\sin Qr_{(\mathrm{C-H})}}{Qr_{(\mathrm{C-H})}}\right) + 4b_{\mathrm{H}}\left(b_{\mathrm{H}} + 3b_{\mathrm{H}}\frac{\sin Qr_{(\mathrm{H-H})}}{Qr_{(\mathrm{H-H})}}\right) \tag{10.24}$$

Taking $r_{(\mathrm{C-H})}$ as 1.08 Å (Aylward and Findley 2002), from the properties of a regular tetrahedron, $r_{(\mathrm{H-H})} = 1.76$ Å. Substituting these into eqn (10.24) we obtain the diffraction pattern in Fig. 10.5.

There is a substantial amount of structure in this diffraction pattern. The first peak, at approximately $Q = 4.5$ corresponds to $d = 1.36$ Å or close to the mean of the C–H and H–H distances. This simplistic interpretation can, however, not be applied to the other peaks in the pattern which can only be correctly interpreted with some prior knowledge and by modelling using eqn (10.23). Note that the maximum Q here is 20 Å^{-1}, requiring a wavelength of 0.628 Å. Most powder diffraction experiments are conducted over a lesser Q range, typically to $Q \cong$ 8 Å^{-1}. The investigation of scattering from gases is typically undertaken using short wavelength neutrons from a 'hot source' or at spallation sources (see §3.1)

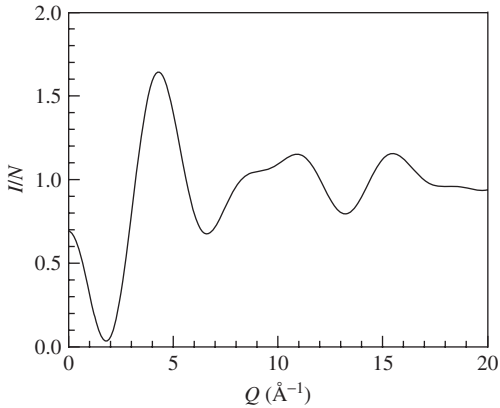

Fig. 10.5 Calculated neutron diffraction pattern from gaseous CH_4 assuming no intermolecular correlation between scattered neutrons.

where a considerable flux of short wavelength neutrons is available. There are, however, several experimental situations in which one might record the diffraction pattern of a gas as part of the background of a powder diffraction experiment. These include the high pressure hydrogenation (or deuteration) of hydrogen storage alloys during *in situ* studies. Equation (10.24) and Figure 10.5 demonstrate that for simple gases, it is not difficult to model the contribution of the gas in these situations.

10.4.3 Liquids and amorphous solids

Liquids and amorphous solids such as glasses have both a far greater density of scattering centres (atoms) and a far greater correlation length, that is, each atom has many shells of neighbours over which some coherent scattering may be established. In many cases, the system adopts an essentially random configuration[154] in which each atom may be regarded as having an average local environment characterized by a radial distribution function. The radial distribution function is given in terms of a density function $\rho(r)$ by

$$g(r) = 4\pi r^2 \rho(r) \tag{10.25}$$

such that a differential spherical shell between radius r and $r + dr$ from the given atom will contain on average $g(r)dr = 4\pi r^2 \rho(r)dr$ scattering nuclei. This radial distribution function is all that is required to describe the local atomic environment when only one kind of atom is involved (e.g. a liquid metal), or when the local structures within the material have only physical origins (i.e. governed by atom

[154] Meaning that, although local structures exist, there is no preferred orientation or directionality to the structure.

radii but with all atom types having equal probability of occupying any shell of neighbours without chemical SRO). This latter condition turns out to be quite rare. Liquids and amorphous solids (and as we have seen in §10.3, crystalline solid solutions) tend to have short-range chemical order which also contributes to the scattering. The simple radial distribution function [eqn (10.25)] is no longer sufficient to describe the structure. Instead a series of pair distribution functions (or pair–correlation functions) describing the radial distribution of each kind of atom pair is used. For example, to describe the local structure in a SiO_2 glass, it is necessary to determine $g(r)_{\mathrm{Si-Si}}$, $g(r)_{\mathrm{Si-O}}$, and $g(r)_{\mathrm{O-O}}$.

So far, we have focused on the structure of the liquid or glass rather than its diffraction pattern. As with crystalline solids, the diffraction pattern is related to the structure via a Fourier transform. In the case of a mono-atomic amorphous phase for which eqn (10.25) holds, the (reduced) intensity, here termed structure factor, is given (Warren 1969, 1990) by

$$S(Q) = \frac{I(Q)/N}{b^2} = 1 + \frac{4\pi}{Q}\int_{r=0}^{\infty} r\,[\rho(r) - \rho_a]\sin Qr\,dr \tag{10.26}$$

where ρ_a is the average atom density in the sample.The radial distribution function is obtained from the inverse Fourier transform:[155,156]

$$g(r) = 4\pi r^2\rho(r) = 4\pi r^2\rho_a + \frac{2r}{\pi}\int_0^{\infty} Q\,[S(Q) - 1]\sin Qr\,dQ \tag{10.27}$$

The consideration of polyatomic materials is facilitated by using a renormalized density function $\rho'(r) = \rho(r)/\rho_a$ that tends to unity for large values of r. Equation (10.26) for instance then reads

$$S(Q) = \frac{I(Q)/N}{b^2} = 1 + \frac{4\pi}{Q}\rho_a\int_{r=0}^{\infty} r\left[\rho'(r) - 1\right]\sin Qr\,dr \tag{10.26a}$$

Now suppose that the polyatomic material comprises species A, B, and so on at concentrations c_{A}, c_{B}, and so on and suppose $\rho_{\mathrm{A-B}}(r)$ is the probability per unit volume of finding a nucleus of species A at distance r from a given nucleus of species B, normalized to tend to unity for large values of r. In these circumstances, the structure factor depends on a weighted sum of partial structure factors (Faber and Ziman 1965):

$$S(Q) = \frac{\langle b^2\rangle - \langle b\rangle^2}{\langle b\rangle^2} + \sum_{\mathrm{A}}\sum_{\mathrm{B}} \frac{c_{\mathrm{A}}c_{\mathrm{B}}b_{\mathrm{A}}b_{\mathrm{B}}}{\langle b\rangle^2} S_{\mathrm{A-B}}(Q) \tag{10.28}$$

[155] The similarity to eqn (10.13) is worth noting.

[156] There is considerable variation in the notation encountered in this field. For example, our $g(r)$ is sometimes shown as $RDF(r)$, whereas $g(r)$ is often used for our $\rho'(r)$, and $G(r)$ for our $\rho'(r) - 1$.

where $\langle b \rangle = \sum_{\mathrm{A}} c_{\mathrm{A}} b_{\mathrm{A}}$, $\langle b^2 \rangle = \sum_{\mathrm{A}} c_{\mathrm{A}} b_{\mathrm{A}}^2$, and the partial structure factors are related to the probabilities $\rho_{\mathrm{A-B}}(r)$ by

$$S_{\mathrm{A-B}}(Q) = 1 + \frac{4\pi}{Q} \rho_a \int_{r=0}^{\infty} r \left[\rho_{\mathrm{A-B}}(r) - 1\right] \sin Qr \, dr \tag{10.29}$$

If these partial structure factors can be determined, then the partial pair distribution functions $\rho_{\mathrm{A-B}}(r)$ are obtained via inverse Fourier transforms.

Bhatia and Thornton (1970) have developed an alternative expression for the structure factor for the particular case of binary systems:

$$S(Q) = \frac{1}{\langle b \rangle^2} \left\{ \langle b \rangle^2 S_{\mathrm{NN}}(Q) + 2\Delta b \langle b \rangle S_{\mathrm{NC}}(Q) + (\Delta b)^2 S_{\mathrm{CC}}(Q) \right\} \tag{10.30}$$

where S_{NN}, S_{CC}, and S_{NC} are the number density–number density, concentration–concentration (i.e., chemical order), and cross-term partial structure factors, respectively, $\Delta b = b_{\mathrm{A}} - b_{\mathrm{B}}$, and the other terms are as before. The partial structure factors incorporated here are rather simply related to the partial structure factors in the Faber–Ziman approach (Bhatia and Thornton 1970).

In polyatomic materials, there are several approaches to determining the individual pair distribution functions.

Isotopic substitution

In favourable circumstances, where an isotope of one atom species with a very different coherent scattering length exists, individual pair distribution functions may be obtained.

In a binary system there are three distinct partial structure factors, $S_{\mathrm{A-A}}(Q)$, $S_{\mathrm{A-B}}(Q)$, and $S_{\mathrm{B-B}}(Q)$ to be determined. By working with three different isotopic compositions, we can measure three different $S(Q)$, solve eqn (10.27) for these three partial structure factors, then obtain the partial pair distribution functions from the inverse Fourier transform. The study of molten strontium chloride (McGreevy and Mitchell 1982) making use of the isotopes ^{35}Cl and ^{37}Cl provides an example of this approach. Measurements were made at four different isotopic compositions, and the partial structure factors extracted. The partial pair distribution functions found in this experiment showed significant differences from those calculated in Monte Carlo and molecular dynamics simulations, suggesting that the interatomic potentials used in these simulations needed to be improved.

In the general case of more than two atomic species, the result of isotopic substitution for just one of these, say A, is from eqn (10.28), to change only the coefficients of $S_{\mathrm{A-A'}}$.[157] This means the difference between the (overall)

[157] A′ here represents any of the atomic species A, B, C, etc. In fact $\langle b \rangle$ and $\langle b \rangle^2$ also change, but this is readily taken into account.

pair-distribution functions obtained with and without isotopic substitution yields a pair distribution function involving only the substituted atom species. Studies of the structure of the chloride ion in aqueous solution (Powell *et al.* 1993) and of the coordination of silver and copper atoms in ternary chalcogenide glasses (Salmon and Liu 1996) are example applications. If several substitutions can be made, all of the pair distribution functions are revealed.

Fukunaga *et al.* (1993) have carried out a technically interesting application in studies of 'neutron zero scattering' amorphous alloys. They were produced, at compositions $Ti_{76}Ni_{24}$ and $Ti_{70}Cu_{30}$, by mechanical alloying. These compositions were chosen to make the average scattering lengths, $\langle b \rangle = \sum_\alpha c_\alpha b_\alpha$, comprising positive contributions from Ni and Cu, along with a negative contribution from Ti, zero. It is seen from eqn (10.30) that under these conditions the measured structure factor gives the concentration–concentration partial directly.

Model-based computer simulation

It is often the purpose of dedicated liquids and amorphous scattering studies to estimate experimental partial pair distribution functions against which theoretical calculations of these quantities can be checked. The theories may be Monte Carlo or Molecular Dynamics simulation-based rules for determining atomic interaction, such as a set of empirically determined interatomic potentials (McGreevy and Mitchell 1982; Powell *et al.* 1993). In the case of liquid $SiSe_2$, a more sophisticated, first principles, Molecular Dynamics simulation (Celino and Massobrio 2002) leads to a calculated structure factor in excellent agreement with experiment. A recent development (Cope and Dove 2007) is the addition to the widely used General Utility Lattice Program (GULP) (Gale and Rohl 2003) of a module to calculate pair distribution functions in partially disordered systems.

It might prove possible to vary certain empirical parameters within these theoretical constructs so as to obtain an improved fit to the experimental data, and indeed to determine such parameters by this means. Such approaches have been taken in studies of diffuse scattering from single crystals, but seem not be have been employed in liquids and amorphous work.

Reverse Monte Carlo simulations (RMC)

RMC is a hybrid of model-based methods with the simulated annealing approach to crystal structure solution (see §6.4.3). A Monte Carlo algorithm is used to pose random deviations from the starting ensemble and these deviations are accepted or rejected with some probability based upon the improvement (or otherwise) to the agreement of a computed structure factor with the observed structure factor (Wicks and McGreevy 1995). Chemical and physical rules concerning distances of closest approach, and so on or even the interatomic potentials used in Molecular Dynamics calculations can be incorporated to force a semblance of reality on the solution(s). A great many ensembles can be generated that give the same computed

$S(Q)$; however, their essential features (partial structure factors, individual pair distribution functions, etc.) will generally be the same. This sameness for simulations with different starting points is a good test for the 'correctness' of an RMC calculation.

Since the study of a liquid or amorphous material *per se* is not usually the purpose of a powder diffraction experiment, the method of choice will necessarily be the one that interfaces best with routine powder diffraction analysis software. To date, the greatest inroads have been made using RMC. The most prominent example is RMCPOW (Mellergård and McGreevy 2000; McGreevy 2001) which has already been discussed in §10.3.3 in the context of SRO diffuse scattering.

In many instances, such as in the study of crystallization from liquids or amorphous material, both the short range (liquid or amorphous) *and* the crystal structure, microstructure, and so on of the crystalline solid are of interest. However, in instances where the amorphous scattering is of no scientific interest a more expedient method is available. The method, known as Fourier filtering, involves preliminary work to define the amorphous scattering curve between Bragg peaks (e.g. using the difference profile from Rietveld refinement). These data, stripped of Bragg peaks, are Fourier transformed to give $g(r)$ for the non-crystalline component. In general, the $g(r)$ derived in this way will be a continuous function and back-transformation can be used to reproduce a smoothed form of the amorphous scattering curve for use as the (user supplied) background in a Rietveld refinement. It has been claimed (Richardson 1993) that this procedure has advantages over merely using a fixed interpolated background (in a way, this is just a more sophisticated interpolation routine!).

The final consideration is in regard to quantifying the amount of liquid or amorphous phase within a sample. In Chapter 8 the theory and methodology of QPA from Rietveld refinement scale factors were detailed. The power of the Rietveld refinement QPA method is that, with the low absorption of neutrons, analysis can be performed using eqn (8.6) without the necessity to include a standard material within the sample. But eqn (8.6) was developed on the assumption that all phases were crystalline, and cannot be applied when amorphous material is present. It is also difficult (but not impossible) to make fundamental contact between the intensity of amorphous scattering and the intensity of the Bragg peaks. Fortunately this is not generally necessary as quite simple experimental procedures exist for determining the amorphous content. The inclusion of a known amount (usually 10–15 wt%) of a well-crystallized standard material,[158] which we will identify using subscript S, is all that is required. Reverting first to eqn (8.4)

$$m_p \propto S_p Z_p M_p V_p \tag{8.4}$$

[158] Alumina, yttria, and ceria are often suitable for ceramic or mineralogical samples; and pure Fe, Ni, or other metal powders for metallic samples.

we can determine the mass fraction of each of the crystalline phases in terms of the known mass fraction of the standard, using

$$w_p = \frac{S_p Z_p M_p V_p}{S_S Z_S M_S V_S} w_S \tag{10.31}$$

Then the mass fractions of all the crystalline phases, including the standard, can be summed, and in the presence of a mass fraction w_A of amorphous material, will sum to $1 - w_A$, that is w_A is given by

$$1 - w_A = \sum_{p \neq S} w_p + w_S = \left(\frac{\sum_{p \neq S} S_p Z_p M_p V_p}{S_S Z_S M_S V_S} + 1 \right) w_S \tag{10.32}$$

This method and eqn (10.32) are based upon the assumption of no significant microabsorption (or micro-attenuation by scattering or extinction). Should this not be the case, a Brindley-type correction can be applied provided the respective particle sizes and attenuation factors are known (Taylor and Matulis 1991).

11

Stress and elastic constants

11.1 STRESSES, STRAINS, AND ELASTIC CONSTANTS IN NATURE AND INDUSTRY

This chapter explores an area of neutron diffraction that departs strongly from its original use in solving or refining crystal structures. The notion that diffracting X-rays (and later neutrons) can be used to measure strains within materials has been extant for many decades. The early diffraction-based strain measurements were conducted exclusively using X-rays because the available neutron diffractometers were of too low resolution. However, with modern diffractometers, neutrons readily have sufficient resolution for very precise strain measurements. In addition, they have a number of advantages for these applications including very low absorption in most materials. This allows depth profiling and strain scanning over large volumes of real engineering structures. The chapter begins with an introduction to stress and strain (§11.1) followed by a discussion of the influence of elastic strains on the powder diffraction pattern (§11.2). The application of these principles to neutron diffraction residual stress analysis is discussed in §11.3 and to the determination of single crystal elastic constants in §11.4.

11.1.1 Stress and strain

Any force, F, exerted upon an area, A, of a solid body, causes a stress, $\sigma = F/A$. Consequently, stresses are experienced by all terrestrial solids. The magnitude of the stress varies greatly from the very minor gravitational stresses experienced by small free standing objects at sea level (100 kPa or $\sim$1 atm/kg and 1 cm^2 of base area), to the enormous isostatic stresses[159] experienced within the earth's crust and mantle (up to 30 GPa or 300,000 atm). Technologically imposed stresses span a similar range from the few Pa required to fold a paper envelope to $\geq$ GPa in the contact zone between two hard surfaces in sliding contact.

Stresses are indispensable in almost all forms of human activity from walking to engineering and manufacturing. The harnessing and control of stress is responsible for many of the remarkable technological features of our lives including cantilevered structures; arched windows, doors, and tunnels; the piezoelectric

[159] Same in all directions, also known as hydrostatic stresses.

effect (and hence ultrasonic medical imaging); the internal combustion engine; the very fast trains; and many other technologies.

Stresses are not readily observed directly. Rather, they are observed by the body's response – the strain. Take the simple case of a thin wire. Suspend a mass from it and we observe a longitudinal strain, given by

$$\varepsilon = \ln\left(\frac{l}{l_0}\right) \tag{11.1}$$

where l is the length and l_0 the original length. Note that when defined in this way (so-called true strain), tensile strains (strains that elongate) are positive and compressive strains (strains that shorten) are negative. In the limit of small strains, the approximation

$$\varepsilon = \frac{l - l_0}{l_0} \tag{11.2}$$

known as the 'engineering' strain is generally used. It differs little from the true strain when ε is less than a few percent. Strains may be either elastic (returning to zero upon removal of the stress) or plastic (permanent). In this chapter we are principally interested in elastic strains, although some of the elastic strains of interest are caused by prior plastic deformation. A majority of solid materials have a linear elastic response in which the stress and strain are formally related through Hooke's law, which for this simple uniaxial[160] case may be written as

$$\varepsilon = \frac{\sigma}{E} \tag{11.3}$$

where E is the elastic modulus or Young's modulus.[161] Sometimes it is more convenient to consider the compliance, $S = 1/E$, hence $\varepsilon = S\sigma$.

Equation (11.3) relates only the longitudinal stress to the longitudinal strain for the simple case of a stretched wire. However, the wire not only gets longer, but also gets thinner. Therefore to describe the strain, it is common to also measure Poisson's ratio ν defined as

$$\nu = \frac{-\varepsilon_{\text{lateral}}}{\varepsilon_{\text{longitudinal}}} \tag{11.4}$$

[160] Stress applied in only a single direction.
[161] In most solid materials, E is essentially constant at constant temperature.

11.1.2 Anisotropy

A more rigorous approach is to describe the strain using the second-rank tensor:

$$[\varepsilon_{pq}] = \begin{bmatrix} \varepsilon_{11} & \varepsilon_{12} & \varepsilon_{13} \\ \varepsilon_{21} & \varepsilon_{22} & \varepsilon_{23} \\ \varepsilon_{31} & \varepsilon_{32} & \varepsilon_{33} \end{bmatrix} \tag{11.5}$$

where the main diagonal elements are the strains along three mutually orthogonal reference axes and the off-diagonal elements are shear strains. In our simple uniaxial tension example, the strain tensor becomes

$$[\varepsilon_{pq}] = \begin{bmatrix} \varepsilon_{11} & 0 & 0 \\ 0 & \varepsilon_{22} & 0 \\ 0 & 0 & \varepsilon_{33} \end{bmatrix} \tag{11.6}$$

and we see that a simple uniaxial stress leads to a more complex system of strains. For an elastically isotropic material,[162] $\varepsilon_{22} = \varepsilon_{33}$ and both have opposite sign to ε_{11}.

Simple uniaxial stresses are rare in nature and we find that the stress σ is itself a second-rank tensor usually written as[163]

$$[\sigma_{rt}] = \begin{bmatrix} \sigma_{11} & \sigma_{12} & \sigma_{13} \\ \sigma_{21} & \sigma_{22} & \sigma_{23} \\ \sigma_{31} & \sigma_{32} & \sigma_{33} \end{bmatrix} \tag{11.7}$$

In its simplest form, our simple uniaxial example has all entries zero except for one diagonal element. This simplicity may not be immediately apparent if the stress is not applied directly along one of the reference axes. In this case, a transformation of axes (e.g. Nye 1957; Lovett 1989) is required.

The simple elastic modulus, E in eqn (11.3), must now be replaced by a fourth-rank elasticity tensor c_{pqrt} or compliance tensor s_{pqrt} (Nye 1957; Lovett 1989), giving

$$\varepsilon_{pq} = s_{pqrt}\,\sigma_{rt} \tag{11.8a}$$

or

$$\sigma_{pq} = c_{pqrt}\,\varepsilon_{rt} \tag{11.8b}$$

[162] Same elastic modulus in all directions.

[163] It is more usual to use *ijkl* as indices; however, these have been replaced by *pqrt* to avoid confusion with the Miller indices (*hkl*) or diffraction peak indices *hkl*.

There is an implied summation over p, q, r, t from 1 to 3. For example, in expanded form

$$\begin{aligned}\varepsilon_{11} &= s_{1111}\sigma_{11} + s_{1112}\sigma_{12} + s_{1113}\sigma_{13} + s_{1121}\sigma_{21} + s_{1122}\sigma_{22} \\ &\quad + s_{1123}\sigma_{23} + s_{1131}\sigma_{31} + s_{1132}\sigma_{32} + s_{1133}\sigma_{33} \\ \varepsilon_{12} &= s_{1211}\sigma_{11} + s_{1212}\sigma_{12} + s_{1213}\sigma_{13} + s_{1221}\sigma_{21} + s_{1222}\sigma_{22} \\ &\quad + s_{1223}\sigma_{23} + s_{1231}\sigma_{31} + s_{1232}\sigma_{32} + s_{1233}\sigma_{33}\end{aligned} \tag{11.9}$$

and so on.

To simplify the use of s_{pqrt} and c_{pqrt}, a two-dimensional matrix notation was introduced by Voigt (1910). In their pure form, s_{pqrt} and c_{pqrt} each have 81 elements. However the requirement for static equilibrium allows us to equate σ_{pq} and σ_{qp} (i.e. no turning moment on the object) and similarly $\varepsilon_{rt} = \varepsilon_{tr}$ (no pure rotation of the object). This simplification reduces the number of elements to 36 (Nye 1957; Lovett 1989) and so we see that a 6×6 matrix allows them all to be expressed. The matrix notation also requires the use of contracted suffixes. We replace pq by m and rt by n according to the following rules (Lovett 1989):

Tensor notation	11	22	33	23	32	13	31	12	21
Matrix notation	1	2	3	4	4	5	5	6	6

The new forms of eqns (11.8) are

$$\varepsilon_m = s_{mn}\,\sigma_n \tag{11.10a}$$

$$\sigma_m = c_{mn}\,\varepsilon_n \tag{11.10b}$$

As there are more examples of mixed suffixes (e.g. 13 and 31) than unmixed (e.g. 11), straight forward expansion of eqn (11.10) will not be identical to expansion of eqn (11.8); there will be some factors of 2 or 4 missing. The consequences of this are

1. $s_{pqrt} = s_{mn}$ only for $m = 1, 2, 3$ and $n = 1, 2, 3$
2. $2s_{pqrt} = s_{mn}$ for either m or $n = 4, 5, 6$
3. $4s_{pqrt} = s_{mn}$ for both m and $n = 4, 5, 6$
4. $2\varepsilon_{rt} = \varepsilon_m$ for $m = 4, 5, 6$

The stress and elasticity tensors σ_{pq} and c_{pqrt} are unaffected, that is, $\sigma_{pq} = \sigma_n$ and $c_{pqrt} = c_{mn}$ for all p, q, r, t. When the contracted or matrix notation is used, s_{mn} and c_{mn} are symmetric 6×6 matrices related by a matrix inversion.

Equation (11.10) describes the elastic response of a completely unsymmetrical body under the action of an arbitrary stress. To be usefully studied by a diffraction technique, the body needs to be crystalline. Crystal symmetry greatly simplifies the form of s_{mn} and c_{mn} by reducing the number of independent coefficients as shown in Table 11.1.

Table 11.1 Effect of crystal symmetry on elastic property tensors.

Symmetry	Independent	Coefficients
None (triclinic)	21	$s_{11}, s_{12}, s_{13}, s_{14}, s_{15}, s_{16}, s_{22}, s_{23}, s_{24}, s_{25}, s_{26}, s_{33}, s_{34}, s_{35}, s_{36}, s_{44}, s_{45}, s_{46}, s_{55}, s_{56}, s_{66}$
Monoclinic	13	$s_{11}, s_{12}, s_{13}, s_{15}, s_{22}, s_{23}, s_{25}, s_{33}, s_{35}, s_{44}, s_{46}, s_{55}, s_{66}$
Orthorhombic	9	$s_{11}, s_{12}, s_{13}, s_{22}, s_{23}, s_{33}, s_{44}, s_{55}, s_{66}$
Tetragonal (classes 4, $\bar{4}$, 4/*m*)	7	$s_{11}, s_{12}, s_{13}, s_{16}, s_{33}, s_{44}, s_{66}$
Tetragonal (classes 4*mm*, $\bar{4}2m$, 422, 4/*mmm*)	6	As above with $s_{16} = 0$
Trigonal (classes 3, $\bar{3}$)	7	$s_{11}, s_{12}, s_{13}, s_{14}, s_{25}, s_{33}, s_{44}$
Trigonal (classes 32, $\bar{3}m$, 3*m*)	6	As above with $s_{25} = 0$
Hexagonal	5	As above with $s_{14} = 0$
Cubic	3	s_{11}, s_{12}, s_{44}
Isotropic	2	s_{11}, s_{12}

The entries in Table 11.1[164,165] are the independent coefficients. The other entries in the compliance or elasticity tensor are either zero or are numerically related to the coefficients given here. Relationships between s_{mn} or c_{mn} are best described by diagrams such as in Table 9 of Nye (1957) which is reproduced as Fig. 11.1.

Note that cubic symmetry does not cause elastic isotropy. An elastically isotropic material has $s_{44} = 2(s_{11} - s_{12})$ and $c_{44} = 1/2\,(c_{11} - c_{12})$ whereas in a cubic crystal s_{44} and c_{44} are independent of the other s_{mn} and c_{mn}.

The elastic constants are important in influencing many properties of crystals including thermal expansion, piezoelectric coefficients, optoelectronic effects, and so on. They are also very important in controlling displacive phase transformations in materials. Although single crystals are used in many technological applications, a large majority of engineering and geological materials are polycrystalline. Whereas the elastic constants of a single crystal are anisotropic (sometimes very much so), a polycrystal comprised from randomly oriented crystallites is elastically isotropic. The appropriate macroscopic elasticity equations are (11.3) and (11.4). To connect with the tensor notation we apply the isotropy condition and write $E = 1/s_{11}$, $S = s_{11}$ and $\nu = -s_{12}/s_{11}$.

11.1.3 Micromechanical influences

The macroscopic strain above is only the average of many microscopic strains which remain locally *anisotropic* according to the elastic properties of the

[164] The exact form depends on the axes chosen [see Table 9, Nye (1957) – Fig. 11.1].
[165] All are referred to orthogonal axes defined in Appendix B of Nye (1957).

Form of the (s_{ij}) and (c_{ij}) matrices

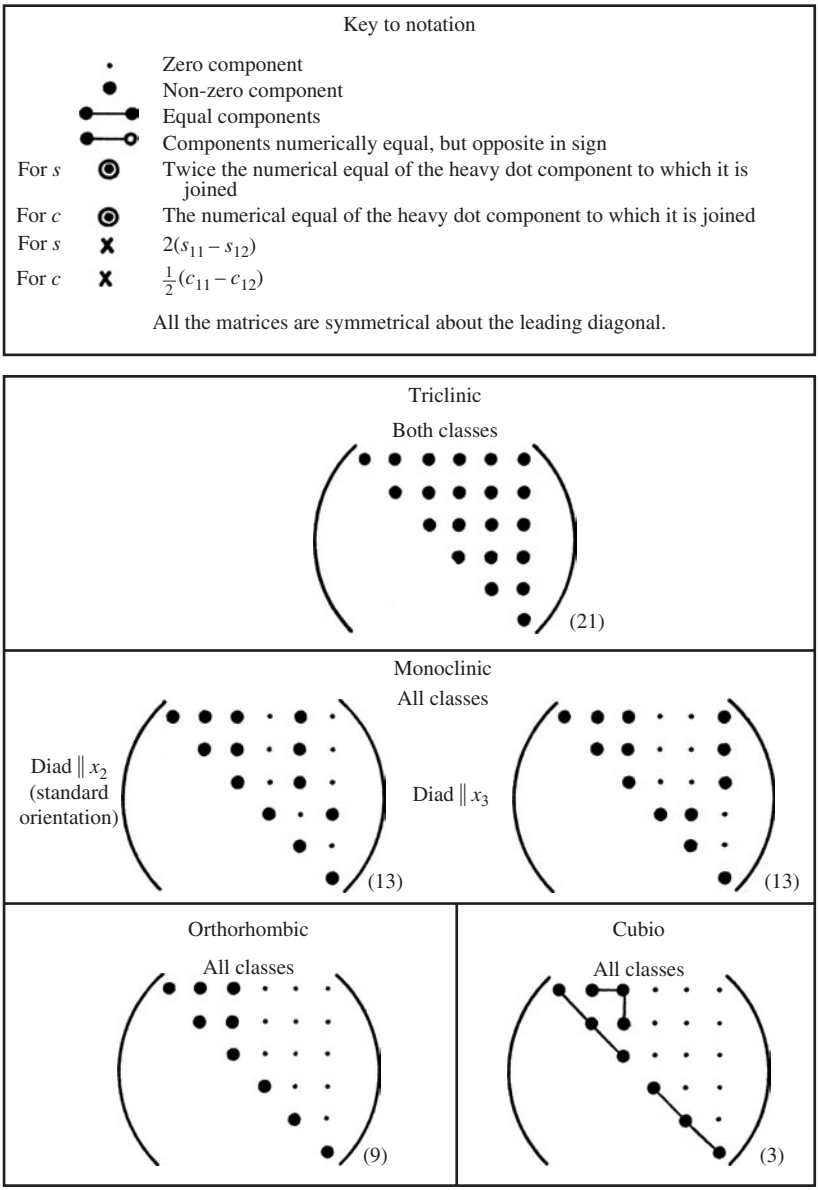

Fig. 11.1 (*Continues*)

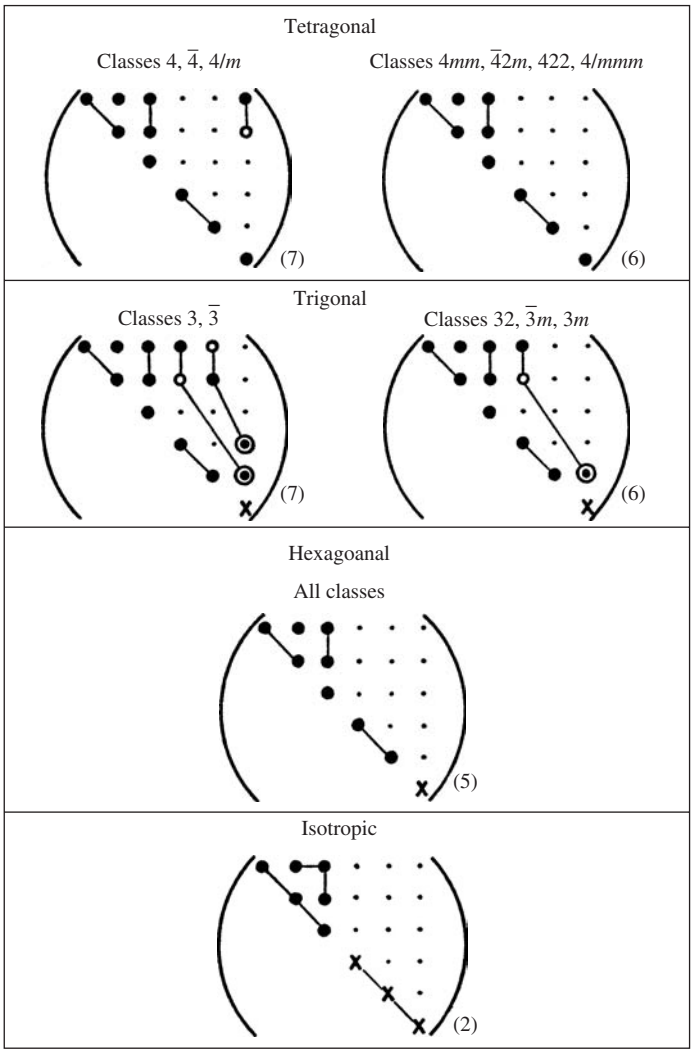

Fig. 11.1 Diagrams from Nye (1957) illustrating the form of the matrix representations (contracted notation) for the elasticity and compliance tensors c_{ij} and s_{ij} in crystals with different symmetry.

crystallites subject to the prevailing micromechanical conditions. The relationship between the single crystal and polycrystal elastic constants for the same material has been the subject of considerable theoretical and experimental activity since early last century. Consider an elastically anisotropic crystal embedded in a solid composed from similar crystals randomly oriented. A two-dimensional schematic

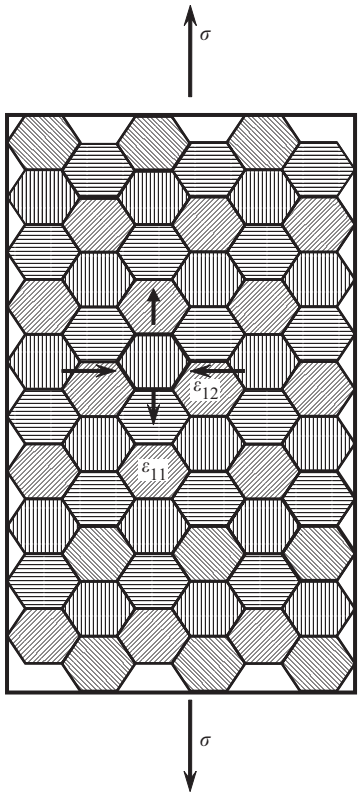

Fig. 11.2 A schematic polycrystal composed from crystals with anisotropic elastic properties for example, such that the planes shown by the lines are normal to the direction of greatest compliance. Any given crystal, such as that shown with a bold border, will develop strains (ε) under an applied stress (σ). However, the strains developed are not the same as for the free crystal due to constraint by neighbouring crystals – also deforming anisotropically.

is shown in Fig. 11.2. As a uniaxial stress is applied, the crystal attempts to distort according to eqn (11.10) and its own s_{mn} and c_{mn}. However, the surrounding crystals also experience the stress and attempt to distort by greater or lesser amounts. At the grain boundaries, crystallites will interact in some way.

Two extreme cases were identified very early. Voigt (1887, 1910) considered the case when each crystallite develops the same *strain*. In that case, the polycrystalline average elastic constants may be most easily found from

$$\overline{C} = \int c_{pqrt}\, d\Phi \tag{11.11}$$

where Φ represents the orientation of the crystallites over which the average is taken. For the case where the crystallites are randomly oriented (no texture) the

result of averaging may be written (Howard and Kisi 1999) as

$$\frac{1}{E} = \frac{6(c_{11}+c_{22}+c_{33})+9(c_{12}+c_{13}+c_{23})+3(c_{44}+c_{55}+c_{66})}{[(c_{11}+c_{22}+c_{33})+2(c_{12}+c_{13}+c_{23})][(c_{11}+c_{22}+c_{33}) -(c_{12}+c_{13}+c_{23})+3(c_{44}+c_{55}+c_{66})]}$$

$$\frac{v}{E} = \frac{3(c_{11}+c_{22}+c_{33})/2+6(c_{12}+c_{13}+c_{23})-3(c_{44}+c_{55}+c_{66})}{[(c_{11}+c_{22}+c_{33})+2(c_{12}+c_{13}+c_{23})][(c_{11}+c_{22}+c_{33}) -(c_{12}+c_{13}+c_{23})+3(c_{44}+c_{55}+c_{66})]} \tag{11.12}$$

It will be seen in §11.2.1 that the effect of strain on diffraction patterns in the Voigt case is very simple, however it is never observed in real polycrystals except when the single crystal elastic constants are relatively isotropic (e.g. a cubic material with $c_{44} \approx {}^1\!/_2\,(c_{11} - c_{12})$). This is because for each elastically anisotropic crystal to distort uniformly requires step changes in the *stress* at the grain boundaries.

Reuss (1929) considered the other extreme, that is, when each crystallite experiences the same *stress*. The polycrystalline average is readily found from

$$\overline{S} = \int s_{pqrt}\, d\Phi \tag{11.13}$$

and for randomly oriented crystallites (no texture) the averaged elastic constants can be written (Howard and Kisi 1999) as

$$\frac{1}{E} = \frac{(s_{11}+s_{22}+s_{33})}{5} + \frac{2(s_{12}+s_{13}+s_{23})}{15} + \frac{(s_{44}+s_{55}+s_{66})}{15}$$

$$\frac{-v}{E} = \frac{(s_{11}+s_{22}+s_{33})}{15} + \frac{4(s_{12}+s_{13}+s_{23})}{15} - \frac{(s_{44}+s_{55}+s_{66})}{30} \tag{11.14}$$

In this case, each crystallite must deform by a differing amount according to its orientation. If the crystals are only allowed to deform by purely elastic mechanisms, this case also should not be realized as it requires *strain* singularities at the grain boundaries. The uniform stress (Reuss) case has however been observed in several metallic materials.

Many geological materials are found to have moduli that lie between the limits set by the Voigt and Reuss cases. Hill (1952) proposed that the numerical average of moduli predicted by the Voigt and Reuss cases would provide satisfactory values for many situations. We shall term this the Voigt–Reuss–Hill (VRH) model. There are two possibilities for the VRH model: one involves taking the mean of the compliances $\overline{S}^{\mathrm{VRH}} = \left(\overline{S}^{\mathrm{Voigt}} + \overline{S}^{\mathrm{Reuss}}\right)/2$ and the other involves the mean of the elasticity tensors $\overline{C}^{\mathrm{VRH}} = \left(\overline{C}^{\mathrm{Voigt}} + \overline{C}^{\mathrm{Reuss}}\right)/2$. Unfortunately, these two distinct estimates from the VRH model do not satisfy the expected reciprocity condition, that is, $\overline{C} \neq \overline{S}^{-1}$. The situation is easily remedied by defining a so-called Super

VRH (Matthies and Humbert 1995) by

$$\overline{S}^{\text{Super}} = \left[\frac{\overline{S}^{\text{VRH}}}{\overline{C}^{\text{VRH}}}\right]^{\frac{1}{2}} = \left(\overline{C}^{\text{Super}}\right)^{-1} \tag{11.15}$$

Another approximation that addresses the reciprocity problem directly is 'Geo' (Matthies *et al.* 2001). Here the averaging is not the arithmetic averaging implied by the integrals in eqns (11.11) and (11.13) but rather the geometric means calculated according to

$$\overline{S}^{Geo} = \exp\left(\int \ln s_{pqrt}\, d\Phi\right) \tag{11.16}$$

$$\overline{C}^{Geo} = \exp\left(\int \ln c_{pqrt}\, d\Phi\right)$$

These now satisfy the relation $\left(\overline{C}^{\text{Geo}}\right)^{-1} = \overline{S}^{\text{Geo}}$.

Beyond the various averages given above are the self-consistent calculations of elastic constants in polycrystalline assemblies. Here each grain is treated as an inclusion in a homogeneous elastic medium comprising all the other grains in the assembly, with 'bare' elastic constants in general different (if only on account of its orientation) from those of the surrounding medium. The idea is to calculate the response of this inclusion to stresses applied to the body as a whole and by this means to calculate the effective elastic constants in the inclusion. The self-consistent condition is that the elastic constants of the inclusion when averaged over all pertinent orientations should equal the elastic constants of the surrounding medium.

The 'simplest' incarnation due to Kröner (1958) is based on Eshelby's (1957) analysis of misfitting inclusions in isotropic media. Eshelby showed that, within an ellipsoidal inclusion that undergoes a uniform strain ε^T_{mn} when free of constraint, the stresses and strains are still uniform when the inclusion is constrained. The constrained strains ε^C_{mn} in the inclusion are linearly related to the unconstrained strains via coefficients A_{mnop}

$$\varepsilon^C_{mn} = A_{mnop}\varepsilon^T_{op} \tag{11.17}$$

and these A_{mnop} form what is now known as the 'Eshelby tensor'. This tensor has been given explicitly for the special case of spherical inclusions. Kröner has taken the Eshelby solution for a misfitting sphere, imposed a uniform strain in the homogeneous elastic medium, then replaced the misfitting inclusion by a single crystal with the same total stress and strain. Next he solved for the strains ε^T_{mn} (and hence ε^C_{mn}) when the elastic constants of the medium (the average over all the other grains) $\overline{C}^{\text{Kröner}}_{mnop}$, the (generally different) elastic constants in the inclusion referred to the same coordinates, $c_{mnop}(\Omega)$, and the applied uniform strain ε_{op} are taken as prescribed. His solution, written for the stress $\sigma_{mn}(\Omega)$ in the included

crystal (here indicated by Ω), is

$$\sigma_{mn}(\Omega) = (\overline{C}_{mnop}^{\text{Kröner}} + r_{mnop}(\Omega))\varepsilon_{op} \tag{11.18}$$

where $r_{mnop}(\Omega)$ is a rather complicated quantity depending on the elastic constants of the crystal and medium, and the various constants of the Eshelby tensor evaluated for a spherical inclusion. Self-consistency requires that, when the average is taken over different possible orientations of the crystal inclusion, the result should be[166]

$$\langle \sigma_{mn}(\Omega) \rangle = \overline{C}_{mnop}^{\text{Kröner}} \varepsilon_{op} \tag{11.19}$$

that is, it requires

$$\left\langle r_{mnop}(\Omega) \right\rangle = 0 \tag{11.20}$$

It is from this last equation that self-consistent estimates of the average elastic constants $\overline{C}_{mnop}^{\text{Kröner}}$ are obtained. There is an analogous result in terms of the strain in the included crystal, ε_{mn} (Ω), given by

$$\varepsilon_{mn}(\Omega) = \left(\overline{S}_{mnop}^{\text{Kröner}} + t_{mnop}(\Omega)\right) \sigma_{op} \tag{11.21}$$

where, like $r_{mnop}(\Omega)$, t_{mnop} (Ω) depends on the elastic constants of the crystal, the medium, and the Eshelby tensor. It can be seen that eqn (11.18) is of the form of the Voigt equation plus a correction term to be applied within the individual crystallite, Ω, and eqn (11.21) is a similar modification of the Reuss equation. As such, although both $\overline{C}_{mnop}^{\text{Kröner}}$ and $\left(\overline{S}_{mnop}^{\text{Kröner}}\right)^{-1}$ lie close to the centre of the limits imposed by the Reuss and Voigt conditions, they do not necessarily meet the reciprocity criterion.

For the mathematical detail, the reader is referred to the original references (Eshelby 1957; Kröner 1958). There are computer programs available to carry out calculations by self-consistent methods, and the methods are now widely applied[167] (Turner and Tomé 1994). Despite the current ascendancy of the self-consistent method in elastic constants calculations, the model in which each crystallite sees its surrounds as a homogeneous elastic medium may be a considerable oversimplification of the interactions between different grains. In a regular polycrystal, each grain has relatively few neighbours each of similar size and shape to itself in a small number of orientations and each with anisotropic elastic constants. The connection to a continuum approximation, however convenient, is not rigorous.

[166] We will use either $\langle\ \rangle$ or a bar to indicate averages, and use uppercase letters with a bar to indicate the averaged macroscopic elastic constants obtained.

[167] These programs encompass plastic deformation as well as the elastic deformation considered here.

Several of the above models (Reuss, VRH, and Kröner) as presented, are sensitive to sample texture. Each can be made to automatically account for sample texture (see §9.8) by conducting the averaging in eqns (11.11), (11.13), (11.16), and (11.20) using the orientation density function (ODF) to apply weightings to the arithmetic or geometric mean. In some cases of one-dimensional texture, a simpler approximation (e.g. the March function) may suffice.

For a given example, it is often the case that the VRH, Kröner and Geo results cluster near the centre of the limits set by the Voigt and Reuss values. For example, for Fe, a cubic material showing significant shear anisotropy ($s_{44} \neq 2\,(s_{11} - s_{22})$), calculations have been carried out by Matthies *et al.* (2001) and their results for Young's modulus presented in Table 11.2. It can be seen that the results from VRH, super VRH, Kröner, and Geo models are virtually indistinguishable.

Whilst the influence of the micromechanical model on computed estimates of the polycrystalline (macroscopic) elastic constants is certainly observable, it is a small effect compared with the effect of micromechanics on the elastic constants needed to determine strains using diffraction data.

11.2 INFLUENCE OF ELASTIC STRAINS ON THE POWDER DIFFRACTION PATTERN

11.2.1 Introduction

We saw in §2.4.1 that the *position* of the diffraction peaks from a powdered or polycrystal sample are very precisely related to the mean spacing of planes of atoms perpendicular to the scattering vector, the so-called d-spacing. In a strained polycrystal, the mean values of the d-spacings change. For a given diffraction peak, in the limit of small strains, the strain along a vector [hkl] parallel to the

Table 11.2 Young's modulus for Fe.[168]

	Voigt	Reuss	VRH(s)	VRH(c)	Super VRH	Kröner	Geo	Observed
E (Gpa)	225.8	194.6	209.0	210.4	209.7	211.6	210.6	205
Difference from Kröner (%)	+6.8	−8.0	−1.2	−0.6	−0.9	0	−0.5	−6.6
Difference from observed (%)	+10.1	−5.1	+2.0	+2.6	+2.3	+3.2	+2.7	0

[168] In Table 11.2 we have added, to the data supplied by Matthies, *et al.* (2001), the observed modulus of Fe and an additional line of differences based on this value rather than Kröner's model.

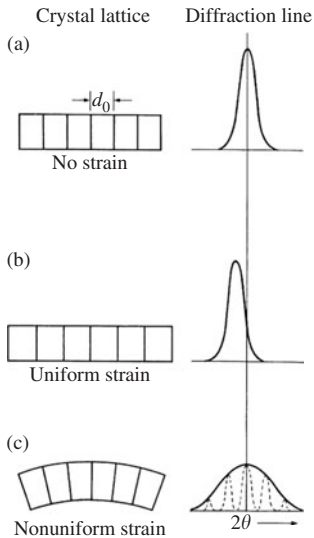

Fig. 11.3 Influence of strain on powder diffraction peaks. (a) no strain, (b) uniform strain, and (c) non-uniform strain (after Cullity 1978).

scattering vector is given by

$$\varepsilon_{hkl} = \frac{d_{hkl} - d^0_{hkl}}{d^0_{hkl}} \tag{11.22}$$

where d^0_{hkl} is the unstrained d-spacing for the planes (hkl). If the strains are distributed widely about this mean value, there is also an associated peak broadening as discussed in §9.3. Figure 11.3 shows schematically the effect of a uniform strain on the diffraction peaks from a metallic sample subjected to an externally applied tensile stress. If the crystals in the material are elastically isotropic (or nearly so) or the stress–strain state in the polycrystal approximates the Voigt condition, then the strain along each scattering vector (i.e. within each set of diffraction planes) will be the same. The effect on the diffraction pattern is simply that of a change in the unit cell dimensions proportional to the change in mean stress. Such cases are rare. In the more general case, for elastically anisotropic crystallites and a non-Voigt stress–strain state, the strains are hkl dependent. For increasing strains, this situation may be recognized by a progressively poorer result from whole-pattern fitting wherein the deviations in the difference plot indicate instances of both positive and negative position shifts with respect to the refined peak positions. An example is shown in Fig. 11.4 (Kisi *et al.* 1997).

If ε_{hkl} is plotted as a function of stress, we obtain data such as portrayed in Fig. 11.5 (Kisi and Howard 1998). The slope of each line on Fig. 11.5 represents the elastic compliance s_{hkl} perpendicular to the appropriate set of diffracting planes. In the data presented in Fig. 11.5, s_{hkl} varies by nearly a factor of 4

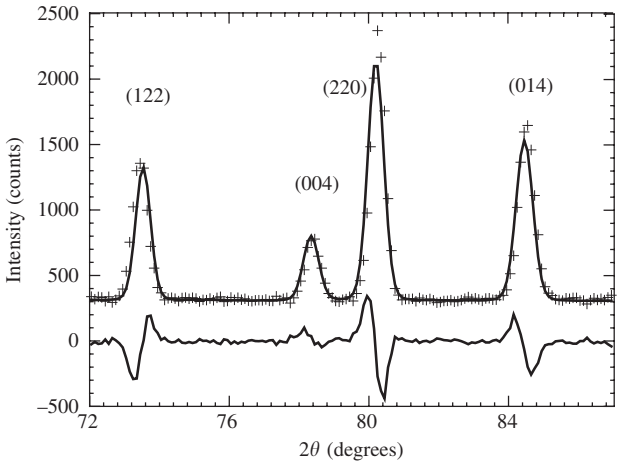

Fig. 11.4 Illustration of the effect of elastic anisotropy on the CW neutron diffraction pattern of ceria-stabilized tetragonal zirconia under applied stress (Kisi *et al*. 1997). Note that the different *hkl* are shifted by differing amounts so that some observed peaks in the Rietveld fit are displaced to higher angle (004, 220, and 014) and others to lower angle (122) with respect to the average calculated positions.

between 004 and 111. These compliances and their inverses (c_{hkl}) are referred to as the *diffraction elastic constants* and are central to the diffraction-based study of both residual stress (§11.3) and single crystal elastic constants (§11.4). As we shall see below, they are related to the single crystal elastic constants by a tensor transformation and are influenced by the micromechanical (stress–strain) state within the polycrystal and any preferred orientation (texture) within the material.

11.2.2 Relationship of diffraction elastic constants to single crystal elastic constants

The crystallites contributing to an observed diffraction peak for planes (*hkl*) in a powder diffraction pattern are those whose plane normals are parallel to the scattering vector. This means that strains measured by diffraction for a particular set of planes, ε_{hkl}, result from the compliance along a common crystallographic vector.[169] The situation is illustrated in Fig. 11.6 (Cullity 1979). The orientation of the crystallites with respect to rotation around the scattering vector is either random or governed by the prevailing sample texture.

The first step in relating the diffraction elastic compliance s_{hkl} to the tensor of single crystal compliances s_{pqrt} is a transformation of the latter onto 'laboratory' axes, one of which is taken to lie parallel to the scattering vector. The treatment

[169] This very useful situation is not the case in some TOF diffractometers with a very wide angular range of detector coverage as patterns are recorded for a great variety of scattering vectors.

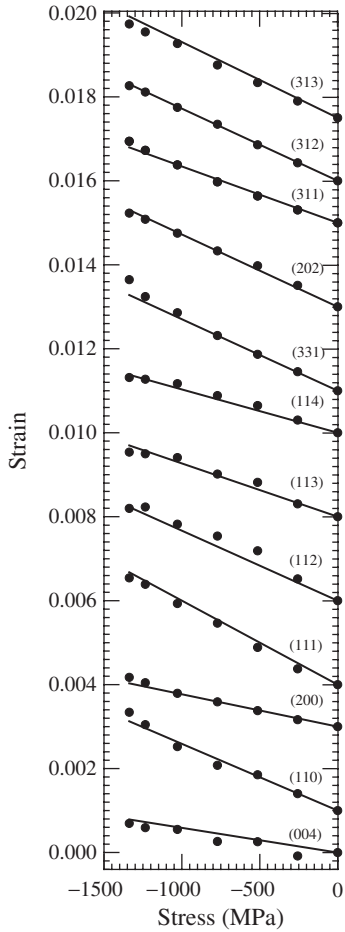

Fig. 11.5 Diffraction elastic compliances for Ce-stabilized tetragonal zirconia polycrystal (Ce-TZP) illustrated as the slope of stress–strain curves for a number of diffraction peaks (Kisi and Howard 1998).

given here follows that by Howard and Kisi (1999). A connection to the nomenclature commonly used in X-ray diffraction residual stress measurements is given in §11.3.

First we define a Cartesian laboratory coordinate system x', y', z' such that the diffraction pattern is recorded in the $x'y'$ plane and the scattering vector for the reflection *hkl* coincides with x'. The conventional orthogonal coordinate axes used to define the elastic constants[170] (see Nye 1957) are termed x, y, z. Next we

[170] These are the axes of the crystallographic unit cell for orthogonal crystals.

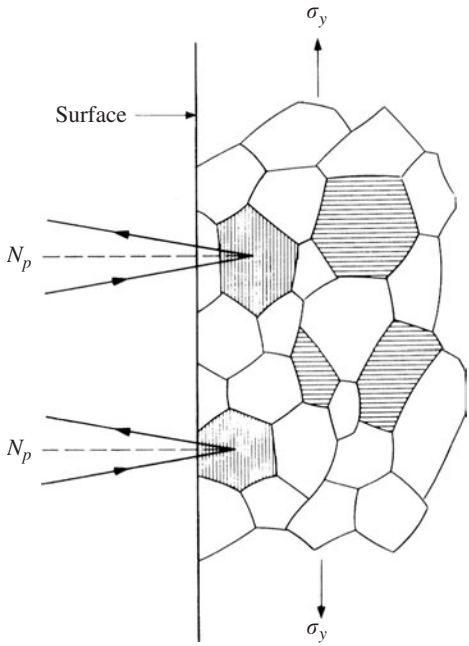

Fig. 11.6 Individual crystals in a polycrystalline aggregate. A tensile stress σ_y causes each crystal to distort. Neutron diffraction into peak *hkl* will occur only in those crystals oriented with (*hkl*) planes perpendicular to the scattering vector as shown (from Cullity 1978).

define a second set of coordinate axes within the crystal, x'', y'', z'', such that x'' too is parallel to the scattering vector. For simplicity, we consider a cubic crystal. Diffraction from (*hkl*) planes means that the scattering vector will be in the direction [*hkl*]. The axes y'' and z'', orthogonal to x'', are conveniently chosen along $[\bar{k}h0]$ and $[\bar{h}\bar{l}\ \bar{k}\bar{l}\ h^2+k^2]$, respectively. If we denote the unit vectors defining the conventional crystallographic axes by $\boldsymbol{i}, \boldsymbol{j}, \boldsymbol{k}$, the unit vectors defining the double primed system are

$$\boldsymbol{i}'' = \frac{h\boldsymbol{i} + k\boldsymbol{j} + l\boldsymbol{k}}{\sqrt{h^2+k^2+l^2}}, \quad \boldsymbol{j}'' = \frac{-k\boldsymbol{i} + h\boldsymbol{j}}{\sqrt{h^2+k^2}}, \quad \text{and} \quad \boldsymbol{k}'' = \frac{-hl\boldsymbol{i} - kl\boldsymbol{j} + (h^2+k^2)\boldsymbol{k}}{\sqrt{h^2+k^2}\sqrt{h^2+k^2+l^2}} \tag{11.23}$$

By definition the x' (laboratory) axis and the x'' (crystallite) axis coincide. The primed (lab) and double-primed (crystallite) systems are then related by a simple rotation about the scattering vector (x', x''). Denoting the angle between z' and z'' as ϕ, we can write the relationship between the crystallite and laboratory

systems as

$$\begin{pmatrix} \boldsymbol{i}' \\ \boldsymbol{j}' \\ \boldsymbol{k}' \end{pmatrix} = \begin{pmatrix} 1 & 0 & 0 \\ 0 & \cos\phi & -\sin\phi \\ 0 & \sin\phi & \cos\phi \end{pmatrix} \begin{pmatrix} \boldsymbol{i}'' \\ \boldsymbol{j}'' \\ \boldsymbol{k}'' \end{pmatrix} \tag{11.24}$$

Combining (11.23) and (11.24) gives the relationship of laboratory axes to the crystallographic (or elasticity) axes

$$\begin{pmatrix} \boldsymbol{i}' \\ \boldsymbol{j}' \\ \boldsymbol{k}' \end{pmatrix} = \begin{pmatrix} 1 & 0 & 0 \\ 0 & \cos\phi & -\sin\phi \\ 0 & \sin\phi & \cos\phi \end{pmatrix} \times \begin{pmatrix} \frac{h}{\sqrt{h^2+k^2+l^2}} & \frac{k}{\sqrt{h^2+k^2+l^2}} & \frac{l}{\sqrt{h^2+k^2+l^2}} \\ \frac{-k}{\sqrt{h^2+k^2}} & \frac{h}{\sqrt{h^2+k^2}} & 0 \\ \frac{-hl}{\sqrt{h^2+k^2}\sqrt{h^2+k^2+l^2}} & \frac{-kl}{\sqrt{h^2+k^2}\sqrt{h^2+k^2+l^2}} & \frac{h^2+k^2}{\sqrt{h^2+k^2}\sqrt{h^2+k^2+l^2}} \end{pmatrix} \begin{pmatrix} \boldsymbol{i} \\ \boldsymbol{j} \\ \boldsymbol{k} \end{pmatrix} \tag{11.25}$$

Multiplying the two square matrices appearing in this expression yields a 3×3 matrix (a_{mn}) of direction cosines of the laboratory (primed) axes relative to the (unprimed) crystallographic axes. The fourth-order compliance (or elasticity) tensor is transformed according to the rule (Nye 1957; Lovett 1989):

$$s'_{pqrt} = a_{pu} a_{qv} a_{rw} a_{tx} s_{uvwx} \tag{11.26}$$

The transformation is algebraically tedious but otherwise straightforward. Noting that for cubic symmetry there are only three independent non-zero components of the compliance tensor, written in abbreviated form as s_{11}, s_{12} and s_{44}, we obtain results such as

$$s'_{1111} = \frac{(h^4+k^4+l^4)}{(h^2+k^2+l^2)^2} s_{11} + \frac{(k^2l^2+h^2l^2+h^2k^2)}{(h^2+k^2+l^2)^2}(2s_{11}+s_{44}) \tag{11.27a}$$

$$\begin{aligned} s'_{1133} = {} & \left\{ \frac{2h^2k^2}{(h^2+k^2+l^2)(h^2+k^2)} + \frac{2(h^4l^2-h^4k^2-h^2k^4+k^4l^2)\cos^2\phi}{(h^2+k^2+l^2)^2(h^2+k^2)} \right. \\ & \left. + \frac{hkl(h^2-k^2)\sin 2\phi}{(h^2+k^2+l^2)^{3/2}(h^2+k^2)} \right\} \left(s_{11} - \frac{s_{44}}{2} \right) \\ & + \left\{ \frac{h^4+k^4+h^2l^2+k^2l^2}{(h^2+k^2+l^2)(h^2+k^2)} + \frac{2(h^4k^2+h^2k^4-h^4l^2-k^4l^2)\cos^2\phi}{(h^2+k^2+l^2)^2(h^2+k^2)} \right. \\ & \left. + \frac{hkl(k^2-h^2)\sin 2\phi}{(h^2+k^2+l^2)^{3/2}(h^2+k^2)} \right\} s_{12} \end{aligned} \tag{11.27b}$$

Note that these compliances are functions of the reflection indices *hkl*. The compliance s'_{1111} measures strain parallel to the scattering vector when that is parallel to the applied stress and as such is independent of rotations, ϕ, of the crystal around the scattering vector; however, the rotation angle remains a variable in expressions for the other compliances (as in eqn 11.27b).

Recall that cubic symmetry was assumed in the analysis above. A similar analysis may be completed for any crystal symmetry, though at the cost of greater complexity.

To make a meaningful connection with the observed d-spacings for the ensemble of crystallites in the sample, it is necessary to

(i) Average eqn (11.27) (or equivalent for other elements of the compliance tensor and/or other crystal systems) for rotation about the scattering vector to give the mean compliances $\langle s'_{pqrt}\rangle_{hkl}$.[171] This may simply be the arithmetic mean if the crystallites are randomly oriented; however, it will need to be weighted by the ODF if the sample is textured. The averages $\langle \boldsymbol{s}'_{pqrt}\rangle_{hkl}$ are the diffraction elastic compliances.

(ii) Use the appropriate form of Hooke's law:

$$\left\langle \varepsilon'_{pq}\right\rangle_{hkl} = \left\langle s'_{pqrt}\right\rangle_{hkl}\left\langle \sigma'_{rt}\right\rangle \tag{11.28}$$

to obtain the mean strains $\langle \varepsilon'_{pq}\rangle_{hkl}$, mean stresses $\langle \sigma'_{rt}\rangle$ or elastic compliances $\langle \boldsymbol{s}'_{pqrt}\rangle_{hkl}$ depending on which are unknown.

There are two ways in which mean strains $\langle \varepsilon'_{pq}\rangle_{hkl}$ measured by diffraction are used. In the first, known values of $\langle \boldsymbol{s}'_{pqrt}\rangle_{hkl}$ are used to determine the stress tensor $\langle \sigma'_{rt}\rangle$ (see §11.3), and in the second, application of stress $\langle \sigma'_{rt}\rangle$ in favourable circumstances allows the determination of unknown single crystal elastic constants by the reverse transformation of $\langle \boldsymbol{s}'_{pqrt}\rangle_{hkl}$ to give s_{pqrt}.

11.3 NEUTRON DIFFRACTION RESIDUAL STRESS ANALYSIS

11.3.1 Introduction to residual stresses

In §11.1 we saw that external forces applied to a solid set up stresses of various kinds. It is often the case that, after some industrial processing operation or geological event, a solid at equilibrium with no externally applied stresses nonetheless contains long-range internal stresses. These stresses are termed *residual* stresses. A very simple example is the welding of both ends of a strut between two rigid beams. As the second weld solidifies and cools, it is predisposed to thermal contraction, a thermal strain. However, the strut is rigidly constrained at the ends. Instead an elastic strain of opposite sign to the thermal contraction develops

[171] We note that the averaging of compliances is well adapted to the Reuss model of the polycrystalline material [cf. eqn (11.13)] and the averaging of elastic constants to the Voigt model.

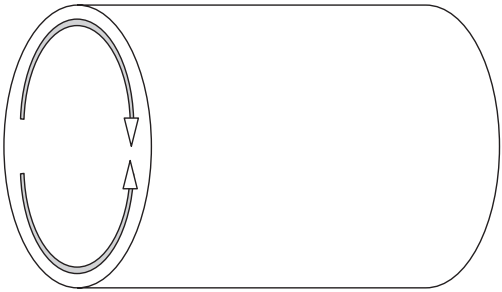

Fig. 11.7 Compressive residual stresses are developed in the surface layers of a case-hardened cylinder.

within the strut and is accompanied by a tensile stress according to eqn (11.3). An analogous geological example would be in the latter stages of cooling of igneous intrusions and the surrounding rocks.[172] Thermal strains are not the only source of residual stresses. A common example arises in the surface hardening of steels by the fcc → bct (body centred tetragonal) martensitic transformation. Here the surface of the steel is heated to 780°C–900°C (depending on carbon content) and quenched.[173] Because carbon that usually precipitates as Fe_3C is trapped in solid solution within the Martensite phase, the specific volume of the Martensite layer is greater than the phases present within the core of the object. Consider the cylinder shown in Fig. 11.7. If unconstrained, the surface would expand[174]; however, it is constrained by the core. The result is that large circumferential compressive stresses arise in the surface. These are considered beneficial in resisting the initiation of fatigue cracks. However, to maintain mechanical equilibrium large tensile stresses are set up in the substrate. The situation is illustrated in Fig. 11.8 showing a schematic residual stress depth profile for the cylinder illustrated in Fig. 11.7. If not properly managed, residual stresses can seriously degrade the performance of engineering materials as they add to externally imposed stresses such as the bending stress (dotted line) in Fig. 11.8. In some cases, the total stress, being the sum of the residual and applied stresses (heavy line in Fig. 11.8), exceeds the yield strength of the steel (dashed line) and can cause premature failure. The size of residual stresses is only limited by the strength of the material and they can easily lead to failure during production (e.g. quench cracks in heat treated steels). More dangerous are undetected residual stresses that are just less than the yield or fracture strength of the material as these will lead to failure under only light externally applied loads.

[172] Geological time frames allow much of the thermal contraction to be accommodated by plastic flow.
[173] Cooled rapidly.
[174] Depending on carbon content, heating, and cooling rates.

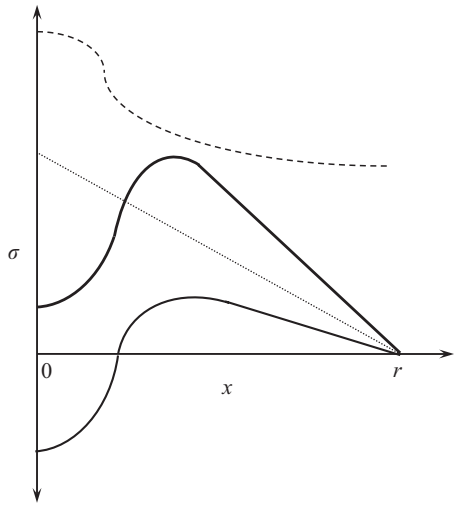

Fig. 11.8 The thin solid line shows a schematic residual stress profile between the surface ($x = 0$) and the centre ($x = r$) of a cylinder like that shown in Fig. 11.7. The dotted line shows the stress associated with an externally applied bending load and the heavy solid line the resultant total stress. The tensile yield *strength* of the material (dashed) varies with depth. Places where the total stress approaches the yield strength are at risk of initiating sub-surface fatigue cracks.

An insidious aspect of residual stresses is that they are undetectable by conventional engineering inspection methods. They may be predicted by careful modelling, for example, using Finite Element Analysis, however, it is not always possible to model all aspects of industrial processes. For example, during the processing of our surface-hardened cylinder, the precise heating profile of the surface, the transformation strains, the amount of creep due to the thermal imbalance on heating and any creep relaxation during and after quenching are all very specific to a given experimental arrangement. It is far too costly and time consuming to determine these factors for each product size and shape, and each production facility and set of operating parameters. Surface residual stresses may be determined experimentally using a roseate of strain gauges glued to the surface of the object. The residual stresses are 'unloaded' by careful drilling and the strains recorded by the gauges are equal in size and opposite in sign to the residual *strains.* Residual strain estimates are then converted to residual stresses using eqn (11.8b). This method, however, damages or destroys the component and must be corrected for relaxation of the stress component perpendicular to the surface which can therefore not be determined.

Another method for determining surface residual stresses, non-destructively this time, is by X-ray diffraction. Conventional laboratory X-rays penetrate most solids to depths of 10 μm or less. The perpendicular stress so near to the surface is close to

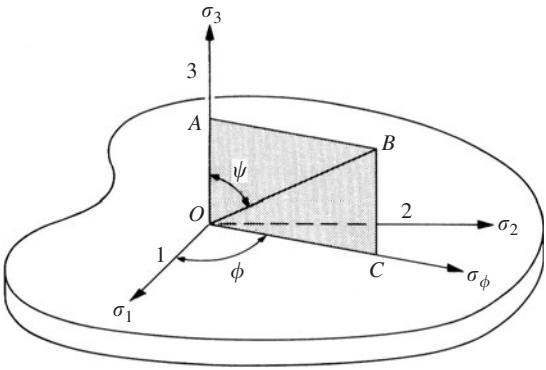

Fig. 11.9 Geometry of X-ray diffraction residual stress determination (Cullity 1978).

zero and is neglected. The surface is then considered to be in a 'biaxial' stress state with principal stresses σ_1 and σ_2. Consider first the case of an elastically isotropic polycrystal. The experimental coordinate system for measuring the stress σ_ϕ at an arbitrary angle (ϕ) to the principal stress σ_1 is shown in Fig. 11.9. Note that although σ_3 is zero, the strain perpendicular to the surface, ε_3, is not zero. It is determined by the Poisson strains due to σ_1 and σ_2, and is the strain most readily measured in a conventional X-ray diffractometer, that is, with the scattering vector normal to the sample surface. It is given by

$$\varepsilon_3 = -\frac{\nu}{\mathrm{E}}(\sigma_1 + \sigma_2) \tag{11.29}$$

Therefore, with a single measurement, only $(\sigma_1 + \sigma_2)$ can be recovered, even for an isotropic material. Now consider data recorded at an angle ψ (Fig. 11.9) to the sample surface. The strain is now given by (Cullity 1979)

$$\varepsilon_\psi = \frac{1}{E}\left[\sigma_\phi(1+\nu)\sin^2\psi - \nu(\sigma_1 + \sigma_2)\right] \tag{11.30}$$

giving by subtraction

$$\varepsilon_\psi - \varepsilon_3 = \frac{\sigma_\phi}{E}(1+\nu)\sin^2\psi \tag{11.31}$$

Expanding the strains in terms of d-spacings gives

$$\frac{d_\psi - d^0}{d^0} - \frac{d_3 - d^0}{d^0} = \frac{d_\psi - d_3}{d^0} \approx \frac{d_\psi - d_3}{d_3} = \frac{\sigma_\phi}{E}(1+\nu)\sin^2\psi \tag{11.32}$$

or

$$\sigma_\phi = \frac{E}{(1+\nu)\sin^2\psi}\left(\frac{d_\psi - d_3}{d_3}\right) \tag{11.33}$$

The approximation taken in eqn (11.32) is to assume that d^0 and d_3 differ so little that either can be used in the denominator. This obviates the need implied by eqn (11.22) for an independent determination of d^0 unless the residual strains are very large. If the principal axes of the strain tensor are known from the sample geometry, then these form ideal directions in which to take measurements. For example in a quenched steel cylinder the hoop, radial, and axial directions are ideal. If the principal directions are not known, then measurements in four directions, normal to the surface, at an angle ϕ, at $\phi + 60°$ and at $\phi - 60°$, can determine the complete biaxial stress state. Greater precision in the measured σ_ϕ may be gained by measuring strains at several values of ψ and measuring the slope of a plot against $\sin^2 \psi$ (the so-called $\sin^2 \psi$ method, see Noyan and Cohen 1987). In the more common case of elastically *anisotropic* materials, it is necessary to work with multiple peaks and to replace E and ν in eqn (11.31) with appropriate diffraction elastic constants $\langle s'_{pqrt} \rangle_{hkl}$ (eqn (11.28)) or, in favourable cases to be discussed later, choosing a diffraction peak that is insensitive to the anisotropy.

The X-ray determination of residual stress is rapid, portable,[175] and non-destructive; however, it only measures the surface stresses and may not be practical for large or complex objects. To investigate sub-surface stresses, often the most dangerous, it is necessary to progressively remove the surface. This practice perturbs the residual stress state and therefore a correction for stress relaxation must be made (Moore and Evans 1958). Some gains have been made with synchrotron X-ray sources where energies as high as 100 keV give penetration depths approaching 1 mm in the lighter engineering materials (e.g. Al-alloys). A spectacular example of the spatial and strain resolution available is the recent direct measurement of triaxial strain fields around ferroelectric domains in $BaTiO_3$ single crystals (Rogan *et al.* 2003). For larger scale engineering applications, such as our surface hardened cylinder in Fig. 11.7, penetration depths of up to 30–50 mm in steel are required to probe the sub-surface strains. This is the realm of neutron diffraction residual stress analysis.

In general, the stress system in a solid polycrystal is triaxial and so the simplified methods described herein can no longer be applied. Even for a neutron diffraction measurement in the near surface region, the large 'gauge volume' (i.e. the volume of the sample that contributes to the observed diffraction pattern) of ≥ 1 mm^3 ensures that the stress is triaxial. Therefore, the appropriate equation to consider is (11.28). A key element of eqn (11.28) is $\langle s'_{pqrt} \rangle_{hkl}$ the diffraction elastic compliances (or $\langle c'_{pqrt} \rangle_{hkl}$ the diffraction elastic constants). Recalling that the aim of residual stress analysis is to obtain measured values of the mean stress tensor (σ'_{rt}) in various positions within a sample, three approaches to determine $\langle s'_{pqrt} \rangle_{hkl}$ can be taken.

[175] Compact diffractometers specifically for measuring one diffraction peak from steels have been available for many years (Cullity 1979; Noyan and Cohen 1987).

11.3.2 Experimental determination of $\langle s'_{pqrt}\rangle_{hkl}$

This is by far the most commonly used approach. A residual-stress-free sample of the material of interest is placed under carefully calibrated external stresses and the strains $\langle \varepsilon'_{pq}\rangle$ determined according to the diffraction peak shifts. The data (e.g. Fig. 11.5) readily yield $\langle s'_{pqrt}\rangle$ for any chosen *hkl*. This apparently trivial procedure has a number of pitfalls.

First, the sample used to determine $\langle s'_{pqrt}\rangle$ must be as close to identical (chemical composition, microstructure, thermal history, etc.) to the residual stress sample as is practicable. This requirement arises because, although the single crystal elastic constants are not significantly altered by minor chemical or processing differences, the micromechanical (stress–strain) state of the material may be strongly influenced (see below).

Second, it is experimentally difficult to create complex stress states and so only $\langle s'_{1111}\rangle$ and $\langle s'_{1133}\rangle$ are readily measured. Experimental arrangements for rapidly determining these two are shown in Fig. 11.10. In constant wavelength situations, the experiment will simultaneously measure the compliance approximately parallel and perpendicular to the scattering vector $(\langle s'_{1111}\rangle$ and $\langle s'_{1133}\rangle)$,

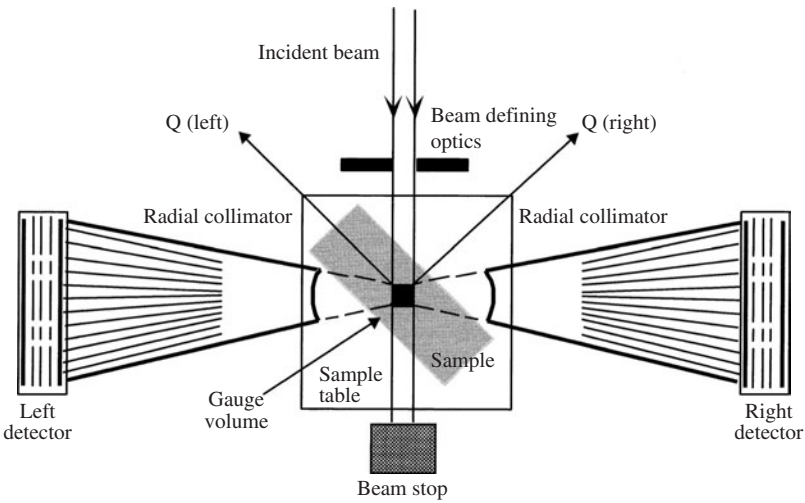

Fig. 11.10 Experimental arrangement, adapted from Johnson and Daymond (2003), for rapid determination of diffraction elastic constants by applying a known stress and simultaneously recording diffraction patterns with scattering vector parallel to the applied stress (left detector) and perpendicular to the applied stress (right detector). In TOF measurements, the geometry is fixed and a whole diffraction pattern is recorded in each detector. In CW measurements, the detectors are either position sensitive or are scanned over a small range whilst the sample is scanned at half the angular rotation speed of the detectors. Only one type of diffraction peak is recorded.

but for one *hkl* only. A wavelength change is required to bring other *hkl* into alignment with the detectors. TOF instruments (e.g. ENGIN-X at ISIS) have the advantage of fixed geometry over a wide range of d-spacing. This allows the determination of diffraction elastic compliances for a large number of peaks simultaneously.

Third, in order to avoid the introduction of errors into the computed $\langle \sigma'_{rt} \rangle$, it is necessary to determine the $\langle s'_{pqrt} \rangle$ very accurately. The greatest precision currently available with neutrons is obtained using the instrument HRPD at ISIS although it is not specifically configured for such measurements. Dedicated instruments such as ENGIN-X at ISIS and SALSA at ILL have slightly lesser resolution, however, with careful experimental and analytical techniques, excellent results are obtained.

Expansion of eqn (11.28) shows that $\langle s'_{1111} \rangle$ and $\langle s'_{1133} \rangle$ are insufficient to resolve complex stress states completely and so this method relies heavily on the experience of the user and geometrical considerations to identify the principal axes. One approach is to expand eqn (11.28) and search for diffraction peaks that are insensitive to the anisotropy (see §11.3.4).

11.3.3 Computation of $\langle s'_{pqrt} \rangle_{hkl}$

Formally, eqn (11.26) is all that is required to relate the elastic compliance of a single crystallite along a specific scattering vector *hkl* to the single crystal compliances. However, just as the macroscopic elastic modulus (Young's modulus) E was influenced by the micromechanical state of the polycrystal in §11.1.3, so too are the diffraction elastic constants. Equations such as (11.27) need to be averaged for rotation ϕ about the scattering vector. In the presence of texturing, the average needs to be weighted by the ODF. The same cases examined in §11.1.3 can be considered.

The uniform strain model

First, the Voigt or uniform strain case may be taken directly from eqns (11.12) by equating

$$\langle s'_{1111} \rangle = \frac{1}{E} \quad \text{and} \quad \langle s'_{1133} \rangle = \frac{-\nu}{E} \tag{11.34}$$

The result is isotropic and may be used in the same way as experimentally determined values of $\langle s'_{1111} \rangle$ and $\langle s'_{1133} \rangle$ (see §11.3.2). It is insensitive to texture and readily applied. Unfortunately, few if any materials behave in this way and so the uniform strain model is not often applicable.

The uniform stress model

The Reuss or uniform *stress* approximation provides the other limiting case. To deal with this case we take compliances such as given in equations such as (11.27) and perform an average over ϕ, corresponding to rotation of crystallites about the scattering vector. In the absence of texture, the averaging reduces to simple integration – the ϕ-dependent terms in eqn (11.27), namely $\cos^2\phi$ and $\sin 2\phi$ average to $1/2$ and 0, respectively. The final results for two components of $\langle s'_{pqrt}\rangle$ and cubic symmetry are then

$$\langle s'_{1111}\rangle = \frac{\left[(h^4+k^4+l^4)s_{11} + (k^2l^2+h^2l^2+h^2k^2)(2s_{11}+s_{44})\right]}{(h^2+k^2+l^2)^2}$$

$$\langle s'_{1133}\rangle = \frac{\left[\begin{array}{l}(k^2l^2+h^2l^2+h^2k^2)(s_{11}-s_{44}/2)\\ \quad +(h^4+k^4+l^4+k^2l^2+h^2l^2+h^2k^2)s_{12}\end{array}\right]}{(h^2+k^2+l^2)^2} \tag{11.35}$$

Results for symmetries down to orthorhombic are given in Howard and Kisi (1999). Results for monoclinic and triclinic symmetries may be obtained from Singh *et al.* (1998) by applying the relationships given by Howard and Kisi (1999).

It is worth pausing to note the effects of different kinds of anisotropy. In a cubic material, the only anisotropy permitted is 'shear' anisotropy, that is, $s_{44} \neq 2(s_{11} - s_{12})$. If we evaluate the expression in eqn (11.35) for steels, using the s_{pq} for Fe, the results given in Table 11.3 are obtained.

Several things are noteworthy in these results. First, the $\langle s'_{1111}\rangle$ are much larger in magnitude than the $\langle s'_{1133}\rangle$ indicating a greater response (on average $1/\nu$ or $\sim$3 for metals). Second, they are of opposite sign(the Poisson effect). Third, the $\langle s'_{1111}\rangle$ are anisotropic by a factor of $\sim$2.4 (i.e. 8.41/3.53) whereas among the $\langle s'_{1133}\rangle$, the

Table 11.3 Diffraction elastic compliances for steels (10^{-12} Pa^{-1}) computed from the single crystal elastic constants for iron, in the Reuss approximation.

hkl	$\langle s'_{1111}\rangle$	$\langle s'_{1133}\rangle$
110	4.75	−1.39
200	8.41	−3.22
211	4.75	−1.39
220	4.75	−1.39
310	7.09	−2.56
222	3.53	−7.78
321	4.75	−1.39
400	8.41	−3.22
Macroscopic constants	$\frac{1}{E} = 4.878$	$\frac{-\nu}{E} = -1.61$

anisotropy is ~5.6 indicating that, despite an overall lower response, $\langle s'_{1133}\rangle$ is far more sensitive to anisotropic effects in this case. Fourth, in iron, s_{44} is much smaller than $2(s_{11} - s_{12})$ indicating that the material is 'stiff' in shear. This fact is visible in the computed $\langle s'_{1111}\rangle$ where 222 is the least compliant (stiffest) and axial peaks such as 200 and 400 are most compliant. The trend is reversed in the $\langle s'_{1133}\rangle$.

In lower symmetry materials, there is the possibility of 'axial anisotropy' in addition to shear anisotropy. For example, in a material belonging to the tetragonal crystal classes $4mm$, $\bar{4}2m$, 422, and $4/mmm$ there are six single crystal elastic constants, s_{11}, s_{33}, s_{12}, s_{13}, s_{44}, and s_{66}. The shear anisotropy conditions are

$$s_{66} \neq 2(s_{11} - s_{12}) \quad \text{and} \quad s_{44} \neq 2(s_{33} - s_{13}) \tag{11.36}$$

Axial anisotropy is indicated by

$$s_{11} \neq s_{33} \tag{11.37}$$

which leads to pairs of similar peaks (e.g. 200, 002) behaving differently.

So far we have only computed two components of $\left\langle s'_{pqrt}\right\rangle$ ($\langle s'_{1111}\rangle$ and $\langle s'_{1133}\rangle$); however, the other elements may be computed using the methods outlined in §11.2.2, followed by appropriate averaging about the scattering vector. In our cubic example, the only missing element is $\langle s'_{44}\rangle = 4\langle s'_{2323}\rangle$. Taking the 110 peak, for example, $\langle s'_{2323}\rangle = 5.68 \times 10^{-12}$ Pa^{-1}, giving a compliance tensor in matrix form:

$$\left[\langle s'_{mn}\rangle_{110}\right] = \begin{bmatrix} 4.75 & -1.39 & -1.39 & 0 & 0 & 0 \\ -1.39 & 4.75 & -1.39 & 0 & 0 & 0 \\ -1.39 & -1.39 & 4.75 & 0 & 0 & 0 \\ 0 & 0 & 0 & 22.7 & 0 & 0 \\ 0 & 0 & 0 & 0 & 22.7 & 0 \\ 0 & 0 & 0 & 0 & 0 & 22.7 \end{bmatrix} \tag{11.38}$$

with units 10^{-12} Pa^{-1}. This may now be used to determine $\langle \sigma'_{rt}\rangle$ using the appropriate form of eqn (11.28).

The effect of sample texture

The integration of equations such as (11.27) has, so far, been conducted on the assumption that the crystallites are completely randomly oriented. We have already noted that the compliance s'_{1111} is independent of the rotation of a crystal around the scattering vector, so we would expect that the measured compliance $\langle s'_{11}\rangle$ would be largely unaffected by texture. For the others, ignoring texture has allowed a convenient but rather arbitrary choice of coordinate system for the tensor transformations, then a simple arithmetic mean or unweighted integral about the scattering vector. The influence of sample texture is to make the macroscopic behaviour of the

solid anisotropic. To fully account for the influence of texture, it is first necessary to determine the ODF from suitably measured pole figures using a four-circle single crystal neutron diffractometer or perhaps one of the powder diffraction techniques outlined in §9.8. Integration about the scattering vector now generally needs to be weighted by pole densities obtained from the ODF for the appropriate integration path. The orientation of the sample texture with respect to the laboratory coordinate axes x', y', z' must be known and properly accounted for in the computation.

A considerable simplification is possible if the texture is one-dimensional – for example, as is usually the case in wires, rods, and solid cylinders.[176] In that case the ODF may be reasonably approximated by a one-dimensional pole density function such as the March function used in §5.5.2 to correct for preferred orientation in powder samples and in §9.8 to model simple textures. The March function describes the distribution of a single preferred orientation vector [*HKL*] as a function of angle,Φ, to the cylinder axis

$$P_{HKL}(\Phi) = (R^2 \cos^2 \Phi + R^{-1} \sin^2 \Phi)^{-\frac{3}{2}} \tag{5.29}$$

where R describes the degree of texture around a neutral value at $R = 1$. An example of March function texture was shown in Fig. 9.39.

To be specific, we consider the computation of $\langle s'_{1133} \rangle$ for the situation in which the applied stress is along the cylinder axis, that is along the reference direction for the March function distribution of the [*HKL*]. Now, the double-primed axes [see eqn (11.23)] are chosen such that

x'' is parallel to the scattering vector [*hkl*] as before
y'' is perpendicular to both x'' and to the preferred orientation vector [*HKL*], that is, as given by the vector product [*HKL*] × [*hkl*] except when [*HKL*] and [*hkl*] are parallel. (In that case, the original choices are satisfactory).
z'' completes the right-handed orthogonal set.

In the cubic case, we have

$$\begin{aligned}
\boldsymbol{i}'' &= \frac{h\boldsymbol{i} + k\boldsymbol{j} + l\boldsymbol{k}}{(h^2 + k^2 + l^2)^{1/2}} \\
\boldsymbol{j}'' &= \frac{(Kl - Lk)\boldsymbol{i} + (Lh - Hl)\boldsymbol{j} + (Hk - Kh)\boldsymbol{k}}{(h^2 + k^2 + l^2)^{1/2}(H^2 + K^2 + L^2)^{1/2}} \\
\boldsymbol{k}'' &= \frac{\begin{aligned}(k^2H + l^2H - hkK - hlL)\boldsymbol{i} + (h^2K + l^2K - hkH - klL)\boldsymbol{j} \\ +(h^2L + k^2L - hlH - klK)\boldsymbol{k}\end{aligned}}{(h^2 + k^2 + l^2)(H^2 + K^2 + L^2)^{1/2}}
\end{aligned} \tag{11.39}$$

[176] Depending on the manufacturing technique.

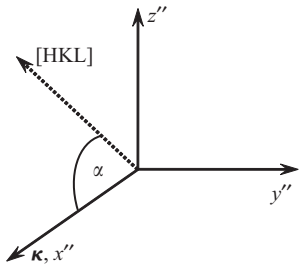

Fig. 11.11 Choice of the double-primed axes used to compute diffraction elastic constants under the March model for one-dimensional texture.

and, writing the coefficients in eqn (11.39) as the elements of a 3 × 3 matrix $\boldsymbol{M}$:

$$\begin{pmatrix} \boldsymbol{i}' \\ \boldsymbol{j}' \\ \boldsymbol{k}' \end{pmatrix} = \begin{pmatrix} 1 & 0 & 0 \\ 0 & \cos\phi & -\sin\phi \\ 0 & \sin\phi & \cos\phi \end{pmatrix} \begin{pmatrix} M_{11} & M_{12} & M_{13} \\ M_{21} & M_{22} & M_{23} \\ M_{31} & M_{32} & M_{33} \end{pmatrix} \begin{pmatrix} \boldsymbol{i} \\ \boldsymbol{j} \\ \boldsymbol{k} \end{pmatrix}$$
$$= \begin{pmatrix} M_{11} & M_{12} & M_{13} \\ M_{21}\cos\phi - M_{31}\sin\phi & M_{22}\cos\phi - M_{32}\sin\phi & M_{23}\cos\phi - M_{33}\sin\phi \\ M_{21}\sin\phi + M_{31}\cos\phi & M_{22}\sin\phi + M_{32}\cos\phi & M_{23}\sin\phi + M_{33}\cos\phi \end{pmatrix} \begin{pmatrix} \boldsymbol{i} \\ \boldsymbol{j} \\ \boldsymbol{k} \end{pmatrix} \tag{11.40}$$

This provides a revised set (a_{mn}) of direction cosines, and the compliances are transformed using eqn (11.26) as before. Using the double-primed system defined above, [HKL] will lie in the x''–z''plane (see Fig. 11.11). From a particular angle ϕ between $z''$and the laboratory axis z' and the known angle, say α, between [HKL] and [hkl], the angle Φ that [HKL] makes with z' is readily calculated, $\Phi = \cos^{-1}(\sin\alpha\cos\phi)$. The probability of occurrence of this angle Φ, as given by the March function eqn (5.29), is used to weight the particular value of ϕ in the final averaging.

The VRH model

As outlined in §11.2, the simplest method to model more complex micromechanical states is to merely take the mean of the Voigt and Reuss models to obtain the VRH model. There is no simplified analytical form for the average. In applying this method to the computation of $\langle s'_{pqrt}\rangle$ (or $\langle c'_{pqrt}\rangle$), it is first necessary to compute individually $\langle s'_{pqrt}\rangle^{\text{Voigt}}$ (reckoned as the inverse of $\langle c'_{pqrt}\rangle^{\text{Voigt}}$) and $\langle s'_{pqrt}\rangle^{\text{Reuss}}$ (corrected for texture if necessary) and then average them to give $\langle s'_{pqrt}\rangle^{\text{VRH}}$. As an

Table 11.4 Comparison of $\langle s'_{1111}\rangle$ and $\langle s'_{1133}\rangle$ using the Reuss, Voigt, and VRH models for Fe. Entries again in units of (10^{-12} Pa^{-1}).

hkl	$\langle s'_{1111}\rangle^{\text{Reuss}}$	$\langle s'_{1111}\rangle^{\text{Voigt}}$	$\langle s'_{1111}\rangle^{\text{VRH}}$	$\langle s'_{1133}\rangle^{\text{Reuss}}$	$\langle s'_{1133}\rangle^{\text{Voigt}}$	$\langle s'_{1133}\rangle^{\text{VRH}}$
110	4.75	4.50	4.63	−1.39	−1.26	−1.33
200	8.41	4.50	6.46	−3.22	−1.26	−2.24
310	7.09	4.50	5.80	−2.56	−1.26	−1.91
222	3.53	4.50	4.02	−7.78	−1.26	−4.52

example, the values of $\langle s'_{1111}\rangle^{\text{Reuss}}$ and $\langle s'_{1133}\rangle^{\text{Reuss}}$ given in Table 11.3 are compared with $\langle s'_{1111}\rangle^{\text{Voigt}}$ and $\langle s'_{1111}\rangle^{\text{VRH}}$ (and corresponding for $\langle s'_{1133}\rangle$) in Table 11.4.[177]

Obviously, the averaging process has the greatest effect on those *hkl* for which $\langle s'_{pqrt}\rangle^{\text{Reuss}}$ is most different from the isotropic (Voigt) value. Within the sample this may be understood to arise because it is in these directions that the strain singularities inherent to the Reuss model are greatest (see §11.1.3) and the constraining effect of the surrounding crystallites will be greatest. Note also that *hhl* peaks such as 110 are little affected by the micromechanical model used. This latter point will be developed in §11.3.4.

Geo

The geometric mean approach or 'Geo' described by Matthies and Humbert (1995) and Matthies *et al.* (2001) may also be applied to the computation of $\langle s'_{pqrt}\rangle$. The presumption here is that the compliances should be evaluated by taking the logarithms of expressions such as (11.27), averaging these logarithms over pertinent values of ϕ, then taking the exponential of the result [*cf.* eqn (11.16)].

The Kröner or self-consistent model

The calculation of diffraction elastic models according to the Kröner self-consistent model is best understood by referring to eqn (11.21) in §11.1.3. We recall that the elastic compliances of the polycrystalline assembly, $\bar{S}^{\text{Kröner}}_{mnop}$, are determined by the condition that the weighted averages of the tensor elements $t'_{mnop}(\Omega)$ over all crystallite orientations are zero. Diffraction elastic constants, such as $\langle s'_{1111}\rangle^{\text{Kröner}}$ and $\langle s'_{1133}\rangle^{\text{Kröner}}$, are obtained from the same equation by averaging the appropriate $t'_{mnop}(\Omega)$, say $t'_{1111}(\Omega)$ or $t'_{1133}(\Omega)$, not over all orientations of the crystallites Ω, but just those that satisfy the Bragg condition for the reflection, *hkl*, of interest. The results for untextured polycrystalline samples comprising crystals of cubic or hexagonal symmetry have been given by Hauk and co-workers

[177] Only unique values of $\langle s'_{1111}\rangle$ are given (e.g. 211 is the same as 110, etc.).

(Bollenrath *et al.* 1967; Evenschor and Hauk 1972). The method can be applied in the presence of texture by weighting the averages using the ODF (Carr *et al.* 2004) or one-dimensional pole density function where it is known (Hirsekorn 1990; Mura 1991).

Overview

In the preceding sections, several micromechanical models have been described which may be used to compute $\langle s'_{pqrt} \rangle_{hkl}$ suitable for residual stress determination. A considerable amount of research effort has been expended on the development and testing of the different models. Comparisons between models are best conducted using model materials with extreme elastic anisotropy. One example is the calculations performed on biotite, an extremely anisotropic material, by Matthies and Humbert (1995). Figure 11.12 is reproduced from their work and shows the variation of the macroscopic compliance (inverse of Young's modulus) with the texture sharpness (see Matthies and Humbert 1995) and the micromechanical model. The Voigt and Reuss values differ by a factor of nearly three in the random polycrystal case; however, the other models cluster near the centre. Of the three tightly clustered models (self-consistent, Geometric mean, and Super VRH), the computationally simpler Super VRH gives answers very similar to the other, computationally intensive models.

For materials with less extreme anisotropy (such as Fe, Table 11.2), the different models are unlikely to be resolvable in the presence of sample variations, measurement errors, and uncertainty in the sample texture as are encountered in

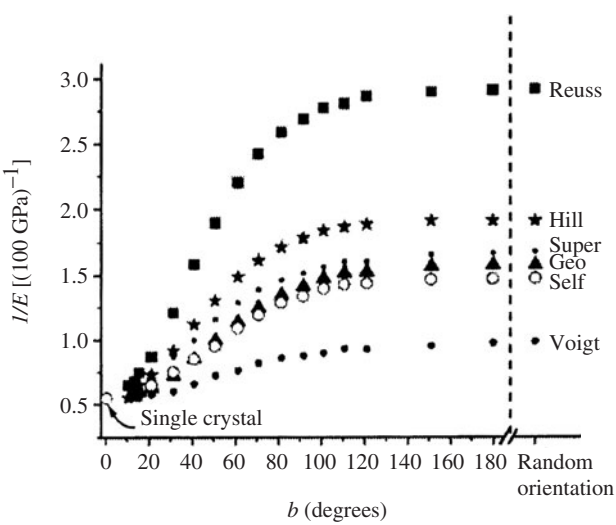

Fig. 11.12 Figure 1 of Matthies *et al.* (2001), illustrating the relative results for calculated Young's modulus using the various micromechanical models and texture effects simulated by rotation of a single crystal through an angle *b*.

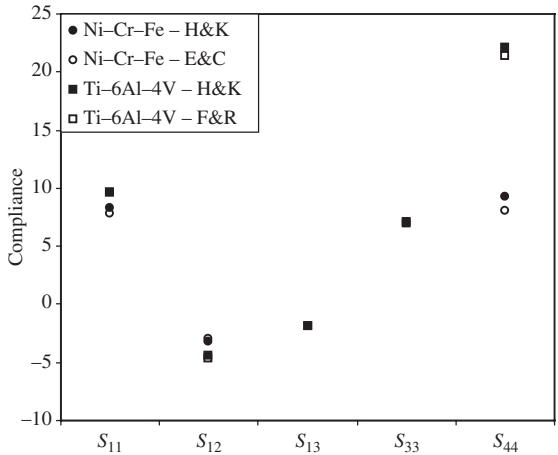

Fig. 11.13 Comparison of the known single crystal elastic compliances for two ductile materials (open symbols, Epstein and Carlson 1967) with those computed under the Reuss approximation using the measured diffraction elastic constants of Butler *et al.* (1989) (solid symbols) by Howard and Kisi (1999). Units are 10^{-12} Pa^{-1}.

experimental data. It is tempting to suggest that this is one reason why no clear consensus on the 'best' model has yet been made.

The diffraction elastic constants are more model sensitive and so offer more prospect for distinguishing between them. We show in Fig. 11.13 that the observed diffraction elastic constants for some metallic materials conform quite closely to the Reuss approximation. Ceramics and minerals on the other hand appear to conform more closely to models that lie between the Reuss and Voigt limits. Therefore, we feel that the key question to be answered in this field is not which micromechanical model is the *best*, but what factor(s) determines the behaviour of particular classes of polycrystals. It has been suggested (Howard and Kisi 1999) that in metals, localized plastic (or anelastic) deformation at stress concentrations accommodates the strain mismatch required under the Reuss model and allows the polycrystal to behave as though in a state of uniform stress. As the ductility of the material decreases (e.g. fcc → cph → bcc metals, hardened steels, ceramics, etc.) localized plasticity becomes more difficult and there is a corresponding shift in the micromechanical model required. This means that a model yielding satisfactory values of $\langle s'_{pqrt} \rangle$ for Fe may be useless for hard iron-based alloys such as Martensitic steels. Further experimentation is required to clarify and quantify this area.

11.3.4 Pseudo-isotropy

In §11.3.2 we explored experimental approaches to determining values for $\langle s'_{pqrt} \rangle$ and in §11.3.3 we saw that computing reliable values of $\langle s'_{pqrt} \rangle$ involves investigating the sample texture as well as a complex calculation based on an assumed micromechanical model. A gleam of hope may be found for the practically oriented reader in the example computations presented in Table 11.4, where it can be noted that whilst $\langle s'_{pqrt} \rangle_{200}$ and $\langle s'_{pqrt} \rangle_{310}$ are very sensitive to the chosen model, $\langle s'_{pqrt} \rangle_{110}$ is relatively insensitive to the model used. By choosing a model guided by previous experience, by considering the ductility of the sample as suggested in the previous section, by comparison of a small number of measured $\langle s'_{pqrt} \rangle$ (see §11.3.2) with the computed values (§11.3.3), or by comparison of the measured E with values computed using the different models, systematic errors due to the choice of micromechanical model can be restricted to $\leq$1%–2%. For the practical purpose of determining residual stress, errors of this magnitude may be considered negligible.

The procedure adopted is then to

1. Compute $\langle s'_{pqrt} \rangle$ for various *hkl* using the Voigt and Reuss limits.
2. Select *hkl* for which $\langle s'_{pqrt} \rangle$ are relatively model insensitive.[178]
3. Select a model to use (see above).
4. Compute $\langle s'_{1111} \rangle$, $\langle s'_{1133} \rangle$ using the chosen model.
5. Proceed as if the sample was isotropic, that is, $s_{44} = 2(s_{11} - s_{12})$.
6. Solve eqn (11.28) $\langle \varepsilon'_{pq} \rangle = \langle s'_{pqrt} \rangle \langle \sigma'_{rt} \rangle$ for the residual stresses $\langle \sigma'_{rt} \rangle$.
7. If necessary, diagonalize $\langle \sigma'_{rt} \rangle$ to obtain the principal stresses.

11.3.5 Experimental considerations and examples

The general layout of diffractometers for residual stress determinations was shown earlier in Fig. 11.10. Instruments for this purpose need to have a very large sample stage, capable of taking the mass of very large engineering components. In addition, to allow strain measurements along an arbitrary direction in the component, the sample stage needs to be equipped with a one- or two-axis goniometer in conjunction with a two- or three-direction translation stage.

The diffractometers are arranged to explore a well-defined region within the sample, termed the 'gauge volume'. The gauge volume is usually defined by collimators in both the incident and diffracted beams. As illustrated in Fig. 11.14, the intersection of the beams allowed by the two slits defines a three-dimensional region within the sample. If square incident and diffracted beam collimators are combined with a Bragg angle of 90°, then the gauge volume is a cube. With neutron diffraction, the gauge volume may be quite large ($\sim$1 cm^3) to ensure sufficient diffracted intensity in a relatively short time; however, most dedicated

[178] If good data for several *hkl* are available (e.g. from TOF) least squares fitting should be used to obtain the best result.

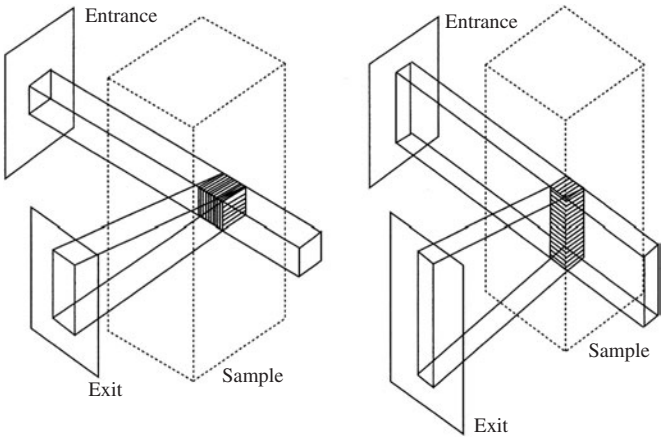

Fig. 11.14 Illustrating how the three-dimensional gauge volume is defined using slits in neutron diffraction residual stress analysis (Pintschovius 2003).

residual stress instruments (e.g. ENGIN-X at ISIS, SALSA at ILL, or KOWARI at the OPAL reactor in Australia) can sample gauge volumes as low as 1 mm^3. Whilst smaller gauge volumes allow the sampling of sharper strain (and residual stress) gradients, there is a practical limit below which the accuracy of the measurements is compromised. The limiting size (assuming sufficient neutron flux and detection capacity to give meaningful data) is determined by the number of crystallites sampled. Therefore, it is determined by the grain or crystallite size in the polycrystal (Matthies *et al.* 2001). As was demonstrated in §11.3.3, the diffraction elastic constants represent averages over ensembles of crystallites. A meaningful sample of the ensemble requires several hundred crystallites to be both within the gauge volume *and* oriented for diffraction by the planes (*hkl*). By allowing reasonable values for the radial and axial beam divergences (0.2° and 5°), we see that only $\sim 0.5 \times 10^{-4}$ of the crystallites in a random polycrystal will be oriented for diffraction. Therefore, a gauge volume containing 10^7 crystallites is required in order for 500 crystallites to diffract at an arbitrary sample setting. If the sample is textured, even greater numbers of crystallites, say 10^8, are necessary to avoid unrepresentative data in directions with a low pole density for the *hkl* of interest. This equates to a crystallite volume of 10 μm^3 or ~ 2 μm crystallite diameter with a gauge volume of 1 mm^3.

Certain economies of effort can be achieved by careful choice of the sample alignment. For example, if the sample has an axis of symmetry then the symmetry axis should be aligned with one of the axes of the laboratory coordinate system $x', y',$ or z'.[179] Additional symmetry axes can be aligned with other axes if possible.

[179] We previously took x' to lie along the (horizontal) scattering vector, z' to be vertical, and y' to complete the orthogonal set.

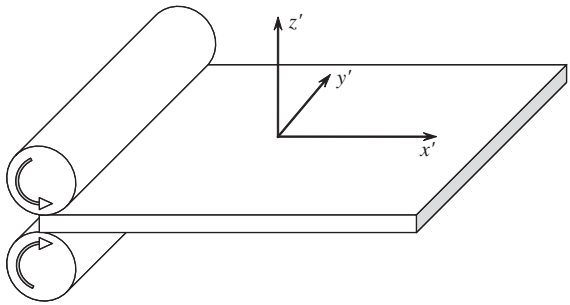

Fig. 11.15 Definition of axes used in the discussion of residual stress in a rolled sheet of metal.

For example, consider a rolled metal sheet. The rolling direction gives an important reference direction. The sheet itself has cylindrical symmetry about the sheet normal, however, the sheet texture does not. The texture will have mirror symmetry about a plane perpendicular to the sheet surface and parallel to the rolling direction. A suitable alignment of the sample in this case is z' perpendicular to the sheet surface, x' parallel to the rolling direction, and y' in the plane of the sheet and perpendicular to the rolling direction (and hence x' and z') as shown in Fig. 11.15. The mirror symmetry means that strain measurements need only be taken on one side of the sheet centre. These axes will almost certainly coincide with the principal stresses and so diagonalization of the stress tensor will not be required. Finally, in order to record all of the principal strains, it is only necessary to permute the axes.

A further consideration in the practical application of neutron diffraction residual stress analysis is the so-called d^0 problem. This arises because the strain determination [eqn (11.22)] relies on a knowledge of d^0_{hkl}. Since d_{hkl} can be altered by a number of factors (elements in solid solution, residual stress, etc.), and these factors will differ for very similar materials given slightly different treatments (fabrication methods, heat treatments, etc.), the appropriate d^0_{hkl} value to use in a given situation is far from obvious. It is sometimes possible to determine d^0 from an independent measurement on part of the sample that contains no residual stresses or has been deliberately unloaded by sectioning or annealing. The determination needs to be made as precisely (i.e. at the highest available resolution) and accurately (i.e. correcting for systematic errors – see Chapter 4) as possible. An accuracy of at least one part in 10^4 is considered necessary (see Noyan and Cohen 1987; Matthies *et al.* 2001). Another approach is to include the zero stress lattice parameters as an unknown in the determination. The decision to adopt this approach *must* be made before recording the experimental data as it seriously influences the experimental plan. Take, for example, the simplest case – a sample comprising a material with a cubic crystal structure for which, probably by virtue of its geometry, the directions of the principal axes of stress are known and can be

aligned with laboratory axes. The principal strains are

$$\begin{aligned}\varepsilon'_{11} &= s'_{1111}\sigma'_{11} + s'_{1122}(\sigma'_{22} + \sigma'_{33})\\ \varepsilon'_{22} &= s'_{1111}\sigma'_{22} + s'_{1122}(\sigma'_{11} + \sigma'_{33})\\ \varepsilon'_{33} &= s'_{1111}\sigma'_{33} + s'_{1122}(\sigma'_{22} + \sigma'_{11})\end{aligned} \tag{11.41}$$

rewriting eqn (11.22) as

$$d = d^0(\varepsilon + 1) \tag{11.42}$$

and applying it to a chosen diffraction peak *hkl*, we get equations such as

$$\begin{aligned}d^1_{hkl} &= d^0_{hkl}\left[s'_{1111(hkl)}\sigma'_{11} + s'_{1122(hkl)}(\sigma'_{22} + \sigma'_{33}) + 1\right]\\ d^2_{hkl} &= d^0_{hkl}\left[s'_{1111(hkl)}\sigma'_{22} + s'_{1122(hkl)}(\sigma'_{11} + \sigma'_{33}) + 1\right]\\ d^3_{hkl} &= d^0_{hkl}\left[s'_{1111(hkl)}\sigma'_{33} + s'_{1122(hkl)}(\sigma'_{22} + \sigma'_{33}) + 1\right]\end{aligned} \tag{11.43}$$

If d^0_{hkl} is known, it is straightforward to extract the unknowns $\sigma'_{11}, \sigma'_{22}, \sigma'_{33}$ from measurements of the d-spacings of a single *hkl* reflection measured in the three principal directions. However, if d^0_{hkl} is also unknown, additional peaks need to be sampled and the results combined via the relationship between d^0_{hkl} and the lattice parameters (a^0, b^0, c^0, α, β, γ – see §2.4.1); in this cubic case

$$d^0_{hkl} = \frac{a_0}{\sqrt{h^2 + k^2 + l^2}} \tag{11.44}$$

By considering the lattice parameter – d-spacing relationships, it becomes apparent that the number of peaks to be sampled rapidly increases as the symmetry is lowered. Additional confidence in the resulting stresses can be obtained by taking measurements in additional orientations, especially if the directions of the principal strains are not known beforehand.

Subject to the statistical requirements of the gauge volume (see above), it is possible by using a small gauge volume to conduct one-, two-, or three-dimensional mapping of residual strains and stresses (strain scanning). This makes it possible to follow residual stress fields with depth in large objects as well as laterally. Consider the example shown in Fig. 11.16 of neutron diffraction strain scanning of a fillet weld in an austenitic stainless steel before and after a post-weld heat treatment. Symmetry allows all of the required information to be obtained in a two-dimensional scan and the lack of any significant variation with depth allowed the results to be plotted one-dimensionally (Spooner 2003). The distance scale is centred on the weld centre and in the un-heat-treated weld [Fig. 11.16(a)] shows a large longitudinal tensile strain in the weld metal which then becomes compressive in the parent metal. The transverse and normal strains are smaller and the normal strain is inverted (i.e. compressive in the weld and tensile in the parent material). The largest strains shown correspond to stresses of ~360 MPa – the approximate

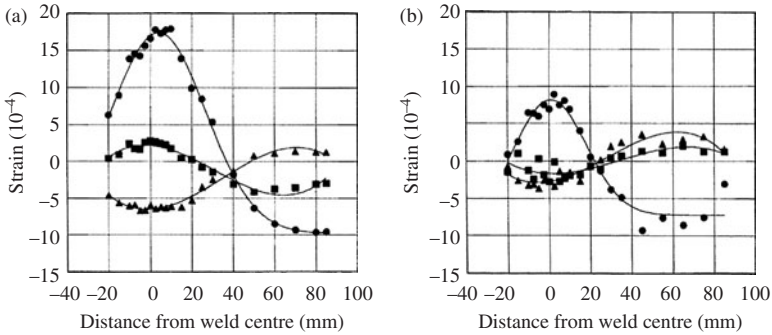

Fig. 11.16 Results of neutron diffraction strain scanning of a fillet weld in an austenitic stainless steel (a) before and (b) after a post-weld heat treatment. Shown are the longitudinal (•), transverse (■) and normal (▲) strains. The largest strains shown correspond to stresses of 360 MPa – the approximate yield strength of the material (Spooner 2003).

yield strength of the material. It can be seen in Fig. 11.16(b) that a post-weld heat treatment reduced the longitudinal residual stresses by about a half and reduced the others to negligible levels.

11.4 DETERMINATION OF SINGLE CRYSTAL ELASTIC CONSTANTS FROM POLYCRYSTALLINE SAMPLES

11.4.1 Single crystal elastic constants

The single crystal elastic constants c_{pqrt} (and s_{pqrt}) determine the response of a crystal not only to a mechanical disturbance (stress) but also to a wide range of other perturbations including temperature (thermal expansion), electric field (piezo-electric coefficients, electrostriction) and magnetic fields (magneto-striction). The mechanical behaviour of individual crystals and ensembles of crystals is critical in determining the fracture toughness of engineering materials and the behaviour of large geotechnical masses.

Single crystal elastic constants are generally measured by determining the longitudinal acoustic wave speed in several directions through large single crystals and solving simultaneously to obtain c_{pqrt} or by analogous acoustic resonance methods. This is only possible once methodologies have been developed for growing large single crystals of the particular material of interest. For many technologically important materials, the growth of large single crystals is not possible due to their complex chemistry (often many elements are present in solid solution). In addition, engineering materials are far too numerous to allow for crystal growth and acoustic measurement of all of them. Many materials of engineering interest are not only polycrystalline but also multi-phase (see §2.2.2). For materials such as these, acoustic methods give only the isotropic average moduli (E, ν) of the ensemble present. The isotropic average moduli are a poor reflection of the single crystal elastic constants. This can be seen in Table 11.5 by a comparison of two cubic

Table 11.5 Comparison of single crystal elastic constants for two cubic materials.

Material	E (GPa)	c_{1111} (GPa)	c_{1122} (GPa)	c_{1212} (GPa)
Fe	205	230	135	114
c-ZrO_2	200	394	91	56

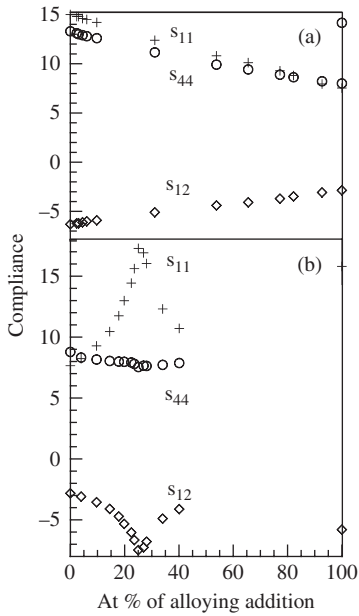

Fig. 11.17 The effect of alloying on single crystal elastic compliances (in units 10^{-12} Pa^{-1}) for (a) Cu–Ni and (b) Fe–Al.

materials, iron and cubic zirconia. They have very similar Young's modulus, E, yet their c_{pqrt} are quite different.

The single crystal elastic constants can also be influenced to a great degree by alloying to form solid solutions. This is illustrated in two cases by Fig. 11.17. In Fig. 11.17(a), which refers to Cu–Ni alloys, intermediate compositions have elastic constants that are a linear combination of those of the constituent elements. On the other hand, for the Fe–Al system, the behaviour [Fig. 11.17(b)] is far from linear. Theories of alloying and bonding in metals are too poorly developed to predict this behaviour for a new material.

It would evidently be advantageous to have a technique for the determination of single crystal elastic constants from readily available polycrystalline samples. Quite some time ago it was realized (Hauk and Kockelmann 1979; Hayakawa *et al.*

1985) that, in favourable circumstances, some of the single crystal constants could be evaluated from the diffraction elastic constants, that is, from strains measured by diffraction at known values of applied stress. Subsequently, several groups have published applications (Kisi and Howard 1998), variations (Bittorf *et al.* 1998; Gnäupel-Herold *et al.* 1998), extensions to non-cubic materials (Howard and Kisi 1999), and commentaries on the technique (Matthies *et al.* 2001). The method, its applications, and its limitations will be explored in the subsequent sections.

11.4.2 Theoretical considerations

The basis of the method is eqn (11.28), that is, Hooke's law for a generalized anisotropic crystal:

$$\langle \varepsilon'_{pq} \rangle_{hkl} = \langle s'_{pqrt} \rangle_{hkl} \langle \sigma'_{rt} \rangle \tag{11.28}$$

where $\langle \varepsilon'_{pq} \rangle_{hkl}$ is the strain measured by diffraction from planes (hkl), $\langle s'_{pqrt} \rangle_{hkl}$ is the mean elastic compliance, and $\langle \sigma'_{rt} \rangle$ represents the applied stress(es). It should be recalled from §11.3.3 that the evaluation of $\langle s'_{pqrt} \rangle_{hkl}$ requires a knowledge of the micromechanical state of the polycrystalline sample or an assumed model (Voigt, Reuss, VRH, Geo, Kröner), as well as knowledge of the sample texture if one exists.

11.4.3 Experimental considerations and examples

In eqn (11.28) $\langle \varepsilon'_{pq} \rangle_{hkl}$ and $\langle \sigma'_{rt} \rangle$ will be measured or known. To simplify the determinations, it is best to apply the stress either along or perpendicular to the scattering vector. Let us assume for now that we have first applied various stresses to a sample in the arrangement shown in Fig. 11.10. To illustrate we will consider a Ce-doped tetragonal zirconia polycrystal (Ce-TZP) at stresses up to 1.2 GPa (Kisi and Howard 1998). Diffraction patterns were recorded at 100 MPa intervals from zero to 1.2 GPa. Individual peak fits were used to obtain d-spacings as a function of applied stress for 12 peaks. The results are shown plotted as strains $\left(\varepsilon = (d - d^0)/d^0\right)$ in Fig. 11.5. The slopes of these curves are the diffraction elastic compliances $\langle s'_{pqrt} \rangle_{hkl}$ (specifically $\langle s'_{1133} \rangle_{hkl}$) that could be used for residual stress analysis in this material. Instead, we wish to use them to extract the single crystal elastic compliances s_{pqrt}. Ce-TZP has a degree of plasticity due to ferroelastic reorientation and the stress-induced tetragonal to monoclinic phase transformation and hence it was assumed that the micromechanical state would be Reuss-like. Under this model, the equation relating the diffraction elastic compliances $\langle s'_{pqrt} \rangle_{hkl}$ to the single crystal compliances s_{pqrt} for crystal class 4/*mmm* in

Table 11.6 Single crystal elastic constants of Ce-TZP determined by diffraction and compared with literature values for cubic and monoclinic zirconia.

	Phase					
	c		*t*		*m*	
Reference	3	4	1	2*	5	6
$s_{11}(10^{-12}\ \mathrm{Pa}^{-1})$	2.76	3.4	3.45	7.78	3.45	3.41
s_{22}					3.35	5.03
s_{33}			4.18	4.45	5.37	6.78
s_{44}	16.7	16.8	16.7	17.9	11.4	10.4
s_{55}					15.3	14.7
s_{66}			15.8	8.06	8.73	8.28
s_{12}	−0.56	−1.0	−1.05	−3.58	−1.28	−1.60
s_{13}			−0.57	−1.15	−0.116	0.608
s_{15}					1.73	1.65
s_{23}					−1.78	−3.71
s_{25}					−2.68	−3.19
s_{35}					2.42	3.10
s_{46}					3.42	1.88
c_{11} (GPa)	401	390	334		358	361
c_{22}					426	408
c_{33}			256		240	258
c_{44}	56	60	60		99.1	99.9
c_{55}					78.7	81.2
c_{66}			63		130	126
c_{12}	96	162	112		144	142
c_{13}			61		67	55
c_{15}					−25.9	−21.3
c_{23}					127	196
c_{25}					38.3	31.2
c_{35}					−23.3	−18.2
c_{46}					38.8	−22.7

1. Kisi and Howard (1998); 2. S-K Chan, private communication (1996); 3. Kandil *et al*. (1984); 4. Howard and Kisi (1999); 5. Nevitt *et al*. (1988); 6. Chan *et al*. (1991).
* Estimated from long wavelength limit of lattice dynamical calculations at 1400 K.

contracted notation is

$$\begin{aligned}\langle s'_{13}\rangle = {} & [(K^2L^2 + H^2L^2 + 2H^2K^2)s_{11} + (K^2L^2 + H^2L^2)(s_{33} - s_{44}) \\ & + (H^4 + K^4 + H^2L^2 + K^2L^2)s_{12} + (H^4 + K^4 + 2L^4 + K^2L^2 \\ & + H^2L^2 + 2H^2K^2)s_{13} - H^2K^2s_{66}]/[2(H^2 + K^2 + L^2)^2] \qquad (11.45)\end{aligned}$$

where $H = h/a$, $K = k/b$, $L = l/c$.

It can be seen that using a single experiment and at least five unique diffraction peaks, four of the six single crystal compliances (s_{11}, s_{12}, s_{13}, s_{66}) along with the combination $s_{33} - s_{44}$ can be obtained. To separate s_{33} and s_{44}, Kisi and Howard used the expression for Young's modulus under the Reuss model (eqn (11.14)) to provide the extra relationship. The compliances were optimized against the full data set by least squares fitting of eqns (11.45) and (11.14) to the observed diffraction elastic constants and known Young's modulus. The fitted strain values are shown as solid lines in Fig. 11.5, and the refined elastic constants are given in Table 11.6.

This method, of combining eqn (11.41) with eqn (11.14) (or equivalent for the other micromechanical models), gives all of the single crystal compliances (or elastic constants by matrix inversion) for cubic and tetragonal symmetries. In lower symmetry crystal systems, other more powerful strategies must be employed. Most powerful is to conduct an identical experiment with the applied stress directed parallel to the scattering vector. On TOF instruments with a pair of symmetrical 90° detectors (e.g. ENGIN-X), it is possible to record data in both orientations at once (see §11.3.2), that is the measurements can yield compliances $\langle s'_{13} \rangle$ and $\langle s'_{11} \rangle$ simultaneously.

For the Ce-TZP example (tetragonal) cited above, the equation for the second compliance is

$$\langle s'_{11} \rangle = [(H^4 + K^4)s_{11} + L^4 s_{33} + (H^2L^2 + K^2L^2)(2s_{13} + s_{44}) + H^2K^2(2s_{12} + s_{66})]/(H^2 + K^2 + L^2)^2$$

So the single crystal s_{33}, which cannot be determined from measurement of $\langle s'_{13} \rangle$ alone, can be obtained immediately from measurements of $\langle s'_{11} \rangle$ for $00l$ reflections.

Other means (as yet untried) of determining the full set would be to conduct a supplementary experiment under hydrostatic pressure and use analogous equations for the bulk modulus or a torsion experiment which is therefore in pure shear (Singh *et al.* 1998).

This method of elastic constant determination shows great promise; however, it is far from being universal and it will never replace careful single crystal measurements when suitable crystals are available. The method is only suitable for solid polycrystals (not powders) for which the texture is known and with sufficient strength to remain intact at sufficiently high stresses to show precisely measurable strains (in the range 200–2000 MPa depending on the instrument used and the stiffness of the material). It is also somewhat dependent on the micromechanical state of the sample, which for a material with completely unknown single crystal elastic constants, cannot be independently determined at this stage. As explained earlier, the ductility of the sample might be taken into account, and an analysis of the micromechanical state of similar materials with known elastic constants might also be useful. Further work is required to formulate a model that predicts the micromechanical state of a polycrystal from measurable physical parameters such as hardness, the number of available slip systems and other deformation mechanisms, and so on.

12

New directions

12.1 INTRODUCTION

Neutron powder diffraction is a somewhat mature field, being more than six decades old (§1.3). Nonetheless, human ingenuity is such that advances continue to be made in all areas. These range from the very powerful new neutron sources now being developed (§12.2) through new instrumentation (§12.3, §12.4) to new methods of analysis (§12.5) that in combination indicate a lasting and expanding role for neutron powder diffraction in the study of solid matter (§12.6).

12.2 NEUTRON SOURCES

With only one exception, the new generation of neutron sources rely upon the spallation of neutrons due to the impact of high-energy protons with heavy metal targets. At the time of writing, the world's largest fully functional spallation source is the ISIS facility at the Rutherford Appleton Laboratory in the United Kingdom. It operates with 3 GeV protons at currents up to 200 μA (i.e. 0.6 MW). ISIS is being upgraded to 300 μA (0.9 MW) and expanded to include an additional target station. The new target station will have seven new instruments in Stage 1 and a further expansion in the near future. As yet, none of these new instruments are powder diffractometers.

The capabilities of ISIS will be matched by a new neutron source – the Japanese Spallation Neutron Source (JSNS) – at the J-PARC site in Tokai. The source is expected to begin operation in late 2008 and the initial suite of 10 instruments will be brought into service over the following few years. The source will utilize 3 GeV protons pulsed at 25 Hz with a pulse width of 1 μs and average current 333 μA, giving overall power 1 MW (Arai 2005). Three hydrogen moderators at 20 K will be used to shape the energy spectrum of the incident neutrons. The peak intensity during the pulse is more than 100 times the intensity of the world's most intense reactor neutron source, the High Flux Reactor (HFR) at the Institut Laue-Langevin (ILL, Grenoble, France); however, the time-averaged intensity is 1/4 of the intensity from the cold source at the ILL. The 25-Hz-pulse cycle is ideal for very long instruments such as high-resolution powder diffractometers and very high-energy resolution inelastic scattering spectrometers. The initial suite of 10 instruments includes no less than *three* powder diffractometers with high resolution, high intensity, and residual stress foci, respectively.

The most powerful source under construction is the (American) Spallation Neutron Source (SNS) at Oak Ridge National Laboratory in the United States. Once fully operational (2008), it will operate at 1.4 MW with staged upgrades to an eventual 4 or 5 MW by 2012. This large increase in power over other spallation sources will give the North American neutron scattering community many opportunities for advancement in the areas of increased Q range, faster sample throughput, smaller samples, and increased resolution. The instrument development programme is staged with 15 instruments planned (2006–2011) including two powder diffractometers and a further two of some interest to powder diffraction work.

An even more intense spallation source – the European Spallation Source (ESS) has been discussed for many years however funding has not been forthcoming. The project as proposed has two 5 MW sources from the outset. Detailed engineering design and instrument planning has yet to be undertaken. Instead, European governments have committed funding to upgrading the neutron scattering facilities available at the ISIS spallation source (as discussed above) and existing reactor-based sources. The principal one has been the Millennium (and beyond) upgrade of the instruments at the ILL. Although this has not included any upgrade of the source flux by increasing reactor power (53 MW), considerable effort has been made to increase the use of existing neutron flux by increasing detector coverage, broadening the acceptance solid angle of guides and beam tubes, and so on.

Contrary to the worldwide trend, we note the development of potentially the last reactor neutron source in the world – the OPAL reactor in Australia. OPAL is a multi-purpose reactor, catering for neutron scattering, isotope production, semiconductor irradiation, radiography, and other research functions. The 30-MW reactor has been designed with supermirror neutron guides in order to deliver a neutron flux in excess of the Ni guides in HFR at ILL. The reactor is operational and the initial suite of instruments is undergoing final commissioning at the time of writing. The neutron scattering capability will begin with nine instruments of which three are powder diffractometers (high resolution, high intensity, and residual stress).

12.3 COMPONENTS

The various components used in the assembly of a neutron powder diffractometer – neutron guides, collimators, monochromators, and detectors – have been introduced in Chapter 3. There are continuing technological developments impacting on all of these.

We remarked in Chapter 3 that neutron guides are used to deliver neutrons to instruments located at some considerable distance from the neutron source. The location of CW neutron powder diffractometers is somewhat a matter of choice and convenience, but for TOF neutron diffractometers the resolution is dependent on $\Delta L/L$ [eqn (3.11)] so remote location (e.g. at 50–100 m from source) is critical for achieving high resolution. The transmission of neutrons along guides is dependent

on mirror reflection of neutrons incident upon the guide walls at angles less than the critical angle, which for Ni (coated on to glass) is about 0.1° per Å wavelength. As intimated in Chapter 3, improvements in transmission can now be achieved through the use of 'supermirrors' (Elsenhans *et al.* 1994). These comprise alternate layers of Ni and Ti, each of thickness some tens of nanometres, such that neutrons incident on the topmost layer of Ni at angles slightly greater than critical undergo Bragg reflection, determined by the repeat dimension of the multilayer structure. By this means, the critical angle can be effectively increased by a factor in the range 3–4. Another recent development is the shaping of guide tubes. Whereas the earlier guides were of constant rectangular cross section, a degree of shaping is now sometimes introduced – for example, a tailored reflectivity along with a gradual reduction in cross section toward the sample end can have the effect of concentrating the neutrons at the sample position.

We also mentioned that neutrons could be transported along a gently curved guide: at the ILL, for example, along a 15 cm wide guide of length 90 m with a 2700 m radius of curvature. This geometry can in principle be scaled down to produce a guide 150 μm wide, 90 mm long, and with a 2.7 m radius of curvature. Guides of such dimensions stacked side by side would serve as a neutron bender. This can be realized in practice via a multilayer construction composed of alternating layers of transmitting (e.g. Al, Si) and reflecting (Ni) materials (Mildner *et al.* 1993). Hollow glass capillaries carry neutrons in a similar manner. This miniaturization of guides has potential for the focusing of neutron beams.

Before and after striking the sample, a degree of collimation of the neutrons is required. A great advance in collimator technology was the replacement, about 25 years ago, of the neutron absorbing metal plates by stretched polymer sheets covered with gadolinium paint. These sheets were thinner and flatter than the metal plates, so could be set closer together, resulting in a more compact assembly. Even more compact devices can be constructed by spacing the absorbers with wafers of (neutron transmitting) silicon (Cussen *et al.* 2001).

The monochromator is a critical component of a CW diffractometer. The usual approach (§3.2.1) is to use Ge or Si crystals plastically deformed so as to increase the mosaic spread and hence the wavelength bandpass of the monochromator. The Brookhaven monochromator (Passell *et al.* 1991) would seem to represent the highest form of the art. Thin wafers (∼0.5 mm) of (113) oriented Ge were first plastically deformed, then pressed and brazed together. Twenty-four segments, each 3 cm wide by 1.25 cm high, were cut from this material, and mounted one above the other on a flexible backing. Each segment can be adjusted horizontally for alignment and bending, while vertical focusing can be achieved by adjustment of the flexible backing. An alternate approach advocated by Popovici and co-workers (Popovici and Yelon 1995) is to use judiciously focused bent perfect crystals rather than plastically deformed ones. It is suggested that these can be used to obtain highly focused beams, as may be very well adapted to measurements of residual stress.

A brief outline of the different types of detectors was given in Chapter 3 (§3.2.3, §3.3.2). Detection must start with the inclusion of a neutron absorbing isotope ('converter'), such as the commonly used ^{3}He, ^{6}Li, ^{10}B, or a small number of additional candidates such as ^{157}Gd. The initial signal may be amplified in a gas, in a scintillator, or in a semiconductor. Different arrangements of electrodes may be used to find the position of the detected neutron. Important considerations in modern applications are the data collection rates that can be achieved, and the rate at which the data can be written to storage (§12.4.2). Excellent accounts of detector state-of-the-art are to be found in recent (2006–2007) issues of *Neutron News*, and this publication should be watched for further developments.

12.4 DIFFRACTOMETERS

12.4.1 High-resolution diffractometers

It is proposed that the new TOF High-Resolution Powder Diffractometer at JSNS (J-PARC) in Japan will have the highest resolution of any neutron powder diffractometer in the world ($\Delta d/d = 3 \times 10^{-4}$) and is aimed at equalling in resolution the best synchrotron X-ray powder diffractometers (Arai 2005). This will be achieved by using a 100m flight path (similar to HRPD at ISIS). The instrument will enable the solution and refinement of complex structures hitherto difficult with neutron diffraction. At this resolution, the influence of sample microstructure (Chapter 9) becomes very apparent. It is unlikely that routine samples will show the full instrument resolution as, even with the crystallite size usually considered optimal for powder diffraction ($\sim$2 μm), there is measurable particle size broadening on such an instrument. The original very high-resolution diffractometer (HRPD at ISIS) has benefited from the recent upgrade to the ISIS source and installation of a new neutron guide system (shaped supermirror guide, §12.3) with increases in neutron flux of between 10 and 40 times (depending on wavelength) whilst still maintaining impressive resolution ($\Delta d/d = 4 \times 10^{-4}$). This allows diffraction patterns from routine samples (2 cm^3) to be recorded in just a few minutes for parametric studies (comparable to, or shorter than, the time for temperature equilibration) or a few tens of minutes for structure studies. Another new TOF instrument capable of recording high-resolution patterns is POWGEN3 at SNS. This is not a dedicated high-resolution diffractometer, but rather a general purpose materials science diffractometer that has one high-resolution detector bank capable of recording patterns at $\Delta d/d = 1 \times 10^{-3}$ (see also §12.4.2).

Other developments in high-resolution diffractometers include the commissioning of an upgraded (Super) D2B at the ILL and a similar diffractometer, ECHIDNA, at the OPAL reactor in Australia. These instruments have extended focusing monochromators (in the case of ECHIDNA the doubly focusing Brookhaven monochromator, §12.3) to increase the neutron flux on the sample, high monochromator take-off angles to enhance resolution (see §3.2), and enhanced detector solid angle through the use of 128 azimuthally aligned linear position sensitive detectors

in an array at 1.25° separation. The detector only needs to be scanned 1.25° to record an entire two-dimensional diffraction pattern spanning 160° 2θ. They are each capable of recording CW diffraction patterns with peak FWHM of $\leq 0.15°$ or less at diffraction angles around $2\theta \approx 2\theta_M$. For the highest resolution, the central portion from each linear detector only is analysed, whereas for higher intensity, the entire two-dimensional pattern is radially averaged to give a single pattern. Using these measures, the instruments can record basic high-resolution patterns from large samples on time frames of a few minutes and high-resolution patterns from a few hundred milligrams of sample in a couple of hours, a feat until recently reserved for the very few ultra-high intensity diffractometers (§12.4.2). As with all CW diffractometers, the d-spacing resolution varies across the diffraction pattern; however, values of around $\Delta d/d = 5 \times 10^{-4}$ are obtained for a small angle range around $2\theta \approx 2\theta_M$. Both diffractometers are configured to give a range of wavelengths (routinely 1–3 Å) and incident collimations. ECHIDNA also offers a choice of monochromator take-off angle so that some trade-off between resolution and intensity may be made. New developments on the high-intensity diffractometer D20 at the ILL allow the recording of patterns with quite respectable resolution ($\Delta d/d \sim 1 \times 10^{-3}$) in very short times as discussed in the next section.

12.4.2 High-intensity diffractometers

The fastest neutron diffractometer in the world, at the instant of writing, is D20 at the ILL. The instrument has a linear 1600 element microstrip detector capable of recording an entire diffraction pattern in just 30 μs. Even with the extremely high incident flux of $\sim 10^8$ n/cm^2 s, this extreme time resolution is only useful in stroboscopic measurements where an excitation in the sample is repeatedly stimulated and allowed to decay. The data collection is synchronized with the stimulation cycle and the repeated data collection runs from equivalent parts of the cycle are added together to give usable neutron counts. For the study of irreversible processes, D20 can record useful diffraction patterns from samples several cm^3 in size in just a few hundred milliseconds with a detector read-out time of between 80 and 400 ms between patterns. D20 has recently been upgraded to include the option of 90° and 120° take-off angles and a radial collimator, both aimed at greater resolution. It is now possible to record patterns with resolution $\Delta d/d \sim 1 \times 10^{-3}$ at time resolutions of tens of seconds to a few minutes depending on sample size.

The new instrument WOMBAT at the OPAL reactor in Australia is designed along the same principles as D20 with a large position sensitive detector. In this case, it is a 30-cm-high curved area detector spanning 120° 2θ. The flux at the sample is slightly greater than on D20 and the detector solid angle is also greater giving the promise of very rapid data acquisition. The detector electronics are configured to allow stroboscopic patterns to be recorded in just 1 μs. The detector is read out sequentially giving essentially 100% duty cycle. Commissioning of the diffractometer is underway to determine how well it meets these expectations.

The highest intensity TOF diffractometer in the world is the GEneral Materials diffractometer (GEM) at ISIS (Hannon 2005). Although not entirely new, having been built in the late 1990s, GEM has shaped the future of powder diffractometers at spallation sources. It uses an enormous detector solid angle (4 steradians) to enhance a moderately high time-averaged incident flux ($\sim 2 \times 10^6$ n/cm^2 s) giving performance in some instances comparable to D20. The highest resolution available on GEM is $\sim 3.4 \times 10^{-3}$. The diffractometer POWGEN3 at SNS is based around the design philosophy of GEM, and when the SNS source reaches full power in 2012 will deliver around an order of magnitude increase in detected neutrons over GEM for the same sample. The medium resolution powder diffractometer at J-PARC is also of similar design, however, with improved resolution ($\sim 9 \times 10^{-4}$ at best).

Whilst the strategy of performing high-speed diffraction at pulsed sources by surrounding the sample with detectors is a sound use of the available neutrons and the TOF technique, there are some limitations. First, detectors arranged to surround the sample deliver a range of resolutions from very low in the forward scattering direction to quite high in backscattering. Whilst this gradation in resolution is also a feature of CW patterns, there it varies smoothly across the recorded diffraction pattern. In the case of instruments like GEM and POWGEN3, there is no sensible way to combine these diffraction patterns into a single diffraction pattern. Second, the time resolution is ultimately limited to the pulse rate of the source (e.g. 20 ms at ISIS) compared with 1–30 μs for the fastest instruments at reactor sources in stroboscopic mode. Third, there is a factor even more restrictive to the time resolution; the time taken to read out several thousand time channels each for several thousand detectors. This currently limits the readout time on such instruments to ~ 10 s.[180]

12.4.3 Residual stress diffractometers

Dedicated X-ray diffractometers for residual stress analysis have been available for approximately four decades. Specialized neutron diffractometers for the same purpose have taken longer to appear, the bulk of early residual stress work having been undertaken on conventional powder diffractometers or on modified triple-axis spectrometers. In more recent times, several very successful dedicated residual stress diffractometer designs have been implemented.

Arguably the best configuration is to use the fixed geometry of a TOF instrument at a pulsed neutron source to full advantage. One such instrument is ENGIN-X at ISIS. Making reference to Fig. 3.12, the instrument lies at the end of a 49 m flight path giving resolution of $\Delta d/d \sim 4 \times 10^{-3}$. The detectors are placed at $\pm 90°$ and when the irradiated volume and diffracted beam are defined by fine slits, the gauge volume is a square prism with height defined by the slit height (often the same

[180] The situation for instruments at the newer pulsed sources was not known at the time of writing.

as the slit width giving a cube). This is a very convenient arrangement for strain scanning as a function of position within an object as the successive gauge-volumes tile three-dimensional space without any special measures. For each gauge volume, two diffraction patterns are recorded simultaneously at ±90° and each contains peaks covering the full accessible d-spacing range. With such an arrangement, it is relatively simple to position a load frame at 45° to the incident beam, that allows the application of uniaxial tensile or compressive stresses to samples *in situ* (see §11.4). The significance of the ±90° detector banks now becomes apparent since one detector bank will record diffraction peaks *hkl* from crystallites oriented so as to have their scattering vector $\boldsymbol{\kappa}_{hkl}$ *parallel* to the applied stress and the other detector bank will record diffraction peaks from crystallites with $\boldsymbol{\kappa}_{hkl}$ *perpendicular* to the applied stress. Similar instruments are under construction at J-PARC (TAKUMI) and SNS (VULCAN). Dedicated residual stress diffractometers are also applicable to reactor sources. Newer variants include SALSA at ILL and KOWARI at the new Australian reactor. Unlike the TOF instruments these instruments generally record data from only one Bragg peak at a time, chosen according to the criteria discussed in Chapter 11.

12.5 DATA ANALYSIS

The analysis of neutron powder diffraction data remains, no doubt, in a state of continuous advancement. In this section we present a selection of relatively recent developments which, in the authors' opinion, are interesting and significant.

First, especially in studies of phase transitions, or of other sequences of closely related structures, we see an increasing role for group theoretical analysis. Of course few crystal structures are solved without reference to the space group tables, published, for example, as *The International Tables for Crystallography Volume A: Space Group Symmetry*. An online version of this invaluable resource can now be purchased. The Bilbao Crystallographic Server (Aroyo *et al.* 2006) provides much of what can be found in these tables, plus useful additional detail. In our work, we have made extensive use of the program ISOTROPY (Stokes and Hatch 1998), which describes the structures obtained when imposing various specific distortions on to a high symmetry parent structure, and indicates the nature of the transitions to be observed. In §5.8.2 we described how the structure of the pseudo-tetragonal phase of the perovskite $SrZrO_3$ was established by combining high-resolution neutron powder diffraction in fine temperature steps with group theoretical analysis. The same methodology could have been useful in our earlier studies of the Ruddlesden-Popper compound $Ca_3Ti_2O_7$ (§5.8.1), and even the much earlier work on the low temperature structure of NaOD (§5.4). In the study of lower symmetry variants of a high symmetry parent structure, it would seem to be a good strategy to anticipate the nature of possible distortions at the outset, then carry out group theoretical analysis so as to limit the structural possibilities. We have used such a strategy to elucidate the structure of the cation-deficient perovskites, such as $Nd_{2/3}TiO_3$ (Zhang *et al.* 2006), and to discover a hitherto

unrecognized phase in WO_3 (Howard *et al.* 2002). The reader is referred to the review article by one of the authors (Howard and Stokes 2005) for detail on the approach outlined here.

It may be that the application of group theory will also assist in structure refinement. Just as group theory can help identify the normal modes of vibration in a high symmetry parent structure, it can be used to decompose the distortion in a lower symmetry structure into normal mode distortions of the parent. That is, the distortion in the lower symmetry structure can be expressed in terms of the amplitudes of these normal modes. This manipulation cannot of course reduce the number of degrees of freedom, which means the number of normal modes must equal the number of variable atomic position parameters in the conventional description of the crystal structure. There are advantages nevertheless in the normal mode description, in that the major distortions can be readily identified, whereas other distortions may be so small they can be ignored. Knight (2008) has decomposed the results from a detailed study of the double perovskite (elpasolite) Ba_2BiSbO_6 to give normal mode amplitudes. He found the dominant distortions were a temperature independent 'breathing' mode corresponding to the size difference between BiO_6 and SbO_6 octahedra, and the ubiquitous (in perovskites) BX_6 octahedral tilting. Knight points out that if in parametric studies (e.g. measurements as a function of temperature) it can be established from a few longer data collection runs that one or more modes have effectively zero amplitude, then in the analysis of shorter runs the number of free parameters can be reduced by setting these same amplitudes to zero. It would seem useful to have a Rietveld code in which the amplitudes of the normal modes (rather than position parameters) were refined variables, and it has been reported (Campbell *et al.* 2007) that the refinement program TOPAS can be adapted to this end.

Chapter 6 was devoted to structure solution *ab initio*, an area in which improvements in instrumentation, methodologies, and computing power should combine to ensure continuing progress. These methods seem well suited to studies of (deuterated) organic materials, including pharmaceuticals. It is probably only the competition from single crystal methods that will inhibit further development in this field.

Improvements in instrumentation (such as represented by GEM) together with the need to study the whole range of materials from amorphous to crystalline have driven new developments in the analysis of the total diffraction, Bragg peaks plus diffuse scattering, to extract a maximum of information from the available data. The nature of the information carried in the diffuse scattering was canvassed long ago, for example, by Sabine (1980). Various means to access this information were introduced in Chapter 10. They include Monte Carlo simulations based on simple but realistic models with relatively few parameters, such as are carried out for single crystal diffuse scattering by Welberry and co-workers (Welberry 2004; Goossens *et al.* 2006), and the Reverse Monte Carlo methods (§10.3.3, §10.4.3) developed mainly by McGreevy and co-workers (Mellergård and McGreevy 2000). The latter approach can involve the random variation of a great number of parameters,

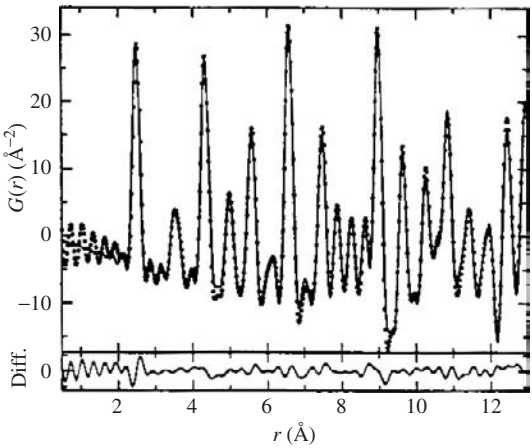

Fig. 12.1 The pair distribution function obtained by Fourier transform of the X-ray scattering from crystalline nickel (Proffen *et al.* 1999). The fitted line is the pair distribution function derived from the known crystal structure.

but if the calculation is often repeated, important features of the ensemble (such as pair distribution functions) should emerge. We also mentioned in §10.4.3 the possibility of Fourier transforming the data, stripped of Bragg peaks, to obtain a pair distribution function $g(r)$ for the non-crystalline component. As recognized by Billinge and co-workers, it can be useful to carry out a Fourier transform of the total scattering – that is, to use eqns (10.26) and (10.27) to obtain a pair distribution function $g(r)$ for the sample as a whole. They show using X-rays, that the method, though developed originally for the study of liquids and amorphous material, works very well for highly crystalline materials such as Ni (Fig. 12.1) and α-AlF_3 – in fact for each of these it proved possible to obtain, from the $g(r)$, values for lattice, positional, and isotropic displacement parameters (Chupas *et al.* 2003). The method requires a wide Q range, to say 30 $Å^{-1}$, but should be well suited to the study of systems exhibiting an intermediate degree of order. The neutron powder diffraction study of the first order co-operative Jahn-Teller (JT) transition at about 750 K in $LaMnO_3$ represents an interesting application (Qiu *et al.* 2005). Below this transition, there is an orthorhombic distortion attributable to the JT effect on the MnO_6 octahedra. Above the transition the material is metrically cubic. The pair distribution function confirms the different Mn–O bond lengths in the MnO_6 octahedra, and remains essentially unchanged through the transition. This indicates that the MnO_6 octahedra are still distorted above the transition, and that it is just the long range ordering of these octahedra that is lost at the transition.

The Fourier relationship between structure factors and scattering lengths and scattering length densities (§2.4.2, §6.4.1) means that in favourable cases, that is, when the phases are known, the scattering length density can be mapped using

eqn (6.11). Fourier inversion is frequently used to obtain electron densities from X-ray structure factors, and in the neutron case might be used to map nuclear densities or, from magnetic neutron scattering, the densities of unpaired electrons. In addition to the formidable problems of extracting structure factors (including phase) from powder diffraction patterns, the Fourier method will lead to termination errors if the series of structure factors [eqn (6.11)] is abruptly terminated at the limit of the observations. Practitioners of Fourier methods routinely make use of the 'difference Fourier', in effect extending the structure factor series beyond experimental limits by calculation based on an approximating model.

Starting from the same data and serving the same purpose as these Fourier methods is a Maximum Entropy Method (MEM) analysis of powder diffraction data, being actively developed by Sakata and co-workers. The first application of MEM seems to have been to image enhancement in astronomy (Gull and Daniel 1978), but it is now applied in many fields. It is said to produce density distributions that are consistent with the given information and least biased with respect to missing information (Wilkins *et al.* 1983) – this implies that the termination errors associated with necessarily incomplete sets of measured structure factors should not occur. In normal application, MEM depends on the fact that the density of scattering material can be assumed to be everywhere positive, and in regard to electron density no problem arises. There is a subtlety in the application to the analysis of neutron powder diffraction data in that scattering lengths may differ in sign. Such is the case for rutile or anatase, TiO_2. This problem was addressed by the application of a 'two-channel' MEM analysis, one channel for nuclei with positive scattering length (O) and one for nuclei with negative scattering length (Ti). The densities of scattering centres in each channel are of course positive. The results from this work (Sakata *et al.* 1993) are density maps showing the nuclei of Ti and O, extended only by the thermal vibration. In a subsequent analysis (Kumazawa *et al.* 1995), the densities of the nuclei are interpreted as forming within one-particle potentials (OPP) and parameters in the OPP functions determined.

Among the more interesting applications of MEM analysis may be those devoted to mapping diffusion paths in fast ion conductors. Yashima *et al.* (2005) have completed an MEM analysis of neutron data recorded at 77 K and room temperature, from the fast lithium-ion conductor $La_{0.62}Li_{0.16}TiO_3$. The density maps (Fig. 12.2) show that at 77 K lithium is isolated on particular sites within a lanthanum-deficient layer, whereas at room temperature scattering density is evident along the diffusion pathways connecting these sites.

Finally, we discuss a development in structure refinement that is a great help to parametric studies and *in situ* studies of, for example, solid state chemical reactions where a sequence of diffraction patterns is recorded against a physical parameter (time, temperature, magnetic field, pressure, etc.) as this is changed. We refer here to sequential Rietveld analyses routines as allowed by some software. These are nothing more than automation of the methodology that individual researchers use, that is, take the converged output parameters from refinement using one diffraction pattern as input parameters for the refinement using the subsequent pattern in the

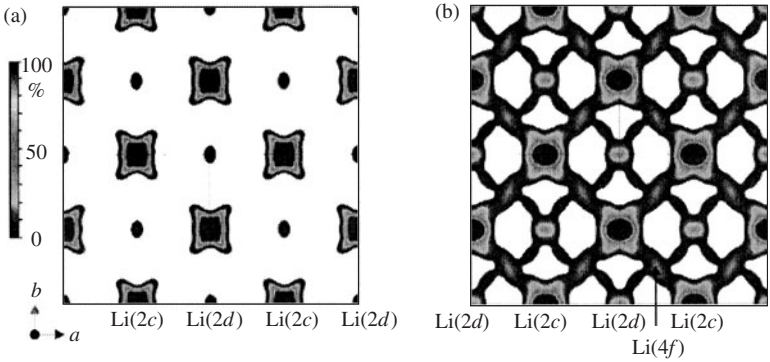

Fig. 12.2 MEM maps of lithium density on the La deficient (002) plane in $La_{0.62}Li_{0.16}TiO_3$ at (a) 77 K and (b) room temperature. Evidently, the Li ions are at isolated sites at 77 K, whereas at room temperature these sites are connected by diffusion pathways (Yashima *et al.* 2005).

sequence. The strategy works especially well in regions of the sequence when the sample is changing slowly from pattern to pattern and fails utterly whenever there is a step change in the phase composition of the sample (e.g. at a first-order phase transition or if a new phase begins to appear through a diffusion controlled transition) at which point a new reference refinement needs to be manually completed and a new sequential refinement series begun. Several Rietveld analysis programs offer this facility, including GSAS which also provides for real-time plotting of the refined parameters to allow user intervention. Of course, a considerable amount of preliminary work is still required to identify all of the phases and structures present at each stage of the reaction, a process which will sometimes require the solution of an unknown crystal structure (Chapter 6) or extensive refinement of a known structure (Chapters 5 and 6) to account for non-stoichiometry, solid solution effects, etc. The complexity of sequential refinements is limited to those which can satisfactorily converge in a single series of refinement cycles from the starting parameters provided by refinement using the previous pattern in the sequence. This is not usually a serious limitation provided that diffraction patterns have been recorded at small steps in the physical stimulus driving changes in the sample (T, P, time, etc.).

12.6 NEW PROBLEMS FOR STUDY BY NEUTRON POWDER DIFFRACTION

In the preceding chapters, we have attempted to cover the types of problems for which neutron powder diffraction is currently in widespread use. In this section we will take a brief excursion into some fields where neutron powder diffraction is beginning to be used, but should be viewed at the time of writing as an emerging technique with great potential.

The first of these fields is that of solid-state chemical reaction kinetics. In Chapter 8 we showed the connection between the diffracted intensity and the total mass of a given phase or compound within a solid and how the neutron data can be used to affect a quantitative phase analysis (QPA). If diffraction patterns are recorded in a time-resolved sequence during a reaction, then the QPA results give a window into the reaction kinetic parameters. Some of the examples used (§8.6.4) dealt with the rates of chemical change within a sample undergoing the ceramic processing method known as reactive sintering. Interest in the rates of solid-state reactions goes well beyond the realm of ceramists to also encompass metallurgists, materials scientists, process engineers, solid-state chemists and physicists, geologists, and mineralogists. Neutron diffraction is particularly suited to this kind of study as often, industrially relevant sample sizes can be studied in transmission geometry without fear of near surface effects biasing the results. As highlighted in Chapter 8, QPA results from neutron diffraction are usually far superior to those obtained with X-rays due to the likely absence of micro-absorption and primary extinction effects. The drawback with neutrons has always been the low intensity of neutron sources and low scattering factors limiting the time resolution of such studies to tens of minutes or more commonly hours. This drawback has been largely overcome. In §12.4.2, new diffractometers capable of recording complete diffraction patterns in as little as 200 ms for irreversible reactions and 30 μs for reversible reactions were described. These then allow solid-state reactions to be studied at the same time resolution as synchrotron X-ray powder diffraction studies. These extremely fast data acquisition rates lead to a further drawback to the study of chemical reaction kinetics by powder diffraction – the extensive amount of data processing required to obtain credible Rietveld analyses at each time slice. A typical 2-day experiment on D20 at ILL may produce in excess of 30,000 diffraction patterns if extreme time resolution is employed. This problem is also largely solved, by the sequential Rietveld refinements described above.

These improvements have allowed the study of a variety of rapid processes in materials such as the formation of Ti_3SiC_2 by combustion synthesis, illustrated in Figs. 12.3 and 12.4. Time resolved data of this kind contain a large amount of information. In this example, we can observe (i) the thermal expansion of the reactants (Ti, SiC, and C), (ii) the $\alpha \rightarrow \beta$ transition in Ti which triggers the chemical reaction, (iii) a small amount of TiC formation, (iv) the <0.5 s combustion event in which the entire 40 g sample converts into a single intermediate phase with a TiC-like structure which persists as the only phase for 5 s, and (v) the precipitation of the product phase Ti_3SiC_2 over the next 35 s. Although recorded in just 0.5 s, each diffraction pattern is quite suitable for Rietveld analyses to extract structural data, thermal expansion, phase quantities, and reaction kinetics (Kisi and Riley 2002; Riley *et al.* 2002; Kisi *et al.* 2006). For example, the pattern labelled (D) in Fig. 12.3 has a highest step intensity of more than 3000 counts.

Switching now from high-intensity diffractometers to high-resolution diffractometers, the size of crystal structures amenable to solution and/or refinement from neutron powder diffraction data has been steadily increasing, fuelled by

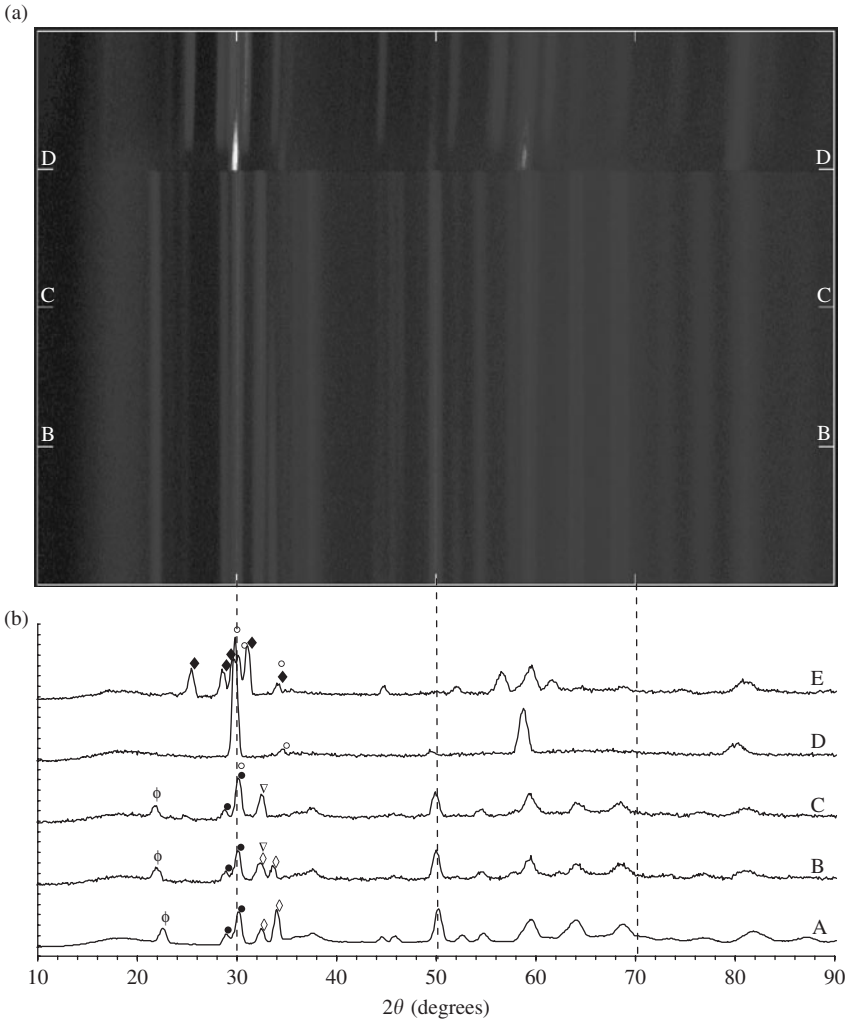

Fig. 12.3 (a) Representation of part of the diffraction patterns collected on D20 at ILL during combustion synthesis of Ti_3SiC_2. The *x*-axis is the diffraction angle $2\boldsymbol{\theta}$, the *y*-axis is time (at 0.9 s per diffraction pattern) and the brightness is the diffracted neutron intensity. All five stages of the reaction are represented here. Most dramatic is the discontinuity created by the SHS reaction. (b) Selected diffraction patterns to represent the five stages of the reaction (pre-heating of the reactants, the $\alpha \rightarrow \beta$ phase transformation in Ti, pre-ignition reactions, an intermediate phase, and the growth of the product phase). Reflections characteristic of each phase are marked as follows: ϕ, C; •, SiC; ◊, α-Ti; *o*, TiC_x; ∇, *β*-Ti; ♦, Ti_3SiC_2 (from Riley *et al*. 2002). (See plate 8)

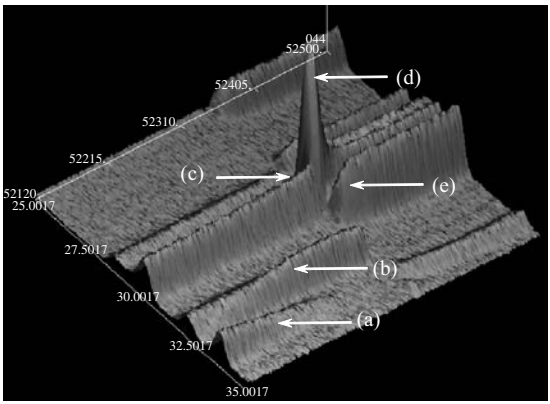

Fig. 12.4 A three-dimensional view of part of Fig. 12.3. The diffraction angle 2θ is shown on the axis running towards the viewer and the pattern sequence number (hence time in 0.9 s steps) on the upper axis running from left to right. Features marked are (a) α-Ti decreasing and (b) β-Ti replacing it, (c) a small amount of TiC forming, (d) the intermediate solid solution of Si in TiC, and (e) growth of the product phase over a 35 s period. (See plate 9)

improvements in instrumentation, analysis methods, and software. An area of particular growth is in the area of molecular solids, for example, *ortho*-xylene, acetaldehyde, dimethyl sulphide, methyl fluoride, dimethyl acetylene, and trichlorofluoromethane as discussed by Ibberson and David (2002). Although *ab initio* structure solution from neutron powder diffraction is hampered by the smaller dynamic range of scattering length (e.g. in Patterson methods) and the weaker intensities (direct methods) many complex structures continue to be successfully solved. A particular advantage in organic structures may be obtained from the negative scattering length of H since these usually lie in an envelope around the positively scattering backbone of the molecule. Under these circumstances, a two-channel positive–negative MEM map will provide greater contrast than from X-ray diffraction where all scattering density is positive. We refer the interested reader to David *et al.* (2002) where a more comprehensive account of structure solution from powder diffraction (neutron and X-ray) is given.

The ultimate level of complexity is of course in the macromolecular crystallography of biological molecules. To the average small molecule crystallographer, materials scientist, or physicist, the idea of attempting macromolecular structures using powder diffraction seems overly ambitious. However, Von Dreele has incorporated data analysis practices used in macromolecular crystallography into the Rietveld refinement section of the program GSAS and applied it to structure solution/refinement of the structure of human insulin–Zn complex formed by grinding single crystals (Von Dreele *et al.* 2000), using a synchrotron X-ray pattern with 4800 data points and 2927 reflections together with 7981 stereochemical restraints in a refinement with 4893 structural parameters! There seem as yet to be no neutron

diffraction equivalents to this feat although in principle, data recorded on HRPD at the ISIS facility and the new high-resolution diffractometer at J-PARC could be used in similar fashion.

In many branches of science and engineering, material properties depend on structure at two length scales, that of atoms (crystal and magnetic structure) and that of crystallites (microstructure) of which nanostructure is but a special case. It is no surprise that the penultimate area we wish to highlight is the potential for the study of microstructure using neutron powder diffraction. As stated in Chapter 9, this is not an area of historical strength for neutron diffraction; however, there are now a great many diffractometers around the world with resolution sufficient to investigate many types of microstructural effects. The analytical means to interpret the data are already relatively well understood from the long history of X-ray work in this area and, where there is a deficiency, guidance has been given (§9.2.2, §9.5). Indeed there is little doubt that microstructural effects are present in many of the high-resolution neutron diffraction patterns recorded around the world – all that is required is that the refined parameters be suitably interpreted using appropriate standards and a correlation made with other microstructural techniques. The strength of neutron diffraction in this area is its suitability to parametric and *in situ* studies in which, under the correct circumstances, structure on both critical length scales can be investigated simultaneously under identical conditions. Apart from X-ray diffraction, there are no other techniques that allow this to be achieved. The significance here should not be taken lightly as with these diffraction techniques, the connection between what is observed (the diffraction pattern) and the structure of the sample is relatively direct compared with other *in situ* techniques such as Raman scattering.

The above discussion on the influence of microstruture leads us naturally to consider how best to tackle problems where the sample is neither a polycrystal nor a single crystal. We refer specifically to multidomain single crystals such as the relaxor ferroelectrics. An example is PZN–PT ($PbZn_{1/3}Nb_{2/3}O_3$–$PbTiO_3$) which can be readily grown as pseudo single crystals but not as polycrystals. In addition to being multidomain, the crystals are pseudo-cubic leading to controversy over their true symmetry. In a CW single crystal study, the position of a peak is determined both by the orientation of the reflecting planes *and* their d-spacing leading to ambiguity. TOF single crystal diffractometers have absolute d-spacing determination, but low resolution. In order to study certain aspects of these materials, for example, their structural response to applied stress or applied electric field, high-resolution powder diffraction-like information is required from single crystal samples. Recently, a technique was demonstrated that appears to enable such experiments (Kisi *et al.* 2007). Crystals of PZN–4.5%PT were mounted on the TOF High-Resolution Powder Diffractometer (HRPD) at ISIS and rotated about a prominent zone axis ([001], [100], [110], etc.). Data were recorded from only the equatorial segments of the backscattering detector and subjected to the usual TOF analysis. This procedure yields a diffraction pattern which is the TOF analogue of the zero layer of a rotating crystal X-ray photograph such as were once

commonly employed in single crystal X-ray diffraction studies. For example, a [001] zone pattern yields only those *hk*0 peaks within the *d*-spacing range of the diffractometer, 0.65–2.5 Å in this case. Depending upon the symmetry of the crystals, as few as two zones may provide enough peaks for unit cell determination (indexing) using powder diffraction techniques *and* structure solution and refinement using extracted intensities and single crystal techniques. The data have the full resolution of the HRPD instrument (4×10^{-4}), well in excess of any single crystal diffractometer, a trait that is essential in the study of multidomain crystals in order to resolve closely overlapping peaks. Certain subtleties regarding the domain structure need to be considered in analysing the data as discussed by Kisi *et al.* (2007).

12.7 CLOSING REMARKS

Powder diffraction is sometimes viewed as the poor relation to single crystal diffraction. Whilst there is no doubt that the *ab initio* solution of crystal and magnetic structures is easier and more certain with single crystals, there are many areas in which powder diffraction has distinct advantages. We hope that this book has demonstrated that the scope of neutron powder diffraction goes well outside simply solving crystal structures into the realm of the detailed analysis of structural systematics; quantitative phase analysis; stresses, strains, and elastic constants; microstructures and much more. When the obvious synergies with X-ray diffraction, transmission electron microscopy, and electron diffraction are exploited, there are few problems in materials science, solid-state physics, solid-state chemistry, or mineralogy where neutron powder diffraction is unable to make a contribution.

Appendix 1

Inter-planar spacing, angles and unit cell volumes

In Tables A1.1, A1.2, and A1.3 expressions are given for inter-planar spacings (d-spacings), inter-planar angles and unit cell volumes, respectively, for the seven crystal classes.

Table A1.1 Distance between successive planes (d-spacing) within the set (hkl).

Symmetry	d-spacing equation
Cubic	$\frac{1}{d^2} = \frac{h^2 + k^2 + l^2}{a^2}$
Tetragonal	$\frac{1}{d^2} = \frac{h^2 + k^2}{a^2} + \frac{l^2}{c^2}$
Hexagonal	$\frac{1}{d^2} = \frac{4}{3}\left(\frac{h^2 + hk + k^2}{a^2}\right) + \frac{l^2}{c^2}$
Rhombohedral	$\frac{1}{d^2} = \frac{\left(h^2 + k^2 + l^2\right)\sin^2\alpha + 2(hk + kl + hl)\left(\cos^2\alpha - \cos\alpha\right)}{a^2\left(1 - 3\cos^2\alpha + 2\cos^3\alpha\right)}$
Orthorhombic	$\frac{1}{d^2} = \frac{h^2}{a^2} + \frac{k^2}{b^2} + \frac{l^2}{c^2}$
Monoclinic	$\frac{1}{d^2} = \frac{1}{\sin^2\beta}\left(\frac{h^2}{a^2} + \frac{k^2\sin^2\beta}{b^2} + \frac{l^2}{c^2} - \frac{2hl\cos\beta}{ac}\right)$
Triclinic	$\frac{1}{d^2} = \frac{1}{V^2}\left[\begin{array}{l} h^2b^2c^2\sin^2\alpha + k^2a^2c^2\sin^2\beta + l^2a^2b^2\sin^2\gamma \\ \quad +2hkabc^2\left(\cos\alpha\cos\beta - \cos\gamma\right) + \\ 2kla^2bc\left(\cos\beta\cos\gamma - \cos\alpha\right) \\ \quad +2hlab^2c\left(\cos\gamma\cos\alpha - \cos\beta\right) \end{array}\right]$

Table A1.2 Angle between two planes $(h_1k_1l_1)$ and $(h_2k_2l_2)$ with d-spacings d_1 and d_2.

Symmetry	Angle ϕ given by
Cubic	$\cos\phi = \dfrac{h_1h_2 + k_1k_2 + l_1l_2}{\sqrt{\left(h_1^2 + k_1^2 + l_1^2\right)\left(h_2^2 + k_2^2 + l_2^2\right)}}$
Tetragonal	$\cos\phi = \dfrac{\dfrac{h_1h_2 + k_1k_2}{a^2} + \dfrac{l_1l_2}{c^2}}{\sqrt{\left(\dfrac{h_1^2 + k_1^2}{a^2} + \dfrac{l_1^2}{c^2}\right)\left(\dfrac{h_2^2 + k_2^2}{a^2} + \dfrac{l_2^2}{c^2}\right)}}$
Hexagonal	$\cos\phi = \dfrac{h_1h_2 + k_1k_2 + \dfrac{1}{2}(h_1k_2 + h_2k_1) + \dfrac{3a^2}{4c^2}l_1l_2}{\sqrt{\left(h_1^2 + k_1^2 + h_1k_1 + \dfrac{3a^2}{4c^2}l_1^2\right)\left(h_2^2 + k_2^2 + h_2k_2 + \dfrac{3a^2}{4c^2}l_2^2\right)}}$
Rhombohedral	$\cos\phi = \dfrac{a^4 d_1 d_2}{V^2}\left[\begin{array}{l}\sin^2\alpha\,(h_1h_2 + k_1k_2 + l_1l_2) \\ \quad + \left(\cos^2\alpha - \cos\alpha\right)(k_1l_2 + k_2l_1 + l_1h_2 \\ \quad + l_2h_1 + h_1k_2 + h_2k_1)\end{array}\right]$
Orthorhombic	$\cos\phi = \dfrac{\dfrac{h_1h_2}{a^2} + \dfrac{k_1k_2}{b^2} + \dfrac{l_1l_2}{c^2}}{\sqrt{\left(\dfrac{h_1^2}{a^2} + \dfrac{k_1^2}{b^2} + \dfrac{l_1^2}{c^2}\right)\left(\dfrac{h_2^2}{a^2} + \dfrac{k_2^2}{b^2} + \dfrac{l_2^2}{c^2}\right)}}$
Monoclinic	$\cos\phi = \dfrac{d_1d_2}{\sin^2\beta}\left[\dfrac{h_1h_2}{a^2} + \dfrac{k_1k_2\sin^2\beta}{b^2} + \dfrac{l_1l_2}{c^2} - \dfrac{(l_1h_2 + l_2h_1)\cos\beta}{ac}\right]$
Triclinic	$\cos\phi = \dfrac{d_1d_2}{V^2}\left[\begin{array}{l}h_1h_2b^2c^2\sin^2\alpha + k_1k_2a^2c^2\sin^2\beta \\ \quad + l_1l_2a^2b^2\sin^2\gamma \\ \quad + (h_1k_2 + h_2k_1)\,abc^2\,(\cos\alpha\cos\beta - \cos\gamma) \\ \quad + (k_1l_2 + k_2l_1)\,a^2bc\,(\cos\beta\cos\gamma - \cos\alpha) \\ \quad + (h_1l_2 + h_2l_1)\,ab^2c\,(\cos\gamma\cos\alpha - \cos\beta)\end{array}\right]$

Table A1.3 Unit cell volume for the seven crystal classes.

Symmetry	Unit cell volume
Cubic	$V = a^3$
Tetragonal	$V = a^2c$
Hexagonal	$V = \frac{\sqrt{3}a^2c}{2}$
Rhombohedral	$V = a^3\sqrt{1 - 3\cos^2\alpha + 2\cos^3\alpha}$
Orthorhombic	$V = abc$
Monoclinic	$V = abc\sin\beta$
Triclinic	$V = abc\sqrt{1 - \cos^2\alpha - \cos^2\beta - \cos^2\gamma + 2\cos\alpha\cos\beta\cos\gamma}$

Appendix 2

Multiplicity factors

Table A2.1 Common multiplicity of lattice planes in the seven crystal systems.[1]

Cubic	hkl	hhl	$0kl$	$0kk$	hhh	$00l$	
	48	24	24	12	8	6	
Hexagonal and	$hk.l$	$hh.l$	$0k.l$	$hk.0$	$hh.0$	$0k.0$	$00.l$
Rhombohedral	24	12	12	12	6	6	2
Tetragonal	hkl	hhl	$0kl$	$hk0$	$hh0$	$0k0$	$00l$
	16	8	8	8	4	4	2
Orthorhombic	hkl	$0kl$	$h0l$	$hk0$	$h00$	$0k0$	$00l$
	8	4	4	4	2	2	2
Monoclinic	hkl	$h0l$	$0k0$				
	4	2	2				
Triclinic	hkl						
	2						

[1] It should be noted that in some space groups, planes which are listed here as equivalent, whilst having the same d-spacing, are allowed distinct structure factors (hence integrated intensity). An example is the tetragonal system in which some space groups (those with Laue group $4/mmm$) have $hk0$ and $kh0$ equivalent (e.g. 210 has the same d-spacing *and* structure factor as 120) whereas in other space groups (with Laue group $4/m$) these planes have the same d-spacing but different structure factors. A full account is given in the International Tables for Crystallography; especially Vol. 1 thereof in which Table 3.5.1 showed relationships between multiplicities in the crystal classes such as might be useful in the study of phase transitions.

References

Abrahams, S.C. and Williams, H.J. (1963). *J. Chem. Phys.* **39**, 2923.

Ahtee, A., Ahtee, M., Glazer, A.M., and Hewat, A.W. (1976). *Acta Crystallogr. B* **32**, 3243.

Ahtee, M., Glazer, A.M., and Hewat, A.W. (1978). *Acta Crystallogr. B* **34**, 752.

Ahtee, M., Nurmela, M., Suorrti, P., and Järvinen, M. (1989). *J. Appl. Crystallogr.* **22**, 261.

Aleksandrov, K.S. and Bartolomé, J. (2001). *Phase Transitions* **74**, 255.

Alexander, L.E. (1950). *J. Appl. Phys*. **21**, 126.

Alexander, L.E. (1954). *J. Appl. Phys*. **25**, 155.

Allegra, G. (1980). In *Theory and practice of direct methods in crystallography* (eds. M.F.C. Ladd and R.A. Palmer), p. 1. Plenum Press, London.

Alvarez, L.W. and Bloch, F. (1940). *Phys. Rev.* **57**, 111.

Anderson, J.S., Bevan, D.J.M., Cheetham, A.K., Von Dreele, R.B., Hutchison, J.L., and Strähle, J. (1975). *Proc. Roy. Soc. London A*, **346**, 139.

Andreev, Y.G. and Bruce, P.G. (2001). *Mater. Sci. Forum* **378–381**, 148.

Arai, M. (2005). *Neutron News* **16**, 25.

Argyriou, D.N. (1994). *J. Appl. Crystallogr.* **27**, 155.

Armstrong, N. and Lynch, P. (2004). In *Diffraction analysis of the microstructure of materials* (eds. E.J. Mittemeijer and P. Scardi), p. 249. Springer-Verlag, Berlin.

Aroyo, M.I., Perez-Mato, J.M., Capillas, C., Kroumova, E., Ivantchev, S., Madariaga, G., Kirov, A., and Wondratschek, H. (2006). "Bilbao crystallographic server I: databases and crystallographic computing programs". *Zeitschrift fuer Kristallographie* **221(1)**, 15. http://www.cryst.ehu.es/

Ashby, M.F. and Jones, D.R.H. (2005). *Engineering materials 1*. Elsevier Butterworth-Heinemann, Oxford.

Avrami, M. (1939). *J. Chem. Phys*. **7**, 1103.

Avrami, M. (1940). *J. Chem. Phys*. **8**, 212.

Avrami, M. (1941). *J. Chem. Phys*. **9**, 177.

Aylward, G.H. and Findley, T.J.V. (2002). *SI Chemical Data*, 5th ed. John Wiley & Sons, Sydney.

Azároff, L.V. (1968). *Elements of X-ray crystallography*. McGraw-Hill, New York.

Bacon, G.E. (1975). *Neutron diffraction.* (3rd ed.) Clarendon Press, Oxford.

Baerlocher, Ch. (1993). In *The Rietveld method* (ed. R.A. Young), p. 186. International Union of Crystallography, Oxford University Press, Oxford.

Baker, H. (ed.) (1992). *Alloy phase diagrams*. ASM International, Ohio.

Balcar, E. and Lovesey, S.W. (1989). *Theory of magnetic neutron and photon scattering*. Oxford University Press, Oxford.

Balucani, U. and Zoppi, M. (1995). *Dynamics of the liquid state*. Oxford University Press, Oxford.

Barsch, G.R. and Krumhansl, J.A. (1984). *Phys. Rev. Lett*. **53**, 1069.

Bastow, T.J., Amm, D.T., Segel, S.W., and Heyding, R.D. (1986a). *Z. Naturforsch.* **41a**, 283.

Bastow, T.J., Elcombe, M.M., and Howard, C.J. (1986b). *Solid State Comm.* **57**, 339.

Beck, P.A. and Hu, H. (1952). *Trans. AIME*, **194**, 83 and 1267.

Berg, H., Rundlov, H., and Thomas, J.O. (2001). *Solid State Ionics* **144**, 65.

Bhatia, A.B. and Thornton, D.E. (1970). *Phys. Rev*. **B2**, 3004.

Bish, D.L. and Howard, S.A. (1988). *J. Appl. Crystallogr.* **21**, 86.

Bittorf, Ch., Matthies, S., and Priesmeyer, H.G. (1998). *Intermetallics* **7**, 1.

Bleif, H.-J. and Dachs, H. (1982). *Acta Crystallogr. A* **38**, 470.

Bloch, F. (1936). *Phys. Rev.* **50**, 259.

Bollenrath, F., Hauk, V., and Müller, E.H. (1967). *Z. Metallkd.* **58**, 76.

Borie, B. (1957). *Acta Crystallogr*. **10**, 89.

Borie, B. (1959). *Acta Crystallogr*. **12**, 280.

Borie, B. (1961). *Acta Crystallogr*. **14**, 472.

Bougrab, H., Inal, K., and Berveiller, M. (2002). *International Union of Crystallography – Commission on powder diffraction*, Newsletter No. 28, p. 16, December 2002.

Boutif, A. and Louër, D. (1991). *J. Appl. Crystallogr.* **24**, 987.

Brandt, S. (1970). *Statistical and computational methods in data analysis.* North Holland Publishing, Amsterdam.

Bruce, P.G. and Andreev, Y.G. (2002). In *Structure determination from powder diffraction data* (eds. W.I.F. David, K. Shankland, L.B. McCusker, and Ch. Baerlocher), p. 286. Oxford University Press, Oxford.

Buerger, M.J. (1959). *Vector space, and its application in Crystal Structure Investigation*, Wiley, New York.

Buerger, M.J. (1980). *X-ray crystallography: an introduction to the investigation of crystals by their diffraction of monochromatic X-radiation*. Huntington, New York.

Bunge, H.J. (1982) *Texture analysis in materials science*. Butterworth, London.

Busing, W.R. (1955). *J. Chem. Phys.* **23**, 933.

Caglioti, G. (1970). In *Thermal neutron diffraction* (ed. B.T.M. Willis), p. 14. Clarendon Press, Oxford.

Caglioti, G. and Ricci, F.P. (1962). *Nucl. Instrum. Methods* **15**, 155.

Caglioti, G., Paoletti, A., and Ricci, F.P. (1958). *Nucl. Instrum. Methods* **3**, 223.

Caglioti, G., Paoletti, A., and Ricci, F.P. (1960). *Nucl. Instrum. Methods* **9**, 195.

Cain, M.G., Bennington, S.M., Lewis, M.H., and Hull, S. (1994). *Phil. Mag. B*. **69**, 499.

Callister, W.D. Jr. (2003). *Materials science and engineering: an introduction*, 6th ed. John Wiley & Sons, New York.

Campbell, B.J., Evans, J.S.O., Perselli, F., and Stokes, H.T. (2007). *International Union of Crystallography – Commission on crystallographic computing*, Newsletter No. 8, November 2007.

Čapková, P., Peschar, R., and Shenk, H. (1993). *J. Appl. Crystallogr.* **26**, 449.

Capponi, J.J., Chaillout, C., Hewat, A.W., Lejay, P., Marezio, M., Nguyen, N., Raveau, B., Soubeyroux, J.L., and Tholence, J.L. (1987). *Eur. Lett.* **3**, 1301.

Carlsson, L. (1967). *Acta Crystallogr.* **23**, 901.

Carpenter, M.A. (2002). Private communication.

Carpenter, M.A., Howard, C.J., Kennedy, B.J., and Knight, K.S. (2005). *Phys. Rev. B* **72**, 024118.

Carr, D.G., Ripley, M.I., Holden, T.M., Brown, D.W., and Vogel, S.C. (2004). *Acta Mater*. **52**, 4083.

Celino, M. and Massobrio, C. (2002). *Comp. Mater. Sci*. **24**, 28.

Chan, S.-K. (1996) Private communication.

Chan, S.-K., Fang, Y., Grimsditch, M., Li, Z., Nevitt, M., Robertson, M.W., and Zouboulis, E.S. (1991). *J. Amer. Ceram. Soc.* **74**, 1742.

Charpak, G. (1968). *Nucl. Instrum. Methods* **62**, 262.

Cheary, R.W. (1991). *Acta Crystallogr. B* **47**, 325.

Cheary, R.W. and Coehlo, A. (1992). *J. Appl. Crystallogr.* **25**, 109.

Cheetham, A.K. and Taylor, J.C. (1977). *J. Solid State Chem.* **21**, 253.

Child, H., Wilkinson, M., Cable, J., Koehler, M., and Wollan, E. (1963). *Phys. Rev*. **131**, 922.

Chupas, P.J., Qiu, X., Hanson, J.C., Lee, P.L., Grey, C.P., and Billinge, S.J.L. (2003). *J. Appl. Crystallogr*. **36**, 1342.

Clapp, P.C. and Moss, S.C. (1966). *Phys. Rev*. **142**, 418.

Clapp, P.C. and Moss, S.C. (1968). *Phys. Rev*. **171**, 754.

Cocking, S.J. and Webb, F.J. (1965). In *Thermal neutron scattering* (ed. P. Egelstaff), p. 141. Academic Press, New York.

Coelho, A.A. (2003). *J. Appl. Crystallogr.* **36**, 86.

Cohen, M.V. (1935). *Rev. Sci. Instr*. **6**, 68.

Cohen, M.V. (1936). *Rev. Sci. Instr*. **7**, 155.

Convert, P., Hansen, T., Oed, A., and Torregrossa, J. (1997). *Physica B* **241**, 195.

Cope, E.R. and Dove, M.T. (2007). *J. Appl. Crystallogr.* **40**, 589.

Corliss, L.M., Hastings, J.M., and Brockman, F.G. (1953). *Phys. Rev.* **90**, 1013.

Cowley, J.M. (1950a). *J. Appl. Phys*. **21**, 24.
Cowley, J.M. (1950b). *Phys. Rev*. **77**, 669.
Cowley, J.M. (1976a). *Acta Crystallogr. A* **32**, 83.
Cowley, J.M. (1976b). *Acta Crystallogr. A* **32**, 88.
Cowley, J.M, (1981). *Diffraction physics.* North Holland, New York.
Cowley, J.M. and Au, A.Y. (1978). *Acta Crystallogr. A* **34**, 738.
Cox, D.E. (1972). *IEEE Trans. Magnet.* **8**, 161.
Craik, D.J. (1971). *Structure and properties of magnetic materials*. Pion, London.
Crangle, J. (1977). *The magnetic properties of solids*. Edward Arnold, London.
Crank, J. (1975). *The mathematics of diffusion*. Clarendon Press, Oxford.
Cullity, B.D. (1978). *Elements of X-ray diffraction*. Addison-Wesley, Reading, Massachusetts.
Cussen, L.D. (2000a). *J. Appl. Crystallogr*. **33**, 1393.
Cussen, L.D. (2000b). *J. Appl. Crystallogr*. **33**, 1399.
Cussen, L.D. (2002). *J. Appl. Crystallogr*. **35**, 615.
Cussen, L.D., Vale, C.J., Anderson, I.S., and Høghøj, P. (2001). *Nucl. Instrum. Methods A* **471**, 392.
Darlington, C.N.W. and Cernik, R.J. (1991). *J. Phys.: Condens. Matter* **3**, 4555.
Darwin, C.G. (1914). *Phil. Mag*. **27**, 315.
David, W.I.F. (1987). *J. Appl. Crystallogr*. **20**, 316.
David, W.I.F. (1990). *Nature* (*London*) **346**, 731.
David, W.I.F. and Jorgensen, J.D. (1993). In *The Rietveld method* (ed. R.A. Young), p. 197. International Union of Crystallography, Oxford University Press, Oxford.
David, W.I.F. and Sivia, D.S. (2002). In *Structure determination from powder diffraction data*. (eds. W.I.F. David, K. Shankland, L.B. McCusker, and Ch. Baerlocher) p. 136. Oxford University Press, Oxford.
David, W.I.F., Ibberson, R.M., Dennis, T.J.S., Hare, J.P., and Prassides, K. (1992). *Eur. Lett*. **18**, 219.
David, W.I.F., Ibberson, R.M., Matthewman, J.C., Prassides, K., Dennis, T.J.S., Hare, J.P., Kroto, H.W., Taylor, R., and Walton, D.R.M. (1991). *Nature* **353**, 147.
David, W.I.F., Shankland, F., Cole, J., Maginis, S., Motherwell, W.D.S., and Taylor, S. (2001). *DASH user manual*. CCDC, Cambridge.
David, W.I.F., Shankland, K., McCusker, L.B., and Baerlocher, Ch. (eds.) (2002). *Structure determination from powder diffraction data*. Oxford University Press, Oxford.
de Keijser, Th., Mittemeijer, E.J., and Rozendaal, H.C.F. (1983). *J. Appl. Crystallogr*. **16**, 309.

de Woff, P.M. (1957). *Acta Crystallogr.* **10**, 590.
de Woff, P.M. (1958). *Acta Crystallogr.* **11**, 664.
de Woff, P.M. (1963). *Adv. X-ray Anal.* **6**, 1.
Debye, P. (1915). *Ann. Phys.* (Leipzig) 809.
Debye, P. and Scherrer, P. (1916). *Z. Physics* **17**, 277.
Delhez, R., De Keijser, Th., Langford, J.I., Louer, D., Mittemeijer, E.J., and Sonneveld, E.J. (1993). In *The Rietveld method* (ed. R.A. Young), p. 132. International Union of Crystallography, Oxford University Press, Oxford.
Dollase, W.A. (1986). *J. Appl. Crystallogr.* **19**, 267.
Dowty, E. (1999). *ATOMS Version 5.07*. Shape Software, Kingsport, Tennessee, 37363, USA.
Egelstaff, P.A. (1994). *An introduction to the liquid state*. Oxford University Press, Oxford.
Elcombe, M.M. and Howard, C.J. (1988). *Mater. Sci. Forum* **27–28**, 71.
Elcombe, M.M., Kisi, E.H., Hawkins, K.D., White, T.J., Goodman, P., and Matheson, S. (1991). *Acta Crystallogr. B* **47**, 305.
Elsenhans, O., Böni, P., Friedli, H.P., Grimmer, H., Buffat, P., Leifer, K., Söchtig, J., and Anderson, I.S. (1994). *Thin Solid Films* **246**, 110.
Erickson, R.A. (1953). *Phys. Rev.* **90**, 779.
Eriksson, T., Bergqvist, L., Nordblad, P., Eriksson, O., and Andersson,Y. (2004). *J. Solid State Chem.* **177**, 4058.
Ernst, Th. (1946). *Nachr. Ges. Wiss. Göttingen*, *Math.-Phys. Kl.* 76.
Eshelby, J.D. (1957). *Proc. Roy. Soc. London Ser. A* **241**, 376.
Estermann, M.A. and David, W.I.F. (2002). In *Structure determination from powder diffraction data* (eds. W.I.F. David, K. Shankland, L.B. McCusker, and Ch. Baerlocher), p. 202. Oxford University Press, Oxford.
Evenschor, P.D. and Hauk, V. (1972). *Z. Metallkd.* **63**, 798.
Faber, J. Jr., Seitz, M.A., and Meuller, M.H. (1976). *J. Phys. Chem. Solids* **37**, 909.
Faber, T.E. and Ziman, J.M. (1965). *Phil. Mag*. **11**, 153.
Federov, E.S. (1895). *Z. Kristallogr*. **24**, 209.
Ferrari, M. and Lutterotti, L. (1994). *J. Appl. Phys*. **76**, 7246.
Feyerherm, R., Loose, A., Rabu, P., and Drillon, M. (2003). *Solid State Sci.* **5**, 321.
Finger, L.W., Cox, D.E., and Jephcoat, A.P. (1994). *J. Appl. Crystallogr.* **27**, 892.
Finlayson, T.R., Gross, A.K, Griffiths, J.R., and Kisi, E.H. (1994). *J. Amer. Ceram. Soc*. **77**, 617.
Fogelson, R.L. (1968). *Fiz. Met. Metalloved.* **25**, 492.
Fogelson, R.L., Ugai, Y.A., Pokoev, A.V., and Akimova, I.A. (1971). *Sov. Phys. Sol. Stat.* **13**, 1028.

Fukunaga, T., Okasaka, K., and Mizutani, U.J. (1993). *J. Non-Cryst. Solids* **156–158**, 120.

Gale, J.D. and Rohl, A.L. (2003). *Mol. Simul.* **29**, 291.

Gamari-Seale, H., Troyanchuk, I.O., Khalyavin, D., Stefanopoulos, K.L., and Hernández-Velasco, J. (2004). *Physica B* **350**, e19.

Gerold, V. and Kim, J. (1987). *Acta Metall.* **35**, 393.

Giacovazzo, C. (1980). *Direct methods in crystallography*. Academic Press, London.

Giacovazzo, C. (1996). *Acta Crystallogr. A* **52**, 331.

Giacovazzo, C., Altomare, A., Burla, M.C., Carrozzini, B., Cascarano, G.L., Guagliardi, A., Moliterni, A.G.G., Polidori, G., and Rizzi, R. (2002). In *Structure determination from powder diffraction data* (eds. W.I.F. David, K. Shankland, L.B. McCusker, and Ch. Baerlocher), p. 190. Oxford University Press, Oxford.

Gibaud, A., Le Bail, A., and Bulou, A. (1986). *J. Phys. C* **19**, 4623.

Gil, A., Kaczorowski, D., Hernandez-Velasco, J., Penc, B., Wawrzynska, E., and Szytula, A. (2004). *J. Alloys Compounds* **384**, L4.

Gilmore, C.J., Shankland, K., and Dong, W. (2002). In *Structure determination from powder diffraction data* (eds. W.I.F. David, K. Shankland, L.B. McCusker, and Ch. Baerlocher), p. 233. Oxford University Press, Oxford.

Glazer, A.M. (1972). *Acta Crystallogr. B* **28**, 3384.

Glazer, A.M., Mabud, S.A., and Clarke, R. (1978). *Acta Crystallogr. B* **34**, 1060.

Gnäupel-Herold, T., Brand, P.C., and Prask, H.J. (1998). *J. Appl. Crystallogr.* **31**, 929.

Goldschmidt, G.H. and Hurst, D.G. (1951). *Phys. Rev.* **83**, 88.

Goossens, D.J., Heerdegen, A.P., Welberry, T.R., and Gutmann, M.J. (2006). *Physica B* **385–386**, 1352.

Goossens, D.J., Robinson, R.A., and Telling, M.T.F. (2004). *Physica B* **352**, 105.

Greaves, C. (1985). *J. Appl. Crystallogr.* **18**, 48.

Green, D.J., Hannink, R.H.J., and Swain, M.V. (1989). *Transformation toughening of ceramics*. CRC Press, Boca Raton, Florida.

Grimley, D.I., Wright, A.C., and Sinclair, R.N. (1990). *J. Non-Cryst. Solids* **119**, 49.

Gull, S.F. and Daniel, G.J. (1978). *Nature* **272**, 686.

Hahn, Th. (ed.) (1987). *International tables for crystallography Volume A: space group symmetry.* D. Riedel Publishing, Dordrecht.

Hall, W.H. (1949). *Proc. Phys. Soc. London A*, **62**, 741.

Hammond, C. (1990). *Introduction to crystallography*. Oxford Science Publications, Oxford.

Hanawalt, J.D., Rinn, H.W., and Frevel, L.K. (1936). *Ind. Eng. Chem. Anal. Ed.* **8**, 244.

Hanawalt, J.D., Rinn, H.W., and Frevel, L.K. (1938). *Ind. Eng. Chem. Anal. Ed.* **10**, 457.

Hannink, R.H.J., Howard, C.J., Kisi, E.H., and Swain, M.V. (1994). *J. Amer. Ceram. Soc.* **77**, 571.

Hannon, A.C. (2005). *Nucl. Instrum. Methods in Phys. Res.* **A 551**, 88.

Harker, D. (1936). *J. Chem. Phys.* **4**, 381.

Hastings, J.B., Thomlinson, W., and Cox, D.E. (1984). *J. Appl. Crystallogr.* **17**, 85.

Hastings, J.M. and Corliss, L.M. (1953). *Rev. Mod. Phys.* **25**, 114.

Hauk, V. and Kockelmann, H. (1979). *Z. Metallkd.* **70**, 500.

Hayakawa, M., Imai, S., and Oka, M. (1985). *J. Appl. Crystallogr.* **18**, 513.

Hendricks, S. and Teller, E. (1942). *J. Chem. Phys.* **10**, 147.

Hewat, A.W. (1973). *J. Phys. C* **6**, 2559.

Hewat, A.W. (1975). *Nucl. Instrum. Methods* **127**, 361.

Hewat, A.W. (1986). *Mater. Sci. Forum* **9**, 69.

Hewat, A.W. and Bailey, I. (1976). *Nucl. Instrum. Methods* **137**, 463.

Hicks, T.J. (1995). *Magnetism in disorder*. Oxford University Press, Oxford.

Hill, R. (1952). *Proc. Phys. Soc. A* **65**, 349.

Hill, R.J. and Flack, H.D. (1987). *J. Appl. Crystallogr.* **20**, 356.

Hill, R.J. and Howard, C.J. (1985). *J. Appl. Crystallogr.* **18**, 173.

Hill, R.J. and Howard, C.J. (1986). Australian Atomic Energy Commission Report M112.

Hill, R.J. and Howard, C.J. (1987). *J. Appl. Crystallogr.* **20**, 467.

Hill, R.J. and Madsen, I.C. (1984). *J. Appl. Crystallogr.* **17**, 297.

Hill, R.J. and Madsen, I.C. (1986). *J. Appl. Crystallogr.* **19**, 10.

Hill, R.J. and Madsen, I.C. (1987). *Powder Diffraction* **2**, 146.

Hirsekorn, S. (1990). *Texture Microstruct.* **12**, 1.

Housley, H.M. and Hess, F. (1966). *Phys. Rev.* **146**, 517.

Howard, C.J. (1982). *J. Appl. Crystallogr.* **15**, 615.

Howard, C.J. and Kisi, E.H. (1990). *J. Amer. Ceram. Soc.* **73**, 3096.

Howard, C.J. and Kisi, E.H. (1999). *J. Appl. Crystallogr.* **32**, 624.

Howard, C.J. and Kisi, E.H. (2000). *J. Appl. Crystallogr.* **33**, 1434.

Howard, C.J. and Stokes, H.T. (1998). *Acta Crystallogr. B* **54**, 782. *Erratum*, *ibid*, *B* **58**, 565.

Howard, C.J. and Stokes, H.T. (2005). *Acta Crystallogr. A* **61**, 93.

Howard, C.J., Ball, C.J., Elcombe, M.M., and Davis, R.L. (1983). *Aust. J. Phys.* **36**, 507.

Howard, C.J., Hill, R.J., and Reichert, B.E. (1988a). *Acta Crystallogr. B* **44**, 116.

Howard, C.J., Hill, R.J., and Sufi, M.A.M. (1988b). *Chem. Aust.* **55**, 367.

Howard, C.J., Kisi, E.H., and Ohtaka, O. (1991). *J. Amer. Ceram. Soc.* **74**, 2321.

Howard, C.J., Kisi, E.H., Roberts, R.B., and Hill, R.J. (1990). *J. Amer. Ceram. Soc.* **73**, 2828.

Howard, C.J., Knight, K.S., Kennedy, B.J., and Kisi, E.H. (2000). *J. Phys.: Condens. Matter* **12**, L677.

Howard, C.J., Luca, V., and Knight, K.S. (2002). *J. Phys.: Condens. Matter* **14**, 377.

Howard, C.J., Withers, R.L., and Kennedy, B.J. (2001). *J. Solid State Chem.* **160**, 8.

Huang, K. (1947). *Proc. Roy. Soc.* **A190**, 102.

Hunter, B.A. (1998). *International Union of Crystallography Commission on powder diffraction*, Newsletter No. 20, p. 21.

Ibberson, R.M. and David, W.I.F. (2002). In *Structure determination from powder diffraction data* (eds. W.I.F. David, K. Shankland, L.B. McCusker, and Ch. Baerlocher), p. 88. Oxford University Press, Oxford.

Inui, H., Yamamoto, T., Hirota, M., and Yamaguchi, M. (2002). *J. Alloys Compounds* **330**, 117.

Irvine, J.S., Feigherg, A.J., Fazz, D.P., and Garcia-Martin, S. (2000). *Solid State Ionics* **136–137**, 879.

Ito, T. (1949). *Nature*, **164**, 755.

Ito, T. (1950). *X-ray studies on polymorphism*, p. 187. Maruzen, Tokyo.

Ivanov, S.A., Eriksson, S.-G., Tellgren, R., and Rundlof, H. (2004). *Mater. Res. Bull.* **39**, 2317.

Izyumov, Y.A. and Ozerov, R.P. (1970). *Magnetic neutron diffraction*. Plenum Press, New York.

Izyumov, Y.A., Naish, V.E., and Ozerov, R.P. (1991). *Neutron diffraction of magnetic materials*. Kluwer Academic, New York.

James, R.W. (1945). *X-ray crystallography*. Methuen, London.

Jansen, E., Schäfer, W., and Will, G. (1988). *J. Appl. Crystallogr.* **21**, 1988.

Jansen, E., Schäfer, W., Will, G., and Knight, K.S. (1996). *Mater. Sci. Forum* **228**, 259.

Johnson, C.K. (1965). *ORTEP: A FORTRAN Thermal Ellipsoid Plot Program for Crystal Structure Illustrations, ORNL-3794* (Rev.). Union Carbide Corporation, Oak Ridge National Laboratory, June 1965.

Johnson, C.K. and Levy, H.A. (1974). *International tables for X-ray crystallography, Vol. 4*, p. 313. Kynoch Press, Birmingham.

Johnson, M.W. and Daymond, M.R. (2003). In *Analysis of residual stress by diffraction using neutron and synchrotron radiation*. (eds. M.E. Fitzpatrick and A. Lodini) p. 146. Taylor & Francis, London.

Jones, H. (1960). *The theory of Brillouin zones and electronic states in crystals*, 1st ed. Amsterdam, North Holland.

Jorgenson, J.D., Beno, M.A., Hinks, D.G., Soderholm, L., Volin, K.J., Hitterman, R.L., Grace, J.D, Schuller, I.K., Segre, C.U., Zhang, K., and Keefisch, M.S. (1987). *Phys. Rev. B* **36**, 3608.

Kakinoki, J. (1967). *Acta Crystallogr.* **23**, 875.

Kakinoki, J. and Tomura, Y. (1965). *Acta Crystallogr.* **19**, 137.

Kallend,J.S. (1998). *Texture and anisotropy: preferred orientations in polycrystals and their effect on materials properties* (eds. U.F. Kocks, C.N. Tome, and H.-R. Wenk). Cambridge University Press, Cambridge.

Kallend, J.S., Kocks, U.F. Rollett, A.D., and Wenk, H.R. (1991). *Mater. Sci. Eng. A*, **132**, 1.

Kamminga, J.-D. and Delhez, R. (2001). *Mater. Sci. Forum* **378–381**, 142.

Kandil, H.M., Greiner, J.D., and Smith, J.F. (1984). *J. Amer. Ceram. Soc.* **67**, 341.

Kariuki, B.M., Belmonte, S.A., McMahon, M.I., Johnston, R.L., Harris, K.D.M., and Nelmes, R.J. (1999). *J. Synchrotron Rad.* **6**, 87.

Karle, J. and Hauptmann, H. (1956). *Acta Crystallogr.* **9**, 635.

Karle, J. and Karle, I. (1966). *Acta Crystallogr.* **21**, 849.

Kasper, J.S. and Lonsdale, K. (eds.) (1959). *International tables for X-ray crystallography, Volume 2.* Kynoch Press, Birmingham.

Khachaturyan, A.G., Semenovskaya, S.V., and Vainshtein, B. (1979). *Krystallografiya*. **24**, 905. [*Sov. Phys. Crystallogr.* **24**, 519.]

Khachaturyan, A.G., Semenovskaya, S.V., and Vainshtein, B. (1981). *Acta Crystallogr. A* **37**, 742.

Khalyavin, D.D., Balagurov, A.M., Beskrovnyi, A.I., Troyanchuk, I.O., Sazonov, A.P., Tsipis, E.V., and Kharton, V.V. (2004). *J. Solid State Chem.* **177**, 2068.

Kim, G.H., Chun, C.H., Lee, S.G., and Lee, J.Y. (1994). *Acta Metall. Mater.* **42**, 3157.

Kim, G.H., Lee, S.G., Lee, J.Y., and Chun, C.H. (1995). *Acta Metall. Mater.* **43**, 2233.

Kisi, E.H. (1988). *Atomic arrangements in the gamma brasses*, PhD thesis. The University of Newcastle, Australia.

Kisi,E.H. (1994). *Materials Forum* **18**, 135.

Kisi, E.H. and Browne, J.D. (1991). *Acta Crystallogr. B* **47**, 835.

Kisi, E.H. and Howard, C.J. (1998). *J. Amer. Ceram. Soc.* **81**, 1682.

Kisi, E.H. and Ma, Y. (1998). *J. Phys.: Condens. Matter* **10**, 3832.

Kisi, E.H. and Riley, D.P. (2002). *J. Appl. Crystallogr.* **35**, 664.

Kisi, E.H., Buckley, C.E., and Gray, E.M. (1992). *J. Alloys Compounds* **185**, 362.

Kisi, E.H., Forrester, J.S., Howard, C.J., and Ibberson, R.M. (2007). *J. Phys.: Condens. Matter* **19**, 232201.

Kisi, E.H., Howard, C.J., and Hill, R.J. (1989). *J. Amer. Ceram. Soc.* **72**, 1757.

Kisi, E.H., Kennedy, S.J., and Howard, C.J. (1997). *J. Amer. Ceram. Soc.* **80**, 621.

Kisi, E.H., Riley, D.P., and Curfs, C.C. (2006). *Physica B* **385–386**, 487.

Kittel, C. (1976). *Introduction to solid state physics*, 5th ed. John-Wiley, New York.

Klimanek, P. and Kužel, R. Jr. (1988). *J. Appl. Crystallogr.* **21**, 59.

Klug, H.P. and Alexander, L.E. (1974). *X-Ray diffraction procedures for polycrystalline and amorphous materials*. John-Wiley & Sons, New York.

Knee, C.S., Field, M.A.L., and Weller, M.T. (2004). *Solid State Sci.* **6**, 443.

Knight, K.S. (2008). *Canadian Mineralogist*, in press.

Koester, L., Rauch, H., and Saymann, E. (1991). *Atomic Data Nucl. Data Tab.* **49**, 65.

Korff, S.A. and Danforth, W.E. (1939). *Phys. Rev. B* **55**, 980.

Kramer, P. (1987). *Acta Crystallogr. A* **43**, 486.

Krivoglaz, M.A. (1969). *Theory of X-ray and thermal neutron scattering by real crystals*. Plenum Press, New York.

Krivoglaz, M.A. and Ryaboshapka, K.P. (1963). *Fiz. Met. Metalloved.* **15**, 18.

Krivoglaz, M.A., Martynenko, O.V., and Ryaboshapka, K.P. (1983). *Fiz. Met. Metalloved.* **55**, 5.

Kröner, E. (1958). *Z. Physik.* **151**, 504.

Kudoh, Y., Takeda, H., and Arashi, H. (1986). *Phys. Chem. Mineral.* **13**, 233.

Kumazawa, S., Takata, M., and Sakata, M. (1995). *Acta Crystallogr. A* **51**, 651.

Ladd, M.F.C. and Palmer, R.A. (1980). *Theory and practice of direct methods in crystallography*. Plenum Press, New York.

Landau, L. (1937). *Phys. Z. Sowj Un*, **12**, 579.

Landau, L.D. and Lifshitz, E.M. (1980). *Statistical physics.* Pergamon Press, New York.

Langford, J.I. and Wilson, A.J.C. (1978). *J. Appl. Crystallogr*. **11**, 102.

Langford, J.I., Louer, D., and Scardi, P. (2000). *J. Appl. Crystallogr*. **33**, 964.

Larson, A.C. and Von Dreele, R.B. (2004). *General structure analysis system*. Los Alamos National Laboratory, Report No. LAUR. 86–748.

Lartigue, C., Le Bail, A., and Porcheron-Guegan, A. (1987). *J. Less Common Metals* **129**, 65.

Le Bail, A. (2001). *Mater. Sci. Forum* **378–381**, 65.

Le Bail, A. (2004). *Powder Diffraction* **19**, 249.

Le Bail, A. and Cranswick, L. (2003). *IUCr Powder diffraction*, Newsletter No. 29, ISSN 1591–9552, http://www.mpi-stuttgart.mpg.de/cpd/html/newsletter.html

Le Bail, A. and Jouanneaus, A. (1997). *J. Appl. Crystallogr*. **30**, 265.

Le Bail, A., Duroy, H., and Fourquet, J.L. (1988). *Mater. Res. Bull.* **23**, 447.

Leineweber, A. (2007). *J. Appl. Crystallogr*. **40**, 362.

Leoni, M., Martinez-Garcia, J., and Scardi, P. (2007). *J. Appl. Crystallogr.* **40**, 719.

Lerch, M., Boysen, H., and Radaelli, P.G. (1997). *J. Phys. Chem. Solids* **58**, 1557.
Levy, H.A. and Peterson, S.W. (1952). *Phys. Rev.* **86**, 766.
Levy, J.H., Taylor, J.C., and Wilson, P.W. (1975a). *Acta Crystallogr. B* **31**, 398.
Levy, J.H., Taylor, J.C., and Wilson, P.W. (1975b). *J. Solid State Chem.* **15**, 360.
Lifshitz, I.M. (1937). *Phys. Z. Sowj Un* **12**, 623.
Lifshitz, I.M. (1939) *J. Exper. Theor. Phys. U.S.S.R.* **9**, 491.
Loopstra, B.O. and Rietveld, H.M. (1969). *Acta Crystallogr. B* **25**, 787.
Louër, D. and Louër, M. (1972). *J. Appl. Crystallogr.* **5**, 271.
Louër, D. and Vargas, R. (1982). *J. Appl. Crystallogr*. **15**, 542.
Lovett, D.R. (1989). *Tensor properties of crystals*. Institute of Physics Publishing, Bristol.
Lutterotti, L. and Scardi, P. (1990). *J. Appl. Crystallogr*. **23**, 246.
Lynch, P. (2003). *X-ray line broadening for gold thin films*, PhD thesis. University of Technology, Sydney.
Ma, Y. and Kisi, E.H. (1998). *J. Phys: Condens. Matter* **10**, 3823.
Ma, Y. and Kisi, E.H. (2005). *J. Amer. Ceram. Soc*. **88**, 2510.
Ma, Y., Kisi, E.H., and Kennedy, S.J. (2001). *J. Amer. Ceram. Soc*. **84**, 399.
Ma, Y., Kisi, E.H., Kennedy, S.J., and Studer, A.J. (2004). *J. Amer. Ceram. Soc.* **87**, 465.
Madsen, I.C., Scarlett, N.V.Y., Cranswick, L.M.D., and Lwin, T. (2001). *J. Appl. Crystallogr*. **34**, 409.
March, A. (1932). *Z. Kristallogr*. **81**, 285.
Marciniak, H., Gierlotka, S., and Palosz, B. (1996). *Mater. Sci. Forum* **228**, 39.
Marshall, W. and Lovesey, S.W. (1971). *Theory of thermal neutron scattering: the use of neutrons for the investigation of condensed matter*. Clarendon Press, Oxford.
Marshall, D.B., James, M.R., and Porter, J.R. (1989). *J. Amer. Ceram. Soc.* **72**, 218.
Matthies, S. and Humbert, M. (1995). *J. Appl. Crystallogr.* **28**, 254.
Matthies, S., Priesmeyer, H.G., and Daymond, M.R. (2001). *J. Appl. Crystallogr.* **34**, 585.
McClune, W.F. (ed.) (2001). *Powder diffraction file*. International Centre for Diffraction Data, Newtown Square, Pennsylvania.
McCusker, L.B., Von Dreele, R.B., Cox, D.E., Louër, D., and Scardi, P. (1999). *J. Appl. Crystallogr.* **32**, 36.
McGreevy, R.L. (1994). *Mater. Sci. Forum* **166–169**, 45.
McGreevy, R.L. (2001). *J. Phys.: Condens. Matter* **13**, R887.
McGreevy, R.L. and Mitchell, E.W.J. (1982). *J. Phys. C* **15**, 5537.
Megaw, H.D. (1973). *Crystal structures: a working approach*. W.B. Saunders Company, London.

Mellergård, A. and McGreevy, R.L. (2000). *Chem. Phys.* **261**, 267.

Mellergård, A. and McGreevy, R.L. (2001). *Mater. Sci. Forum* **378–383**, 71.

Michalewicz, Z. (1996). *Genetic algorithms + data Structures = evolution programs*, 3rd ed. Springer-Verlag, Berlin.

Michalski, E. (1988). *Acta Crystallogr. A* **44**, 640.

Mighell, A.D. and Santoro, A. (1975). *J. Appl. Crystallogr.* **8**, 372.

Mildner, D., Chen, H., Downing, G., and Sharov, V. (1993). *J. Neutron Res.* **1**, 1.

Millis, A.J. (1998). *Nature* **392**, 147.

Mitchell, D.P. and Powers, P.N. (1936). *Phys. Rev.* **50**, 486.

Mitchell, J.F., Argyriou, D.N., Potter, C.D., Hinks, D.G., Jorgensen, J.D., and Bader, S.D. (1996). *Phys. Rev. B* **54**, 6172.

Moisy-Maurice, V., Lorenzelli, N., De Novion, C.H., and Convert, P. (1982). *Acta Metall.* **30**, 1769.

Moore, M.G. and Evans, W.P. (1958). *Trans. SAE*, **66**, 340.

Moore, M.J. and Kasper, J.S. (1968). *Nature* **24**, 848

Morniroli, J.P. (2004). *Large angle convergent beam electron diffraction: applications to crystal defects*. Taylor & Francis, CRC Press, Boca Raton, Florida.

Moss, S.C. and Clapp, P.C. (1968). *Phys. Rev.* **171**, 764.

Muddle, B.C. (1985). *Metals Forum* **2–3**, 93.

Mura, T. (1991). *Micromechanics of defects in solids*. Kluwer, Dordrecht.

Mursic, Z., Vogt, T., and Frey, F. (1992). *Acta Crystallogr. B* **48**, 584.

Nevitt, M.V., Chan, S.-K., Liu, J.Z, Grimsditch, M.H., and Fang, Y. (1988). *Physica B* **150**, 230.

Nield, V.M. and Keen, D.A. (2000). *Diffuse neutron scattering from crystalline materials*. Oxford University Press, Oxford.

Nield, V.M., McGreevy, R.L., Keen, D.A., and Hayes, W. (1994). *Physica B* **202**, 159.

Nix, F.C., Beyer, H.G., and Dunning, J.R. (1940). *Phys. Rev.* **58**, 1031.

Noeraj, T. and Mills, M.J. (2001). *Mater. Sci. Eng. A* **319–321**, 415.

Noyan, I.C. and Cohen, J.B. (1987). *Residual stress – measurement by diffraction and interpretation.* Springer-Verlag, New York.

Nye, J.F. (1957). *Physical properties of crystals*. Oxford University Press, Oxford.

Oed, A, (2001). *Neutron Data Booklet* (eds. A.-J. Dianoux and G. Lander). ILL, Orrendole.

Oed, A. (1988). *Nucl. Instrum. Methods A* **263**, 351.

Ohtaka, O, Yamanaka, T., Kume, S., Hara, N., Asano, H., and Izumi, F. (1990). *Proc. Jpn. Acad. Ser. B* **66**, 193.

Otes, A., Kajzar, F., Kucab, M., and Sikorn, W. (1976). *Magnetic structures determined by neutron diffraction.* Polska Akademia Nank, Warsaw.

Ouyang, Z.W., Wang, F.W., Hang, Q., Liu, W.F., Liu, G.Y., Lynn, J.W., Liang, J.K., and Rao, G.H. (2005). *J. Alloys Compounds* **390**, 21.

Passell, L., Bar-Ziv, S., Gardner, D.W., Cox, D.E., and Axe, J.D. (1991). *Mater. Sci. Forum* **79–82**, 475.

Paul-Boncour, V., André, G., Bouréé, F., Guillof, M., Wiesingar, G., and Percheron-Guégan, A. (2004). *Physica B* **350**, 27.

Pawley, G.S. (1981). *J. Appl. Crystallogr.* **14**, 357.

Peschar, R., Etz, A., Jansen, J., and Schenk, H. (2002) In *Structure determination from powder diffraction data* (eds. W.I.F. David, K. Shankland, L.B. McCusker, and Ch. Baerlocher), p. 179. Oxford University Press, Oxford.

Peterse, W.J.A.M. and Palm, J.H. (1966). *Acta Crystallogr.* **20**, 147.

Pierson, H.O. (1996). *Handbook of refractory carbides and nitrides*. Noyes, Westwood, New Jersey.

Pintschovius, L. (2003). In *Analysis of residual stress by diffraction using neutron and synchrotron radiation* (eds. M.E. Fitzpatrick and A. Lodini), p. 133. Taylor & Francis, London.

Popa, N.C. (1992). *J. Appl. Crystallogr.* **25**, 611.

Popa, N.C. (1998). *J. Appl. Crystallogr.* **31**, 176.

Popova, M.N., Klimin, S.A., Malkin, B.Z., Kasalkina, L.A., Gao, G., and Crow, J. (1996). *Phys. Lett.* **A223**, 308.

Popovici, M.M. and Yelon, W.B. (1995). *J. Neutron Res.* **3**, 1.

Pototskaja, V.I. and Ryaboshapka, K.P. (1968). *Metallofizika* **24**, 97.

Powell, D.H., Neilson, G.W., and Enderby, J.E. (1993). *J. Phys.: Condens. Matter* **5**, 5723.

Prince, E. (1982). *Mathematical techniques in crystallography and materials science*. Springer-Verlag, New York.

Prince, E. (1983). *J. Appl. Crystallogr.* **16**, 508.

Prince, E. (1993). In *The Rietveld method*. (ed. R.A. Young) p. 43. International Union of Crystallography, Oxford University Press, Oxford.

Prince, E. (ed.) (2006). *International tables for crystallography Volume C: Mathematical, physical and chemical tables*. Springer-Verlag, Berlin.

Proffen, T. and Billinge, S.J.L. (1999). *J. Appl. Crystallogr*. **32**, 572.

Putz, H., Schön, J.C., and Jansen, M. (1999). *J. Appl. Crystallogr.* **32**, 864.

Qiu, X., Proffen, T., Mitchell, J.F., and Billinge, S.J.L. (2005). *Phys. Rev. Lett*. **94**, 177203.

Rafaja, D. (2000). *Materials Structure* **7**, 43.

Reefman, D. (1999). In *Defect and microstructure analysis by diffraction* (eds. R.L. Snyder, J. Fiala, and H.J. Bunge), p. 652. Oxford University Press, Oxford.

Reinhard, L. and Moss, L.C. (1993). *Ultramicroscopy* **52**, 223.

Reuss, A. (1929). *Z. Angew. Math. Mech.* **9**, 49.

Richardson, J.W. (1993). In *The Rietveld method* (ed. R.A. Young). International Union of Crystallography, Oxford University Press, Oxford.

Rietveld, H.M. (1967). *Acta Crystallogr.* **22**, 151.

Rietveld, H.M. (1969). *J. Appl. Crystallogr.* **2**, 65.

Riley, D.P., Kisi, E.H., Hansen, T.C., and Hewat, A.W. (2002). *J. Amer. Ceram. Soc*. **85**, 2417.

Robertson, J. (2002). *Mater. Sci. Eng. R*, **37**, 129.

Rogan, R.C., Tamura, N., Swift, G.A., and Ustundag, E. (2003). *Nat. Mater.* **2**, 379.

Roth (1958). *Phys. Rev.* **110**, 1333.

Ruis, J. (2002). In *Structure determination from powder diffraction data* (eds. W.I.F. David, K. Shankland, L.B. McCusker, and Ch. Baerlocher), p. 219. Oxford University Press, Oxford.

Runge, C. (1917). *Z. Physik*. **18**, 509.

Sabine, T.M. (1980). *Aust. J. Phys.* **33**, 565.

Sabine, T.M. (1988). *Acta Crystallogr. A* **44**, 368.

Sabine, T.M. (1993). In *The Rietveld method* (ed. R.A. Young), p. 55. International Union of Crystallography, Oxford University Press, Oxford.

Sakata, M., Uno, T., Takata, M., and Howard, C.J. (1993). *J. Appl. Crystallogr.* **26**, 159.

Salje, E. (1990). *Phase transitions in ferroelastic and co-elastic crystals*. Cambridge University Press, Cambridge.

Salmon, P.S. and Liu, J. (1996). *J. Non-Cryst. Solids* **205–207**, 172.

Savitky, A. and Golay, M.J.E. (1964). *Anal. Chem.* **36**, 1627.

Sayre, D. (1952). *Acta Crystallogr.* **5**, 60.

Scarlett, N.V.Y., Madsen, I.C., Cranswick, L.M.D., Lwin, T., Groleau, E., Stephenson, G., Aylmore, M., and Agron-Olshina, N. (2002). *J. Appl. Crystallogr.* **35**, 383.

Schäfer, W. and Will, G. (1979). *Acta Crystallogr. B* **35**, 588.

Schenk, H. (ed.) (1991). *Direct methods of solving crystal structures*. Plenum Press, New York.

Scherrer, P. (1918). *Nachr. Ges. Wiss. Göttingen* **2**, 98.

Schobinger-Papamantellos, P., Buschow, K.H.J., and Ritter, C. (2004). *J. Alloys Compounds* **384**, 12.

Schoenflies, A. (1891). *Krystallsysteme und Krystallstructur.* Teubner, Leipzig.

Scott, H.G. (1975). *J. Mater. Sci*. **10**, 1527.

Semenovskaya, S.V. and Khachaturyan, A.G. (1985). *Sov. Phys. Crystallogr*. **30**, 22.

Semenovskaya, S.V., Khachaturyan, K.A., and Khachaturyan, A.G. (1985). *Acta Crystallogr. A* **41**, 268.

Senechal, M. (1995). *Quasicrystals and geometry*. Cambridge University Press, New York.

Shankland, K. and David, W.I.F. (2002). In *Structure determination from powder diffraction data* (eds. W.I.F. David, K. Shankland, L.B. McCusker, and Ch. Baerlocher), p. 252. Oxford University Press, Oxford.

Sheldrick, G. (2007). http://shelx.uni-ac.gwdg.de/SHELX/

Shirane, G. (1959). *Acta Crystallogr.* **12**, 282.

Shirane, G. and Takei, W.J. (1962). *J. Phys. Soc. Jpn. Suppl. BIII*, **17**, 35.

Shirley, R. (1984). *Methods Appl. Crystallogr. Comput.*, Int. Summer School (eds. S.R. Hall and T. Ashida). Clarendon Press Oxford.

Shubnikov, A.V. (1951). *Symmetry and antisymmetry of finite figures*. Moscow (in Russian).

Shubnikov, A.V. and Belov, N.V. (1964). *Coloured symmetry*. Pergamon, Oxford.

Shull, C.G. (1995). *Rev. Mod. Phys.* **67**, 753.

Shull, C.G. and Siegel, S. (1949). *Phys. Rev.* **75**, 1008.

Shull, C.G. and Smart, J.S. (1949). *Phys. Rev.* **76**, 1256.

Shull, C.G. and Wilkinson, M.K. (1955). *Phys. Rev.* **97**, 304.

Shull, C.G. and Wollan, E.O. (1951). *Phys. Rev.* **81**, 527.

Shull, C.G. and Yamada, Y. (1962). *J. Phys. Soc. Jpn. Suppl. BIII* **17**, 1.

Shull, C.G., Strauser, W.A., and Wollan, E.O. (1951a). *Phys. Rev.* **83**, 333.

Shull, C.G., Wollan, E.O., and Koehler, W.C. (1951b). *Phys. Rev.* **84**, 912.

Shull, C.G., Wollan, E.O., Morton, G.A., and Davidson, W.L. (1948). *Phys. Rev.* **73**, 842.

Sidhu, S.S., Heaton, Le Roy, Zauberis, D.D., and Campos, F.P. (1956). *J Appl. Phys*. **27**, 1040.

Singh, A.K., Mao, H.K., Shu, J., and Hemley, R.J. (1998). *Phys. Rev. Lett.* **80**, 2157.

Snyder, R.L., Fiala, J., and Bunge, H.J. (eds.) (1999). *Defect and microstructure analysis by diffraction*. Oxford University Press, Oxford.

Sørby, M.H., Mellergård, A., Delaplane, R.G., Wannberg, A., Hauback, B.C., and Fjellvåg, H. (2004). *J. Alloys Compounds* **363**, 209.

Spooner, S. (2003). In *Analysis of residual stress by diffraction using neutron and synchrotron radiation* (eds. M.E. Fitzpatrick and A. Lodini), p. 296. Taylor & Francis, London.

Squires, G.L. (1978). *Introduction to the theory of thermal neutron scattering*. Cambridge University Press, London.

Stehr, H. (1967). *Z. Kristallogr*. **125**, 332.

Stephens, P. (1999). *J. Appl. Crystallogr*. **32**, 281.

Stirling, W.G. and Cooper, M.J. (1999). *J. Magnetism Magnetic Materials* **200**, 755.

Stokes, A.R. (1948). *Proc. Phys. Soc. London* **61**, 382.

Stokes, H.T. and Hatch, D.M. (1998) ISOTROPY software suite, http://stokes.byu.edu/isotropy.html

Storms, E.K. (1967). *The refractory carbides*. Academic Press, New York.

Stout, G.H. and Jensen, L.H. (1968). *X-ray structure determination: a practical guide*. Macmillan, New York.

Taylor, D.R. (2000). *Solid State Comm.* **116**, 447.

Taylor, D.R. and Swainson, I.P. (1998). *J. Phys: Condens. Matter* **10**, 10207.

Taylor, J.C. and Matulis, C.E. (1991). *J. Appl. Crystallogr.* **24**, 14.

Taylor, J.C. and Wilson, P.W. (1974). *Acta Crystallogr. B* **30**, 2664.

Taylor, J.C. and Wilson, P.W. (1975). *J. Solid State Chem.* **14**, 378.

Taylor, J.C., Wilson, P.W., and Kelly, J.W. (1973). *Acta Crystallogr. B* **29**, 7.

Thompson, P., Cox, D.E., and Hastings, J.M. (1987a). *J. Appl. Crystallogr.* **20**, 79.

Thompson, P., Reilly, J.J., Corliss, L.M., Hastings, J.M., and Hempelmann, R. (1987b). *J. Phys. F* **16**, 675.

Tilley, R. (2006). *Crystals and crystal structures*. John Wiley & Sons, New York.

Toby, B.H. (2001). *J. Appl. Crystallogr.* **34**, 210.

Tokar, V.J. (1985). *Phys. Lett*. **A110**, 453.

Toraya, H. (1988). *J. Appl. Crystallogr.* **21**, 192.

Treacy, M.M.J., Newsam, J.M., and Deem, M.W. (1991). *Proc. Roy. Soc. London A* **433**, 499.

Trigunayat, G.C. (1991). *Solid State Ionics* **48**, 2.

Trueblood, K.N., Bürgi, H.-B, Burzlaff, H., Dunitz, J.D., Gramaccioli, C.M., Schulz, H.H., Shmueli, U., and Abrahams, S.C. (1996). *Acta Crystallogr. A* **52**, 770.

Turner, P.A. and Tomé, C.N. (1994). *Acta Metallurgica et Materialia* **42**, 4143.

Ungar, T., Leoni, M., and Scardi, P. (1999). *J. Appl. Crystallogr.* **32**, 290.

Unman, J. and Houska, C.R. (1976). *J. Appl. Phys.* **47**, 4336.

Valot, C.M., Floquet, N., Mesnier, M.T., and Niepce, J.C. (1996). *Mater. Sci. Forum* **228–231**, 59.

van Laar, B. and Yelon, W.B. (1984). *J. Appl. Crystallogr.* **17**, 47.

Van Vlack, L.H. (1975). *Elements of materials science: an introductory text for engineering students*. Addison-Wesley, Reading, Massachusetts.

Visser, J.W. (1969). *J. Appl. Crystallogr.* **2**, 89.

Vogt, T., Woodward, P.M., and Hunter, B.A. (1999). *J. Solid State Chem.* **144**, 209.

Voigt, W. (1887). *Abh. Kgl. Ges. Wiss. Göttingen Math. Kl.* **34**, 1.

Voigt, W. (1910). *Lehrbuch der Kristallphysik*, 1st ed. Taubner, Leipzig.

Von Dreele, R.B. (1997). *J. Appl. Crystallogr.* **30**, 517.

Von Dreele, R.B. and Cheetham, A.K. (1974). *Proc. Roy. Soc. London A* **338**, 311.

Von Dreele, R.B., Jorgensen, J.D., and Windsor, C.G. (1982). *J. Appl. Crystallogr.* **15**, 581.

Von Dreele, R.B., Stephens, P.W., Smith, G.D., and Blessing, R.H. (2000). *Acta Crystallogr. D* **56**, 1549.

von Halban, H. and Preiswerk, P. (1936). *C.R. Acad. Sci. Paris* **203**, 73.

Walker, C.B. and Keating, D.T. (1961). *Acta Crystallogr*. **14**, 1170.

Warren, B.E. (1933). *Z. Kristallogr*. **86**, 305.

Warren, B.E. (1934). *J. Amer. Ceram. Soc*. **17**, 249.

Warren, B.E. (1969). *X-ray diffraction*. Addison–Wesley, Reading, Massachusetts.

Warren, B.E. (1990). *X-ray diffraction*. Dover Publications, New York.

Warren, B.E. and Averbach, B.L. (1950). *J. Appl. Phys*. **21**, 595.

Warren, B.E. and Averbach, B.L. (1952). *J. Appl. Phys*. **23**, 497.

Weertman, J. and Weertman, J.R. (1964). *Elementary dislocation theory*. Macmillan, New York.

Welberry, T.R. (2004). *Diffuse X-ray scattering and models of disorder*. International Union of Crystallography, Oxford University Press, Oxford.

Wenk, H.-R. (2006). *Reviews in Mineralogy and Geochemistry*, Vol. 63, p. 399.

Wenk, H.-R., Matthies, S., and Lutterotti, L. (1994). *Mater. Sci. Forum* **157–162**, 473.

Werner, P.E. (1964). *Z. Kristallogr.* **120**, 375.

Werner, P.E. (2002). In *Structure determination from powder diffraction data* (eds. W.I.F. David, K. Shankland, L.B. McCusker, and Ch. Baerlocher), p. 118. Oxford University Press, Oxford.

Werner, P.E., Eriksson, L., and Westdahl, M. (1985). *J. Appl. Crystallogr.* **18**, 367.

Wertheim, G.K., Butler, M.A., West, K.W., and Buchanan, D.N.E. (1974). *Rev. Sci. Instrum.* **45**, 1369.

Wessels, T., Baerlocher, Ch., McCusker, L.B., and David, W.I.F. (2002). In *Structure determination from powder diffraction data* (eds. W.I.F. David, K. Shankland, L.B. McCusker, and Ch. Baerlocher), p. 162. Oxford University Press, Oxford.

Wicks, J.W. and McGreevy, R.L. (1995). *J. Non-Cryst. Solids* **192–193**, 23.

Wilkens, M. (1970). *Phys. Status Solidi A* **2**, 359.

Wilkens, M. (1976). *Krist. Tech.* **11**, 1159.

Wilkens, M. (1987). *Physica Status Solidi A – Appl. Res.* **104**, K1.

Wilkins, S.W., Varghese, J.N., and Lehmann, M.S. (1983). *Acta Crystallogr. A* **39**, 47.

Will, G., Jansen, E., and Schäffer, W. (1982). In *Neutron Scattering – 1981* (*AIP Conf. Proc. No*. 89), p. 205.

Will, G., Parrish, W., and Huang, T.C. (1983). *J. Appl. Crystallogr.* **16**, 611.

Williamson, G.K. and Hall, W.H. (1953). *Acta Metall*. **1**, 22.

Willis, B.T.M. (1970). *Acta Crystallogr. A* **26**, 396.

Willis, B.T.M. and Pryor, A.W. (1975). *Thermal vibrations in crystallography*. Cambridge University Press, Cambridge.

Wilson, A.J.C. (1942). *Proc. Roy. Soc. London A* **180**, 277.

Wilson, A.J.C. (1943). *Proc. Roy. Soc. London A* **181**, 360.

Wilson, A.J.C. (1962a). *Nature* **193**, 568.

Wilson, A.J.C. (1962b). *Proc. Phys. Soc.* (*London*) **80**, 286.

Windsor, C. and Sinclair, R. (1982). *Phys. Bull*. **33**, 290.

Wollan, E.O. and Koehler, W.C. (1955). *Phys. Rev.* **100**, 545.

Wollan, E.O. and Shull, C.G. (1948). *Phys. Rev.* **73**, 830.

Woolfson, M.M. (1970). *An introduction to X-ray crystallography*. Cambridge University Press, Cambridge.

Worlton, T.G., Jorgensen, J.D., Beyerlein, R.A., and Decker, D.L. (1976). *Nucl. Instrum. Methods* **137**, 331.

Wright, A.C. and Wagner, C.N.J. (1998). *J. Non-Cryst. Solids* **106**, 85.

Wu, E., Gray, E.M., and Kisi, E.H. (1998b). *J. Appl. Crystallogr.* **31**, 356.

Wu, E., Kisi, E.H., and Gray, E.M. (1998a). *J. Appl. Crystallogr.* **31**, 363.

Wu, E., Kisi, E.H., Kennedy, S.J., and Studer, A. (2001). *J. Amer. Ceram. Soc*. **84**, 2281.

Wu, E., Kisi, E.H., Riley, D.P., and Smith, R.I (2005). *J. Eur. Ceram. Soc*. **25**, 3503.

Wu, E., Kisi, E.H., Riley, D.P., and Smith, R.I. (2002). *J. Amer. Ceram. Soc*. **85**, 3084.

Yashima, M., Itoh, M., Inaguma, Y., and Morii, Y. (2005). *J. Amer. Chem. Soc*. **127**, 3491.

Young, R.A. (1993). In *The Rietveld method*, (ed. R.A. Young), p. 1. International Union of Crystallography, Oxford University Press, Oxford.

Zhang, Z., Howard, C.J., Knight, K.S., and Lumpkin, G.R. (2006). *Acta Crystallogr. B* **62**, 60.

Zolliker, P., Yvon, K., and Baerlocher, Ch. (1986). *J. Less Common Metals* **115**, 65.

Index

ab initio structure solution 192
absorption:
  by scattering 62
  micro 19, 33, 293, 402
  of neutrons 19, 40, 43–45, 157–58, 236, 287
  true 43–45
absorption coefficients 44, 61–63
  calculation for compounds and mixtures 63
  table 44
AgBr 391
Al_2O_3 100, 376–78
$AlF_3(\alpha)$ 451
amorphous materials:
  amorphous solids 35–6, 170, 381, 397–402, 450–51
  effect on quantitative phase analysis 401–02
  gases 397
  liquids 397–402
anharmonic thermal displacement 2, 239
annealing 102, 243, 363, 392, 436
asymmetry 11–12, 127–28, 159, 169, 346–72
atom coordinates 23–25, 34, 135, 143–46, 153–56, 177, 218–221, 232–34
attenuation, *see* absorption
attenuation factor, *see* absorption
AuMn 258, 263
Au_2Mn 4, 259, 261, 263, 266
Au_2MnAl 266
Austenite 287–89

Ba_2BiSbO_6 450
background:
  contributing factors 44, 47, 69–70, 86, 92–3
  functions 170
  models in Rietveld analysis 159, 170, 236
  radiation 64, 68, 95, 111
$BaPrO_3$ 281–83
$BaTiO_3$ 134, 352, 355, 357, 424
Bragg cut-off 19, 72, 132
Bragg peak 83, 129, 163, 170, 222, 268
Bragg's Law 51–55
Bravais lattice:
  crystal 23–24, 139
  magnetic 254–58
broadening, *see* peak broadening

$Ca_3Ti_2O_7$ 116, 132, 182–85, 201–22
calculated diffraction pattern 117, 154–55
centred lattice 23–25, 140–43, 151–53, 211
CH_4 396–97
coherent scattering 8, 42–5
  cross-section 42, 49
  length 42–45, 63, 72
  magnetic 45–48
cold source 18, 67, 69
collimator 70–72, 425, 435, 444, 445
  effect on resolution 73–75, 128–29
  radial 447
  Soller 45, 69, 83
constant wavelength technique 51, 53, 65, 70–77, 80
constraints 173–74, 179, 234–35, 391
convergence in structure refinement 178, 220, 221, 232–34
cost function 227, 230–31
Cr 259–60
critical angle 68–9, 445
cryostat 86–88
crystal structure 134–191
  ab initio solution 192–250
  basics 3, 9, 11, 14–7, 21–5
  interplanar spacing 55
  lattice 21
  lattice parameters 23, 118, 120–24
  long range order 30
  Miller indices 26, 27
  refinement 82, 155–82, 232–49

crystal structure *(Cont.)*
short range order 30, 385–95
solution 82, 150–54, 182–250
space groups 140–44
symmetry 136–44
unit cell 23, 120–25, 193–205
crystal structure examples:
β-brass (CuZn) 29, 376, 392–94
$Ca_3Ti_2O_7$ 182–84
diamond 72, 100, 372–73
fluorite (CaF_2) 25, 114, 240, 289
graphite 72
MnF_2 412
NaOD 150–54
crystal systems 23, 61, 139, 142, 146, 281
crystallite size, *see* peak broadening
Cu_9Al_4 120, 249–50
CuBr 391
$CuFeS_2$ 294–95
CuZn, *see* crystal structure examples

D_2O 108–9, 245
data analysis:
for crystal structure solution 146, 193, 205
for microstructural analysis 308
for quantitative phase analysis 287
new methods 449
preliminary 106
Debye:
scattering equation 357, 395–96
temperature 235, 237
–Waller factor 158, 160–62
Debye-Scherrer:
cones or rings 53–55, 60, 64, 70, 103, 127, 164, 285
geometry 61, 104, 119, 165
detector:
BF_3 75
^3He 76
micro-strip 76
multi-wire proportional 76
position sensitive 76, 379
scintillation 79
de–Wolff's method, *see* Ito's method
diffractometer 4–8, 13–4, 53–55
constant wavelength (CW) 54, 70–77, 125–27
high-intensity 82, 447–48
high-resolution 82, 446- 47
residual stress 425, 434–35, 448–49
time-of-flight (TOF) 77–80, 127–29
diffuse scattering 381
amorphous solids 397–402
definition 43, 381
gaseous 395–97
liquids 397–402
magnetic 267
short range order 30, 385–95
size effect 388–91
thermal 170, 382–85
direct methods of structure solution 192, 223–26
dislocations:
definition 31, 358–60
peak broadening due to 82, 337, 361–68
displacement parameter 57–8, 161–63, 235–39
interpretation 161–63, 236–39, 246–49
Displex™ 87
disproportionation 103
dominant zone 195, 210–08
d-spacing:
definition 27
effect on powder diffraction pattern 53
equations 55, 459
DyCuSi 275

elastic compliance:
definition 404
diffraction 415
effect of symmetry 407
elastic constants:
definition 404–05
determination 438–42
effect of symmetry 407
elastic modulus, *see* also elastic compliance, elastic constants:
polycrystalline solid 411–14
single crystal 405
electric field 90
electrochemical cell 92
$ErCu_{25}Ge_2$ 274
Ewald construction 52–54
experiment design 80–100

Fe-Al 439
FeCo 4, 9
Fe_2O_3 13
Fe_3O_4 13, 293
FeS_2 294–95
flight tube 70–71
Fourier:
  analysis 212–22, 389, 399
  deconvolution 315–17, 342–44
  filtering 401
  integral theorem 315
  map 21, 180
  transform 52, 57–8, 212–22
furnace 84–7

genetic algorithms 229–30
global optimisation 226–31

H_2O 100, 108, 245
helimagnetic structure 37, 263–66, 274
high pressure 4, 88–90
Hill average elastic moduli 411–12
$HoCu_{33}Ge_2$ 274
HoCuSi 275
HoN 270
hot source 18, 67, 396

ILL 5, 14, 66
incoherent scattering 42, 44, 48, 72
  attenuation due to 62
  magnetic 47
indexing of powder patterns 109, 120–23, 146, 193–205
intensity:
  background 30, 111, 125, 159, 170
  of a diffraction peak (I) 55–64
  of a point in a diffraction pattern (y_{obs}) 106, 155–56
interference function 311–14, 321–24, 371
inter–planar spacing, *see* *d*-spacing
ISIS 5, 15, 66
isotopic substitution 4, 45, 222, 239, 245
ISOTROPY 184, 187, 258
Ito's method for powder pattern indexing 195–97

$KAlF_4$ 369
kinetics of solid state reactions 305–07, 454
Kröner approach to elastic moduli 412–13, 431

LaB_6 345
$La_{1-x}Ca_xMnO_3$ 4, 13
$La_{0.62}Li_{0.16}TiO_3$ 452
$LaMnO_3$ 13, 451
$LaNi_5$ 45, 245, 319, 325, 337, 366–68
least-squares refinement 155, 159, 179, 234
Le Bail extraction 111, 132–33, 177–78
$LiCuCl_{3.2}H_2O$ 268
line broadening, *see* peak broadening
long range order parameter 30, 385, 394–95
Lorentz factor 58–60, 163–64

magnetic:
  Bravais lattice 256–57
  diffraction 2, 4, 6, 10, 260–66
  form factor 45
  moment 19
  ordering 10–13, 36–39, 253–55
  scattering 45–48, 260
  space group 257–58
  unit cell 38, 256
magnetic structure:
  antiferromagnetic 4, 11, 38, 254, 258, 262, 268
  collinear 253–54
  commensurate 253–59, 262
  ferrimagnetic 253–54
  ferromagnetic 253–54
  helical 263–66
  incommensurate 259–60, 263–66
  intermetallic compounds 273–74
  organic-inorganic compounds 279–81
  oxides 276–78
  silicides and germanides 274–76
  solution 267–72
  spiral, *see* helical, incommensurate
Maxwellian distribution of neutron wavelengths 18–19
$MgFe_2O_4$ 13

Mg_2NiH_4 373
Mg-PSZ 113–18, 189–91, 289–91, 294–302
$Mg_2Zr_5O_{12}$ 113–14, 189, 289, 295–300
Mg-Zr-O-N 391
micromechanics:
  definition 407
  influence on elastic constants 407–14, 426–33
microstrain:
  anisotropic 334–40
  broadening 330
  isotropic 330–34
Miller indices 26–27
Mitchell and Powers experiment 3, 5
MnO 4, 11–12
molecular dynamics simulations 399–400
monochromator 15, 70–73
  definition 70–71
  focussing 73
  germanium 71–72
  materials 72
  new 445
Monte Carlo methods 198, 227, 346, 390, 399–400, 450
multiple site occupancy 239–249
multiplicity factor 60–61, 462
  magnetic 271
NaCl 4, 6, 9, 213, 239
NaD 4, 10
NaH 4, 9–10
NaOD 135, 150–54, 156, 175
NaOH 150–51
$Nd_{2/3}TiO_3$ 449
ND_4Cl 9

neutron:
  absorption 40
  absorption cross-section 19, 43–45
  De Broglie equation 18,78
  elastic scattering 20, 39–45
  flux 4, 6, 13–14, 18, 39–40, 64–68
  magnetic moment 4, 6–7, 10–12, 19, 45–48, 272
  properties 19
  thermal 18–19
  wavelength 18
neutron guides 68–69
  new 445
neutron scattering:
  by a sample 39
  by an assembly of atoms 42
  by an atom 39
  coherent 42–45
  incoherent 42
  magnetic 45–48, 260
neutron sources 14, 15, 65–70, 443
  cold 18–19
  hot 18–19
  location of 66–67
  reactor 65–67
  spallation 69–70
  new 443
Ni_3Fe 4, 12
$NiFe_2O_4$ 13
$Ni(OD)_2$ 327
$Ni(OH)_2$ 326
null-matrix alloys 45, 83, 88

overlapping peaks:
  experimental separation 209
  theoretical separation 208

particle size, *see* peak broadening – due to small particle size
particle size distribution 318–25
Patterson map 208, 216
Patterson synthesis 212–18
Pawley fit 132, 231
$PbFe_{2/3}W_{1/3}O_3$ 276, 278
PbO 335
PbS 294
$PbZn_{1/3}Nb_{2/3}O_3$ 352
$PbZn_{1/3}Nb_{2/3}O_3$-$PbTiO_3$ 457
peak:
  asymmetry 111–12, 127–28, 159, 169, 346–48, 369
  position 115–16, 119–20
  shape 124–28
  variance 317
  width 128–31
peak broadening:
  anisotropic 325–30, 334–40, 360–62, 367–69
  due to chemical gradients 347–52
  due to dislocations 358–68
  due to small particle size 309–330
  due to stacking faults 368–74

due to strain 330–40
due to strain gradients 352–58
isotropic 308–325, 330–34, 340–46
size and strain combined 340–46
peak positions:
determination 115
sources of systematic error 119–20
peak shape:
constant wavelength 125–27
functions 125–28, 159, 166–69, 317–18
Gaussian 125, 159, 168
Lorentzian 125, 168
pseudo-Voigt 125–27, 168
time-of-flight (TOF) 127–28, 168
Voigt 125, 168
peak widths 128–31
perovskite 3, 13, 110–11, 143–45, 182–88, 201–08
phase identification 33, 113–18
phase quantification 96, 284–307
preferred orientation 64, 101, 103–04, 113, 158, 164–66, 292, 301–02, 374–80
primitive unit cell 23, 37, 139, 141–43

quantitative phase analysis:
examples 294–307
individual peak methods 287–92
polymorph method 287–92
Rietveld refinement method 292–93
standards 291–92
theory 285–87
whole pattern fitting 292–93

RbOD 335
RbOH 335
reactor neutron source, *see* neutron source – reactor
reciprocal lattice 27, 51–54, 57, 146, 160, 164, 193–94
refinement of crystal structures 155–177, 232–49
reflection broadening, *see* peak broadening
reflection conditions 146–50, 152–53, 183
residual stress diffractometer 425, 448
resolution 5, 14, 73–75, 77, 79, 81–83, 94, 102, 109, 110, 130–31, 167, 198, 394
Reuss approach to elastic moduli 411, 413, 427–28, 431–34
reverse Monte Carlo methods 390–91, 400–01
R-factors 175–76
Rietveld method, *see* Rietveld refinement
Rietveld refinement 4, 14, 131, 155–78

sample environment 2–3, 80, 83–93
scale factor 132, 155, 158, 160, 177, 286, 292
scattering:
coherent 42–45, 63, 72
incoherent 42
scattering length table 44
scattering vector 42, 46–47, 50–54
Scherrer:
constant 320, 325, 327
equation 314, 318, 324
semi-exhaustive powder pattern indexing 197
short range order 385–95
Cowley parameters 385–88
simulated annealing 227–29, 231, 400
SiO_2 35, 92, 104, 294, 398
$SiSe_2$ 400
site occupancy 239–249
multiple 240–43
space group 135–150
determination 146–50
symbol 141–42
spallation neutron source 69–70
spottiness 101
$Sr_3Ti_2O_7$ 183
$SrZrO_3$ 110–12, 184–89
stacking faults:
definition 31–32
effect on powder diffraction pattern 82, 368–374
standard samples 83, 99–100, 103, 106, 108, 120, 123, 131, 291
static displacements 29, 160, 236–39
steel 3, 104, 284, 287–88, 340, 421, 424, 427, 437
stress 403–05
effect on powder diffraction pattern 330–40, 414–20
residual stress analysis 420–38

structure:
crystal 21–25, 134–191
magnetic 36–39, 251–283
structure factor:
crystal 56, 146
magnetic 260–66
structure solution:
crystal 150–55
magnetic 267–72
successive dichotomy 197
symmetry:
configurational 258–59
crystal 135–50
magnetic 252–260
space group 135–150
translational 139–40
symmetry operators (Table) 138
systematic absences, *see* reflection conditions

$TbBaCo_{2-x}Fe_xO_{5+\gamma}$ 278
$TbCo_2$ 273–74
TbCuSi 275
TbN 270
temperature factor, *see* displacement parameter
texture, *see* also preferred orientation:
definition 374
determination using powder diffraction 375–380
thermal diffuse scattering, *see* diffuse scattering – thermal
Ti-6Al-4V 433
TiC 302–07
Ti_7Cu_3 400
$Ti_{76}Ni_{24}$ 400
Ti_3SiC_2 115, 117, 302–07, 454–56
$Ti_5Si_3C_x$ 246, 247, 303–06
time-of-flight 15, 51, 65, 77–80, 108, 127, 380
TiO_2 100, 294, 391, 452
titanium silicon carbide, *see* Ti_3SiC_2
TmCuSi 275
TOF, *see* time-of-flight

unit cell:
crystal 22–25, 52, 55
magnetic 12, 252–66
unit cell parameters:
definition 22, 458–60
determination 118–23
refinement 123–24, 131–33

$VD_{0.8}$ 391–92
visual inspection 109–113
Visser's method for powder pattern indexing, *see* Ito's method for powder pattern indexing
Voigt approach to elastic moduli 410–414
Voigt function peak shape 125–27, 167–69

Warren-Averbach method 342–44
whole pattern fitting, *see* also Rietveld refinement 120, 124–25, 131–33, 155–78, 272, 318, 344–46
Williamson-Hall plot 326, 334, 340–41
WO_3 450
Wyckoff position 144, 151, 154, 161, 234

X-ray diffraction 1–3, 10, 16, 43, 81, 113, 181, 213–16, 244, 286–94

$YBa_2Cu_3O_{7-\delta}$ 15, 278, 356
$YFe_2(D_{1-x}H_x)_{4.2}$ 273
$Y_2O_3-ZrO_2$ 391
$Y_2O_3-ZrO_2-Nb_2O_5$ 391
$Y_2O_3-ZrO_2-TiO_2$ 391
$Y-ZrO_2$ 293, 391

zirconia 25, 191, 240, 293, 299, 391, 439
zone indexing method of powder pattern indexing, *see* Ito's method for powder pattern indexing
$ZnFe_2O_4$ 13
ZnS 79, 294
$Zr_{0.82}Mg_{0.18}O_{1.82}$ 299
ZrO_2 25, 191, 240, 293, 299, 391, 439

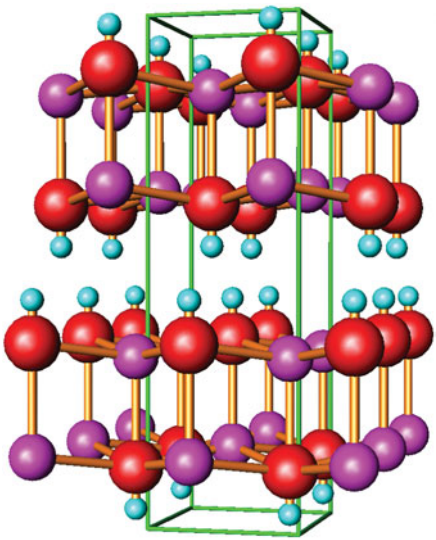

Plate 1

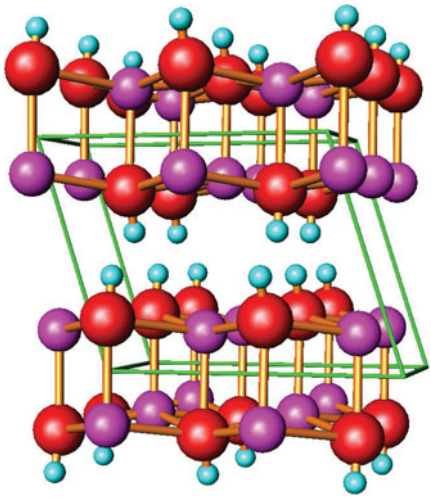

Plate 2

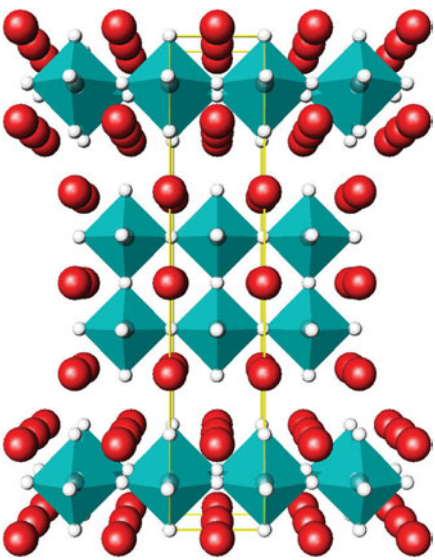

Plate 3

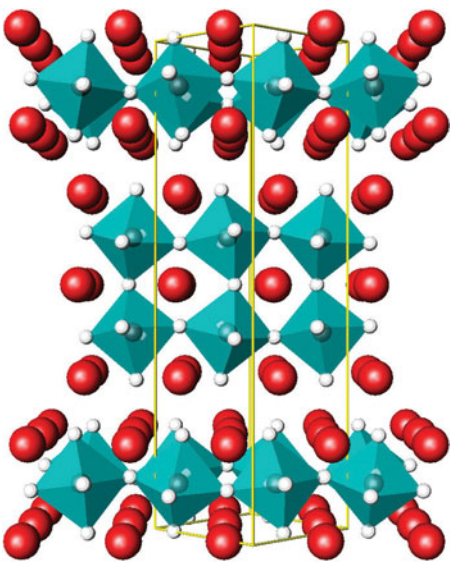

Plate 4

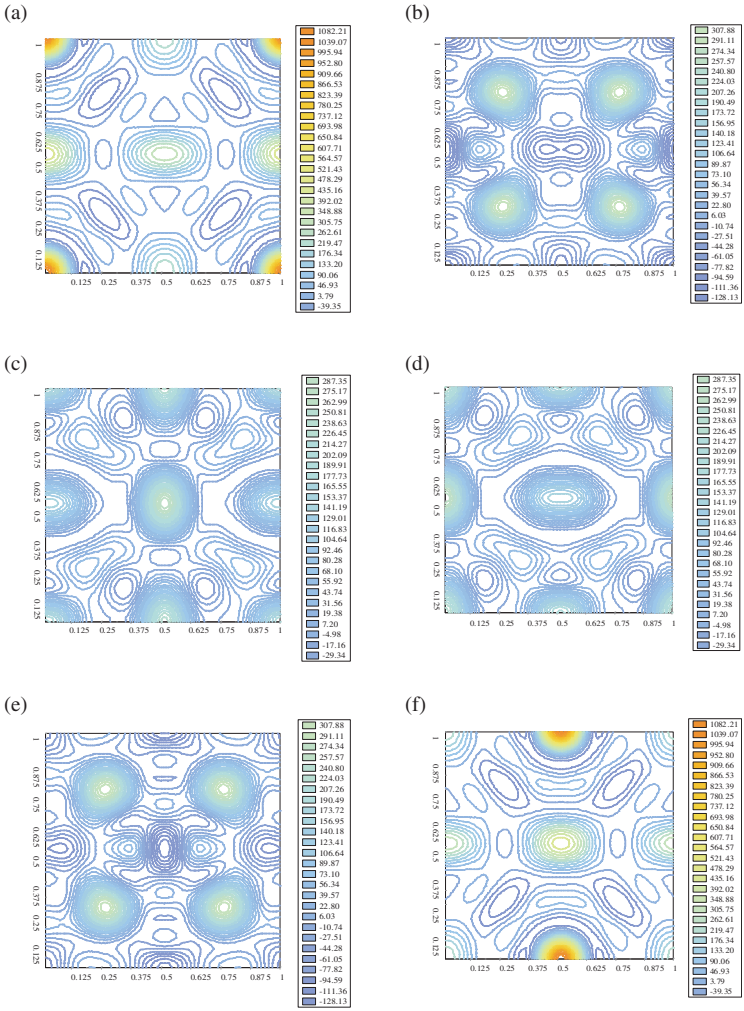
(a)
1082.21
1039.07
995.94
952.80
909.66
866.53
823.39
780.25
737.12
693.98
650.84
607.71
564.57
521.43
478.29
435.16
392.02
348.88
305.75
262.61
219.47
176.34
133.20
90.06
46.93
3.79
-39.35
(b)
307.88
291.11
274.34
257.57
240.80
224.03
207.26
190.49
173.72
156.95
140.18
123.41
106.64
89.87
73.10
56.34
39.57
22.80
6.03
-10.74
-27.51
-44.28
-61.05
-77.82
-94.59
-111.36
-128.13
(c)
287.35
275.17
262.99
250.81
238.63
226.45
214.27
202.09
189.91
177.73
165.55
153.37
141.19
129.01
116.83
104.64
92.46
80.28
68.10
55.92
43.74
31.56
19.38
7.20
-4.98
-17.16
-29.34
(d)
287.35
275.17
262.99
250.81
238.63
226.45
214.27
202.09
189.91
177.73
165.55
153.37
141.19
129.01
116.83
104.64
92.46
80.28
68.10
55.92
43.74
31.56
19.38
7.20
-4.98
-17.16
-29.34
(e)
307.88
291.11
274.34
257.57
240.80
224.03
207.26
190.49
173.72
156.95
140.18
123.41
106.64
89.87
73.10
56.34
39.57
22.80
6.03
-10.74
-27.51
-44.28
-61.05
-77.82
-94.59
-111.36
-128.13
(f)
1082.21
1039.07
995.94
952.80
909.66
866.53
823.39
780.25
737.12
693.98
650.84
607.71
564.57
521.43
478.29
435.16
392.02
348.88
305.75
262.61
219.47
176.34
133.20
90.06
46.93
3.79
-39.35
0.125 0.25 0.375 0.5 0.625 0.75 0.875 1

Plate 5

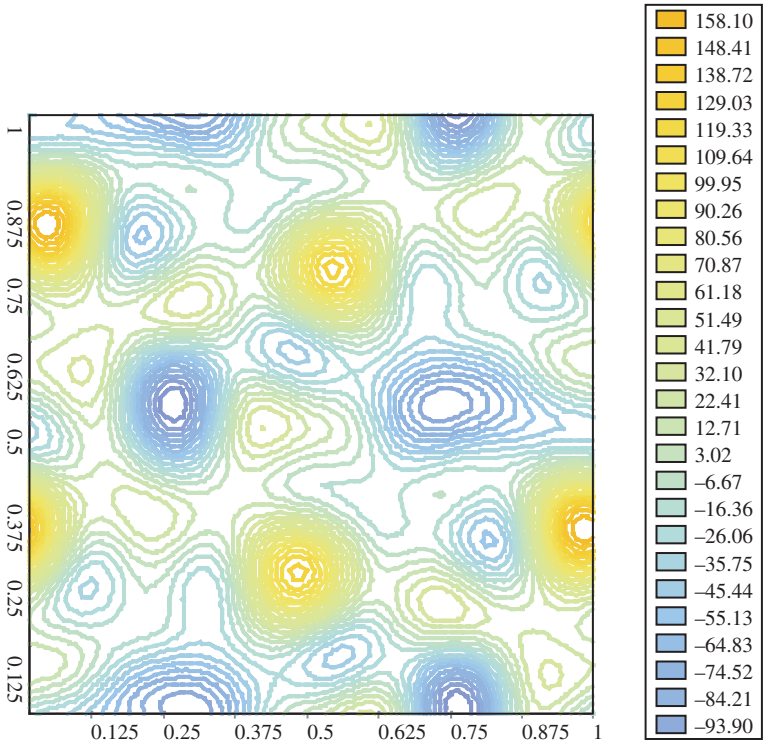

Plate 6

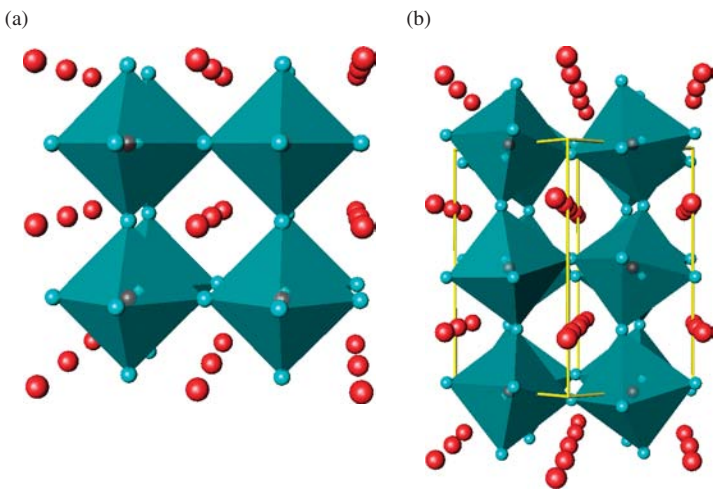

Plate 7

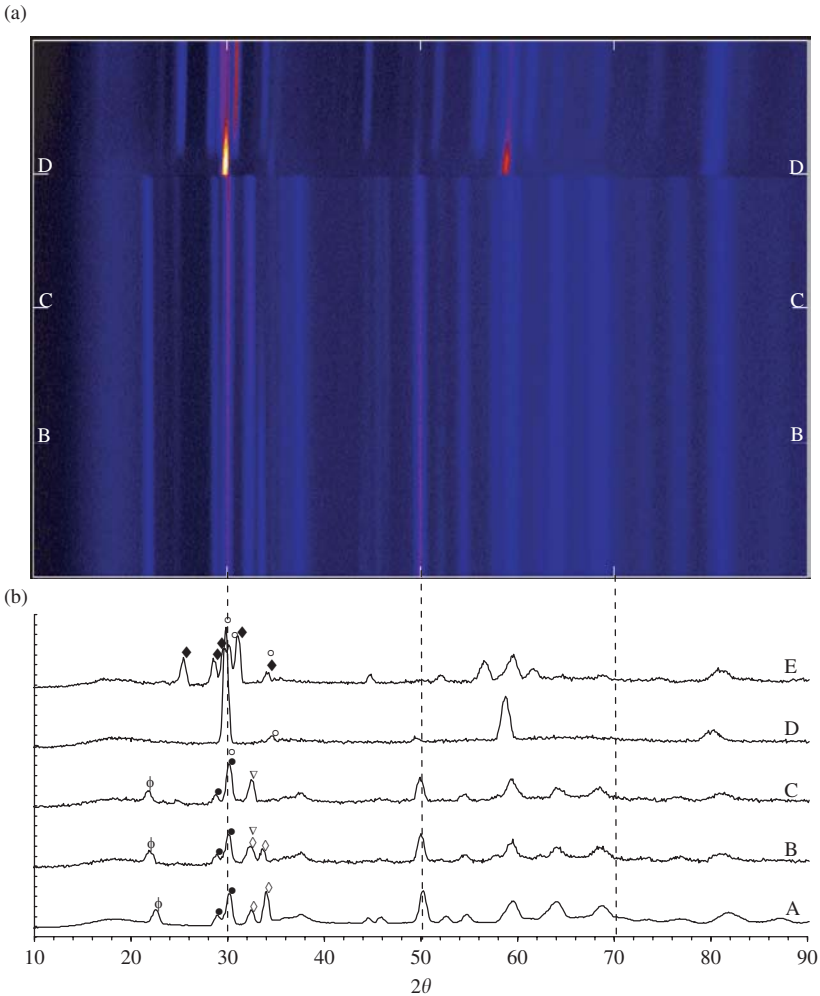

Plate 8

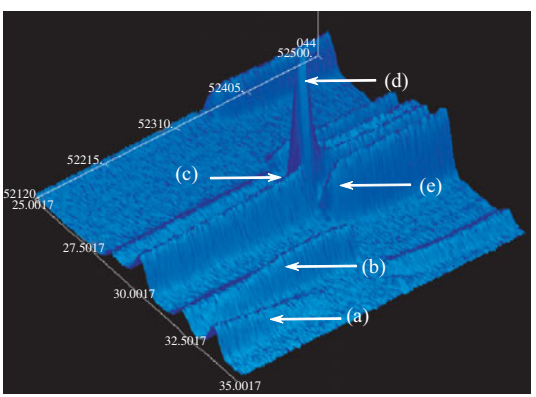

Plate 9